UNIVERSIDADE DE SÃO PAULO
Escola de Engenharia de São Carlos

Advances in Open Source Hydroinformatics for Flood Modeling and Disaster Education

Candidate: Marcus Nóbrega Gomes Júnior
Advisor: Eduardo Mario Mendiondo
Co-Advisor: Marcio Hofheinz Giacomoni

EESC · USP

University of São Paulo
São Carlos School of Engineering

Advances in Open Source Hydroinformatics for Flood Modeling and Disaster Education

Marcus Nóbrega Gomes Júnior

Doctoral dissertation presented at São Carlos School of Engineering, University of Sao Paulo, in partial fulfilment of the requirements for obtaining the Degree of Doctor in Science: Hydraulic Engineering and Sanitation.

Concentration Area: Hydraulics and Sanitation

Advisor: Dr. Eduardo Mario Mendiondo
Co-advisor: Dr. Marcio Hofheinz Giacomoni

Corrected Version
São Carlos
2023

Ficha catalográfica elaborada pela Biblioteca Prof. Dr. Sérgio Rodrigues Fontes da EESC/USP com os dados inseridos pelo(a) autor(a).

Nóbrega Gomes Júnior, Marcus
N633a Advances in open source hydroinformatics for flood modeling and disaster education / Marcus Nóbrega Gomes Júnior; orientador Eduardo Mario Mendiondo; coorientador Marcio Hofheinz Giacomoni. São Carlos, 2023.

Tese (Doutorado) - Programa de Pós-Graduação em Engenharia Hidráulica e Saneamento e Área de Concentração em Hidráulica e Saneamento -- Escola de Engenharia de São Carlos da Universidade de São Paulo, 2023.

1. 1D/2D Flood Modeling. 2. Stormwater Real-time Control. 3. Pollutant Transport and Fate. 4. Spatially-distributed Modeling. 5. Flood Hazard. 6. Dam-Break. 7. Disaster Education. I. Título.

Eduardo Graziosi Silva - CRB - 8/8907

FOLHA DE JULGAMENTO

Candidato: Engenheiro **MARCUS NÓBREGA GOMES JÚNIOR**.

Título da tese: "Avanços em Hidroinformática de Código Aberto para Modelagem de Inundações e Educação em Desastres".

Data da defesa: 27/11/2023.

Comissão Julgadora	Resultado
Prof. Dr. Eduardo Mario Mendiondo (Orientador) (Escola de Engenharia de São Carlos/EESC-USP)	Aprovado
Prof. Dr. Rodrigo Cauduro Dias de Paiva (Universidade Federal do Rio Grande do Sul/UFRGS)	Aprovado
Dr. Ayan Santos Fleischmann (Instituto de Desenvolvimento Sustentável Mamirauá/IDSM)	Aprovado
Prof. Dr. Marco Aurélio Holanda de Castro (Universidade Federal do Ceará/UFC)	Aprovado
Prof. Dr. José Goes Vasconcelos Neto (Auburn University)	Aprovado

Coordenador do Programa de Pós-Graduação em Engenharia Hidráulica e Saneamento:
Prof. Assoc. **Juliano Jose Corbi**

Presidente da Comissão de Pós-Graduação:
Prof. Titular **Carlos De Marqui Junior**

DEDICATION

To those who are trying to see the astonishing beauty and unknown underlying laws of nature that we are constantly seeking and attempting almost naively to comprehend.

ACKNOWLEDGMENTS

These almost 4 years have made me face so many varied, complex, and challenging things that I never thought I would be able to face. The pursuit of a doctorate degree made me a better person, not only through the knowledge that I received but also by the life lessons that this journey taught me. By constantly looking for new challenges, methods, visualization tools or even trying to solve sometimes never solved problems, I think my life will never be the same. The concept of what is something difficult has changed. Pursuing a Ph.D. helped me pursue a better life filled with desire, joy, and willingness to become a better person.

There must be someone somewhere who gave me the strength and put me in the right place and at the right time multiple times. I thank God for that. If you asked me by the time I finished my undergraduate that I would be able to have a Master's degree and eventually two Ph.D.s, I would say that it was impossible. For God, nothing is impossible if you believe in him and have an open mind enough to face the unknown path under his guidance, even if you are scared.

Several important people gave me the tools, strength, and support to cope with such difficult times, especially during the 2020-2022 pandemic. I would like to give a more than special thanks to all the support given by Eudiana Sousa, whom I personally admire and think was fundamental. I have learned a lot from you. I would also like to thank my parents, Edeliar T. Saraiva, and Marcus N. Gomes, my brother Eduardo. T. N. Gomes, and my sister, Ana C. Gomes. Without your support, I would not have been able to.

Without agency funding, this research would be impossible. I greatly appreciate the support received from CNPQ, CAPES, FAPESP, and the San Antonio River Authority to partially fund my research. It is relatively unfair to only thank a couple of friends and colleagues who helped me. Therefore, I thank all PPGSHS and CPG, especially Sá, Rose, Tatiana, and César. I also thank the Wadi Lab, and all friends and colleagues that helped during this process. I had excellent talks with professors from USP and UTSA, also during conferences at AGU, EWRI, and SBRH, or even talks during short courses with outstanding professors that inspired me to believe that we can develop high-level technology in Brazil. However, I need to be specific with some estimated friends and colleagues.

My gratitude is infinite toward my supervisors, Dr. Eduardo M. Mendiondo from USP and Dr. Marcio H. Giacomoni from UTSA. Mario always believed in me without any proof at first. He simply gambled in my potential and showed me that somehow he knew more about me than I at the beginning of my academic career. Sometimes we just need someone to push us forward, someone who trusts us and gives us confidence to try to perform our best work. Besides the academia, Mario is a friend, someone that I have the pleasure to say that I can count on not only for my formal education, but also for life in general. Thank you, Mario.

Another absolutely great example of guidance and supervision is what I had the pleasure of receiving from Dr. Giacomoni. I believe that one of the most important things in my education was the weekly meetings we had for almost 2 years and the weekly state-of-the-art discussion of recent published papers in the top journals. The power of explaining complex concepts in a digestible and meaningful manner, the ability to summarize, to be concise, and to be specific are just a few of the things that I learn from this admirable individual. Marcio is an example of a responsible and hard-working person that I inspire to be similar. I had important conversations with him about my career, my life and my future. Thank you for always giving me the tools, the environment, and the opportunity to grow, Marcio. I also must mention Dr. Ahmad Taha, a professor who sharpened my mathematical and modeling skills to a new level. I believe that taking your doctoral courses in electrical engineering simply changed my view for the better in the field of hydrology and water resources.

I came to UTSA a month before the pandemic, in 2020. A new country, a new language, a

new and way colder environment at the time, a new worldwide never-known pandemic. Dr. Cesar do Lago, Ph.D student at the time, was my old brother that I never had and best friend who helped me so much that I cannot put in words. All the hard-working, the papers, the codes, and also the beers and bottles of wine merged with universe and black hole conversations were certainly a valve to escape all pressure from the time. I also especially thank Jonathan Tran, who was always a wonderful friend and helped me a lot in San Antonio during this time.

Finally, I would like to give special thanks to Luis Castillo. After returning to Brazil in 2022, we had worked almost daily and developed a friendship and camaraderie that will always be appreciated. Thanks also to my other friends and colleagues at Wadi Marcos R. Benso, Fabricio Navarro, Matheus Schorender, Maria de Andrade, Mateo Hernandez. All support is greatly appreciated.

PRESENTATION

This Ph.D. dissertation was carried out within the Graduate Program in Hydraulic Engineering and Sanitation (PPGSHS) at the Sao Carlos School of Engineering (EESC) of the University of Sao Paulo. The supervision was provided by Prof. Eduardo Mario Mendiondo, with co-supervision from Prof. Marcio Hofheinz Giacomoni. Financial support for the research was received through a doctoral scholarship from the Coordination for the Improvement of Higher Education Personnel (CAPES) under process number 88887.663281/2022-00 covering the period from February 2022 to December 2023.
The author of this Ph.D. dissertation pursued a dual-degree Ph.D. and was enrolled at the University of Sao Paulo and at the University of Texas at San Antonio (UTSA) throughout the execution of this Ph.D. dissertation. From January 2020 to December 2021, the author received funding from the city of San Antonio, Texas, through the San Antonio River Authority (SARA) while enrolled in the Ph.D. program in Civil and Environmental Engineering at UTSA, under the supervision of Prof. Marcio Giacomoni. Additionally, support from PROEX (CAPES) through PPGSHS facilitated the author's participation in various events. Included below is a collection of selected journal articles, conference papers, and open-source software derived from partial results of this Ph.D dissertation.

Journal Articles

1. *Chapter - 2:* **M. N. Gomes Jr.**, M. H. Giacomoni, A. F. Taha, and E. M. Mendiondo, Flood risk mitigation and valve control in stormwater systems: State-space modeling, control algorithms, and case studies, *Journal of Water Resources Planning and Management*, vol. 148, no. 12, p. 04022067, 2022. [Online]. Available: 10.1061/(ASCE)WR.1943-5452.0001588.

2. *Chapter - 3:* **M. N. Gomes Jr.**, C. A. F. do Lago, L. M. C. Rápalo, P. T. S. Oliveira, M. H. Giacomoni, and E. M. Mendiondo, HydroPol2D Distributed Hydrodynamic and Water Quality Model: Challenges and Opportunities in Poorly-Gauged Catchments, *Journal of Hydrology*, 2023, DOI: https://doi.org/10.1016/j.jhydrol.2023.129982

3. *Chapter - 4:* **M. N. Gomes Jr.**, M.H. Giacomoni, F.A. Navarro, and E.M. Mendiondo, 2024. Global Optimization-Based Calibration Algorithm for a 2D Distributed Hydrologic-Hydrodynamic and Water Quality Model. *Environmental Modelling and Software* (under review).

4. *Chapter - 5:* **M. N. Gomes Jr.**, J. Vijay, and E.M. Mendiondo, 2024. Exploring the Impact of Rainfall Temporal Distribution and Critical Durations on Flood Hazard Modeling. *International Journal of Disaster Risk Reduction* (under review).

5. *Chapter - 6:* **M. N. Gomes Jr.**, L. M. C. Rápallo, P. T. S. Oliveira, M. H. Giacomoni, C. A. F. do Lago, and E. M. Mendiondo, Modeling unsteady and steady 1-d hydrodynamics under different hydraulic conceptualizations: Model/software development and case studies, *Environmental Modelling and Software*, 2022. DOI: https://doi.org/10.1016/j.envsoft.2023.105733.

6. *Chapter - 7:* **M. N. Gomes Jr.**, M. A. R. A. Castro, P. G. C. da Silva, M.H. Giacomoni, E.M. Mendiondo, 2024. Increasing Flood Awareness Through Dam-Breach Serious Games. *International Journal of Disaster Risk Reduction* (under review).

Conference Papers

1. **M. N. Gomes Jr.**, Giacomoni, M.H., Taha, A.F. and Mendiondo, E.M., 2022, August. Model Predictive Control for Stormwater Reservoirs: Investigating Effects of Climate Change and Urbanization. *IEEE Conference on Control Technology and Applications (CCTA)* (pp. 691-698). IEEE.

2. **M. N. Gomes Jr.**, C. A. F. do Lago, M. H. Giacomoni, E. M. Mendiondo, "Expanding the 2-Dimentional Green-Ampt and Non-linear Reservoir Hydrological Model from SWMM to MATLAB", *AGU Fall Meeting*, 2021.

3. **M. N. Gomes Jr.**, L. M. C. Rápalo, E. M. Mendiondo, A Serious Game for societal risk perception of dam-break flood assessment using a hydrodynamic model, *Latin American Hydraulic Congress*, (2022). *Award of Best Paper*.

4. **M. N. Gomes Jr.**, C. A. F do Lago, M. H. Giacomoni, E. M. Mendiondo, Assessing the role of cross-section shape for flood routing under compound flood events using a hydrodynamic model, *Latin American Hydraulic Congress*, (2022).

5. **M. N. Gomes Jr.**, M. H. Giacomoni, E. M. Mendiondo, A. F. Taha, "Real-Time Control of Stormwater Reservoirs for Flood Risk Mitigation", *The 2nd International Symposium on Water System Operations*, 2021.

6. **M. N. Gomes Jr.**, E. O. Pavan, L. M. C. Rápallo, M. H. Giacomoni, E. M. Mendiondo, "Modelo Hidrodinâmico e de Qualidade da Água Bidirecional (2DCAWQ): Desafios de Modelagem em Bacias com Dados Escassos: Aplicação na Bacia do Tijuco Preto - São Carlos", *XIV Encontro Nacional de Águas Urbanas e IV Simpósio de Revitalização de Rios Urbanos*, 2022 (In Portuguese).

7. **M. N. Gomes Jr.**, M. H. Giacomoni, E. M. Mendiondo, "The role of raster resolution into overland flow and total suspended solids modeling in small urban catchments", *Simpósio Brasileiro de Recursos Hídricos*, (2021).

8. **M. N. Gomes Jr.**, M. H. Giacomoni, A. T. Papagiannakis, "Spatial Assessment of Overland Flow, Pollutant Concentration, and First Flush Using a 2D Non-Point Source Pollution and Hydrological Model for Urban Catchments", *World Environmental and Water Resources Congress*, 2021, 397-413.

Open-Source Software

1. *CHAPTER - 2:* RTC-Stormwater: A coupled model of watersheds, reservoirs, and channels adapted to real-time control, available at:
   https://github.com/marcusnobrega-eng/RTC---Flood-and-Water-Quality.
2. *CHAPTER - 2:* 2D Watershed Model: A simple quasi-2D kinematic wave hydrologic-hydrodynamic model, available at:
   https://github.com/marcusnobrega-eng/2D_Watershed_Model
3. *CHAPTERS - 3, 4, and 5:* HydroPol2D: A catchment 2D hydrologic-hydrodynamic coupled with pollutant transport and fate, available at:
   https://github.com/marcusnobrega-eng/HydroPol2D
4. *CHAPTERS - 6 and 7:* HydroHP-1D: A full momentum hydrodynamic model adapted for various conceptualizations of flow resistance, available at:
   https://github.com/marcusnobrega-eng/HydroHP
5. *CHAPTER - 7:* Dam-Break Module: A guided user interface application for the simulation of 1D dam-break, available at:
   https://github.com/marcusnobrega-eng/Dam_Break_Module.

EPIGRAPH

"I'll tell you what changed my whole life: I finally discovered that it's all risky. The minute you got born it got risky. If you think trying is risky, wait until they hand you the bill for not trying".

Jim Rohn

ABSTRACT

Advances in Open Source Hydroinformatics for Flood Modeling and Disaster Education

Floods are one of the deadliest natural disasters and are affected by increased urbanization and climate change effects. Associated with floods are the pollutant transport and fate, reducing the water quality of rivers. The proper modeling of rainfall into runoff and the carrying of pollutants through overland flow depends on the scale of the time and space discretization of the watershed. To this end, one-dimensional (1D) or two-dimensional (2D) models are usually used to express the hydrodynamics. The objective of this work is to advance hydroinformatics of catchment-scale hydrology and hydrodynamics by the development of new computational tools adapted for flood and water quality problems, especially adapted to perform simulations in poorly gauged catchments although not limited to. By coupling a hydrologic model to a hydrodynamic model, it is possible to investigate effects such as estimating the impacts of unprecedented floods in vulnerable catchments or improving flood awareness through a serious gaming approach. This paper is divided into an introductory chapter 1, six research papers from Chapter 2 to Chapter 7, and the conclusions chapter. Chapter 2 shows an integrated hydrologic-hydrodynamic modeling framework used for real-time-control that accounts for catchment quasi-2D kinematic overland flow, lumped reservoir routing considering controllable orifices and weirs, and 1-D diffusive-like channel. Chapter 3 shows an innovative approach for 2D diffusive-like overland flow modeling (HydroPol2D), accounting for a more complete fully distributed hydrologic model (i.e., Green-Ampt infiltration and non-linear reservoir for stage-discharge overland flow modeling) coupled with evapotranspiration and groundwater recharge modeling. Chapter 4 presents a Global Optimization strategy to perform automatic calibration of HydroPol2D water quantity and quality parameters under single or multi-site, multi-event, observations. Chapter 5 enhances HydroPol2D by including a Human-Instability modeling capacity to estimate not only flood areas, but also risk of dragging due to the flood wave propagation in the 2D mesh grid. HydroPol2D is a 2D fully distributed model suitable for overland flow; therefore, some enhancements would be required to accurately simulate 1D unsteady flow when inertial terms of the shallow water equations are dominant. To this end, Chapters 6 and 7 develop a full momentum 1D solver suitable for regular and irregular cross-sections modeling with overbanks parametrized with different roughness coefficients. Chapter 6 develops the model (HydroHP) and Chapter 7 shows an application of 1D Dam-Break for 20 dams in Brazil, including the Brumadinho Dam. Finally, Chapter 8 shows the conclusions and future steps to continue the development of the models presented in this dissertation.

Keywords: 1D/2D Flood Modeling, Stormwater Real-time Control, Pollutant Transport and Fate, Spatially-distributed Modeling, Flood Hazard, Dam-Break *Disaster education*

RESUMO

Avanços em Hidroinformática de Código Aberto para Modelagem de Inundações e Educação em Desastres

As inundações são uma das catástrofes naturais mais impactantes e são afetadas pelo aumento da urbanização e pelos efeitos das alterações climáticas. Associados às enchentes estão o transporte e o destino dos poluentes, reduzindo a qualidade da água dos rios. A modelagem adequada da conversão de precipitação em escoamento e do transporte de poluentes através do escoamento superficial depende da escala da discretização temporal e espacial da bacia hidrográfica. Para tanto, modelos unidimensionais (1D) ou bidimensionais (2D) são normalmente utilizados para expressar a hidrodinâmica. O objetivo deste trabalho é avançar o campo da hidroinformática da hidrologia e hidrodinâmica em escala de bacia hidrográfica através do desenvolvimento de novas ferramentas computacionais adaptadas para problemas de inundação e qualidade da água, especialmente para o caso de bacias com escassez de dados observados, embora a metodologia proposta é limitada apenas a esses casos. Ao acoplar um modelo hidrológico a um modelo hidrodinâmico, é possível investigar efeitos como estimar os impactos de cheias sem precedentes em bacias hidrográficas vulneráveis ou aumentar a percepção de risco de cheias através de uma abordagem de jogo sério. Este artigo está dividido em um Capítulo introdutório 1, 6 artigos de revista que vão do Capítulo 2 ao Capítulo 7 e o Capítulo de conclusões. O Capítulo 2 mostra uma estrutura integrada de modelagem hidrológica-hidrodinâmica usada para controle em tempo real que leva em conta o escoamento superficial modelado pela onda cinemática, quasi-2D, que deságua em um reservatório com seu escoamento propagado considerando orifícios e vertedores controláveis. O reservatório deságua em um canal modelado pelo modelo da onda difusa, 1D. O Capítulo 3 mostra uma abordagem inovadora para modelagem 2D de escoamento superficial por onda difusa (HydroPol2D), representando um modelo hidrológico totalmente distribuído mais completo (ou seja, infiltração pelo método de Green-Ampt e propagação do escoamento pelo reservatório não linear para conversão de lâmina em vazão) juntamente com evapotranspiração e modelagem de recarga de águas subterrâneas. O Capítulo 4 apresenta uma estratégia de Otimização Global para realizar a calibração automática dos parâmetros de quantidade e qualidade da água HydroPol2D com observações de vários eventos, em um ou vários locais. O Capítulo 5 aprimora o HydroPol2D ao incluir uma capacidade de modelagem de instabilidade humana para estimar não apenas áreas de inundação, mas também o risco de arrasto devido à propagação das ondas de inundação na grade de malha 2D. HydroPol2D é um modelo 2D totalmente distribuído adequado para escoamento superficial; portanto, algumas melhorias seriam necessárias para simular com precisão o fluxo instável 1D quando os termos inerciais das equações de águas rasas são dominantes. Com essa finalidade, os Capítulos 6 e 7 desenvolvem uma solução do escoamento 1D considerando as equações completas de Saint-Venant, tornando-se adequado para modelagem de seções transversais regulares e irregulares com margens parametrizadas com diferentes coeficientes de rugosidade. O Capítulo 6 desenvolve o modelo (HydroHP) e o Capítulo 7 apresenta uma aplicação do problema de Dam-Break 1D para 21 barragens no Brasil, incluindo a Barragem de Brumadinho. Por fim, o Capítulo 8 mostra as conclusões e passos futuros para continuar o desenvolvimento dos modelos apresentados nesta tese de doutorado.

Palavras-chave: 1D/2D Modelagem de Inundações, Controle em Tempo Real de Sistemas Pluviais, Modelagem Espacialmente Distribuída, Perigo de Inundações, Rompimento de Barragens, *Educação em desastres*

LIST OF FIGURES

LIST OF TABLES

LIST OF CONTENTS

1 GENERAL INTRODUCTION

The increasing access to non-expensive sensors, computing power, and more accurate forecasting of storm events provides unique opportunities to shift flood management practices from static approaches to an optimization-based real-time control (RTC) of urban drainage systems. Recent studies have addressed a plethora of strategies for flood control in stormwater reservoirs; however, advanced control theoretic techniques have not yet been fully investigated and applied to these systems. In addition, there is an absence of a coupled integrated control model for systems composed of watersheds, reservoirs, and channels for flood mitigation. To this end, we develop a novel non-linear state-space model of hydrologic and hydrodynamic processes in watersheds, reservoirs, and one-dimensional channels. The model is tested under different types of reservoir control strategies based on real-time measurements (reactive control), and based on predictions of the future behavior of the system (predictive control) using rainfall forecasting. We apply the modeling approach to a system composed of a single watershed, a reservoir, and a channel connected in series, respectively, for the San Antonio observed rainfall data. Results indicate that for flood mitigation, the predictive control strategy outperforms the reactive controls not only when applied for synthetic design storm events, but also for a continuous simulation. Moreover, the predictive control strategy requires smaller valve operations, while still guaranteeing efficient hydrological performance. From the results, we recommend the use of the non-linear model predictive control strategy to control stormwater systems due to the ability to handle different objective functions, which can be altered according to rainfall forecasting and shift the reservoir operation from flood-based control to strategies focused on increasing detention times, depending on the forecasting.

Flood damage is expected to increase in the future due to climate change and the unplanned urbanization process that leads to new land developments in susceptible flood areas, increasing the population's exposure to flood risks (Johnson et al., 2020). Strategies to mitigate these damages vary from increasing urban drainage control measures such as stormwater reservoirs (Che e Mays, 2015), improving control of existing stormwater facilities by implementing real-time control strategies (Wang et al., 2018; Sharior et al., 2019a), and avoiding development in floodplains (Johnson et al., 2020). Water resources planning and management usually require capable models to simulate complex phenomena as flood routing in two-dimensional (2D) floodplains, sediment transport and fate, as well as the modeling of pollutant dynamics under storm events. The development and validation of these models require extensive computational tests and applications in synthetic and real-world cases (Guidolin et al., 2016; Downer e Ogden, 2004; Panday e Huyakorn, 2004b), especially when applied to real-time control.

In the following sections of this chapter, we provide a brief description of some main concepts developed and applied in the remainder of this dissertation.

1.1 Real-Time Control Models

The increasing access to non-expensive sensors, computing power, and more accurate forecasting of rain storm events provides unique opportunities to shift flood management practices from static approaches to optimization-based real-time control (RTC) of urban drainage systems. Stormwater facilities can potentially increase their efficiency by deploying Real-Time control strategies. These strategies can vary from ruled-based or predictive-based approaches, where actions could be taken according to pre-defined rules or in terms of predictions on how the controlled system would behave in the future. Moreover, the way hydrological devices (e.g., reservoirs, channels) are controlled could be derived from optimization-based controls. In this case, a proper hydrologic model capturing the main

dynamics of the hydrologic system is required and used in optimization problems. An example of a predictive and optimization-based algorithm for Real-Time control is the Model Predictive Controllers, where several optimization problems are solved in Real-Time defining an optimal control schedule over time.

1.2 Hydrologic and Hydrodynamic Models

Hydrologic models can be classified into (a) lumped-parameter models, (b) semi-distributed models and (c) fully-distributed models. The differences are primarily related to how the hydrologic system of equations is conceptualized. Lumped models often referred to the so-called conceptual models, for instance, do not track spatial distribution of states such as flows and water surface depths and are generally used for designing purposes or when the lack of data makes the use of more complete models impossible. Lumped models are often used with synthetic storm events, or, when used as conceptual models, can be adapted to simulate long-term water balances. They generally require fewer parameters compared to distributed models and are relatively simpler and faster. Semi-distributed models solve the hydrology and sometimes a hydrodynamic problem by assuming hydrologic units (i.e., spatial entities where parameters are space-invariant), often considered as sub-catchments but not limited to. Each individual sub-catchment can be modeled through a lumped model. The flow is propagated through all subcatchments and then routed in channels using channel routing methods, ultimately reaching reservoirs and water receptor systems.

Fully distributed models, however, are typically defined by a series of interactions between individual hydrology units connected by topological relationships. Software packages such as Stormwater Management Model (SWMM) (Rossman et al., 2010) and the Hydrologic Engineering Center - Hydrologic Modeling System (HEC-HMS) (Feldman, 2000) are examples of semi-distributed models, and software as the Gridded Surface and Subsurface Hydrologic Analysis (GSSA) (Downer e Ogden, 2004), and the Hydrologic Engineering Center River Analysis System (HEC-RAS) (Brunner, 2002) are fully distributed for 2-dimensional (2D) floodplain routing studies.

Depending on the desired level of accuracy in modeling flood depths, flows, or stages, different models are applicable, considering time and space resolution. The choice between one-dimensional (1D) or two-dimensional (2D) models depends on how the flow is confined in the floodplain, allowing representation of the 3D Navier-Stokes Equations in Shallow Water Equations (SWE). In inundation studies, high-resolution elevation data, land-use coverage, and rainfall data are typically essential. Software packages with 2D solvers of SWE, such as HEC-RAS, Infoworks, and MIKE 21, are generally well-suited for 2D floodplain analysis. Hydrodynamic models find application in various scenarios, including estimating discharges and stages in open channels under steady or unsteady flow, simulating dam breaks, real-time control of stormwater facilities, and spatial assessment of flood hazards through flood propagation.

1.3 Water Quality Models

Estimating the dynamics of pollutants transport and fate is complex and generally requires hydrologic-hydraulic models to estimate flow velocities, water surface depths, and shear stresses. Recently, software such as GSSHA (Downer e Ogden, 2004), Soil & Water Assessment Tool (SWAT) (Arnold et al., 2012) and the Water Quality Analysis Simulation Program (Shabani et al., 2021) addressed the water quality problem of the advective and diffusion processes. SWMM, on the other hand, assumes a simplified problem considering the build-up and wash-off approach, where coefficients are

fitted to represent pollutant accumulation and washing over time (Rossman e Huber, 2016; Deletic, 1998).

1.4 Numerical Schemes

The flow and water quality dynamics can be solved with different discrete numerical schemes, although can be solved analytically for only highly limited cases (Maxwell et al., 2014a; Panday e Huyakorn, 2004b). The selection between one method or another depends on the degree of stability, accuracy, and computational time required for a given problem.

Explicit solutions, often written as a finite-difference forward Euler scheme (Hindmarsh et al., 1984), are unconditionally unstable and require that spatial and time resolution satisfy stability criteria to guarantee convergence. This scheme generally requires finer mesh-grids and solutions from a given time-step $(t + \Delta t)$ only depend on known values from time (t). This is particularly important, since parallelization and GPU processing in a graphics card can be applied to solve problems with this property (Guidolin et al., 2016).

Implicit schemes, however, can provide unconditionally stability, independent of the mesh-grid properties since solutions from a given time (t) can be implicitly written depending on the values of the past $(t - \Delta t)$ or future $(t + \Delta t)$, as well as the actual time step (t) (Brunner, 2002). In this case, there are more unknowns than equations, and numerical solvers (e.g., Newton-Raphson) are required. Although more computational resources seem necessary for implicit methods, it allows using larger time-steps compared to explicit schemes, ultimately leading to faster computations for single core processing.

1.5 Research Need

There are not enough tools to simulate the hydrologic and hydrodynamic behavior of stormwater systems such as reservoirs and channels, especially adapted for catchments where data is scarce. Assessing the performance of stormwater systems for flood and pollution control requires stable, accurate, and computationally efficient mathematical models. In addition to being used as a tool to simulate the hydrological and hydrodynamic response of stormwater systems, these models can be used for other purposes such as learning, teaching, and increasing flood awareness through serious games.

1.6 Research Objectives

The main goal of this doctoral dissertation is to develop computationally efficient novel mathematical models to represent flood routing and water quality transport that can be used for designing, planning, being used for real-time control of stormwater facilities and ultimately being adapted for learning and teaching through the adaptation of serious games. To accomplish this research goal, the following specific research objectives are proposed:

- **Research Objective 1**: Develop an integrated fully-distributed kinematic-wave watershed model coupled with Green-Ampt infiltration modeling, connected to a reservoir modeled as a storage node with controllable orifices that releases water to a downstream channel. The real-time control model developed in this objective automatically defines the valve opening in the reservoir to minimize inundation in the downstream channel. Therefore, more specifically, this research objective has the goal of investigating the benefits of retrofitting stormwater facilities with real-time control capabilities that control runoff.

- **Research Objective 2**: Investigate the performance of a developed diffusive-like 2D fully distributed water quantity and quality model that accounts for spatially varied rainfall, infiltration, flood routing, and water quality routing. By performance herein is understood the performance in terms of accurately predicting the hydrodynamic and pollutant states as well as the computational performance.

- **Research Objective 3**: Develop a full momentum, GPU-Based, hydrodynamic model to simulate complex dam-break and channel routing problems adapted for complex cross-sections.

These research objectives are explored from Chapter 2 to 8. More specifically, Research Objective 1 is explored in Chap. 2, while Research Objective 2 is explored in Chapters 2 to 5, while Chapters 6 to 7 explore Research Objective 3.

1.7 Scientific Gaps and Fundamental Contributions

1.7.1 Real-Time Control of Stormwater Systems - Research Objective 1

Although SWMM or the Gridded Surface Subsurface Soil Analysis (GSSHA) are capable of solving the usually complex shallow water equations, their use in optimization for large systems can be intractable for real-time control and a simplified plant model of the flow dynamical model is needed (Lund et al., 2018). Moreover, exploring the impacts of water quality controls on flood control performance is not yet investigated in the literature. In this study, these issues are addressed and the trade-offs between various control strategies with regard to flood mitigation are explored.

To this end, we develop a novel state-space representation of the main processes of the water cycle related to urban catchments (i.e., infiltration, overland flow, reservoir storage, channel routing), using cells, reservoirs, sub-reaches of channels connected as networked dynamical systems. This state-space model is based on the energy, continuity, and momentum equations. We approach the non-linearities of the flow dynamics by performing successive linearizations in each time-step of the model using data from previous time-steps as operational points. Although we are able to linearize most of the system's equations, we are unable to do it for the rainfall intensity because of the absence of differentiable models for that. Therefore, we assume a known rainfall input time-series in the model, and we model the watershed as a non-linear dynamical system.

In addition to the development of the novel state-space model, we want to assess how varied valve control strategies behave in the system. To this end, we develop a model predictive controller (MPC) algorithm to improve valve operation in stormwater reservoirs, minimizing a composed cost function related to flood performance. Moreover, we compare the efficiency of reactive controls (i.e., controls based on real-time measurements of the states) with MPC solved with a gradient-based method (Interior-Point).

The fundamental contributions of this paper are described below:

- We present an overall mathematical representation including the flow dynamics in watersheds using the non-linear reservoir, and the Green-Ampt infiltration model (Green e Ampt, 1911), coupled with reservoir routing and 1-D channel dynamics in a non-linear state-space representation. It allows optimization and real-time control of urban drainage systems without requiring extensive software packages (i.e., only MATLAB is required).

- We derive the non-linear dynamics of watersheds, and linearize the dynamics of reservoirs and channels. Since no continuous and differentiable model is currently available for rainfall intensity, we assume a known time series of rainfall as a piecewise continuous input data.

- We provide a comprehensive analysis of reactive controls (i.e., some ruled-based and other optimally controlled) for flood mitigation and tested the efficiency of water quality ruled-based algorithms presented in Sharior et al. (2019a) for flood mitigation.

- We develop and apply a servo-control algorithm (Young e Willems, 1972) used in the discrete linear quadratic integrator (DLQI) reactive control. This is a new application for this control technology in urban drainage systems. This algorithm allows tracking a specific state and can be used in reservoirs with specified minimum water surface depths (e.g., wetlands or retention ponds).

- We evaluate and discuss the performance of reactive RBCs (passive, on/off, detention control) and reactive optimization-based controls (discrete linear quadratic regulator and discrete linear quadratic integrator) compared to the predictive control strategy. In addition, we explore the caveats of consecutive design storms and also compared the flood performance of reactive and predictive algorithms in a continuous simulation, providing a methodology to assess the efficiency of control algorithms for flood mitigation.

1.7.2 2-D Diffusive-Like Hydrologic and Hydrodynamic Model - Research Objective 2

Despite some of the models are capable of estimating the several components of hydrologic processes, such as groundwater recharge or flood routing, there is still a lack of models to perform a fully distributed water quality modeling applicable not only for rural catchments, but especially for urban areas (Downer e Ogden, 2004; Arnold et al., 2012; Rossman et al., 2010).

On the one hand, the Gridded Surface Subsurface Hydrological Analysis (GSSHA) model, for example, is limited to a 10-m grid resolution and despite some applications for water quality being performed in recent literature, it has not been extensively applied for water quality and sediment transport (Johnson e Gerald, 2006). This resolution can play an important role and can be considerably coarse to model, for instance, green infrastructure (GI) inflows and incoming pollutant mass for highly sensitive pollutants.

On the other hand, the Storm Water Management Model (SWMM), even though some studies have successfully calibrated and validated the model for water quantity and quality (Di Modugno et al., 2015; Piro e Carbone, 2014), fails to represent time spatial distribution of pollutants by considering a semi-distributed water quality model in a network of connected sub-catchments. Therefore, we overcome it by developing a fully distributed hydrologic-hydraulic model to estimate water flood depths and wash-off mass in space and time, considering known watershed boundary conditions. Moreover, using an explicit matrixwise numerical scheme, we allow model parallelization and processing in GPUs.

Most studies in pollutant dispersion and transportation address pollution generated by the agricultural sector that discharges nitrogen and phosphorus to water bodies (Ferrant et al., 2011; Johnson e Gerald, 2006; Whitehead et al., 2011). For urbanized catchments, however, total suspended solids (TSS) is considered a comprehensive metric that represents the global state of pollution in stormwater runoff (Di Modugno et al., 2015; Han et al., 2006), although only a few studies assess their spatial distribution (Al Ali et al., 2018). Enhancing the understanding and modeling of 2-D overland flows and pollutants distribution in a urban catchment is important for the following reasons: (1) spatial flood risk assessment, (2) spatial comprehensive assessment of first flush, and hence enhancing of waste water treatment plants (WWTP) design or Low Impact Development (LID) allocation.

The fundamental contributions derived from this research objective are described below:

- A 2-D hydrologic, hydrodynamic, and water quality model based on non-linear reservoir model, Green-Ampt model, coupled with buildup and washoff water quality approach is developed

- An automatic calibration algorithm using genetic algorithms in a single objective optimization problem is developed to estimate infiltration, roughness, and abstraction parameters based on multi-site, multi-event runoff observations.
- The model can be used for a comprehensive first flush analysis, identifying critical areas prone to pollutant accumulation.
- We expand the weighted cellular automata model (Guidolin et al., 2016) to account for 5 different land use and land cover types, including different roughness and Green-Ampt parameters, and we allow the simulation of spatially-varied rainfall and evapotranspiration.
- Water quality modeling through a fully distributed 2D model is included, accounting for exponential equations for build-up accumulation, and rating curve for wash-off.
- Two adaptive time step calculations are implemented, one based on the Courant Number (Chang e Wang, 2002) and the other based on stability criteria for raster hydrological models (Hunter et al., 2005).
- The performance of a fully distributed model is contrasted with software as GSSHA, SWMM, and HEC-RAS
- We expand the model (Gomes Jr. et al., 2021b) into a fully matrixwise representation considering a time-varying domain scheme, which can be used for CPU or GPU processing in an optimized fashion in terms of memory allocation.

1.7.3 1-D Full Momentum Hydrodynamic Model and Dam-Break Simulation - Research Objective 3

Full momentum hydrodynamic models account for important hydrodynamic factors that diffusive-like models neglect, especially under rapid changes in topography, flow acceleration, dam-breaks, or when very mild or event-absence slopes occur in the domain. Although these factors might be irrelevant for large-scale or coarse-resolution hydrodynamic simulations, for catastrophic events such as a dam-break, a model capable of considering these features is necessary. Several models account for these dynamic features; however, they may require a substantial number of parameters and data, sometimes making their application complex and user-interface. We attempt to provide a mathematical accurate model that solves the dynamic wave equations explicitly, in parallelizable fashion, but with a simple interface and with the flexibility of allowing the simulation of rectangular, asymmetric trapezoidal, circular, hyperbolical, or even irregular cross-section. In addition, the developed framework is also flexible enough to simulate space- and depth-varying roughness coefficients calculated for different formulae. While the advances in hydrodynamic modeling are evident and the modeling framework is flexible (i.e., input data from Excel sheets and model fully open source in Matlab), we also provide a dam-break application with a guided-user interface to allow the spread use of a relatively complete and complex manner but in a simple and ludic way. This model is adapted to be used for a serious gaming approach due to these characteristics.

The fundamental contributions of this research are described as follows:

- We develop novel generalized algorithms to determine the hydraulic properties (HP) for regular and irregular cross-sections.
- We assess the uncertainty in modeled-based rating curve estimations.
- We assess the role of Manning's roughness coefficient in conveyance estimation.

- We develop a modified Single-Channel-Method (SCM) equivalent to the Divided-Channel-Method (DCM) model coupled with additional shear stress at the interface within the overbanks and the main channel.
- We develop a method for estimating dynamic rating curves using a full-momentum hydraulic model.
- We compare the dynamical rating curve estimations with the normal flow rating curve estimations.
- We develop a serious game with guided used interfaces (GUI) to solve the 1-D dam breach problem.
- We allow two versions of the game: one with the GUI and another, more flexible, with the open source code and with input data derived from Excel spreadsheets.
- We solve the full momentum 1-D Saint-Venant Equations by simplifying the data entry to the minimum as possible; although still maintaining the physical meaning of the simulations for the GUI version. For the complete version, users can use several different types of cross-sections, including irregular cross-sections (Gomes Jr et al., 2023a).
- We create a framework that is in the state-of-the-art in the mathematically modeling of the hydrodynamics but can be adapted to require only simple input data that could be derived by students in a class of Hydraulics or Geographical Information Systems, for example. Therefore, the methods and results of this paper can be used in a serious gaming approach to increase the perception of flood impacts induced by dam-break events.

1.8 Modeling Input Data and Capabilities

In this section, we briefly introduce some of the modeling capabilities of the following models: RTC-Stormwater (Cap. 2), HydroPol2D (Cap. 3-5), and HydroHP-1D (Cap. 6-7). These models are developed and described in the following chapters. The summary of each input and capability of the models is presented in the Tab. 1.1 and Tab. 1.2. A few of the definitions in this table are also elucidated in the following chapters.

References

Al Ali, S., Rodriguez, F., Bonhomme, C., e Chebbo, G. (2018). Accounting for the spatio-temporal variability of pollutant processes in stormwater tss modeling based on stochastic approaches. *Water*, 10(12):1773.

Arnold, J. G., Moriasi, D. N., Gassman, P. W., Abbaspour, K. C., White, M. J., Srinivasan, R., Santhi, C., Harmel, R., Van Griensven, A., Van Liew, M. W., et al. (2012). Swat: Model use, calibration, and validation. *Transactions of the ASABE*, 55(4):1491–1508.

Brunner, G. W. (2002). Hec-ras (river analysis system). In *North American Water and Environment Congress & Destructive Water*, pages 3782–3787. ASCE.

Chang, S. e Wang, X. (2002). Courant number insensitive ce/se euler scheme. In *38th AIAA/ASME/SAE/ASEE Joint Propulsion Conference & Exhibit*, page 3890.

Che, D. e Mays, L. W. (2015). Development of an optimization/simulation model for real-time flood-control operation of river-reservoirs systems. *Water Resources Management*, 29(11):3987–4005.

Deletic, A. (1998). The first flush load of urban surface runoff. *Water research*, 32(8):2462–2470.

Input Data	RTC-Stormwater	HydroPol2D	HydroHP-1D
DEM Raster	X	X	
LULC Raster	X	X	
SOIL Raster	X	X	
LULC-Based Hydrodynamic Parameters	X	X	
SOIL-Based Hydrological Parameters	X	X	
Outlet Boundary Conditions	X	X	X
Internal Boundary Conditions	X	X	X
Rainfall Boundary Conditions	X	X	
Inflow Boundary Conditions	X	X	X
Stage-Hydrograph Boundary Conditions	X	X	X
Reservoir stage-area data	X		X
Reservoir porosity	X		
Reservoir outlet hydraulic parameters	X		
Channel section-by-section roughness coefficient	X		
Channel section-by-section width	X		
Channel section-by-section elevation	X		
Build-up and Washoff Parameters		X	
Adaptive Time-Stepping Parameters	X	X	X
Cellular Automata Parameters			X
Cross-Section Data			X
Slope Profile			X

Table 1.1. Overall input data required to run RTC-Stormwater (Chapter 2), HydroPol2D (Chapters 3 - 5), and HydroHP-1D (Chapters. 6-7)
. DEM = Digital Elevation Model, LULC = Land Use and Land Cover Model.

Model Capabilities	Stormwater-RTC	HydroPol2D	HydroHP
Spatial Rainfall Modeling	X	X	
Synthetic Rainfall Modeling		X	
Persiann Rainfall Modeling		X	
Evapotranspiration Modeling	X	X	
Groundwater Replenishing Modeling	X	X	
Reservoir Modeling	X		
Channel Modeling	X		X
Full Momentum 1D Channel Modeling			X
Diffusive-wave 1D Channel Modeling	X		
GPU Processing		X	
Human-Instability Modeling		X	
Adapted to Real-Time Control	X	X	X
Adapted to Simulate Green-Infrastructure	X	X	
Adapted to Simulate Dam-Break			X
Transient Flow Modeling		X	X
Kinematic Wave Modeling	X		
Diffusive-Wave Modeling		X	
Dynamic-Wave Modeling			X
Evapotranspiration Modeling	X	X	
Dam-Break Capabilities		X	X
Gradually-Variable Flows		X	X
Highly-Variable Flows			X
Groundwater Replenishment	X	X	
.CSV files with numerical simulation results	X	X	X
.MP4 and GIFs of the simulation results	X	X	X
Rasters of the states simulated	X	X	
Open-Source Code	X	X	X

Table 1.2. Overall modeling capabilities of RTC-Stormwater (Chapter 2), HydroPol2D (Chapters 3 - 5), and HydroHP-1D (Chapters 6-7)

Di Modugno, M., Gioia, A., Gorgoglione, A., Iacobellis, V., La Forgia, G., Piccinni, A. F., e Ranieri, E. (2015). Build-up/wash-off monitoring and assessment for sustainable management of first flush in an urban area. *Sustainability*, 7(5):5050–5070.

Downer, C. W. e Ogden, F. L. (2004). Gssha: Model to simulate diverse stream flow producing processes. *Journal of Hydrologic Engineering*, 9(3):161–174.

Feldman, A. D. (2000). *Hydrologic modeling system HEC-HMS: technical reference manual*. US Army Corps of Engineers, Hydrologic Engineering Center.

Ferrant, S., Oehler, F., Durand, P., Ruiz, L., Salmon-Monviola, J., Justes, E., Dugast, P., Probst, A., Probst, J.-L., e Sanchez-Perez, J.-M. (2011). Understanding nitrogen transfer dynamics in a small agricultural catchment: Comparison of a distributed (tnt2) and a semi distributed (swat) modeling approaches. *Journal of Hydrology*, 406(1-2):1–15.

Gomes Jr, M. N., Giacomoni, M. H., de Macedo, M. B., do Lago, C. A. F., Brasil, J. A. T., de Oliveira, T. R. P., e Mendiondo, E. M. (2023a). A modeling framework for bioretention analysis: Assessing the hydrologic performance under system uncertainty. *Journal of Hydrologic Engineering*, 28(9):04023025.

Gomes Jr., M. N., Giacomoni, M. H., Papagiannakis, A. T., Mendiondo, E. M., e Dornelles, F. (2021b). Spatial Assessment of Overland Flow, Pollutant Concentration, and First Flush Using a 2- D Non-Point Source Pollution and Hydrological Model for Urban Catchments. In *World Environmental and Water Resources Congress 2021: Planning a Resilient Future along America's Freshwaters - Selected Papers from the World Environmental and Water Resources Congress 2021*, pages 397–413.

Green, W. H. e Ampt, G. A. (1911). Studies on soil phyics. *The Journal of Agricultural Science*, 4(1):1–24.

Guidolin, M., Chen, A. S., Ghimire, B., Keedwell, E. C., Djordjević, S., e Savić, D. A. (2016). A weighted cellular automata 2d inundation model for rapid flood analysis. *Environmental Modelling & Software*, 84:378–394.

Han, Y., Lau, S., Kayhanian, M., e Stenstrom, M. K. (2006). Correlation analysis among highway stormwater pollutants and characteristics. *Water Science and Technology*, 53(2):235–243.

Hindmarsh, A., Gresho, P., e Griffiths, D. (1984). The stability of explicit euler time-integration for certain finite difference approximations of the multi-dimensional advection–diffusion equation. *International journal for numerical methods in fluids*, 4(9):853–897.

Hunter, N. M., Horritt, M. S., Bates, P. D., Wilson, M. D., e Werner, M. G. (2005). An adaptive time step solution for raster-based storage cell modelling of floodplain inundation. *Advances in water resources*, 28(9):975–991.

Johnson, B. E. e Gerald, T. K. (2006). Development of nutrient submodules for use in the gridded surface subsurface hydrologic analysis (gssha) distributed watershed model1. *JAWRA Journal of the American Water Resources Association*, 42(6):1503–1525.

Johnson, K. A., Wing, O. E., Bates, P. D., Fargione, J., Kroeger, T., Larson, W. D., Sampson, C. C., e Smith, A. M. (2020). A benefit–cost analysis of floodplain land acquisition for us flood damage reduction. *Nature Sustainability*, 3(1):56–62.

Lund, N. S. V., Falk, A. K. V., Borup, M., Madsen, H., e Steen Mikkelsen, P. (2018). Model predictive control of urban drainage systems: A review and perspective towards smart real-time water management. *Critical Reviews in Environmental Science and Technology*, 48(3):279–339.

Maxwell, R. M., Putti, M., Meyerhoff, S., Delfs, J.-O., Ferguson, I. M., Ivanov, V., Kim, J., Kolditz, O., Kollet, S. J., Kumar, M., et al. (2014a). Surface-subsurface model intercomparison: A first set of benchmark results to diagnose integrated hydrology and feedbacks. *Water resources research*, 50(2):1531–1549.

Panday, S. e Huyakorn, P. S. (2004b). A fully coupled physically-based spatially-distributed model for evaluating surface/subsurface flow. *Advances in water Resources*, 27(4):361–382.

Piro, P. e Carbone, M. (2014). A modelling approach to assessing variations of total suspended solids (tss) mass fluxes during storm events. *Hydrological Processes*, 28(4):2419–2426.

Rossman, L. e Huber, W. (2016). Storm water management model reference manual. *Volume II–Hydraulics, Tech. Rep. EPA/600/R-17/111, US EPA Office of Research and Development, Water Systems Division, avaialable at: https://nepis. epa. gov/Exe/ZyPDF. cgi*.

Rossman, L. A. et al. (2010). *Storm water management model user's manual, version 5.0*. National Risk Management Research Laboratory, Office of Research and Development, U.S. Environmental Protection Agency.

Shabani, A., Woznicki, S. A., Mehaffey, M., Butcher, J., Wool, T. A., e Whung, P.-Y. (2021). A coupled hydrodynamic (hec-ras 2d) and water quality model (wasp) for simulating flood-induced soil, sediment, and contaminant transport. *Journal of Flood Risk Management*, 14(4):e12747.

Sharior, S., McDonald, W., e Parolari, A. J. (2019a). Improved reliability of stormwater detention basin performance through water quality data-informed real-time control. *Journal of Hydrology*, 573:422–431.

Wang, Y., Chen, A. S., Fu, G., Djordjević, S., Zhang, C., e Savić, D. A. (2018). An integrated framework for high-resolution urban flood modelling considering multiple information sources and urban features. *Environmental modelling & software*, 107:85–95.

Whitehead, P., Jin, L., Baulch, H., Butterfield, D., Oni, S., Dillon, P., Futter, M., Wade, A., North, R., O'Connor, E., et al. (2011). Modelling phosphorus dynamics in multi-branch river systems: A study of the black river, lake simcoe, ontario, canada. *Science of the Total environment*, 412:315–323.

Young, P. C. e Willems, J. (1972). An approach to the linear multivariable servomechanism problem. *International journal of control*, 15(5):961–979.

2 FLOOD RISK MITIGATION AND VALVE CONTROL IN STORMWATER SYSTEMS: STATE-SPACE MODELING, CONTROL ALGORITHMS, AND CASE STUDIES

A modified version was published as: Gomes Júnior, M.N., Giacomoni, M.H., Taha, A.F. and Mendiondo, E.M., 2022. Flood risk mitigation and valve control in stormwater systems: State-space modeling, control algorithms, and case studies. *Journal of Water Resources Planning and Management*, 148(12), p.04022067.

Abstract

The increasing access to non expensive sensors, computing power, and more accurate forecasting of storm events provides unique opportunities to shift flood management practices from static approaches to an optimization-based real-time control (RTC) of urban drainage systems. The recent studies have addressed a plethora of strategies for flood control in stormwater reservoirs; however, advanced control theoretic techniques are not yet fully investigated and applied to these systems. In addition, there is an absence of a coupled integrated control model for systems composed of watersheds, reservoirs, and channels for flood mitigation. To this end, we develop a novel nonlinear state-space model of hydrologic and hydrodynamic processes in watersheds, reservoirs, and one-dimensional channels. The model is tested under different types of reservoir control strategies based on real-time measurements (reactive control), and based on predictions of the future behavior of the system (predictive control) using rainfall forecastings. We apply the modeling approach in a system composed by a single watershed, reservoir, and a channel connected in series, respectively, for the San Antonio observed rainfall data. Results indicate that for flood mitigation, the predictive control strategy outperforms the reactive controls not only when applied for synthetic design storm events, but also for a continuous simulation. Moreover, the predictive control strategy requires smaller valve operations, while still guaranteeing efficient hydrological performance. From the results, we recommend the use of the non-linear model predictive control strategy to control stormwater systems due to the ability to handle different objective functions, which can be altered according to rainfall forecasting and shift the reservoir operation from flood-based control to strategies focused on increasing detention times, depending on the forecasting.
Keywords: Real-time control, Smart urban drainage systems, Control theory, Model predictive control, Linear quadratic regulator, Ruled-Based Control.

2.1 Introduction

Floods are the deadliest natural disaster in US and worldwide (Wing et al., 2020). Estimated global flood damages from 1980 to 2019 exceed USD 750 billion, with a peak in 2012 of nearly USD 70 billion (Our World in data, 2021). Storm events are expected to become more frequent and intense due to climate change, likely increasing not only economic, but also social and environmental impacts, posing flood control as one of the greatest challenges for future planning and management of water resources (Gasper et al., 2011). Flood control measures in urban stormwater infrastructures are typically performed by static operations of valves, gates, pumps and/or tunnels based on pre-defined heuristic rules. With the advances in real-time control strategies such as the advent of non expensive sensors, wireless communication, microprocessors and microcontrollers, opportunities to enhance flood management are evident. Therefore, control theory methods can be applied to enhance water resources management by deploying optimization-based control algorithms. Despite the fact that control theoretic methods have been applied to control combined sewer systems, reservoirs and drinking water

systems (Duchesne et al., 2001; Troutman et al., 2020a; Wang et al., 2021), it is a relatively new technique for drainage systems with separated infrastructure for stormwater and sanitary sewage (Wong e Kerkez, 2018; Lund et al., 2018).

Most drainage infrastructure in major cities was built to operate as static systems. These systems, in order to convey and/or store large storms (e.g., 100-yr storms), typically require relatively large dimensions. However, over the lifespan, the aging infrastructure, lack of proper maintenance, or the increasing of expected surface runoff (e.g., climate change and urbanization) can decrease the system reliability and hence increase the risk of flooding (Kessler, 2011; Zhang et al., 2018). Real-Time Control (RTC) of the existent systems (e.g., watersheds, reservoirs, channels) can change the flow-storage regime by controlling actuators such as valves and pumps and ultimately restore or increase the level of protection against flooding. On the other hand, new stormwater systems designed for RTCs could require smaller surface areas and volumes, potentially leading to an overall cost reduction for the same level of expected performance (Wong e Kerkez, 2018; Brasil et al., 2021; Xu et al., 2021).

2.1.1 Literature Review

The literature reviewed shows several applications of optimization of flow characteristics in a hydraulic structure (i.e., reservoir, channel, pipe, tunnel) in order to provide multiple benefits and increase the average performance to different water-related problems. An optimized control of the drainage facilities can enhance erosion control (Schmitt et al., 2020), provide stormwater runoff treatment due to higher detention times (Sharior et al., 2019b), increase navigability conditions in canals (Horváth et al., 2014), and not only reduce flood downstream locally but also reshape the hydrographs in a desired way set by the developed optimization problem (Wong e Kerkez, 2018).

Another example of RTC approaches applied to water systems is on the topic of combined sewer overflows, which contains an extensive literature (García et al., 2015; Ocampo-Martínez e Puig, 2010; Joseph-Duran et al., 2015). However, only a few cities worldwide had applied optimization-based RTC in their drainage systems (Lund et al., 2018). Nonetheless, only a few studies assessed the benefits of RTCs in separated drainage systems. In general, there are 2 types of control strategies: Reactive Controls (i.e., based on Real-Time measurements), and Predictive Controls (i.e., based on predictions of the future behavior of the system). Reactive Controls can be used with heuristic or ruled-based approaches and with optimization-based approaches. Predictive Controls are typically solved with optimization-based approaches. Recently, (Schmitt et al., 2020) assessed the role of heuristic and reactive control rules (i.e., based on Real-Time measurements) applied to valves in stormwater reservoirs (i.e., actions are made based on measured states), focusing on control of erosive flows. The RTC efficiency was assessed through flow-duration curves, providing exceedance probabilities for any given flow. Although the RTC application provided a significant flow reduction for relatively small flows, its implementation for larger storms (i.e., $>$ 1yr) had nearly less or equal peak flow reduction as the passive control. In several assessed storms, the outflows were larger than the inflows, indicating that the RTC increased the likelihood of large flows. Since the controls were guided to increase water quality by increasing detention times (e.g., the control algorithm principle relies on storing the water for one or two days for any particular event), when sequential storm events occur, flood risks increased because the storage capacity was nearly complete from previous storms.

The research conducted by (Wong e Kerkez, 2018) presents an optimization methodology towards the control of stormwater reservoirs to identify optimal, but yet reactive control based on measured states. A Stormwater Management Model (SWMM) (Rossman, 2010) model was used to estimate the flow dynamics in a watershed with several reservoirs and links. The model outputs were used in a linear quadratic regulator (LQR) control to decide the valve openings schedule in a set of

controlled assets. Although the control schedule given by the LQR reduced peak flows in several ponds, a few of them had higher outflow peaks in some of the most intense storms assessed, mostly due to the lack of predictability of the future states of the system. Their results illustrate how RTC can increase flood control performance of urban drainage systems, but also indicate that without predictions, its practicality might be limited.

In contrast to heuristic and reactive controls, (Shishegar et al., 2019a) develop an optimization-based approach using a model predictive controller for operating valves in a stormwater detention pond. The authors used a calibrated SWMM model for the watershed and formulated the water balance dynamical problem in the reservoir by linear programming with flows as decision variables. Their approach reshaped hydrographs out of the stormwater reservoir according to the control objective, although several simplifications were adopted: (a) perfect 48-hours rainfall forecasting was used in the prediction horizon, (b) evaporation was neglected, and (c) linear hydraulics releasing outflows in a linear fashion.

Other recent applications of RTC approaches using heuristic controls for water quality enhancement as the on/off and detention control (Sharior et al., 2019b), fuzzy-logic and data-driven algorithms with genetic algorithms (Li, 2020), and deep learning (Mullapudi et al., 2020) are found in the literature and addresses different applications of RTC of urban drainage than our study. From these studies, we categorize RTC for separated urban drainage systems into (a) Static and/or Optimization-Based Reactive Controls (i.e., control algorithm according to measured or estimated states) and (b) Predictive / Optimization-Based Controls (i.e., control algorithms that considers future states estimation using rainfall forecasting and hydrological models). It is important to note that several ruled-based control (RBC) algorithms do not even require a hydrological modeling, although it is mandatory for predictive controllers (Lund et al., 2018).

2.1.2 Paper Objectives and Contributions

We observe from the aforementioned studies a lack of coupled model for the main processes related to floods as overland flow, infiltration, reservoir routing, and channel routing that allows the use of advanced control theory techniques. Although SWMM or the Gridded Surface Subsurface Soil Analysis (GSSHA) are capable of solving the usually complex shallow water equations, their use in optimization for large systems can be intractable for real-time control and a simplified plant model of the flow dynamical model is needed (Lund et al., 2018). Moreover, exploring the differences between water quality controls as detention control, on/off control, further discussed in the next sections, into flood control performance are not yet investigated in the literature. In this paper, we address these issues and explore the trade-offs between reactive and predictive control strategies in regards to flood mitigation. A schematic of the modeled system is shown in Fig. 2.1 representing the three modeled systems: watersheds discretized in cells, reservoirs receiving outflows from watershed, and channels discretized into sub-reaches receiving outflows from reservoirs. In this model, we are only interested in floods generated by excess of overland flow. Therefore, sub-surface flow are not considered and stored volumes are assumed as overland flow volumes.

To this end, we develop a novel state-space representation of the main processes of the water cycle related to urban catchments (i.e., infiltration, overland flow, reservoir storage, channel routing), using cells, reservoirs, sub-reaches of channels connected as networked dynamical systems. This state-space model (i.e., a matrix and vector representation of the system dynamics) is based on energy, continuity, and momentum equations. We approach the non-linearities of the flow dynamics by performing successive linearizations in each time-step of the model using data from previous time-steps as operational points. Although we are able to linearize most of the system's equations based on physics

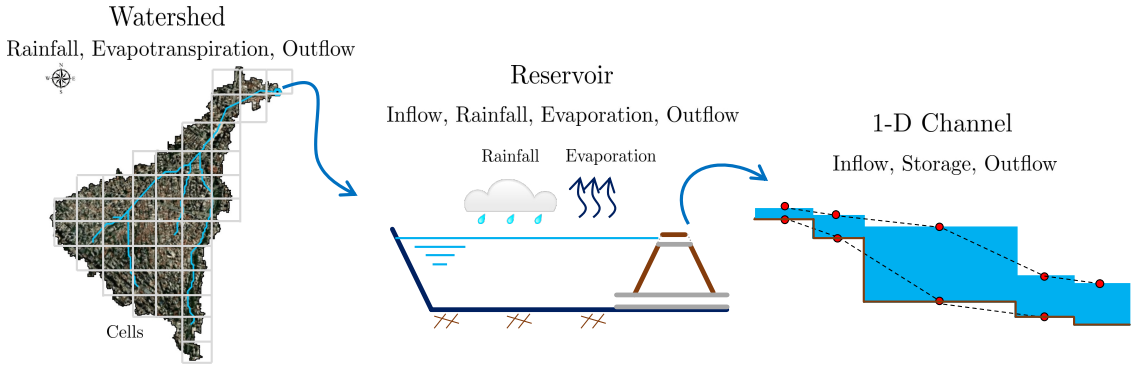

Figure 2.1. System of sub-systems where the watershed is discretized in cells in a 2-D space, and the channel is discretized in 1-D cells. Service Layer Credits: Source: Esri, Maxar, GeoEye, Earthstar Geographics, CNES/Airbus DS, USDA, USGS, AeroGRID, IGN, and the GIS User.

laws (e.g., water balances, energy conservations), we are unable to do it for the rainfall intensity due to the complexity and absence of differentiable models for that. Therefore, we assume a known rainfall input time-series in the model and we model the watershed as a non-linear dynamical system.

In addition to the development of the novel state-space model, we want to assess how varied valve control strategies behave in the system. To that end, we develop a model predictive controller (MPC) algorithm to enhance the operation of valves in stormwater reservoirs, minimizing a composed cost function related to flood performance. Moreover, we compare the efficiency of reactive controls (i.e., controls based on real-time measurements of the states) with MPC solved with a gradient-based method (Interior-Point).

The fundamental contributions of this paper are described below:

- We present an overall mathematical representation including the flow dynamics in watersheds using the non-linear reservoir, and the Green-Ampt infiltration model (Green e Ampt, 1911), coupled with reservoir routing and 1-D channel dynamics in a non-linear state-space representation. It allows optimization and real-time control of urban drainage systems without requiring extensive software packages (i.e., only MATLAB is required).

- We derive the non-linear dynamics of watersheds, and linearize the dynamics of reservoirs and channels. Since no continuous and differentiable model is currently available for rainfall intensity, we assume a known time series of rainfall as a piecewise continuous input data.

- We provide a comprehensive analysis of reactive controls (i.e., some ruled-based and other optimally controlled) for flood mitigation and tested the efficiency of water quality ruled-based algorithms presented in Sharior et al. (2019b) for flood mitigation.

- We develop and apply a servo-control algorithm (Young e Willems, 1972) used in the discrete linear quadratic integrator (DLQI) reactive control. This is a new application for this control technology in urban drainage systems. This algorithm allows tracking a specific state and can be used in reservoirs with minimum specified water surface depths (e.g., wetlands or retention ponds).

- We evaluate and discuss the performance of reactive RBCs (passive, on/off, detention control) and reactive optimization-based controls (discrete linear quadratic regulator and discrete linear quadratic integrator) compared with the predictive control strategy. Moreover, we explore the caveats of consecutive design storms and also compared the flood performance of reactive and predictive algorithms in a continuous simulation, providing a methodology to assess the efficiency of control algorithms for flood mitigation.

The remainder of the paper is organized as follows. Section 2.2 develops the state-space model for watersheds, reservoirs, and 1-D channels flow routing dynamics. Next, Section 2.3 describes the tradional reactive controls applied to control of stormwater reservoirs. Moreover, in this section we develop a novel non-linear MPC optmization problem focusing on flood mitigation in channels and reservoirs. Following, in Section 2.4 we present a case study to test the controls presented in the aforementioned sections, including two scenarios: 2 consecutive design storms of 25-yr, 12-hr and 10-yr, 12-hr, respectively and a continuous simulation scenario from 04/23/2021 to 07/23/2021 in San Antonio - Texas. Section 2.5 shows the results and discussion of the model application and Section 2.6 the conclusions, limitations, and future works. The paper notation for this paper is introduced next.

Paper's Notation: Italicized, boldface upper and lower case characters represent matrices and column vectors: a is a scalar, $\boldsymbol{a}$ is a vector and $\boldsymbol{A}$ is a matrix. Matrix $\boldsymbol{I}_n$ denotes an identity square matrix of dimension n-by-n, whereas $\boldsymbol{O}_{m\times n}$ and $\boldsymbol{1}_{m\times n}$ denotes a zero and one matrix with size m-by-n, respectively. The notations $\mathbb{R}$ and $\mathbb{R}_{++}$ denote the set of real and positive real numbers. Similarly, $\mathbb{N}$ and $\mathbb{N}_{++}$ denote the set of natural and positive natural numbers. The notations $\mathbb{R}^n$ and $\mathbb{R}^{m\times n}$ denote a column vector with n elements and an m-by-n matrix in $\mathbb{R}$. The element-wise product or Hadamard product is defined as $\boldsymbol{x}\circ\boldsymbol{y} \coloneqq [x_1y_1, x_2y_2, \ldots, x_ny_n]^T$ multiplications. Similarly, the element-wise division or Hadamard is defined as $\boldsymbol{x}\oslash\boldsymbol{y} \coloneqq [\frac{x_1}{y_1}, \frac{x_2}{y_n}, \ldots, \frac{x_n}{y_n}]^T$. The element-wise p power of a matrix $\boldsymbol{A}$, $(\boldsymbol{A}^{\circ p})$, with $\boldsymbol{A}\in\mathbb{R}^{m\times n}$ and $p\in\mathbb{R}$ is given by $a_{i,j}^p$ for $i\in\mathbb{N}_{++}$, and $j\in\mathbb{N}_{++}$ The number of elements in a set $\boldsymbol{A}\cup\boldsymbol{B}$ is $\mathbf{n}(\boldsymbol{A}\cup\boldsymbol{B}) = \mathbf{n}(\boldsymbol{A}) + \mathbf{n}(\boldsymbol{B}) - \mathbf{n}(\boldsymbol{A}\cup\boldsymbol{B})$. A normally distributed random number with average μ and variance σ^2 is notated by $\mathcal{N}(\mu,\sigma^2)$. Given a vector $\boldsymbol{x}\in\mathbb{R}^n$, the notation $\boldsymbol{x}(i:j)$ with i and $j\in N_{++}$ represents a cut in $\boldsymbol{x}$ from i$^{\text{th}}$ to j$^{\text{th}}$ entries.

2.2 Mathematical Model Development

The stormwater flow dynamical problem solves physics-based governing equations in each watershed, reservoir, and channel using physically-based input data. The model (RTC-Stormwater) is implemented in Matlab. Since mass balance equations are solved, we postulate the stormwater flow dynamical system as nonlinear difference-algebraic equation (DAE) state-space model. All variables used in this paper are summarized in Tab. S1 in the supplemental material.

The model requires matrices and vectors to represent the dynamical and algebraic parts of the simulated hydrological systems, as presented in Eq. 2.1. Specifically, matrix $\boldsymbol{E}$ enables the representation of the dynamics and algebraic constraints of the coupled watershed-reservoir-channel model in a single state-space model. Moreover, linear time-varying parts are represented by matrices $\boldsymbol{A}(k), \boldsymbol{B}(k)$, while $\boldsymbol{C}$ represents time-invariant output matrix, as the sensors are assumed to have fixed geographic placements. In addition, offsets, non-linearities from the watershed model, operational points, rainfall intensity in each cell, outflows/inflows connectivity from watersheds to reservoirs and from reservoirs to channels, and integrator reference setpoints are given by $\boldsymbol{\psi}(\cdot)$. The mathematical development of these matrices and vectors are detailed in the following sections. In this paper, we develop the DAE state space model for a system composed of a single watershed, reservoir, and channel. We collect a vector of water surface depths in cells, reservoirs, and channels, accumulated infiltration depths in each cell, and outflows from catchments and reservoirs as the state vector, such that $\boldsymbol{x}(k) = [\boldsymbol{h}_{ef}^w(k), \boldsymbol{f}_d^w(k), q_{out}^w(k), h^r(k), q_{out}^r(k), \boldsymbol{h}^c(k)]^T$. We also assume a control vector given by $\boldsymbol{u}(k) = u^r(k)$. The model parameters, states, outputs, and sources of uncertainty are presented in Table 2.1. The state-space representation can be written as

$$\boldsymbol{E}\boldsymbol{x}(k+1) = \boldsymbol{A}(k)\boldsymbol{x}(k) + \boldsymbol{B}(k)\boldsymbol{u}(k) + \boldsymbol{\psi}(k, \boldsymbol{x}(k), \boldsymbol{x}_*^r, \boldsymbol{u}_*^r) \tag{2.1a}$$

$$\boldsymbol{y}(k) = \boldsymbol{C}x(k) \tag{2.1b}$$

Table 2.1. Systems, Parameters, States, Outputs and Uncertainty features of the model, where q, n_r and n_c represents the number of cells, reservoirs and channel sub-reaches, and the state vector dimension n is equal $(2q + 1 + 2n_r + n_c)$.

System	Parameters	States (Symbols)	Outputs (Symbols)	Uncertainty
Cells	Infiltration Parameters Surface Roughness Initial Abstraction Digital Elevation Model Land Use and Land Cover	Water Surface Depth in each cell ($\boldsymbol{h}_{ef} \in \mathbb{R}^q$) in (mm), Infiltrated Depths ($\boldsymbol{f}_d \in \mathbb{R}$) in (mm), and Outflow ($q^w_{out}$) in ($m^3/s$)	Outflow in each cell and in the outlet ($\boldsymbol{q}_{out} \in \mathbb{R}^q$) in ($mm.h^{-1}$)	Manning's Coefficient and Rainfall Spatial Distribution
Reservoirs	Stage-Discharge Relationships Area-Volume Function Porosity	Water Surface Depth ($\boldsymbol{h}^r \in \mathbb{R}^{n_r}$) in (m), and Outflow q^r_{out} in (m^3/s)	Maximum Water Surface Depth ($\max(\boldsymbol{h}^r) \in \mathbb{R}$) in (m)	Water Surface Depth Measurement Noise
Channels	Stage-Discharge Relationships Manning's Coefficient Hydraulic Radius Gridded Bathymetry	Water Surface Depth ($\boldsymbol{h}^c \in \mathbb{R}^{n_c}$) in each sub-reach of the Channel (m)	Maximum Water Surface Depth ($\max(\boldsymbol{h}^c) \in \mathbb{R}^{n_c}$) in (m)	Manning's Coefficient

where $\boldsymbol{E}$ is a singular matrix with some zero rows representing the algebraic constraints of flow equations, $\boldsymbol{A}(k) \in \mathbb{R}^{n \times n}$, is the state or system matrix, $\boldsymbol{x}(k) \in \mathbb{R}^n$ is the state vector, $\boldsymbol{B}(k) \in \mathbb{R}^{n \times m}$ is the input matrix, $\boldsymbol{u}(k) \in \mathbb{R}^m$ is the input vector, $\boldsymbol{\psi}(k, \boldsymbol{x}^r_*, \boldsymbol{u}^r_*)$ is a disturbance vector, $\boldsymbol{x}^r_*$ and $\boldsymbol{u}^r_*$ are operational points which are updated each time-step, $\boldsymbol{C} \in \mathbb{R}^{p \times m}$ is the output matrix, and $\boldsymbol{y}(k)$ is the output function and k is a time-step index. The vectors $\boldsymbol{h}^w_{ef}, \boldsymbol{h}^r$, and $\boldsymbol{h}^c$ are water surface depths in each system, $\boldsymbol{f}_d$ is the accumulated infiltration depth in the cells of the watershed, and q^w_{out} and q^r_{out} are the watershed outflow, and reservoir outflow, respectively. In the following sections, we define each system and their governing equations, as well the linerizations.

For cases with more watersheds, reservoirs, and channels, the state vector can be augmented to include the new systems, concatenating each individual state (e.g., $\boldsymbol{h}^w_{ef}(k) = [\boldsymbol{h}^w_{ef,1}, \ldots, \boldsymbol{h}^w_{ef,s}]^T$) such that $\boldsymbol{x}(k) = [\boldsymbol{h}^w_{ef}(k), \boldsymbol{f}^w_d(k), \boldsymbol{q}^w_{out}(k), \boldsymbol{h}^r(k), \boldsymbol{q}^r_{out}(k)]^T$, $\boldsymbol{u}(k) = [u^r_1(k), \ldots u^r_s(k)]^T$, where s is the number of systems composed by watersheds, reservoirs, and channels. In this paper, we present the mathematical formulation for a watershed-reservoir-channel system.

2.2.1 Watershed Overland Flow Modeling

In this section we derive the mathematical formulation to estimate overland flow in watersheds using a fully-distributed hydrologic model. Excess of infiltration (Hortonian Flow) and/or saturation (Dunnian Flow) generates overland flow in storage cells (Maxwell et al., 2014b). In urban environments with high impervious areas, hortonian flows governs the overland flow generation and occur when infiltration capacity is smaller than the inflow rate (i.e., net precipitation, inflow from neighbour cells, ponding depth).

The infiltration losses are estimated using the Green and Ampt Infiltration Model. This model is physically-based and derived from simplifications of the Richards' Equation (Richards, 1931; Green e Ampt, 1911). All parameters of the model can be estimated in laboratory tests. However, substantial studies are available in the literature providing good parameter's estimates according to the soil characterization (Green e Ampt, 1911; Rossman, 2010). Furthermore, Green-Ampt soil properties are typically available in spatially distributed Geographical Information System (GIS) databases in many parts of the world, which facilitates the application of this model.

For each cell of a pre-defined grid domain, the (i) saturated hydraulic conductivity, (ii) suction head pressure (capillarity), (iii) initial and saturated soil moisture and (iv) initial infiltrated water content are required. Extractions of ASCII files from delineated watershed rasters can be used to define the matrices representing the digital elevation model (DEM) and the imperiousness map. More details of these files and for the model construction are found in Gomes Jr. et al. (2021b,a). The Mannings equation is used to relate water surface depth to flow for the cells (Akan, 1993; Chow, 2010b). To

perform the calculations, input data such as (a) Mannings coefficient and (b) Central Elevation of each cell of the grid are required.

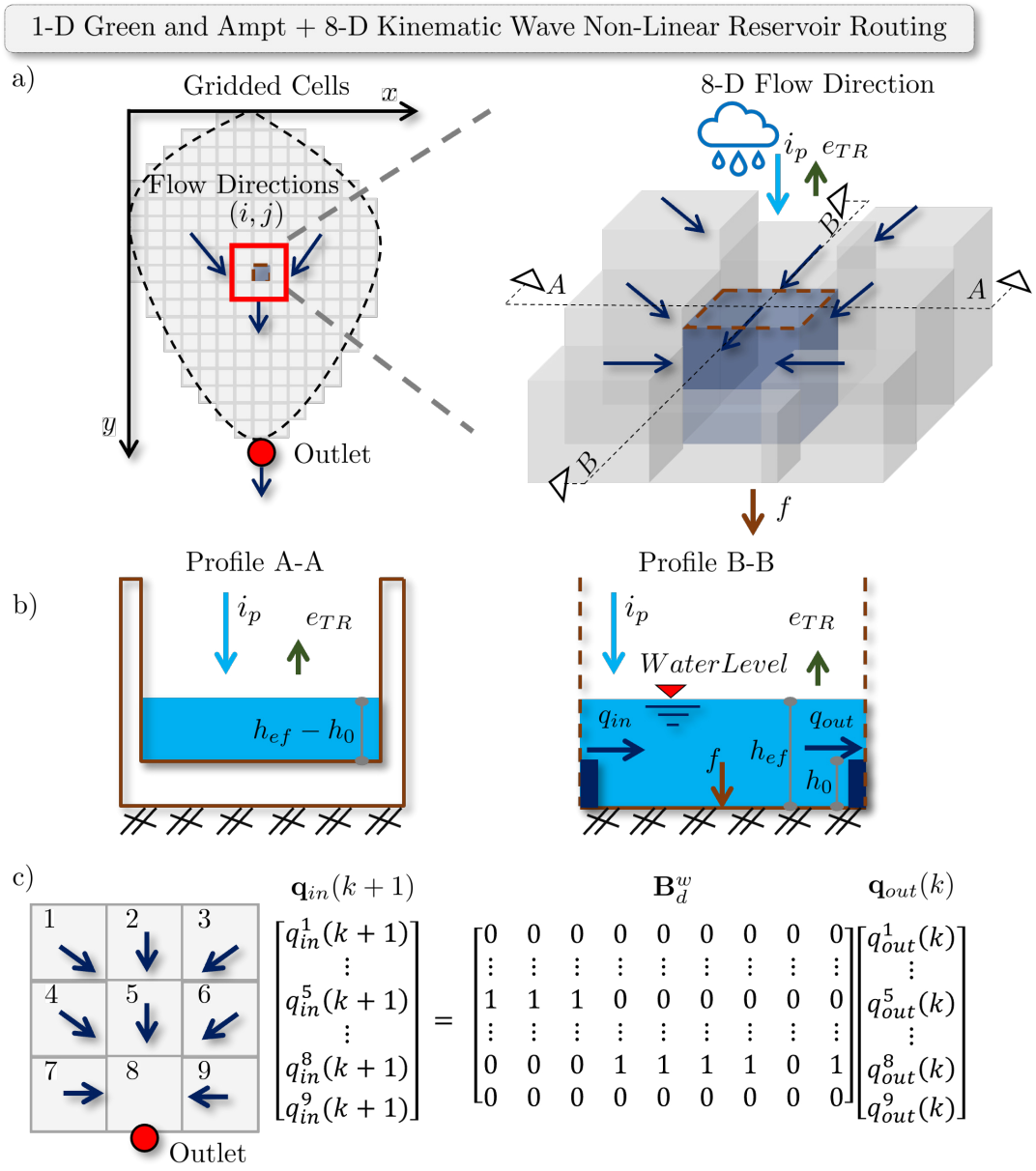

Figure 2.2. (a) Watershed conceptual model, a) is the plan view of the watershed, b) is the profiles of a cell and c) is the 8-D flow direction matrix based on the steepest slope, where $q_{in}, i_p, e_{TR}, q_{out}, f, d$ and h_0 are the inflow, rainfall intensity, evapotranspiration, outflow, infiltration, water surface depth and the initial abstraction of a specific cell of the grid.

2.2.1.1 1-D Vertical Infiltration Model

The Green-Ampt model is applied to each grid cell to estimate the infiltration capacity at any given time and is used to estimate the available depth to be routed to downstream cells. The infiltration capacity is estimated as

$$c^{i,j}(t) = k_{sat}^{i,j}\left[1 + \frac{\left(\zeta^{i,j} + h_{ef}^{i,j}(t)\right)\left(\theta_s^{i,j} - \theta_i^{i,j}\right)}{f_d^{i,j}(t)}\right], \tag{2.2}$$

where the sub-index i and j indicate the cell position in the grid, $c(t)$ is the infiltration capacity (mm.h^{-1}), k_{sat} is the saturated hydraulic conductivity in (mm.h^{-1}), ζ is the suction head pressure (mm),

$h_{ef}(t)$ is the water depth in the cell (mm), ($\Delta\theta = \theta_s - \theta_i$) is the effective soil moisture, $f_d(t)$ is the time-varying accumulated infiltration (mm).

The infiltration model is a non-linear time-varying function of the accumulated infiltrated volume $I_i^{i,j}(t)$, and is dynamically computed in an explicit 1st order finite difference discretization, written as

$$f_d^{i,j}(t+\Delta t) = f_d^{i,j}(t) + f^{i,j}(t)\Delta t = f_d^{i,j}(t) + \overbrace{\left[\min\left(c^{i,j}(t), q_{in}^{i,j}(t) + i_p^{i,j}(t) - e_{TR}^{i,j}(t)\right)\right]}^{f^{i,j}(t)}\Delta t, \tag{2.3}$$

where i_p is the rainfall intensity (mm.h^{-1}), e_{TR} is the real evapotranspiration intensity (mm.h^{-1}), Δt is the model time-step, $f_d^{i,j}(t)$ is the accumulated infiltration depth in (mm), $q_{in}^{i,j}(t)$ is the inflow discharge rate (mm.h^{-1}), and $h_{ef}^{i,j}$ is the runoff water depth (mm) in cell i, j.

In the previous equation, we model the soil drying only by assuming a flux of evapotranspiration occurring at pervious surfaces such that in drying periods, the soil storage depth is decreased. Moreover, we limit the accumulated infiltrated soil depth f_d to a minimum threshold typically assumed as 5 mm.

2.2.1.2 Vertical Water Balance

Hydrological processes of infiltration, precipitation, surface runoff and evaporation occur simultaneously. However, an analytical solution of the continuous functions of these inputs into the overall water balance is typically not available for real case scenarios, especially due to the rainfall. With proper stable time-step resolution, an alternative to solve the overland flow dynamics is to derive an explicit system of equations from the time derivative of the storage variation in each cell, expressed as follows (Rossman, 2010)

$$\frac{\mathrm{d}s^{i,j}(t)}{\mathrm{d}t} = \left[q_{in}^{i,j}(t) + i_p^{i,j}(t) - e_{TR}^{i,j}(t) - q_{out}^{i,j}(t) - f^{i,j}(t)\right]\omega^w \tag{2.4a}$$

$$\frac{\mathrm{d}h_{ef}^{i,j}(t)}{\mathrm{d}t} = \frac{1}{\omega^w}\frac{\mathrm{d}s^{i,j}(t)}{\mathrm{d}t}, \tag{2.4b}$$

where $s^{i,j}$ is the ponded water storage (m^3), $\omega^w = \Delta x^w \Delta y^w$ is the cell area in (m^2), Δx^w and Δy^w are the cell resolution in x and y in (m), $q_{out}^{i,j}(t)$ is the outflow discharge rate (mm/hr) and $f^{i,j}(t)$ is the infiltration rate (mm/hr).

Generalizing Eq. (2.4b) for a vector notation concatenating the number of rows and columns into a vector of dimension q, changing the units for water surface depth instead of storage, and including a constraint to account for the initial abstraction, we can derive the following expression

$$\boldsymbol{h_{ef}}(k+1) = \boldsymbol{h_{ef}}(k) + \frac{\Delta t}{600}\Big(\boldsymbol{q}_{in}(k) + \boldsymbol{i}_p(k) - \boldsymbol{e}_{TR}(k) - \boldsymbol{q_{out}}(k) - \boldsymbol{f}(k)\Big), \tag{2.5}$$

where k is a time-step index, $\boldsymbol{h}_{ef}$, $\boldsymbol{q}_{in}$, $\boldsymbol{i}_p$, $\boldsymbol{e}_{TR}$, $\boldsymbol{q}_{out}$, and $\boldsymbol{f} \in \mathbb{R}^q$.

2.2.1.3 Outflow Discharge

The outflow discharge is simplified to be a function of the steepest 8-Direction slope, cell roughness and water surface depth in a kinematic-wave shallow-water simplification approach. This approximation is implemented since the goal of the watershed model is to determine flows and not high-resolution surface water flood depths. According to the gridded elevation, first we define a flow direction matrix similar as presented in Fig. 2.2, part b). This matrix is determined calculating the steepest topographic slope of each cell assuming 8 boundary cells (i.e., Moore neighborhood grid).

According to the steepest slope direction, a number is assigned to each cell. This matrix defines the boundary conditions among each cell in the grid.

Using the Mannings equation (Chow, 2010b) and assuming the energy slope as bottom slope, we can estimate the outflow discharge for a specific cell as following in a matrix notation

$$\boldsymbol{q}_{out}(k) = \overbrace{\left(k_f \frac{\Delta x^w + \Delta y^w}{2}\right) \boldsymbol{s}_0^{\circ 1/2} \oslash \boldsymbol{n}}^{\boldsymbol{\lambda}} \circ \Big(\max(\boldsymbol{h}_{ef}(k) - \boldsymbol{h}_0), 0\Big)^{\circ 5/3} \tag{2.6}$$

where k_f is a conversion factor equals 1×10^{-5}, $\boldsymbol{s_0}$ is the steepest topographic slope (m/m), n is the Mannings roughness coefficient in (sm$^{-1/3}$), and $\boldsymbol{\lambda}$ lumps the hydraulic properties of the cells into a single vector. $\boldsymbol{s}_0$, $\boldsymbol{h}_0$, $\boldsymbol{q}_{out}$, and $\boldsymbol{\lambda} \in \mathbb{R}^q$. All the other equations are in the international system of units.

To guarantee continuity in the hydrological model, a pre-processing in the digital elevation model is performed. Natural sinks are filled to ensure all cells have an outlet slope. Moreover, the outlet boundary condition of the watershed is modeled assuming a normal flow hydraulic condition (Kollet e Maxwell, 2006a).

2.2.1.4 Inflow Discharge

The inflow discharge is a function of the flow direction matrix and outflow discharge. Defining a matrix $\boldsymbol{B}_d^w \in \mathbb{R}^{q \times q}$ to represent the direction relationship among the cells in the form of a sparce matrix filled with ones (i.e., outflows becomes inflow for the downstream cell) and zeros (i.e., no flow connection between cells, see Fig. 2.2 part c), we can write

$$\boldsymbol{q}_{in}(k) = \boldsymbol{B}_d^w \boldsymbol{q}_{out}(k), \tag{2.7}$$

where $\boldsymbol{B_q} \in \mathbb{R}^{q \times q}$ is the direction boolean matrix containing the relationship between each cell.

Substituting Eqs. (2.7) and (2.6) into Eq. (2.5), tracking the accumulated infiltration depth (f_d), and the watershed outflow (q_{out}^w), the watershed sub-system from Eq. (2.1) can be written in a state-space representation, given by

$$\overbrace{\begin{bmatrix} \boldsymbol{I}_{2q} & 0 \\ 0 & 0 \end{bmatrix}}^{\boldsymbol{E}^w} \overbrace{\begin{bmatrix} \boldsymbol{h}_{ef}(k+1) \\ f_d(k+1) \\ q_{out}^w(k+1) \end{bmatrix}}^{\boldsymbol{x}^w(k+1)} = \overbrace{\boldsymbol{I}_{2q+1}}^{\boldsymbol{A}^w(k)} \boldsymbol{x}^w(k)$$

$$+ \Delta t \overbrace{\begin{bmatrix} 1/600\Big((\boldsymbol{B}_d^w - \boldsymbol{I}_q) \circ \boldsymbol{\lambda} \circ \max\Big(\boldsymbol{h}_{ef}(k) - \boldsymbol{h}_0, 0\Big)^{\circ 5/3} + \boldsymbol{i}_p'(k) - \boldsymbol{f}(k)\Big) \\ \boldsymbol{f}(k) \\ \frac{-0.277 \times 10^{-6}}{\Delta t} ||\boldsymbol{\lambda}^{i_0, j_0} \max\Big(\boldsymbol{h}_{ef}^{i_0, j_0}(k) - \boldsymbol{h}_0, 0\Big)^{\circ 5/3} \omega^w|| \end{bmatrix}}^{\boldsymbol{\psi}^w(k, \boldsymbol{x}^w(k))}, \tag{2.8}$$

where $\boldsymbol{x}^w(k) = [\boldsymbol{h}_{ef}^w(k), \boldsymbol{f}_d^w(k), q_{out}^w(k)]^T$, $\boldsymbol{i}'(k) = \boldsymbol{i}_p(k) - \boldsymbol{e}_{TR}(k)$, $\boldsymbol{f}(k)$ is modeled in Eq. (2.3), $\boldsymbol{i}_0$ and $\boldsymbol{j}_0$ represent the indexes of the outlet cells, and $\boldsymbol{\lambda}^{i_0, j_0}$ concatenates λ for outlet cells.

2.2.2 Reservoir Dynamics

In this section, the reservoir routing dynamics is described and we provide a fully linearizable model to account for valve control in stormwater reservoirs with hydraulic devices as orifices and spillways.

2.2.2.1 Orifice Modeling

The control signal $u(k)$ represents the percentage of the orifice area that allows flow to be routed to downstream channels. Therefore, applying the energy equation in the reservoir (Chow, 2010b) and including $u(k)$ in the effective orifice area, we can derive the controlled orifice equation, such that

$$q_o(h^r(k), u(k)) = u^r(k) c_{d,o} a_o \sqrt{2g(\max(h^r(k) - (h_o + h_m), 0))} = u^r(k) k_o \sqrt{\hat{h}^r(k)}, \tag{2.9}$$

where q_o is the orifice discharge, $c_{d,o}$ is the orifice discharge coefficient, a_o is the orifice area and g is the gravity acceleration, $\hat{h}^r(h^r(k)) = \max(h^r(k) - (h_o + h_m), 0)$ is the effective water depth at the orifice, u is the control input representing the valve opening between 0 and 1, h_o is the bottom elevation of the orifice and h_m is the minimum water surface depth to begin the outflow (i.e., typically 20% of the hydraulic diameter of the outlet) (Chow, 2010b).

2.2.2.2 Spillway Modeling

The spillway is also assumed to be discharging at the atmospheric pressure. The Francis Spillway equation is typically used for detention reservoirs and can be modeled as follows

$$q_s(h^r(k)) = c_{d,s} l_{ef} (h^r(k) - p)^{3/2} = k_s (h^r(k) - p)^{3/2}, \tag{2.10}$$

where q_s is the spillway discharge, p is the spillway depth from the bottom, $c_{d,s}$ is the spillway discharge coefficient and l_{ef} is the effective length of the spillway (Chow, 2010b).

2.2.2.3 Reservoir Outflow

The outflow in a reservoir is a function of the water surface depth $h^r(k)$ and is described by the energy conservation applied into the orifice and spillway, and thus has two governing equations. The first case is where $h^r(k) \leq p$, and is given by Eq. (2.9) (Chow, 2010b). When the water level reaches the spillway level, the reservoir outflow (q^r_{out}) is the sum of the orifice and spillway flow. Therefore, the reservoir outflow function be derived as follows

$$q^r_{out}(h^r(k), u^r(k)) = \begin{cases} u^r(k) k_o \sqrt{\hat{h}^r(k)} & \textbf{if } h^r(k) \leq p, \textbf{ else} \\ u^r(k) k_o \sqrt{\hat{h}^r(k)} + k_s (h^r(k) - p)^{3/2} \end{cases} \tag{2.11}$$

We compute the jacobian of q^r_{out} with respect to h^r and u to obtain a linearized flow equation neglecting the high order terms of the Taylor's series, resulting in the following equations:

$$\frac{\partial q^r_{out}(h^r(k), u^r(k))}{\partial h} \approx \left\{ \frac{u^r(k) k_o}{2\sqrt{\hat{h}^r(k)}} + \frac{3 k_s [\max((h^r(k) - p)^{1/2}, 0)]}{2} \right\} = \alpha(h^r(k), u^r(k)) \tag{2.12}$$

$$\frac{\partial q^r_{out}(h^r(k), u^r(k))}{\partial u} = k_o \sqrt{\hat{h}^r(k)} = \beta(h^r(k), u^r(k)). \tag{2.13}$$

Therefore, a linearized model for the outflow in terms of the stored water surface depth and valve opening is given as

$$q^r_{out}(h^r(k), u^r(k)) = \overbrace{q^r_{out}(h^r_*)}^{\gamma(k)} + \overbrace{\alpha|_{h=h^o, u=u^r_*}}^{\tilde{\alpha}(k)} (h^r(k) - h^r_*) + \overbrace{\beta|_{h=h^o, u=u^r_*}}^{\tilde{\beta}(k)} (u^r(k) - u^r_*), \tag{2.14}$$

where γ is the offset, $\tilde{\alpha}$ is the linear coefficient with respect to h^r, $\tilde{\beta}$ is the linear coefficient in terms of u and u^r_* and h^r_* are operation points given by the states and controls of the previous time-step, such that $u^r_*(k) = u^r(k-1)$ and $h^r_*(k) = h^r(k-1)$.

2.2.2.4 Reservoir Water Balance

The temporal evolution of storage in a reservoir depends on the inflow, precipitation, evaporation, water surface area and stage-discharge function of the outlet hydraulic devices. Applying evaporation and precipitation in the reservoir surface area, we can derive an expression for the water storage dynamics, given by

$$\frac{\partial s^r(h^r(k),u^r(k))}{\partial t} = \overbrace{q^w_{out}(k) + \Big(i(k) - e_v(k)\Big)\omega^r(h^r(k))}^{q^r_{in}(k,h^r(k))} - q^r_{out}(h^r(k),u^r(k)), \tag{2.15}$$

where s^r is the stored volume of stormwater runoff in the reservoir, $\omega^r(h^r(k))$ is the reservoir surface area in terms of $h^r(k)$, e_v is the evaporation in the reservoir surface area, q^w_{out} is the inflow from upstream catchment, q^r_{in} is the total inflow i is the rainfall intensity. Assuming an average porosity η representing the stage-storage relationship in the reservoir (e.g., for free surface reservoirs, the porosity is 1), the water surface depth dynamics can be derived as

$$\frac{\partial h(k,h^r(k),u^r(k))}{\partial t} = \frac{1}{\omega^r(h^r(k))\eta}\Big[q^r_{in}(h^r(k)) - q^r_{out}(h^r(k),u^r(k))\Big]. \tag{2.16}$$

The storage dynamics in a reservoir can be very slow depending on the area of the reservoir, which might contribute for low degrees of controllability for reactive controls, even in events with high inflows. Substituting the linearized reservoir outflow, Eq. (2.14), into the water balance equation, it follows that

$$\frac{\partial h(h^r(k),u^r(k))}{\partial t} = \overbrace{\frac{1}{\omega^r(h^r(k))\eta}}^{\mu(h^r(k))}\Big[q^r_{in}(k,h^r(k)) - \tilde{\alpha}(k)(h^r(k) - h^r_*) - \tilde{\beta}(k)(u^r(k) - u^r_*) - \gamma(k)\Big]. \tag{2.17}$$

Assuming an approximated finite-difference scheme by the forward Euler method applied in the water surface depth partial derivative equation, we obtain

$$\frac{\partial h(h^r(k),u^r(k))}{\partial t} \approx \frac{h^r(k+1) - h^r(k)}{\Delta t}. \tag{2.18}$$

Generalizing the reservoir dynamics for more than one reservoir per watershed ($n_r > 1$ and $\boldsymbol{u}^r(k) \in \mathbb{R}^{n_r}$), substituting Eq. (2.17) into Eq. (2.18), and expanding for a matrix notation, the water depth dynamics in reservoirs is given by Eq. (2.19), the reservoirs sub-system from Eq. (2.1) is given by

$$\begin{aligned}\boldsymbol{h}^r(k+1) = &\overbrace{\left(\boldsymbol{I}_{\boldsymbol{n}_r} - \operatorname{diag}\left(\Delta t\tilde{\boldsymbol{\alpha}}(k)\circ\boldsymbol{\mu}(\boldsymbol{h}^r(k))\right)\right)}^{\tilde{\boldsymbol{A}}^r(k)}\boldsymbol{h}^r(k) + \overbrace{\left(-\operatorname{diag}(\Delta t\tilde{\boldsymbol{\beta}}(k)\circ\boldsymbol{\mu}(\boldsymbol{h}^r(k)))\right)}^{\tilde{\boldsymbol{B}}^r(k)}\boldsymbol{u}^r(k)\\ &+\overbrace{\Delta t\boldsymbol{\mu}(\boldsymbol{h}^r(k))\circ\left(\tilde{\boldsymbol{\alpha}}(k)\circ\boldsymbol{h}^r_* + \tilde{\boldsymbol{\beta}}(k)\circ\boldsymbol{u}^r_* - \boldsymbol{\gamma}(k) + \boldsymbol{q}^r_{in}(k)\right)}^{\tilde{\boldsymbol{\psi}}^r(k,\boldsymbol{u}^r_*,\boldsymbol{x}^r_*)},\end{aligned} \tag{2.19}$$

where $\boldsymbol{h}^r(k), \tilde{\boldsymbol{\alpha}}(k), \tilde{\boldsymbol{\beta}}(k)$ and $\tilde{\boldsymbol{\psi}}_r(k,\boldsymbol{u}^r_*,\boldsymbol{x}^r_*) \in \mathbb{R}^{n_r}$, n_r is the number of reservoirs, $\tilde{\boldsymbol{A}}(k)$ and $\tilde{\boldsymbol{B}}_r(k) \in \mathbb{R}^{n_r\times n_r}$ and $\boldsymbol{q}^r_{in}(k)$ captures the watershed-reservoir outflow/inflow connection.

Moreover, generalizing the method for s systems with n_r reservoirs per watershed, we can define $z = n_r s$ resulting in the reservoir state space non-linear dynamics tracking the reservoir outflows such that:

$$\overbrace{\begin{bmatrix}\boldsymbol{I}_z & \boldsymbol{O}_{z\times z}\\ \boldsymbol{O}_{z\times z} & \boldsymbol{O}_{z\times z}\end{bmatrix}}^{\boldsymbol{E}^r_s}\overbrace{\begin{bmatrix}\boldsymbol{y}^r_s(k+1)\\ \boldsymbol{\varphi}^r_{out,s}(k+1)\end{bmatrix}}^{\boldsymbol{x}^r_s(k+1)} = \overbrace{\begin{bmatrix}\tilde{\boldsymbol{A}}^r_1(k) & \boldsymbol{O} & \dots & \boldsymbol{O} & \boldsymbol{O}\\ \boldsymbol{O} & \tilde{\boldsymbol{A}}^r_2(k) & \dots & \boldsymbol{O} & \boldsymbol{O}\\ \vdots & \vdots & \ddots & \vdots & \vdots\\ \boldsymbol{O} & \boldsymbol{O} & \dots & \tilde{\boldsymbol{A}}^r_s(k) & \boldsymbol{O}\\ \boldsymbol{O} & \boldsymbol{O} & \dots & \boldsymbol{O} & -I_z\end{bmatrix}}^{\boldsymbol{A}^r_s(k)}\overbrace{\begin{bmatrix}\boldsymbol{h}^r_1(k)\\ \boldsymbol{h}^r_2(k)\\ \vdots\\ \boldsymbol{h}^r_s(k)\\ \boldsymbol{\varphi}^r_{out,s}(k)\end{bmatrix}}^{\boldsymbol{x}^r_s(k)} +$$

$$\overbrace{\begin{bmatrix} \tilde{\boldsymbol{B}}_1^r(k) & \boldsymbol{O} & \dots & \boldsymbol{O} \\ \boldsymbol{O} & \tilde{\boldsymbol{B}}_2^r(k) & \dots & \boldsymbol{O} \\ \vdots & \vdots & \ddots & \vdots \\ \boldsymbol{O} & \boldsymbol{O} & \dots & \tilde{\boldsymbol{B}}_s^r(k) \\ \boldsymbol{O} & \boldsymbol{O} & \boldsymbol{O} & \boldsymbol{O} \end{bmatrix}}^{\boldsymbol{B}_s^r(k)} \overbrace{\begin{bmatrix} \boldsymbol{u}_1^r(k) \\ \boldsymbol{u}_2^r(k) \\ \vdots \\ \boldsymbol{u}_s^r(k) \end{bmatrix}}^{\boldsymbol{\sigma}_s^r(k)} + \overbrace{\begin{bmatrix} \tilde{\boldsymbol{\psi}}_1^r(k) \\ \tilde{\boldsymbol{\psi}}_2^r(k) \\ \vdots \\ \tilde{\boldsymbol{\psi}}_s^r(k) \\ \boldsymbol{\sigma}_s^r(k) \circ \boldsymbol{k}_o^* \circ (\hat{\boldsymbol{h}}_s^r(k))^{\circ 1/2} + \boldsymbol{k}_s^* \circ (\max(\boldsymbol{y}_s^r - \boldsymbol{p}, 0))^{\circ 3/2} \end{bmatrix}}^{\boldsymbol{\psi}_s^r(k)} \tag{2.20}$$

where $\boldsymbol{k}_o^*$ and $\boldsymbol{k}_s^*$ collects k_o and k_s for all reservoirs in all systems, respectively. Similarly, $\boldsymbol{p}$ collects spillway elevations. Vectors $\boldsymbol{\varphi}_{out}^r, \boldsymbol{y}_s^r$, and $\boldsymbol{\sigma}_s^r$ are defined as follows. Matrices $\boldsymbol{E}_s^r$ and $\boldsymbol{A}_s^r \in \mathbb{R}^{2z \times 2z}$, matrix $\boldsymbol{B}_s^r \in \mathbb{R}^{2z \times z}$, while $\boldsymbol{x}_s^r \in \mathbb{R}^{2z}$, $\boldsymbol{\psi}_s^r \in \mathbb{R}^{2z}$, and $\boldsymbol{\sigma}_s^r \in \mathbb{R}^z$. Vectors $\boldsymbol{\varphi}_{out,s}^r, \boldsymbol{y}_s^r$, and $\boldsymbol{\sigma}_s^r$ are defined as follows:

$$\boldsymbol{\varphi}_{out,s}^r(k) = [\overbrace{\boldsymbol{q}_{out,1}^{r,1}(k), \dots, \boldsymbol{q}_{out,1}^{r,n_r}(k)}^{\boldsymbol{q}_{out,1}^r(k)}, \dots, \overbrace{\boldsymbol{q}_{out,s}^{r,1}(k) \dots \boldsymbol{q}_{out,s}^{r,n_r}(k)}^{\boldsymbol{q}_{out,s}^r(k)}]^T \tag{2.21a}$$

$$\boldsymbol{y}_s^r(k) = [\overbrace{\boldsymbol{h}_1^{r,1}(k), \dots, \boldsymbol{h}_1^{r,n_r}(k)}^{\boldsymbol{h}_1^r(k)}, \dots, \overbrace{\boldsymbol{h}_s^{r,1}(k) \dots \boldsymbol{h}_s^{r,n_r}(k)}^{\boldsymbol{h}_s^r(k)}]^T \tag{2.21b}$$

$$\boldsymbol{\sigma}_s^r(k) = [\overbrace{\boldsymbol{u}_1^{r,1}(k) \dots \boldsymbol{u}_1^{r,n_r}(k)}^{\boldsymbol{u}_1^r(k)} \dots \overbrace{\boldsymbol{u}_s^{r,1}(k) \dots \boldsymbol{u}_s^{r,n_r}(k)}^{\boldsymbol{u}_s^r(k)}]^T. \tag{2.21c}$$

2.2.3 1-D Channel Dynamics

The flow dynamics in rivers or channels can be modeled using hydrologic or hydraulic routing modeling approaches (USACE, 2000). The first is governed by the water balances in the inlet and outlet sections of a sub-reach. The continuity equation and storage-outflow relationships are used to estimate the outflow in the last sub-reach (McCarthy, 1938; Cunge, 1969). However, this approach is suitable only for estimating flows. Moreover, hydrologic routing is not flexible enough to explain more detailed phenomena such as backwater effects from downstream reservoirs or flood waves in channels with very flat slopes (Cunge, 1969). Another issue is the time-related coefficients associated with the hydrologic routing equations. Typically, to ensure model's stability, coefficients are in the order of several hours and days. This poses as a drawback for real-time monitoring of urban channels (Kumar et al., 2011). We propose a diffusive wave simplification in the Saint-Venant Equations (SVE) to represent the flow dynamics in the 1-D channels.

Recently, an application of the full one-dimensional Saint-Venant equations allowed the state-space representation in channels (Bartos e Kerkez, 2021). The authors developed a backward Euler implicit scheme solving continuity and momentum equations via a sparce matrix system of equations. While model stability is theoretically increased with this implicit numerical scheme, in order to develop a full state-space representation of watersheds, reservoirs, and channels, a implicit derivation for the other systems would be required. Therefore, we solve the 1-D flow dynamics using an Euler explicit numerical scheme as used in Eq. (2.8) and Eq. (2.20).

2.2.3.1 Channel Water Depth Dynamics

To represent the channel 1-D dynamics in space and time, we develop an explicit diffusive-wave simplification in SVE, assuming the friction slope from Manning's resistance equation. Fig. 2.5 part c) shows a scheme of a 1-D channel. The outflow in each segment is calculated through Mannings equation as follows (Panday e Huyakorn, 2004b):

$$q_{out}^c(h_i^c(k)) = \frac{a_i^c(k)(r_{h,i}(k))^{2/3}}{n_i} \boldsymbol{s}_{f,i}{}^{1/2} \tag{2.22}$$

where a_i^c is the wetted area, $r_{h,i}$ is the hydraulic radius, h_i^c is the channel water surface depth at cross section i, y is the channel's longitudinal direction and $s_{f,i}(k)$ is the friction slope. The previous expression is expanded in a vector format given by:

$$\boldsymbol{q}_{\boldsymbol{out}}^{\boldsymbol{c}}\left(\boldsymbol{h}^{\boldsymbol{c}}(k)\right) = \mathbf{1}_{n_c\times 1} \oslash \boldsymbol{n}^{\boldsymbol{c}} \circ \boldsymbol{a}^{\boldsymbol{c}}\left(\boldsymbol{h}^{\boldsymbol{c}}(k)\right) \circ \left(\boldsymbol{r}_{\boldsymbol{h}}^{\boldsymbol{c}}\left(\boldsymbol{h}^{\boldsymbol{c}}(k)\right)^{\circ 2/3} \circ \boldsymbol{s}_{\boldsymbol{f}}{}^{1/2}, \tag{2.23}$$

where $\boldsymbol{n}^{\boldsymbol{c}}$, $\boldsymbol{a}^{\boldsymbol{c}}$, $\boldsymbol{r}_{\boldsymbol{h}}^{\boldsymbol{c}}$, is the Manning's coefficient, cross section area function, and hydraulic radius for each sub-reach.

A channel is discretized into sub-reaches with appropriate spatial resolution to be suitable for the time-step of the model (Chang e Wang, 2002). Therefore, the model simulates steady non uniform flow assuming initial boundary conditions from $q_{out}^r(k)$ and from the outlet normal friction slope (Panday e Huyakorn, 2004b; Maxwell et al., 2014b). The conservation of mass and momentum equations are given by:

$$\frac{\partial q_i^c(k)}{\partial y} = -\frac{\partial a_i^c(k)}{\partial t} \tag{2.24a}$$

$$\frac{\partial h_i^c(k)}{\partial y} = s_0^c - \overbrace{\left(\frac{q_i^c(k) n_i^c}{a_i(k) r_{h,i}(k)^{2/3}}\right)^2}^{s_{f,i}(k)} \tag{2.24b}$$

where y represents the longitudinal channel dimension, q_i^c is the net flow within cross sections, s_0^c is the bottom slope, n_i^c is Manning's roughness coefficient, and $s_{f,i}$ is the friction slope.

2.2.3.2 Channel Water Surface Depth Dynamics

We can expand Eq. (2.24a), resulting in a vectorized channel water surface depth mass balance as:

$$\boldsymbol{h}^{\boldsymbol{c}}(k+1) = \boldsymbol{h}^{\boldsymbol{c}}(k) + \Delta t \mathbf{1}_{n_c\times 1} \oslash (\Delta \boldsymbol{x} \circ \Delta \boldsymbol{y}) \overbrace{\left(\boldsymbol{q}_{\boldsymbol{in}}^{\boldsymbol{c}}(k) - \boldsymbol{q}_{\boldsymbol{out}}^{\boldsymbol{c}}(k)\right)}^{\Delta \boldsymbol{q}(\boldsymbol{h}^{\boldsymbol{c}}(k))}, \tag{2.25}$$

where h_c is the water surface depth in each sub-reach of the channel, the outflow Q^c is given by the Mannings equation that depends on known functions of cross section area and hydraulic radius for each reach of the channel and length ($\Delta \boldsymbol{y}$) and width ($\Delta \boldsymbol{x}$). For the first sub-reach, q_{in}^c is equal the reservoir outflow (q_{out}^r). Flows $q_{in,i}^c(k)$ and $q_{out,i}^c(k)$ are equal to q_{i-1}^c and q_i^c, respectively.

To explicit solve Eq. (2.25), we need to derive an expression for $\Delta \boldsymbol{q}^{\boldsymbol{c}}(\boldsymbol{h}^{\boldsymbol{c}}(k))$. To this end, we apply the energy conservation within two consecutive cross sections neglecting the velocity head to develop a vector representation for the friction slope assuming normal depths, such that for a particular cell (i) in a 1-D channel domain, we can write:

$$s_{f,i} = \frac{1}{\Delta y_i}\left(e_{l,i} + h_i^c(k) - e_{l,i+1} - h_{i+1}^c(k)\right)\Big) \tag{2.26}$$

where e_l is the bottom elevation of the sub-reach segment and $\frac{\partial h_i^c(k)}{\partial y}$ is the water surface slope in the cell i at step k.

Expanding the previous equation in a vector format, we can derive the momentum equation from Eq. (2.24b) for all sub-reaches as a linear combination of $\boldsymbol{h}^{\boldsymbol{c}}(k)$ (see Eq. (2.23), such that:

$$\frac{\partial \boldsymbol{h}^{\boldsymbol{c}}(k)}{\partial \boldsymbol{y}} = \boldsymbol{A}_{slope}\boldsymbol{h}^{\boldsymbol{c}}(k) + \boldsymbol{b}_{slope}, \tag{2.27}$$

where $\frac{\partial \boldsymbol{h}^{\boldsymbol{c}}}{\partial \boldsymbol{y}} \in \mathbb{R}^{n_c}$ is a vector representing the water slopes in each reach of the channel, $\boldsymbol{A}_{slope} \in \mathbb{R}^{n_c \times n_c}$ and $\boldsymbol{b}_{slope} \in \mathbb{R}^{n_c}$ are derived from Eq. (2.26) assuming 1-D connections between cells, computing the water surface slopes, and including the outlet slope boundary condition.

2.2.3.3 1-D Flow in Open Channels

Similarly, to the overland flow model for the watershed model, we can compute $\left(\boldsymbol{q}_{in}^{c}(k)-\boldsymbol{q}_{out}^{c}(k)\right)$ as a function of a flow direction matrix and the flow through Manning's equation. Therefore, the net flow $\Delta\boldsymbol{q}^{c}(\boldsymbol{h}^{c}(k))=\boldsymbol{q}_{in}^{c}(k)-\boldsymbol{q}_{out}^{c}(k)$ for all sub-reaches can be given as

$$\Delta\boldsymbol{q}^{c}(\boldsymbol{h}^{c}(k))=\boldsymbol{B}_{d}^{c}\boldsymbol{q}_{out}^{c}(\boldsymbol{h}^{c}(k))+\boldsymbol{w}(k), \tag{2.28}$$

where $\boldsymbol{B}_{d}^{c}$ is a topology matrix linking each sub-reach segment with the previous one and $\boldsymbol{w}(k)$ is a zero vector where only the first entry is equal the reservoir outflow ($q_{out}^{r}(k)$).

However, to estimate the 1-D flow propagation in channels, we do not assume a simplified hydraulic radius and define a constant $\boldsymbol{\lambda}$ due to the relatively small width of the sub-reaches when compared to the gridded cells from the watershed system (Liu e Singh, 2004). To estimate $\boldsymbol{\lambda}$, functions that describe the cross section area ($\boldsymbol{a}_{h}^{c}$(k)) and hydraulic radius ($\boldsymbol{r}_{h}^{c}(k)$) are required and can be derived in terms of topographic properties of the channel. For a rectangular channel (i.e., condition of the case study), $\boldsymbol{a}_{h}^{c}\left(\boldsymbol{h}^{c}(k)\right)=\Delta\boldsymbol{x}\circ\boldsymbol{h}^{c}(k)$, and $\boldsymbol{r}_{h}^{c}\left(\boldsymbol{h}^{c}(k)\right)=\boldsymbol{a}_{h}^{c}(\boldsymbol{h}^{c}(k))\oslash(\Delta\boldsymbol{x}+2\boldsymbol{h}^{c}(k))$.

2.2.3.4 Linearized Channel Dynamics

We can substitute Eq. (2.28) into Eq. (2.25), resulting in a matrix expression for the channel non-linear dynamics given by

$$\begin{aligned}\boldsymbol{h}^{c}(k+1)=\boldsymbol{h}^{c}(k)+\Delta t\mathbf{1}_{n_c\times 1}\oslash(\Delta\boldsymbol{x}\circ\Delta\boldsymbol{y})\circ\Big[\boldsymbol{B}_{d}^{c}\mathbf{1}_{n_c\times 1}\oslash\boldsymbol{n}^{c}\circ\boldsymbol{a}_{h}^{c}\left(\boldsymbol{h}^{c}(k)\right)\circ\boldsymbol{r}_{h}^{c}\left(\boldsymbol{h}^{c}(k)\right)^{\circ 2/3}\\ \circ\left(\boldsymbol{A}_{slope}\boldsymbol{h}^{c}(k)+\boldsymbol{b}_{slope}\right)^{\circ 1/2})+\boldsymbol{w}(k)\Big].\end{aligned} \tag{2.29}$$

Finally, we can obtain a linearized expression around an operation point $\boldsymbol{h}_{0}^{c}$, applying the jacobian in the previous equation, such that

$$\overbrace{\boldsymbol{I}_{n_c}}^{E^{c}}\boldsymbol{h}^{c}(k+1)=\overbrace{(\boldsymbol{I}_{n_c}+\nabla\boldsymbol{h}^{c}(\boldsymbol{h}_{0}^{c}))}^{\boldsymbol{A}^{c}(k)}\boldsymbol{h}^{c}(k), \tag{2.30}$$

where ∇ is the gradient of Eq. (2.29) and can be obtained knowing the cross section area and hydraulic radius functions of each sub-reach and can be computationally derived with symbolic functions on MATLAB, for instance. The gradient and the operational point from Eq. (2.30) are refreshed each model time-step.

2.2.4 State-Space Representation

The derivation of the state-space model for a single watershed, reservoir, and channel is performed merging the dynamical state-space representation for each sub-system from Eqs. (2.8), (2.20), (2.30), and applying in Eq. (2.1), the watershed-reservoir-channel dynamical system can be defined as

$$\begin{aligned}\overbrace{\begin{bmatrix}\boldsymbol{E}^{w}&\boldsymbol{O}&\boldsymbol{O}\\ \boldsymbol{O}&\boldsymbol{E}^{r}&\boldsymbol{O}\\ \boldsymbol{O}&\boldsymbol{O}&\boldsymbol{E}^{c}\end{bmatrix}}^{\boldsymbol{E}}\overbrace{\begin{bmatrix}\boldsymbol{x}^{w}(k+1)\\ \boldsymbol{x}^{r}(k+1)\\ \boldsymbol{x}^{c}(k+1)\end{bmatrix}}^{\boldsymbol{x}(k+1)}&=\overbrace{\begin{bmatrix}\boldsymbol{A}^{w}(k)&\boldsymbol{O}_{(2q+1)\times 1}&\boldsymbol{O}_{(2q+1)\times n_c}\\ \boldsymbol{O}_{1\times(2q+1)}&\boldsymbol{A}^{r}(k)&\boldsymbol{O}_{1\times n_c}\\ \boldsymbol{O}_{n_c\times(2q+1)}&\boldsymbol{O}_{n_c\times 1}&\boldsymbol{A}^{c}(k)\end{bmatrix}}^{\boldsymbol{A}(k)}\overbrace{\begin{bmatrix}\boldsymbol{x}^{w}(k)\\ \boldsymbol{x}^{r}(k)\\ \boldsymbol{x}^{c}(k)\end{bmatrix}}^{\boldsymbol{x}(k)}+\\ &\overbrace{\boldsymbol{B}^{r}(k)}^{\boldsymbol{B}(k)}\boldsymbol{u}(k)+\overbrace{\begin{bmatrix}\boldsymbol{\psi}^{w}(k,\boldsymbol{x}^{w}(k))\\ \boldsymbol{\psi}^{r}(k,x_{*}^{r},u_{*}^{r})\\ \boldsymbol{O}_{n_c\times 1}\end{bmatrix}}^{\boldsymbol{\psi}(k)}\end{aligned} \tag{2.31}$$

Similarly, the derivation of the state-space dynamics for the general case with multiple watersheds, more than one reservoir per watershed, and more than 1 channel per reservoir can be done using Eqs. (2.20) and (2.8). It is noted that the watershed is an autonomous system, whereas the reservoir is governed by the control law, and the channel depends on the outflow from the reservoir, although is not directly controlled.

2.3 Reactive and Predictive Control Strategies

The control strategies tested in this paper are focused on reducing flood effects. Here in this paper, we define it as a composite function accounting for local floods in reservoirs and channels, while minimizing rapid changes in valve operation. We can generally write the flood performance as a function defined for (n_s) systems accounting for flooding (e.g., reservoirs and channels) with different number of components per each system that impacts the flood performance ($c(i)$) (e.g., flood performance for reservoirs is associated with water levels and control deviations, whereas for channels is only associated with water levels). Therefore, we can generally write flood performance as linear combinations between weights and functions for each component of each system associated with floods, such that:

$$\text{Flood Performance} = \sum_{i_s=1}^{n_s} \sum_{j_c=1}^{c(i)} \alpha_{i_s,j_c} f_{i_s,j}(\boldsymbol{X}) \tag{2.32}$$

where $\boldsymbol{X}$ is the state matrix concatenating $\boldsymbol{x}(k)$ for all simulation time.

The aforementioned equation is detailed defined in the objective function used to describe the flood mitigation performance in Sec. 2.3.4. This particular function operates in all modeled states returning a number a real number. Although the flood performance was defined here, only the Model Predictive Control strategy is able to control all parts of the system (e.g., channels and reservoirs) and act directly to maximize it, since the reactive controls are developed only using the reservoir dynamics. This section is organized as follows: first we describe the reactive control strategies tested in this paper and following that, we introduce a non-linear model predictive control algorithm to control valve operations in stormwater reservoirs.

2.3.1 Discrete Linear Quadratic Regulator

Given a linearized time-invariant state space representation of the reservoir dynamics, the linear quadratic regulator strategy finds an optimal control signal for time step k minimizing a quadratic cost function, solved as an unconstrained convex optimization problem given by

$$\min_{\boldsymbol{u}} J(\boldsymbol{u}) = \sum_{n=1}^{\infty} \left[(\boldsymbol{h}^r(k))^T \boldsymbol{Q} \boldsymbol{h}^r(k) + (\boldsymbol{u}^r(k))^T \boldsymbol{R} \boldsymbol{u}^r(k) \right], \tag{2.33}$$

where $\boldsymbol{Q}$, and $\boldsymbol{R}$ are tuned symmetric positive semi-definite matrices representing the setpoints, cost of the states, cost of controls and cross-term costs.

This particular control strategy only considers the reservoir dynamics. Therefore, the coupled flood performance of this case only focus on reservoir water depth and control energy as shown in aforementioned equation. During the period where the dynamics are unchanged (e.g., steady inflows from the watersheds), the performance of the LQR control is optimal (Wong e Kerkez, 2018). The solution of this equation given by the discrete algebraic Riccati equation (DARE) (Pappas et al., 1980), consists into finding a $\boldsymbol{P}(k)$ matrix (cost-to-go) and a closed-loop feedback gain $\boldsymbol{K}(k)$, such that

$$\boldsymbol{K}(k) = \left(\boldsymbol{R} + (\boldsymbol{B}^r(k))^T \boldsymbol{P}(k) \boldsymbol{B}^r(k) \right)^{-1} (\boldsymbol{B}^r(k))^T \boldsymbol{P}(k) \boldsymbol{A}^r(k). \tag{2.34}$$

where the aforementioned matrices $\boldsymbol{P}(k)$ and $\boldsymbol{K}(k)$ can be solved using the *dlqr* function on Matlab.

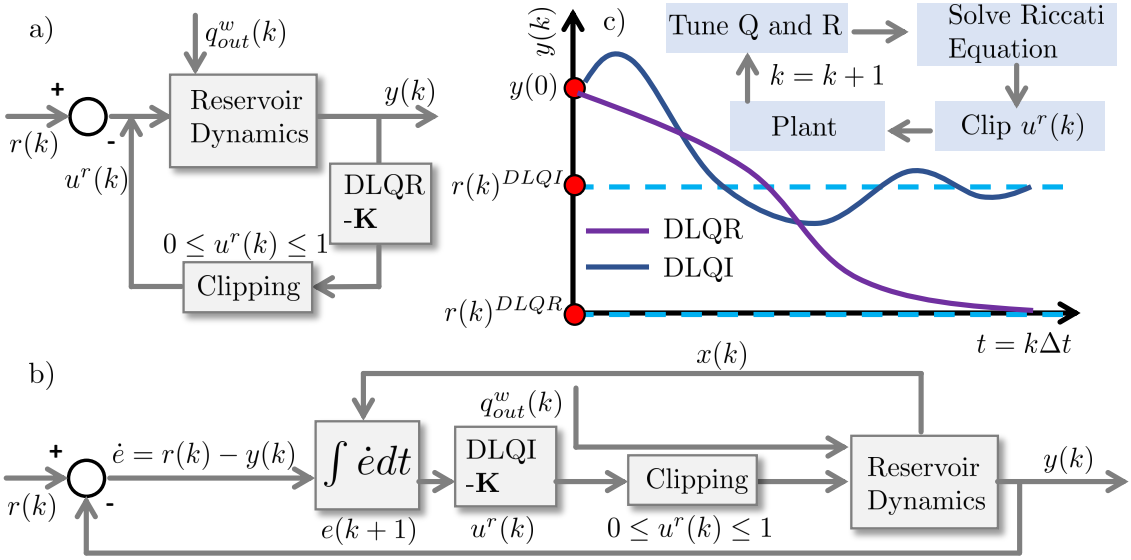

Figure 2.3. Controls based on the solution of Riccati Equation. Part a) represents the closed-loop system of the discretized linear quadratic regulator, Part b) is the block diagram of the discretized linear quadratic integrator with servo control, and part c) represents a schematic objective of the control approach.

A schematic detail of the closed-loop system for DLQR is presented in Fig. 2.3 part a). In this control algorithm, we are only using the reservoir plant in the dynamics. To design the state feed-back gain matrix $\boldsymbol{K}$, we can first tune $\boldsymbol{Q} = \boldsymbol{C}^T\boldsymbol{C}$ and $\boldsymbol{R} = \boldsymbol{I}_{n_r}$ as a first attempt. Basically, the DLQR control tends to find an optimal control for time $(k+1)$ that ultimately stabilize the reservoir dynamics or, in other words, tends to release the water considering the costs of rapid changes in the valves. To ensure physical constraints in the inputs (Wong e Kerkez, 2018), we limit the feed-back gain to

A schematic detail of the closed-loop system for DLQR is presented in Fig. 2.3 part a).

$$\boldsymbol{u}^r(k) = -\boldsymbol{K}\boldsymbol{h}^r(k) \tag{2.35a}$$

$$0 \leq u_i^r(k) \leq 1, \quad i = \{1, 2, \ldots, n_r\}. \tag{2.35b}$$

2.3.2 Discrete Linear Quadratic Integrator

The linear quadratic integrator works similarly to the DLQR control; however, an augmented dynamical system to account for a reference tracking setpoint (Young e Willems, 1972) is developed. The system dynamics is augmented to include the temporal evolution of the integral of the error between the reference and the output. The setpoint reference can be a constant value or a time-varying function representing the goal of the control technique. Assuming the error between states and outputs as $\dot{\boldsymbol{e}}(k) = \boldsymbol{r}(k) - \boldsymbol{y}(k)$ and discretizing it by an explicit forward Euler method in terms of the error integral ($\boldsymbol{e}(k)$), the augmented dynamical system can be given as

$$\begin{bmatrix} \boldsymbol{h}^r(k+1) \\ \boldsymbol{e}(k+1) \end{bmatrix} = \begin{bmatrix} \boldsymbol{A}^r(k) & \boldsymbol{O}_{n_r \times n_r} \\ -\boldsymbol{C}^r & \boldsymbol{I}_{n_r} \end{bmatrix} \begin{bmatrix} \boldsymbol{h}^r(k) \\ \boldsymbol{e}(k) \end{bmatrix} + \begin{bmatrix} \boldsymbol{B}^r(k) \\ \boldsymbol{O}_{n_r \times n_r} \end{bmatrix} \boldsymbol{u}^r(k) + \tilde{\boldsymbol{\psi}}^r(k, \boldsymbol{x}_*^r, \boldsymbol{u}_*^r) + \Delta t \begin{bmatrix} \boldsymbol{O}_{n_r \times 1} \\ \boldsymbol{1}_{n_r \times 1} \end{bmatrix} \boldsymbol{r}(k) \tag{2.36}$$

where $\boldsymbol{r}(k)$ is a setpoint or reference goal (e.g., minimum water surface depth to maintain natural ecosystems in the reservoir) and $\boldsymbol{C}^r = I_{n_r}$.

The closed-loop system for the DLQI is presented in Fig. 2.3 part b). A known input given is by $q^w_{out}(k)$, which changes the dynamics over time. The solution of the DARE is performed with

Table 2.2. Types of static ruled-based controls.

Type	Description
Passive Control (a)	Valve always 100% open
Detention Control (b)	If an event occurs, valve opening = 0% After the event, valve opening = 0% for t_d Else, valve opening = 100%
On/Off (c)	If $h < h_{cr}$, valve opening = 0% If $h \geq h_{cr}$, valve opening = 100% Else, valve opening = 0%

the coefficients of matrix $\boldsymbol{Q}$ (see Eq. (2.33) and Fig. 2.3) representative of the deviations in states, outputs and from matrix $\boldsymbol{R}$ control signal of $1 \times 10^0, 1.5 \times 10^3$ and 1×10^2, respectively. The number of integrators is assumed to be equal the number of outputs, hence all nodes are considered observable. After determining the optimal feedback gain, to ensure physical constraints, we also clip the control signal following Eq. (2.35) as shown in Fig. 2.6 part b). The control input can be separated into

$$\boldsymbol{u}^r(k) = -\begin{bmatrix} \boldsymbol{k}_s & \boldsymbol{k}_e \end{bmatrix} \begin{bmatrix} \boldsymbol{h}^r(k) \\ \boldsymbol{e}(k) \end{bmatrix}, \tag{2.37}$$

where $\boldsymbol{k}_s$ is the system feedback gain and $\boldsymbol{k}_e$ the servo feedback gain.

The ultimate objectives of DLQR and DLQI are presented in Fig. 2.3 part c). While DLQR tends to find a control schedule steering the output function to zero (e.g., rapidly release stored water and decrease $h^r(k)$ considering control energy), DLQI does a similar approach but for a reference water level $r(k)^{DLQI}$ (i.e., a given expected reservoir water level).

2.3.3 Ruled-Based Controls

Typically, stormwater systems are passive or controlled by ruled-based reactive and local controls, sometimes even manually performed by operators (Schmitt et al., 2020; Shishegar et al., 2019a; García et al., 2015). Although the control rule of these methods seem logical and easily applicable for simple storm events, they can fail to control more complex cases as fast consecutive storms by not predicting the future behavior of the system (Lund et al., 2018; Sharior et al., 2019b). Some of the most common rules for reservoirs for flood control are presented in Table 2.2 and tested in this paper. Some control decisions are made for these type of heuristic controls, such as the critical water surface depth to open the valves for the on-off approach and the required retention time after a storm event to start releasing water for the detention control approach. These parameters were assumed as h_{cr} = 3 m (i.e., representing a critical level in terms of flood management) and t_d = 6 hrs (i.e., representing a minimum detention time for sedimentation).

2.3.4 Model Predictive Control

For a given time, the Model Predictive Control strategy estimates the future behavior of the system, finds the solution of an optimization problem and defines a control trajectory. The control strategy is estimated with actual and predicted states. As a result, a simplified plant of the complete dynamical system (e.g., a simplified version of the Shallow Water Equations for 1-D and 2-D overland and channel flow) is utilized. The use of a simplified plant is typically a requirement in order to have a relatively fast model that could be run in real-time. The MPC approach can be time-consuming due to consecutive optimizations, therefore defining the proper model simplifications in the plant while maintaining accurate solutions is a challenge (Lund et al., 2018).

Moreover, due to the nature of hydraulic and hydrological systems, the selection of the optimizer solver is also important. We test state-of-the-art optimizers as Global Search (Kearfott, 2013), and Genetic Algorithms (Giacomoni e Joseph, 2017; Vose, 1999), and the Interior-Point method was selected due to its robustness and faster computation. Therefore, in this paper, we develop a non-linear MPC solved with the Interior-Point method (Potra e Wright, 2000). A flowchart of the MPC control algorithm is presented in Fig. 2.4. Generally, an optimal control trajectory is solved for a prediction horizon, although only a few of the control signals are implemented in real-time (see red line in the control signal chart at Fig. 2.4. Following that, a new optimization problem is solved resulting in the green line (see Fig. 2.4). The solution of the MPC optimization problem is an optimal control trajectory vector $\boldsymbol{U}_k = [u_1, u_2 \dots u_{N_p-1}]^T$ such that the following optimization problem is satisfied:

$$\min_{\boldsymbol{U}_k} \sum_{k=0}^{N_p-1} \boldsymbol{J}(\boldsymbol{x}(k+1), \boldsymbol{u}(k+1)) = \rho_u \Delta \boldsymbol{U}_k^T \Delta \boldsymbol{U}_k + \rho_x \Delta \boldsymbol{H}_k^T \Delta \boldsymbol{H} + \rho_r \left(\max \left(\boldsymbol{H}_k - \boldsymbol{h}_{ref}^r, 0 \right) \right) + \rho_c \left(\max \left(\boldsymbol{H}_k^c - \boldsymbol{h}_{ref}^c, 0 \right) \right) \tag{2.38}$$

$$\boldsymbol{E}\boldsymbol{x}(k+1) = \boldsymbol{A}(k)\boldsymbol{x}(k) + \boldsymbol{B}(k)\boldsymbol{u}(k) + \boldsymbol{\psi}(\boldsymbol{x}(k), \boldsymbol{x}_*^r, \boldsymbol{u}_*^r) \tag{2.39a}$$

$$\Delta u_{min} \leq \Delta u\,(k) \leq \Delta u_{max} \tag{2.39b}$$

$$\boldsymbol{y}\,(k) = \boldsymbol{C}\boldsymbol{x}(k) \tag{2.39c}$$

$$\boldsymbol{u}(k) \in \mathcal{U} \tag{2.39d}$$

$$\boldsymbol{x}(k) \in \mathcal{X} \tag{2.39e}$$

where $\boldsymbol{J}$ is the cost function (e.g., a function where weights are given for the control input (ρ_u), for the water surface depths in the reservoirs (ρ_r) and water surface depth in the channels ρ_c. N_p is the prediction horizon, $\Delta u(k) = u(k) - u(k-1)$, $\Delta \boldsymbol{U}_k = [\Delta u_1 \dots \Delta u_{N_p-1}]^T$ $\boldsymbol{H}_k = [h_1^r, \dots h_{N_p-1}^r]^T$, $\boldsymbol{H}^c = [\boldsymbol{h}_1^c, \dots \boldsymbol{h}_{N_p-1}^c]^T$ and $\mathcal{U}$ and § are the feasible sets of the control signal (i.e., $u(k) \in [0; 1]$ and $\boldsymbol{x}(k) \geq \boldsymbol{0}$). This objective function penalizes control schedules that generate states violating the threshold values for the maximum water surface depth in the channel and in the reservoir, while minimizing control energy.

2.4 Mathematical Model Application

This section describes the numerical case studies that we apply the modeling approach. All codes are available in a open repository (Gomes Jr., 2021). We attempt to answer the following questions:

- Q1: *How do control strategies primarily focused on increasing detention times affect flood control?*
- Q2: *How do state-of-the-art reactive controls based on real-time measurements perform against a predictive control based on rainfall forecasting?*
- Q3: *Do reactive controls perform better than passive control?*
- Q4: *Does the decrease in the control interval compensate the lack of predictability of reactive controls compared to a predictive control?*

To enable feasibility to use the controls in real world, we assume a control interval of 15-min for the reactive controls. Therefore, the control signal is assumed as a continuous piecewise within two intervals of 15-min. For the predictive control strategies, we assume a control interval of 60-min.

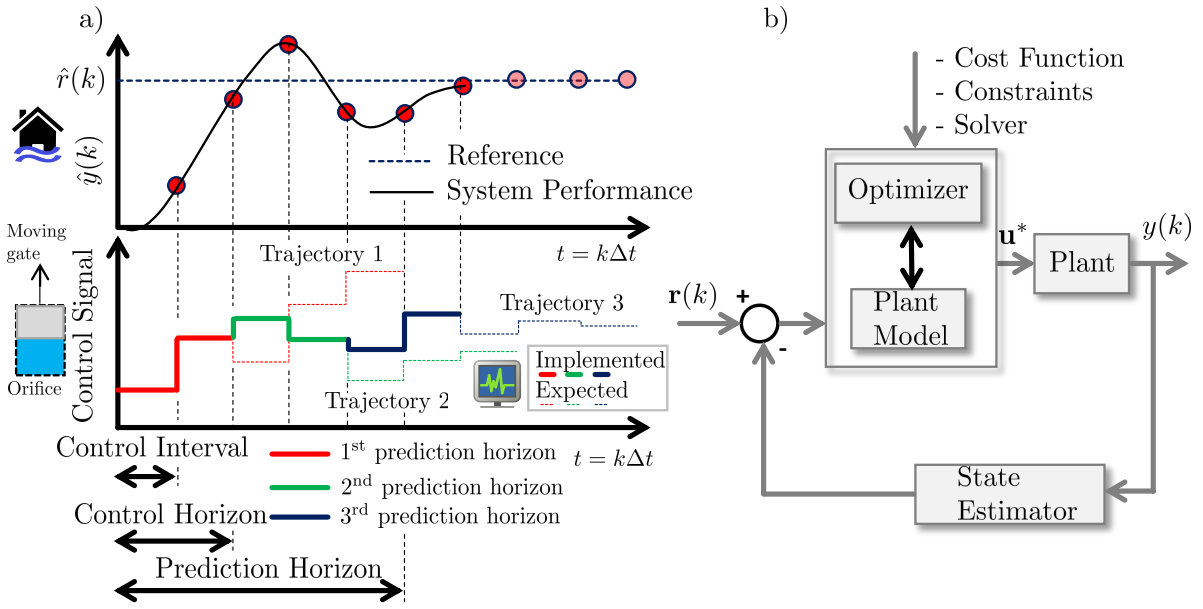

Figure 2.4. MPC schematic (a) and block diagram (b), where trajectories are generated for each moving prediction horizon, controls are assumed for every control horizon and are considered a constant piecewise within the control interval.

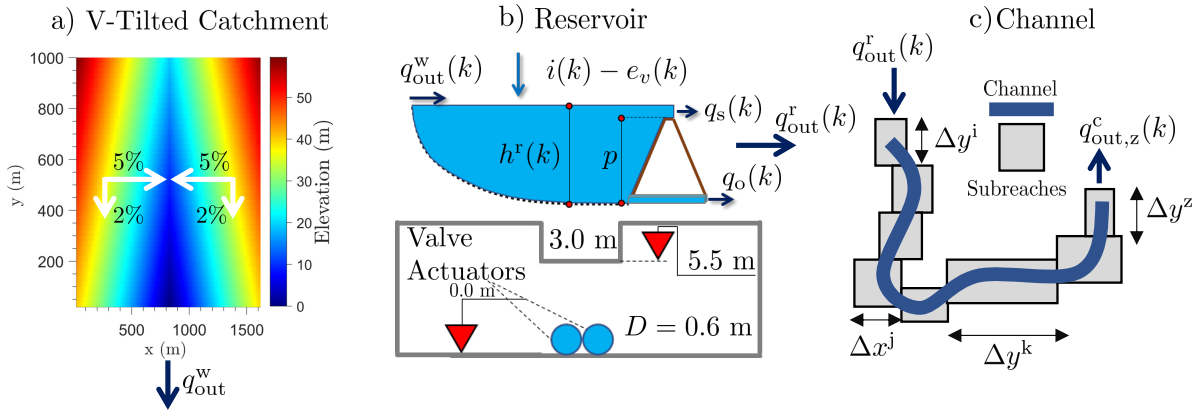

Figure 2.5. System composed by an autonomous watershed, a controlled reservoir and an autonomous channel receiving flow from the reservoir, where a) represents the watershed, (b) the reservoir, including spillway and orifice information, and c) a schematic representation of the 1-D channel.

We test the effects of RTC in a system defined by a watershed (a), reservoir (b) and channel (c), as shown in Fig. 2.5. The V-Tilted catchment has only one cell as the outlet (i_0 and $j_0 \in \mathbb{R}$) and dimensions of 1.62 km $\times$1 km and is composed by two rectangular planes of 0.8 km $\times$1 km m and a channel of 20 m in the connection within the planes (Fry e Maxwell, 2018a; Panday e Huyakorn, 2004b). The $x - x$ slopes in the hillslopes is 5% and the $y - y$ slope in the channel longitudinal direction is 2%. Two types of land cover are assumed, one for the hillslopes representing the watershed and another for the channel representing the main open channel drainage collector. The reservoir area is defined as 0.65% of the catchment area. The time step is assumed as 1 sec to ensure model numerical stability. All parameters of the model for each system are presented in the Table 2.3.

2.4.1 Numerical Case Study 1: Consecutive Design Storms

Typically, stormwater reservoirs are designed to hold rare storms such as 50 or 100-yr storms. However, two consecutive more recurrent storms can provide more flood risks in cases where the soil is likely more saturated and when control strategies focused on water quality by increasing retention

Table 2.3. Parameters required in the numerical case studies, where * represents changed values for the continuous simulation analysis.

System	Parameter	Value	Unit	Description
Watershed	R_w	20	m	Cell Resolution
	n_{per}	0.3, 0.18*	s.m$^{-1/3}$	Manning's coefficient
	ζ_{per}	110, 0.6*	mm	Suction Head
	$\Delta\theta_{per}$	0.453, 0.386*	cm^3.cm^{-3}	Moisture Deficit
	$k_{sat,per}$	10.92, 1.2*	mm.h^{-1}	Saturated Hydraulic Conductivity
	$h_{0,per}$	10, 10*	mm	Initial Abstraction
	$h_{0,imp}$	0, 0*	mm	Initial Abstraction
	$F_{d_0,imp}$	10, 10*	mm	Initial Infiltrated Volume
	n_{imp}	0.018	s.m$^{-1/3}$	Manning's coefficient
	e_t	2	mm.day^{-1}	Daily Evapotranspiration Rate
	Hillslopes	5	%	Slopes in x direction
	Channel Slope	2	%	Slopes in y direction
	n_{cells}	4050	-	Number of cells
	A_d	1.62	km^2	Drainage Area
Reservoir	$\omega^r(h^r)$	10,530	m^2	Reservoir Area
	k_o	1.538	m$^{1/2}$s^{-1}	Orifice coefficient
	k_s	6.3	m	Spillway coefficient
	h_s	5.5	m	Spillway elevation
	η	1	-	Reservoir average porosity
Channel	x	3	m	Channel width
	y	30	m	Sub-reach length
	n	0.3	s.m$^{-1/3}$	Manning's coefficient
	Sub-reaches	100	-	Number of reaches
	s_0	2.5	%	Channel bottom slopes
	$\frac{\partial h_o^c}{\partial y}$	2.5	%	Outlet Boundary Condition

times are implemented. Therefore, we test the efficiency of the control strategies for a 25-yr followed by a 10-yr design storm using a fitted Sherman intensity-duration-frequency curve for the available data for San Antonio - Texas (NOAA-Atlas, 14). The consecutive rainfalls have volumes of 7.5 and 6.3 inches, respectively. The landuse and landcover assumed for the watershed is equivalently to a recharge zone, with a relatively high infiltration capacity and can also be considered as a shrub forest for the hillslopes (Sharif et al., 2013; Rawls et al., 1983; Rossman, 2010). For the main channel, however, a concrete Manning's coefficient was considered. Using a moving prediction horizon of 8 hours, control horizons of 2 hours and control intervals of 1 hour, the performance of the predictive optimization-based control algorithm is compared to reactive approaches.

2.4.2 Numerical Case Study 2 - Continuous Simulation

In order to assess the trade-offs between flood mitigation and control efforts, we test the mathematical model through a real observed rainfall time series that occurred between 04/22/2021 and 07/22/2021 in San Antonio Texas (USGS, 2021). The cumulative rainfall in this period exceeds the average 30-yr rainfall pattern and can be considered an intense rainy season (Gregg Eckhardt, 2021). Moreover, we also test a change in the land cover from a recharge zone to a clay soil (Furl et al., 2018). The hillslopes roughness were also changed to represent urban areas. Using a moving prediction horizon of 2 hours (e.g., most radars have a good precision within this interval) (Lund et al., 2018), control horizons of 2 hours and control intervals of 1 hour, the performance of the optimization-based control algorithm is compared to static-rules approaches.

2.4.3 Performance Evaluation

The metrics used in this paper to evaluate the control performance were the (a) Peak Flow Reduction η_p, (b) Relative Maximum Flood Depth η, (c) Relative Control Effort η_c, and (d) Flood Duration η_d. Each metric is applied for all control methods with m representing the index of the control strategy. Given a duration from a initial time-step k_b and a final time-step k_f, the duration $\Delta k = k_f - k_b$ are defined to capture a particular important time (e.g., maximum outflow peak). The concatenated states at this interval are vectors with Δk rows for outflows and controls and matrices with Δk rows for the channel water depth. We denote the symbol † for concatenated states spanned over time. Therefore, the evaluation metrics are represented as follows:

$$\eta_{p,m} = \frac{\max(\boldsymbol{q}_{out}^{w,\dagger}(k_b : k_f)) - \max(\boldsymbol{q}_{out,m}^{r,\dagger}(k_b : k_f))}{\max(\boldsymbol{q}_{out}^{w,\dagger}(k_b : k_f))}, \tag{2.40}$$

$$\eta_{r,m} = \frac{\max(\boldsymbol{H}_m^{c,\dagger}(k_b : k_f))}{h_{lim}^c}, \tag{2.41}$$

$$\eta_{c,m}(k) = \frac{\sum_{i=k_b}^{k_f} \Delta u_m^{r,\dagger}(i)}{\max\limits_{m \in \mathfrak{C}} \sum_{i=k_b}^{k_f} \Delta u^r(i)}, \tag{2.42}$$

$$\eta_{d,m}(k) = \mathbf{n}\Big(\bigcup_{t \in \mathfrak{T}} (\boldsymbol{h}_{c,m}^{\dagger} > h_c^{lim})\Big)\Delta t, \tag{2.43}$$

where h_{lim}^c is the maximum allowable water surface depth in the channel, $\mathfrak{C}$ is the set of assessed controls, m is the assessed control, $\mathfrak{T}$ is the duration set of the analysis. Other similar metrics applied to real-time controls can be found in Wong e Kerkez (2018); Shishegar et al. (2019a); Schmitt et al. (2020).

2.5 Results and Discussion

This section presents results and discussions on how MPC can increase flood performance compared to other reactive control strategies. First, we assess the control performance to critical consecutive design storms in San Antonio in Sec. 2.5.1. Following that, we perform a continuous simulation with observed data and assess the performance of MPC in contrast to reactive controls in Sec. 2.5.2

2.5.1 Design Storms

The comparison between reactive and predictive control approaches is shown in Fig. 2.6. The events produced similar peaks due to the initial saturation provided from the first storm. Outflow peaks in the reservoir increased from the first to the second storm, even though the runoff from the catchment decreased. The performance summary of ruled-based control against model predictive control is shown in Table 2.4. The control approach that generated the highest outflow peak was the detention control. This approach basically started to release the stored water at 18 hours from the beginning of the first event (i.e., 6-hours from the end of the first storm event) and it matched with the start of the intense inflow runoff volume at the detention basin originated from the second storm. Only the detention control and the on/off strategy reached the spillway elevation and hence had the higher outflows. For the MPC control, smaller flows than all RBCs are observed. From these results it is noted that reactive controls, especially the ones primarily designed for water quality purposes, can increase flood and consequently erosion downstream for large storm events (Schmitt et al., 2020).

The detention pond dumps faster on the passive control strategy as expected. However the temporal evolution of the water surface depth in the reservoir had a similar behavior compared to DLQI and DLQR controls. It suggests that using reactive controls for relatively large floods might be

Table 2.4. Comparison within control strategies for a consecutive 25-yr, 12-hr and 10-yr, 12-hr design storm in San Antonio for a watershed in a recharge zone.

Type of Control	Control Strategy	Peak Flow Reduction 1st peak (%)	Peak Flow Reduction 2nd peak (%)	Relative Maximum Flood Depth (%)	Relative Control Effort (%)	Flood Duration (hr)
Static / Reactive	Passive	73.08	68.67	26.57	0.0	10.40
	On/Off	37.97	27.81	148.89	93.46	10.98
	Detention Control	15.01	1.09	229.87	15.58	8.38
	DLQI	72.11	67.54	30.18	61.37	11.15
	DLQR	72.42	67.91	29.01	53.74	10.83
Optimization-based / Predictive	Interior-Point Optimizer	79.39	76.02	2.55	48.91	2.2

as effective as the passive control. For the DLQI is noted that the state $h^r(k)$ is steered to the reference setpoint ($r(k) = 1$ m) where the system dynamics is not changing dramatically (i.e., cases where the inflow is steady). This type of control strategy is more suitable where constraints of minimum water depths are required in the reservoir (e.g., wetlands). Significant differences between the controls approaches; however, are depicted in the channel stage variation over time. For all reactive controls, periods of flooding occurred whereas the MPC control largely avoided it, although we assumed a perfect 8-hour rainfall forecasting.

For the MPC, a solution of a non-linear optimization problem is developed for each control horizon. We used the interior-point method, which is a gradient-based method dependent on the initial estimated control decision. Therefore, to initialize the optimization algorithm, we assume this initial point as a random combination from the previous control signal. Basically, a normal distributed random number with 0 average and 0.2 variance is generated ($\delta =\sim \mathcal{N}(0, 0.2)$), and applied to the previous control, such that the initial point for the optimization is $u_0(k+1) = u(k)(1+\delta)$. Defining this initial estimate; however, does not imply solutions only within this interval but actually can substantially decrease the computational time by starting in initial points nearby the previous control state.

2.5.2 Continuous Simulation

The comparison between reactive approaches with an optimized-based/predictive control approach in a continuous simulation is shown in Fig. 2.7 and the trade-offs between control effort and flood duration for the continuous modeling are shown in Fig. 2.8. In this analysis, we assume a 2-hour rainfall forecasting, showing the performance of RTC for low degrees of uncertainty in rainfall. In Fig. 2.7, a detail of the storm event that occurred in May 1st of 2021 shows the hydrographs and the water surface depths in the reservoir and channels, as well as the control schedules over time.

This rainfall event was rapid and intense, producing a high inflow peak due to the initial saturation of the soil from previous rainfall events. The hydrograph shows that the on/off and detention control had the highest outflows peak. The valves were mostly closed for all reactive control strategies in the arriving of the inflow peak since no relatively high water stages were yet observed. However, the on/off started this event with approximately 3 m of water stage (i.e., its control strategy is regulated by this water depth).

While almost all other control strategies (i.e., except detention control) were able to release the accumulated volume with reasonable maximum channel water depths, the On/Off strategy, however, produced the highest outflow peak. It occurred due to opening both orifices lately without avoiding spillway outflow. The risk of flooding is generally increased with this strategy. Although the detention control had some of the inflow volume spilled, all the stored volume correspondent to approximately

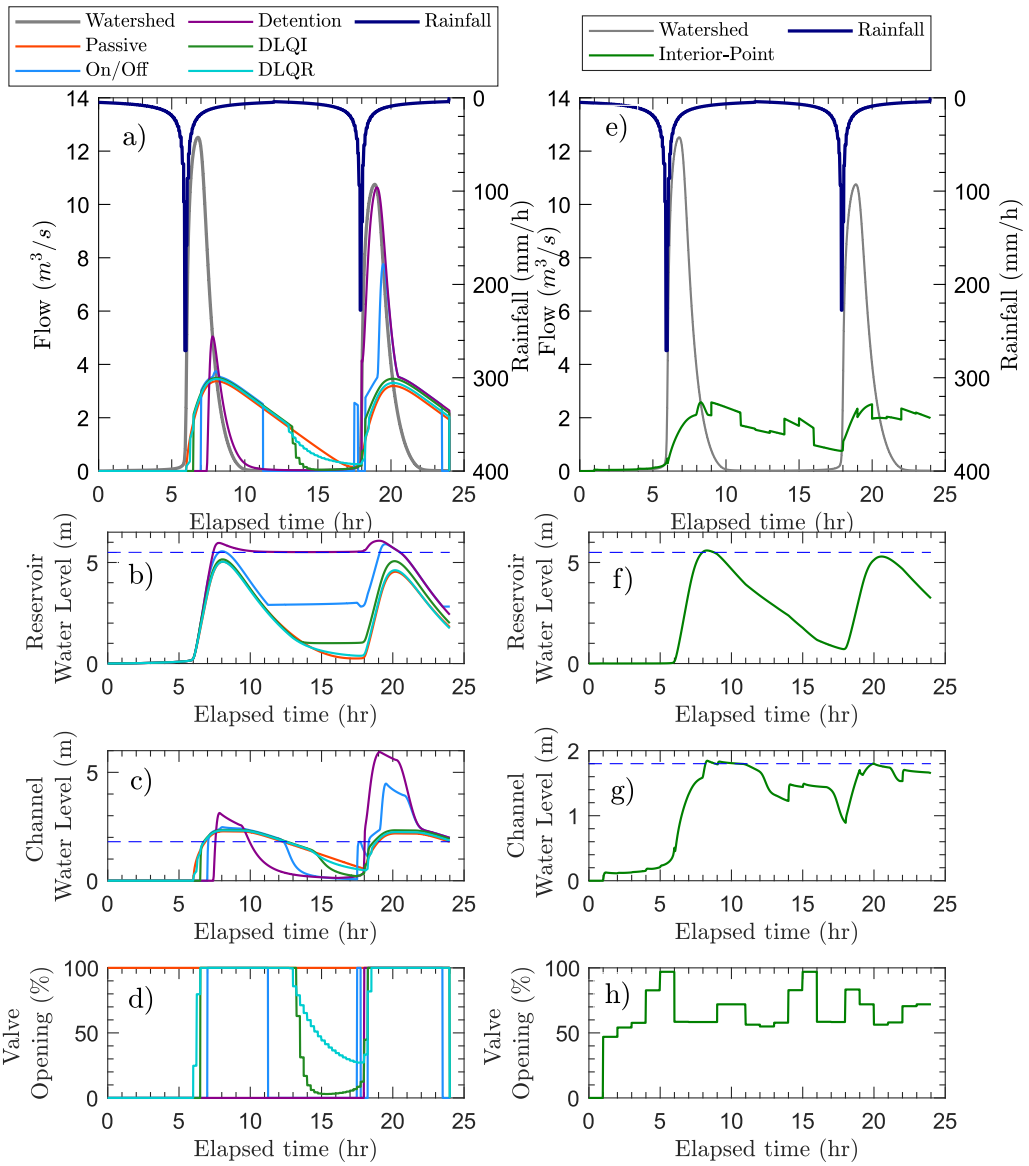

Figure 2.6. Control performance of ruled-based approaches in comparison with optimization-based control using the Interior-Point method, where the dashed blue lines in b) and f) represent the spillway elevation and in c) and g) they represent the allowed water surface depth in the channel for a 25-yr, 12-hr storm followed by a 10-yr, 12-hr storm.

2.5 m (i.e., 5.5 m - 3.0 m) of the pond stored volume (see Fig. 2.7 part b) was successfully released 6 hours following the end of the rainfall event. As shown in Sec. 2.5.1, this available time might not always be feasible if a new storm event occur in this interval.

The DLQI, DLQR and Passive control strategies had had similar outflows. The common reaction of the regulators is to stabilize the changing dynamics described by $\boldsymbol{\psi}(k, \boldsymbol{x}(k), \boldsymbol{u}(k))$ due to $q^{w}_{out}(k)$ (see Fig. 2.3), therefore, rapid valve openings is a common solution chosen by these controls depending on the tunned matrices Q and R. One also can tune these matrices differently to favorably change the relative importance of variations in control schedule and water stage over time.

It is noted from Fig. 2.7 that the the detention control and the on/off control had the highest stored water surface depths, which is in accordance with (Sharior et al., 2019b). The latter control; however, returned for the regulated water surface depth relatively fast due to decide to open the valves after reaching 3 m whereas the detention control only released the flow hours afterwards. Moreover, even after the event, some volume is still stored for all controls. Outflow discharge only occurs when

$h^r(k) > \max(h_o, 0.2 \times D_h)$, where D_h is the hydraulic diameter. Thus, the minimum water surface depth is approximately 0.24 m.

An interesting result is the fact that the predictive control had a relatively larger stored water surface depth in the reservoir compared to the other controls. Despite this fact, it still regulated the maximum water surface depth in the channel below the reference h_{ref} of 1.8 m, as shown in Fig. 2.7 c). During the peak of the storms, the predictive control decided to partially close the valves, which was a feasible decision because the water surface depth in the pond was below the spillway elevation and no intense inflow was expected within the next few hours. This type of decision is counter intuitive and pinpoints the benefit of using predictive optimization-based control algorithms rather than solely expertise-based manually operations in real-time.

Frequency plots presented in Fig. 2.9 shows the exceedance probability of outflows and stages in the reservoir and channel. The on/off control is more likely to release high flows, which can cause erosion (Schmitt et al., 2020). This control is similar to a pond with the spillway in an elevation of 2.5 m above the ground. It certainly has the benefits of water quality enhancement due to larger retention times (Sharior et al., 2019b; Wong e Kerkez, 2018) but this approach was the one with higher outflows and hence water surface depths in the channel. The DLQR had the more spread flow-duration curve, indicating that this control typically can release flows throughout a larger period of time in a relatively small magnitude. This is particularly important since the pond can be slowly emptied when no future inflow is forecasted. The DLQI, as well as the on/off, had a flat duration curve around their regulated water surface depths of 3 m and 1 m, respectively, which indicates that they can satisfy their control goals over a rainy season.

Results shown in Fig. 2.9 part c) and d) show an estimate of the flood probability in the channel. They indicate that the passive control is the most suitable reactive control to avoid flood in the channel. However, the DLQR had approximately the same effect for mitigating the flood in the channel, but added the benefit of maintaining water in the channel and in the reservoir for longer periods of time. This type of RTC can, therefore, increase the period of time in the channel with some sort of baseflow (Xu et al., 2021). The predictive control had no probability of flood in the channel, as desired from the optimization function.

Another interesting analysis is the trade-offs between the control efforts and the flood duration. The largest controls efforts were provided by the on/off, detention control and DLQI. Since we tune Q with a high weight in the output deviation ($\dot{e} = r(k) - y(k)$), the control law rapidly tries to steer the system back to the defined reference setpoint, thus generating intense control efforts. This tuning can represent the operator preferences (Troutman et al., 2020a; Fraternali et al., 2012) and could be a time-varying function in terms of the rainfall forecastings, although most of control algorithms assume a constant value. The control approach with least control effort was the predictive control, which nearly had 10% of the detention control approach. The MPC problem for the continuous simulation was solved in approximately 30 minutes in a single core machine.

2.6 Conclusions, Limitations, and Future Works

The real-time control of watersheds, reservoirs and channels can decrease the risk of flooding in stormwater systems by better controlling their flow release over time. The application of different types of optimization-based and reactive controls algorithms was tested in a case study, and given the questions posed in Section 2.4, the results support the following conclusions.

- A1: The reactive controls have lower flood mitigation performance when compared to the predictive strategy, especially the water-quality controls of the on/off control and the detention control.

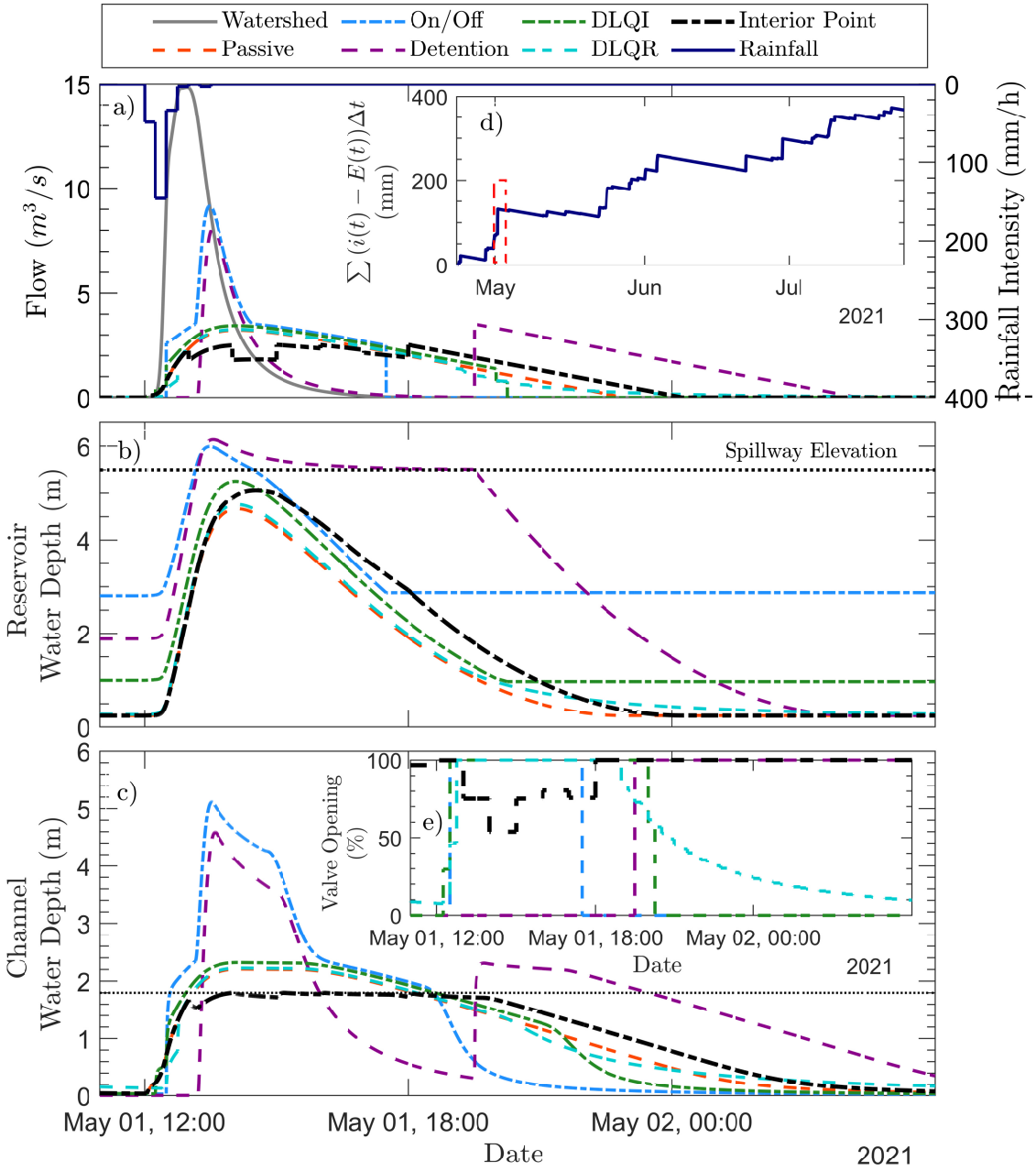

Figure 2.7. Control Performance of ruled-based approaches in comparison with optimization-based control using the Interior-Point method for the rainy season of 2021 in San Antonio, where the dotted black lines in b) and c) represent the spillway elevation and maximum allowable water surface depth in the channel, respectively. Parts d) and e) represent the net rainfall and control schedule of the assessed control algorithms, respectively.

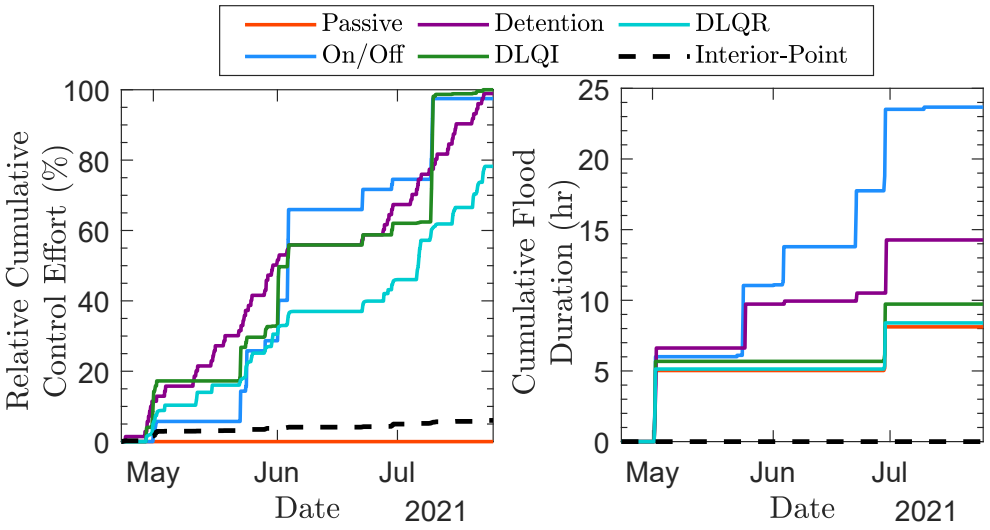

Figure 2.8. Trade-offs between control effort and flood duration for a rainy season in an urbanized watershed with poor infiltration capacity.

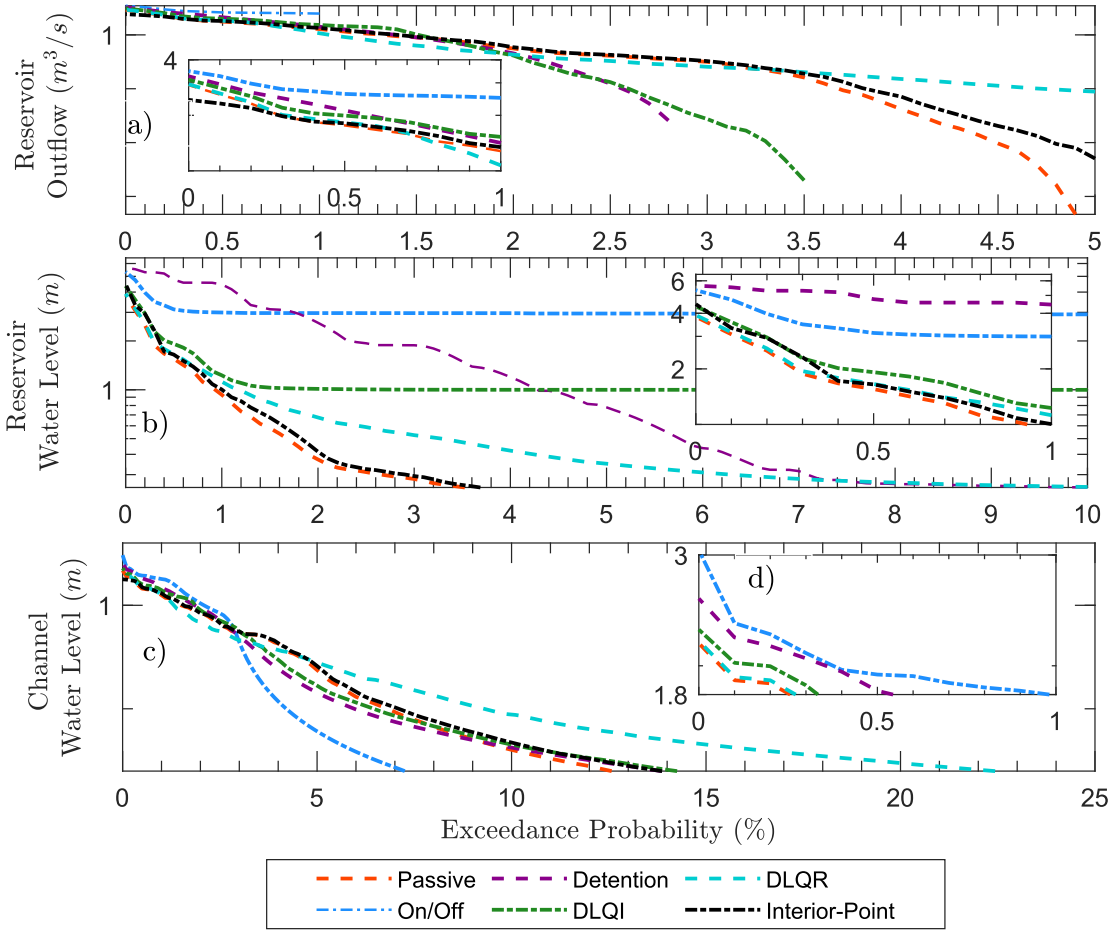

Figure 2.9. Duration curves comparing reactive and predictive controls, where a), b), c), represent the exceedance probability of flows and levels in the reservoir, and levels in the channel, respectively, and d) represents a zoom of the channel flood exceedance probability.

- A2: The MPC control outperforms all other control strategies for flood mitigation performance and also require less control effort.
- A3: The DLQR and DLQI are as effective as the passive control for flood mitigation in the channel. However, they add more specific benefits as maintain a desired water surface depth in the pond (DLQI) and increase residence times and low flows (DLQR). However, tuning the weighing matrices $\boldsymbol{Q}$ and $\boldsymbol{R}$ from the DLQR and LQR optimization problems can be complex due to different units in the objective function. Therefore, using normalized objective functions could be an alternative.
- A4: Despite the reactive controls were applied each 15-min and the predictive control each 60-min, the larger opportunity to change the valve operation had not compensate the lack of predictability of the states for the reactive controls, neither for large critical design storms events, nor for observed rainfall events.

Although only flood performance is evaluated in this paper, this type of modeling approach can be flexible enough to combine different control purposes according to the expected rainfall forecastings. Depending on the estimated future states of the system, one can change the objective functions of the system to shift from a flood focused strategy to a water quality control, increasing detention times. Moreover, since uncertainty in forecasting increase over the predicted horizon, it is possible to tune the weight matrices in the objective function following the uncertainty associated in the forecasting and thus giving more importance for short duration forecastings by increasing the cost weights associated with this duration.

Future application of the developed approach will consider scenarios of uncertainty in rainfall, model parameters, and measurements noise. Moreover, the approach needs to be tested in real case studies, such as the Upper San Antonio river watershed, which contains some of the most advanced flood protection systems in the US. Comparisons of the simplified dynamical system with the state of the art hydraulic and hydrologic models, such as SWMM, GSSHA, HEC-RAS, InfoWorks, and many others are also warranted. This methodology can be easily expanded for systems with many watersheds, reservoirs, and channels.

2.7 Data Availability Statement

Some or all data, models, or code generated or used during the study are available in a repository or online in accordance with funder data retention policies. All functions, scripts, and input data including the state-space non-linear model, the model predictive control algorithm, and the ruled-based algorithms are available in Gomes Jr. (2021).

Acknowledgment

The authors gratefully acknowledge the support by the City of San Antonio, by the San Antonio River Authority, and by the National Science Foundation (NSF) under Grant 2015671.

2.8 Supplemental Materials

Tab. S1 is available online in the ASCE Library (www.ascelibrary.org).

References

Akan, O. A. (1993). *Urban stormwater hydrology: a guide to engineering calculations*. Crc Press.

Bartos, M. e Kerkez, B. (2021). Pipedream: An interactive digital twin model for natural and urban drainage systems. *Environmental Modelling & Software*, 144:105120.

Brasil, J., Macedo, M., Lago, C., Oliveira, T., Júnior, M., Oliveira, T., e Mendiondo, E. (2021). Nature-based solutions and real-time control: Challenges and opportunities. *Water*, 13(5):651.

Chang, S. e Wang, X. (2002). Courant number insensitive ce/se euler scheme. In *38th AIAA/ASME/SAE/ASEE Joint Propulsion Conference & Exhibit*, page 3890.

Chow, V. t. (2010b). *Applied hydrology*. Tata McGraw-Hill Education.

Cunge, J. (1969). On the subject of a flood propagation computation method (musklngum method). *Journal of Hydraulic Research*, 7(2):205–230.

Duchesne, S., Mailhot, A., Dequidt, E., e Villeneuve, J. P. (2001). Mathematical modeling of sewers under surcharge for real time control of combined sewer overflows. *Urban Water*, 3(4):241–252.

Fraternali, P., Castelletti, A., Soncini-Sessa, R., Ruiz, C. V., e Rizzoli, A. E. (2012). Putting humans in the loop: Social computing for water resources management. *Environmental Modelling & Software*, 37:68–77.

Fry, T. J. e Maxwell, R. M. (2018a). Using a distributed hydrologic model to improve the green infrastructure parameterization used in a lumped model. *Water*, 10(12):1756.

Furl, C., Ghebreyesus, D., e Sharif, H. O. (2018). Assessment of the performance of satellite-based precipitation products for flood events across diverse spatial scales using gssha modeling system. *Geosciences*, 8(6):191.

García, L., Barreiro-Gomez, J., Escobar, E., Téllez, D., Quijano, N., e Ocampo-Martinez, C. (2015). Modeling and real-time control of urban drainage systems: A review. *Advances in Water Resources*, 85:120–132.

Gasper, R., Blohm, A., e Ruth, M. (2011). Social and economic impacts of climate change on the urban environment. *Current Opinion in Environmental Sustainability*, 3(3):150–157.

Giacomoni, M. e Joseph, J. (2017). Multi-objective evolutionary optimization and monte carlo simulation for placement of low impact development in the catchment scale. *Journal of Water Resources Planning and Management*, 143(9):04017053.

Gomes Jr. (2021). https://github.com/marcusnobrega-eng/Stormwater-RTC-Model. https://github.com/marcusnobrega-eng/Stormwater-RTC-Model.

Gomes Jr., M. N., Giacomoni, M. H., e Eduardo M. Mendiondo (2021a). Simpósio brasileiro de recursos hídricos. In *The role of raster resolution into overland flow and total suspended solids modeling in small urban catchments*, Belo Horizonte - Brazil. ABRH.

Gomes Jr., M. N., Giacomoni, M. H., Papagiannakis, A. T., Mendiondo, E. M., e Dornelles, F. (2021b). Spatial Assessment of Overland Flow, Pollutant Concentration, and First Flush Using a 2- D Non-Point Source Pollution and Hydrological Model for Urban Catchments. In *World Environmental and Water Resources Congress 2021: Planning a Resilient Future along America's Freshwaters - Selected Papers from the World Environmental and Water Resources Congress 2021*, pages 397–413.

Green, W. H. e Ampt, G. A. (1911). Studies on soil phyics. *The Journal of Agricultural Science*, 4(1):1–24.

Gregg Eckhardt (2021). Regional Climate and Water Availability.

Horváth, K., Petreczky, M., Rajaoarisoa, L., Duviella, E., e Chuquet, K. (2014). Mpc control of water level in a navigation canal-the cuinchy-fontinettes case study. In *2014 European Control Conference (ECC)*, pages 1337–1342. IEEE.

Joseph-Duran, B., Ocampo-Martinez, C., e Cembrano, G. (2015). Output-feedback control of combined sewer networks through receding horizon control with moving horizon estimation. *Water Resources Research*, 51(10):8129–8145.

Kearfott, R. B. (2013). *Rigorous global search: continuous problems*, volume 13. Springer Science & Business Media.

Kessler, R. (2011). Stormwater strategies: cities prepare aging infrastructure for climate change.

Kollet, S. J. e Maxwell, R. M. (2006a). Integrated surface–groundwater flow modeling: A free-surface overland flow boundary condition in a parallel groundwater flow model. *Advances in Water Resources*, 29(7):945–958.

Kumar, D. N., Baliarsingh, F., e Raju, K. S. (2011). Extended muskingum method for flood routing. *Journal of Hydro-environment Research*, 5(2):127–135.

Li, J. (2020). A data-driven improved fuzzy logic control optimization-simulation tool for reducing flooding volume at downstream urban drainage systems. *Science of the Total Environment*, 732:138931.

Liu, Q. e Singh, V. (2004). Effect of microtopography, slope length and gradient, and vegetative cover on overland flow through simulation. *Journal of Hydrologic Engineering*, 9(5):375–382.

Lund, N. S. V., Falk, A. K. V., Borup, M., Madsen, H., e Steen Mikkelsen, P. (2018). Model predictive control of urban drainage systems: A review and perspective towards smart real-time water management. *Critical Reviews in Environmental Science and Technology*, 48(3):279–339.

Maxwell, R. M., Putti, M., Meyerhoff, S., Delfs, J.-O., Ferguson, I. M., Ivanov, V., Kim, J., Kolditz, O., Kollet, S. J., Kumar, M., Lopez, S., Niu, J., Paniconi, C., Park, Y.-J., Phanikumar, M. S., Shen, C., Sudicky, E., e Sulis, M. (2014b). Surface-subsurface model intercomparison: A first set of benchmark results to diagnose integrated hydrology and feedbacks. *Water Resources Research*, 50:1531–1549.

McCarthy, G. T. (1938). The unit hydrograph and flood routing. In *proceedings of Conference of North Atlantic Division, US Army Corps of Engineers, 1938*, pages 608–609.

Mullapudi, A., Lewis, M. J., Gruden, C. L., e Kerkez, B. (2020). Deep reinforcement learning for the real time control of stormwater systems. *Advances in Water Resources*, 140:103600.

NOAA-Atlas (14). Precipitation-frequency atlas of the united states.

Ocampo-Martínez, C. e Puig, V. (2010). Piece-wise linear functions-based model predictive control of large-scale sewage systems. *IET control theory & applications*, 4(9):1581–1593.

Our World in data (2021). Global damage costs from natural disasters, All natural disasters, 1980 to 2019.

Panday, S. e Huyakorn, P. S. (2004b). A fully coupled physically-based spatially-distributed model for evaluating surface/subsurface flow. *Advances in water Resources*, 27(4):361–382.

Pappas, T., Laub, A., e Sandell, N. (1980). On the numerical solution of the discrete-time algebraic riccati equation. *IEEE Transactions on Automatic Control*, 25(4):631–641.

Potra, F. A. e Wright, S. J. (2000). Interior-point methods. *Journal of computational and applied mathematics*, 124(1-2):281–302.

Rawls, W. J., Brakensiek, D. L., e Miller, N. (1983). Green-ampt infiltration parameters from soils data. *Journal of hydraulic engineering*, 109(1):62–70.

Richards, L. A. (1931). Capillary conduction of liquids through porous mediums. *Physics*, 1(5):318–333.

Rossman, L. A. (2010). *Storm water management model user's manual, version 5.0*. National Risk Management Research Laboratory, Office of Research andă. . . .

Schmitt, Z. K., Hodges, C. C., e Dymond, R. L. (2020). Simulation and assessment of long-term stormwater basin performance under real-time control retrofits. *Urban Water Journal*, 17(5):467–480.

Sharif, H. O., Chintalapudi, S., Hassan, A. A., Xie, H., e Zeitler, J. (2013). Physically based hydrological modeling of the 2002 floods in san antonio, texas. *Journal of hydrologic Engineering*, 18(2):228–236.

Sharior, S., McDonald, W., e Parolari, A. J. (2019b). Improved reliability of stormwater detention basin performance through water quality data-informed real-time control. *Journal of Hydrology*, 573(March):422–431.

Shishegar, S., Duchesne, S., e Pelletier, G. (2019a). An integrated optimization and rule-based approach for predictive real time control of urban stormwater management systems. *Journal of Hydrology*, 577(June):124000.

Troutman, S. C., Love, N. G., e Kerkez, B. (2020a). Balancing water quality and flows in combined sewer systems using real-time control. *Environmental Science: Water Research and Technology*, 6(5):1357–1369.

USACE (2000). Hydrologic Modeling System Technical Reference Manual. *Hydrogeology Journal: Hydrologic Modeling System: Technical Reference Manual*, (March):145.

USGS (2021). USGS Current Conditions for Texas.

Vose, M. D. (1999). *The simple genetic algorithm: foundations and theory*. MIT press.

Wang, S., Taha, A. F., e Abokifa, A. A. (2021). How effective is model predictive control in real-time water quality regulation? state-space modeling and scalable control. *Water Resources Research*, 57(5):26.

Wing, O. E., Pinter, N., Bates, P. D., e Kousky, C. (2020). New insights into us flood vulnerability revealed from flood insurance big data. *Nature communications*, 11(1):1–10.

Wong, B. P. e Kerkez, B. (2018). Real-Time Control of Urban Headwater Catchments Through Linear Feedback: Performance, Analysis, and Site Selection. *Water Resources Research*, 54(10):7309–7330.

Xu, W. D., Burns, M. J., Cherqui, F., e Fletcher, T. D. (2021). Enhancing stormwater control measures using real-time control technology: A review. *Urban Water Journal*, 18(2):101–114.

Young, P. C. e Willems, J. (1972). An approach to the linear multivariable servomechanism problem. *International journal of control*, 15(5):961–979.

Zhang, W., Villarini, G., Vecchi, G. A., e Smith, J. A. (2018). Urbanization exacerbated the rainfall and flooding caused by hurricane harvey in houston. *Nature*, 563(7731):384–388.

3 HYDROPOL2D - DISTRIBUTED HYDRODYNAMIC AND WATER QUALITY MODEL: CHALLENGES AND OPPORTUNITIES IN POORLY-GAUGED CATCHMENTS

A modified version was published as: M. N. Gomes, C. A. F. do Lago, L. M. C. Rápalo, P. T. S. Oliveira, M. H. Giacomoni, E. M. Mendiondo, HydroPol2d Distributed Hydrodynamic and Water Quality model: Challenges and Opportunities in Poorly Gauged Catchments, *Journal of Hydrology* 625 (2023) 129982.

Graphical Abstract

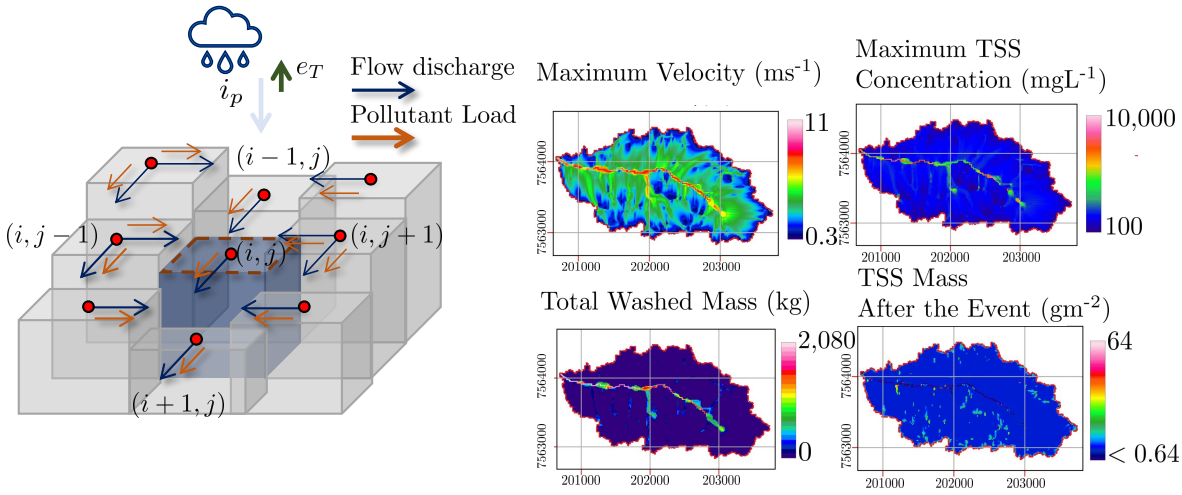

Highlights

- A new coupled hydrodynamic and water quality 2D model is developed (HydroPol2D).
- The spatial-temporal dynamics of Total Suspended Solids (TSS) is investigated.
- We estimate TSS transport rates and first flush for a 1-year return period.
- The maximum TSS load is 2.56 ± 0.4 kgs^{-1}km^{-2} for a 40% uncertainty in water quality parameters.
- HydroPol2D can also be used for flood inundation mapping, infiltration, and evapotranspiration modeling.

Abstract

Floods are one of the deadliest natural hazards and are exacerbated by changes in land-use and climate. Urban development decreases infiltration by reducing pervious areas and increases the accumulation of pollutants during dry weather. It also decreases infiltration by reducing pervious areas and increases the accumulation of pollutants during dry periods. During rainy events, there is an increase in pollution concentrations and runoff that may be a source of water supply during drought periods. Modeling the quantity and quality dynamics of stormwater runoff requires a coupled hydrodynamic module capable of estimating the transport and fate of pollutants. In this paper, we evaluate the applicability of a distributed hydrodynamic model coupled with a water quality model (HydroPol2D). First, the model is compared to GSSHA and WCA2D in the V-Tilted catchment, and the limitation of the critical velocity of WCA2D is investigated. We also applied the model in a

laboratory wooden board catchment, focusing on the validation of the numerical approach to simulate water quality dynamics. Then, we apply HydroPol2D in the Tijuco Preto catchment, in Sao Carlos - Brazil, and compare the modeled results with the full momentum solver of the HEC-RAS 2D. This catchment shares similar characteristics with many poorly-gauged and human-impacted catchments worldwide. The implementation of the model, the governing equations, and the estimation of input data are discussed, indicating the challenges and opportunities to scale HydroPol2D into the reality of data scarcity of larger poorly-gauged catchments. For a 1-yr return period of rainfall and antecedent dry days, and assuming an uncertainty of 40% in the water quality parameters, the results indicate that the maximum concentration of total suspended solids (TSS), the maximum load and the mass of the pollutant washed in 30% of the volume are, 456 $\pm$ 260 $mgL^{-1}km^{-2}$, 2.56 ± 0.4 $kgs^{-1}km^{-2}$, and 89% $\pm$ 10%, respectively.
Keywords: 2D Hydrodynamic Model, Water Quality Model, Build-up and Wash-off, Water-Adaptive-Design, Low Impact Development, Pollutant Transport and Fate.

3.1 Introduction

The spatial scale is a determinant factor to decide which tools to apply in water resources problems such as flood management (Kreibich et al., 2022), flood modeling (Gomes Jr et al., 2023c), and spatial analysis of pollutants transport (Yanxia et al., 2022). Solutions to these problems typically require numerical modeling, and the quality of these models usually depends on data availability and the actual state-of-the-art conceptual models used to express complex phenomena of the water cycle.

Hydrologic, hydrodynamic, and pollutant transport models are fundamental tools for decision-making about mitigating floods and poor water quality (Fan e Collischonn, 2014). In the literature, there are a variety of models that aid in the quantification of hydrodynamic processes at different temporal and spatial scales. At the watershed scale, where these phenomena are usually expressed on larger time scales (e.g., hourly or daily), the Large-Scale Hydrological Model (MGB-IPH) (Collischonn et al., 2007; De Paiva et al., 2013) and the Hydrological Modeling and Analysis Platform (HyMAP) (Getirana et al., 2012) are examples.

At the scale of rapid response events and urban catchments, the Weighted Cellular Automata 2D (WCA2D) model (Guidolin et al., 2016), which uses the cellular automata approach to distribute runoff and estimate water surface flood maps, is another available model. Other fast flood models are available in the literature and focus mainly on simplifying non-linear hydrodynamic equations through assumptions such as the use of logic and linear runoff distribution rules (Jamali et al., 2018) or by data-driven approaches such as training neural networks to predict flood inundation maps (Kabir et al., 2020; do Lago et al., 2023).

Process-based models are typically more laborious than rapid flood models; however, they can better model events on the urban or rural scale and are not limited to the study area where they are applied. GSSHA (Gridded Surface / Subsurface Hydrologic Analysis) (Downer e Ogden, 2004) and SWAT (Soil and Water Assessment Tool) (Arnold et al., 2012), are examples of process-based models. GSSHA is often used to estimate hydrological-hydrodynamic processes and is also able to model sediment transport and fate (Furl et al., 2018; Sharif et al., 2017b). However, few studies have used it for water quality assessment (Downer et al., 2015). Their approach to simulate soil detachment, sediment routing, and fines deposition is based on advection-dispersion equations, complete mixed reactors, and Shield's law. Similarly, other models such as the Water Quality Analysis Simulation Program (WASP) also use equations based on advection-dispersion to estimate the dynamics of sediment and water quality (Knightes et al., 2019).

Most of these methods require empirical parameters to represent hydraulic conditions, which

can increase the complexity of the calibration due to the requirement of substantially more data, especially in poorly gauged catchments (Fu et al., 2019). Some recent examples of the application of 2D water quantity and quality models can be found in Shabani et al. (2021) and (Yanxia et al., 2022). The research carried out in Shabani et al. (2021) coupled the Hydrologic Engineering Center - River System Analysis 2D (HEC-RAS 2D) with the Water Quality Analysis Simulation Program (WASP) and the results illustrate an approach of evaluation of the spatial distribution of soil detachment and Total Suspended Solids (TSS) during a flood event. Using a 2D diffusive-wave and advection-diffusion model, (Yanxia et al., 2022) evaluated the concentrations of total phosphorus and total nitrogen. Both aforementioned investigations, however, were feasible to be validated due to extensive available field observations of discharges, concentrations, and pollutant loads.

In general, most studies on the dispersion and transport of pollutants address the pollution generated by agricultural sectors (Zia et al., 2013). For instance, the SWAT model has been used to predict and analyze the impacts of agricultural management practices at the watershed scale (Volk et al., 2016). Although able to model events on a sub-daily scale, only few articles worldwide used this model capability, and no articles with case studies in Brazil used it until 2019 (Brighenti et al., 2019).

The dynamics of pollutants in urban areas is complex and requires not only a complete description of physical, chemical, and biological phenomena at a proper spatial-temporal scale, but also a proper hydrological-hydrodynamic model that can explain the transport of pollutants in surface runoff (Vartziotis et al., 2022). These requirements are quite challenging in poorly gauged catchments. This could be the reason why many water quality analyzes are performed primarily with diluted metrics, such as event concentrations (EMC) or total maximum daily loads (TDML), rather than high-resolution pollutographs (Rossman e Huber, 2016).

For the sub-daily and sub-hourly temporal scales, a model capable of simulating water quality dynamics in a semi-distributed fashion is the Stormwater Management Model (SWMM). Although SWMM is typically applied for urban catchments, their conceptual model of semi-distributed modeling presents a limitation for the temporal-spatial distribution of pollutants in the catchment domain because modeled results are only visualized at nodes of links or at the outlet of sub-catchments. Simulating hydrodynamic and water quality processes and presenting results as maps with proper resolution is essential for understanding multiple issues. Spatial-temporal results can be used for problems such as (i) identifying prone areas to implement Low Impact Developments (LIDs) by estimating the potential pollutant retention, (ii) identifying areas prone to floods, and (iii) estimating pollutant concentrations in different locations in the domain. Therefore, to aid in the modeling of catchments with rapid hydrological response, the HydroPol2D (Hydrodynamic and Pollution 2D Model) is developed. The model allows the distributed hydrodynamic modeling of surface runoff and the transport of pollutants in catchments and allows estimation of water quality and quantity dynamics at user-defined temporal and spatial resolutions.

HydroPol2D contributes to the field of hydrologic and hydrodynamic models by allowing a 2D flood and water quality modeling with the simulation of floodplain momentum transfer, spatially distributed infiltration and evapotranspiration calculation, and simulation of pollutant transport and fate. HydroPol2D also advances hydroinformatics by creating a fully explicit numerical model coupled with an adaptive time-stepping method to guarantee numerical stability for the water quantity and quality models of HydroPol2D. Moreover, HydroPol2D also allows the use of Graphics Processing Unit (GPU) calculations and have open source versions in Matlab and Python . This set of model capabilities is currently not available in the literature.

The main objective of the present work is to investigate the dynamics of surface runoff and water quality in a watershed with few available data - the Tijuco Preto catchment (TPC) in São Carlos/Brazil - and to highlight the potential of applying HydroPol2D in poorly gauged catchments. TSS

as the overall water quality indicator (Di Modugno et al., 2015) and is modeled with HydroPol2D. In addition to simulating hydrodynamics and TSS transport in a poorly gauged catchment, we provide calibration and validation tests of HydroPol2D water quantity and quality components by applying the model in different case studies. To this end, the specific objectives of this paper are (i) to assess the velocity limitation of WCA2D by comparing HydroPol2D with GSSHA and WCA2D (Numerical Case Study 1), (ii) to calibrate and validate the water quality model of HydroPol2D (Numerical Case Study 2), and (iii) to compare HydroPol2D with HEC-RAS (Numerical Case Study 3), as well as to provide a comprehensive TSS spatial-temporal analysis.

3.2 Material and Methods

3.2.1 HydroPol2D Model

The main concept of the model is to simulate the transport of water and pollutant mass through the interaction between a central cell and its 4 neighbors (Von Neumann grid). HydroPol2D allows assessing the variation of surface runoff along the catchment in space and time based on their physical and morphological characteristics. The model consists of 3 major components: infiltration model (i.e., hydrologic model), non-linear reservoir + cellular automata approach (i.e., hydrodynamic model) and build-up and wash-off model (i.e., water quality model).

The main parameters of the model are presented in Table 3.1. In addition, the model requires georeferenced .TIFF rasters that represent topography (Digital Elevation Model), land use and cover (LULC), and soil type. From these maps, we derive distributed parameters for each component of the model. Hydrologic Model parameters are determined in terms of the soil raster (e.g., infiltration parameters of Green-Amp model (Green e Ampt, 1911)), whereas the parameters of the Hydrodynamic Model (e.g., Manning's coefficient (Chow, 2010a)) are described by the LULC. Similarly, the Water Quality Model parameters (e.g., Build-up and Wash-off parameters (Rossman e Huber, 2016)) are also entered as a function of LULC. All model components can have initial values entered according to each category of its input data, or can have input maps representing initial conditions. More details on how to obtain and estimate the parameters used in the model can be found in Gomes Jr et al. (2021). The flowchart of the model steps is presented in Fig. 3.1.

First, HydroPol2D reads the input data and the boundary conditions of rain-on-grid, inflow hydrograph, and stage-hydrograph. The model requires at least one of the aforementioned boundary conditions to perform the numerical calculations. It also reads the downstream boundary condition that can be modeled either as normal flow or critical flow (Kollet e Maxwell, 2006a). Then, HydroPol2D discretizes the time domain and calculates two main processes: it solves the water quantity dynamic system presented in Eq. (3.3), and the water quality dynamic system shown in Eq. (3.9). Following this process, it decides whether to change the time step or not following Eq. (3.19), append rasters and vectors of the main states (e.g., water depths, infiltrated depths, stored pollutant mass) and check if the simulation time (t_f) is reached. The numerical modeling is carried out until t_f = simulation time.

3.2.1.1 Water Quantity Model - 2D Conservation of Mass and Momentum

The HydroPol2D model solves mass balance and momentum conservation equations using the diffusive wave approximation to estimate the outflow of each cell O (mmh^{-1}) in Eq. (3.1). However, the diffusive wave equation is only solved for the steepest water surface slope for each cell. Each cell can potentially have four flow directions and hence 4 water surface slopes gradients. Therefore, the mo-

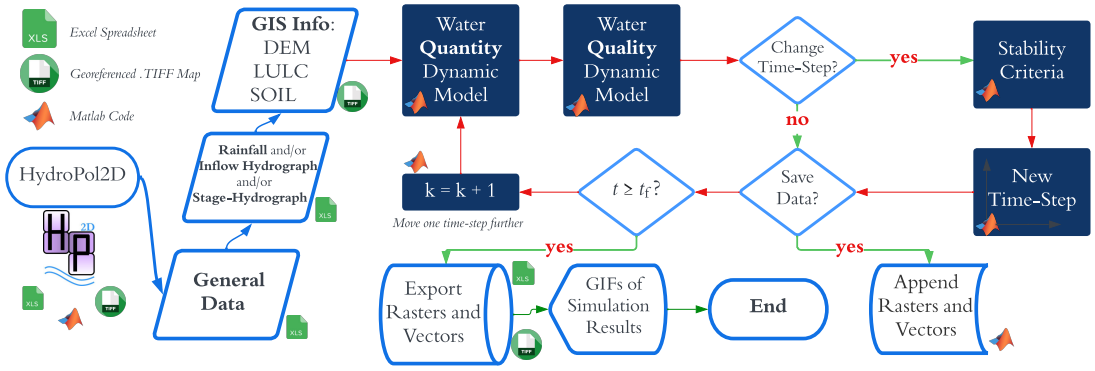

Figure 3.1. HydroPol2D model flowchart, where t_f represents the final simulation time and k represents the current time-step number. The *General Data* input sets final processing parameters, stability, and all other numerical parameters, i.e., not in matrix or vector format; The *Rainfall and/or Inflow Hydrograph and/or Stage-Hydrograph* sets the input rain-on-the-grid boundary conditions and/or punctual inflows and stages at internal nodes of the model. In addition, it defines the cells that receive this input hydrograph. At least one internal boundary condition has to be set. Finally, the *GIS Info* input data defines the digital elevation model and the land use and occupation map.

Table 3.1. Input data as a function of LULC and Soil Maps. HydroPol2D require the units for each variable as presented in this table. The model requires 11 parameters to simulate the water quantity and quality dynamics.

Model	Variable	Symbol (units)	Source of Uncertainty
Hydrologic Model	Saturated Hydraulic Conductivity	k_{sat} (mmh^{-1})	Spatial Variability
	Suction Head	ψ (mm)	Seasonality and Soil Loss
	Moisture Deficit	$\Delta\theta$ (cm^{3}cm^{-3})	Inter-event Variability
	Initial Soil Moisture	I_0 (mm)	Inter-event Variability
Hydrodynamic Model	Mannings Roughness Coefficient	n (sm$^{-1/3}$)	Stage Variability
	Initial Abstraction	h_0 (mm)	Spatial Variability
	Initial Water Surface Depth	d_0 (mm)	Warm-up Process
Water Quality Model	Linear Build-up Coefficient	C_1 (kgha^{-1})	Spatial Variability
	Exponential Build-up Coefficient	C_2 (day^{-1})	Temporal Variability
	Linear Wash-off Coefficient	C_3 (-)	Spatial Variability
	Exponential Wash-off Coefficient	C_4 (-)	Spatio-Temporal Variability

del solves the non-linear Manning's equation (i.e., relatively computationally expensive due to power functions required) only once per cell. For the remainder of the directions, it solves the distribution of runoff through simplification using rules of cellular automata (Guidolin et al., 2016) based on the available void volume in the boundary cells. The primary input data for the hydrological module are the spatial and temporal distribution of rainfall intensity, inflow hydrographs, stage-hydrographs, as well as the identification of downstream boundary conditions. Cell topology and connections between them, follow the Cartesian directions in a 2D spatial mesh of Von Neumann with $y-y$ and $x-x$ flow directions.

Let $\mathcal{D}$ be the catchment domain containing all cells that represent the physical region of interest and let the superscript (i,j) represent the i $-$ th and j $-$ th cell $\in \mathcal{D}$. Also, let $\mathcal{N}^{i,j}$ be the sub-domain represented by the four neighbors of the cell i,j. The following description of the model equations are dimensionally homogeneous with units in the international system, except when clearly stated different. Combining the main elements of the mass balance in a cell (i.e., a pixel with known resolution), we can describe the rate of change in water surface depth in cell i,j as (Rossman et al., 2010):

$$\frac{\partial d^{i,j}(t)}{\partial t} = \left[\sum_{\mathcal{N}^{i,j}} I^{i,j}(t) - \sum_{\mathcal{N}^{i,j}} O^{i,j}(t) + i^{i,j}(t) - f^{i,j}\left(d^{i,j}(t), F_d^{i,j}(t)\right) - e_{\mathrm{T}}^{i,j}(t)\right] \tag{3.1}$$

where $d^{i,j}(t)$ is the water surface depth (m), $I^{i,j}(t)$ is the inflow rate (LT^{-1}), $O^{i,j}(t)$ is the outflow rate (LT^{-1}), $i^{i,j}(t)$ is the rainfall intensity (LT^{-1}), $f^{i,j}(t)$ is the infiltration rate (LT^{-1}), $F_d(t)$ is the infiltrated depth of water into the soil (L), and $e_T^{i,j}(t)$ is the evapotranspiration rate (LT^{-1}).

Infiltration of water into the soil is represented using the Green and Ampt (GA) model (Green e Ampt, 1911), which can be derived from a simplification of Richards equation (Richards, 1931), and is applied to each cell of the spatial mesh created for the discretization of the catchment. Infiltration capacity is modeled as:

$$C_f^{i,j}(t) = k_{\text{sat}}^{i,j}\left[1 + \frac{\left(\psi^{i,j} + d^{i,j}(t)\right)}{L^{i,j}(t)}\right] \tag{3.2}$$

where $C_f^{i,j}(t)$ is the infiltration capacity (LT^{-1}), $k_{\text{sat}}^{i,j}$ is the saturated hydraulic conductivity (LT^{-1}), $L(t) = \frac{F_d(t)}{\Delta\theta}$ is the wetting front depth (L), and $\psi^{i,j}$ is the suction head (L).

The infiltration rate is the minimum value between the infiltration capacity and the water availability rate and can be calculated for a time $t + \Delta t$ with inflow rates, depths, and infiltrated depths from t. Expanding Eq. (3.1) by a 1st order Taylor's approximation, we can derive a forward in time explicit numerical solution for the 2D water surface dynamics problem by neglecting the high order terms, such that:

$$\begin{aligned} d^{i,j}(t+\Delta t) = {} & d^{i,j}(t) \\ & + \Delta t\left[\sum_{\mathcal{N}^{i,j}} I^{i,j}(t) - \sum_{\mathcal{N}^{i,j}} O^{i,j}(t) + i^{i,j}(t) - f^{i,j}\left(d^{i,j}(t), F_d^{i,j}(t)\right) - e_{\text{T}}^{i,j}(t)\right] \end{aligned} \tag{3.3}$$

The current version of the model allows for the simulation of soil moisture restitution during dry weather periods and the spatial simulation of evapotranspiration through Penman-Monteith simulation, which aids in the modeling of droughts (Melo et al., 2023). Although these characteristics are not directly investigated in this article, they are available in the model repository (Gomes Jr., 2023). During wet weather periods, the state variable $L^{i,j}(t)$ (i.e., the saturated depth of the wetting front) is calculated only by integrating the infiltration rate over time (Gomes Jr et al., 2021). Therefore, the initial value of $L^{i,j}(0)$ can be calibrated to represent the initial conditions of proper soil moisture and can be entered as an input map in the model that represents the initial conditions of soil moisture for each cell.

The conversion of depth to flow is done through the calculations of I and O of Eq. (3.1) based on the Manning's equation using the friction slope that is calculated from the water surface elevation the steepest gradient. In this model, the friction slope is assumed to be equal to the slope of the energy line (i.e., diffusive wave (Vieira, 1983)). Therefore, to distribute the volumes of surface runoff to the boundary cells, a system of weighted averages is performed in terms of the void volumes available between neighboring cells, substantially reducing the calculations by calculating the runoff velocity only for the direction of the highest slope of the water surface (Guidolin et al., 2016) and distributing the surface runoff volume as a function of this weighted average.

It is important to note that although the Manning equation is typically used for steady-state and uniform flow, it does not necessarily occur in the HydroPol2D model because the slope of the energy line is not assumed as the bottom slope. Therefore, this modeling capability allows HydroPol2D to estimate hydraulic transients and to dynamically change flow direction according to water surface elevation slopes. Moreover, HydroPol2D can also simulate backwater effects and river networks with bifurcations due to its adaptive flow direction scheme according to water surface elevations. A detailed pseudo-code of the model internal processes to solve Eq. (3.3) with the Celular-Automata approach is presented in the Supplemental Material.

3.2.1.2 Critical Velocity Limitation

Two versions of the HydroPol2D model were developed with respect to how flow velocities are treated, herein we name them as HydroPol2D (a) and HydroPol2D (b). For example, the research conducted in Guidolin et al. (2016) restricted flow velocities to the critical velocities in their WCA2D model - a similar modeling approach to HydroPol2D. However, several studies point out that hydrodynamic modeling, especially in significant flooding events, can present a mixed flow regime (i.e., the regime can change from sub-critical to super-critical flow rapidly) (Farooq et al., 2019). Therefore, some areas in the domain might have flow velocities larger than the critical velocity. The two adaptations of the HydroPol2D model (a) and (b) are available and are described below with respect to the critical velocity as follows:

- HydroPol2D (a): Change of hydraulic regime is allowed and the flow velocity is unconstrained; however, hydraulic jump is not modeled due to diffusive wave model that does not account for convective and local acceleration features presented in full dynamic wave models. This model assumption is more applicable for high-resolution flood inundation mapping and modeling.
- HydroPol2D (b): The flow velocity is constrained to the critical flow, ensuring only sub-critical or fluvial flow regime in all cells of the domain. In this case, there are relatively lower velocities and, as a consequence, longer time-steps and shorter simulation durations. Moreover, this limitation might affect flood wave propagation and hence delay peak times.

These two variations of the model can be controlled by a factor f_m and result from the limitation of the maximum flow velocity, given by Eq. (3.4) and Eq. (3.5):

$$v_{\mathrm{m}}^{i,j}(t) = \min\left(f_{\mathrm{m}}\sqrt{g h_{ef}^{i,j}(t)}, \frac{1}{n^{i,j}}\Delta x\left(h_{ef}^{i,j}(t)\right)^{\frac{5}{3}}\sqrt{s_e^{i,j}(t)}\right) \tag{3.4}$$

$$h_{ef}^{i,j}(t) = \max\left(d^{i,j}(t) - h_0^{i,j}, 0\right) \tag{3.5}$$

where v_m is the maximum velocity calculated for the steepest direction (ms^{-1}), g gravity acceleration (ms^{-2}), d is the water surface depth (m), f_m is a factor assumed to account for models HydroPol2D (a) and HydroPol2D (b), s_e (mm^{-1}) is the steepest slope of the water surface calculated from the water surface elevation map, Δx is the spatial discretization of cells (m), n is the Mannings roughness coefficient ($sm^{-1/3}$), and h_{ef} is the effective water surface depth considering losses through the initial abstraction (m) (h_0), with h_0 in (m).

In the case of model HydroPol2D (a), f_m can be assumed to tend to infinity, such that it does not limit the flow to the critical velocity, otherwise $f_m = 1$. The previous formula is applied to each time-step, for all cells of the domain, but only to the direction of the steepest water surface slope.

3.2.1.3 Water Quality Modeling - 2D Build-up and Wash-off

The mathematical model used to determine the transport and fate of pollutants is based on the build-up and wash-off model (Deletic, 1998; Rossman e Huber, 2016). The term build-up refers to the accumulation of pollutants in the catchment during dry periods, and the term wash-off refers to the washing and transport of these pollutants during wet periods events (Rossman e Huber, 2016). Several mathematical formulations for this model are proposed and, in this article, an adaptation of the exponential build-up and wash-off model is assumed. Furthermore, the increase in pollutants (ΔB) in the catchment during dry weather periods is assumed as a variable dependent only on the number of consecutive dry days (ADD), as shown in Eq. (3.6):

$$\Delta B_l^{i,j} = 10^{-4} A_c \left[C_{1,l}^{i,j} \exp\left\{ -C_{2,l}^{i,j} \mathrm{ADD} \right\} \right] \pm R_l(\mathrm{ADD}) \tag{3.6}$$

where C_1 is the build-up coefficient, function of land use and land cover (kgha^{-1}), C_2 is the daily accumulation rate of build-up (day^{-1}), ADD is the antecedent dry days (days), A_c is the catchment area of (m^2), l represents the classification of land use (e.g., pervious or impervious areas) and we introduce a source term R to allow modeling of a non-conservative mass balance due to self-degradation or chemical reaction, varying for each land use and land cover (kgha^{-1}).

The Eq. (3.6) is valid in dry periods and calculates the build-up increment which, if added to the initial build-up, represents the amount of mass available in each cell at the end of the ADD time (Deletic, 1998). Typically, for total suspended solids, R can be neglected. The original equation of the exponential wash-off model, which acts on the equation of the build-up variation during the wet weather periods, can be modeled as follows in Eq. (3.7)

$$\frac{\mathrm{d}B(t)}{\mathrm{d}t} = -W_{out}(t) = 10^{-4} A_c \left(-C_3^* q(t)^{C_4^*} B(t) \right) \tag{3.7}$$

where C_3^* and C_4^* are wash-off coefficients in terms of specific flow rates (i.e., flow divided by catchment area) instead of flow discharges in each cell. The variable $q(t)$ is the flow rate usually given in (mmh^{-1}) or (inh^{-1}) and can be inferred by dividing the outlet flow by the catchment area when the catchment is modeled in a concentrated model (Xiao et al., 2017). The units of C_3^* depend on the units of $q(t)$, which is used in the conversion factor of C_4^* so that it guarantees that the wash-off rate W has units of mass / time or (e.g., kgh^{-1}). In summary, for the international system of units C_3 has dimensions of (LT^{-1})^{C_4}T^{-1}, depending on $q(t)$ (Rossman e Huber, 2016).

The Eq. (3.7) is used in the SWMM software and is applied in a concentrated hydrologic conceptual model, assuming a single representative value for the entire sub-catchment, as aforementioned. To represent the wash-off phenomenon, we have used a variation of the previously presented exponential model of wash-off (Shaw et al., 2006; Tu e Smith, 2018; Wicke et al., 2012; Wijesiri et al., 2015a). The adaptation made in HydroPol2D is the following: instead of modeling the wash-off using functions dependent on specific flow rates (equivalent depth per unit of time), the model calculates the transport of pollutants, that is, rate of pollution washed, as a function of the flow discharges leaving each cell and its available mass to be washed. Another significant difference is that pollutants enter and leave cells simultaneously wet weather periods. This feature changes the mass balance equation so that the equation for the rate of change of the mass of pollutants can be written as a combination of inputs and outputs of pollutant mass given by:

$$\frac{\partial B^{i,j}(t)}{\partial t} = \sum_{\forall \text{ dir}} W_{\text{in,dir}}^{i,j}(t) - \sum_{\forall \text{ dir}} \overbrace{C_3 \left(Q_{\text{dir}}^{i,j}(t) \right)^{C_4} f\left(B(t) \right)}^{W_{\text{out,dir}}^{i,j}(t)}, \tag{3.8}$$

where W is the wash-off load (kgh^{-1}), the sub-index *in* and *out* represent the inlet and outlet of the cells, respectively. The sub-index dir represents the flow direction, varying among leftwards, rightwards, upwards, and downwards, respectively, following the Cartesian directions. $W_{\text{in,dir}}(t)$ is the rate of pollutant inflow in direction dir, and the term $\sum_{\forall \text{ dir}} W_{\text{in,dir}}^{i,j}(t)$ calculates the pollutant inflow rate and depends on the topology of the problem. Q_{dir} is the outflow discharge (m^{3}s^{-1}) into direction dir, and $f(B(t))$ is explained further.

Discretizing Eq. (3.8) using a forward Euler scheme, it follows that:

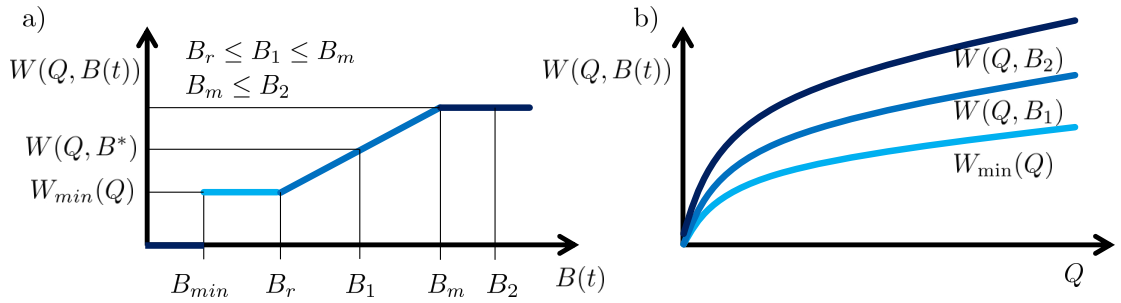

Figure 3.2. Scheme of pollutant washing curves. Part a) represents the washing rate as a function of accumulated mass for several cases, assuming a constant flow rate Q. Part b) represents the pollutant rating curve as a function of the accumulated mass in terms of the flow discharge. This figure shows the envelope of rating curves assumed for the pollutant washing.

$$B^{i,j}(t+\Delta t) = B^{i,j}(t) + \Delta t \overbrace{\left(\sum_{\forall \text{ dir}} W^{i,j}_{\text{in,dir}} - \sum_{\forall \text{ dir}} W^{i,j}_{\text{out,dir}}(t) \right)}^{\Delta W^{i,j}(t)} \tag{3.9}$$

The function $f(B(t))$ varies the equation of pollutant washing according to the mass accumulated in the cells. For values of $B(t)$ smaller than B_{min}, the pollutant flux is assumed to be zero. This is the typical case of pollutants that are fixed on the soil and surface and are difficult to wash-off. For values greater than B_{min} but smaller than a threshold B_{r}, which depends on the type of pollutant, the washing rate follows a sediment rating curve independent of the accumulated mass; therefore, washing is exclusively dependent on the rating curve coefficients, which are equal to the wash-off coefficients. Note that B_{r} can be assumed equals B_{min}, that is, the effect of the rating curve can be neglected. For the cases where the available mass is between B_{r} and B_{m}, where B_{m} is an upper bound, the wash rate is scaled (see Fig. 3.2) by the mass of pollutants in the cell, following the typical exponential wash-off model (Rossman et al., 2010). In the cases where $B(t)$ is greater than B_{m}, the maximum output rate is limited to the representative value of B_{m}. These conditions are expressed in Eq. (3.10), such that:

$$f\Big(B\,(t)\Big) = \begin{cases} 0, \text{ if } B\,(t) \leq B_{\text{min}} \\ 1, \text{ if } B_{\text{min}} \leq B\,(t) \leq B_{\text{r}} \\ (1 + \ B\,(t) - B_{\text{r}})\,, \text{ if } B_{\text{r}} \leq B\,(t) \geq B_{\text{m}} \\ (1 + B_{\text{m}} - B_{\text{r}})\,, \text{ if } B\,(t) \geq B_{\text{m}}. \end{cases} \tag{3.10}$$

The imposition of a B_{min} value on the pollutant washing rate substantially improves the computational performance of the model by avoiding calculations in cells where the accumulated mass tends to zero and, therefore, avoids the minimum time-step tending to zero. Furthermore, the choice of the limit B_r is effective as it ensures that pollutants follow a rating curve model for relatively low accumulated masses but larger than a minimum value B_{r}. For instance, if the conventional wash-off model were used (Eq. (3.7)), the mathematical operation to calculate the wash-off rate $C_3\ Q^{C_2} B(t)$ would tend to zero if B(t) tends to zero. This might result in a non-realistic case, especially when considering a relatively low available pollutant mass washed by a large flow rate that would have nearly no wash-off because B(t) tends to zero.

Previous modeling results indicate that for TSS, $B_{\text{min}} = 1$ gm^{-2}, $B_{\text{r}} = 10$ gm^{-2}, and $B_{\text{m}} = 100$ gm^{-2} is consistent with TSS modeling in urban areas. These values can also be calibrated for different pollutants. Other studies of build-up and wash-off modeling (Hossain et al., 2012; Wicke et al., 2012) have applied the exponential wash-off equation presented in Eq. (3.7) in the form of specific flow rates (i.e., outlet flow divided by the catchment area) instead of the flow discharges. However, in these studies, concentrated hydrological models of the watershed are used to represent the dynamics of surface runoff in the watershed. If we write the flow as a function of the specific flow rate (q), we can

derive the relationship between the two modeling approaches and compare the coefficients adopted in the literature. Assuming that the specific flow rate is given in (mmh^{-1}) and the modeled flow is in (m^3s^{-1}), we can write Eq. (3.11) relating the specific flow rate to the cell outlet flow discharge, such that:

$$Q_d\left(t\right) = \left(\frac{1}{3600 \times 1000}\right) q\left(t\right) \Delta x^2 \tag{3.11}$$

Finally, analogously using Eq. (3.7) and Eq. (3.8), we can relate the coefficients C_3^* and C_4^* (that is, the coefficients considering the catchment as concentrated) with C_3 and C_4 (i.e., coefficients for distributed modeling), resulting in:

$$C_3 = \overbrace{\left(\frac{3600 \times 1000}{\Delta x^2}\right)^{C_4^*}}^{f_c} C_3^*, \quad C_4 = C_4^* \tag{3.12}$$

where f_c converts C_3^* developed for q(t) in (mmh^{-1}) to the model proposed here using flow discharges in (m^3s^{-1}). The usual values of f_c are presented in the supplemental materior for various values of C_4 and can be used for comparison between SWMM parameters and the parameters suggested in the HydroPol2D model.

Using the previous states modeled with the aforementioned equations, we calculate water quality dynamic indicators such as the instantaneous pollutant concentrations in Eq. (3.13) and pollutant loads (Eq. (3.13)) as follows:

$$C_{\text{dir}}^{i,j}(\text{t}) = \lim_{\Delta t \to 0} \left(\frac{W_{\text{out,dir}}^{i,j}(t)\Delta t}{Q_{\text{out,dir}}^{i,j}\left(t\right)\Delta t} \right) \tag{3.13}$$

$$L_{\text{dir}}^{i,j}(t) = C_{\text{dir}}^{i,j}(t) Q_{\text{out,dir}}^{i,j}(t) \tag{3.14}$$

The HydroPol2D model also allows the calculation of event mean concentration (EMC) and the first-flush curve that combines the normalized pollutant washed mass (m/M) with the normalized runoff volume (v/V)(Di Modugno et al., 2015). Let t_f be the end of an event and ϕ represent the outlet cells, one can calculate these time-varying metrics as follows:

$$\text{EMC}^{\phi}(t) = \frac{\int_0^t W_{out}^{\phi}(t)\text{d}t}{\int_0^{t_f} Q_{\text{out}}^{\phi}\left(t\right)\text{d}t} \tag{3.15a}$$

$$\frac{m^{\phi}(t)}{M^{\phi}} = \frac{\int_0^t W_{\text{out}}^{\phi}\left(t\right)\text{d}t}{\int_0^{t_f} W_{\text{out}}^{\phi}\left(t\right)\text{d}t} \tag{3.15b}$$

$$\frac{V^{\phi}(t)}{V^{\phi}} = \frac{\int_0^t Q_{\text{out}}^{\phi}\left(t\right)\text{d}t}{\int_0^{t_f} Q_{\text{out}}^{\phi}\left(t\right)\text{d}t} \tag{3.15c}$$

3.2.1.4 Numerical Stability and Adaptive Time-Stepping

For the numerical solution, either constant or adaptive time-steps can be used. The adaptive time-step values depend on the propagation conditions of the information along the cell computational mesh grid. In other words, to ensure that the information (i.e., wave propagation) does not exceed more than one cell in a time-step, the Courant - Friedrichs - Lewy (*CFL*) condition is considered as the numerical stability criterion, expressed in Eq. (3.16) as (Courant et al., 1928):

$$\Delta t^r\left(t\right) = \min_{\mathcal{D}} \left(\frac{\alpha^r \max\limits_{\forall \text{ dir}} \left(u_{\text{dir}}^{i,j}\left(t\right)\right)}{\Delta x}, \Delta t^* \right) \quad \forall\, i,j \;\in \mathcal{D} \tag{3.16}$$

where α^{r} is a factor < 1 that ensures a courant number below the unit for the modeling of surface runoff, Δt^{*} is the maximum time-step assumed in the simulation, the sub-index (dir) represents an orthogonal direction from cell $i, j \in \mathcal{D}$, and u is the wave celerity, given by Eq. (3.17):

$$u_{\text{dir}}^{i,j}(t) = \left| v_{\text{dir}}^{i,j}(t) \right| \pm \sqrt{g d^{i,j}(t)} \tag{3.17}$$

where v is the wave velocity.

Some degree of numerical diffusion occurs when using very low values of α^{r} and must be previously assessed to ensure more accurate numerical solutions (Lantz, 1971). For water quality, we must ensure that the available pollutant mass does not reach negative values in each time-step. This is the typical case when a long time-step is used. Fig. 3.3 presents a schematic of the pollutant transport model that illustrates the processes of numerical stability and mass balances. By dividing the available pollutant mass by the pollutant wash-off for all cells in the domain, the minimum time-step is obtained to ensure numerical stability, expressed in Eq. (3.18) as:

$$\Delta t^{q}(t) = \min_{\mathcal{D}} \left(3600 \frac{\alpha^{q} B^{i,j}(t)}{\left| \Delta W^{i,j}(t) \right|}, \Delta t^{*} \right) \;\; \forall\, i, j \in \mathcal{D},\ \text{If } \Delta W^{i,j}(t) < 0 \tag{3.18}$$

where ΔW is the outflow flux of pollutants leaving the cell (i.e., the net wash-off) considering the 4 directions, that is, the difference between outflow and inflow of pollutant loads (kgh^{-1}), and Δt^{*} is the minimum time-step assumed in the model (sec).

Theoretically, the model should not have a minimum time-step constraint Δt^{*} to be considered numerically stable. However, as shown in Eq. (3.18), the time-step tends to zero as $B(t)$ approaches zero. This implies that after the first-flush, which eventually washes most of the initial pollutants out of the catchment and causes $B(t)$ to tend to zero, the time-step would also tend to zero. Therefore, we assume the minimum water quality time-step (Δt^{*}). Finally, the chosen time-step of the model considers the stability of both water quality and quantity models as follows:

$$\Delta t(t) = \min \left[\Delta t^{r}(t), \Delta t^{q}(t) \right] \tag{3.19}$$

3.2.2 Numerical Case Study 1 V-Tilted Catchment

The first case study is performed in a synthetic catchment (V-Tilted Catchment) that has been used to test surface runoff models (Fry e Maxwell, 2018a; Gomes Jr. et al., 2022; Kollet e Maxwell, 2006a) and we compare HydroPol2D in this catchment with GSSHA. The objective of this numerical case study is twofold: assess the influence of space and time discretization and investigate the limitation of critical velocity. This theoretical catchment has only one outlet pixel and is assumed to have a width equal to the spatial discretization resolution of the cell grid (20 m x 20 m). The V-Tilted catchment corresponds to a catchment of $1,620$ m x $1,000$ m (area = 1.62 km^2) composed of two rectangular planes (i.e., hillslopes) measuring 800 m x 1000 m, each coupled with a vegetated channel in the connection of the two planes (Gomes Jr. et al., 2022). The slope in the $x - x$ direction is 5%, while the slope in the $y - y$ direction is 2%, as shown in Fig. 3.4a).

Two types of ground cover are assumed: channel (n = 0.15 sm$^{-1/3}$) and hillslopes (n = 0.015 sm$^{-1/3}$). Only surface runoff flow is evaluated; therefore, infiltration, water quality, and runoff generated by excess saturation are not modeled in this first test. A constant rainfall rate of 10.8 mmh^{-1} in 90 min is applied uniformly in the catchment. The gradient boundary condition (e.g., normal flow at the outlet) was assumed for a slope equal to the natural slope of the outlet channel. The calculation time is defined as 240 min to ensure the propagation of the hydrograph through the catchment. Fig. 3.4a) represents the digital terrain. Different time-step discretizations are tested, ranging from 0.1

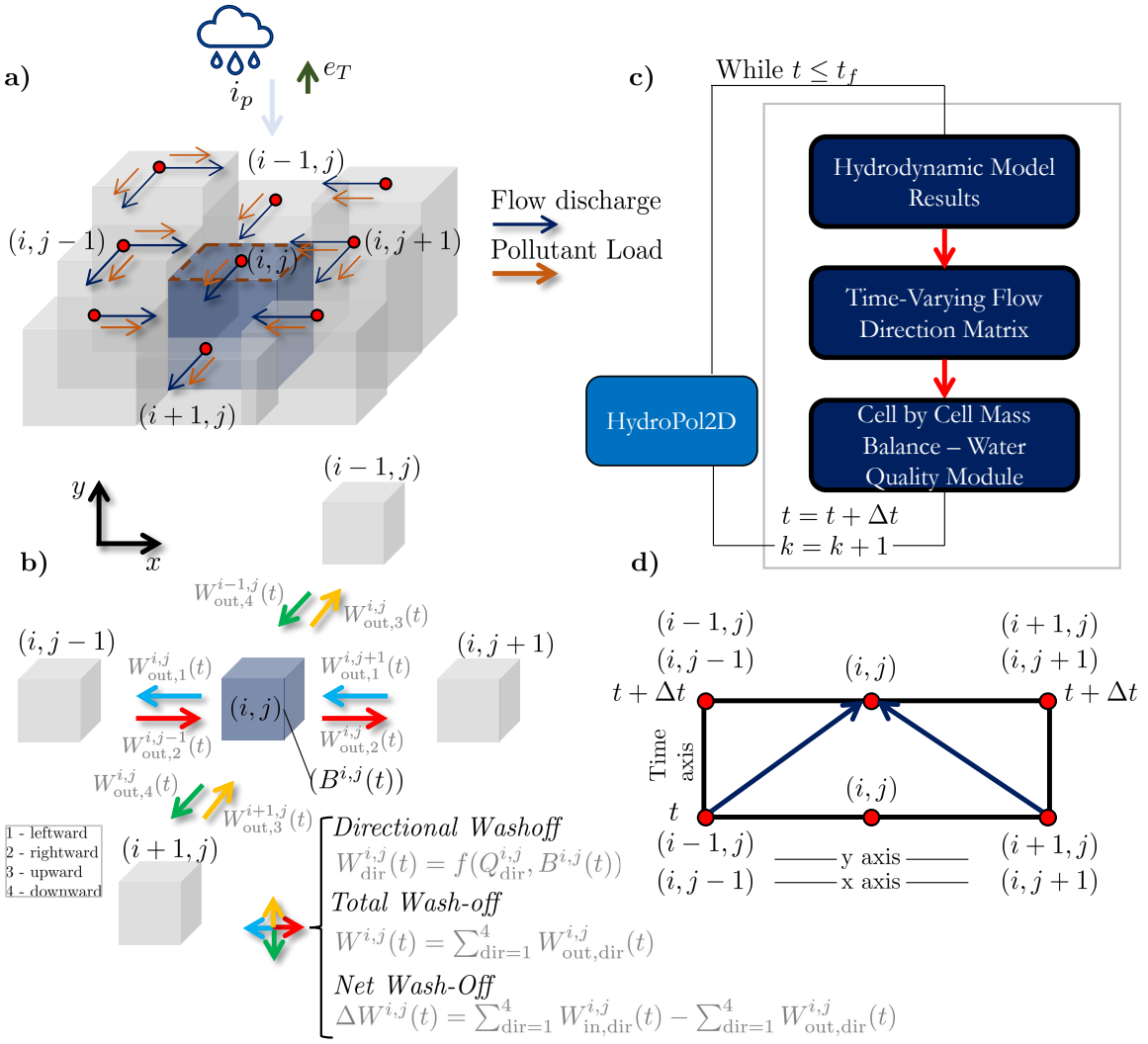

Figure 3.3. Scheme of the pollutant transport model, where a) represents a 3D schematic of a watershed with inflows and outflows and pollutants, b) represents a cell with pollutant outflow rates W with pollutant outflow and inflow rates as a function of the flow direction matrix, c) represents a detail of the computational scheme of the model related to water quality modeling and d) represents the computational mesh, where the water quality states of the time a posteriori depends on the states of the neighboring cells and the time to the prior time-step. Furthermore, pollutant flow rates depend on the flow rate Q_{dir} for each direction. These flow rates are a function of the hydrodynamic model.

to 60 seconds. In addition, an adaptive time-step numerical scheme is also evaluated, and simulated hydrographs with different computational meshes are compared.

3.2.3 Numerical Case Study 2 - Wooden-Plane Catchment

This numerical case study aims to validate the proposed distributed water quality modeling. The water quality model, however, requires a calibrated water quantity model to predict discharges, and hence the pollutant rates. We applied the HydroPol2D model in a wooden board catchment of 3 m length and 1.5 m width that represents an impervious surface, as shown in Fig. 3.4b) (Xiao et al., 2017; Zhang et al., 2020). The Manning's roughness coefficient (n) is spatially invariant and is assumed to be equal to 0.04 $\text{sm}^{-1/3}$, and the initial depth of the water is assumed to be 0.5 mm (Zhang et al., 2020). Rainfall is uniformly distributed in the catchment. All experimented events had a rainfall duration of 28 min. Previous modeling comparisons of HydroPol2D with flow observations in this catchment presented in Xiao et al. (2017) show good agreement. Therefore, the water quantity results were

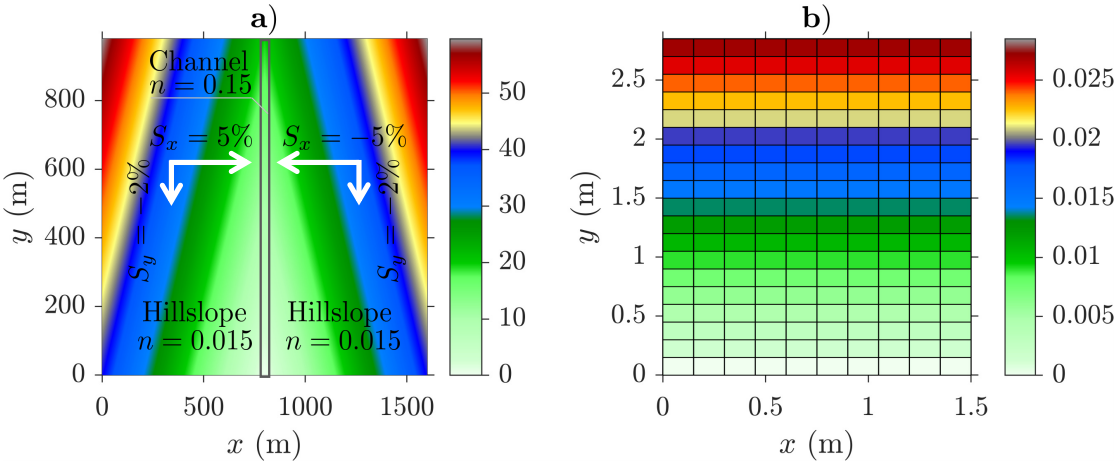

Figure 3.4. Catchments of Numerical Case Study 1 and 2. Part a) is the V-Tilted Catchment Digital Elevation Model (m), with smoother hillslopes and a rougher central channel. The outlet boundary condition is assumed as normal depth with slope of 0.02. The pixel dimension is 20 m. Infiltration is not modeled and the rainfall is spatially and temporally uniform with 10.8 mmh^{-1} during 90 min. Part b) is the Wooden-Plane catchment digital elevation model (m) (Zhang et al., 2020) with pixels of 0.15 m with time and space invariant rainfall, and slope (s_0) of 1°, although it varies for some events assessed further. The outlet boundary condition of normal slope following the plane slope is assumed. Infiltration is also neglected, and an initial solute mass of 125 g is uniformly distributed in the catchment.

assumed as calibrated. In the study presented in Zhang et al. (2020), salt was used as the solute and all the experiments carried out were carried out evenly distributing 125 g of salt through the wooden board.

In this paper, we selected two cases of experiments presented in Zhang et al. (2020) with different conditions of rainfall and slope. Events 1 to 4 have slopes of 0.5° with rainfall intensities of 24.22, 43.16, 63.81 and 76.34 mmh^{-1}, respectively. Events 5 to 8 have slopes of 2° and rainfall intensities of 20.76, 41.72, 78.26 ,83.99 mmh^{-1}, respectively. From these 8 events, we perform a single calibration and validation test for each slope. For events 1 to 4 (i.e., $s_0 = 0.5°$), we select event 4 for calibration and the remainder for validation. In addition, for events 5 to 8 (i.e., $s_0 = 2°$), event 7 was used for calibration and the others for validation. To this end, we develop a calibration optimization problem minimizing the root-square mean error (RMSE) between modeled and observed salt concentrations. This procedure is fully described in the Supplemental Material. The decision variables for the optimization problem are the wash-off coefficients C_3 and C_4 and the problem is solved with the genetic algorithm for a 40 generation and population size of 100. The build-up coefficients C_1 and C_2 were not used in the calibration since the initial mass of salt is known.

3.2.4 Numerical Case Study 3 The Tijuco Preto Catchment in Sao Carlos Sao Paulo / Brazil

The third case study tested the HydroPol2D model in the Tijuco Preto catchment (TPC), in São Carlos - São Paulo. The TPC is characterized by 95% of impervious areas (Baptista et al., 2021). The digital elevation model (DEM) was built based on elevation data with horizontal and vertical spatial resolution of 12.5 and 1 m, respectively, obtained from the Alos database Palsar (Rosenqvist et al., 2007). The LULC raster was obtained from the mapbiomas project, available at (Souza et al., 2020) and was later reclassified into two main land uses: impermeable and permeable surfaces. Subsequently, a downscaling procedure was performed, using the nearest-neighbor method, on these data from 30 m to 12.5 m of horizontal resolution to match the DEM spatial resolution. Despite possible errors due to data resampling, this procedure is justified because the Alos Palsar data are the product of resampling the SRTM data from 30 to 12.5 m. Furthermore, the delineation of flood inundation maps with a

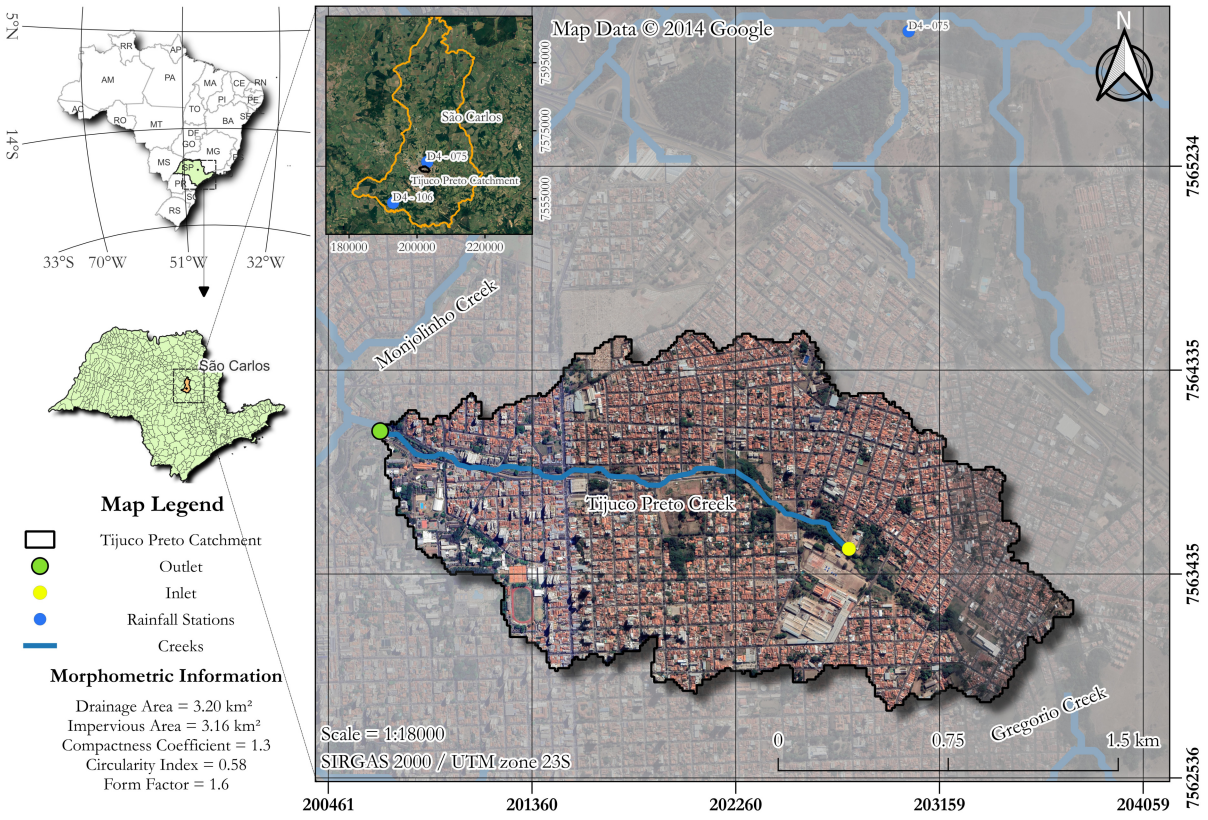

Figure 3.5. Tijuco Preto catchment located in São Carlos - SP. Data source: Map data ℓ′ 2015 Google and IBGE.

resolution of 12.5 m provides a better level of detail in the modeling outputs, as it allows the capture of the flow path of streets and avenues.

This case of study is located in São Carlos - Brazil, which has experienced intense urbanization in recent decades (Ohnuma Jr e Mendiondo, 2014). This catchment is comparable in characteristics of many highly urbanized catchments with a lack of high-resolution data on rainfall, elevation, and almost an absence of water quantity and quality observations.

The modeling efforts presented here aim to explain the transport phenomenon of TSS mobilized only as a function of surface runoff. TSS was chosen due to its good representation of the general state of water quality (Di Modugno et al., 2015; Rossman e Huber, 2016). To this end, the modeling of maximum water depths, maximum pollutants concentrations, and potential pollutant retention is evaluated. The TPC is shown in Fig. 3.5.

Despite the absent monitored data in this catchment, both in terms of high-resolution precipitation (e.g, sub-hourly intervals) and in terms of water depths or flows observed in the stream, the objective of this case study is to quantify in probabilistic terms the expectation of specific water depths of flood inundation depths, flow discharges, concentrations, and pollutant loads in pixels of the catchment, especially at the outlet. The rainfall on the grid boundary condition is a design spatially-invariant storm hyetograph distributed with the Alternated Blocks method (Keifer e Chu, 1957b).

3.2.4.1 Probabilistic Distribution of Daily Rainfall and Antecedent Dry Days

For the maximum annual dry days and the subsequent creation of the ADD curve for the TPC, rainfall data was sought in the website of the Hydrological Database of the Department of Water and Electricity (DAEE), available at (Prodesp, 2022). The rainfall station with prefix D4 − 075 (see

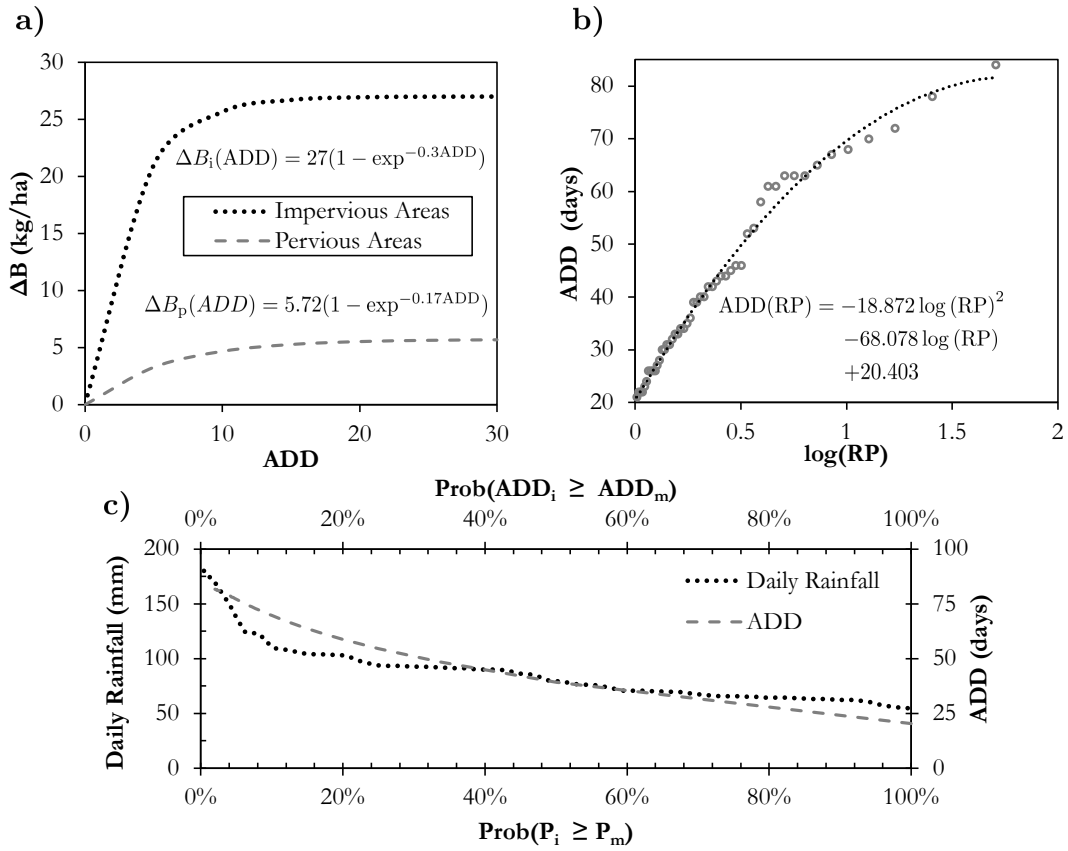

Figure 3.6. Accumulation of pollutants (build-up) as a function of the interval of dry days (ADD), b) Adjustment of dry days concerning empirical return periods simulated by the Weibull relation, and c) Probability distribution of ADD and daily rainfall. The rainfall is assumed space invariant in the catchment.

Fig. 3.3), named São Carlos SAAE, located in the geographic coordinates 21°59′12″S, 47°52′33″W was chosen. However, this station lacks rainfall data between 1996 and 2013, and, in this case, we used the station $D4-106$, named "Fazenda Santa Bárbara- located at coordinates 22ř05'38"S, 47ř58'30"W.

To estimate the maximum annual dry days in the TPC, data from station $D4-075$ were used between 1970 and 1995, and for the years 2014 to 2018. For the period from 1996 to 2013 and 2019, station $D4-106$ was used. Both stations do not have data for May 2016, so this year was not used for the analysis. It is observed that the expected values of ADD are on the order of 25 days for a RP of 1 year. The daily rainfall data presented in Fig. 3.6 were obtained from the DAEE platform and used to fit an updated IDF curve for São Carlos (Gomes Jr et al., 2021), with Sherman-type parameters of $K = 819.67$, $a = 1.388$, $b = 10.88$, and $c = 0.75$.

3.2.4.2 DEM Treatment and Reconditioning

Raw elevation information contains noise, accumulation points, depressions, and plateaus due to the low accuracy of the data. The elevation data was subjected to sequential processes to refine the hydraulic pathways in the catchment. First, a slope-based filter was used to remove possible noise from the elevation data, generating a raster that contains the terrain without peaks with a slope greater than 30ř (*DTM filter* - SAGA (Passy e Théry, 2018)). This slope represents an elevation difference of 7.21 m between the boundary cells and the cells and could represent urban features such as buildings that should be removed from the terrain model. After this operation, a raster is generated with several areas left without data, and, in the absence of such data, a bilinear interpolation filter was used to smooth the terrain lines (*r.fillnuls* GRASS (Lacaze et al., 2018)). This process ensures smoother flow

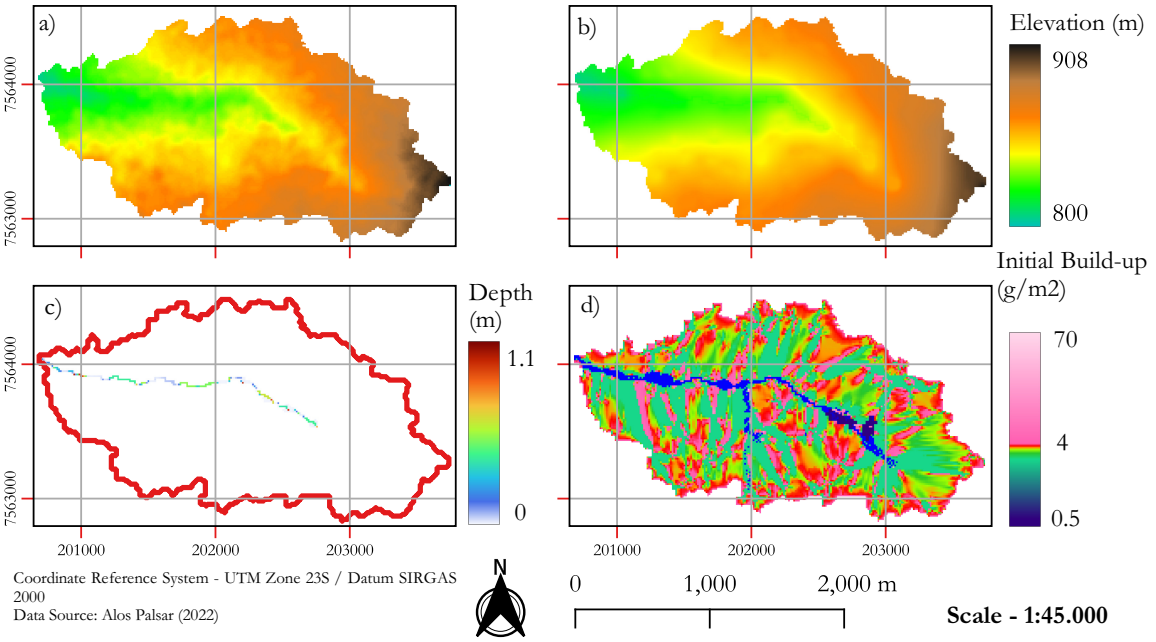

Figure 3.7. Relationship between the original DEM and the reconditioned DEM developed to ensure hydrological continuity and warm-up data. Part a) is the original elevation data, b) is the reconditioned DEM, c) is the warm-up depth, and d) is the initial TSS mass (initial build-up).

lines. The final product of the procedure is shown in Fig. 3.7.

3.2.4.3 Warm-Up Process and Initial Values for Modeling

In HydroPol2D, users can enter initial maps of water surface depths, pollutant mass, or enter a constant value per land use and land cover classification as warm-up data. In this paper, we performed a water quantity and quality warm-up by subjecting the catchment domain to an inflow hydrograph 0.3 m^3s^{-1} for 24 h followed by a rain on the grid boundary condition with return period of 1-yr and 1-hour duration with the Alternated Blocks rainfall distribution. The pollutant initial build-up were estimated for a return period of 1/12 years, representing the available TSS mass in the catchment with RP, which results in ADD of 10 days. More details of the warm-up process can be found in the Supplemental Material.

3.2.4.4 Composite Design Event

The event simulated in this study corresponds to a combination of two consecutive events: frequent annual drought (e.g., RP = 1 year) followed by frequent annual rainfall (e.g., RP = 1 year). Thus, the return period of the composite event, which corresponds to the product of each RP event, also results in RP = 1 year. This design event was chosen because it represents a common event in the catchment in terms of both the accumulation of pollutants and the volume of precipitation. Furthermore, more frequent rainfall events tend to produce higher average concentrations because they carry a higher amount of pollutants in a smaller volume of surface runoff (Di Modugno et al., 2015). On the other hand, very frequent events (e.g., RP $<$ 1/12 years) might not even produce surface runoff to carry pollutants. The base parameters assumed in the simulation were obtained based on the literature and studies such as (Zaffani, 2012) for the TPC, presented in Table 3.2.

Table 3.2. Parameters of the base scenario adopted in the simulation.

Land Use Classification	Parameters							
	k_{sat} (mmh^{-1})	$\Delta\theta$ ($cm^3 cm^{-3}$)	n ($sm^{-1/3}$)	h_0 (mm)	C_1 ($kg\ ha^{-1}$)	C_2 (day^{-1})	C_3 -	C_4 -
Impervious Areas	0	0	0.018	10	27.6	0.2	1200	1.2
Pervious Areas	10	0.4	0.100	20	5.72	0.17	1200	1.2

3.2.4.5 Parameter Estimations and Local Sensitivity Analysis

The absence of monitoring makes the formal calibration and validation of the model intractable. The parameters of the water quantity model were assumed a priori, based on satellite information on the catchment and inspections on site. The Manning coefficient and the losses by abstraction were assumed on the basis of the land use and land cover of the catchment, classified as permeable and impermeable. Since the catchment is almost entirely impermeable (i.e., there are relatively few losses through infiltration), the calibration of the hydrodynamic model would only consider the Manning's coefficient if we neglect the effect of the initial abstraction in impermeable areas. The assumed values of the Manning's coefficient are twofold: one that represents impermeable areas and other that represent shrub and grass, since we have 2 land use and land cover classification in the catchment (Chow, 2010a). For the water quality wash-off parameters, we perform a first estimate based on the scarce observations presented in Ohnuma Jr e Mendiondo (2014). Furthermore, we evaluate the uncertainty in the wash-off parameters by a local sensitivity analysis varying the parameters $+40\%$ to -40% in terms of loads, concentrations and EMC of TSS.

In addition, we compared the HydroPol2D model with the HEC-RAS 2D full-momentum Pardiso fully implicit numerical solver (Brunner, 2016b; Gomes Jr et al., 2023d) to check the ability of the model to predict hydrographs at the outlet. In this analysis, we simulate the same design event but without infiltration and the initial abstraction effect.

3.2.5 Performance Indicators

The performance indicators are used to evaluate the modeling prediction capacity of HydroPol2D for water quantity and water quality estimation. In this paper, we use the Nash-Sutcliffe-Efficiency (Nash e Sutcliffe, 1970), the coefficient of determination, the Root-Mean-Square-Error (Fisher et al., 1920), and the PBIAS (Neyman e Pearson, 1936). The equations of each indicator are detailed in the Supplemental Material.

3.3 Results and Discussions

3.3.1 Numerical Case Study 1: The Role of Velocity Limitation and Numerical Stability

The mathematical model is developed by numerical discretization of differential equations solved by explicit finite differences in a forward Euler fashion. Thus, this case study aims to assess the impact of different temporal discretization on the hydrodynamic modeling of the V-Tilted Catchment, typically used to assess the performance of hydrologic and hydrodynamic models. In this analysis, several time steps were used to evaluate the numerical validation of the solution considered, limiting or not limiting the velocity to the critical velocity. Since we use forward Euler's discretization method, care must be taken to select the proper computational temporal meshgrid because the method is unconditionally unstable. In this section, we compare several hydrographs with constant time-step, with guaranteed stability and evident instability, with simulations made using the adaptive stable time-step scheme, as illustrated in Fig. 3.8.

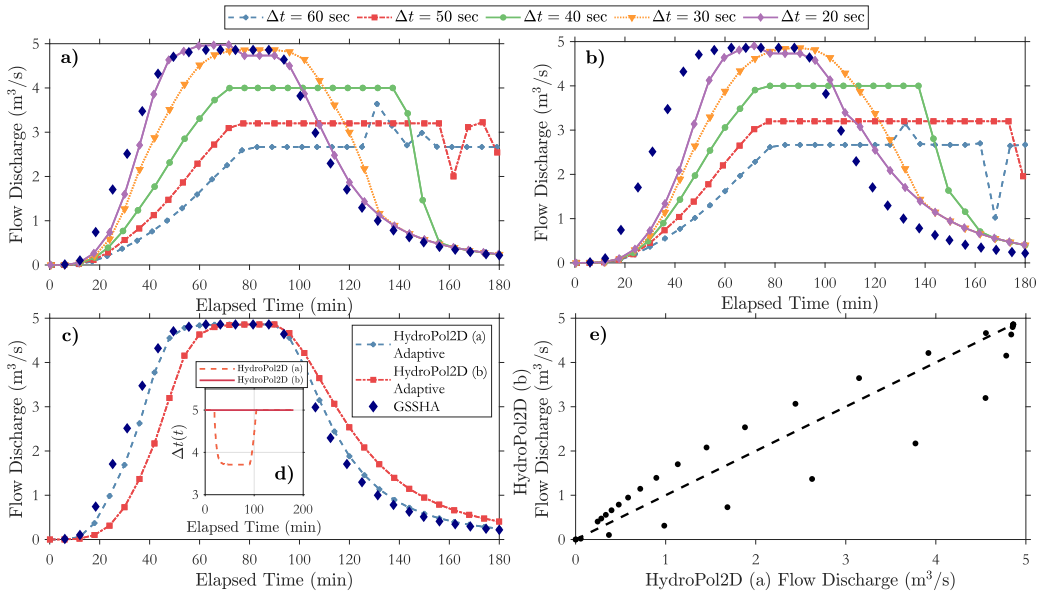

Figure 3.8. Comparison of hydrographs generated by different computational meshes; where (a)-(b) represent hydrographs for simulated for unstable meshes. Part (a) represents unstable meshes of HydroPol2D (a) while part (b) represents unstable meshes of HydroPol2D (b). Part (c) shows GSSHA results compared with stable results of HydroPol2D (a) and (b) with adaptive time-step, with the time-steps presented in Part d). Finally, part e) shows a scatter plot of stable meshes of HydroPol2D (a) and (b).

The different computational meshes used in the model reveal that the surface runoff modeling is practically invariant to cases where stable time-steps are chosen (see parts b and c in Fig. 3.8). This implies that once the CFL conditions are verified; the model can accurately predict hydrographs at the catchment outlet. The same is not true when we choose time-steps greater than 20 seconds. The system starts to show divergences from this value for both HydroPol2D models (a) and (b), generating a total loss of accuracy and numerical instability of the method for a time-step of 1 minute.

Significant differences occur when the HydroPol2D model restricts its maximum wave velocity. Although theoretically neglecting the hydraulic regime change would mean relatively smaller velocities and, therefore, allow longer time-steps, it is not consistent with the reality of more intense flow phenomena, especially in the case of large floods with high velocities. In these cases, the modeling allowing regime switching is closer to the results simulated with the GSSHA, assumed as the base scenario in this case study. Both HydroPol2D models (a) and (b) accurately predicted the peak flow; however, only model (a) was able to capture the time to peak more precisely, as it did not limit the flow velocity. The HydroPol2D model (b) is identical to the model proposed by (Guidolin et al., 2016), except that the HydroPol2D model allows one to calculate infiltration, water quality, and simulate different uses and land covers.

3.3.2 Numerical Case Study 2: Water Quality Model Validation

The results of the numerical calibration are presented in detail in the Supplemental Material. The pollutographs of all eight events simulated with the statistics of RMSE, NSE, r^2, and PBIAS are presented in Fig. 3.9. The temporal dynamics of the solute was properly captured by the HydroPol2D model. The resulting calibrated parameters for events 1-4 are $C_3 = 9036.83$ and $C_4 = 0.2435$, while for events 5-8, $C_3 = 7445.11$ and $C_4 = 0.1916$. Although HydroPol2D can accurately capture the dynamics of the solute, calibration of water quality parameters is required and varies according to the physiographic characteristics of the catchment, such as slope, length, width, and roughness (Xiao et al., 2017; Zhang et al., 2020).

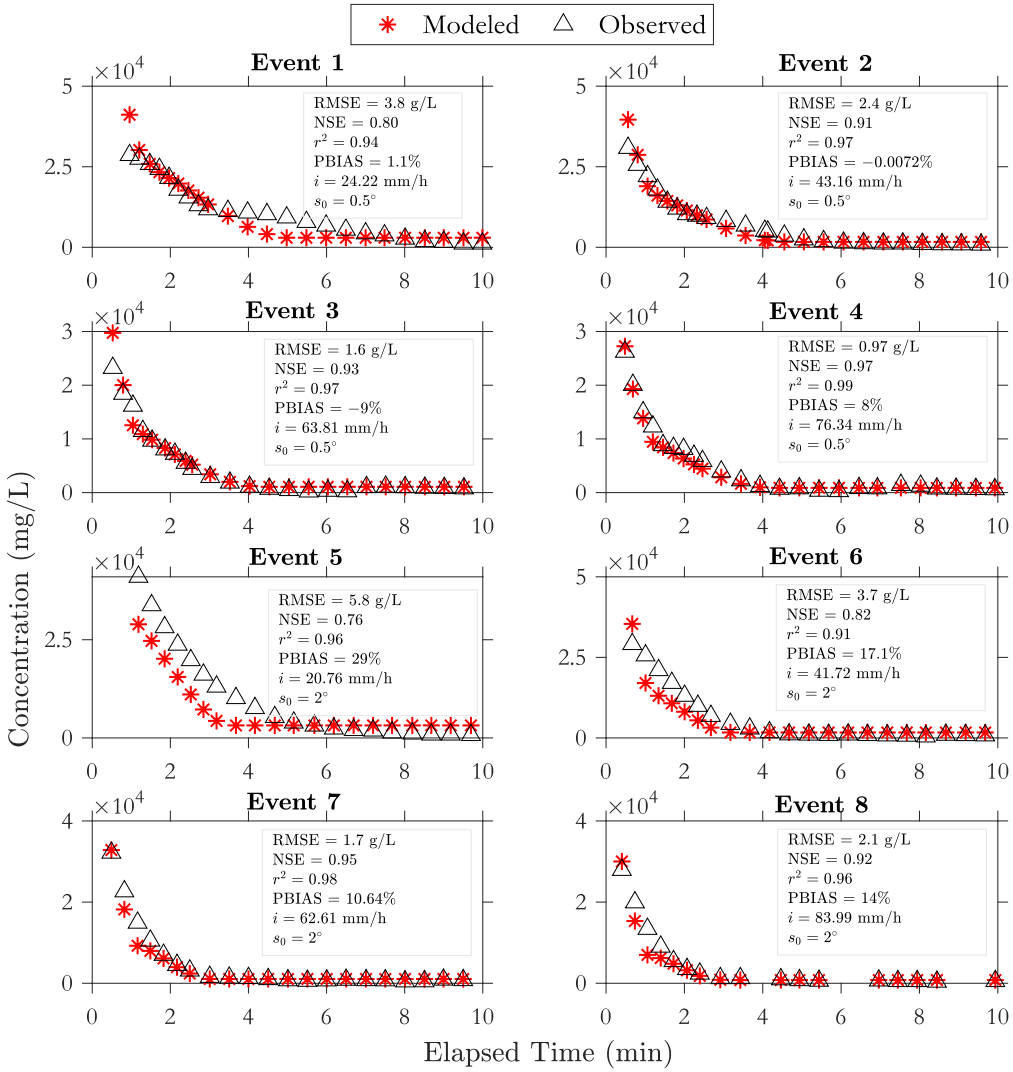

Figure 3.9. Comparison between HydroPol2D pollutographs with observed concentration of salt in a laboratory wooden board catchment of 4.5 m^2 (Zhang et al., 2020). The initial mass of salt is 125 g and is uniformly distributed.

3.3.3 Numerical Case Study 3: Dynamics of Water Quantity and Quality in Poorly Gauged Catchments

3.3.3.1 Comparison Between HEC-RAS and HydroPol2D

The results indicated in Fig. 3.10 show the goodness of fitness between HydroPol2D and HEC-RAS 2D in the Tijuco Preto catchment compared to the HydroPol2D model. The NSE index is 0.97, the r^2 is 0.98 and the PBIAS is 4.4%, indicating a good agreement between both models for all evaluated metrics.

3.3.3.2 Local Sensitivity Analysis

Although the parameter estimates are based on previous studies (Ohnuma Jr e Mendiondo, 2014), a local sensitivity analysis was carried out to identify the most sensitive parameters in the water quality model. Fig. 3.11 a) shows the sensitivity of C_3, which was more sensitive to changes in maximum concentration. However, the results of Fig. 3.11 a) indicate that the wash-off coefficient (i.e., the ratio between the washed mass and the initially available mass) was not very sensitive to this variation, suggesting that the error in this parameter does not have a large effect on the total washed

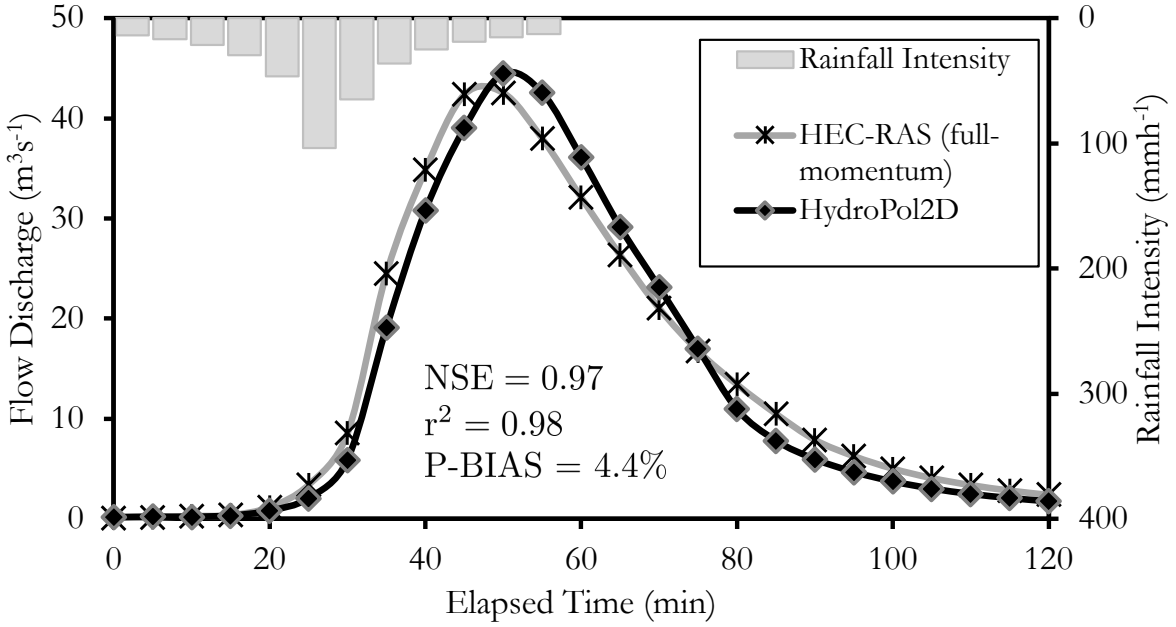

Figure 3.10. Outlet hydrograph comparison between the full momentum solver used in HEC-RAS and the diffusive-like numerical solution approach used in the HydroPol2D model. Both outlet boundary conditions were assumed as normal depth with gradient slope of 2% and the catchment hydrological processes were simulated without infiltration and initial abstraction.

mass at the outlet. Both the EMC and the maximum load had a low sensitivity to C_3, indicating that its error does not compromise the average and diluted analyzes (e.g., EMC), but the dynamic ones such as the maximum concentration.

The results presented in Fig. 3.11 b) show an opposite scenario than that shown in Fig. 3.11 a). However, in general, decreasing C_4 increases peak concentrations and loads, which is explained by a greater mass swept at flow rates smaller than 1 m^3s^{-1}(see Eq. 3.8). Since the wash-off is a flow-dependent rating curve, lower C_4 exponents at flows lower than 1 (i.e., 1 m^3s^{-1}) increase the washed rates. Thus, larger masses washed in smaller volumes tend to increase the concentration. This is a numerical characteristic of the wash-off model used in this article. Another mathematical alternative to pollutants that do not follow the proposed rating curve is to add a factor μ to the flow, so that the flow used in the modeling of pollutants is $(Q + \mu)$, in order to avoid this numerical problem.

The maximum load rates of TSS increase with increasing C_4, indicating a higher instantaneous washing rate at the outlet in a given time. However, these loads occur only at large flows greater than 1 m^3s^{-1}; therefore, the increase in C_4, despite increasing the maximum load, decreases the wash-off coefficient because most flows are smaller than 1 m^3s^{-1}. This implies that higher values of C_4 work well on heavy pollutants mobilized in large flows; however, as pollutants are mobilized only in large flows, the total mass washed is less than a case of lower C_4. On the basis of this same hypothesis, C_4 is concluded to have a strong relationship with the density and mean diameter of the pollutant.

Fig. 3.11 c) presents the first-flush curve for each scenario evaluated. The critical cases of the first flush (that is, larger masses washed in smaller volumes) are more evident in the variation of C_3 (scenarios 1, 2, 3). In all cases except for scenario 8, more than 60% of the pollutants were washed with 30% by volume (Di Modugno et al., 2015), indicating a strong first-flush. This implies that even with eventual changes in the wash-off parameters, the first flush effect is mostly observed as a result of the high impervious rate of the catchment, which quickly washes the pollutant toward the outlet. The pollutograph showed high variability, as shown in Fig. 3.11 d), with higher peaks for higher values of C_4 and C_3.

Therefore, if we consider a maximum uncertainty of 40% in the water quality parameters,

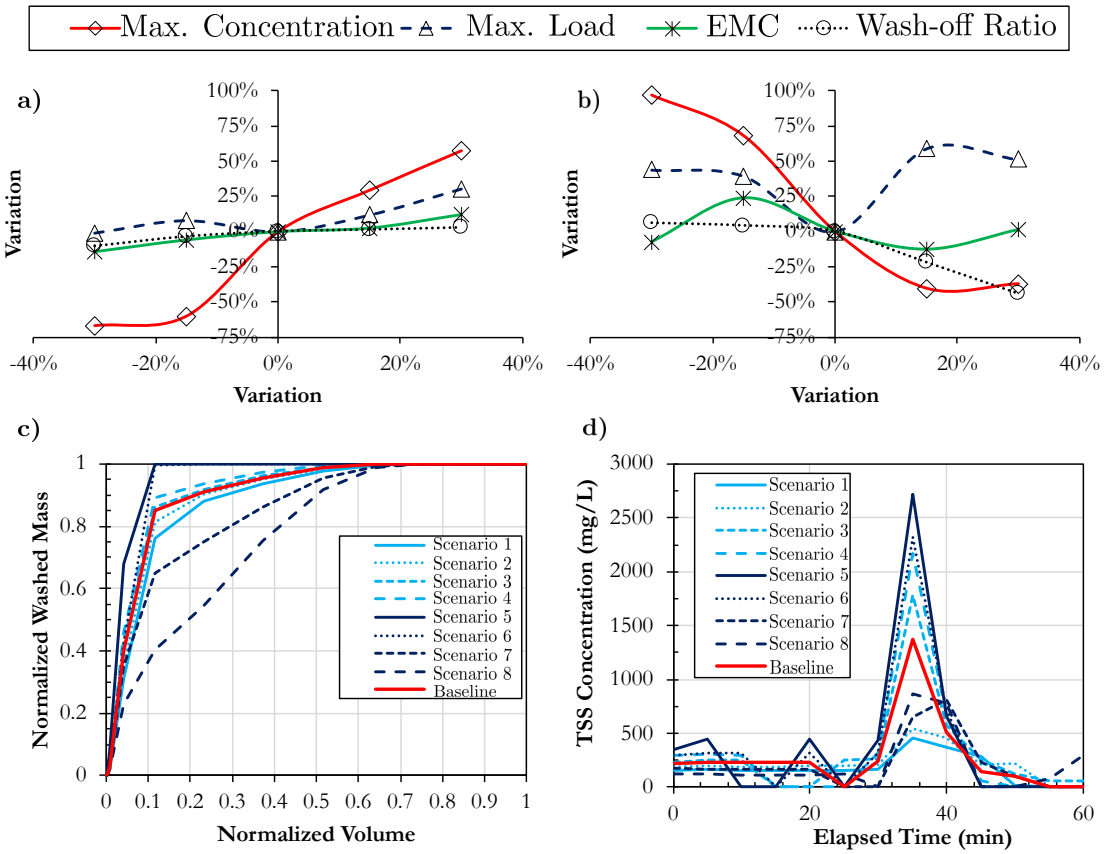

Figure 3.11. Results of the model sensitivity analysis for an event of RP = 1 year, C_3 = 1,200 and C_4 = 1.2. Parts a) and b) represent the sensitivity of the maximum concentration, maximum load, and average concentration of the event for variations of C_3 (a) and C_4 (b). Parts c) and d) represent the first-flush curves and pollutographs of each simulated scenario, detailed in Table 3.3. The wash-off ratio is defined as the ratio between the washed mass and the available mass in the catchment.

Table 3.3. Data used in the sensitivity analysis and its respective modeling results.

Scenario	C_3	C_4	Maximum instantaneous Concentration (mgL^{-1})	Maximum Load (kgh^{-1})	EMC (mgL^{-1})	Washoff-Ratio
1	840	1.2	455.19	6.25	112.55	0.62
2	1020	1.2	548.33	6.81	123.83	0.67
3	1380	1.2	1786.73	7.06	135.18	0.70
4	1560	1.2	2174.31	8.22	148.11	0.71
5	1200	0.84	2716.02	9.09	121.85	0.74
6	1200	1.02	2319.25	8.81	163.13	0.72
7	1200	1.38	817.91	10.04	114.81	0.54
8	1200	1.56	862.95	9.55	133.29	0.39
Baseline	1200	1.2	1377.75	6.31	131.81	0.69

Fig. 3.11 (c and d) would represent first-flush and pollutogram envelopes for the simulated event. Statistically, this indicates that in 30% of the volume, 89% ś 10% of the TSS of the catchment is swept away. Similarly, the maximum load and the maximum concentration of TSS are 8.22 ś 1.29 kgs^{-1} and 1,460 ś 832 mgL^{-1}, respectively, and the wash-off coefficient and EMC are 0.63 ś 0.11 and 131.59 ś 16 mgL^{-1}, respectively. Normalizing these values by the catchment area, the Load = 2.56 ś 0.4 $kgs^{-1}km^{-2}$, TSS = 456 ś 260 $mgL^{-1}km^{-2}$, EMC = 41 ś 5 $mgL^{-1}km^{-2}$. These values are within the expected values for moderate rainfall in urbanized areas (Rossman e Huber, 2016).

3.3.3.3 Simulation Results for RP = 1 year

The simulation of the TPC for 1 year return period event for rainfall and for the number of dry days is shown in Fig. 3.12. Fig. 3.12 b) shows the maximum flood depth in the catchment, identifying areas susceptible to flooding with maximum depths of up to 1.50 m for an 1 hour of rainfall and 32 mm of volume distributed in Alternated Blocks. Fig. 3.12 a) shows the maximum velocity map, which exceeded 10 ms^{-1} in the stream. Note that the maximum velocities are not necessarily associated with this maximum depth due to the rise and recession of the hydrographs with the propagation of the diffusive wave. The surface runoff generated was approximately equal to the total rainfall volume of 32 mm, except for the volume infiltrated in permeable areas, illustrated in Fig. 3.12 e). In this figure, it is possible to observe infiltrated volumes greater than the precipitated volume. This occurred because the pervious areas receive runoff volume from several cells upstream, which increases the ponding depth and therefore increases the infiltration capacity. Although most of the catchment is impervious, flood depths occurred mainly in the stream, falling toward the overbanks only in a few areas, as illustrated in Fig. 3.12 b). This occurred due to the relatively low return period assumed in the modeling.

Regarding the TSS transport, Fig. 3.12 d) shows how much pollutants have flowed to each cell during the event studied. Naturally, the stream is the area with the greatest passage of pollutants. However, it is possible to identify locations outside the urban stream that also have a high level of pollution transport. These results could be strategically used to identify possible candidate areas for the implementation of LIDs. Therefore, this methodology makes it possible to quantitatively identify the most suitable areas to maximize the capture of pollutants carried by surface runoff, especially the TSS.

After the rainfall event, the remaining mass in the catchment is shown in Fig. 3.12 f). This map illustrates the relatively clean stream and some areas with a relatively large accumulation of pollutants (e.g., $>$ 60 gm^{-2} or 9.3 kg of TSS in each pixel of 156.25 m^2). Therefore, this map can help identify areas of accumulation and can serve as information for model calibration when used for sediment modeling. Despite being more dynamic and instantaneous, the maximum concentration also allows one to identify the maximum polluting potential of surface runoff water, as illustrated in Fig. 3.12 c).

The analysis of the normalized outlet hydrograph result is presented in Fig. 3.13. It is possible to observe the hysteresis phenomenon (Aich et al., 2014), which shows that the concentration peak occurs approximately 25 min before the surface runoff peak. First, the rainfall peak occurs, following the concentration, load, and discharge peak, respectively. The first flush chart also shows that more than 90% of the TSS are washed in 30% of the volume. The same chart allows us to estimate (i) the time of concentration for this event, (ii) the peak time of flow discharges, concentrations, and loads, and allows comparison of results with other catchments, since all values are normalized by the catchment area.

3.3.4 Challenges and Limitations of the Application of Distributed Models in Poorly-Gauged Catchments

Depending on the purpose and scale of the study, elevation data may be crucial in applying hydrological and water quality models. In the case of modeling focused on the delineation of flood inundation maps, FEMA, the Federal Emergency Agency of the United States, recommends as a minimum criterion hydrodynamic simulations with a resolution of up to 3 m with a vertical resolution of at most 1 cm. Detailed elevation data are available in countries such as Brazil only in some large cities, e.g. São Paulo, making it difficult to apply them at several important points where floods occur (Santos et al., 2016).

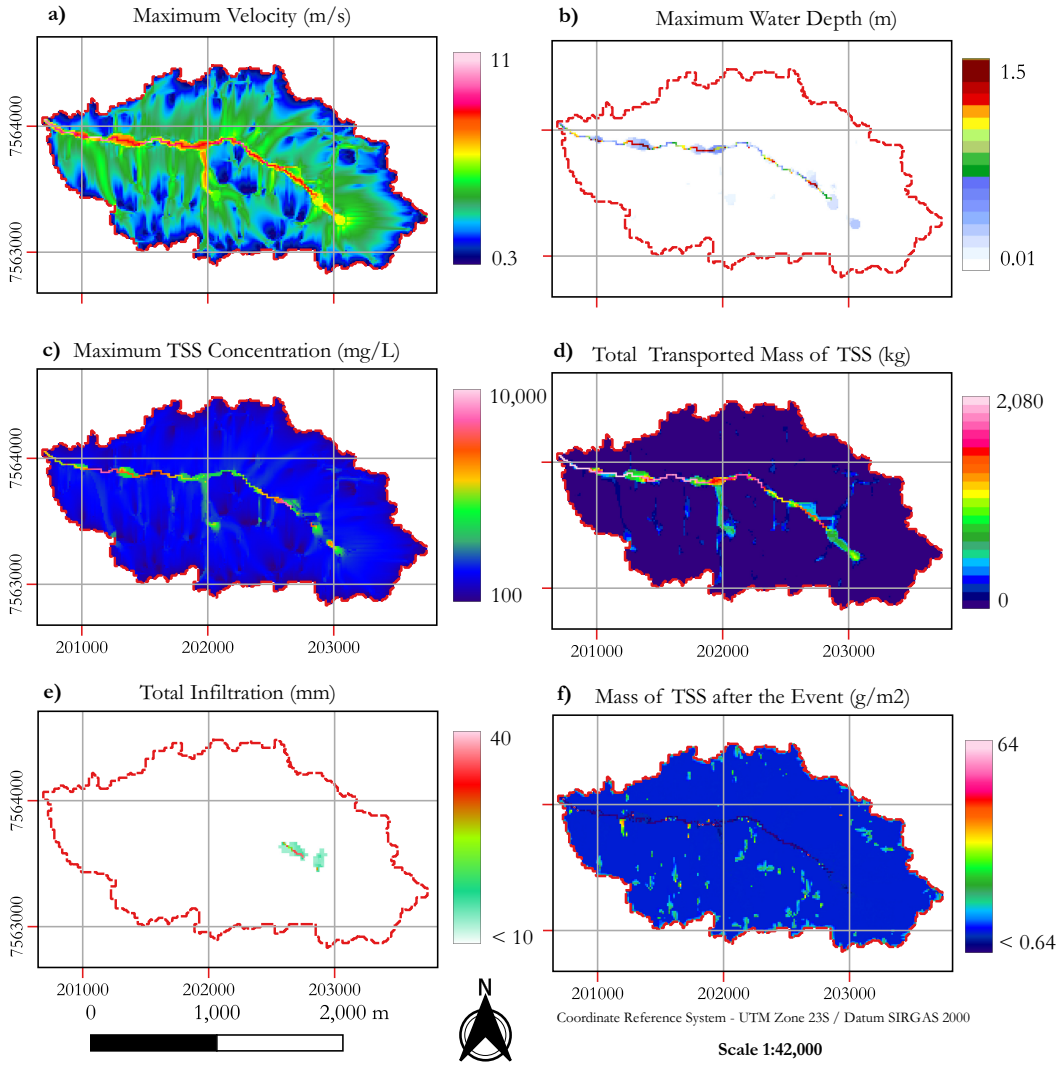

Figure 3.12. Simulation results with baseline scenario parameters, where a) is the maximum velocity, b) is the map of maximum depths, c) the maximum instantaneous concentration of TSS, d) is the map that represents the total mass that passed through each cell. The catchment boundaries are given by the red dashed lines.

The most recurring application of hydrodynamic models is the study and delineation of flood inundation areas (do Lago et al., 2021; Erena et al., 2018; Fava et al., 2022). Although the HydroPol2D model does not solve the complete Saint-Venant 2D equations, its diffusive wave methodology is promising for determining flood areas in catchments where convective and local acceleration phenomena do not act as the main hydrodynamic governing processes. The flood inundation depth coupled with the velocity maps can serve as a basis to calculate the risk of human instability during a flood event (Rotava et al., 2013), to assess potential flood damage (Jamali et al., 2018) or as input data for estimating the value of flood insurance policies (Aerts e Botzen, 2011). Furthermore, the model can be used to estimate the time of concentration without requiring calculating it by empirical formulae (Manoj et al., 2012), as previously presented. Additionally, flows at the catchment outlet can be estimated without the need for unit hydrographs.

Examples of the use of distributed models to determine hydrographs are presented in Furl et al. (2018); Sharif et al. (2010) and (Sharif et al., 2013). To this end, however, if the information on where the stream passes is dissolved in the coarse resolution of the elevation pixels, it is necessary to recondition the terrain model, smoothing thalweg lines and elevation peaks, or sometimes imposing lower elevations in channel sections as presented in this paper. Another application is the spatial asses-

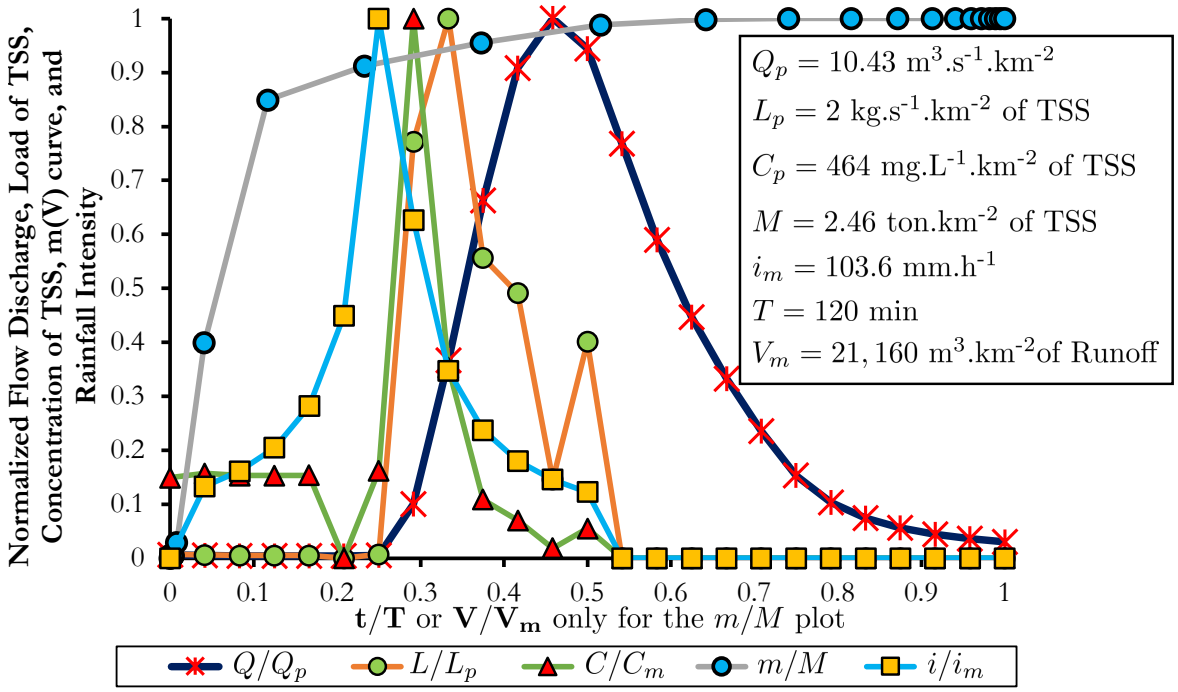

Figure 3.13. Normalized modeling results, where all values are divided by their next maximum values and are typically divided by the watershed area of 3.20 km^2. Q is the flow discharge, Q_p is the peak flow, L is the pollutant load, L_p is the maximum pollutant load, C is the pollutant concentration, C_p is the maximum pollutant concentration m is the washed pollutant mass, M is the total mass of pollutant washed, i is the rainfall intensity, i_m is the maximum rainfall intensity, t is the time and T is the total duration.

sment of infiltration, which can be important in some urban areas and plays a major role in rural areas. This analysis can aid in spatial quantification of infiltration, which can aid in the decision about the implanted or chosen crop (Paudel et al., 2011). These examples show that, although modeling aimed at delineating flooded areas via 2D modeling requires high spatial resolution DEM, the determination of flows and, at least, the identification of critical points in the catchment can be identified with free data derived from satellite products (e.g., SRTM (Drusch et al., 2012) and Alos Palsar (Rosenqvist et al., 2007)).

The most uncertain variable that is very difficult to estimate is the initial build-up map (Wijesiri et al., 2015b). Several studies indicate that the use of the build-up equation with ADD as a dependent variable may not correctly represent the pollutant accumulation process in urban catchments (Bonhomme e Petrucci, 2017; Zhang et al., 2019). Variables such as the predominant wind speed and direction, atmospheric pressure, humidity, and the geographic position of the catchment near roads and highways, among others, can play an essential role in the accumulation of pollutants (Pandey et al., 2016). Furthermore, the build-up model assumes a uniform accumulation for each land use, disregarding accumulation characteristics (e.g., source pollution release). All these limitations must be taken into account when modeling water quality. The HydroPol2D model, although developed for non-point source pollution, allows the modeling of source pollution by entering load rates at specific cells as external boundary conditions.

Despite the difficulties in model calibration, most parameters can be estimated, at least at the preliminary analysis level, based on the literature (Rossman et al., 2010). Sensitivity analysis reveals that the most important parameters of the model are the Manning's roughness coefficients and the wash-off coefficients, especially the exponent (C_4). Both parameters can be derived as a function of land use classifications. The model makes it possible to identify, using mostly physically-based equations, the hydrological, hydrodynamic, and distribution behavior of diffusive pollution in catchments where

Hortonian processes govern the flow. The model allows for the estimation of important factors at the outlet level and spatialized values throughout the catchment. Therefore, one of the applications is to determine the critical areas of accumulation of pollutants in the catchment during and after precipitation events. This information can be used in master plans for better water quality management and to define potential areas to implement LID techniques focused on treating part of surface runoff (Batalini de Macedo et al., 2022b; McClymont et al., 2020; de Oliveira et al., 2021).

Furthermore, the model can be used to evaluate the spatial impact of LIDs at the watershed scale by modeling its pixels with different land use and elevation properties (e.g., reducing the pixel elevation to simulate the ponding layer on the surface). This analysis can be done to quantify water quality and estimate the volumes of surface runoff retention. Furthermore, at the outlet of the catchment, dynamic factors such as the load and concentration of pollutants are estimated and are indicators of the response of the catchment to simulated events. Finally, the first flush modeling can be performed using the HydroPol2D model, which is an important evaluation for urbanized catchments.

3.4 Conclusions

Evaluating the impacts of surface runoff quality and quantity in urbanized catchments requires the temporal and spatial quantification of flood depths, pollutant transport, and fate. With this focus, the HydroPol2D model was designed and first applied in the V-tilted catchment to identify the role of the maximum flow velocity limitation. Our results indicates that limiting velocities to critical, reduce the model performance. The HydroPol2D water quality module was calibrated and validated with the observed data provided from a wooden board catchment. Subsequently, the model was applied in the Tijuco Preto catchment in São Carlos - focusing on the qualitative and quantitative quantification of the spatial-temporal behavior of surface runoff. Even with the lack of observed or high-resolution elevation data, it was possible to evaluate the quali-quantitative dynamics of the stormwater runoff for a return period of 1 year, both for rainfall and the number of antecedent dry days. An event composed of drought followed by a flood was evaluated. The results of the numerical simulation for the Numerical Case Study 3 indicate the following:

- The maximum load and the maximum TSS concentration at the outlet are 8.22 ± 1.29 kgs^{-1} and $1,460 \pm 832$ mgL^{-1}. Normalizing by the catchment area of 3.20 km^2 it follows that the maximum concentration of TSS is 456 ± 260 mgL^{-1}km^{-2} and the maximum load of TSS is 2.56 ± 0.4 kgs $^{-1}$km^{-2} for a 1-yr flood-drought event.
- The Washoff-Ratio coefficient and the EMC were 0.63 ± 0.11 and 131.59 ± 16 mgL^{-1}, respectively, for a 1-yr flood-drought event.
- The volume of TSS washed in 30% of the runoff volume was $89\% \pm 10\%$, indicating a high first-flush phoenomen in the catchment, considering an uncerntainty in wahs-off parameters from -40% to 40%.

The results of this article show how quali-quantitative modeling can be used to determine possible areas for applying LIDs, delineating areas prone to flooding, analysis of maximum flow velocities, and therefore risk of human instability due to floods. Furthermore, it allows to identify maps of maximum pollutant concentration. Despite the impossibility of calibrating the model for the TPC catchment due to lack of data, the calibration of quali-quantitative parameters is encouraged and can be done in the model via automatic calibration using optimization packages in Matlab (Higham e Higham, 2016).

Furthermore, the analysis performed can be replicated for other combinations of RPs for rainfall and antecedent dry days. Future studies will incorporate resilience metrics, not only for

short-term forecasts but also for scenario-based climate change predictions in large-scale watersheds. Thus, HydroPol2D can flexibly assess floods, drought-flood composite events, and water quality to aid decision-making in warning systems. Moreover, future work will incorporate modeling via continuous simulation. In this case, spatially varied climatological forcing and even drought-flood pooling under anthropic land-use change can be performed through HydroPol2D. Finally, testing the simulation computational time performance of the model against state-of-the-art software is also desired.

As in other distributed models, the challenge for the quality of the results presented by HydroPol2D is related to the quality of the input data, especially the topography and land use and land cover data. However, the model requires relatively few parameters to describe the hydraulic properties of the terrain and allows us to simulate quantity and/or quality. When simulating only water quantity, significant differences in processing time are obtained with HydroPol2D. Another advantage is the model's applicability, which, if the hydrological processes are predominantly Hortonian, allows simulating catchments at all spatial scales. Future studies will incorporate spatial variability of rainfall and evapotranspiration for large-scale watersheds, especially for modeling under periods of persistent droughts with unprecedented floods. Ultimately, the HydroPol2D model can become a tool for a wide range of purposes, either in real-time forecasting or even in scenarios, by incorporating distributed modeling of hydrodynamics and pollutant transport and fate.

Acknowledgment

The authors appreciate the support of the City of San Antonio, by the San Antonio River Authority, CAPES Ph.D Scholarship, and the PPGSHS PROEX Graduate Program. The authors also appreciate the support by Grant # FAPESP 22/08468-0 "Flash drought event evolution characteristics and response mechanism to climate change", Grant # FAPESP 14/50848-9 "INCTMC2 Nat. Inst. of Sci. & Tech. for Climate Change Phase 2 Water Security Subcomponent, and Grant 139529Q/3281199 Univ Montpellier I-SITE Excellence Program, Campus France.

Appendix A. Supplementary Material

Supplementary data related to this article can be found at:
https://github.com/marcusnobrega-eng/HydroPol2D.

Data Availability Statement

Algorithms and data used are available in an open repository at (Gomes Jr., 2023).

References

Aerts, J. C. e Botzen, W. W. (2011). Climate change impacts on pricing long-term flood insurance: A comprehensive study for the netherlands. *Global environmental change*, 21(3):1045–1060.

Aich, V., Zimmermann, A., e Elsenbeer, H. (2014). Quantification and interpretation of suspended-sediment discharge hysteresis patterns: how much data do we need? *Catena*, 122:120–129.

Arnold, J. G., Moriasi, D. N., Gassman, P. W., Abbaspour, K. C., White, M. J., Srinivasan, R., Santhi, C., Harmel, R., Van Griensven, A., Van Liew, M. W., et al. (2012). Swat: Model use, calibration, and validation. *Transactions of the ASABE*, 55(4):1491–1508.

Baptista, M. V., Scarpinella, G. D., e Menezes, D. B. (2021). Idas e vindas do processo de degradação e recuperação de um córrego urbano. *SIMPÓSIO NACIONAL DE GESTÃO E ENGENHARIA URBANA*, 3:87–95.

Batalini de Macedo, M., Nobrega Gomes Junior, M., Pereira de Oliveira, T. R., H. Giacomoni, M., Imani, M., Zhang, K., Ambrogi Ferreira do Lago, C., e Mendiondo, E. M. (2022b). Low impact development practices in the context of united nations sustainable development goals: A new concept, lessons learned and challenges. *Critical Reviews in Environmental Science and Technology*, 52(14):2538–2581.

Bonhomme, C. e Petrucci, G. (2017). Should we trust build-up/wash-off water quality models at the scale of urban catchments? *Water research*, 108:422–431.

Brighenti, T. M., Bonumá, N. B., Srinivasan, R., e Chaffe, P. L. B. (2019). Simulating sub-daily hydrological process with swat: a review. *Hydrological Sciences Journal*, 64(12):1415–1423.

Brunner, G. W. (2016b). Hec-ras river analysis system modeling user's manual us army corps of engineers hydrologic engineering center. *Information on http://www. hec. usace. army. mil*.

Chow, T. (2010a). V (2010). applied hydrology.

Collischonn, W., Allasia, D., Da Silva, B. C., e Tucci, C. E. (2007). The mgb-iph model for large-scale rainfallrunoff modelling. *Hydrological Sciences Journal*, 52(5):878–895.

Courant, R., Friedrichs, K., e Lewy, H. (1928). Über die partiellen differenzengleichungen der mathematischen physik. *Mathematische annalen*, 100(1):32–74.

de Oliveira, T. R. P., de Macedo, M. B., Oliveira, T. H., do Lago, C. A. F., Gomes Jr, M. N., Brasil, J. A. T., e Mendiondo, E. M. (2021). Different configurations of a bioretention system focused on stormwater harvesting in brazil. *Journal of Environmental Engineering*, 147(12):04021058.

De Paiva, R. C. D., Buarque, D. C., Collischonn, W., Bonnet, M.-P., Frappart, F., Calmant, S., e Bulhões Mendes, C. A. (2013). Large-scale hydrologic and hydrodynamic modeling of the amazon river basin. *Water Resources Research*, 49(3):1226–1243.

Deletic, A. (1998). The first flush load of urban surface runoff. *Water research*, 32(8):2462–2470.

Di Modugno, M., Gioia, A., Gorgoglione, A., Iacobellis, V., La Forgia, G., Piccinni, A. F., e Ranieri, E. (2015). Build-up/wash-off monitoring and assessment for sustainable management of first flush in an urban area. *Sustainability*, 7(5):5050–5070.

do Lago, C. A., Giacomoni, M. H., Bentivoglio, R., Taormina, R., Junior, M. N. G., e Mendiondo, E. M. (2023). Generalizing rapid flood predictions to unseen urban catchments with conditional generative adversarial networks. *Journal of Hydrology*, 618:129276.

do Lago, C. A. F., Hofheinz Giacomoni, M., Olivera, F., e Mário Mendiondo, E. (2021). Assessing the impact of climate change on transportation infrastructure using the hydrologic-footprint-residence metric. *Journal of Hydrologic Engineering*, 26(5):04021014.

Downer, C. W. e Ogden, F. L. (2004). Gssha: Model to simulate diverse stream flow producing processes. *Journal of Hydrologic Engineering*, 9(3):161–174.

Downer, C. W., Pradhan, N. R., Ogden, F. L., e Byrd, A. R. (2015). Testing the effects of detachment limits and transport capacity formulation on sediment runoff predictions using the us army corps of engineers gssha model. *Journal of Hydrologic Engineering*, 20(7):04014082.

Drusch, M., Del Bello, U., Carlier, S., Colin, O., Fernandez, V., Gascon, F., Hoersch, B., Isola, C., Laberinti, P., Martimort, P., et al. (2012). Sentinel-2: Esa's optical high-resolution mission for gmes operational services. *Remote sensing of Environment*, 120:25–36.

Erena, S. H., Worku, H., e De Paola, F. (2018). Flood hazard mapping using flo-2d and local management strategies of dire dawa city, ethiopia. *Journal of Hydrology: Regional Studies*, 19:224–239.

Fan, F. M. e Collischonn, W. (2014). Integração do modelo mgb-iph com sistema de informação geográfica. *Rbrh: revista brasileira de recursos hídricos. Porto Alegre, RS. Vol. 19, n. 1 (jan./mar. 2014), p. 243-254*.

Farooq, M., Shafique, M., e Khattak, M. S. (2019). Flood hazard assessment and mapping of river swat using hec-ras 2d model and high-resolution 12-m tandem-x dem (worlddem). *Natural Hazards*, 97(2):477–492.

Fava, M. C., Macedo, M. B. d., Buarque, A. C. S., Saraiva, A. M., Delbem, A. C. B., e Mendiondo, E. M. (2022). Linking urban floods to citizen science and low impact development in poorly gauged basins under climate changes for dynamic resilience evaluation. *Water*, 14(9):1467.

Fisher, R. A. et al. (1920). 012: A mathematical examination of the methods of determining the accuracy of an observation by the mean error, and by the mean square error. *Monthly Notices of the Royal Astronomical Society*.

Fry, T. J. e Maxwell, R. M. (2018a). Using a distributed hydrologic model to improve the green infrastructure parameterization used in a lumped model. *Water*, 10(12):1756.

Fu, B., Merritt, W. S., Croke, B. F., Weber, T. R., e Jakeman, A. J. (2019). A review of catchment-scale water quality and erosion models and a synthesis of future prospects. *Environmental modelling & software*, 114:75–97.

Furl, C., Ghebreyesus, D., e Sharif, H. O. (2018). Assessment of the performance of satellite-based precipitation products for flood events across diverse spatial scales using gssha modeling system. *Geosciences*, 8(6):191.

Getirana, A. C., Boone, A., Yamazaki, D., Decharme, B., Papa, F., e Mognard, N. (2012). The hydrological modeling and analysis platform (hymap): Evaluation in the amazon basin. *Journal of Hydrometeorology*, 13(6):1641–1665.

Gomes Jr. (2023). Hydropol2d v.0.0.1. https://github.com/marcusnobrega-eng/HydroPol2D.

Gomes Jr, M., Giacomoni, M., Papagiannakis, A., Mendiondo, E., e Dornelles, F. (2021). Spatial assessment of overland flow, pollutant concentration, and first flush using a 2-d non-point source pollution and hydrological model for urban catchments. In *World Environmental and Water Resources Congress*, pages 397–413.

Gomes Jr., M. N., Giacomoni, M. H., Taha, A. F., e Mendiondo, E. M. (2022). Flood risk mitigation and valve control in stormwater systems: State-space modeling, control algorithms, and case studies. *Journal of Water Resources Planning and Management*, 148(12):04022067.

Gomes Jr, M. N., Rápalo, L. M., Oliveira, P. T., Giacomoni, M. H., do Lago, C. A., e Mendiondo, E. M. (2023c). Modeling unsteady and steady 1d hydrodynamics under different hydraulic conceptualizations: Model/software development and case studies. *Environmental Modelling & Software*, page 105733.

Gomes Jr, M. N., Rápalo, L. M., Oliveira, P. T., Giacomoni, M. H., do Lago, C. A., e Mendiondo, E. M. (2023d). Modeling unsteady and steady 1d hydrodynamics under different hydraulic conceptualizations: Model/software development and case studies. *Environmental Modelling & Software*, page 105733.

Green, W. H. e Ampt, G. A. (1911). Studies on soil phyics. *The Journal of Agricultural Science*, 4(1):1–24.

Guidolin, M., Chen, A. S., Ghimire, B., Keedwell, E. C., Djordjević, S., e Savić, D. A. (2016). A weighted cellular automata 2d inundation model for rapid flood analysis. *Environmental Modelling & Software*, 84:378–394.

Higham, D. J. e Higham, N. J. (2016). *MATLAB guide*. SIAM.

Hossain, I., Imteaz, M. A., e Hossain, M. I. (2012). Application of a catchment water quality model for an east-australian catchment. *International journal of global environmental issues*, 12(2-4):242–255.

Jamali, B., Löwe, R., Bach, P. M., Urich, C., Arnbjerg-Nielsen, K., e Deletic, A. (2018). A rapid urban flood inundation and damage assessment model. *Journal of Hydrology*, 564:1085–1098.

Kabir, S., Patidar, S., Xia, X., Liang, Q., Neal, J., e Pender, G. (2020). A deep convolutional neural network model for rapid prediction of fluvial flood inundation. *Journal of Hydrology*, 590:125481.

Keifer, C. J. e Chu, H. H. (1957b). Synthetic storm pattern for drainage design. *Journal of the hydraulics division*, 83(4):1332–1.

Knightes, C. D., Ambrose Jr, R. B., Avant, B., Han, Y., Acrey, B., Bouchard, D. C., Zepp, R., e Wool, T. (2019). Modeling framework for simulating concentrations of solute chemicals, nanoparticles, and solids in surface waters and sediments: Wasp8 advanced toxicant module. *Environmental Modelling & Software*, 111:444–458.

Kollet, S. J. e Maxwell, R. M. (2006a). Integrated surface–groundwater flow modeling: A free-surface overland flow boundary condition in a parallel groundwater flow model. *Advances in Water Resources*, 29(7):945–958.

Kreibich, H., Van Loon, A. F., Schröter, K., Ward, P. J., Mazzoleni, M., Sairam, N., Abeshu, G. W., Agafonova, S., AghaKouchak, A., Aksoy, H., et al. (2022). The challenge of unprecedented floods and droughts in risk management. *Nature*, 608(7921):80–86.

Lacaze, B., Dudek, J., e Picard, J. (2018). Grass gis software with qgis. *QGIS and generic tools*, 1:67–106.

Lantz, R. (1971). Quantitative evaluation of numerical diffusion (truncation error). *Society of Petroleum Engineers Journal*, 11(03):315–320.

Manoj, K., Fang, X., Yi, Y.-J., Li, M.-H., Cleveland, T. G., e Thompson, D. B. (2012). Estimating time of concentration on low-slope planes using diffusion hydrodynamic model. In *World Environmental and Water Resources Congress 2012: Crossing Boundaries*, pages 360–371.

McClymont, K., Cunha, D. G. F., Maidment, C., Ashagre, B., Vasconcelos, A. F., de Macedo, M. B., Dos Santos, M. F. N., Júnior, M. N. G., Mendiondo, E. M., Barbassa, A. P., et al. (2020). Towards urban resilience through sustainable drainage systems: A multi-objective optimisation problem. *Journal of Environmental Management*, 275:111173.

Melo, L. S., Costa, V. A., e Fernandes, W. S. (2023). Assessing the anthropogenic and climatic components in runoff changes of the são francisco river catchment. *Water Resources Management*, pages 1–15.

Nash, J. E. e Sutcliffe, J. V. (1970). River flow forecasting through conceptual models part ia discussion of principles. *Journal of hydrology*, 10(3):282–290.

Neyman, J. e Pearson, E. S. (1936). Contributions to the theory of testing statistical hypotheses. *Statistical research memoirs*.

Ohnuma Jr, A. A. e Mendiondo, E. M. (2014). Análise de cenários com proposição de medidas de recuperação ambiental para a micro-bacia do tijuco preto, são carlos-sp. *Brazilian Journal of Environmental Sciences (Online)*, pages 42–51.

Pandey, A., Himanshu, S. K., Mishra, S. K., e Singh, V. P. (2016). Physically based soil erosion and sediment yield models revisited. *Catena*, 147:595–620.

Passy, P. e Théry, S. (2018). The use of saga gis modules in qgis. *QGIS and generic tools*, 1:107–149.

Paudel, M., Nelson, E. J., Downer, C. W., e Hotchkiss, R. (2011). Comparing the capability of distributed and lumped hydrologic models for analyzing the effects of land use change. *Journal of hydroinformatics*, 13(3):461–473.

Prodesp (2022). Daee.

Richards, L. A. (1931). Capillary conduction of liquids through porous mediums. *Physics*, 1(5):318–333.

Rosenqvist, A., Shimada, M., Ito, N., e Watanabe, M. (2007). Alos palsar: A pathfinder mission for global-scale monitoring of the environment. *IEEE Transactions on Geoscience and Remote Sensing*, 45(11):3307–3316.

Rossman, L. e Huber, W. (2016). Storm water management model reference manual. *Volume II–Hydraulics, Tech. Rep. EPA/600/R-17/111, US EPA Office of Research and Development, Water Systems Division, avaialable at: https://nepis. epa. gov/Exe/ZyPDF. cgi*.

Rossman, L. A. et al. (2010). *Storm water management model user's manual, version 5.0*. National Risk Management Research Laboratory, Office of Research and Development, U.S. Environmental Protection Agency.

Rotava, J., Mendiondo, E. M., e Souza, V. C. B. (2013). Simulação de instabilidade humana em inundações: primeiras considerações. *XX Simpósio Brasileiro de Recursos Hídricos*, pages 1–8.

Santos, M. A., Carvalho, S. M., e Antoneli, V. (2016). Suscetibilidade de enchentes a partir da análise das variáveis morfométricas na bacia hidrográfica rio bonito em irati-pr-brasil. *Revista Equador*, 5(5):152–167.

Shabani, A., Woznicki, S. A., Mehaffey, M., Butcher, J., Wool, T. A., e Whung, P.-Y. (2021). A coupled hydrodynamic (hec-ras 2d) and water quality model (wasp) for simulating flood-induced soil, sediment, and contaminant transport. *Journal of Flood Risk Management*, 14(4):e12747.

Sharif, H. O., Al-zahrani, M., e Hassan, E. A. (2017b). Driven by gpm satellite rainfall over an urbanizing arid catchment in saudi arabia.

Sharif, H. O., Chintalapudi, S., Hassan, A. A., Xie, H., e Zeitler, J. (2013). Physically based hydrological modeling of the 2002 floods in san antonio, texas. *Journal of hydrologic Engineering*, 18(2):228–236.

Sharif, H. O., Sparks, L., Hassan, A. A., Zeitler, J., e Xie, H. (2010). Application of a distributed hydrologic model to the november 17, 2004, flood of bull creek watershed, austin, texas. *Journal of hydrologic engineering*, 15(8):651–657.

Shaw, S. B., Walter, M. T., e Steenhuis, T. S. (2006). A physical model of particulate wash-off from rough impervious surfaces. *Journal of Hydrology*, 327(3-4):618–626.

Souza, C. M., Z. Shimbo, J., Rosa, M. R., Parente, L. L., A. Alencar, A., Rudorff, B. F. T., Hasenack, H., Matsumoto, M., G. Ferreira, L., Souza-Filho, P. W. M., de Oliveira, S. W., Rocha, W. F., Fonseca, A. V., Marques, C. B., Diniz, C. G., Costa, D., Monteiro, D., Rosa, E. R., Vélez-Martin, E., Weber, E. J., Lenti, F. E. B., Paternost, F. F., Pareyn, F. G. C., Siqueira, J. V., Viera, J. L., Neto, L. C. F., Saraiva, M. M., Sales, M. H., Salgado, M. P. G., Vasconcelos, R., Galano, S., Mesquita, V. V., e Azevedo, T. (2020). Reconstructing three decades of land use and land cover changes in brazilian biomes with landsat archive and earth engine. *Remote Sensing*, 12(17).

Tu, M.-C. e Smith, P. (2018). Modeling pollutant buildup and washoff parameters for swmm based on land use in a semiarid urban watershed. *Water, Air, & Soil Pollution*, 229(4):1–15.

Vartziotis, E., Ulm, F., Boukin, K., Pellenq, R. J., Magnin, Y., e Ioannidou, K. (2022). Modeling inundation flooding in urban environments using density functional theory.

Vieira, J. D. (1983). Conditions governing the use of approximations for the saint-venant equations for shallow surface water flow. *Journal of Hydrology*, 60(1-4):43–58.

Volk, M., Bosch, D., Nangia, V., e Narasimhan, B. (2016). Swat: Agricultural water and nonpoint source pollution management at a watershed scale.

Wicke, D., Cochrane, T., e O'sullivan, A. (2012). Build-up dynamics of heavy metals deposited on impermeable urban surfaces. *Journal of Environmental Management*, 113:347–354.

Wijesiri, B., Egodawatta, P., McGree, J., e Goonetilleke, A. (2015a). Influence of pollutant build-up on variability in wash-off from urban road surfaces. *Science of the Total Environment*, 527:344–350.

Wijesiri, B., Egodawatta, P., McGree, J., e Goonetilleke, A. (2015b). Process variability of pollutant build-up on urban road surfaces. *Science of the Total Environment*, 518:434–440.

Xiao, Y., Zhang, T., Wang, L., Liang, D., e Xu, X. (2017). Analytical and experimental study on dissolved pollutant wash-off over impervious surfaces. *Hydrological processes*, 31(25):4520–4529.

Yanxia, S., Qi, Z., e Chunbo, J. (2022). A dynamic bidirectional coupling model for watershed water environment simulation based on the multi-grid technique. *Science of the Total Environment*, 843:156760.

Zaffani, A. G. (2012). *Poluição difusa da drenagem urbana com base ecohidrológica: diagnóstico atual e cenários de longo prazo em bacias urbanas de São Carlos, SP*. PhD thesis, Universidade de São Paulo - Escola de Engenharia de São Carlos.

Zhang, K., Deletic, A., Bach, P. M., Shi, B., Hathaway, J. M., e McCarthy, D. T. (2019). Testing of new stormwater pollution build-up algorithms informed by a genetic programming approach. *Journal of Environmental Management*, 241:12–21.

Zhang, T., Xiao, Y., Liang, D., Tang, H., Xu, J., Yuan, S., e Luan, B. (2020). A physically-based model for dissolved pollutant transport over impervious surfaces. *Journal of Hydrology*, 590:125478.

Zia, H., Harris, N. R., Merrett, G. V., Rivers, M., e Coles, N. (2013). The impact of agricultural activities on water quality: A case for collaborative catchment-scale management using integrated wireless sensor networks. *Computers and electronics in agriculture*, 96:126–138.

4 GLOBAL OPTIMIZATION-BASED CALIBRATION ALGORITHM FOR A 2D DISTRIBUTED HYDROLOGIC-HYDRODYNAMIC AND WATER QUALITY MODEL

A modified version was submitted to *Environmental Modelling and Software* as: Gomes Jr., M.N., Giacomoni, M.H., Navarro, F.A. and Mendiondo, E.M., 2024. Global Optimization-Based Calibration Algorithm for a 2D Distributed Hydrologic-Hydrodynamic and Water Quality Model.

Graphical Abstract

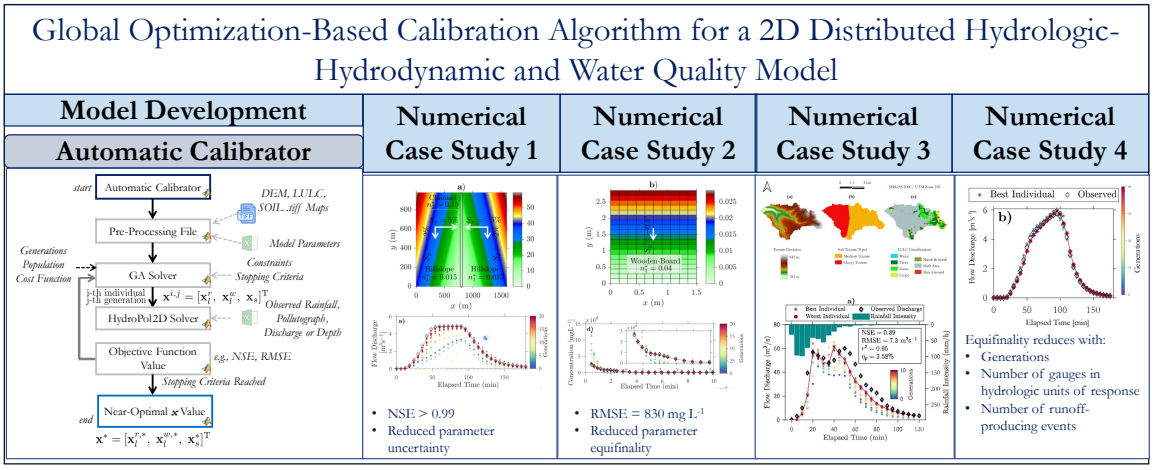

Highlights

- An automatic optimization calibration algorithm for spatially-distributed flood and water quality is developed.
- The algorithm uses HydroPol2D model and is able to calibrate water quantity and quality parameters globally.
- Source data in observed gauges such as discharges, depths, and concentration is required for the calibration.
- Equifinality is investigated and increases with the use of non-producing runoff events and increases with poor gauge locations.

Abstract

Hydrodynamic models with rain-on-the-grid capabilities are usually computationally expensive. This makes the use of automatic calibration algorithms hard to apply due to the large number of model runs. However, with the recent advances in parallel processing, computational resources, and increasing high-resolution climatologic and GIS data, high-resolution hydrodynamic models can be used for optimization-based calibration. This paper presents a global optimization-based algorithm to calibrate a fully distributed hydrologic-hydrodynamic and water quality model (HydroPol2D) using observed data (i.e., discharge, or pollutant concentration) as input. The algorithm can find a near-optimal set of parameters to explain observed gauged data. The modeling framework presented here, although applied in a poorly-gauged catchment, can be adapted for catchments with more detailed observations. We applied the algorithm in different cases of the V-Tilted Catchment, the Wooden-Board

catchment, and in an existing urban catchment with heterogeneous data. The results of automatic calibration indicate NSE = 0.99 for the V-Tilted catchment, RMSE = 830 mgL^{-1} for salt concentration pollutographs (i.e., 8.3% of the event mean concentration), and NSE = 0.89 for the urban catchment case study. This paper also explores the issue of equifinality in modeling calibration (EqMC). Equifinality is defined as the set of different parameter combinations that can provide equally good or accepted results, within the physical parameter ranges. EqMC decreases with the number of events and increases with the choice of partially or nonproducing runoff ones. Furthermore, results indicate that providing more accurate parameter ranges based on a priori knowledge of the catchment is fundamental to reduce the chances of finding a set of parameters with equifinality.

Keywords: Automatic Calibration, HydroPol2D, Parameter Estimation, Genetic Algorithm.

4.1 Introduction

The advances in computational processing, high resolution GIS data availability, and relatively more complete physically-based models enables the application of fully distributed hydrodynamic and pollutant transport and fate models (Yang et al., 2010; Gomes Júnior et al., 2022). Although the application of fully distributed models (i.e., models that discretize the catchment domain into finite cells) remotes to the early 1970s (Zhang et al., 1990), the demands for high-resolution modeling, especially for flood and pollution assessment, make optimization-based calibration (i.e., herein referred to as automatic calibration) complex, time-consuming, and dependent on prior knowledge of the modeler (Blasone et al., 2008) due to the relatively high computational effort required to perform numerical hydrodynamic simulations with high-resolution data (Blasone et al., 2008; Brath et al., 2004).

The complexity comes because the Shallow-Water-Equations dynamic problem forms a set of hyperbolic partial differential equations with no analytical solution for complex real-world cases (Bermudez e Vazquez, 1994), requiring finite-volume or finite-difference numerical schemes to solve the problem (Brunner, 2016b). The hydrodynamic problem can be simplified into diffusive-like problems when local acceleration and inertial terms can be neglected (Akan e Iyer, 2021) and these can reduce computational effort (Gomes et al., 2023); however, the number of required simulations for a full calibration still makes the process laborious. Since the governing equations of flow and pollutant routing are generally performed for each element in the grid domain either as a matrix-wise expression or as an element-wise approach, the numerical modeling process can be challenging for finer mesh grids, such as the ones required for flood mapping (do Lago et al., 2023). This might be one of the reasons why only a few articles attempted to develop automatic calibration algorithms for 2D hydrodynamic and pollutant transport and fate models (Afshar et al., 2011).

The parameter discretization of distributed models is usually performed by the discrete categorical values of Land Use and Land Cover (LULC) and Soil type classifications. This information is entered as georeferenced maps, and each cell of the computational domain is assigned with the parameters associated with each input map. For example, in HydroPol2D (Gomes et al., 2023), hydrological parameters (i.e. Green-Ampt parameters) are assigned with the Soil raster, and hydrodynamic (i.e., Manning's roughness coefficient and initial abstraction) and water quality (i.e., build-up and wash-off parameters) are assigned according to the LULC raster.

The automatic calibration of distributed models can be a taunting task due to the degrees of freedom of the optimization problem and the number of calibration variables that could increase proportionally to the number of land uses and soil classifications (Debele et al., 2008). Moreover, due to the nonlinear behavior of hydrology and hydrodynamics, the use of convex optimization to find global optima is unfeasible, unless several simplifications are performed in the modeling equations

(Wang et al., 2020). Additionally, defining the appropriate ranges for model parameters can also lead to unrealistic parameter estimations, especially when the physical boundaries of the parameters are incorrectly treated (Domeneghetti et al., 2012). Due to the complexity of automatic parameter estimations, several studies have successfully performed manual calibrations using distributed models (Ardıçlıoğlu e Kuriqi, 2019; Phillips et al., 2005; Li et al., 2021). Despite these challenges, calibrating a complex model with a relatively large number of parameters can be even more complex.

Although successful calibrations are presented in the literature, one of the yet unsolved and considerably complex problem is the total reduction of equifinality for a relatively large number of model parameters and ranges (Fatichi et al., 2016). This paper does not attempt to provide a definitive solution to this issue; rather, we explore the factors associated with the chances of finding parameter equifinality in automatic calibration. Investigating the trade-offs between the number of observation points, intensity of rainfall events, and combination of different associations of gauges that can affect parameter equifinality.

Several physically-based models are available in the literature, such as the Hydrologic Engineering Center - River System Analysis (Brunner, 2016b), the Stormwater Management Model - SWMM (Rossman et al., 2010), and the Gridded Surface and Subsurface Analysis (Downer e Ogden, 2004). However, only a few studies used the aforementioned models or developed new models that can take advantage of automatic calibration capabilities (Cho e Lee, 2015; Dung et al., 2011; Hong et al., 2019).

Research conducted in Cho e Lee (2015) used a genetic algorithm solver to calibrate observations with modeling results; however, as most studies in automatic calibration of hydrologic models (Gupta et al., 1999; Confesor Jr e Whittaker, 2007) they used a semi-distributed model that cannot account for some important hydrodynamic features such as backwater effects or hydrologic characteristics such as spatial distribution of soil moisture and pollutants inside the subcatchments. Other recent research using the SWMM model attempts to develop automatic calibration algorithms for semi-distributed models, as shown in Behrouz et al. (2020); Swathi et al. (2019).

The research conducted in Hong et al. (2019), however, considered a physically based fully distributed model that assumes various wash-off processes such as detachment and transport of particulate, resulting in six wash-off parameters that, in addition to the water quantity model parameters, must be calibrated altogether. This dramatically increases the decision variable space and might result in relatively longer simulations, as well as increase the chance of finding a different set of parameters that could explain the modeling results within a defined physically-based parameter range (i.e., Equifinality effect (Beven e Freer, 2001)). In addition to calibrating the model, an essential part is the model validation/evaluation that can be done to understand the model capability to represent the behavior of the system outside the calibration range (Shen et al., 2022).

The validation of conceptual lumped-paramater hydrological models as the ones presented in Shen et al. (2022) does not require detailed description of the surface topography. For fully distributed models, however, if all parameters are correct but the Digital Elevation Model (DEM) does not allow proper continuity of the flow, the model performance is affected. Poor DEMs are one of the limiting factors of applyng distributed models. DEMs usually contain noises, bridges, and are affected by vegetation (Hawker et al., 2018). Raster-based algorithms such as HydroPol2D might be hydraulically affected by such issues in the DEM, requiring a pre-processing filtering to allow proper flow paths and continuity. To this end, filtering algorithms to smooth DEM flow paths (Schwanghart e Scherler, 2014), remove vegetation noises (De Paiva et al., 2013), reduce sharp elevations (Conrad et al., 2015), or smooth hillslopes (Milledge et al., 2009), can be applied to treat DEMs.

4.1.1 Paper objectives and Contributions

Although several studies successfully calibrated distributed hydrodynamic models, most of the calibration studies were performed manually. With advances in computational processing and parallel computing, models that take advantage of these techniques can be applied and used for automatic optimization-based calibration. Only a few studies developed automatic calibration algorithms for fully distributed, high-resolution, hydrological-hydrodynamic models. This is likely due to complexity of due to the complex computational models with a high number of cells, states, and relatively high nonlinear underlying physical laws.

The objective of this paper is to derive a flexible framework to apply a formal HydroPol2D (Hydrodynamic and Pollution 2D model) calibration-optimization problem (i.e., a 2D distributed water quantity and quality model) using only source data at observed gauges as input. Although we use HydroPol2D in this paper, the methods developed here are valid for any other hydrodynamic model used to estimate information at gauge stations.

More specifically, in this paper, we develop a modeling framework that calibrates HydroPol2D for gauged information such as hydrographs and / or stage hydrographs and / or pollutographs using rainfall, initial soil moisture and initial water surface depths from the warm-up process as initial conditions for the model. All other hydrological-hydrodynamic and pollutant transport and fate parameters can be automatically obtained by the calibrator module developed in this paper. The method is of particular interest in catchments that already have point source gauged data in observed nodes (e.g., outlet), and these data can be used to generate spatiotemporal information within the catchment by running a calibrated HydroPol2D model in the catchment (Brath et al., 2004).

The fundamental contributions of this paper are:

- We develop an automatic calibration routine to estimate HydroPol2D parameters requiring only point-source information such as depths, flows, or pollutant concentrations.
- We provide a framework capable of calibrating HydroPol2D for various events for water quantity and/or water quality modeling.
- We improved the model presented in Gomes et al. (2023) by allowing not only a Von-Neuman (4-D) cell topology but also by adding a Moore grid (8-D) topology (i.e., four in the cardinal direction and four in the diagonal direction), allowing cells to have more flow directions, eventually decreasing the flow paths.
- We also expand (Gomes et al., 2023) by allowing raster-based DEM pre-processing algorithms to enhance flow continuity in coarse resolution DEMs.

4.2 Model Background

HydroPol2D model is a 2D model of transport and fate of hydrodynamic and water quality. The watershed is discretized into finite cells with known resolution Δx and the equations of conservation of runoff mass, momentum and conservation and transport of pollutant mass are all solved matrix-wise. For a more complete description of the model, please refer to (Gomes et al., 2023). Let n and p be the number of rows and columns in the watershed domain. In this paper, we show the main equations for the 2D surface water dynamics in Eq. (4.1) and 2D pollutant transport (4.2)-(4.3). To ensure proper mathematical notation for the modeling equations, we introduce the paper notation as follows:

Paper's Notation: Italicized, boldface upper and lower case characters in boldface represent matrices and column vectors: a is a scalar, $\boldsymbol{a}$ is a vector, and $\boldsymbol{A}$ is a matrix. Matrix $\boldsymbol{I}_n$ denotes an identity square matrix of dimension n-by-n, while $\boldsymbol{O}_{m\times n}$ and $\boldsymbol{1}_{m\times n}$ denotes a zero and one matrix of size m-by-n, respectively. The notations $\mathbb{R}$ and $\mathbb{R}_{++}$ denote the set of real and positive real numbers. The notations $\mathbb{R}^n$ and $\mathbb{R}^{m\times n}$ denote a column vector with n elements and an m-by-n matrix in $\mathbb{R}$. The element-wise product or Hadamard product is defined as $\boldsymbol{x}\circ\boldsymbol{y} \coloneqq [x_1y_1, x_2y_2, \ldots, x_ny_n]^T$ multiplications. Similarly, the element-wise division or Hadamard is defined as $\boldsymbol{x}\oslash\boldsymbol{y} \coloneqq [\frac{x_1}{y_1}, \frac{x_2}{y_n}, \ldots, \frac{x_n}{y_n}]^T$. The element-wise p power of a matrix $\boldsymbol{A}$, $(\boldsymbol{A}^{\circ p})$, with $\boldsymbol{A}\in\mathbb{R}^{m\times n}$ and $p\in\mathbb{R}$ is given by $a_{i,j}^{p}$ for $i\in\mathbb{N}_{++}$, and $j\in\mathbb{N}_{++}$.

$$\begin{aligned}\boldsymbol{H}(t+\Delta t) = &\overbrace{\boldsymbol{H}(t) + \Delta t\left(\boldsymbol{B}_{\mathrm{i}}\boldsymbol{I}(t) + \frac{1}{A}\boldsymbol{B}_{\mathrm{Q}}\boldsymbol{Q}(t) - \boldsymbol{F}(\boldsymbol{H}(t), \boldsymbol{F}_{\mathrm{d}}(t), \boldsymbol{E}_{\mathrm{TR}}) - \boldsymbol{E}_{\mathrm{TR}}(t)\right)}^{\boldsymbol{H}_{\mathrm{ef}}(t)} \\ &+ \Delta t\sum_{i=1}^{m}\left[\boldsymbol{Q}_{\mathrm{in}}^{i}\Big(\boldsymbol{H}(t)\Big) - \boldsymbol{Q}_{\mathrm{out}}^{i}\Big(\boldsymbol{H}(t)\Big)\right],\end{aligned} \tag{4.1}$$

where $\boldsymbol{H}_{\mathrm{ef}}(t)\in\mathbb{R}^{\mathrm{n}\times\mathrm{p}}$ is the effective depth for overland flow routing, $\boldsymbol{B}_i$ defines the cells that receive rain-on-the-grid boundary condition values from $\boldsymbol{I}$, $\boldsymbol{B}_{\mathrm{Q}}$ defines the cells that receive inflow hydrograph boundary conditions from $\boldsymbol{Q}$, $\boldsymbol{F}$ is the infiltration rate, $\boldsymbol{F}_d$ is the cumulative infiltration depth, $\boldsymbol{E}_{\mathrm{TR}}$ is the evapotranspiration rate, $\boldsymbol{Q}_{\mathrm{in}}^{i}$ is the inflow rate for direction i, calculated from the outflow rate $\boldsymbol{Q}_{\mathrm{out}}$ with the time-varying flow-direction matrix.

To solve Eq. (4.1), we develop a weighted cellular automata approach using Manning's equation to estimate matrix $\boldsymbol{Q}_{\mathrm{out}}\in\mathbb{R}^{\mathrm{n}\times\mathrm{p}\times\mathrm{m}}$, with m being the number of flow directions (i.e., 4 or 8), and using topological relationships between cells, we derive $\boldsymbol{Q}_{in}(t)\in\mathbb{R}^{\mathrm{n}\times\mathrm{p}\times\mathrm{m}}$ in terms of $\boldsymbol{Q}_{\mathrm{out}}(t)\in\mathbb{R}^{\mathrm{n}\times\mathrm{p}}$ by calculating the sparse time-varying flow direction matrix $\boldsymbol{B}_d(\boldsymbol{H}(t))\in\mathbb{R}^{\mathrm{np}\times\mathrm{np}\times\mathrm{m}}$. $\boldsymbol{F}(\boldsymbol{H}(t), \boldsymbol{F}_d(t), \boldsymbol{E}_{\mathrm{TR}})\in\mathbb{R}^{\mathrm{n}\times\mathrm{p}}$ is the infiltration rate, which is calculated with the Green-Ampt model (Green e Ampt, 1911) and depends on soil hydraulic properties. Details of how to solve the problem can be found (Gomes et al., 2023; Guidolin et al., 2016) and a pseudo-code of the Celular-Automata (CA) used in this paper is presented in Algorithm 1. In brief, the CA algorithm calculates the friction slope to the steepest water surface direction using Manning's equation, determines the maximum velocity to this direction, uses a weighted-average system based on the available void volume of neighbor cells, and distributes the runoff according to the weights given for each neighbor. In addition, it restricts the maximum outflow volume to avoid checkerboard oscillations between two adjacent cells (Hunter et al., 2005).

During dry weather periods, the initial mass of pollutant available in the catchment domain varies according to each Land Use and Land Cover (LULC) classification (Rossman et al., 2010), and can be calculated using the build-up equation as follows:

$$\boldsymbol{B}(t+\mathrm{ADD}) = \boldsymbol{C}_1\circ(\boldsymbol{1}_{\mathrm{n}\times\mathrm{p}} - \boldsymbol{e}_{\mathrm{n}\times\mathrm{p}}^{\circ\boldsymbol{C}_3\mathrm{ADD}}) + \boldsymbol{B}(t), \tag{4.2}$$

where $\boldsymbol{C}_1\in\mathbb{R}^{\mathrm{n}\times\mathrm{p}}$ is the buildup maximum concentration (kg.ha^{-1}), $\boldsymbol{C}_2\in\mathbb{R}^{\mathrm{n}\times\mathrm{p}}$ is a fitted decreasing factor (day^{-1}) and ADD is the antecedent dry days prior to the event (days).

During wet-weather periods, the pollutant mass balance equation is calculated in terms of the discharges in each direction and is given by:

$$\sum_{l=1}^{m}\boldsymbol{B}_{\mathrm{out}}^{i}(t) = \boldsymbol{W}_{\mathrm{out}}^{\mathrm{tot}}(t) = \Delta t\sum_{i=1}^{m}\left[\boldsymbol{C}_3\circ(\boldsymbol{Q}_{\mathrm{out}}^{i}(\boldsymbol{H}(t))^{\circ\boldsymbol{C}_4}\circ\boldsymbol{B}(t)\right], \tag{4.3}$$

where $\boldsymbol{W}_{\mathrm{out}}^{\mathrm{tot}}(t)\in\mathbb{R}^{\mathrm{n}\times\mathrm{p}}$ is the total amount of pollutant in kg that left each cell considering all directions.

Algorithm 1: Celular automata pseudocode

input: Cell elevations ($\boldsymbol{E}$), initial surface water depths (**WSE**), matrices of Manning's roughness ($\boldsymbol{N}$), initial abstraction ($\boldsymbol{H}_0$), time-step (Δt), grid discretization (Δx), friction slope at the outelt for normal flow (s_0^b), large number (c), Velocity to the steepest direction ($\boldsymbol{V}_\mathrm{m}$), Intercell Volume ($\boldsymbol{I}_{tot}$) outflow volumes from previous time-step ($\boldsymbol{I}_{tot}^p$), Minimum water depth (Δh_min) Set of cells in the catchment domain ($\mathbb{C}$), set of cells at the outlet ($\mathcal{O}$), Domain borders ($\mathbb{B}$), number of flow directions (m), gravity acceleration (g), cell area (A).
for *i = 1 to m* **do**
  compute: $\Delta \boldsymbol{H}_{\mathrm{ef,i}} = \mathbf{WSE} - \mathbf{WSE}_i$, $\Delta \boldsymbol{H}_\mathrm{ef} \in \mathbb{R}^{\mathrm{n}\times\mathrm{p}\times(\mathrm{m}+1)}$, $\mathbf{WSE} \in \mathbb{R}^{\mathrm{n}\times\mathrm{p}}$
end for
if *Outlet Type = 1* **then**
  compute: $\Delta \boldsymbol{H}_{\mathrm{ef,m}+1} = s_0^b \Delta x \; \forall \; \mathbb{C} \in \mathbb{O}$
else
  compute: $\Delta \boldsymbol{H}_{\mathrm{ef,m}+1} = \boldsymbol{H}_\mathrm{ef}^{\circ -1/6} g^{0.5} \circ \boldsymbol{N} \; \forall \; \mathbb{C} \in \mathbb{O}$
end if
$\boldsymbol{H}_{\mathrm{ef,m}+1} \leftarrow 0 \; \forall \; \mathbb{C} \in \mathbb{B}$
$\boldsymbol{\Delta H}_\mathrm{ef} \leftarrow 0 \; \forall \; \Delta \boldsymbol{H}_\mathrm{ef} \leq \Delta h_\mathrm{min}$
compute: $\Delta \boldsymbol{V} = A \Delta \boldsymbol{H}_\mathrm{ef}$, $\Delta \boldsymbol{V} \in \mathbb{R}^{\mathrm{n}\times\mathrm{p}\times(\mathrm{m}+1)}$
$\Delta \boldsymbol{V} \leftarrow c, \; \forall \; \Delta \boldsymbol{V} = 0$
compute: $\Delta \boldsymbol{V}_\mathrm{max} = \max(\Delta \boldsymbol{V})$, $\Delta \boldsymbol{V}_\mathrm{max} \in \mathbb{R}^{\mathrm{n}\times\mathrm{p}}$
compute: $\Delta \boldsymbol{H}_\mathrm{ef,max} = \max(\Delta \boldsymbol{H}_\mathrm{ef})$, $\Delta \boldsymbol{H}_\mathrm{ef,max} \in \mathbb{R}^{\mathrm{n}\times\mathrm{p}}$
compute: $\Delta \boldsymbol{V}_\mathrm{min} = \min(\Delta \boldsymbol{V})$, $\Delta \boldsymbol{V}_\mathrm{min} \in \mathbb{R}^{\mathrm{n}\times\mathrm{p}}$
compute: $\boldsymbol{\Omega} = (\Delta \boldsymbol{V}_\mathrm{tot} + \Delta \boldsymbol{V}_\mathrm{min}) \oslash \Delta \boldsymbol{V}$, $\boldsymbol{\Omega} \in \mathbb{R}^{\mathrm{n}\times\mathrm{p}\times(\mathrm{m}+1)}$
compute: $\boldsymbol{\Omega}_\mathrm{max} = \max(\boldsymbol{\Omega})$, $\boldsymbol{\Omega}_\mathrm{max} \in \mathbb{R}^{\mathrm{n}\times\mathrm{p}}$
compute:
$\boldsymbol{V}_\mathrm{m} = \min\left(\sqrt{g}\boldsymbol{H}_\mathrm{ef}^{\circ 0.5}, \boldsymbol{N} \oslash \max(\boldsymbol{H}_\mathrm{ef} - \boldsymbol{H}_0)^{\circ 2/3} \circ (\boldsymbol{H}_\mathrm{ef,max}(1/\Delta x))^{\circ 0.5}\right)$, $\boldsymbol{V}_\mathrm{m} \in \mathbb{R}^{\mathrm{n}\times\mathrm{p}}$
compute: $\boldsymbol{I}_\mathrm{tot}^* = \min(\omega \boldsymbol{H}_\mathrm{ef}, (\Delta x/\Delta t)\boldsymbol{V}_\mathrm{m} \circ \boldsymbol{H}_\mathrm{ef}, \boldsymbol{I}_\mathrm{tot}^p + \Delta \boldsymbol{V}_\mathrm{min})$, $\boldsymbol{I}_\mathrm{tot}^* \in \mathbb{R}^{\mathrm{n}\times\mathrm{p}}$
compute: $\boldsymbol{I}_\mathrm{tot}^* \leftarrow \mathrm{sum}_3(\boldsymbol{\Omega} \circ \boldsymbol{I}_\mathrm{tot}^*)$
compute: $\boldsymbol{Q}_\mathrm{out} = 1/(\Delta t A)\boldsymbol{I}_\mathrm{tot}^*$, $\boldsymbol{Q}_\mathrm{out} \in \mathbb{R}^{\mathrm{n}\times\mathrm{p}\times\mathrm{m}}$
compute: $\boldsymbol{H}_\mathrm{ef} \leftarrow \boldsymbol{H}_\mathrm{ef} - (1/\omega)\boldsymbol{I}_\mathrm{tot}^*$
output: $\boldsymbol{Q}_\mathrm{out}$ from Eq. (4.1), , $\boldsymbol{H}_\mathrm{ef}$, $\boldsymbol{I}_\mathrm{tot}^*$

The available pollutant mass is calculated using Euler's forward finite difference scheme applied in Eq. (4.3), such that:

$$\boldsymbol{B}(t + \Delta t) = \boldsymbol{B}(t) + \left[\boldsymbol{B}_d(t)\boldsymbol{W}_{out}(t)\right], \tag{4.4}$$

where $\boldsymbol{W}_\mathrm{out}(t) \in \mathbb{R}^{\mathrm{n}\times\mathrm{p}\times\mathrm{m}}$ is the pollutant washed mass for each Von-Neumann or Moore (Torres et al., 2022) direction (i.e., moving from 1 to m clockwise, with 1 being the leftwards direction).

4.2.1 Decision Variables in HydroPol2D Automatic Calibration Problem

In HydroPol2D, parameters are spatially derived as a function of the Land Use and Land Cover (LULC) and Soil rasters. Minimum and maximum values of each decision variable are entered for each classification of these rasters. Let n_l be the number of land use classifications and n_s be the number of soil classifications in a catchment. Also, let n_v^l be the number of decision variables related to the LULC map and n_v^s be those related to the soil map; therefore, we have a decision vector $\boldsymbol{x} \in \mathbb{R}^{n_x}$ with $n_x = n_l n_v^l + n_s n_v^s$.

We classify the decision variables into water quantity variables (superscript r), water quality variables (superscript w), and soil related parameters (subscript s). Furthermore, we classify the variables as LULC-based and soil-based into subscripts 1 to n_l and 1 to n_s, respectively. The decision

variable of the calibration problem can be written as $\boldsymbol{x} = [\boldsymbol{x}_l^q,\ \boldsymbol{x}_l^w,\ \boldsymbol{x}_s^q]^{\mathrm{T}}$, such that:

$$\boldsymbol{x}_l^r = [n_1,\ \ldots, n_{n_l},\ h_{0,1},\ \ldots,\ h_{0,n_l}]^{\mathrm{T}} \tag{4.5a}$$

$$\boldsymbol{x}_l^w = [C_{1,1},\ \ldots, C_{1,n_l},\ C_{2,1},\ \ldots,\ C_{2,n_l}, C_{3,1}, \ldots C_{3,n_l},\ C_{4,1},\ \ldots C_{4,n_l}]^{\mathrm{T}} \tag{4.5b}$$

$$\boldsymbol{x}_s = [k_{sat,1},\ \ldots, k_{sat,n_s},\ \Delta\theta_1,\ \ldots,\ \Delta\theta_{n_s}, \psi_1,\ \ldots \psi_{n_s}]^{\mathrm{T}}, \tag{4.5c}$$

where n is the Manning's roughness coefficient ($\mathrm{sm}^{-1/3}$), h_0 is the initial abstraction (mm), k_{sat} is the saturated hydraulic conductivity of the soil (mmh^{-1}), $\Delta\theta$ is the soil moisture deficit (-), and ψ is the soil suction head (mm), C_1 is the build-up coefficient, C_2 is the build-up.

4.2.2 Initial Values for the Simulation

In addition to the parameters, in the automatic calibrator of the HydroPol2D model, we can enter initial maps of water surface depth and soil moisture to accurately represent the initial conditions for simulation, for each event. The code is designed to calibrate at last 10 events with 10 observation points of discharge, water depth, and pollutant concentration. Another input map that could be entered is the distributed pollutant mass in the catchment domain prior to the simulation; however, in this paper we opted to calculate this mass in terms of the antecedent dry days and assume that it is uniformly distributed according to the land use classification.

4.2.3 Fitness Functions

In this section we show the fitness functions allowed in the automatic calibrator. These functions can be used for the calibration of hydrographs, stage-hydrographs, and pollutographs at the catchment outlet. Detailed mathematical descriptions of these functions are available in the Supplemental Material. In this paper, we use the Nash-Sutcliffe-Efficiency (NSE) (Nash e Sutcliffe, 1970), the coefficient of determination (r^2), the root-mean-square-error (RMSE) (Fisher et al., 1920), the Peak Flow Bias, and the relative runoff volume error.

In addition to the previously defined functions, users can have the flexibility to write their own fitness function since all codes are open source. Some examples that are predefined in the model and not fully detailed here for the sake of parsimony are the (i) mean average error, (ii) event mean concentration, (iii) PBIAS, and (iv) runoff volume mean error.

4.2.4 Optimization Constraints

The optimization problem is subject to 4 constraints. First, the model is constrained to HydroPol2D dynamical model that has conservation of mass and conservation of momentum constraints and pollutant transport and fate dynamics. Moreover, the optimization problem is constrained to equality constraints (e.g., the case where a parameter is known or cannot vary). In addition, we can add equality constraints in the model and, finally, we can add the minimum and maximum parameter ranges for each decision variable.

4.2.5 Objective Function

We can calibrate a single or multiple events together. Therefore, let the index j represent the j-th event used for calibration. Moreover, let f collect fitness functions such that a possible scenario of objective functions could be $f_1 = -\mathrm{NSE}$, $f_2 = -r^2$, $f_3 = -\mathrm{RMSE}$, and $f_4 = \mathrm{Jq}$, for example. The problem is set as a single-objective minimization problem, and the objective function used in this paper can be written as a function of linear combinations between each individual fitness function for each event, such that:

$$O_f = \sum_{j=1}^{n_e} \beta_j \Big[\Big(\sum_{i=1}^{n_f} \alpha_i f_i \Big) \Big], \tag{4.6}$$

where n_f is the number of fitness functions used in the optimization α defines the relative weight of each individual function f_i, n_e is the number of events used in the calibration, and B_j is the weight given by the objective function values for each event.

It is important to mention that the factor α_i must be such that it normalizes the varied objective functions used, to avoid over-weighting in fitness functions with different scales of magnitude and units.

4.2.6 Automatic Calibration Optimization Problem

In this section, we define the automatic calibration optimization problem. Although the nature of hydrological model calibration can be inherently multiobjective (Shafii e De Smedt, 2009), for the sake of parsimony and to allow practical application, we focus on developing a single objective automatic calibration problem. It can be written by minimizing the objective function, subject to HydroPol2D dynamics. Users can define equality constraints in case few of the parameters are known or inequality constraints whenever a linear relationship among them is available, such that we can write the problem as:

$$\min_{\boldsymbol{x}} O_f = \sum_{j=1}^{n_e} \beta_j \Big[\Big(\sum_{i=1}^{n_f} \alpha_i f_i \Big) \Big] \tag{4.7a}$$

$$\tag{4.7b}$$

$$\text{s.t. HydroPol2D Dynamics in Eqs. (4.1) } - \text{ (4.4)} \tag{4.7c}$$

$$\boldsymbol{A}_{\text{eq}} \boldsymbol{x} = \boldsymbol{B}_{\text{eq}} \tag{4.7d}$$

$$\boldsymbol{x}_l \leq \boldsymbol{x} \leq \boldsymbol{x}_m \tag{4.7e}$$

The problem posed in Eq. (4.7) is non-linear and non-convex. The use of evolutionary strategies such as the Shuffled Complex Evolution (SCE) (Naeini et al., 2019) has been used for this type of calibration problems (Tigkas et al., 2016). In Matlab, several solvers are available to solve problems as Eq. (4.7), such as *Global-Search*, *Patter-Search* or *Genetic-Algorithms* (GA) (Higham e Higham, 2016). Herein, we choose GA due to its flexibility to deal with non-linear problems (Giacomoni e Joseph, 2017) and its ability to use parallelization in Matlab. The GA is a population-based probabilistic optimization method that emulates the principles of genetics and natural selection (Tigkas et al., 2016). Since the goal of hydrologic-hydrodynamic model calibration is not essentially finding the global optima but a physically possible set of parameters trying to avoid equifinality, we set all problems to run with a relatively low number of generations, but still with a relatively large number of population to allow a proper exploration of the decision variable space.

4.2.6.1 Genetic Algorithm Properties

We set the problem to run for (10-40) generations with a 100 population. The stopping criteria were twofold: (i) simulation would stop if the number of maximum generations is reached, (ii) if no improvement in the objective function were found in 30 min. All parameters of the genetic algorithm are set as standard values from Matlab (Higham e Higham, 2016). A flowchart of the optimization process is presented in Fig. 4.1.

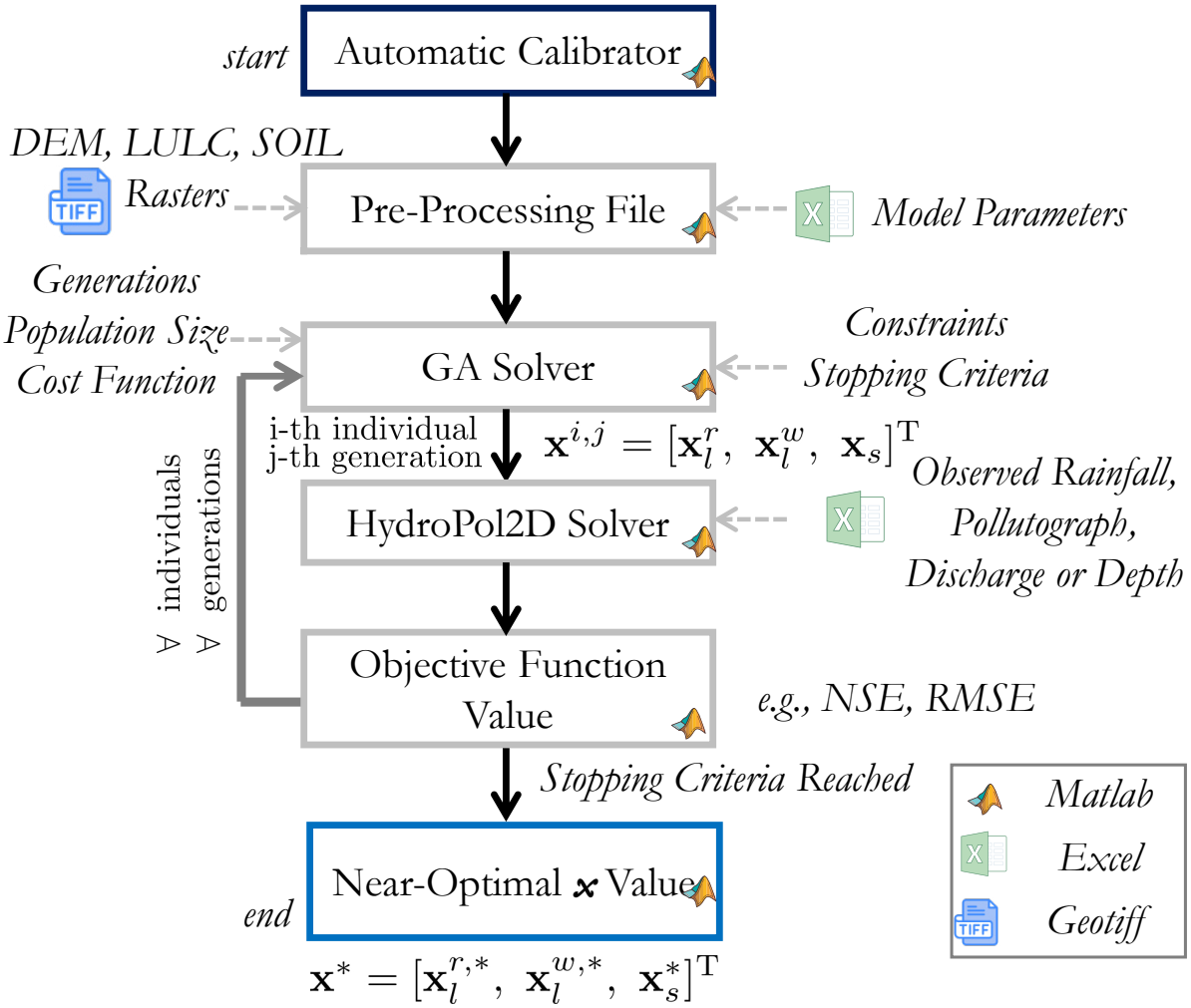

Figure 4.1. Automatic calibrator flowchart. First, the model reads the automatic calibration inputs, then it runs a pre-processing files, defining the required numerical input for HydroPol2D, such as the DEM, LULC, and Soil Maps. Following this phase, the model runs the GA solver, that uses HydroPol2D to estimate the objective function values and this process is looped until the stopping criteria is reached.

4.3 Case Studies

4.3.1 Numerical Case Study 1 - V-Tilted Catchment

The objective of this numerical case study is to test the ability of the optimization model to predict the Manning's roughness coefficient of the catchment and to check if the model can predict that there are no initial abstractions and no infiltration in this case study. Essentially, we want to answer the following question:

- Q1: *Can the automatic calibration algorithm identify the Manning's roughness coefficients of hillslopes and main channel, as well as the initial abstraction values of these land uses? In addition, can it identify whether infiltration is being considered or not in this case study?*

We choose the V-Tilted catchment as a virtual experiment inverse problem (Fatichi et al., 2016). The catchment has 4,050 cells of 20 x 20 m in size and has a reasonable fast computation, allowing the use of meta-euristics that rely on multiple computations of the objective function. To answer Q1, we define the decision vector of this problem as:

$$x = [n_1, n_2, h_{0,1}, h_{0,2}, k_{\mathrm{sat},1}, \Delta\theta_1, \psi_1]^{\mathrm{T}},$$

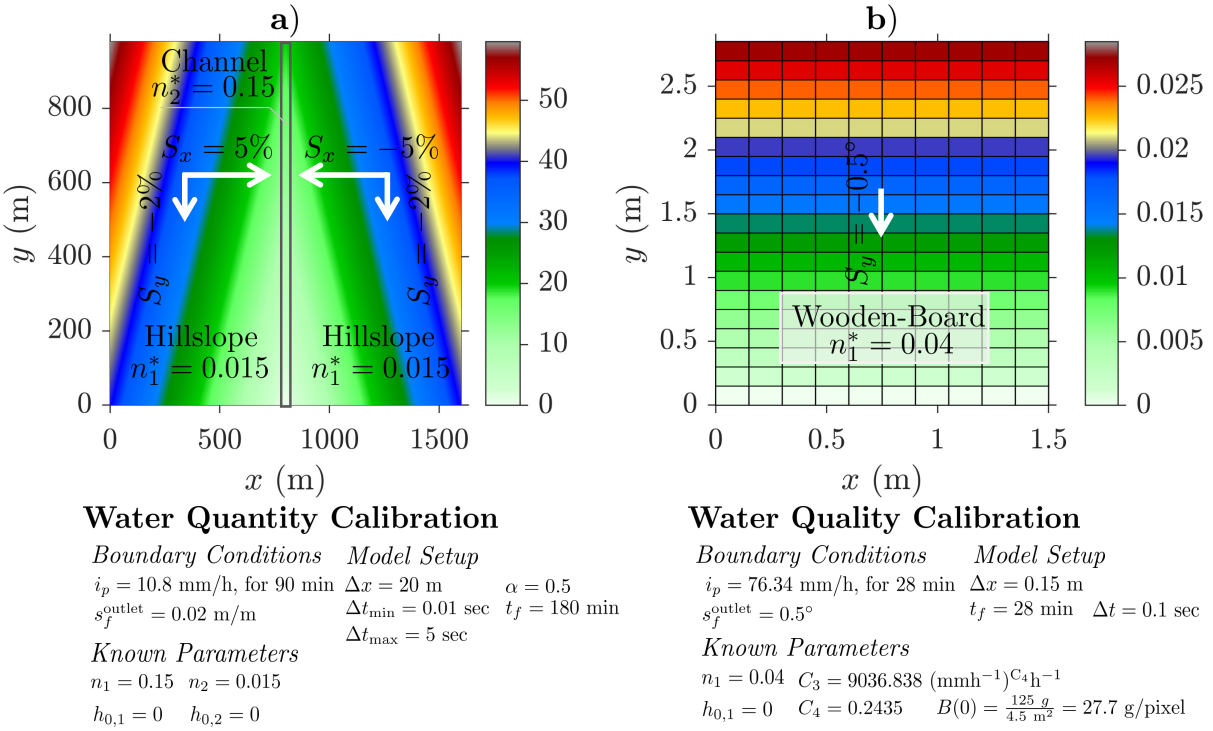

Figure 4.2. Numerical Case Study 1 and 2 digital elevation models in meters. Part a) is the V-Tilted Catchment whereas part b) is the Wooden-Board catchment. The parameters of each case are shown in the figure, where i_p is the constant rainfall rate, s_f^{outlet} is the friction slope at the outlet, Δx is the pixel size, Δt is the constant time-step assumed, and t_f is the end of the simulation.

where subscripts 1 and 2 are the LULC classifications in the catchment (i.e., 1 are the hillslopes and 2 is the channel, see Fig. 4.2a)). It is assumed that there is only one type of soil in the catchment such that $n_s = 1$. To set only the water quantity variables as decision variables, we add an equality constraint in Eq. (4.8d) by entering the known parameters in $\boldsymbol{B}_{\text{eq}}$. In this problem, we choose the NSE as the objective function, since we are focused on calibrating the modeled flow discharge with the observed discharge at the outlet. This case study has no infiltration or initial abstraction and is a reverse problem since we know the right parameters (Kollet e Maxwell, 2006a); however, we decided to include infiltration variables in the optimization problem formulation to see if the algorithm can identify this condition. The formal optimization problem can be written as:

$$\min_{\boldsymbol{x}} \; O_f = \text{NSE} \tag{4.8a}$$

$$\tag{4.8b}$$

$$\text{s.t. HydroPol2D Dynamics in Eqs. (4.1) – (4.4)} \tag{4.8c}$$

$$\begin{bmatrix} \boldsymbol{O}_4 & \boldsymbol{O}_{4\times4} & \boldsymbol{O}_{4\times3} \\ \boldsymbol{O}_{8\times4} & \boldsymbol{I}_8 & \boldsymbol{O}_{8\times3} \\ \boldsymbol{O}_{3\times4} & \boldsymbol{O}_{3\times4} & \boldsymbol{O}_{3\times3} \end{bmatrix} \begin{bmatrix} \boldsymbol{x}_l^q \\ \boldsymbol{x}_l^w \\ \boldsymbol{x}_s \end{bmatrix} = \begin{bmatrix} \boldsymbol{O}_{4\times1} \\ \boldsymbol{C}_{8\times1} \\ \boldsymbol{O}_{3\times1} \end{bmatrix} \tag{4.8d}$$

$$[0.009,\ 0.1,\ 0,\ 0,\ \boldsymbol{C}^{\text{T}},\ 0,\ 0,\ 0]^{\text{T}} \leq \boldsymbol{x} \leq$$
$$[0.027,\ 0.3,\ 30,\ 30,\ \boldsymbol{C}^{\text{T}},\ 50,\ 0.45,\ 300]^{\text{T}}, \tag{4.8e}$$

where $\boldsymbol{C}$ is a constant vector and each entry of the vector follows the aforementioned definition of $\boldsymbol{x}$ for this problem.

This is a problem with a relatively short decision space, in which equifinality effects are hypothesized to be minimized.

4.3.2 Numerical Case Study 2 - Wooden-Board Catchment - Pollutant Concentration

The objective of this numerical case study is to test the ability of the optimization model to predict the salt concentrations at the outlet of the catchment, the initial salt mass and the wash-off parameters of the model. This is a fairly more complex optimization problem if not only the water quantity parameters are required to calibrate, but also the water quality ones. In addition, the water quality parameters have a wider sensitivity as shown in Gomes et al. (2023). In this problem, we assume that the water quantity parameters (i.e., n and h_0) are already calibrated (Zhang et al., 2020), so that the decision vector for this problem is $\boldsymbol{x}_l^w = [C_{1,1},\ C_{2,1},\ C_{3,1},\ C_{4,1}]^{\mathrm{T}}$. To set only the water quality variables as the decision variables, we add an equality constraint in Eq. (4.7d). In this problem, we only choose RMSE as the fitness function.

This case study is a controlled experiment in a wooden-catchment as shown in Fig. 4.2b). The wooden-board has 4.5 m^2 and 300 cells. The initial mass of the solute is 125 g and it is assumed that it is uniformly distributed in the catchment area (Zhang et al., 2020). However, in this paper, we do not assume that the initial solute mass is known, and we let the model search for the near-optimal solute mass considering C_1 and C_2 as decision variables. Naturally, this controlled experiment is not a direct case of applying the build-up equation that calculates the available mass of the pollutant in terms of the ADD, as shown in Eq. (4.2). However, fixing ADD = 10 days, for example, we can estimate C_1 and C_2, calculate the initial build-up by solving Eq. (4.2) and compare with the initial mass of 125 g known from the experiment. Ultimately, what matters for HydroPol2D is the initial pollutant mass available in each cell of the domain. The reason we consider build-up as a function of ADD and LULC is that in most cases, the initial pollutant mass varying cell-by-cell is unknown and these direct measurements are either intractable, hardly ever available, and would result in an intractable decision-space if all cells are treated individually in the optimization problem. The parameter ranges were estimated from a 60% variation from the previous calibrated ones, assuming that the initial pollutant mass was 125 g (Gomes et al., 2023). In this Numerical Case Study, we want to answer the following question:

- Q2: *Assuming the water quantity parameters known, can the algorithm find the initial mass of salt (build-up model parameters) and the wash-off parameters to match with the observed pollutograph at the outlet?*

To answer this question, we build a formal optimization problem for this case study that can be written as follows.

$$\min_{\boldsymbol{x}} \ O_f = \text{RMSE} \tag{4.9a}$$

$$\tag{4.9b}$$

$$\text{s.t. HydroPol2D Dynamics in Eqs. (4.1)} - \text{(4.4)} \tag{4.9c}$$

$$\begin{bmatrix} \boldsymbol{I}_2 & \boldsymbol{O}_{2\times 7} \\ \boldsymbol{O}_{7\times 2} & O_{7\times 7} \end{bmatrix} \begin{bmatrix} n_1 \\ h_{0,1} \\ \boldsymbol{x}_l^w \\ \boldsymbol{x}_s \end{bmatrix} = \begin{bmatrix} 0.04 \\ 0 \\ \boldsymbol{O}_{7\times 1} \end{bmatrix} \tag{4.9d}$$

$$[0.04,\ 0,\ 166.71,\ 0.51,\ 5422.10,\ 0.14612,\ 0,\ 0,0]^{\mathrm{T}}$$

$$\leq \boldsymbol{x} \leq$$

$$[0.04,\ 0,\ 388.99,\ 1.19,\ 12651.57,\ 0.34096,\ 0,\ 0,0]^{\mathrm{T}},$$

4.3.3 Numerical Case Study 3 - Gregorio Catchment in Sao Carlos / Brazil

The Gregório catchment is located in the municipality of São Carlos in the state of São Paulo, Brazil. The climate in the state of São Paulo is influenced by Atlantic Tropical and Continental and Atlantic Polar air masses, complemented by Continental Equatorial air masses coming from the Western Amazon. The months with the largest rainfall events are in summer, from October to March, and the dry weather period varies from April to September in winter. The average annual precipitation of the city of São Carlos is approximately 1492 mm (de Meteorologia., 2022) and the city has been prone to critical rainfall events yearly (Abreu, 2019). The catchment area is 18.64 km^2, the length of the main channel is 8.6 km and its morphological characteristics indicate an elongated to strongly elongated catchment, which presents a compactness coefficient (C_c) of 2.030, a circularity ratio (R_c) of 0.120 and a form factor (R_f) of 0.289, as shown in Fig. 4.3. Although the morphometric characteristics would indicate a resilient catchment to floods, the large impervious rate, mean slope, and the channelization of the main creek increase the vulnerability of the area in terms of floods.

To perform hydrodynamic modeling, we built maps of Digital Elevation Model (DEM), Land Use Land Cover (LULC) and Soil Texture as presented in Fig. 4.4. Due to the lack of high-resolution data in the catchment, we use freely available worldwide datasets for all input maps; therefore, the methods applied here are replicable in other poorly-gauged catchments (Gomes et al., 2023). However, when available, higher resolution maps can be used.

The pedology of the catchment is composed of yellow-red latosoil (YRL) and small areas of purple latosoil (PL) (de Geografia e Estatística , IBGE). The soil texture within the catchment can be classified into medium and clayey texture (de Geografia e Estatística , IBGE) (see Fig. 4.4). The headwaters of Gregorio catchment remains relatively undeveloped, with a predominance of pervious areas with crops, grass, and shrub areas. Downstream the creek, impervious rates dramatically increase with the urbanization, which almost makes the catchment impervious towards the outlet, as presented in Fig. 4.3 and Fig. 4.4. This catchment covers large proportion of the urbanized area in the municipality of São Carlos with the most commercial activities of the city being carried out in this area. For this reason, due to the climatic and hydraulic characteristics of the catchment, floods are constantly recorded, especially in the summer. A recent flood picture is shown in Fig. 4.3 in the Local Market (Abreu, 2019; Sarmento Buarque et al., 2020).

The specific question of this Numerical Case Study is:

- Q3: *Given the reality of scarce data in poorly-gauged catchments, can the algorithm find the near-optimal hydrodynamic parameters, within physical limits, to match with the observed hydrograph? Can this set of parameters be used to estimate catchment-scale information?*

4.3.3.1 DEM - Preprocessing

A 30-m DEM might be considered high-resolution for rural catchments. For urban areas, however, the complexity of the built environment with detailed infrastructure would require a more detailed resolution. Information in such detail is typically unavailable in developing countries. Nonetheless, poorly-gauged areas are usually those that often suffer from floods (Fava et al., 2020). Raster-based flood routing models are, therefore, affected by DEM quality. Typically, DEMs are required to be hydrologically corrected, ensuring that the flow directions are continuous and connected toward the outlet. However, especially in urban areas with bridges, culverts, and stormwater reservoirs, DEMs usually have to be burned to allow proper flow directions and connection. Herein, we provide 4 algorithms to treat low-quality DEMs (i.e., gaussian filter (Young e Van Vliet, 1995), constrained regularized smoothing of the channel length profile (CRS) (Schwanghart e Scherler, 2014), and reduction of DEM

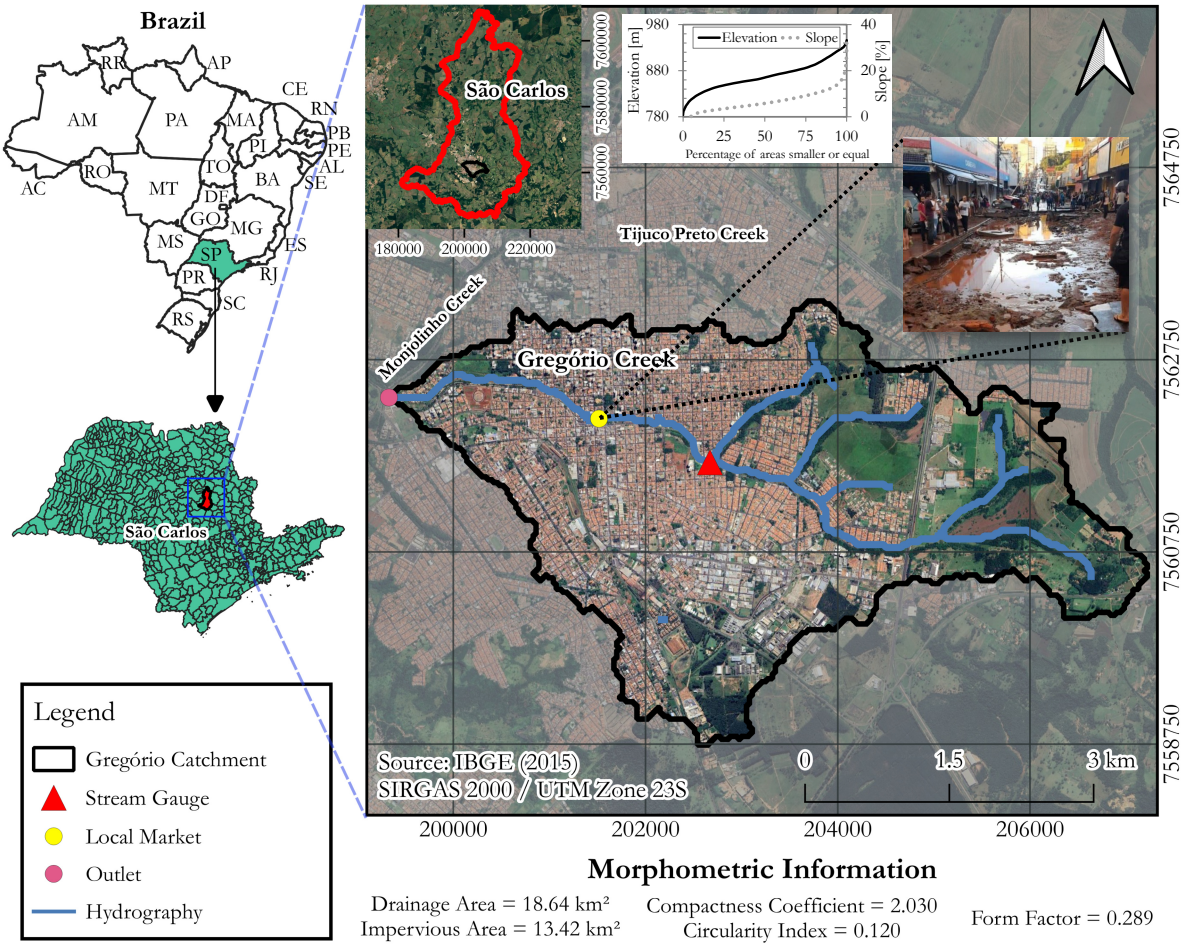

Figure 4.3. Gregorio Catchment location map with hypsometric curves of elevation and slope, and a figure of the flood-related impacts in the Local Market point of Sao Carlos.

elevation to consider water surface depths based on (De Paiva et al., 2013). These methods are detailed in the Supplemental Material.

4.3.3.2 Data Collection

Rainfall intensity and depth of the water surface are recorded in a limited way each minute and upscaled to 5-min intervals, and the rainfall and stream gauge station is shown in Fig. 4.3. From the monitoring campaign provided in Souza (2008), only one event had a sufficiently large rainfall volume and quality discharge observations. To collect data, a Campbell Scientificő CR10 station was installed and calibrated to record the data to be collected after each rainfall event (Souza, 2008). A calibrated rating curve (Gomes Jr et al., 2023e) converts water depth into flow discharge by the following relationship (Lima et al., 2007):

$$Q(h) = 8.278h^{2.2517},\ r^2 = 0.99, \tag{4.10}$$

where Q is the observed flow discharge at the gauge station, and h is the measured water depth taken from the channel invert.

The recorded level was converted into flow discharges using Eq. (4.10) and used for the calibration of HydroPol2D.

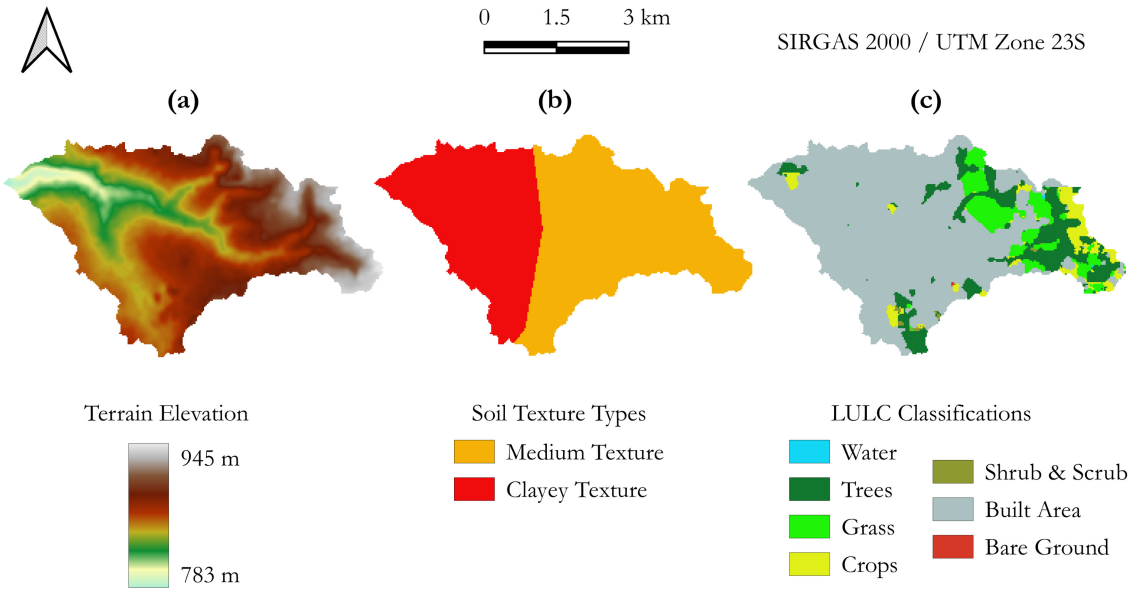

Figure 4.4. Input maps to the hydrodynamic simulation in HydroPol2D for the Gregorio catchment, where a) is the digital elevation model, b) is the soil texture map, and c) is the land use and land cover map.

4.3.3.3 Initial Conditions

We assumed the initial soil moisture in the soil calculated with the cumulative rainfall prior to the event coupled with the SCS-CN (SCS, 1986) infiltration model. A Curve-Number map was developed by (Souza, 2008) and used to estimate spatial infiltration in pervious areas. For the initial water surface depth, previous modeling results indicate that no warm-up is necessary, and current visits to the study area indicate a minimum effect of non-hortonian flows. It is also seen from the observed hydrographs that the initial flow is null, indicating an intermittent creek.

4.3.3.4 Boundary Conditions and Running Control Parameters

The model is simulated with a space-invariant and time-variant rainfall hyetograph distributed to all cells of the grid. In addition, we assume a gradient outlet boundary condition at the outlet with the friction slope $s_f = 0.02$ m/m. Although we assume normal flow at the catchment outlet, the flow is considered transient in the gauging station as it is an internal node of the domain (see Fig. 4.3). To guarantee numerical stability, we define minimum and maximum time steps of 0.1 and 5 sec, respectively, and we set HydroPol2D model to change time-steps each 60 seconds of the simulation time. We use a Courant number bound of 0.4, such that time-steps are adapted to match this input (Gomes et al., 2023). The model is run for 120 min of simulation and point and raster results are retrieved each 5-min.

4.3.3.5 Parameter Ranges

The parameter ranges used for calibration and for the construction of the calibration optimization problem of Eq. (4.7) are given in Tab. 4.1 and Tab. 4.2. The physically bounds used in this paper were derived from the literature and recent published papers and manuals (Soliman et al., 2022; Rossman et al., 2010; Brunner, 2016b).

Classification	n_{min} [$sm^{-1/3}$]	n_{max} [$sm^{-1/3}$]	n [$sm^{-1/3}$]	$h_{0,min}$ [mm]	$h_{0,max}$ [mm]	h_0 [mm]
Water	0.0250	0.0400	0.0400	0.00	0.00	0.00
Trees	0.0250	0.0400	0.0268	0.00	10.00	0.8259
Grass	0.0200	0.0350	0.0244	0.00	5.00	0.2740
Flooded Vegetation	0.0250	0.0400	0.0381	0.00	10.00	1.2281
Crops	0.0200	0.0350	0.0236	0.00	10.00	0.1564
Scrub/Shrub	0.0300	0.0400	0.0358	0.00	10.00	7.6289
Built Areas	0.0150	0.0300	0.0216	0.00	2.00	0.0625
Bare Ground	0.0200	0.0300	0.0260	0.00	2.00	1.6101

Table 4.1. Parameter ranges and calibrated values for the LULC-Based parameters of HydroPol2D for Numerical Case Study 3.

Type	$k_{sat,min}$	$k_{sat,nax}$	k_{sat}	$\Delta\theta_{min}$	$\Delta\theta_{max}$	$\Delta\theta$	ψ_{min}	ψ_{min}	ψ
	[$mm.h^{-1}$]	[$mm.h^{-1}$]	[$mm.h^{-1}$]	[-]	[-]	[-]	[mm]	[mm]	[mm]
Medium	1.00	10.00	1.14	0.25	0.60	0.29	0.00	230.00	33.56
Clayey	0.20	10.00	6.23	0.25	0.60	0.40	0.00	312.50	281.10

Table 4.2. Parameter ranges and calibrated values for the SOIL-Based parameters of HydroPol2D for Numerical Case Study 3.

4.3.3.6 Sensitivity Analysis

A one-at-the-time sensitivity analysis is performed in the model to identify the most sensitive parameters prior to the automatic calibration procedure (Gomes Jr et al., 2023a). We define three output functions and calculate the variance of each perturbation in the decision variables in terms of the variance in the output functions. We evaluated the output variance of Peak Flow, Runoff Volume, and Time to Peak, as they are closely related to the hydrograph properties. We also evaluated flood areas. More details of the output functions are found in the Supplementary Material. The parameters ranged from 10% to 190% the baseline parameters, with 10% intervals, and the baseline parameters are defined as the average of the parameter ranges presented in Tables 4.1 and 4.2.

4.3.4 Numerical Case Study 4 - Exploring Equifinality

In this case study, our objective is to explore the parameter equifinality problem in the calibration of the hydrological and hydrodynamic model. Equifinality tends to decrease with the number of observations and with the decrease in the model parameters (Her et al., 2019). To this end, we create a synthetic case study without uncertainty in rainfall, initial soil moisture, and observed discharge, mimicking a perfect gauging system. Therefore, the error in the parameter measurements is only due to the lack of accuracy in the optimization solver, number of generations, population size, genetic algorithm properties that might change the behavior of the exploration of the decision space, and due to the conceptual model of HydroPol2D. The spatial-variability of rainfall is a challenge that could be also explored, but is out of scope of this paper. To explore the equifinality problem in a scenario of certain rainfall and perfect measurements in the gauges, we formulate the following question.

- *Q4-1: How does parameter equifinality affect the calibration of HydroPol2D for different parameter ranges, number of events, magnitude of the rainfall intensity, and location of the gauging stations?*

Therefore, we assess the near-optimal calibrated parameters in an inverse problem using the V-Tilted catchment as a surrogate case study, varying the number of gauges, the number of rainfall

events, and its intensities. This catchment is used as a virtual laboratory to test the hypothesis raised in this case study (Fatichi et al., 2016). We altered the original watershed to have 3 classifications of soils and LULC, following the left hillslope (1), the middle channel (2), and the right hillslope (3), each of them with different n, h_0, k_{sat}, $\Delta\theta$, and ψ. The left and right hillslopes can be classified into hydrologic units with the same roughness and infiltration properties. Consequently, having a gauge station in each of the hillslopes would possibly reduce the uncertainty in the parameters.

The problem has ten unknown parameters (i.e., five parameters for each hillslope) and five known parameters (i.e., the main channel parameters are kept constant). We apply the model to calibrate three different storms of 10.8 mmh^{-1}, 21.6 mmh^{-1}, and 32.4 mmh^{-1} with 90-min duration and later we calibrate only using the first event of 10.8 mmh^{-1}. Detailed results of the modeling of each of the three rainfall events are presented in the Supplemental Material. The number of gauges (1 - outlet, 2 - left hillsope, and 3 - right hillslope) is combined, resulting in 7 possible cases (1-2-3, 1-2, 1-3, 2-3, 1, 2, and 3). The left and right gauges are defined by the channel neighborhood cell located at the half middle of the V-tilted length (i.e., $y = 500$ m) spanned 20 m from the channel i.e ($x = 780$ m, and $x = 820$ m, see Fig. 4.2a)).

We formulate the calibration problem with a wide parameter range (see Supplemental Material) mimicking no prior knowledge of the system except by the input data that discretize the domain into 3 areas (i.e., left hilslope, channel, right hillslope). We compare the results of this case with a condition with more knowledge of the system, that is, the parameter range is half of the previous one, hence reducing the decision space.

The calibration of hydrological models is inherently multi-objective (Shafii e De Smedt, 2009). For example, minimizing RMSE might give good objective function values, correctly matching the peaks, but might fail during the recession time, thus altering the overall mass balance that is accounted for in soil moisture, for example (Lindström, 1997). To this end, we use two metrics as our composite objective function, that is, the NSE and the relative volume error. The NSE varies from ∞ to 1 and the relative volume error should be minimized, such that we would want to maximize the NSE while minimizing the volume error. By introducing a penalizing factor as a function of the relative volume error in the NSE, we seek solutions that have a good NSE and reduced volume errors. Therefore, the objective function also varies from $-\infty$ to 1, where 1 indicates a perfect NSE and no volume error.

To transform this hypothesis into a minimizing optimization problem, we assume that each gauge has the same importance (i.e., $\gamma = 1/n_g$, with n_g as the number of gauges), assuming the NSE with weight $\alpha_1 = 1$ and the volume error with weight $\alpha_2 = 0.5$ as well, and we assume that each event also has the same importance (i.e., $\beta_j = 1/n_e \;\forall\; j$, with n_e being the number of events). Therefore, we can write the objective function as (4.6) (Lindström, 1997).

$$O_f = \frac{-1}{n_e}\sum_{j=1}^{n_e}\Big[\frac{1}{n_g}\sum_{i=1}^{n_g}\Big(\alpha_1 \overbrace{\text{NSE}^{\text{i,j}}}^{f_1} - \alpha_2 \overbrace{\left|\frac{\sum_{k=1}^{T_j}(Q_{\text{m}}^{\text{i,j,k}} - Q_{\text{obs}}^{\text{i,j,k}})}{\sum_{k=1}^{T_j}(Q_{\text{obs}}^{\text{i,j,k}})}\right|}^{f_2}\Big)\Big], \tag{4.11}$$

where i is the gauge index, j is the event index, and k is a time-step index.

The previous objective function attempts to maximize NSE while trying to maintain important hydrological features such as volume conservation (Gomes Jr et al., 2023a; Lindström, 1997). The negative sign in the first fraction is to transform the objective function suitable for the minimization of the optimization problem.

The calibration of hydrologic-hydrodynamic models is a necessary but not sufficient condition to the application of the model under different input ranges. The validation process is usually performed with different hydrologic conditions, typically represented by storms different from those used for the calibration. In order to gain confidence in the estimated parameters, we provide a vali-

Classification	n	h_0	k_{sat}	$\Delta\theta$	ψ
	[$sm^{-1/3}$]	[mm]	[mmh^{-1}]	[−]	[mm]
Left Hillslope	0.06	1	8	0.6	20
Channel	0.15	0	0	0.1	0
Right Hillslope	0.015	4	2	0.15	100

Table 4.3. Known parameters of the inverse problem of Numerical Case Study 4.

dation test under different storm volumes, intensities, temporal distributions, and volumes. To attach these issues, we formulate the following question.

- *Q4-2: Using only the observed data at the outlet, is it possible to obtain a sufficiently accurate model that can be used not only for the calibration events but also for the validation under different storms intensities, durations and temporal distributions?*

For the purpose of answering Q4-2, we calibrate the model with only the outlet gauge as the source information for the optimization calibration algorithm. To ensure different rainfall characteristics, we change the durations and volumes, as well as the rainfall temporal distribution. The rationale behind this is to have rainfall events with 50 or 150% values from the calibration events, whenever possible to represent relatively different conditions from the calibration phase. Therefore, we alter the durations from the 90-min rainfall duration used from the calibration events, resulting in rainfall durations of either 45 or 135 minutes. However, reducing the rainfall volumes to 50% of the smallest rainfall event used for calibration would generate events without runoff. Therefore, for this case, we fix the intensity as 10.8 mmh^{-1} but change the duration of the rainfall. To consider the effect of unsteady-state rainfall, we use the Huff 1st quartile hyetograph (Huff, 1967) as a proxy rainfall distribution to represent the temporal dynamics of the rainfall.

4.4 Results and Discussion

4.4.1 Numerical Case Study 1

The modeling results of the V-Tilted catchment calibration problem are presented in Fig. 4.5. The near optimal value of the decision vector is found after 20 generations with 100 population are $n_1 = 0.0132$ $sm^{-1/3}$, $n_2 = 0.1703$ $sm^{-1/3}$, $h_{0,1} = 0.02$ mm $k_{sat} = 0$, $\Delta\theta = 0.07$ cm^3cm^{-3}, and $\psi = 15.21$ mm. The hydrographs at the catchment outlet are presented in Fig. 4.5d), where the best and worst individual's hydrographs are plotted for each generation. Some of the worst individuals had no outflow due to large values of initial abstraction and/or k_{sat}, likely due to the decision space exploration of GA. However, as the generation moves, the worst individuals predict better hydrographs with NSE closing to unity as shown in Fig. 4.5e), that shows the performance of the best and worst individuals throughout the generations. In nearly 1 generation, it is possible to note that the best individual already gets good results for hydrological models (i.e., NSE > 0.85) (Nash e Sutcliffe, 1970).

The best individuals rapidly move to NSE closer to the unit, even though the parameters are not 100% correct. Some of the parameter ranges used in this case study had nearly a 200% variation from the minimum and maximum values (e.g., n_1 and n_2, as shown in Eq. (4.8e)) and the model still had minor errors compared to the expected values, as shown in Fig. 4.5f). The model also predicted that no infiltration would occur in this catchment since the near optimal k_{sat} is 0 mmh^{-1}. However, it predicted some initial abstraction of 0.02 mm, but this value is nearly negligible. Overall, the optimization problem resulted in a near-optimal solution that, at least for hydrological purposes, is a sufficient and physically based solution. It preserves the peak flow and overall shape of the hydrograph and has an

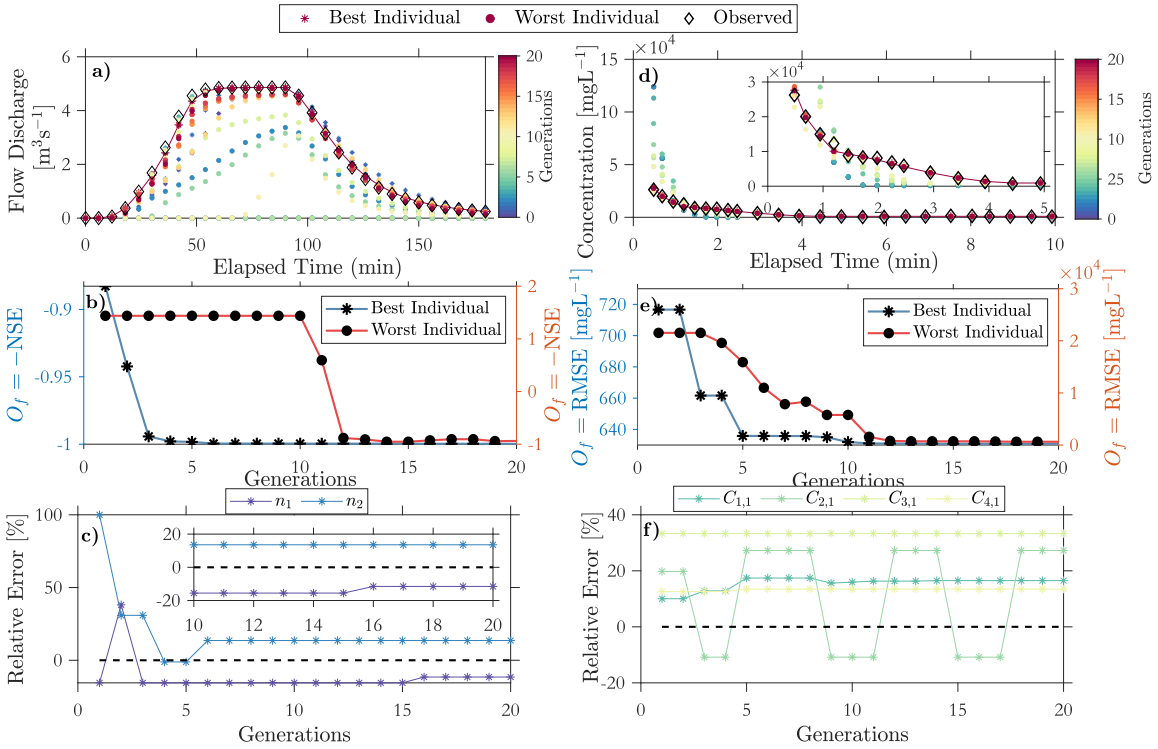

Figure 4.5. Modeling Results of Numerical Case Studies 1 and 2. Parts a) - c) are the hydrograph, objective function chart, and relative error of parameters for the V-Tilted catchment. Parts d) - f) represent the pollutograph, objective function chart, and relative error chart for the Wodden-Plane catchment. Only the best and the worst individuals of each generation are plotted in a) and d). Only the parameters of the best individuals are plotted nin c) and f).

optimal NSE compared to the outlet hydrograph. However, relying solely on NSE might produce great solutions, with feasible parameter estimations within the parameter boundaries but may be affected by equifinality, as shown in Fig. 4.5f), where it is noted that the Manning's roughness coefficient had a range of approximately 20% around the expected values.

4.4.2 Numerical Case Study 2

The modeling results of the Wooden-Plane catchment are presented in Fig. 4.5(a)-(c). In this problem, the RMSE was chosen as the objective function and the nearly-optimal objective function value was approximately 630 mg/L. For other modeling pollutants, such as copper, zinc, or phosphate, a RMSE of this magnitude would result in an inaccurate model (Batalini de Macedo et al., 2021); however, we are modeling salt concentrations that had mean concentrations of approximately 30.000 mg/L, as shown in Fig. 4.5a). The goodness of fitness can also be visualized in the inserted chart in Fig. 4.5a), where the model nearly predicted the same concentrations as the observations.

The values of the objective function for the best and worst individuals of each generation are also shown in Fig. 4.5b). Results are already relatively good for the 1st generation and finds a near-optimal plateau after the 5th generation. Although the optimization model found good results for fitting the observed concentrations, it came at the cost of estimating a larger mass of salt in the beginning of the simulation. The overprediction of C_1 and C_2 can be seen in Fig. 4.5c), where $C_1 = 323.68$, $C_2 = 1.081$, $C_3 = 12.045,03$, $C_4 = 0.2763$. In particular, the combined values of C_1, C_2, and ADD would result in an initial salt mass of 145 g, which is approximately 16% more than the value reported by (Hong et al., 2019). The black dashed line in this figure is the result of the same problem, using the same model (HydroPol2D), calibrating for C_3 and C_4, but assuming the initial mass of 125 g

(Gomes et al., 2023). It is inferred that a larger mass was expected with a larger washing capacity, since all water quality parameters were larger for the simulations presented in this numerical case study.

4.4.3 Numerical Case Study 3

The model has 8 LULC and 2 Soil classifications, resulting in 22 hydrologic-hydrodynamic parameters (16 from LULC and 6 from the soil parameters). Using the average of the parameter range presented in Tab. 4.1 and Tab. 4.2, the one-at-the-time sensitivities of these parameters are depicted in Figs. 4.6 and 4.7. The average of the parameters might be the baseline used when only the parameter ranges are known. The output functions used for this evaluation are mainly related to the hydrograph shape. We used peak flow, runoff volume at the end of the event, and time-to-peak variances as hydrograph shape evaluation functions. Furthermore, we evaluate the sensitivity of the parameters to flood areas (i.e., areas with maximum flood depth greater than 0.5 m). From Fig. 4.6 it is observed that the most sensitive parameters in terms of hydrograph shape are the Manning's roughness coefficient of the Built Areas (i.e., the watershed has nearly 70% of built areas), followed by those in the areas of trees. A reduction in roughness is fairly more expressive than an increase in terms of peak flow. However, for runoff volume, time to peak, and flooded areas, the Manning's variation seems to follow a linear relationship with these outputs.

It is interesting to note that reducing the n values reduces the total volume that leaves the catchment at the end of the event and also decreases flooded areas, which does not necessarily mean that areas with risks of human instability would also decrease (Rotava et al., 2013). The larger velocities that resulted from the reduced Manning's coefficient might increase areas of instability risks. The initial abstraction (h_0) also had some sensitivity, but presented a very non-linear behavior for all output functions used, indicating that it could be assumed in some cases rather than calibrated. This non-linear behavior might be due to Eq. 19 from Algorithm 1, which allows storing water in cells if the surface runoff depths are smaller than or equal to h_0, while allowing infiltration. We hypothesize that h_0 would have more influence for values larger than 10 mm and this parameter can be used to represent the storage of low impact development (LID) facilities that do not change surface roughness, such as rain barrels. Parameters n and h_0 can be proxy representations of LID facilities such as rain barrels (i.e., increasing h_0 in pixels), green roofs, permeable pavements, or bioretention systems, as they represent the storage and delay of the flood wave passing through cells (Damodaram et al., 2010).

These parameters associated with the infiltration parameters shown in Fig. 4.7 can be used to assess the effects of retrofitting the catchment into a more sustainable scenario with green infrastructure (McClymont et al., 2020) or can also represent a scenario of increase in urbanization and hence represent the effects of post-development conditions (Gomes Jr et al., 2023a). Due to the limited area for infiltration in the catchment, the results presented in Fig. 4.7 indicate that the soil properties have less influence than the roughness coefficients but greater influence than the initial abstraction, especially $k_{sat,2}$, which can be seen from Fig. 4.4 that most of the pervious areas are derived from this type of soil.

The model calibration results are presented in Fig. 4.8. Part a) shows the hydrograph for the best and worst individuals of each generation, while part b) shows the evolution of the objective function (i.e., - NSE) through the generations. The calibration results present a NSE = 0.89, RMSE $= 7.3\ m^3/s$, and $r^2 = 0.95$, and $\eta_p = 3.58\%$. Although we ran the optimization algorithm for 10 generations, 100 population, it was fundamentally impossible to capture the second peak of the two-peak observed hydrograph, as well as the observed runoff volume in the falling limb of the hydrograph. Other objective functions could also be tested; especially that account for peak flows and runoff volumes, but for the sake of simplicity, we only used the NSE. Several factors might have influenced

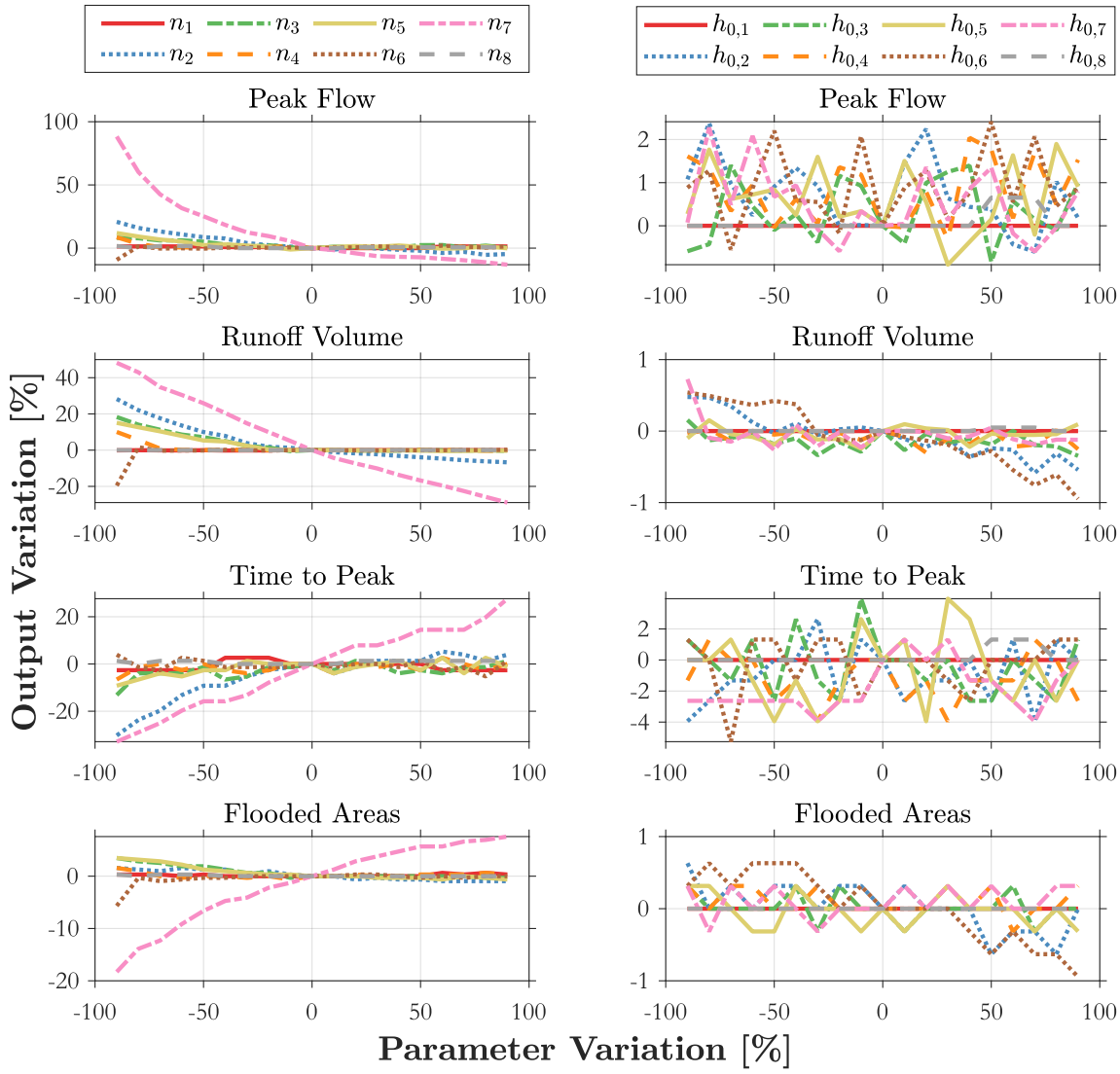

Figure 4.6. One-at-the-time sensitivity analysis of the LULC-Based parameters using the average parameters from the parameter range presented in Tab. 4.1 and Tab. 4.2 for Numerical Case Study 3. LULC-Based subscripts 1 = water, 2 = trees, 3 = Grass, 4 = Flooded Vegetation, 5 = Crops, 6 = Schrub/Scrub, 7 = Built Areas, and 8 = Bare Ground.

this behavior, and we hypothesize that the most important are the quality of the digital elevation model, the spatial variability of rainfall in the catchment, and the uncertainty in the rainfall measurements and transformation of stage into discharge, as well as the inherent uncertainty of the conceptual model of HydroPol2D. The calibrated parameters are shown in Tables 4.1 and 4.2.

As in Numerical Case Studies 1 and 2, after the first generation, the model performs similar to the last generation (i.e., NSE = 0.85), indicating that relatively fewer simulations can be required to reach accepted modeling results (Moriasi et al., 2015). As shown in Fig. 4.9, none of the parameters reached the boundaries of the range defined for the upper and lower bounds. However, a relatively large Manning's roughness coefficient is noted. Using a coarser DEM and filtering the DEM with Gaussian filters, CRS, and carving water surface depths in the channel, we hypothesized that the flow paths were shortened and smoothed in such a way that increasing n was necessary. However, not including these filters might cause water ponding in areas with DEM noise. Furthermore, by using a 30-m DEM, the terrain details that would be captured with a relatively high resolution DEM and would eventually create larger flow paths (i.e., more contact area between the flow and the surface

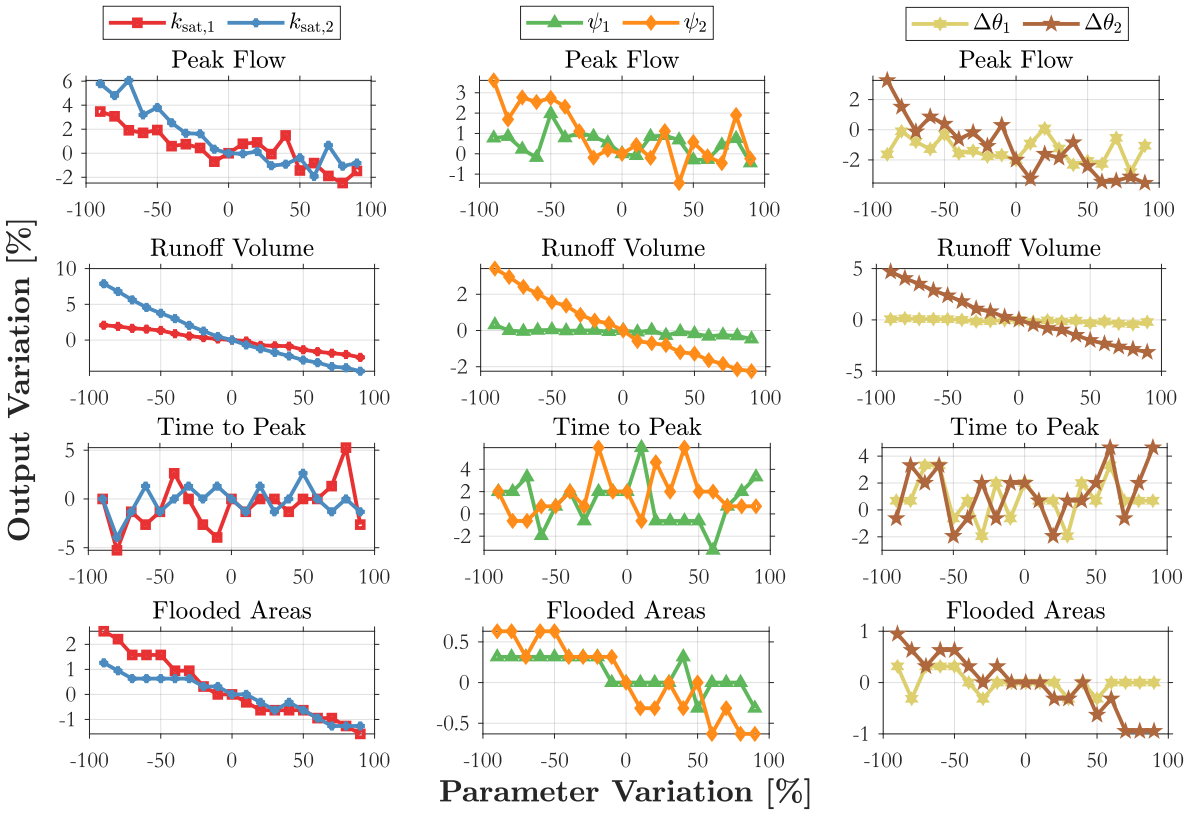

Figure 4.7. One-at-the-time sensitivity analysis of the SOIL-Based parameters using the average parameters from the parameter range presented in Tab. 4.1 and Tab. 4.2 for Numerical Case Study 3. Soil-Based subscripts 1 = Medium and 2 = Clayey.

resulting in larger head losses) would have played a role in the relatively larger n values. By having a shorter flow path (i.e., coarse resolution versus high resolution DEMs), for the same head loss, the n values would have to increase.

Using calibrated parameters, HydroPol2D can be applied and determine flood maps, human instability maps, infiltration, and other components of the water balance as shown in Gomes et al. (2023). Fig. 4.10 shows the spatialized results derived from the calibrated model using the source point data from the observed gauge. It is possible to assess flood, infiltration, and velocity maps, as well as the outlet hydrograph. The Supplemental Material contains HydroPol2D outputs that can improve flood risk management if a calibrated model is available.

4.4.4 Numerical Case Study 4

The relative parameter error assuming a considerably wide parameter range that would represent no prior knowledge about the parameters is shown in Fig. 4.11. Overall, the algorithm can find suitable sets of n and k_{sat}, i.e., the most sensitive parameters using the outlet gauge in combination with some of the other gauges, but have larger errors in the other less sensitive Green-Ampt parameters and in the initial abstraction, as shown in Fig. 4.11a). These other parameters are less sensitive and could have been assumed otherwise without prejudice to the overall representation of the hydrology and hydrodynamics.

When using gauges 2 or 3, that is, gauges from the left and right hillslopes, the error in the parameters of the opposite hillslope is relatively larger since the parameters were randomly chosen because no information about the discharges of that area is available, as shown in Fig. 4.11b). Using gauges 2 and 3 together, the error in the parameters is reduced since information from both hillslopes

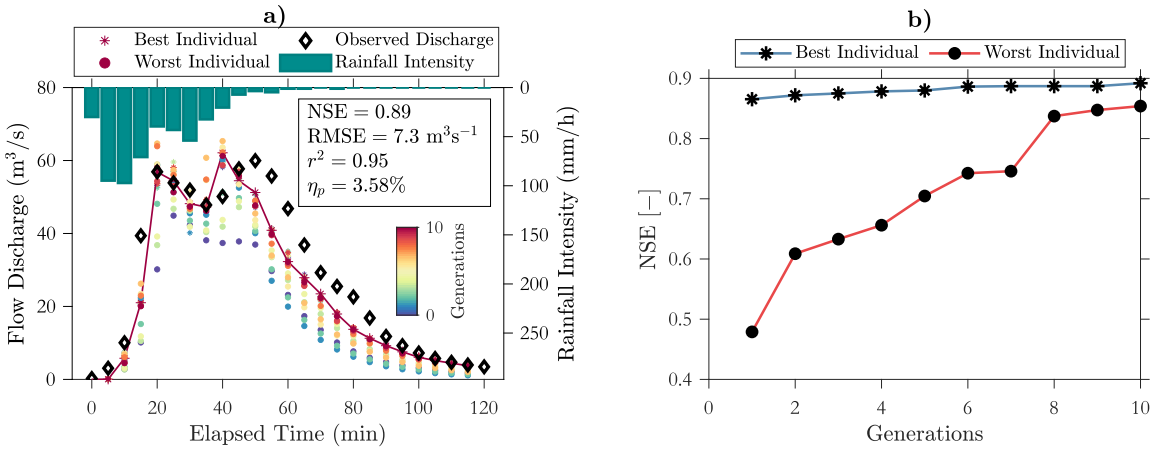

Figure 4.8. Calibration problem results with the catchment simulated with 30 m spatial resolution under an observed rainfall event. Part a) shows the hydrographs of the best and worst individuals, for each generation, as well as the rainfall intensity. Part b) shows the objective function (i.e., −NSE) values for the best and worst individuals.

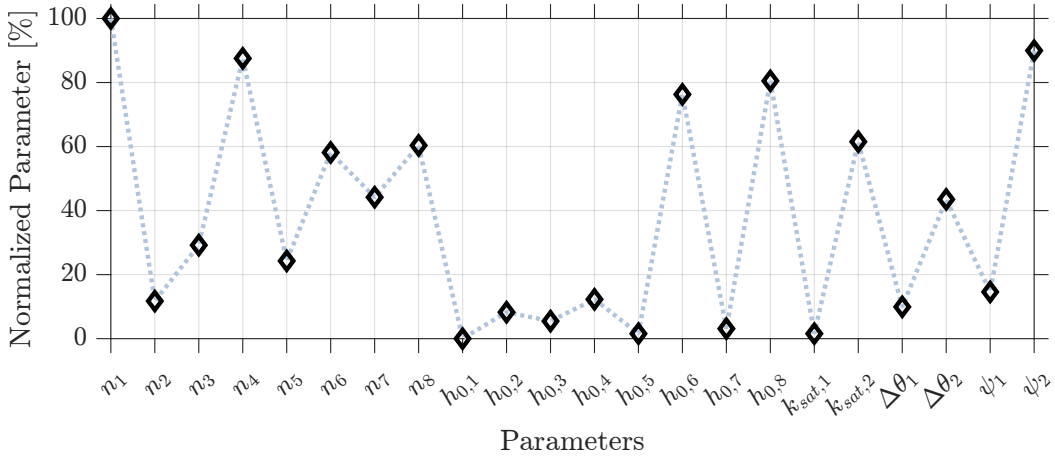

Figure 4.9. Near-Optimal normalized parameter, where 0 and 100% are the boundaries of the decision vector $\boldsymbol{x}$. LULC-Based subscripts 1 = water, 2 = trees, 3 = Grass, 4 = Flooded Vegetation, 5 = Crops, 6 = Schrub/Scrub, 7 = Built Areas, and 8 = Bare Ground. Soil-Based subscripts 1 = Medium and 2 = Clayey.

(i.e., areas with similar hydrologic characteristics) is available. Using only gauge 1 as the source of information for calibration, a good objective function value is found (see Fig. 4.11c)) but a very poor description of the parameters is found, as shown in Fig. 4.11b), indicating a high chance of equifinality if no minimum knowledge of the parameters is known. This result shows the importance of experts defining proper parameter ranges and that a previous, at least minimum, parameter range of the system is very important. All objective function performances could be considered feasible solutions with high fitness values if no prior knowledge of the system is known, as shown in Fig. 4.11c), increasing the equifinality issues.

When comparing the performance of solutions without prior knowledge of the parameters with solutions with a smaller decision space, the equifinality tends to decrease, as shown in Fig. 4.11 compared to Fig. 4.12 and the values of the objective function are generally higher. This result indicates that a reduction in decision space to a more reduced space can substantially decrease equifinality. Some parameters less influential as $h_{0,l}$ had larger errors but little sensitivity and could have been assumed rather than calibrated.

The number of events in the calibration also plays an important role in the reduction of equifinality. By using a relatively small rainfall event that is not a runoff producing event in the left hillslope,

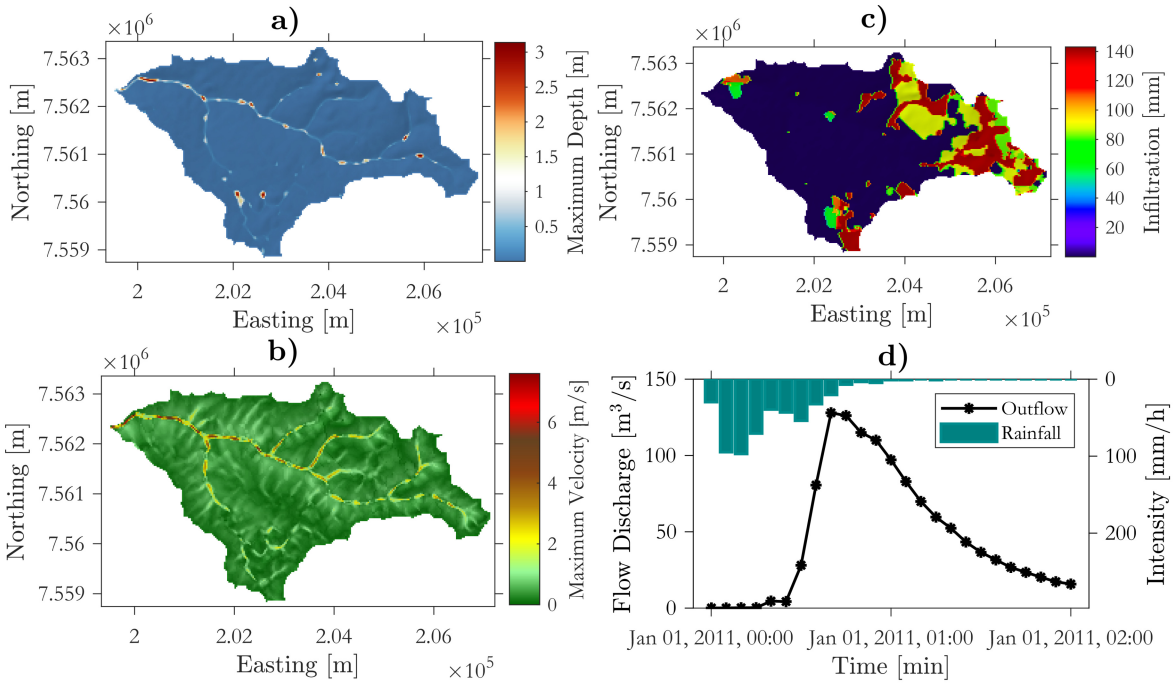

Figure 4.10. Some of the states modeled with HydroPol2D derived from a calibrated model with source point data used. Part a) is the maximum water surface depth, b) is the maximum overland flow velocity, c) is the infiltrated depth at the end of the event, and d) is the outlet hydrograph. The maps are projected in SIRGAS 2000 UTM 23 S.

no quality information is available for the calibration of the hydrodynamic and infiltration parameters of this hillsope. The left gauge in event 1, with 10.8 mmh^{-1} did not record runoff. Therefore, any combination of parameters such that all water infiltrates in the soil are a solution with full performance of the objective function. An infinite number of combinations of parameters would satisfy this condition (e.g., $h_{0,l} > 16.2$ mm, $k_{sat,l} > 10.8$ mmh^{-1}), leading to high equifinality due to poor gauging location and selection of the event for calibration. However, for the right gauge, runoff is observed, and the parameters can be relatively well estimated, although not perfectly. The problem of distributed physically-based modeling in small catchments with events that produce little or no runoff is a complex problem and models typically have lower performance for hortonian small flows (Senarath et al., 2000; Downer e Ogden, 2004).

This idea is illustrated in Tab. 4.4. Overall, by choosing only one poor event, the calibration performance is nearly optimal for all combinations of gauges, but the parameter estimation is faulty. Therefore, calibrating the model for longer hydrological periods or choosing a combination of events that would encompass relatively high and low flows is desirable to increase the available information and reduce parameter equifinality. However, the uncertainty in the boundary conditions and in the initial simulation values, especially the initial soil moisture (Senarath et al., 2000), is challenging. Even in a perfect virtual experiment without uncertainty in rainfall values, initial soil moisture, model boundary conditions, and perfect gauging data, the uncertainty in the parameters is substantially affected by a poor parameter range.

One of the advantages of this calibration approach is the use of the model to calibrate the parameters using only the outlet data as the sole gauge, which would be the case of many poorly-gauged and flood-prone catchments such as the Gregorio Catchment. To this end, we use a relatively high optimization resource, that is, we run the optimization model for 40 generations and 100 population size and optimize Eq. (4.8) using only the outlet as the observed gauge for all events available. The rationale

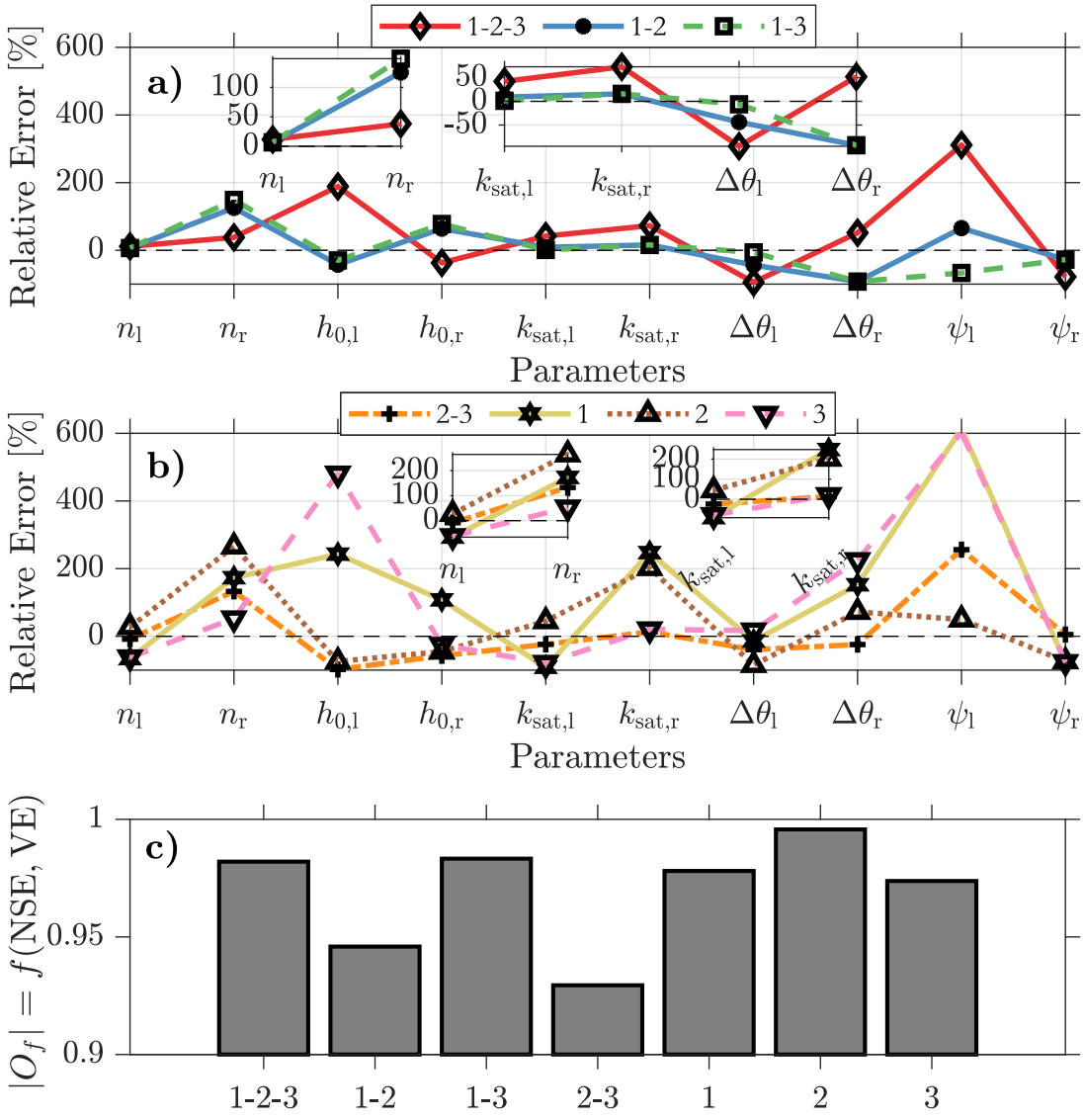

Figure 4.11. Relative Parameter Error for Numerical Case Study 4, assuming no prior knowledge of the parameter boundaries where 1 = Outlet, 2 = left gauge, 3 = right gauge. Black dashed lines are the expected values. Part a) is the relative error for cases where the outlet and at least one more gauge is observed and case, Part b) are single gauges or a combination of gauges that are not at the outlet and Part c) are the objective function values given by Eq. (4.8). All cases were simulated with 10 generations and 100 populations.

.

behind using a larger number of generations is to extract the maximum resource of the single-point observed information, since it is only at one gauge. Using a larger number of generations would likely decrease the possibility of finding local optima in the optimization model. Therefore, the uncertainty would probably be due to equifinality since there is no uncertainty in rainfall and observations.

In this analysis, we assume the initial abstractions of the left and right gauges as the correct parameters, since they do not play an important role in the hydrological response of the catchment, as mentioned above in this section. The other parameter ranges are the same as those used in the simulated cases with prior knowledge of the system (see Tab. S1). The results in Fig. 4.13 show the hydrographs for the outlet (a)-(c) and for the other gauges not considered in the calibration (i.e., left gauge (d)-(f), and right gauge (g)-(i)). Even calibrating with only the outlet of the catchment, the model can still find a reasonable, physically-based, and bounded parameter set, although the parameters are not equal as the one of the inverse problem. This result points to the scenario that, given a sufficient number of runoff-producing events and reasonable computational resources, it is possible to calibrate HydroPol2D only with data at the outlet and later use the calibrated model to derive important catchment response information such as those presented in Fig. 4.10. The calibrated parameters of this analysis are $n_l = 0.0536$ sm$^{-1/3}$, $n_r = 0.0168$, $k_{\text{sat,l}} = 3.56$ mmh^{-1}, $k_{\text{sat,r}} = 1.77$ mmh^{-1}, $\Delta\theta_l = 0.625$, $\Delta\theta_r = 0.346$, $\psi_l = 91.36$ mm, $\psi_r = 49.92$ mm.

By comparing the calibrated parameters with the ones of the inverse problem shown in Tab. 4.3, it is noticed that a trade-off between $k_{\text{sat,l}}$ and ψ_{l} is found for the left hilslope. While $k_{\text{sat,l}}$ decreases, $\Delta\theta_{\text{l}}$ and ψ_{l} increase, counterbalancing the reduction in $k_{\text{sat,l}}$. However, even though the parameter equifinality is evident, the model performance and the errors are visually minimal, as shown in Fig. 4.14 and Figs. 4.15. In addition, the performance metrics are also accepted in most gauges, as shown in Tab. 4.5.

For steady-state events, the model presented acceptable results for all events, with all volume errors smaller than 6% and all NSE larger than 0.996. For unsteady-state hyetographs, as expected, the model presented a relatively reduced performance for the left gauge, especially for event 6, that is, the event with the smallest duration and volume. As shown in Fig. 4.15, event 6 generated a very small runoff rate that was observed in the inverse problem and not predicted by the calibrated model. In addition, for the right gauge, a relatively large volume error can be observed. For the outlet, however, the results are still quite accurate; although relatively faulty for the left and right gauges. Disregarding this event, the simulation results had volume errors smaller than 20% and NSE larger than 0.992. Overall, using the calibrated parameters that were obtained only with the outlet gauge is sufficient to explain the events used for calibration and can accurately represent the hydrological response of events that are outside the hydrological characteristics of the events used for calibration. Even though some errors are found in the internal gauges, the performance of the model measured in the outlet can be considered very good for all validation events.

4.4.5 Limitations, Challenges, and Opportunities of this Modeling Approach

Calibrating a fully-distributed hydrodynamic and water quality model requires not only field observations, but also depends extensively on the quality and resolution of the terrain, soils, and land use and land cover models. However, as presented in this paper, this modeling approach can be easily applied worldwide in catchments with scarce time-series observations of rainfall and/or a representing variable of the flow dynamics such as discharge depths and/or a variable representing the pollutant such as the pollutant concentration. Since pollutant concentrations are inherently associated with accurate discharge modeling, calibrating water quantity and quality parameters altogether might result in high equifinality if only pollutographs are the optimization criteria.

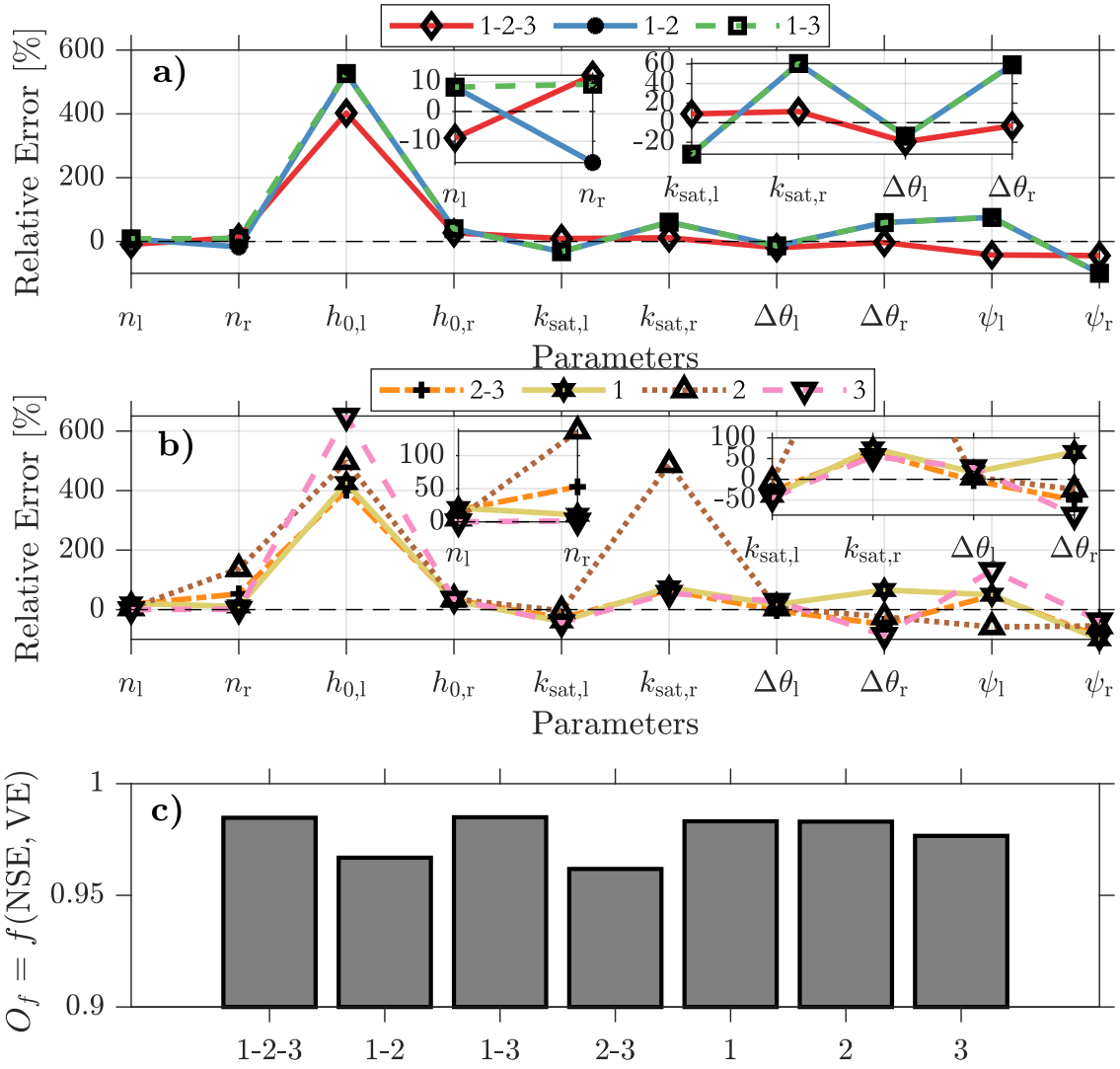

Figure 4.12. Relative Parameter Error for Numerical Case Study 4, assuming a prior knowledge, that is, half of the parameter range from Fig. 4.11 of the parameter boundaries where 1 = Outlet, 2 = left gauge, 3 = right gauge. Black dashed lines are the expected values. Part a) is the relative error for cases where the outlet and at least one more gauge is observed and case, Part b) are single gauges or combination of gauges that are not at the outlet and Part c) are the objective function values given by Eq. (4.8). All cases were simulated with 10 generations and 100 population.

Gauges	n_l [sm$^{-1/3}$]	n_r [sm$^{-1/3}$]	$h_{0,l}$ [mm]	$h_{0,2}$ [mm]	$k_{sat,l}$ [mmh^{-1}]	$k_{sat,r}$ [mmh^{-1}]	$\Delta\theta_l$ [-]	$\Delta\theta_r$ [-]	ψ_l [mm]	ψ_r [mm]	OF [-]
1-2-3	0.036	0.019	9.17	5.25	8.986	3.44	0.65	0.04	92.34	8.33	-0.99
1-2	0.047	0.015	9.73	7.68	10.059	1.30	0.52	0.11	14.49	13.80	-0.99
1-3	0.068	0.015	5.36	7.68	5.395	1.78	0.64	0.11	15.26	13.80	-0.98
2-3	0.050	0.014	5.24	5.61	2.761	2.48	0.68	0.16	54.34	20.14	-0.98
1	0.040	0.013	9.95	5.51	3.191	3.12	0.77	0.27	0.61	0.17	-0.99
2	0.063	0.048	7.12	8.76	9.004	0.91	0.74	0.17	36.91	51.51	-1.00
3	0.032	0.020	6.44	5.14	6.630	3.36	0.73	0.04	38.00	23.21	-0.97

Table 4.4. Near-optimal solutions for different combinations of gauges and for only 1 storm of 10.8 mmh^{-1} during 90 minutes. The known parameters are $n_l = 0.06$ sm$^{-1/3}$, $n_r = 0.015$, $h_{0,l} = 1$ mm, $h_{0,r} = 4$ mm, $k_{sat,l} = 8$ mmh^{-1}, $k_{sat,r} = 2$ mmh^{-1}, $\Delta\theta_l = 0.6$, $\Delta\theta_r = 0.15$, $\psi_l = 20$ mm, and $\psi_r = 100$ mm.

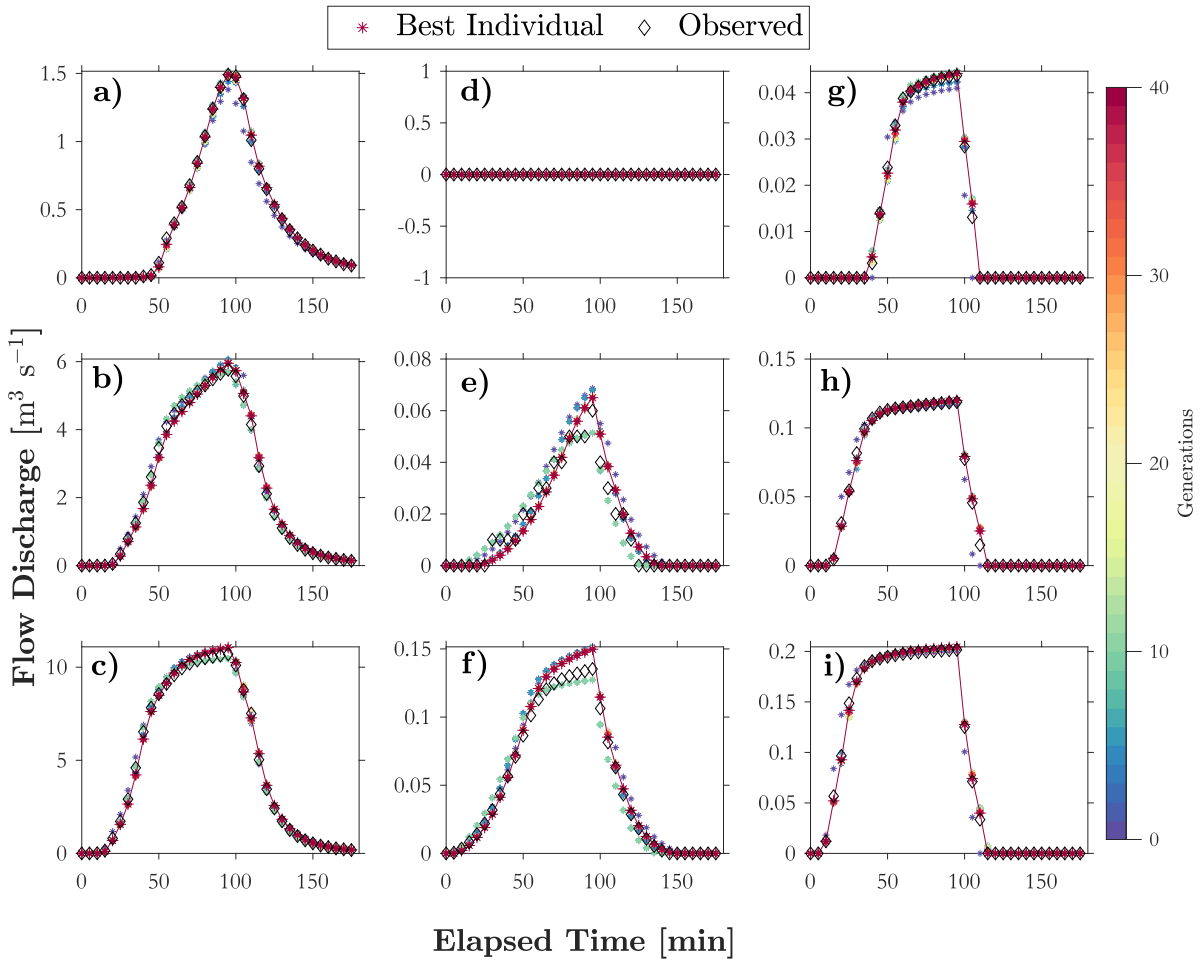

Figure 4.13. Automatic calibration results of considering the 3 events but only the outlet as the observable gauge. Therefore, the charts (d)-(i) are shown, but the modeled results were not considered in the calibration of the model and were simulated with the parameters that were obtained by calibrating the model only with the outlet gauge. The first row are the events of 10.8 mm h^{-1}, followed by 21.6 mm h^{-1} and 32.4 mm h^{-1}. Parts (a)-(c) are results for the outlet, whereas (d)-(f) are from the left gauge and (g)-(i) are from the right gauge.

This approach can be enhanced and easily expanded by allowing calibration not only with time series but also with maps of flood extent, magnitude, or by socio-hydrological information (Fava et al., 2022) such as maximum depths in certain flood points, especially in catchments with no gauge stations (Gomes et al., 2023). The challenge, however, is to find a suitable single objective cost function that can normalize different optimization criteria into a single and homogeneous cost function. In addition, the minimum requirement, however, is the rainfall intensity time-series in a proper resolution that depends on the catchment response. Regarding rainfall, this approach could also be improved by allowing space-variant rainfall that could be derived from radar, satellite imagery, or by interpolation of source-gauged rainfall stations.

It is recommended that a sensitivity analysis be performed before automatic calibration to avoid wasting computational resources on variables that do not play a substantial role in the hydrologic-hydrodynamic behavior of the catchment. Although the results presented in this paper indicate that some parameters might be more sensitive than others, the results can vary dramatically for different catchments with different topography and soil properties.

The use of worldwide datasets to represent LULC and SOIL allows a proper definition of model parameters such as n or k_{sat}, as shown in Soliman et al. (2022); Gupta et al. (2021). Studies such as the aforementioned ones might facilitate the parametrization of fully distributed models and can be

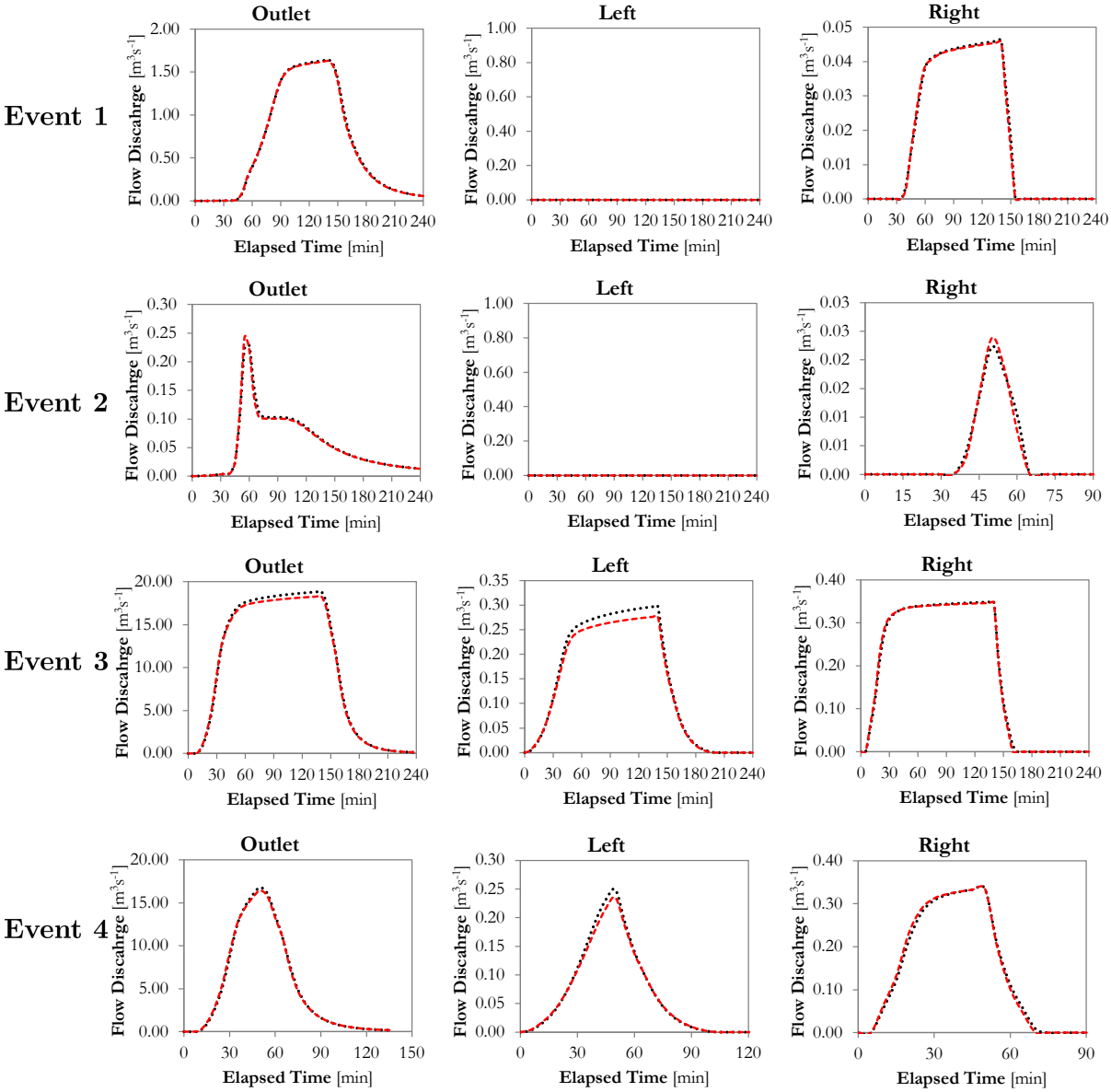

Figure 4.14. Steady-state rainfall validation hydrographs of Numerical Case Study 4, for Events 1 to 4 described in Tab. 4.5. Black dotted lines are modeled results with the calibrated model using only the outlet gauge data, and red dashed lines are the results with the parameters of the inverse problem.

opportunities for worldwide application.

4.5 Conclusions

An optimization-based algorithm was developed and applied to calibrate a fully distributed hydrological-hydrodynamic and water quality model (HydroPol2D). The algorithm can find near-optimal set of parameters to explain the observed gauged information, such as flow discharge, pollutant concentration, or flood depths. The results of Numerical Case Studies 1, 2, from the real-world case study in Numerical Case Study 3, and from the Equifinality analysis in Numerical Case Study 4 support the following:

- A1: The model can accurately predict not only the Green-Ampt infiltration parameters but also Manning's roughness coefficients and initial abstraction values, as shown in Numerical Case Study

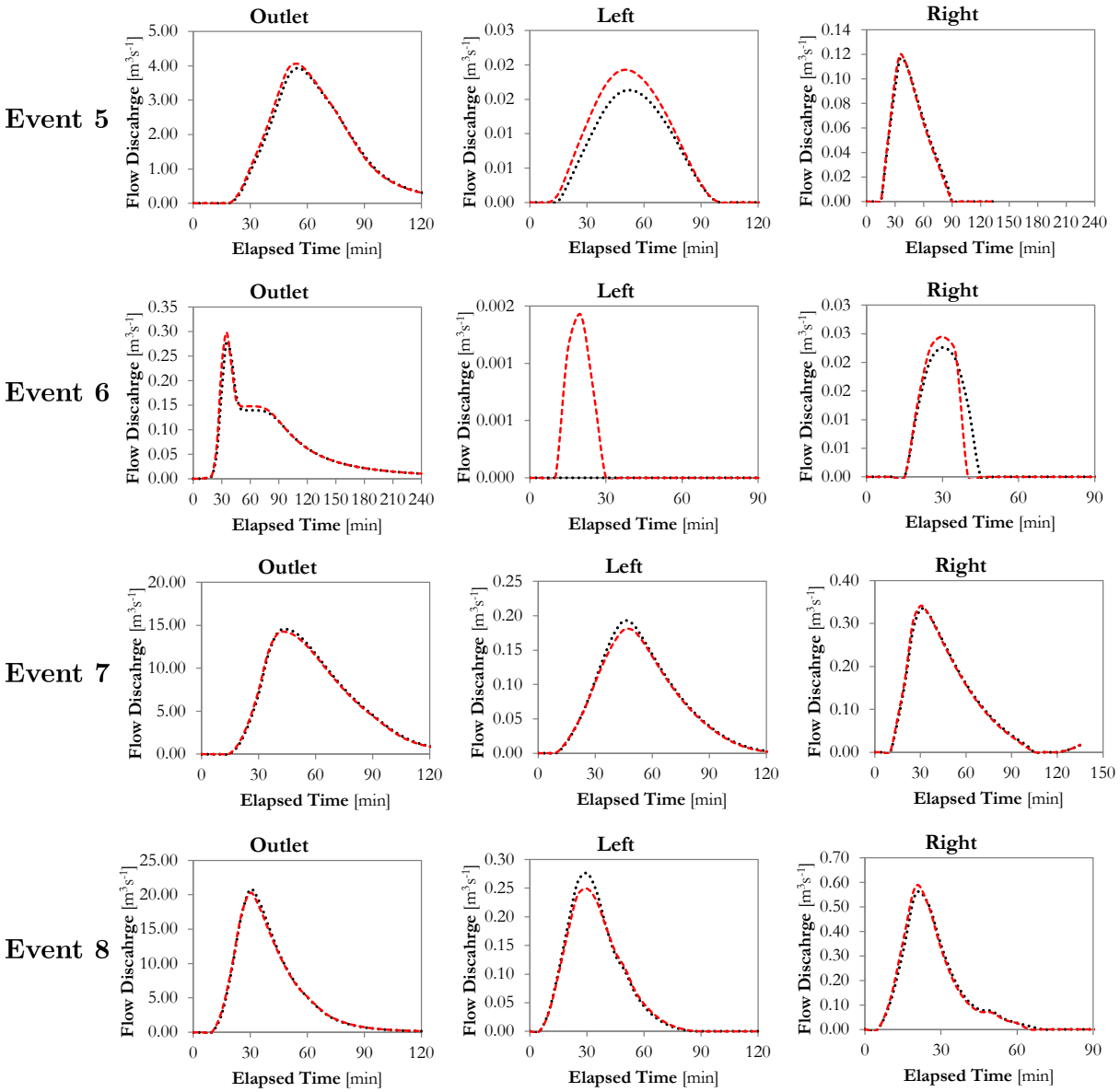

Figure 4.15. Unsteady-state rainfall results of Numerical Case Study 4, for Events 5 to 8 described in Tab. 4.5. The rainfall is simulated with Huff 1st quartile hyetograph. Black dotted lines are modeled results with the calibrated model using only the outlet gauge data, and red dashed lines are the results with the parameters of the inverse problem.

Event	Rainfall Boundary Condition	Rainfall Duration [min]	Rainfall Volume [mm]	Gauge	NSE [-]	Vol Error [%]	r^2 [-]	PBIAS [%]
1	Steady State	135	24.3	Outlet	0.999	1.076	1.000	0.347
				Left	[-]	[-]	[-]	[-]
				Right	0.999	0.951	0.999	0.589
2	Steady State	45	8.1	Outlet	0.993	1.847	0.997	1.184
				Left	[-]	[-]	[-]	[-]
				Right	0.989	1.456	0.995	5.171
3	Steady State	135	48.6	Outlet	0.998	2.121	1.000	0.494
				Left	0.990	5.961	1.000	1.269
				Right	0.999	0.224	1.000	0.381
4	Steady State	45	36.45	Outlet	0.999	0.378	1.000	0.712
				Left	0.996	3.227	1.000	1.696
				Right	0.998	-0.483	0.999	1.119
5	Huff 1st Quartile	135	24.3	Outlet	0.997	-2.505	0.999	1.189
				Left	0.960	-20.399	0.997	4.777
				Right	0.997	0.226	0.999	1.401
6	Huff 1st Quartile	45	8.1	Outlet	0.983	-3.425	0.993	1.862
				Left	-0.061	[-]	[-]	59.408
				Right	0.895	6.872	0.946	15.927
7	Huff 1st Quartile	135	48.6	Outlet	0.999	1.310	1.000	0.684
				Left	0.996	4.049	1.000	1.358
				Right	0.998	0.059	0.999	0.972
8	Huff 1st Quartile	45	36.45	Outlet	0.999	0.708	1.000	1.022
				Left	0.992	3.125	0.998	2.573
				Right	0.995	-0.424	0.998	2.571

Table 4.5. Validation metrics for events outside of the calibration conditions. Each row represent results of one event, for different gauges. Events 1-2 are with the smallest rainfall intensity used in calibration (i.e., 10.8 mmh^{-1}, while events 3-4 are with the largest one (i.e., 32.4 mmh^{-1}. Similarly, the events with unsteady-state rainfall follow the same pattern, resulting in the same rainfall volumes but temporally distributed with Huff 1st quartile hyetographs.

1. The Predicted hydrographs match, with NSE > 0.99 the considered real observed hydrograph in Numerical Case Study 1.

- A2: The algorithm can find not only the wash-off parameters, but also the initial mass (error $< 15\%$) of the pollutant in the wooden-plane catchment to match the observed pollutgraph, as shown in Numerical Case Study 2.

- A3: The model can still find a physically bounded near-optimal set of parameters to calibrate the observed hydrograph with NSE = 0.89, indicating good accuracy. In addition, using this set of parameters were possible to determine (i) infiltration maps, maximum flow velocities (ii), maximum flood depths, (iii) outlet hydrograph.

- A4-1: The equifinality problem is reduced by the addition of runoff-producing events and by choosing at least one gauge in hydrological unit regions. Using only the outlet gauge as the information might produce a feasible (i.e., within the parameter range) but wrong parameter set that explains the observed data. This set of parameters tends to produce small errors in peaks and hydrograph sha-

pes and relatively larger errors in runoff volumes. The use of runoff-producing events with different flow parameters typically produces better parameter estimation. The parameter estimation error is reduced by a more reduced parameter range that can be attached by experts or by GIS available worldwide datasets to reduce parameter ranges.

- A4-2: The model presented accurate results when calibrated only with the outlet gauge hydrograph as the sole information for calibration. Although the equifinality is observed by the compensation of the infiltration parameters, the model presented acceptable results in most cases of different rainfall volumes, intensities, and distributions. A reduced model performance is observed for events with little or no observed runoff in the gauges. However, in general, the model presented accepted results in gauges not used for calibration for different rainfall durations, volumes, intensities, and rainfall distributions even with the model calibrated with only the outlet gauge. This indicates an opportunity to move towards conceptual and simplified lumped models flood assessment to physically-based, fully-distributed analysis, since both models can be calibrated with the same input data.

Therefore, the methods applied in this paper can be replicated in all catchments with observations at least at one point. The more points with runoff observations, the better the reduction of equifinality. Using only freely available datasets, this method can be applied for catchments with observations at gauging stations to extrapolate results in the whole catchment domain moving from typically limited lumped-parameter models to fully-distributed physically-based analysis. However, the methodology strategy developed in this paper is only applicable if some constraints are satisfied, such as:

- The overland flow is predominantly hortonian.
- The effect of human made drainage systems such as reservoirs, dams, polders, or any other hydraulic structure operation does not govern the whole catchment hydrodynamics.
- The catchment can be modeled with space-invariant precipitation.
- The optimization cost function is relatively fast, allowing multiple evaluations in a reasonable time.

The aforementioned requirements are typically satisfied in relatively small to mid-size catchments. Advancing these limitations and developing a framework capable of adapting to whatever data is available could help modelers use distributed models and improve flood and water quality spatial analysis.

4.6 Data Availability Statement

Some or all data, models, or code generated or used during the study are available in a repository or online in accordance with funder data retention policies. All software, figures, and data can be freely downloaded in Gomes et al. (2023).

Acknowledgment

The authors appreciate the support of the City of San Antonio, by the San Antonio River Authority, CAPES Ph.D Scholarship, and the PPGSHS PROEX Graduate Program.

Supplemental Materials

Supplementary data related to this article can be found at (Gomes Jr., 2023).

References

Abreu, F. G. d. (2019). *Quantificação dos prejuízos econômicos à atividade comercial derivados de inundações urbanas*. PhD thesis, Universidade de São Paulo.

Afshar, A., Kazemi, H., e Saadatpour, M. (2011). Particle swarm optimization for automatic calibration of large scale water quality model (ce-qual-w2): Application to karkheh reservoir, iran. *Water resources management*, 25:2613–2632.

Akan, A. O. e Iyer, S. S. (2021). *Open channel hydraulics*. Butterworth-Heinemann.

Ardıçlıoğlu, M. e Kuriqi, A. (2019). Calibration of channel roughness in intermittent rivers using hec-ras model: Case of sarimsakli creek, turkey. *SN applied Sciences*, 1:1–9.

Batalini de Macedo, M., Pereira de Oliveira, T. R., Halmenschlager Oliveira, T., Nóbrega Gomes Junior, M., Teixeira Brasil, J. A., Ambrogi Ferreira do Lago, C., e Mendiondo, E. M. (2021). Evaluating low impact development practices potentials for increasing flood resilience and stormwater reuse through lab-controlled bioretention systems. *Water Science and Technology*, 84(5):1103–1124.

Behrouz, M. S., Zhu, Z., Matott, L. S., e Rabideau, A. J. (2020). A new tool for automatic calibration of the storm water management model (swmm). *Journal of Hydrology*, 581:124436.

Bermudez, A. e Vazquez, M. E. (1994). Upwind methods for hyperbolic conservation laws with source terms. *Computers & Fluids*, 23(8):1049–1071.

Beven, K. e Freer, J. (2001). Equifinality, data assimilation, and uncertainty estimation in mechanistic modelling of complex environmental systems using the glue methodology. *Journal of hydrology*, 249(1-4):11–29.

Blasone, R.-S., Madsen, H., e Rosbjerg, D. (2008). Uncertainty assessment of integrated distributed hydrological models using glue with markov chain monte carlo sampling. *Journal of Hydrology*, 353(1-2):18–32.

Brath, A., Montanari, A., e Toth, E. (2004). Analysis of the effects of different scenarios of historical data availability on the calibration of a spatially-distributed hydrological model. *Journal of Hydrology*, 291(3-4):232–253.

Brunner, G. W. (2016b). Hec-ras river analysis system modeling user's manual us army corps of engineers hydrologic engineering center. *Information on http://www. hec. usace. army. mil*.

Cho, J. H. e Lee, J. H. (2015). Watershed model calibration framework developed using an influence coefficient algorithm and a genetic algorithm and analysis of pollutant discharge characteristics and load reduction in a tmdl planning area. *Journal of Environmental Management*, 163:2–10.

Confesor Jr, R. B. e Whittaker, G. W. (2007). Automatic calibration of hydrologic models with multi-objective evolutionary algorithm and pareto optimization 1. *JAWRA Journal of the American Water Resources Association*, 43(4):981–989.

Conrad, O., Bechtel, B., Bock, M., Dietrich, H., Fischer, E., Gerlitz, L., Wehberg, J., Wichmann, V., e Böhner, J. (2015). System for automated geoscientific analyses (saga) v. 2.1. 4. *Geoscientific Model Development*, 8(7):1991–2007.

Damodaram, C., Giacomoni, M. H., Prakash Khedun, C., Holmes, H., Ryan, A., Saour, W., e Zechman, E. M. (2010). Simulation of combined best management practices and low impact development for sustainable stormwater management 1. *JAWRA Journal of the American Water Resources Association*, 46(5):907–918.

de Geografia e Estatística (IBGE), I. (2022). Panorama população, território e ambiente.

de Meteorologia., I. I. N. (2022). Gráficos climatólogicos.

De Paiva, R. C. D., Buarque, D. C., Collischonn, W., Bonnet, M.-P., Frappart, F., Calmant, S., e Bulhões Mendes, C. A. (2013). Large-scale hydrologic and hydrodynamic modeling of the amazon river basin. *Water Resources Research*, 49(3):1226–1243.

Debele, B., Srinivasan, R., e Parlange, J.-Y. (2008). Coupling upland watershed and downstream waterbody hydrodynamic and water quality models (swat and ce-qual-w2) for better water resources management in complex river basins. *Environmental Modeling & Assessment*, 13:135–153.

do Lago, C. A., Giacomoni, M. H., Bentivoglio, R., Taormina, R., Junior, M. N. G., e Mendiondo, E. M. (2023). Generalizing rapid flood predictions to unseen urban catchments with conditional generative adversarial networks. *Journal of Hydrology*, 618:129276.

Domeneghetti, A., Castellarin, A., e Brath, A. (2012). Assessing rating-curve uncertainty and its effects on hydraulic model calibration. *Hydrology and Earth System Sciences*, 16(4):1191–1202.

Downer, C. W. e Ogden, F. L. (2004). Gssha: Model to simulate diverse stream flow producing processes. *Journal of Hydrologic Engineering*, 9(3):161–174.

Dung, N. V., Merz, B., Bárdossy, A., Thang, T. D., e Apel, H. (2011). Multi-objective automatic calibration of hydrodynamic models utilizing inundation maps and gauge data. *Hydrology and Earth System Sciences*, 15(4):1339–1354.

Fatichi, S., Vivoni, E. R., Ogden, F. L., Ivanov, V. Y., Mirus, B., Gochis, D., Downer, C. W., Camporese, M., Davison, J. H., Ebel, B., et al. (2016). An overview of current applications, challenges, and future trends in distributed process-based models in hydrology. *Journal of Hydrology*, 537:45–60.

Fava, M. C., Macedo, M. B. d., Buarque, A. C. S., Saraiva, A. M., Delbem, A. C. B., e Mendiondo, E. M. (2022). Linking urban floods to citizen science and low impact development in poorly gauged basins under climate changes for dynamic resilience evaluation. *Water*, 14(9):1467.

Fava, M. C., Mazzoleni, M., Abe, N., Mendiondo, E. M., e Solomatine, D. P. (2020). Improving flood forecasting using an input correction method in urban models in poorly gauged areas. *Hydrological Sciences Journal*, 65(7):1096–1111.

Fisher, R. A. et al. (1920). 012: A mathematical examination of the methods of determining the accuracy of an observation by the mean error, and by the mean square error. *Monthly Notices of the Royal Astronomical Society*.

Giacomoni, M. e Joseph, J. (2017). Multi-objective evolutionary optimization and monte carlo simulation for placement of low impact development in the catchment scale. *Journal of Water Resources Planning and Management*, 143(9):04017053.

Gomes, M. N., do Lago, C. A. F., Rápalo, L. M. C., Oliveira, P. T. S., Giacomoni, M. H., e Mendiondo, E. M. (2023). Hydropol2d distributed hydrodynamic and water quality model: Challenges and opportunities in poorly-gauged catchments. *Journal of Hydrology*, 625:129982.

Gomes Jr. (2023). Hydropol2d v.0.0.1. https://github.com/marcusnobrega-eng/HydroPol2D.

Gomes Jr, M. N., Giacomoni, M. H., de Macedo, M. B., do Lago, C. A. F., Brasil, J. A. T., de Oliveira, T. R. P., e Mendiondo, E. M. (2023a). A modeling framework for bioretention analysis: Assessing the hydrologic performance under system uncertainty. *Journal of Hydrologic Engineering*, 28(9):04023025.

Gomes Jr, M. N., Rápalo, L. M., Oliveira, P. T., Giacomoni, M. H., do Lago, C. A., e Mendiondo, E. M. (2023e). Modeling unsteady and steady 1d hydrodynamics under different hydraulic conceptualizations: Model/software development and case studies. *Environmental Modelling & Software*, page 105733.

Gomes Júnior, M. N., Giacomoni, M. H., Taha, A. F., e Mendiondo, E. M. (2022). Flood risk mitigation and valve control in stormwater systems: State-space modeling, control algorithms, and case studies. *Journal of Water Resources Planning and Management*, 148(12):04022067.

Green, W. H. e Ampt, G. A. (1911). Studies on soil phyics. *The Journal of Agricultural Science*, 4(1):1–24.

Guidolin, M., Chen, A. S., Ghimire, B., Keedwell, E. C., Djordjević, S., e Savić, D. A. (2016). A weighted cellular automata 2d inundation model for rapid flood analysis. *Environmental Modelling & Software*, 84:378–394.

Gupta, H. V., Sorooshian, S., e Yapo, P. O. (1999). Status of automatic calibration for hydrologic models: Comparison with multilevel expert calibration. *Journal of hydrologic engineering*, 4(2):135–143.

Gupta, S., Lehmann, P., Bonetti, S., Papritz, A., e Or, D. (2021). Global prediction of soil saturated hydraulic conductivity using random forest in a covariate-based geotransfer function (cogtf) framework. *Journal of Advances in Modeling Earth Systems*, 13(4):e2020MS002242.

Hawker, L., Bates, P., Neal, J., e Rougier, J. (2018). Perspectives on digital elevation model (dem) simulation for flood modeling in the absence of a high-accuracy open access global dem. *Frontiers in Earth Science*, 6:233.

Her, Y., Yoo, S.-H., Cho, J., Hwang, S., Jeong, J., e Seong, C. (2019). Uncertainty in hydrological analysis of climate change: multi-parameter vs. multi-gcm ensemble predictions. *Scientific reports*, 9(1):4974.

Higham, D. J. e Higham, N. J. (2016). *MATLAB guide*. SIAM.

Hong, Y., Liao, Q., Bonhomme, C., e Chebbo, G. (2019). Physically-based urban stormwater quality modelling: An efficient approach for calibration and sensitivity analysis. *Journal of environmental management*, 246:462–471.

Huff, F. A. (1967). Time distribution of rainfall in heavy storms. *Water resources research*, 3(4):1007–1019.

Hunter, N. M., Horritt, M. S., Bates, P. D., Wilson, M. D., e Werner, M. G. (2005). An adaptive time step solution for raster-based storage cell modelling of floodplain inundation. *Advances in water resources*, 28(9):975–991.

Kollet, S. J. e Maxwell, R. M. (2006a). Integrated surface–groundwater flow modeling: A free-surface overland flow boundary condition in a parallel groundwater flow model. *Advances in Water Resources*, 29(7):945–958.

Li, W., Kiaghadi, A., e Dawson, C. (2021). High temporal resolution rainfall–runoff modeling using long-short-term-memory (lstm) networks. *Neural Computing and Applications*, 33:1261–1278.

Lima, G, d., Boldrin, R. S., Mendiondo, E. M., Mauad, F. F., e Ohnuma Jr, A. (2007). Análise de incertezas de observações hidrológicas e sua influência na modelagem de pequenas bacias urbanas. *Revista Brasileira de Recursos Hídricos*, 12(1):107–116.

Lindström, G. (1997). A simple automatic calibration routine for the hbv model. *Hydrology Research*, 28(3):153–168.

McClymont, K., Cunha, D. G. F., Maidment, C., Ashagre, B., Vasconcelos, A. F., de Macedo, M. B., Dos Santos, M. F. N., Júnior, M. N. G., Mendiondo, E. M., Barbassa, A. P., et al. (2020). Towards urban resilience through sustainable drainage systems: A multi-objective optimisation problem. *Journal of Environmental Management*, 275:111173.

Milledge, D., Lane, S., e Warburton, J. (2009). The potential of digital filtering of generic topographic data for geomorphological research. *Earth Surface Processes and Landforms*, 34(1):63–74.

Moriasi, D. N., Gitau, M. W., Pai, N., e Daggupati, P. (2015). Hydrologic and water quality models: Performance measures and evaluation criteria. *Transactions of the ASABE*, 58(6):1763–1785.

Naeini, M. R., Analui, B., Gupta, H., Duan, Q., e Sorooshian, S. (2019). Three decades of the shuffled complex evolution (sce-ua) optimization algorithm: Review and applications. *Scientia Iranica*, 26(4):2015–2031.

Nash, J. E. e Sutcliffe, J. V. (1970). River flow forecasting through conceptual models part ia discussion of principles. *Journal of hydrology*, 10(3):282–290.

Phillips, B., Yu, S., Thompson, G., e De Silva, N. (2005). 1d and 2d modelling of urban drainage systems using xp-swmm and tuflow. In *10th international conference on urban drainage*, pages 21–26. Citeseer.

Rossman, L. A. et al. (2010). *Storm water management model user's manual, version 5.0*. National Risk Management Research Laboratory, Office of Research and Development, U.S. Environmental Protection Agency.

Rotava, J., Mendiondo, E. M., e Souza, V. C. B. (2013). Simulação de instabilidade humana em inundações: primeiras considerações. *XX Simpósio Brasileiro de Recursos Hídricos*, pages 1–8.

Sarmento Buarque, A. C., Bhattacharya-Mis, N., Fava, M. C., Souza, F. A. A. d., e Mendiondo, E. M. (2020). Using historical source data to understand urban flood risk: a socio-hydrological modelling application at gregório creek, brazil. *Hydrological Sciences Journal*, 65(7):1075–1083.

Schwanghart, W. e Scherler, D. (2014). Topotoolbox 2–matlab-based software for topographic analysis and modeling in earth surface sciences. *Earth Surface Dynamics*, 2(1):1–7.

SCS, U. (1986). Urban hydrology for small watersheds, technical release no. 55 (tr-55). *US Department of Agriculture, US Government Printing Office, Washington, DC*.

Senarath, S., Ogden, F., Downer, C., e Sharif, H. (2000). On the calibration and verification of distributed, physically-based, continuous, hortonian hydrologic models. *Water Resour. Res*, 36(6):1495–1510.

Shafii, M. e De Smedt, F. (2009). Multi-objective calibration of a distributed hydrological model (wetspa) using a genetic algorithm. *Hydrology and Earth System Sciences*, 13(11):2137–2149.

Shen, H., Tolson, B. A., e Mai, J. (2022). Time to update the split-sample approach in hydrological model calibration. *Water Resources Research*, 58(3):e2021WR031523.

Soliman, M., Morsy, M. M., e Radwan, H. G. (2022). Assessment of implementing land use/land cover lulc 2020-esri global maps in 2d flood modeling application. *Water*, 14(23):3963.

Souza, T. F. d. (2008). *Drenagem urbana sob cenários de longo prazo visando incentivos ambientais*. PhD thesis, Universidade de São Paulo.

Swathi, V., Srinivasa Raju, K., Varma, M. R., e Sai Veena, S. (2019). Automatic calibration of swmm using nsga-iii and the effects of delineation scale on an urban catchment. *Journal of hydroinformatics*, 21(5):781–797.

Tigkas, D., Christelis, V., e Tsakiris, G. (2016). Comparative study of evolutionary algorithms for the automatic calibration of the medbasin-d conceptual hydrological model. *Environmental Processes*, 3:629–644.

Torres, M. A., Chávez-Cifuentes, J. F., e Reinoso, E. (2022). A conceptual flood model based on cellular automata for probabilistic risk applications. *Environmental Modelling & Software*, 157:105530.

Wang, S., Taha, A. F., Sela, L., Giacomoni, M. H., e Gatsis, N. (2020). A new derivative-free linear approximation for solving the network water flow problem with convergence guarantees. *Water Resources Research*, 56(3):no–no.

Yang, C., Raskin, R., Goodchild, M., e Gahegan, M. (2010). Geospatial cyberinfrastructure: past, present and future. *Computers, Environment and Urban Systems*, 34(4):264–277.

Young, I. T. e Van Vliet, L. J. (1995). Recursive implementation of the gaussian filter. *Signal processing*, 44(2):139–151.

Zhang, H., Haan, C., e Nofziger, D. (1990). Hydrologic modeling with gis: An overview. *Applied Engineering in Agriculture*, 6(4):453–458.

Zhang, T., Xiao, Y., Liang, D., Tang, H., Xu, J., Yuan, S., e Luan, B. (2020). A physically-based model for dissolved pollutant transport over impervious surfaces. *Journal of Hydrology*, 590:125478.

5 EXPLORING THE IMPACT OF RAINFALL TEMPORAL DISTRIBUTION AND CRITICAL DURATIONS ON FLOOD HAZARD MODELING

A modified version was submitted to *International Journal of Disaster Risk Reduction* as: Gomes Jr, M.N., Jalihal, Vijay,and Mendiondo, E.M., 2024. Exploring the Impact of Rainfall Temporal Distribution and Critical Durations on Flood Hazard Modeling.

Graphical Abstract

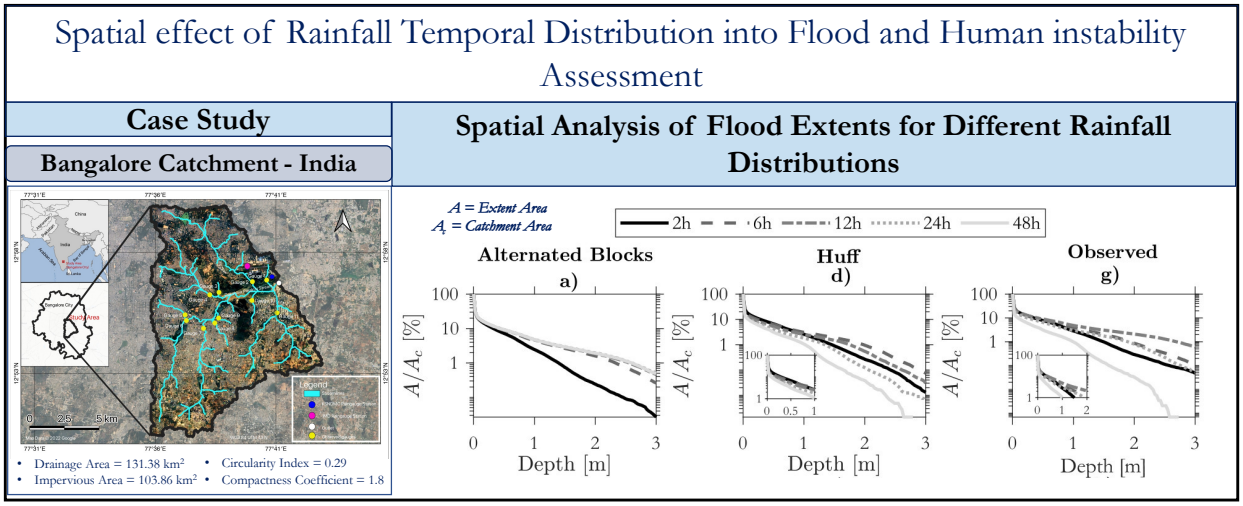

Highlights

- The effects of rainfall temporal distribution in flood hazard are investigated.
- The concept of critical rainfall duration is defined to maximize a spatial flood hazard metric.
- We compare synthetic Huff curves, Alternating Block Method and median observed hyetograph curves effects in flood hazard modeling.
- The observed rainfall distribution is the most critical for human instability hazard.

Abstract

Urbanization and climate change amplify challenges posed by floods for both city dwellers and planners. Flood modeling, rooted in geosciences and atmospheric sciences, operates in a non-linear and multi-modal fashion, marked by uncertainties from factors like soil infiltration characteristics, floodplain roughness, and spatio-temporal variations in rainfall volume, distribution, and intensities. This paper addresses these challenges by introducing a flood mapping methodology that incorporates synthetic design storms and compares them with a fitted median rainfall distribution derived from high-resolution observed rainfall data in the catchment. The flood hazard effect of choosing different rainfall temporal distribution methods is investigated. The Alternating Blocks Method and the Huff curves method, one of the most widely used methods in engineering hydrology, were chosen as representative synthetic rainfall methods for flood mapping assessment and compared against the measured median rainfall distribution. The framework was applied in a 131 km^2 flood-prone urban catchment in Bangalore, India. Evaluation of different rainfall distributions reveals a potential 50%

smaller areas with flood hazard, for the same return period and duration, simply by selecting a specific rainfall distribution compared to the expected fitted median rainfall distribution based on observed data. This research not only underscores the importance of appropriate rainfall distribution selection and critical rainfall duration, but also highlights the need for accurate data-driven methodologies in flood mapping, particularly in the face of urbanization and climate-induced complexities.

Keywords: Flood Mapping, Huff Curves, Alternated Blocks Method, Rainfall Distribution, Flood Hazard

5.1 Introduction

Urban flood inundation mapping is affected by a phletora of hydrological phenomena varying from the rainfall dynamics, to the non-linear spatio-temporal representation of infiltration (Cheng et al., 2020). Typically, the use of so-called event-based design storms is used to delineate flood-prone areas (Mei et al., 2020; Kang et al., 2013), especially when high-resolution quality data of rainfall is lacking (Gomes et al., 2023). Multiple areas across the world use the 100-yr return period as the common return period used to define flood-risk areas (Huang e Wang, 2020; Dottori et al., 2022), although the definition of the rainfall duration and temporal distribution are hardly ever specified (Krvavica e Rubinić, 2020).

The importance of flood modeling and mapping associated with rainfall return periods is evident for instances such as aiding in the development of flood insurance plans (Mani et al., 2014) or even by being used to define multifaceted risk areas that would depend not only on hydrological but also socioeconomic information (Roldán-Valcarce et al., 2023; Pregnolato et al., 2024; Zare et al., 2024). Even though multiple applications use products derived from flood simulation results, a large uncertainty can arise from not clearly defining the proper duration and temporal distribution of the rainfall that would maximize the expected flood hazard (e.g., maximum water surface depth).

Two storms with the same return period can have dramatically different catchment responses simply by varying the temporal rainfall distribution and / or the rainfall duration. We hypothesize that a proper definition of these rainfall characteristics must be made focusing on heuristic search of the duration that maximizes a spatial flood hazard criterion. Flood hazard can be defined as a function of a variety of features, such as the floodplain area with significant flood depth, velocity or ultimately, areas with human instability hazards (Lazzarin et al., 2024). The latter can be simply estimated via flood momentum equations and dynamic friction modeling (Jonkman e Penning-Rowsell, 2008).

The commonly accepted definition of critical rainfall duration is based on the duration leading to the maximum outflow peak (Krvavica e Rubinić, 2020). However, this definition may not align with other critical flood hazard metrics, such as the maximization of areas prone to human instability or those with substantial flood depth. Additionally, there is a lack of consensus on widely accepted rainfall temporal distribution and duration, with many engineering design studies arbitrarily selecting these rainfall characteristics (Krvavica e Rubinić, 2020).

In this paper, we define a heuristic method using a 2D hydrologic-hydrodynamic modeling approach to estimate the critical rainfall duration that maximizes flood hazard indicators such as floodplain extent, areas with relatively high velocities, and areas with human instability hazards. The methods developed in this paper are tested in a real-world catchment in Bangalore, India.

5.1.1 Literature Review

Challenges in sub-daily rainfall data are primarily rooted in the scarcity of prolonged, reliable records encompassing extreme rainfall events at shorter time scales (Westra et al., 2014). Key

impediments include the lack of comprehensive global repositories for sub-daily data, limitations in instruments measuring short yet intense rainfall, evolving technological incompatibilities, and variations in quality assessment methods. These challenges hinder our capacity to ascertain whether extreme sub-daily rainfall is increasing due to climate change and subsequently impact our understanding of whether flood hazard frequencies align with rainfall trends.

Flood hydrologic reponse is influenced by the spatio-temporal variability in rainfall (Zhu et al., 2018; Chen et al., 2023). The study conducted by (Breinl et al., 2021) found that regions with convective rain patterns exhibit increased variability in extreme rainfall, whereas orographic rain regions display greater variability in streamflow runoff. In essence, the research suggests that the characteristics of rainfall intensity, duration, and frequency, as well as streamflow runoff, are influenced by factors including spatial distribution of rain, geological features, and soil storage capacity. In the same direction, the research carried out in Cristiano et al. (2017) emphasizes the intricate spatial and temporal variability characterizing hydrological processes within urban environments. This variability is particularly heightened by the influence of impervious surfaces and the diverse land use patterns present that influences the flow dynamics within urban catchments.

The investigation conducted by Bezak et al. (2018) exposes the reliance of critical rainfall duration, particularly in maximizing peak flows within Huff curves (Huff, 1967), on the catchment time of concentration. Nevertheless, they emphasize the lack of a universally defined method within the engineering community to estimate this critical duration. Furthermore, Bezak et al. (2018) notes that prolonging rainfall duration amplifies disparities in peak discharge and time-to-peak. Scenarios featuring extended rainfall durations, while adhering to the same Huff curve, yield smaller peak discharge values compared to cases where rainfall duration closely matches the catchment time of concentration. The study indicates that more research is required to advance the understanding of critical rainfall duration.

Many studies aimed at determining critical duration primarily concentrate on identifying the duration that maximizes flood hazard, often focusing on catchment-integrated hydrological subproducts, particularly the maximum peak flow (Yuan et al., 2021; Bezak et al., 2018). While the maximum peak flow is connected to flood characteristics, its limitation lies in neglecting the impact on floodplain extent, especially in smaller urbanized areas with diverse land use patterns contributing to nonlinear runoff. This highlights the need for a spatialized metric to define critical rainfall duration and temporal distribution, with a specific emphasis on maximizing considerations for spatial flood hazard assessment.

With urban floods posing a lot of challenges to city dwellers and planners, several spatial and temporal hydrological models were developed for authorities to have better decision-making in further flood prevention and risk management. Models using StormWater Management Model (SWMM) (Rossman, 2010), Machine learning techniques (Mosavi et al., 2018), Neural Networks (do Lago et al., 2023), and physically-based fully distributed models (Gomes et al., 2023) are some of the solutions being developed by the research community all over the world to analyse, predict and control flood risks enabling the decision-makers and city authorities to formulate a plan to improve the infrastructural conditions (Teng et al., 2017).

Flood or hydrodynamic modeling can be uncertain and difficult in data-scarce areas and scenarios. However, these areas are generally the areas with relatively higher exposure and vulnerability of the population (Batalini de Macedo et al., 2022a; Membele et al., 2022). An example of such cases is of the floods in Bellandur, a very urbanized catchment in Bagalore, India. Although we apply our methods in this catchment, we attempt to develop a case-study free analysis that uses only freely-available datasets and can be adapted not only to poorly-gauged catchments but also to catchments with more climatologic-hydrologic data.

While recent literature offers diverse analyses for flood hazard modeling and mitigation, the absence of proper high-resolution rainfall and terrain data remains a challenge for assessing floods in poorly-gauged watersheds. Despite data limitations, the development of a method providing meaningful results for flood hazard in these areas holds relevance for decision-makers. Additionally, there is no consensus on the use of synthetic design storms, rainfall durations, and return periods critical for flood inundation mapping and modeling. Moreover, there is a gap in research investigating the impact of rainfall duration and temporal distribution on human instability hazard. We address these issues by presenting a flood hazard zoning method that evaluates varied rainfall durations and temporal distributions.

Our ultimate goal is not to provide a definitive solution for determining the duration times and temporal distributions of critical rainfall in terms of flood hazard. These are closely related to catchment and climate signatures. Instead, we seek to elucidate the impact of neglecting these catchment-specific characteristics and its potential effects in flood hazard modeling. The framework herein developed relies solely on freely available global datasets, ensuring broad applicability within the engineering community. The fundamental contributions of this paper are:

- We develop a flood mapping framework for relatively small poorly-gauged catchments using 2D hydrodynamic modeling approach that requires only a catchment GIS data and a rainfall intensity-duration-frequency (IDF) curve. Therefore, this framework can be used to generate first-order site-specific catchment information, such as flood mapping and areas with human instability.
- We evaluate the effects of the rainfall duration and temporal distribution on the modeling assessment of water surface depths, velocities, human instability, and infiltrated depths, providing a comprehensive analysis of the effects of not choosing a critical rainfall duration and temporal distribution.

5.2 Material and Methods

5.2.1 Mathematical Model

HydroPol2D, as detailed by (Gomes et al., 2023), is a comprehensive hydrological-hydrodynamic and transport and fate model. It employs the Green-Ampt equation (Green e Ampt, 1911) for estimating hortonian overland flow and converts shallow water depths into discharge through the nonlinear reservoir model (Rossman, 2010). Functioning as a diffusive-like cellular automata model, HydroPol2D utilizes the steepest slope of the water surface elevation at each time-step to estimate the momentum term within the diffusion wave 2D system of equations. These equations include a mass balance equation and a momentum equation.

5.2.1.1 Conservation of Mass and Momentum

The elementwise cell-by-cell mass balance equation can be written:

$$^{t+\Delta t}d^{i,j} = {}^{t}d^{i,j} + \Delta t\left[\sum_{\mathcal{N}^{i,j}} {}^{t}I^{i,j} - \sum_{\mathcal{N}^{i,j}} {}^{t}O^{i,j} + {}^{t}r^{i,j} - {}^{t}f^{i,j}\left({}^{t}d^{i,j}, {}^{t}F_{d}^{i,j}\right) - {}^{t}e_{T}^{i,j}\right], \tag{5.1}$$

where t is the time, d is the water surface depth, Δt is the time-step, I is the inflow rate, O is the outflow rate, r is the rainfall rate, f is the infiltration rate, F_d is the cumulative infiltration depth, e_T is the real evapotranspiration, and $\mathcal{N}$ represents the domain subset of all neighbors of cell i, j (Gomes et al., 2023).

The term $(\sum_{\mathcal{N}^{i,j}} {}^{t}I^{i,j} - \sum_{\mathcal{N}^{i,j}} {}^{t}O^{i,j})$ is calculated in terms of the change in inter-cell volume between each neighboring cell using a cellular automata approach and topological relationships.

By assuming a diffusive-wave approximation in the momentum equation (Akan e Iyer, 2021), we can consider that:

$$ {}^{t}s_{f}^{i,j} = \max\left(\frac{\partial({}^{t}d^{i,j} + z^{i,j})}{\partial x}, \frac{\partial({}^{t}d^{i,j} + z^{i,j})}{\partial y}\right) \tag{5.2} $$

where ∂x and ∂y are incremental cell sizes in x and y directions on 2D plan, whereas z is the ground elevation from the DTM.

Using the friction slope formulation derived from previous Eq. (5.2) into Manning's equation, the maximum intercell flow velocity is given by:

$$ {}^{t}v_{m}^{i,j} = \frac{1}{n^{i,j}}\Delta x\left(\max\left({}^{t}d^{i,j} - h_{0}^{i,j}, 0\right)\right)^{\frac{5}{3}}\sqrt{{}^{t}s_{f}^{i,j}}, \tag{5.3} $$

where n is the Manning's roughness coefficient, Δx is the cell area, h_0 is the initial abstraction or storage depression. This maximum intercell velocity is then constrained by volumetric rules of the cellular automata, reducing checkerboard effects (Hunter et al., 2005; Guidolin et al., 2016). The velocities for the other outflow direction from a given cell are calculated in terms of the void volume between the centering cells and its neighbors, in a weighthed cellular automata approach (Gomes Jr et al., 2023b; Gomes et al., 2023; Guidolin et al., 2016).

Using the states modeled by HydroPol2D, it is possible to determine drag forces and to calculate the human instability risk due to friction. This method is further explained.

5.2.1.2 Human Instability Modeling

During flood events, effects of sliding and toppling can occur depending on the velocities and water surface depth magnitudes. In this paper, we estimate the occurrence of these effects by calculating the forces associated with the flow following the methodology proposed in Jonkman e Penning-Rowsell (2008). In brief, the friction instability occurs when the available static friction (i.e., calculated using the difference between the weight of a person and its buoyancy) is smaller or equal to the hydrodynamic force associated with the perpendicular flow (Jonkman e Penning-Rowsell, 2008). The governing equations to calculate the human instability hazard (f_r) , considering a cell (i, j) in the domain, are shown as follows:

$$ V_{c} = L_{p}B_{p}d \tag{5.4a} $$

$$ F_{p} = mg \tag{5.4b} $$

$$ F_{q} = \frac{1}{2}\rho C_{d}B_{p}dv^{2} \tag{5.4c} $$

$$ F_{b} = \rho V_{c}g \tag{5.4d} $$

$$ F_{f} = \mu\left(F_{p} - F_{b}\right) \tag{5.4e} $$

$$ f_{r} = \max\left(\frac{F_{q}}{F_{f}}, 1\right) \tag{5.4f} $$

where the subscripts p, q, b, and f represents person, flow, buyoance, and friction. The person's height, length, and width are given by H_p, L_p, and B_p. Parameters g, C_d, and μ are the gravity acceleration, the drag coefficient, and the kinematic static factor and the water density is given by ρ. The product Bh represents the person area in the flow direction. A value of $f_r = 1$ represents that a person would be dragged in the water.

The previous set of equations (5.4) are solved for each computational time-step and after the end of the simulation, the time-dependent maps of f_r are plotted, as well as the maximum values of f_r per cell that would define the human instability flood hazard map. For the sake of parsimony, we assumed $u = 0.5$, $m = 75$ kg, $C_d = 1.1$, $\rho_p = 1000$ kg $\cdot$ m^{-3}, $H_p = 1.75$ m, $L_p = 0.3$ m, $B_p = 0.3$ m, and $g = 9.81$ m $\cdot$ s^{-2}.

5.2.2 Design Hyetographs

The intensity-duration-frequency curve is given by a Sherman type, such that:

$$i = \frac{K\mathrm{RP}^a}{(b + t_\mathrm{d})^c}, \tag{5.5}$$

where K, a, b, and c are fitted parameters using a theoretical distribution frequency curve (e.g., Gumbel), and RP is the return period.

5.2.2.1 ABM - Chicago Hyetograph

The method assumes that the rainfall volume obtained by the IDF curve distributes following a peak factor γ, such that if $\gamma = 0.5$, the maximum intensity value of rainfall would be centered. The Chicago method hence equals the ABM if $\gamma = 0.5$ (Gomes Jr et al., 2023a).

$$i(t) = \frac{K\mathrm{RP}^a(\frac{t_1}{\gamma}(1-c)+b)}{(\frac{t_1}{\gamma}+b)^{1+c}} \text{ for } t = t_1 \leq \gamma t_\mathrm{d} \tag{5.6a}$$

$$i(t) = \frac{K\mathrm{RP}^a(\frac{t_2}{\gamma}(1-c)+b)}{(\frac{t_1}{1-\gamma}+b)^{1+c}} \text{ for } t = t_2 > \gamma t_\mathrm{d} \tag{5.6b}$$

where γ is a peak factor assumed as 0.5 to represent the rainfall peak at 50% of the storm duration and Eqs. (5.6a) and (5.6b) represent equations for durations before peak and after peak.

5.2.2.2 Huff Hyetographs

The polynomial equations used in the model to represent the Huff temporal distribution are presented as follows (Gomes Jr et al., 2023a):

$$P(t) = 0.2558\Big(\frac{t}{t_\mathrm{d}}\Big)^4 + 1.5586\Big(\frac{t}{t_\mathrm{d}}\Big)^3 - 4.346\Big(\frac{t}{t_\mathrm{d}}\Big)^2 + 3.603\Big(\frac{t}{t_\mathrm{d}}\Big) - 0.0579 \tag{5.7a}$$

$$P(t) = 6.1888\Big(\frac{t}{t_\mathrm{d}}\Big)^4 - 14.996\Big(\frac{t}{t_\mathrm{d}}\Big)^3 + 10.861\Big(\frac{t}{t_\mathrm{d}}\Big)^2 - 1.0758\Big(\frac{t}{t_\mathrm{d}}\Big) + 0.0235 \tag{5.7b}$$

$$P(t) = 71.986\Big(\frac{t}{t_\mathrm{d}}\Big)^6 + 206.68\Big(\frac{t}{t_\mathrm{d}}\Big)^5 - 211.78\Big(\frac{t}{t_\mathrm{d}}\Big)^4 - 92.488\Big(\frac{t}{t_\mathrm{d}}\Big)^3 + 16.973\Big(\frac{t}{t_\mathrm{d}}\Big)^2 - 0.5697\Big(\frac{t}{t_\mathrm{d}}\Big) + 0.0041 \tag{5.7c}$$

$$P(t) = -58.036\Big(\frac{t}{t_\mathrm{d}}\Big)^6 + 154.96\Big(\frac{t}{t_\mathrm{d}}\Big)^5 - 151.59\Big(\frac{t}{t_\mathrm{d}}\Big)^4 + 68.269\Big(\frac{t}{t_\mathrm{d}}\Big)^3 - 13.978\Big(\frac{t}{t_\mathrm{d}}\Big)^2 + 1.3842\Big(\frac{t}{t_\mathrm{d}}\Big) - 0.008 \tag{5.7d}$$

where Eqs (5.7a), (5.7b), (5.7c), and (5.7d) represent polynomial equations for Huff's 1$^{\mathrm{st}}$, 2$^{\mathrm{nd}}$, 3$^{\mathrm{rd}}$, and 4$^{\mathrm{th}}$ quartiles, respectively. Variables t and t_d are the time and the rainfall duration.

5.2.3 Case Study

Floods are one of the deadliest natural disasters, and India is a country prone that not only gets affected by ecosystems and infrastructure, but also lead to casualties (De et al., 2013). India has a diverse topography and rich natural bio-diversity ranging from deserts to glacial mountain regions. It is the 7th largest country by size and one of the most populous countries in the world with over 1.4 Billion people and is expected to surpass the 1.5 billion mark by 2025 and surpass China within a decade (Kc et al., 2018). With this increase in population and economic growth over the last few

decades, India saw an increase in urbanization as the rural population started migrating towards the cities for better employment opportunities and a better standard of living (Bhagat, 2011).

Bangalore or also known as Bengaluru is the capital and the largest city in the southern Indian state of Karnataka. It is popularly known as the "Garden City"or the "Silicon Valley of India". Bangalore is located at 12°59′ north latitude and 77°57′ east longitude, almost equidistant from the eastern and western coasts of the South Indian peninsula. It is situated at an altitude of 920 m above mean sea level (MSL) with an area of 741km^2. The mean annual total rainfall is about 900mm (Ramachandra e Aithal, 2019). The summer temperature ranges from 18°C to 38°C, while the winter temperature ranges from 12°C to 25°C. Thus, Bangalore enjoys a salubrious climate around the year (Ramachandra e Aithal, 2019). Bangalore is also the third most populous city with a population of more than 8.5 million and a metropolitan population of 11 million as of the 2011 Census (Avinash et al., 2018).

The topography of the city is located over a natural ridge delineating four major watersheds, viz. Hebbal, Koramangala, Challaghatta and Vrishabhavathi valley pass from the citys ridge in the north to an enclosed lake system at the perimeter of Bangalore. Waterbodies are part of these four major waterways valley systems, which drain the majority of the citys stormwater to large tanks or lakes, which were traditionally used for recreation and water supply for irrigation.

These waterways with interconnected lakes in addition to their primary function as flood carriers, have provided the city with reasonable ecological and recreational values. The urban growth in recent times, not guided by strong strategic planning or development control measures to minimise the impacts on existing infrastructure, on the surrounding environment, and in particular on the stormwater system, had severe impacts on waterways. This has led to the depletion of waterways in addition to pollution and wastewater discharge to the stormwater system (Ramachandra e Mujumdar, 2009).

Due to the size of the Bangalore stormwater system, we concentrate our study on the Bellandur Watershed (see Fig. 5.1) which is located in the Koramangala-Challagatta valley (K&C Valley), lies between longitude 77°39′ W - 77°40′ E and latitude 12°60′ N - 12°50′ S (Chandrashekar et al., 2003) with an area of approximately 131 km^2.

We fitted a Sherman-type IDF curve for the catchment using 30 years of daily rainfall records, resulting in $K = 447.01$, $a = 0.19$, $b = 0.03$, and $c = 0.67$ from Eq. (5.5). Detailed methodology and results for the derivation of the parameters are shown in the Supplemental Information (SI) section.

5.2.3.1 DEM and Land Use Land Cover Treatment

The DEM was converted into a digital terrain model (DTM) using the DTM-Filter tool followed by the SAGA close gaps function, (Conrad et al., 2015), such that areas with slope greater than 30% are interpolated, resulting in a smoother DEM. The spatial resolution of the DTM and of the other rasters are 30 m for x and y directions, resulting in 145,556 squared computational cells. In addition, flow paths were smoothed using the constrained regularized smoothing (CRS) (Schwanghart e Scherler, 2014). This algorithm calculates the DEM streams with a user defined flow accumulation threshold (e.g., herein we assume streams start at 0.5 km^2) and smooths paths, reducing DEM noises and enhancing flow continuity. Furthermore, we reduce DEM elevations in streams in terms of the flow accumulation following an exponential relationship between DEM reduction and flow accumulation (De Paiva et al., 2013).

The Land Use and Land Cover (LULC) dataset from Dynamic World(Brown et al., 2022), delineating nine distinct LULC types, was utilized for the temporal range period from January 1, 2021, to January 1, 2022 to generate the LULC for the watershed in this study. The DEM and the LULC maps are shown in Fig. 5.2.

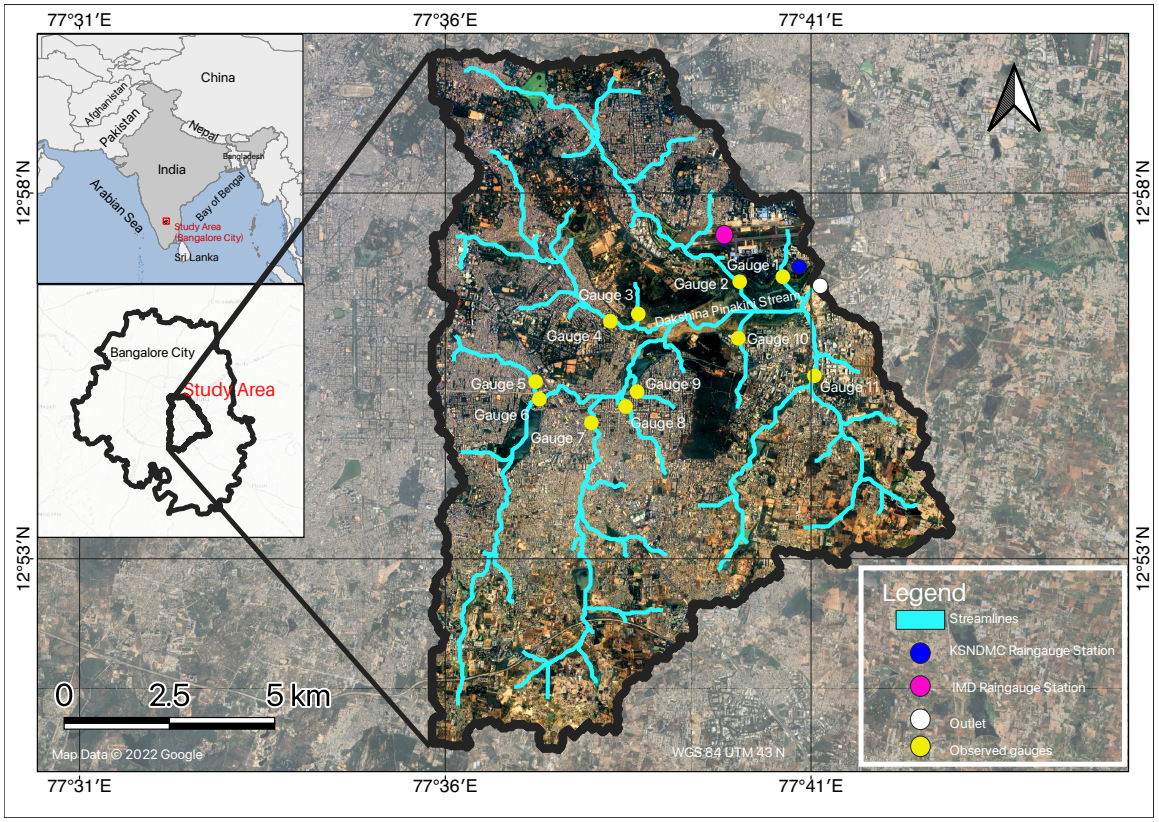

Figure 5.1. Bellandur Watershed study area. The IMD Raingauge Station have daily rainfall recordings and were used to derive the IDF curve whereas the KSNDMC Raingauge stations records 15-min rainfall and was used to derive rainfall distribution patterns in the catchment. The "virtual"(i.e., not real points with observation) gauges are selected to represent the hydrology and hydrodynamics of each subcatchment prior to the effect of the main reservoir.

5.2.3.2 Observed Rainfall Distribution

Using the only available 6 years of 15-min resolution rainfall data retrieved from India Meteorological Department(IMD) and Karnataka State Natural Disaster Monitoring Centre (KSNDMC), we develop a statistical analysis to determine the rainfall distribution in the watershed by calculating the percentiles associated with each bin of time. The algorithm developed moves in finite durations up to the end of simulation.

In brief, the algorithm considers each rainfall duration of interest, denoted as t_d^i. For every t_d^i, the algorithm defines n^i possible rainfalls by shifting in time by Δt (i.e., the time resolution of rainfall), where Δt is set to 15 minutes since the rainfall records are in this interval. Subsequently, the algorithm identifies potential rainfall events with a duration of t_d^i by moving a time window through the whole observed rainfall data time series. Rainfall volume computation follows, with only events exceeding a threshold ($\tau = 2$ mm) considered in the analysis. Collecting these events with duration t_d^i for all durations of the analysis that have volume larger than τ allows the creation of normalized rainfall distribution charts, similar to those introduced by Huff (Huff, 1967). These normalized charts express values relative to the rainfall duration t_d^i and precipitated volume P_t^i, utilizing normalized duration t/t_d^i and normalized rainfall volume P/P_t^i for each rainfall event.

5.2.3.3 Model Parameters and Initial Inputs

HydroPol2D assigns hydrodynamic, hydrologic, and water quality parameters to all cells of the domain according to LULC and SOIL maps. The parameters used in the model are shown in

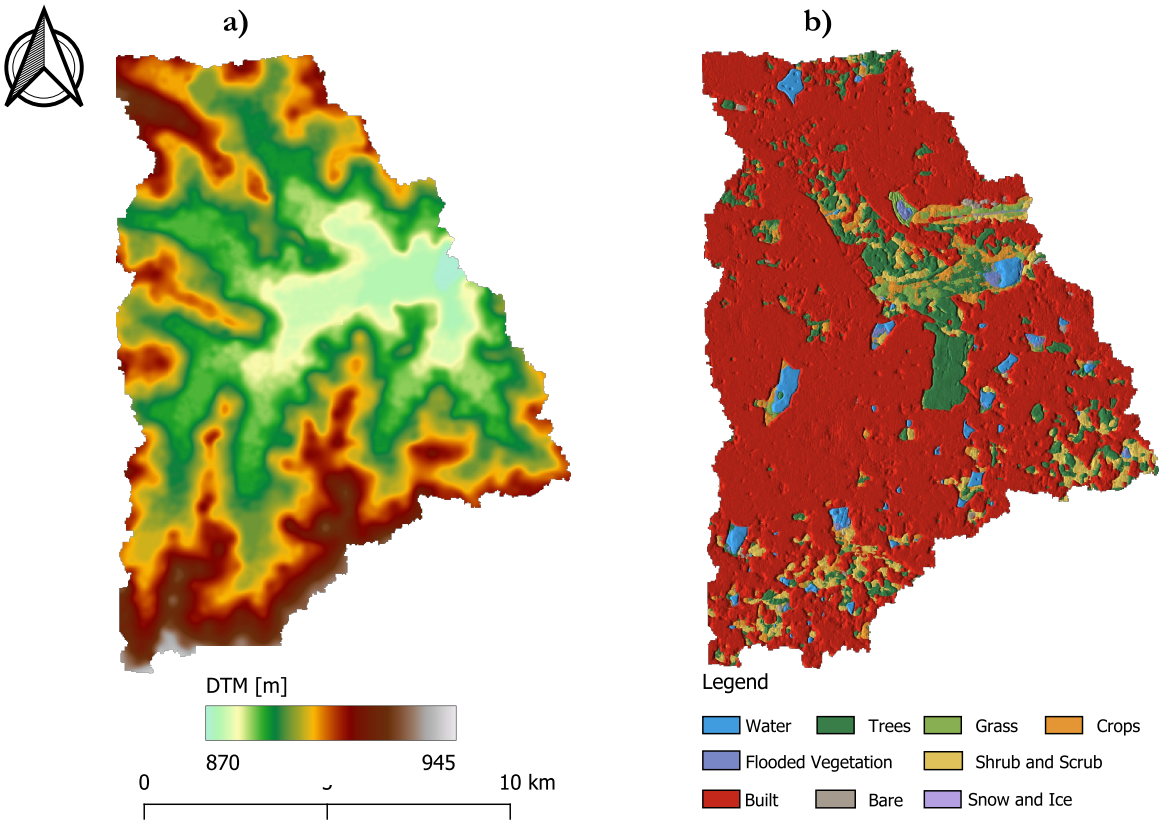

Figure 5.2. (a) Digital Terrain Model (DTM) and (b) Land Use and Land Cover classification from the Dynamic World (Brown et al., 2022) (LULC).

LULC Classification	Index	n [$s \cdot m^{-1/3}$]	h_0 [mm]
Water	0	0.025	0
Trees	1	0.035	8
Grass	2	0.03	2
Flooded Vegetation	3	0.04	4
Crops	4	0.035	5
Shrub and Scrub	5	0.045	5
Built Areas	6	0.025	0
Bare Ground	7	0.028	0.5

Table 5.1. LULC-Based parameters, where n is the Manning's roughness coefficient and h_0 is the initial abstraction or depression storage.

Tab. 5.1 and were estimated based on data from the literature (Te Chow, 1959; Rossman, 2010). There is only one soil type in the catchment and the Green-ampt parameters of saturated hydraulic conductivity ($k_{sat} = 5$ mm $\cdot$ h^{-1}), moisture deficit ($\Delta\theta = 0.427$), and suction head ($\psi = 40$ mm) (Brunner, 2016a). Another degree of freedom in the analysis could be explored by the initial soil moisture content; however, the influence of this watershed condition is out of the scope of the paper. The initial soil moisture condition represented by the initial soil moisture depth was assumed as 10 mm for all pervious cells.

To evaluate the possible uncertainties in the parameter estimations, we perform a one-at-the-time sensitivity analysis in the hydrologic and hydrodynamic parameters of the model to identify the potential variations in flooded areas and areas with human instability hazard.

Rainfall Duration [h]	i_{max}^{ABM} [mm · h^{-1}]	i_{max}^{H} [mm · h^{-1}]	i_{max}^{OBS} [mm · h^{-1}]	Rainfall Volume [mm]
2	174	130	131	87
6	174	42	92	125
12	174	26	73	157
24	174	16	52	197
48	174	11	15	248

Table 5.2. Summary of events tested with maximum intensities given in 15-min intervals, where subscripts ABM, H, and OBS represent the rainfall distributions of ABM, Huff, and Observed.

5.2.3.4 Design Flood Mapping under Uncertainty

The lack of proper spatio-temporal rainfall data is a challenge for urban planning and definition of critical areas prone to floods. To this end, in this paper we develop a flood mapping analysis considering design storms with different durations and temporal distributions. We select the ABM and the Huff as the design storms tested for flood mapping assessment. In addition, we use the median observed hyetograph derived from the 15-min high resolution rainfall data to compare with these synthetic design storms. The HydroPol2D model is then run with rainfall of 2, 6, 12, 24, and 48 hours distributed with ABM, Huff, and with the median observed hyetograph.

5.3 Results and Discussion

Rainfall maximum intensities and volumes are discretized for each distribution and duration, detailed in Table 5.2. The larger 15-minute intensities are sourced from the ABM. Noticeably, it is observed that the maximum rainfall intensities are consistently smaller for the Huff hyetographs compared to both Observed and ABM, despite having the same rainfall volume. Fig. 5.3 presents the cumulative observed normalized rainfall for various durations, and Fig. 5.4 illustrates all 12-hour rainfall events within the total sample. Using the median of the distribution, Fig. 5.5 displays a normalized rainfall distribution hyetograph, revealing distinct characteristics. Shorter rainfall durations exhibit peaks near half of the duration, while longer events show peaks at the 3rd quartile (i.e., 24 hours) or an unclear peak, resulting in a dispersed pattern (i.e., 48 hours).

Median storms, representing a probability of 50%, predominantly occur within 10% to 80% of the rainfall duration. With the exception of the 2-hour rainfall, all other events exhibit a two-peak hyetograph. These meteorological characteristics can be easily derived using high-resolution rainfall data and effectively encapsulate the median temporal distribution behavior of the catchment.

The comprehensive results, outlining instability risk areas, flooded areas, areas with velocities larger than 3 m · s^{-1} and areas with infiltration larger than 100 mm in the Bellandur catchment for different rainfall distributions and durations are presented in Fig. 5.6. The critical combination of rainfall distribution and duration, across all methods of rainfall temporal distribution, was identified as the 12-hour rainfall duration using the observed rainfall distribution, resulting in a human instability hazard area of 6.17 km^2, as shown in Fig. 5.6a). In particular, the duration of the critical rainfall duration was 24 hours for the ABM method (6.10 km^2) and 6 hours for the Huff rainfall distribution (4.01 km^2). These results reveal discrepancies between the critical rainfall duration due to several non-linear factors such as the infiltration modeling. The figure also highlights that, except for the 2-hour rainfall duration, the Huff hyetograph is less critical compared to both ABM and Observed hyetographs, in line with findings from other studies (Balbastre-Soldevila et al., 2019; Pan et al., 2017; Na e Yoo, 2018). For relatively longer durations (>12 hours), the ABM proves to be more critical.

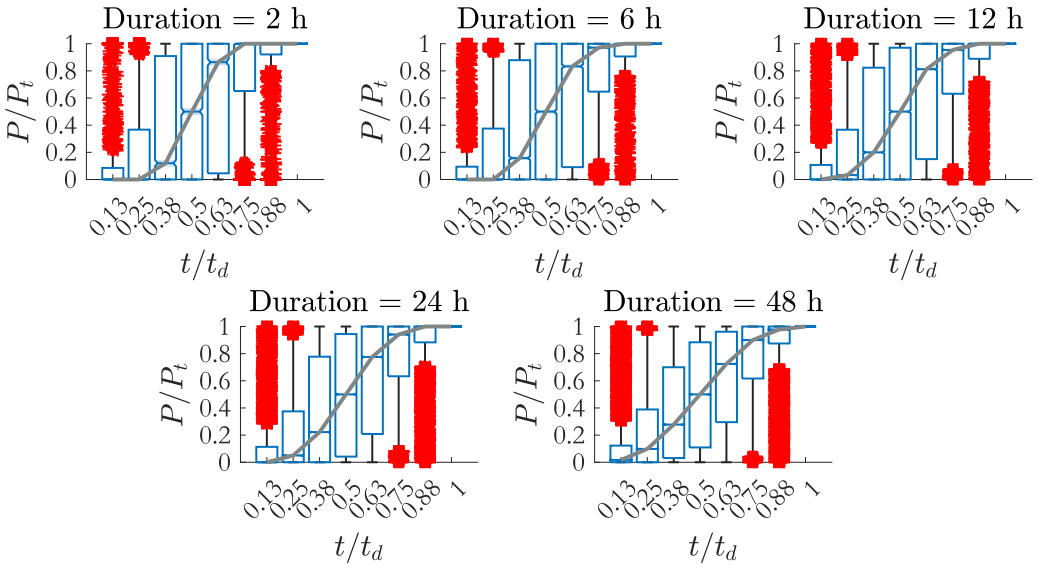

Figure 5.3. Cumulative normalized observed rainfall distribution for different rainfall durations. The gray line connects all median (i.e., 50%) values for each normalized duration. The data is shown discretizing the time into 8 equal intervals for the sake of parsimony, although it could be discretized in 15-min time-steps. All possible rainfalls of t_d duration with volume larger than 2 mm are recorded, normalized and box-plotted in this figure.

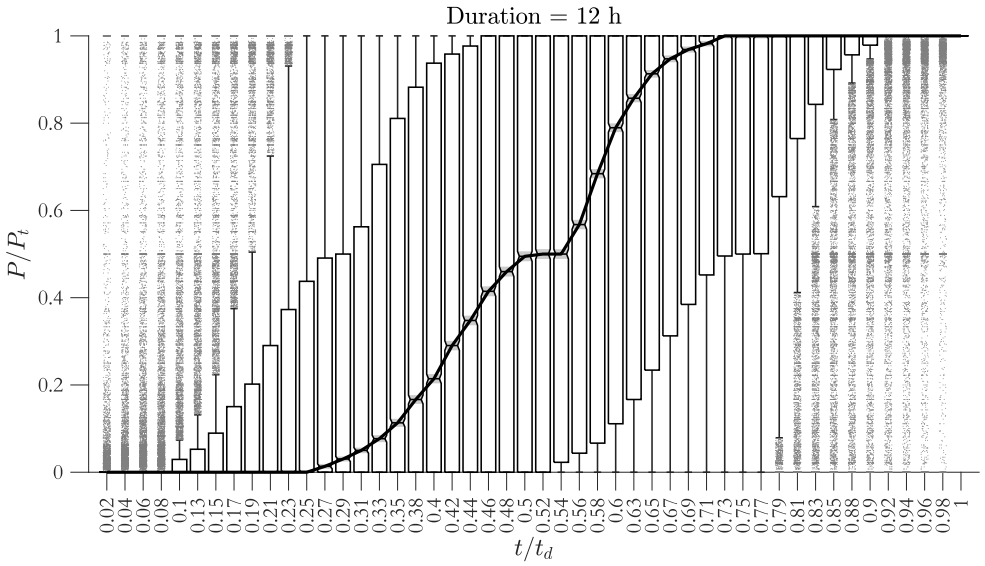

Figure 5.4. Rainfall temporal distribution of all 210,432 possible events of 12 hour duration derived from the observed high resolution data. Results are discretized into 15-min time-steps. The black line represents the median distribution. The normalized median rainfall distribution is used throughout the further analyses

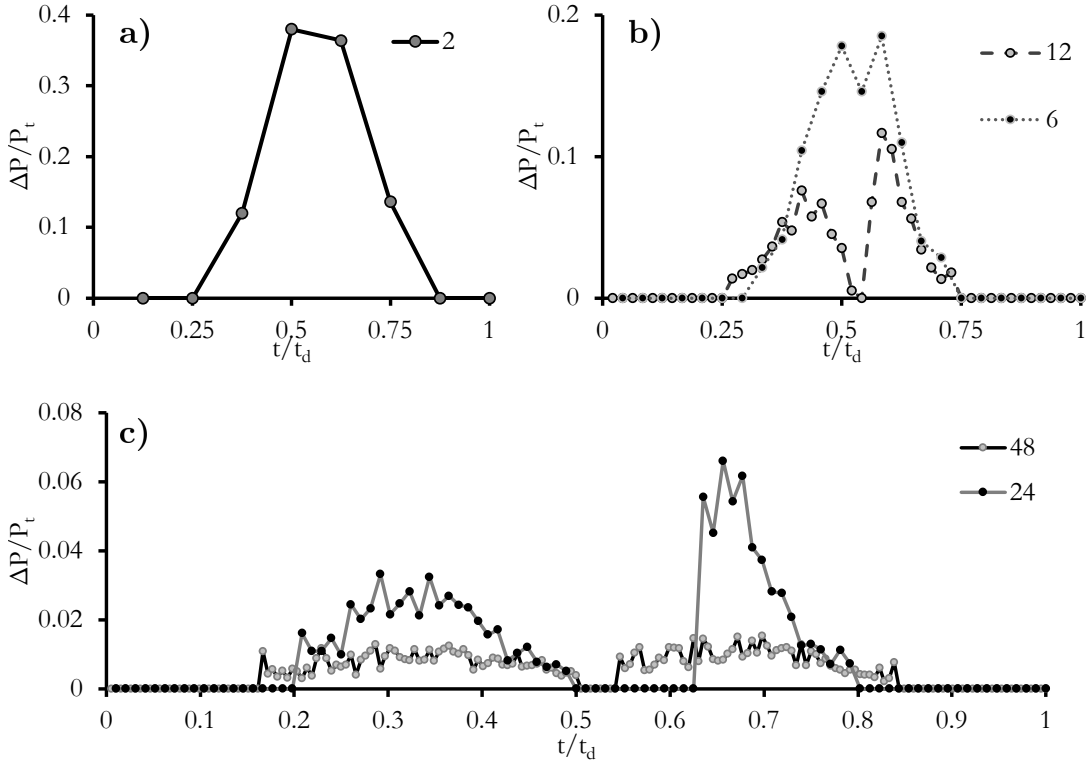

Figure 5.5. Median rainfall distribution for 2, 6, 12, 24, and 48 hours. All charts are designed with 15-min rainfall resolution and normalized by the rainfall duration t_d. The total precipitation P_t is calculated from the IDF curve, RP, and t_d. Part a) shows the normalized hyetograph for 2-hours, b) shows for 12-h and 6-h, and c) shows for 24-h and 48-h.

Importantly, rainfall durations that exceed the time of concentration do not necessarily increase flood areas.

However, the analysis does not account for flood exposure in human risk instability. Human risk instability areas were calculated based on the maximum drag forces surpassing available friction, without considering the duration where this exposure is effective. While exposure duration impacts human flood resistance, an alternative approachcalculating instability risk multiplied by the duration of occurrencefalls beyond the scope of this article but could offer insights into areas with varying levels of hazard exposure.

The analysis of maximum velocities in Fig. 5.6b) indicates consistently lower values for Huff across all tested durations. The 12-hour observed median rainfall distribution remains critical for this hazard. As expected, a strong correlation between human instability areas and maximum velocities is observed.

The critical duration and temporal distribution for flooded areas with depths larger than 0.5 m is, as opposed to the aforementioned hazard metrics, the ABM with 12-h of rainfall duration, as observed in Fig. 5.6c), however with a difference of only 5% from the observed rainfall distribution. The ABM appears to be overall more critical, except for the 2-h and for the 12-h rainfall that have the observed distribution as the critical, as shown in Fig. 5.6c). This result indicates that having larger flood extents does not necessarily mean larger areas with human instability risk or relatively high flood velocities. This may be due to the generation of overland flow due to the excess of infiltration caused by the relatively high rainfall intensities derived from the ABM rainfall distribution, increasing flooded areas. It is noted that the flooded areas are 2-4 times larger than the areas of instability risk, by comparing Fig. 5.6a) with Fig. 5.6c). This is due to the fact that some areas are natural reservoirs and floodplains with high resistance, which ultimately leads to relatively low flow velocities and hence

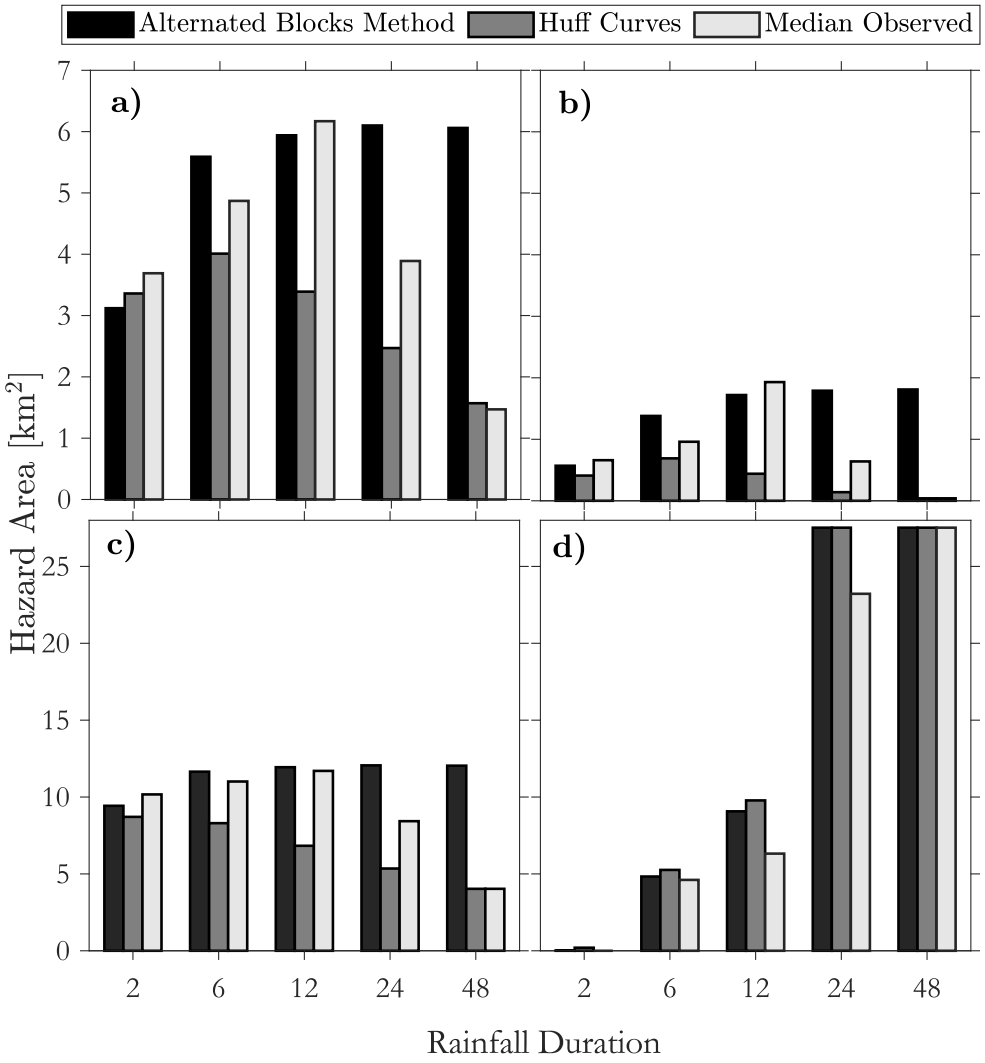

Figure 5.6. Hazard Areas in terms of human instability, maximum flow velocity, water surface depths, and infiltrated depths. Part (a) illustrates the overall areas prone to human instability, calculated by accounting for flood hydrodynamics and ground friction. Part (b) represents areas exceeding flow velocities greater than 3 m $\cdot$ s^{-1}. Cumulative areas surpassing flood depths of 0.5 m are shown in Part (c), while Part (d) displays total areas exceeding 100 mm of soil infiltration.

smaller drag forces, while still getting flooded. Similarly to flood area analysis.

Regarding areas with infiltrated depths exceeding 100 mm (commonly found in regions with high flow accumulation and pervious areas), the Huff rainfall distribution outperformed the other two methods in generating more infiltration, as evidenced in Fig. 5.6d). While these infiltration depths can be viewed as a positive metric for aquifer recharge, they also pose a flood hazard by potentially reducing the infiltration capacity for incoming storms.

In summary, adhering to local regulatory constraints in flood modeling, assuming a requirement for a 100-year return period analysis, and utilizing the Huff hyetograph for a 12-hour rainfall duration (identified as the critical duration in this analysis) would result in significantly smaller risk areas with human instability. Specifically, these areas would be 45% smaller compared to the Observed Distribution and 42% smaller compared to the ABM. This holds notable implications, as insurance plans and the definition of risk areas for urban zoning often rely on the delineation of flood hazard areas. Opting for a noncritical rainfall distribution could potentially indicate nearly 50% fewer areas at risk of flooding.

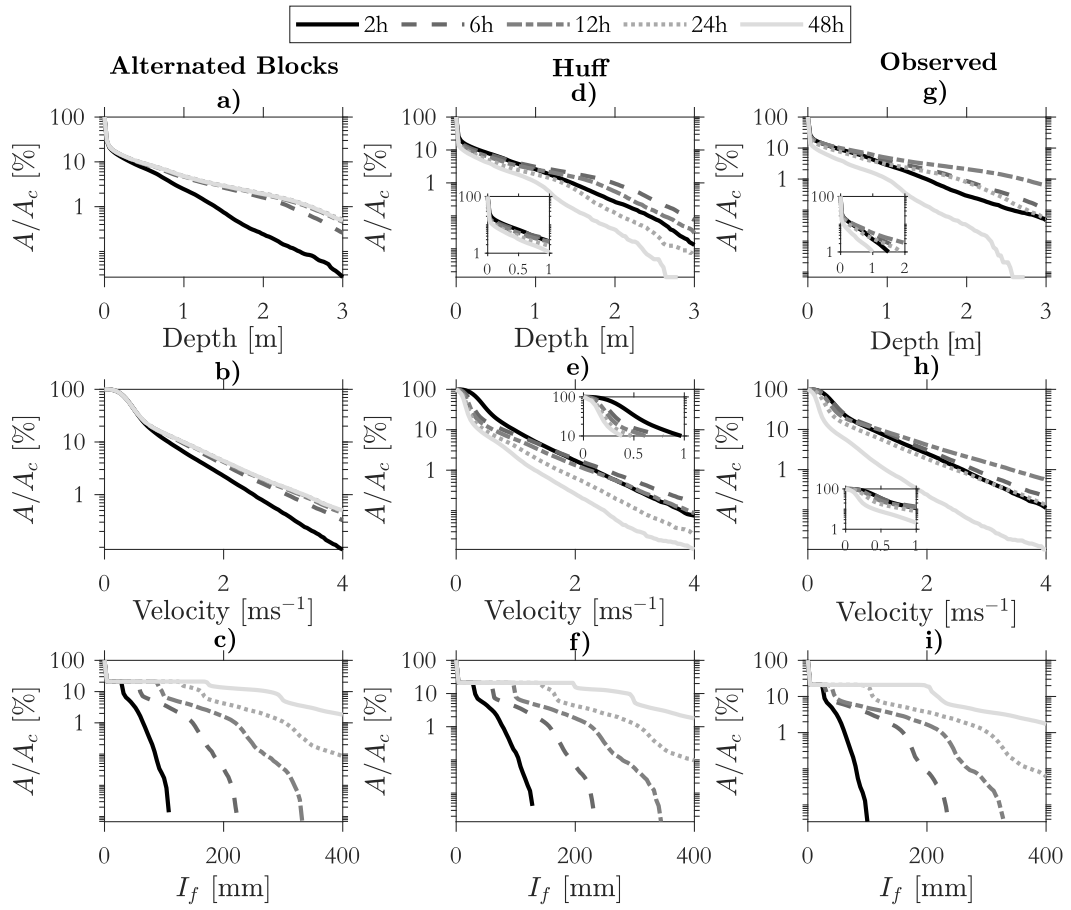

Figure 5.7. Normalized spatial analysis of flood depths, velocity, and infiltrated depth, where (a)-(c) are results for the ABM, (d)-(f) are for the Huff rainfall distributions, and (g)-(i) are median observed distribution. The x values of all plots are defined as $x \leq x_m$, with x being the independent (e.g., Depth) variable and x_m a reference value (e.g., 2 ms^{-1}). Results are plotted for each rainfall duration tested. Areas are normalized by the catchment area $A_c = 131.37$ km^2.

The results of the previous analysis are limited by the definition of the thresholds for water depth, velocity, and infiltration. To this end, we assess the sensitivity of the extent areas where a threshold is surpassed in terms of depths, velocities, and infiltration depths. Results of Fig. 5.7 show hypsometric analysis of these variables for each rainfall duration and distribution. While the 48-hour duration is the one that produce that larger extent areas for the ABM in terms of depths and velocities (see Fig. 5.7a)-b)), it is the least critical for the Observed and Huff distributions (see Fig. 5.7d)-e) and g)-h)). This result shows the effect of rainfall temporal distribution variability in terms of flood characteristics.

For deep water surface depths (i.e., $>$ 1 m), the durations of 6-12 hours are more critical for the Huff and Observed hyetograph, in terms of velocities and depths, while 48-hours is the critical for ABM. Therefore, if one has to choose a critical rainfall duration and a critical rainfall distribution in terms of maximizing flood areas, it could be 12 hours distributed with the median observed rainfall pattern (Gomes Jr et al., 2023a).

In terms of infiltrated depths, figures (c), (f), and (i) of Fig. 5.7 show similar patterns, indicating that infiltration is not intensively governed by rainfall distribution in this catchment; however, in catchments with more pervious areas, this would not be the case.

Assuming a 12-hour duration as the critical rainfall duration, Fig. 5.8 illustrates the sensitivity of the threshold τ for water surface depth, flow velocity, and infiltrated depth. The results of this analysis can be used to establish varying levels of protection for flood insurance plans, among

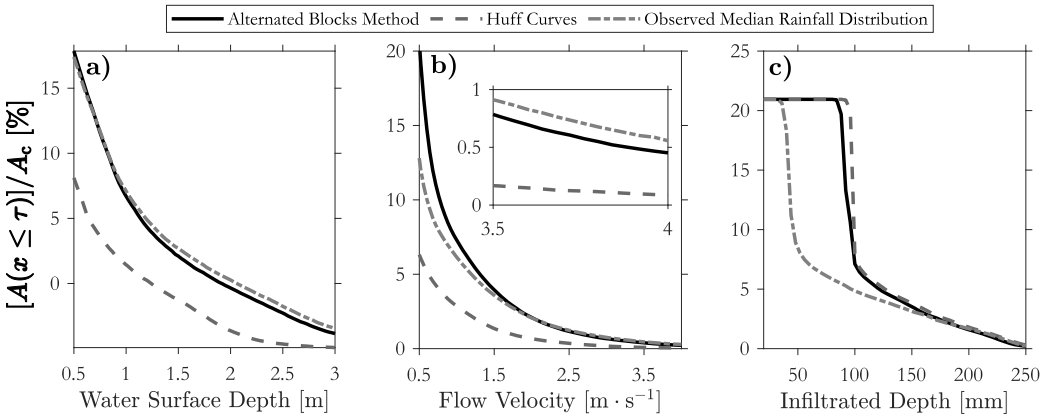

Figure 5.8. Effect of the threshold τ in the definition of the flood hazards related to the water surface depth (a), maximum flow velocity (b), and infiltrated depth into the permeable areas (c) for the critical duration of 12-h.

other applications. It should be noted that, consistently, the Huff method produced nearly 50% fewer flooded areas for all thresholds of water depth ranging from 0.5 to 3 m, whereas the observed and ABM methods yielded very similar results, with the observed rainfall distribution slightly higher (see Fig. 5.8a). In part (b) of Fig. 5.8, it is evident that for relatively high velocities, the hazard areas are 5-6 times larger for the observed distribution and ABM compared to the Huff distribution. In part (c) of Fig. 5.8, a distinctive scenario emerges in which a rapid decline is evident in areas with substantial infiltration, particularly in the observed rainfall distribution. While both Huff and ABM maintain sizable areas with high infiltration, the observed rainfall distribution, notably influenced by the two-peak pattern (refer to Fig. 5.5b)), promotes overland flow generation during the second peak due to an excess of infiltration resulting from the infiltrated depth during the first peak.

To illustrate the effects of not choosing a critical rainfall distribution method, we compare the results for a 12-h duration of the observed rainfall and Huff curves, as presented in Fig. 5.9. The results presented in Fig. 5.8 can be seem spatially from the maps presented in Fig. 5.9. In particular, larger flooded areas and areas with human instability are expected for the median observed rainfall distribution; consequently, larger infiltration is observed for the Huff distribution when comparing both methods.

The results presented in Fig. 5.7 and 5.8 can be influenced by the choice of the model parameters presented in Tab. 5.1, since no observed discharges were available to perform a proper model calibration. Therefore, a sensitivity analysis would allow one to assess the associated uncertainty effects in the calculations, as well as to quantify the impacts of retrofitting the catchment with LIDs or by increasing urbanized areas. The one-at-the-time sensitivity analysis of the hydrodynamic parameters and soil parameters is presented in Fig. 5.10 and Fig. 5.11, respectively.

As anticipated, the Built Areas and Water land use/land cover (LULC) classifications exhibit the highest sensitivity, given the significant urbanized areas and water bodies within the catchment. The surface roughness coefficient demonstrates more pronounced elasticity to parameter reduction than to an increase. Even with a 20% uncertainty range in roughness coefficients, errors in flood areas and human instability areas remain below 5%, indicating a relatively low level of uncertainty associated with the parameters and, consequently, with the previously provided estimations of flood hazard.

Nevertheless, for variations exceeding 20% in the parameter estimation, the sensitivity of human instability areas becomes more pronounced. Notably, an intriguing observation is that elevating the Manning's roughness coefficient (n) results in an increase in flooded areas but induces a more substantial reduction in human instability areas, as depicted in Fig. 5.10a)-b). Consequently, retrofitting urban areas with green infrastructure may expand flood-prone regions, yet it concurrently diminishes

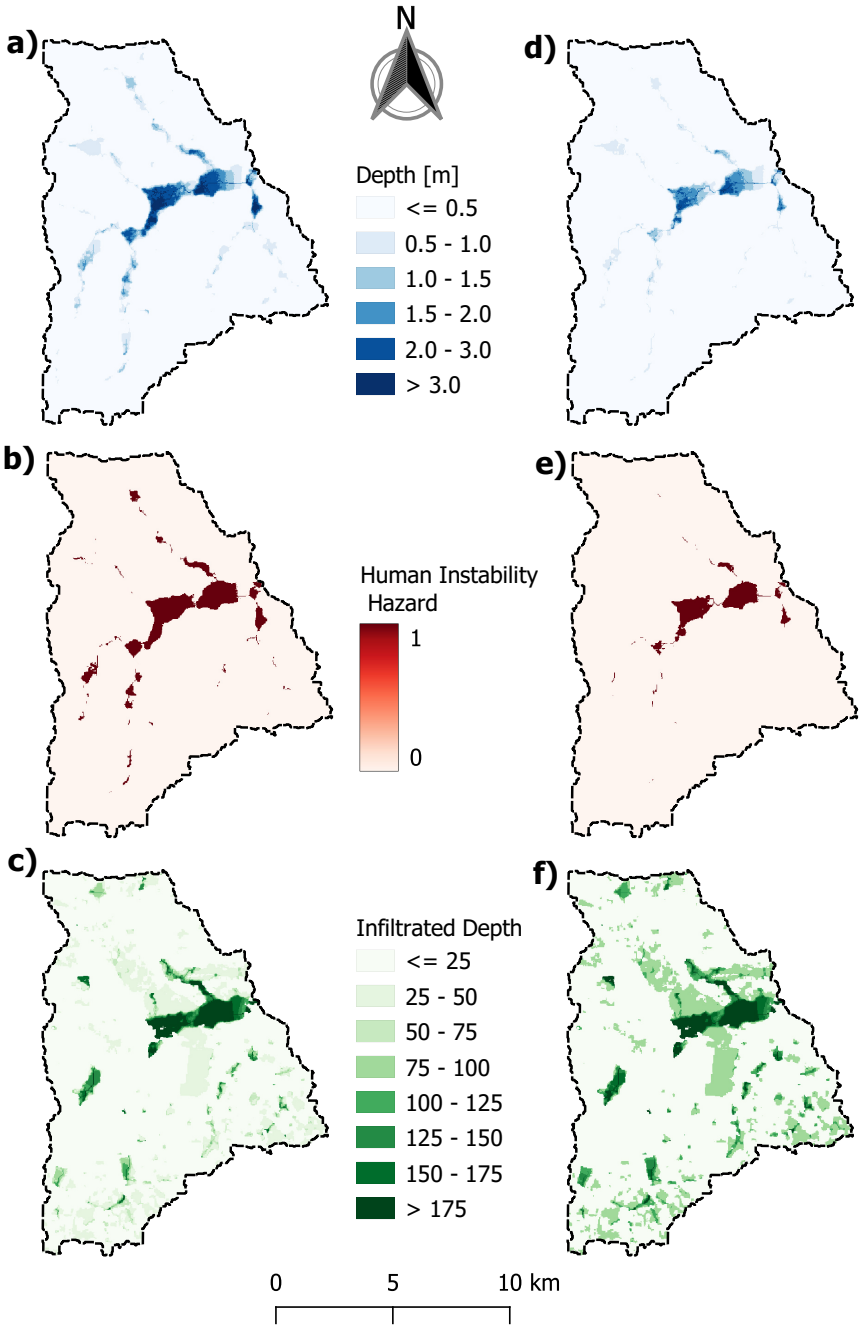

Figure 5.9. Comparison between Observed Rainfall Distribution (left) with Huff Distribution (right), where (a)-(c) show water surface depths, f_r [Eq. (5.4)] values such that dark red areas have human instability hazard, and infiltrated depths, respectively. Similarly, (d) to (f) show the same results but for the Huff rainfall distribution. All results are shown assuming a critical rainfall duration of 12-h.

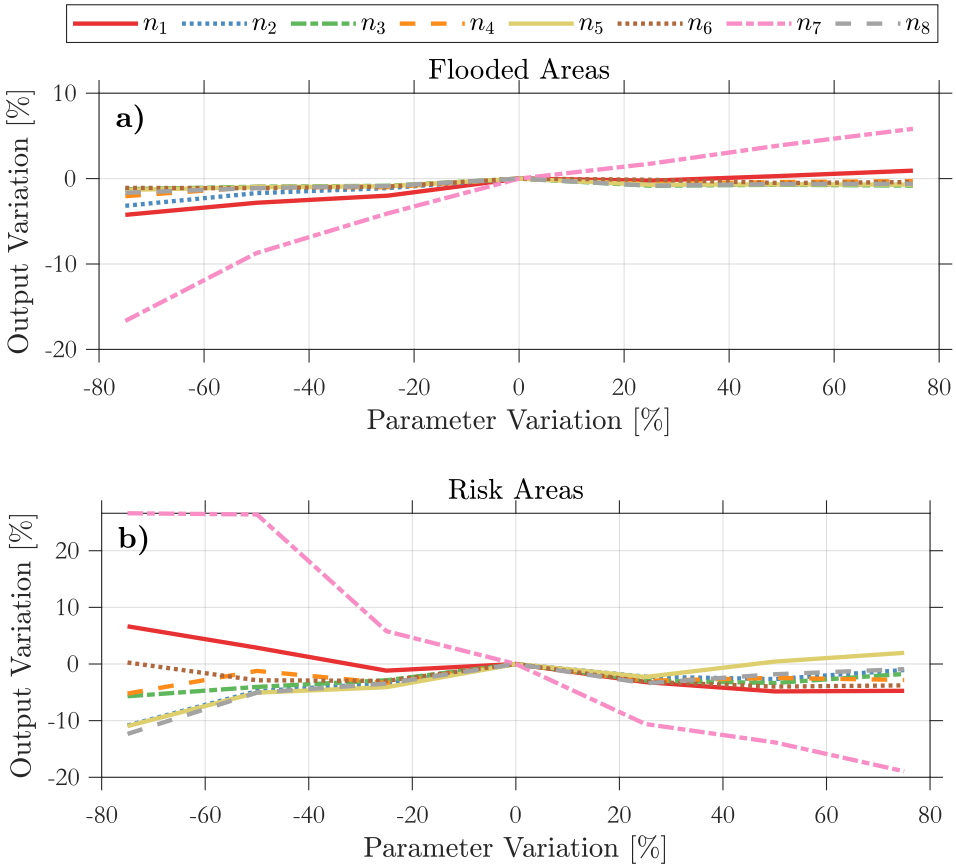

Figure 5.10. One-at-the-time sensitivity analysis on Manning's roughness coefficient for the 12-h observed hyetograph with a 100-yr return period, where 1 = water, 2 = Trees, 3 = Flooded Vegetation, 4 = Crops, 5 = Shrub/Scrub, 7 = Built Areas, and 8 = Bare Ground.

risks of human instability to a greater extent. This suggests that green infrastructure could serve as an effective strategy for mitigating human instability areas and that only flooded areas might be an incomplete metric to assess flood hazard.

This finding holds significance for flood insurance programs exclusively reliant on flooded areas, as an increase in flooded areas does not necessarily correlate with a reduction in human instability areas. Integrating human instability maps into the formulation of flood insurance policies could offer a more comprehensive perspective, providing a more accurate estimation of the real impacts of floods.

The flooded area extents, as indicated in Fig. 5.11, exhibited relatively low sensitivity to Green-Ampt soil properties. Conversely, soil parameters play a more crucial role in influencing variations in areas with human instability risks. Increasing the saturated hydraulic conductivity (k_{sat}) by 80%, from 5 to 9 mm $\cdot$ h^{-1} in pervious areas, has the potential to reduce areas of human instability by 10%. Implementing engineering strategies such as building infiltration techniques or enhancing macropores could achieve this reduction. While altering saturated hydraulic conductivity might pose challenges, it serves as a straightforward proxy for assessing the impacts of increased infiltration in the catchment. This result, coupled with an increase in Manning's roughness coefficient (n), underscores the advantages of implementing green infrastructure retrofits in the catchment, leading to a reduction in areas with flood hazards (McClymont et al., 2020; Borah et al., 2023).

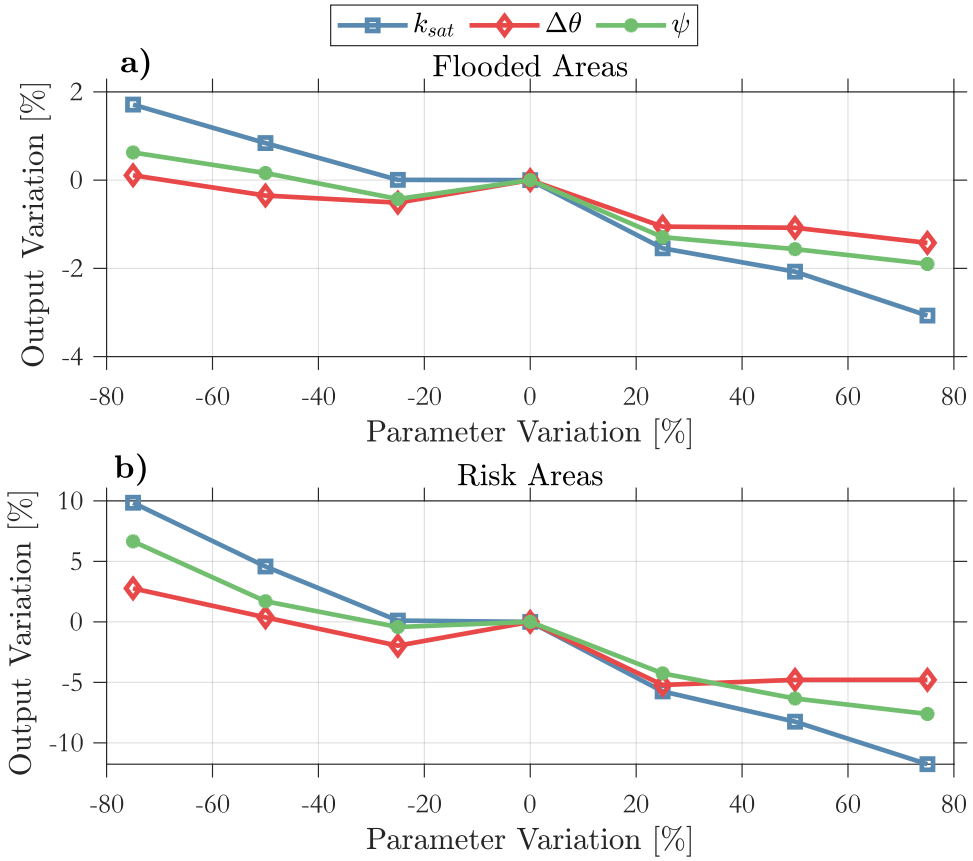

Figure 5.11. One-at-the-time sensitivity analysis on Green-Ampt parameters for the infiltration model for the 12-h observed hyetograph with a 100-yr return period, where a) are the sensitivity in Flood Areas and b) in human instability areas.

5.4 Conclusions

A flood inundation model, incorporating a human instability module and employing both synthetic and observed rainfall distribution methods, was developed and implemented in the Bellandur catchment in Bangalore, India. The study investigated the impact of various rainfall distributions on flood characteristics, including inundation extents, depths, velocities, and soil infiltration. This analysis aimed to assess the uncertainty associated with assuming an a priori synthetic rainfall distribution for flood inundation mapping and modeling and the potential impacts in flood hazard assessment. The discrepancies can be even larger if not only the rainfall distribution is not critical, but also the rainfall duration.

The preselection of a synthetic rainfall distribution for flood mapping and modeling, without evaluating the sensitivity of various synthetic rainfall distribution methods or incorporating observed fitted rainfall distributions, may result in a considerable uncertainty, potentially leading to a misrepresentation of up to 45% smaller areas with flood hazards related to human instability for a 100-year flood event.

The sensitivity analysis of the hydrodynamic and hydrologic parameters of the catchment indicates a relatively lower degree of sensitivity in flood areas and human instability areas (i.e., smaller than 20% for a variation of 80% in all parameters), allowing a relatively safe use of the model without formal calibration that would require inaccessible stream flow and spatially distributed rainfall. This indicates a scenario where the application of 2D hydrologic-hydrodynamic modeling can generate useful information for catchments with lack of observed hydrological data but prone to floods.

The automatic one-at-a-time sensitivity algorithms, developed and implemented in the HydroPol2D model in this study, serve as a valuable tool for comprehending the consequences of retrofitting the catchment with various low-impact development scenarios. Additionally, HydroPol2D allows for straightforward sensitivity analysis of different rainfall distributions, durations, and return periods. Replicating the methods established in this paper to other ungauged or poorly-gauged catchments provides an alternative for furnishing valuable information in areas lacking data but facing potential unprecedented floods in the future due to urbanization and climate change. The application of this strategy to other highly urbanized and flood-prone catchments is justified.

Future studies can incorporate the spatial behavior of rainfall and its impacts on human instability metrics, especially because the center of the rainfall can influence the total potential energy that ultimately would convert to larger flood velocities downstream the catchment.

Acknowledgments

The authors appreciate the support of the City of San Antonio, by the San Antonio River Authority, CAPES Ph.D Scholarship, and the PPGSHS PROEX Graduate Program.

5.5 Supplemental Information

The supplemental information illustrates the HydroPol2D model setup to run all simulations and results of testing the model for a critical rainfall event that occured in 28th November of 2012, the Hurrican Nilam. In addition, the SI contains tables with the numeric values of Fig. 5.6.

References

Akan, A. O. e Iyer, S. S. (2021). *Open channel hydraulics*. Butterworth-Heinemann.

Avinash, S., Prasad, K. L., Reddy, G., e Mukund, D. (2018). Urban flood forecast system-a case study of bangalore, india. *Univ Rev*.

Balbastre-Soldevila, R., García-Bartual, R., e Andrés-Doménech, I. (2019). A comparison of design storms for urban drainage system applications. *Water*, 11(4):757.

Batalini de Macedo, M., Gomes Júnior, M. N., Jochelavicius, V., de Oliveira, T. R. P., e Mendiondo, E. M. (2022a). Modular design of bioretention systems for sustainable stormwater management under drivers of urbanization and climate change. *Sustainability*, 14(11):6799.

Bezak, N., Šraj, M., Rusjan, S., e Mikoš, M. (2018). Impact of the rainfall duration and temporal rainfall distribution defined using the huff curves on the hydraulic flood modelling results. *Geosciences*, 8(2):69.

Bhagat, R. B. (2011). Emerging pattern of urbanisation in india. *Economic and political weekly*, pages 10–12.

Borah, A., Bardhan, R., e Bhatia, U. (2023). Protecting heritage: Insights into effective flood management using green infrastructure in a highly urbanized environment. *International Journal of Disaster Risk Reduction*, 98:104075.

Breinl, K., Lun, D., Müller-Thomy, H., e Blöschl, G. (2021). Understanding the relationship between rainfall and flood probabilities through combined intensity-duration-frequency analysis. *Journal of Hydrology*, 602:126759.

Brown, C. F., Brumby, S. P., Guzder-Williams, B., Birch, T., Hyde, S. B., Mazzariello, J., Czerwinski, W., Pasquarella, V. J., Haertel, R., Ilyushchenko, S., et al. (2022). Dynamic world, near real-time global 10 m land use land cover mapping. *Scientific Data*, 9(1):251.

Brunner, G. W. (2016a). Hec-ras river analysis system: Hydraulic reference manual, version 5.0. *US Army Corps of Engineers–Hydrologic Engineering Center*, 547.

Chandrashekar, J., Babu, L., e Somashekar, R. (2003). Impact of urbanization on bellandur lake, bangalore- a case study. *Journal of Environmental Biology*, 24(3):223–227.

Chen, G., Hou, J., Hu, Y., Wang, T., Yang, S., e Gao, X. (2023). Simulated investigation on the impact of spatial–temporal variability of rainstorms on flash flood discharge process in small watershed. *Water Resources Management*, 37(3):995–1011.

Cheng, T., Xu, Z., Yang, H., Hong, S., e Leitao, J. P. (2020). Analysis of effect of rainfall patterns on urban flood process by coupled hydrological and hydrodynamic modeling. *Journal of Hydrologic Engineering*, 25(1):04019061.

Conrad, O., Bechtel, B., Bock, M., Dietrich, H., Fischer, E., Gerlitz, L., Wehberg, J., Wichmann, V., e Böhner, J. (2015). System for automated geoscientific analyses (saga) v. 2.1. 4. *Geoscientific Model Development*, 8(7):1991–2007.

Cristiano, E., ten Veldhuis, M.-c., e Van De Giesen, N. (2017). Spatial and temporal variability of rainfall and their effects on hydrological response in urban areas–a review. *Hydrology and Earth System Sciences*, 21(7):3859–3878.

De, U., Singh, G., e Rase, D. (2013). Urban flooding in recent decades in four mega cities of india. *J. Ind. Geophys. Union*, 17(2):153–165.

De Paiva, R. C. D., Buarque, D. C., Collischonn, W., Bonnet, M.-P., Frappart, F., Calmant, S., e Bulhões Mendes, C. A. (2013). Large-scale hydrologic and hydrodynamic modeling of the amazon river basin. *Water Resources Research*, 49(3):1226–1243.

do Lago, C. A., Giacomoni, M. H., Bentivoglio, R., Taormina, R., Junior, M. N. G., e Mendiondo, E. M. (2023). Generalizing rapid flood predictions to unseen urban catchments with conditional generative adversarial networks. *Journal of Hydrology*, 618:129276.

Dottori, F., Alfieri, L., Bianchi, A., Skoien, J., e Salamon, P. (2022). A new dataset of river flood hazard maps for europe and the mediterranean basin. *Earth System Science Data*, 14(4):1549–1569.

Gomes, M. N., do Lago, C. A. F., Rápalo, L. M. C., Oliveira, P. T. S., Giacomoni, M. H., e Mendiondo, E. M. (2023). Hydropol2d distributed hydrodynamic and water quality model: Challenges and opportunities in poorly-gauged catchments. *Journal of Hydrology*, 625:129982.

Gomes Jr, M. N., Giacomoni, M. H., de Macedo, M. B., do Lago, C. A. F., Brasil, J. A. T., de Oliveira, T. R. P., e Mendiondo, E. M. (2023a). A modeling framework for bioretention analysis: Assessing the hydrologic performance under system uncertainty. *Journal of Hydrologic Engineering*, 28(9):04023025.

Gomes Jr, M. N., Giacomoni, M. H., Navarro, F. A., e Mendiondo, E. M. (2023b). Global optimization-based calibration algorithm for a 2d distributed hydrologic-hydrodynamic and water quality model. *arXiv preprint arXiv:2308.16864*.

Green, W. H. e Ampt, G. A. (1911). Studies on soil phyics. *The Journal of Agricultural Science*, 4(1):1–24.

Guidolin, M., Chen, A. S., Ghimire, B., Keedwell, E. C., Djordjević, S., e Savić, D. A. (2016). A weighted cellular automata 2d inundation model for rapid flood analysis. *Environmental Modelling & Software*, 84:378–394.

Huang, X. e Wang, C. (2020). Estimates of exposure to the 100-year floods in the conterminous united states using national building footprints. *International Journal of Disaster Risk Reduction*, 50:101731.

Huff, F. A. (1967). Time distribution of rainfall in heavy storms. *Water resources research*, 3(4):1007–1019.

Hunter, N. M., Horritt, M. S., Bates, P. D., Wilson, M. D., e Werner, M. G. (2005). An adaptive time step solution for raster-based storage cell modelling of floodplain inundation. *Advances in water resources*, 28(9):975–991.

Jonkman, S. e Penning-Rowsell, E. (2008). Human instability in flood flows 1. *JAWRA Journal of the American Water Resources Association*, 44(5):1208–1218.

Kang, M., Goo, J., Song, I., Chun, J., Her, Y., Hwang, S., e Park, S. (2013). Estimating design floods based on the critical storm duration for small watersheds. *Journal of Hydro-environment Research*, 7(3):209–218.

Kc, S., Wurzer, M., Speringer, M., e Lutz, W. (2018). Future population and human capital in heterogeneous india. *Proceedings of the National Academy of Sciences*, 115(33):8328–8333.

Krvavica, N. e Rubinić, J. (2020). Evaluation of design storms and critical rainfall durations for flood prediction in partially urbanized catchments. *Water*, 12(7):2044.

Lazzarin, T., Chen, A. S., e Viero, D. P. (2024). Beyond flood hazard. mapping the loss probability of pedestrians to improve risk estimation and communication. *Science of the total environment*, 912:168718.

Mani, P., Chatterjee, C., e Kumar, R. (2014). Flood hazard assessment with multiparameter approach derived from coupled 1d and 2d hydrodynamic flow model. *Natural Hazards*, 70:1553–1574.

McClymont, K., Cunha, D. G. F., Maidment, C., Ashagre, B., Vasconcelos, A. F., de Macedo, M. B., Dos Santos, M. F. N., Júnior, M. N. G., Mendiondo, E. M., Barbassa, A. P., et al. (2020). Towards urban resilience through sustainable drainage systems: A multi-objective optimisation problem. *Journal of Environmental Management*, 275:111173.

Mei, C., Liu, J., Wang, H., Li, Z., Yang, Z., Shao, W., Ding, X., Weng, B., Yu, Y., e Yan, D. (2020). Urban flood inundation and damage assessment based on numerical simulations of design rainstorms with different characteristics. *Science China Technological Sciences*, 63:2292–2304.

Membele, G. M., Naidu, M., e Mutanga, O. (2022). Examining flood vulnerability mapping approaches in developing countries: A scoping review. *International Journal of Disaster Risk Reduction*, 69:102766.

Mosavi, A., Ozturk, P., e Chau, K.-w. (2018). Flood prediction using machine learning models: Literature review. *Water*, 10(11):1536.

Na, W. e Yoo, C. (2018). Evaluation of rainfall temporal distribution models with annual maximum rainfall events in seoul, korea. *Water*, 10(10):1468.

Pan, C., Wang, X., Liu, L., Huang, H., e Wang, D. (2017). Improvement to the huff curve for design storms and urban flooding simulations in guangzhou, china. *Water*, 9(6):411.

Pregnolato, M., West, C., Evans, B., Lam, M.-Y., Chen, A. S., Ahmadian, R., e Djordjević, S. (2024). Using multi-stakeholder causal mapping to explore priorities for infrastructure resilience to flooding. *International Journal of Disaster Risk Reduction*, 101:104189.

Ramachandra, T. e Aithal, B. H. (2019). Bangalore. *The Wiley Blackwell Encyclopedia of Urban and Regional Studies*, pages 1–21.

Ramachandra, T. e Mujumdar, P. P. (2009). Urban floods: Case study of bangalore. *Disaster Dev*, 3(2):1–98.

Roldán-Valcarce, A., Jato-Espino, D., Manchado, C., Bach, P. M., e Kuller, M. (2023). Vulnerability to urban flooding assessed based on spatial demographic, socio-economic and infrastructure inequalities. *International journal of disaster risk reduction*, 95:103894.

Rossman, L. A. (2010). *Storm water management model user's manual, version 5.0*. National Risk Management Research Laboratory, Office of Research andă. . . .

Schwanghart, W. e Scherler, D. (2014). Topotoolbox 2–matlab-based software for topographic analysis and modeling in earth surface sciences. *Earth Surface Dynamics*, 2(1):1–7.

Te Chow, V. (1959). *Open channel hydraulics*.

Teng, J., Jakeman, A. J., Vaze, J., Croke, B. F., Dutta, D., e Kim, S. (2017). Flood inundation modelling: A review of methods, recent advances and uncertainty analysis. *Environmental modelling & software*, 90:201–216.

Westra, S., Fowler, H. J., Evans, J. P., Alexander, L. V., Berg, P., Johnson, F., Kendon, E. J., Lenderink, G., e Roberts, N. (2014). Future changes to the intensity and frequency of short-duration extreme rainfall. *Reviews of Geophysics*, 52(3):522–555.

Yuan, W., Tu, X., Su, C., Liu, M., Yan, D., e Wu, Z. (2021). Research on the critical rainfall of flash floods in small watersheds based on the design of characteristic rainfall patterns. *Water Resources Management*, 35:3297–3319.

Zare, N., Maknoon, R., et al. (2024). Urban flood resilience assessment & stormwater management (case study: District 6 of tehran). *International Journal of Disaster Risk Reduction*, page 104280.

Zhu, Z., Wright, D. B., e Yu, G. (2018). The impact of rainfall space-time structure in flood frequency analysis. *Water Resources Research*, 54(11):8983–8998.

6 MODELING UNSTEADY AND STEADY 1D HYDRODYNAMICS UNDER DIFFERENT HYDRAULIC CONCEPTUALIZATIONS: MODEL/SOFTWARE DEVELOPMENT AND CASE STUDIES

A modified version was published as: Gomes Jr, M.N., Rápalo, L.M., Oliveira, P.T., Giacomoni, M.H., do Lago, C.A. and Mendiondo, E.M., 2023. Modeling unsteady and steady 1D hydrodynamics under different hydraulic conceptualizations: Model/Software development and case studies. *Environmental Modelling & Software*, p.105733.

Graphical Abstract

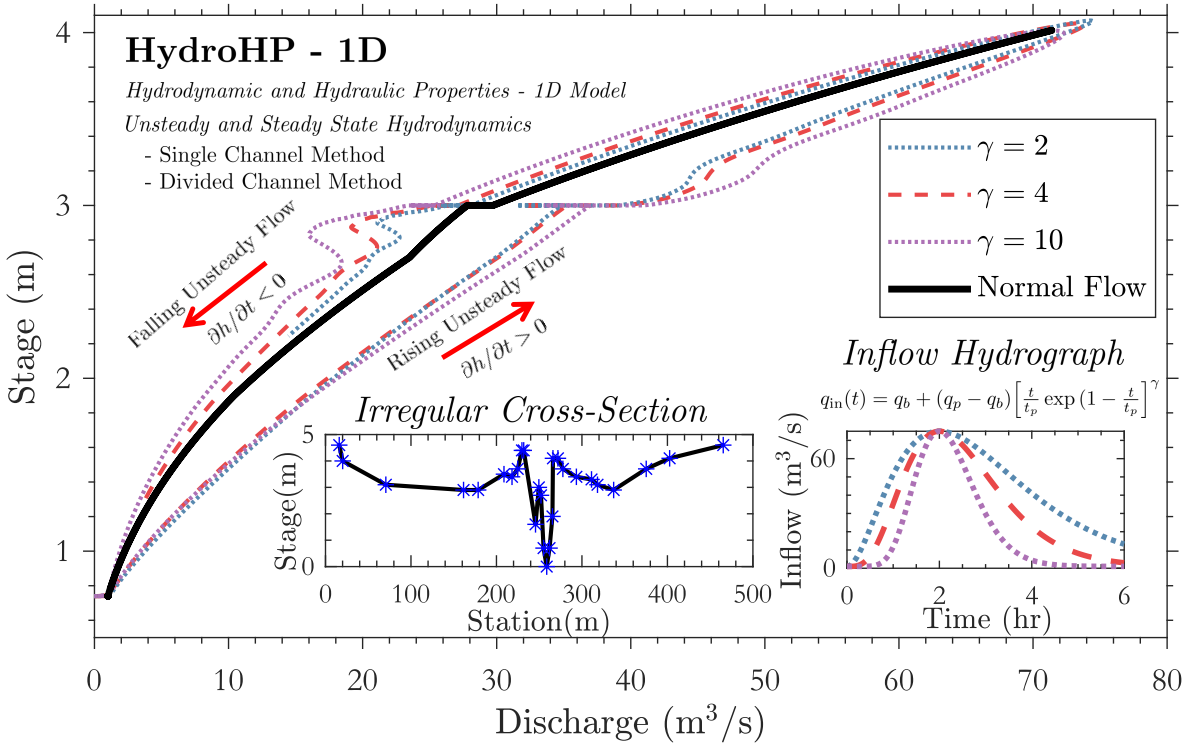

Highlights

- We develop a tool for estimating stage-varying hydraulic properties of open channels.
- HydroHP - 1D allows simulating steady and unsteady dynamics of 1D channels.
- Modeling results of flood routing can be visualized through videos and GIFs.
- The single channel method (SCM) and divided channel method (DCM) are assessed.
- Application in remote areas, like the Upper Negro River (Amazon basin), indicates a good accuracy.

Abstract

The stage-discharge relationship is affected by hysteresis, especially in 1D river cross-sections with very mild slopes, and/or where backwater effects occur. To model these cases, hydraulic property (HP) estimations (e.g., hydraulic radius and conveyance) are usually required as closed-form functions

of stage. However, these are typically unavailable for complex cross-sections with overbanks. For no sediment-laden flows, we created the HydroHP - 1D tool to solve the 1D Saint Venant Equations aided by the cross-section HP stored in tables. It also simulates irregular and composite hydraulic cross-sections, allows hydrodynamic simulation using the single-channel method (SCM), and proposes the divided channel method (DCM) for steady and unsteady flow analysis. A wide range of applications in rivers such as the Little Washita River and the Upper Negro River, and comparisons with NOAA normal depth solver, HEC-RAS, and with an analytical solution shows a promising scenario of applying HydroHP - 1D to estimate 1D steady and unsteady hydrodynamics.
Keywords: Saint-Venant Equations, Unsteady Rating-Curve, Hydrodynamic Modeling, Divided Channel Method, Hysteresis, Channel Routing.

6.1 Introduction

Stage-discharge relationships, also referred to as rating curves are one of the main tools for hydraulic engineering. These tools are dependent on cross-section geometry, longitudinal slope, friction, and shear stress variations. Two forms of rating curve derivation are typically performed: biunivocal steady rating curves and looped unsteady rating curves. The latter is derived from the application of Newton's 2^{nd} laws, where two-dimensional space dimensions are orders of magnitude larger than vertical dimensions. In this case, the Shallow-Water Equations (SWE) are derived from coupling mass balance, friction, and conservation of momentum in a partial differential system of equations usually numerically solved. This type of modeling is also known as dynamic wave and is used in software as the Storm Water Management Model (Rossman et al., 2010). For steady-flow modeling, however, we simplify the shallow-water dynamics by assuming the friction slope as the bottom slope, and we apply a resistance equation such as Manning's or Darcy-Weisbach equations to compute friction losses. In this case, we assume a kinematic wave flood-wave approximation in SWE.

SWE are usually applied to estimate the hydraulic flow behavior on one-dimensional (1D) channels and two-dimensional (2-D) floodplain dynamics. Focusing on the 1D modeling, the Saint-Venant Equations (SVE) are the special case when the flow is assumed to be unidimensional with the same longitudinal velocity throughout the whole cross-section. In other words, vertical acceleration is considered negligible. These equations form a set of hyperbolic partial differential equations derived from 3-D Navier-Stokes equations, applicable to solving the conservation of mass and momentum in channels. The equations are versatile to represent flows at atmospheric pressure, full pressurized pipe flows with the Preissmann slot concept (Cunge, 1980), and also sub-atmospheric full pipe flows if adjustments are made in SVE (Vasconcelos et al., 2006). In most cases, however, no analytical solution is available, especially for complex cases such as irregular cross-sections. Therefore, numerical methods are typically applied to solve the SVE (Strelkoff, 1970; Zarmehi et al., 2011; Roohi et al., 2020; Chen et al., 2013). In these cases, classic method approaches use closed-form equations representing hydraulic functions such as wetted area, wetted perimeter, channel's top width, and the relative centroid position to the surface in terms of water surface depth. These functions are functions of water surface depth and are relatively simple to derive for common regular shapes such as rectangular, asymmetric trapezoid, triangular, or parabolic channels (Simões et al., 2017).

However, natural rivers are generally defined by irregular geometry, and closed-form equations of hydraulic properties (HP) are not available, as shown in Farina et al. (2015) and (Gleason, 2015). Abrupt increases in perimeters cause discontinuities in hydraulic radius functions that ultimately cause sharp variations in the rating curve. In addition, channels are generally conceptualized with a constant Gauckler-Manning-Strickler coefficient (here simply denoted as Manning's coefficient) for the entire main channel and sometimes with different values for overbanks (Petikas et al., 2020). However, Man-

ning's coefficient is an empirical representation of friction at the cross-section perimeter, representing the friction properties of the interface between the flow and the cross-section. Therefore, it probably changes with water surface depth (Chow, 2010b). Manning's equation was derived for fully turbulent, steady, uniform flow at normal depth with mild slopes, which is the typical conditions of river flooding (Chanson, 2004).

Although software such as the Hydrologic Engineering Center - River Analysis System (HEC-RAS) (Brunner, 2016b) and the Stormwater Management Model (SWMM) (Rossman et al., 2010) have 1D full momentum solvers, their HP algorithms to determine hydraulic properties are not explicitly specified in their manuals. This poses a drawback for new modeling developments using other software packages, such as Matlab or Python. We overcome these issues here by developing two different algorithms to estimate HP in regular, irregular, and compound cross-section channels and pinpointing various applications of the algorithms developed for steady and unsteady rating curve estimations. The following section assesses the literature review on the aforementioned topics. The tool developed in this paper is easy to use and can be used for teaching and educational purposes.

6.1.1 Literature Review

Since the beginning of the 20th century, the literature has shown that applications of stage-discharge relationships are extensive. The research carried out in Garbrecht (1990) advanced the analytical definition of irregular cross-section hydraulic functions using coupled power fitness functions for the main channel and overbank areas. These functions were fitted using elevation and station data for each breakpoint in the surveyed channel. The author created a methodology to derive these functions, considering different roughnesses in the main channel and at the left and right overbanks. Similarly, (Dingman, 2007) derived analytical "at-station"HP for more generalized cases using not only Manning's equation but also Chezy's. Another method for estimating HP in rivers using polynomial functions is found in Hrafnkelsson et al. (2021). Instead of creating power-law functions with constant exponents, the authors proposed a depth-varying term in the standard rating curve function to fit better river-changing dynamics over time.

A significant model consideration in rating-curve estimations is how friction is modeled. The application in Abril e Knight (2004) shows a depth-averaged model using the Darcy-Weisbach friction model applied in a depth-averaged unsteady model to determine unsteady rating curves in regular sections. Another rating curve method based on the conservation of the mass and momentum equations is described in Dottori et al. (2009). There is no consensus on which friction model should be applied for open channel rating curve models; however, Manning's friction model is more common, probably due to its simplicity and number of studies.

The propagation of the hydrograph in the channel length causes energy losses, flow attenuation (i.e., diffusive effects), and flow delay (i.e., kinematic effects). In addition to these effects, convective and local acceleration change the relationship between stage and discharge. The rising and falling limb of the hydrograph converts a single biunivocal rating curve into a looped rating curve due to hysteresis (Petersen-Øverleir, 2006; Perret et al., 2022; Wolfs e Willems, 2014). The methodology presented in Dottori et al. (2009) is related to this issue and is particularly important in channels where local and convective acceleration play an important role (i.e., channels with very mild slopes and large friction). When using data to compare modeling results with observations, one of the main problems is the lack of observation data for large flows, especially because observations of low-frequency flows, that is, relatively large flows, are rare (Lang et al., 2010) and difficult to obtain. This poses the hydraulic modeling of rating curves as an important tool to determine the probabilities of exceedance of flows and depths that could lead to downstream flood damage (Moncoulon et al., 2014). However, when

data are available on a large scale, data-driven algorithms can also be used to predict stage-discharge in streams, as shown in Muste et al. (2022).

Determining rating curves based on hydraulic models in river cross-sections usually require detailed bathymetric data. This gives rise to a drawback for ungauged rivers with neither flow observations to empirically fit a rating curve (Manfreda, 2018) nor detailed cross-section data (Zheng et al., 2018) to model flow-discharge relationships. To this end, the study conducted in Zheng et al. (2018) developed a continental-scale flood mapping data set based on a 1/3 arc-second (10m) grid cross-section data derived directly from Digital Elevation Models provided by USGS. Their method, based on Manning's uniform flow equation, was comparable to products derived from the Federal Emergency Management Agency (FEMA) with substantially fewer data required compared to full-momentum 2-D models while presenting reasonable results.

In terms of the hydraulic limitations of various approaches to determine steady rating curves in open channels, studies, as presented in HOSSEINI (2004); Stephenson e Kolovopoulos (1990); Fernandes (2021b); Khodashenas e Paquier (1999), show that the interface within the main channel and the overbanks have shear stresses that are not considered when dividing the cross-section into homogeneous parts. In contrast, when considering a single section method with a single average velocity for the inbank and overbanks, discharge passes through discontinuities when flow depth reaches overbank levels with a relatively low hydraulic radius (Sahu et al., 2011). Following these cases, two main alternatives have been implemented to determine normal discharges in channels in most hydraulic engineering procedures (HOSSEINI, 2004):

- a) Dividing the channel into theoretically homogeneous sections (Brunner, 2016b) each with its own Manning's roughness coefficient changing in terms of the stage or for each surveyed cross-section break-point. Moreover, Manning's coefficient could be considered constant, changing only for inbank and over-banks.

- b) Calculating hydraulic properties as a single cross-section (SCM). The Manning's roughness coefficient can vary for each break-point, with stage or assumed constant for inbank and overbank areas.

The fundamental difference between procedures (a) and (b) is the way the velocity is considered. In (a), the velocity can be different for the inbank, overbanks, or even when the roughness changes under the inbank conditions. Therefore, the flow is calculated as an algebraic sum of each flow. In procedure (b), however, velocity is assumed uniform for the whole cross-section. This assumption implies that overbank areas, typically with large perimeters and friction, would have the same velocity as the inbank areas; which might not always be a good assumption. A more detailed theoretical alternative was developed in HOSSEINI (2004) by the introduction of a coherence factor into modeled conveyances with cases a) and b) to correct velocities in the overbanks and the main channel. However, in general, hydraulic engineering calculations, which are often performed by engineers using pieces of software such as HEC-RAS, mainly focus on solutions using the aforementioned alternatives a) or b).

Shear stress occurs when a compound channel exchanges flow from the main channel to the overbanks, and a momentum transfer (Hua et al., 2007) occurs. As mentioned, the velocity in overbank areas is generally lower than in the main channel due to relatively high roughness coefficients in overbanks and relatively larger perimeters. In these cases, the energy and momentum equations can be corrected by the introduction of *Coriolis* (i.e., energy correction) and *Boussinesq* (i.e., momentum correction) coefficients. However, accurate determination of them is a daunting task, as shown by the research conducted in Yang et al. (2018).

The aforementioned literature shows different methods, applications, and correction factors, but no consensus is found when modeling relatively common problems such as determining the normal discharge in a compound or irregular channel. Exploring these issues and providing more guidance related to uncertainty in different model conceptualizations is needed. In this article, we pinpoint their main differences. The uncertainty in the rating curves has not been shown to be negligible in several studies, as presented in Domeneghetti et al. (2012); Ghanghas et al. (2022); Kuczera (1996); Clarke et al. (2000). We want to explore these issues and provide more guidance related to uncertainty in different model conceptualizations and pinpoint their differences in our case studies.

The methods proposed herein can be used in various applications, such as: determining design rating curves in ungauged rivers, 1D hydraulic works as channels, gutters, or Low Impact Development facilities as vegetated swales. Especially in poorly-gauged watersheds where stream gauges are typically unavailable, this methodology can be a tool aiding planning and management of floods. Nonetheless, even when stream gauges are available, the correct measurement of high-level flows is a taunting task because of the typical high turbulence and measurement noise in these cases. The algorithms are developed in Matlab, and cross-sectional information is input into the model in a .xlsx file. The results are displayed graphically, in tables, and printed as PDF automatically.

6.1.2 Paper Objectives and Contributions

Despite experimental and modeling research attached to the problem of determining flow rates in regular and irregular cross-sections, we observe from these aforementioned studies a lack of generalized algorithms to estimate HP in rivers of composite, regular and irregular sections. Studies presented in HOSSEINI (2004); Fernandes (2021b) make clear the impact of shear stress in compound regular cross-sections; however, little has been researched for modeling more complex regular and irregular cross-sections with single stage roughness or depth-varying roughness coefficients. The specific objectives of this study are described as follows:

- Develop novel generalized algorithms to determine HP for regular and irregular cross-sections. Algorithm 2 focuses on the plane geometry, while Algorithm 2, available in the Supplemental Material, focuses on the finite-element method.
- Assess the uncertainty in modeled-based rating curve estimations.
- Assess the role of Manning's roughness coefficient in conveyance estimation.
- Develop a modified SCM equivalent to the DCM model coupled with additional shear stresses at the interface within the overbanks and the main channel.
- Develop a method for estimating dynamic rating curves using a full momentum hydraulic model.
- Compare the dynamical rating curve estimations with the normal flow rating curve estimations.

The remainder of the paper is organized as follows. Section 6.2 develops the mathematical model used in the paper, describing the hydraulic property functions used in the algorithms developed, and detailing the governing equations. In addition, this section explains the methods used to assess rating curve uncertainty and the methods used to evaluate dynamical rating curves by hydraulic modeling. Next, Section 6.3 describes each numerical case study in which the methods were applied in this paper. Following the case studies, Section 6.4 shows the results of all numerical case studies and discusses their main implications, as well as the strengths and weaknesses of the model in Sec. 6.4.6. Section 6.5 discusses the conclusions and future work. Finally, the Supplemental Material details the

governing equations and pseudocode for Algorithm 2, data acquisition, and cross-section determination for synthetic cross-sections tested in this paper. The paper notation for this paper is introduced next.

Paper's Notation: Italicized, boldface upper and lower case characters represent matrices and column vectors: a is a scalar, $\boldsymbol{a}$ is a vector and $\boldsymbol{A}$ is a matrix. Italicized, regular upper and lower case characters represent scalars: q is a scalar, Q is also a scalar. The notation $\mathbb{R}$ denote a set of real numbers. The notations $\mathbb{N}$ and $\mathbb{N}_{++}$ denote the set of natural and positive natural numbers. A normally distributed random number with average μ and variance σ_n^2 is notated by $\mathcal{N}(\mu, \sigma_n^2)$. Given a vector $\boldsymbol{x} \in \mathbb{R}^n$, the notation $\boldsymbol{x}(i:j)$ with i and $j \in N_{++}$ represents a cut in $\boldsymbol{x}$ from i$^{\text{th}}$ to j$^{\text{th}}$ entries. The notations $\mathbb{R}^n$ and $\mathbb{R}^{m \times n}$ denote a column vector with n elements and an m-by-n matrix in $\mathbb{R}$.

6.2 Material and Methods

The process of estimating the HP of irregular cross-sections, although has been addressed by research conducted in Garbrecht (1990) and (Dingman, 2007), still lacks a general algorithm procedure capable of working in irregular, regular, and compound cross-sections. In this paper, we solve this issue by providing two types of algorithms to determine HP assuming surveyed cross-sectional data at different stations. The algorithms and data used in this article are available in an open repository at (Gomes Jr., M. N., 2022). Sec 6.2.8 details governing equations valid for Algorithm 2, whereas the Supplemental Material explains the same for Algorithm 2. The following sub-sections apply to both algorithms.

6.2.1 Cross-section Data

Here, we follow the left-right convention for the cross-section data. Input data is organized in terms of breakpoints. Each breakpoint has its x and y coordinates. Manning's roughness coefficient is defined in three ways: (i) it can be entered for each break-point, (ii) for each stage, or (iii) a constant value for inbank and overbank. The method used in the model can also be chosen (i.e., SCM or DCM). The friction slope (i.e., typically assumed as the bottom slope in normal flow rating curves) is also entered. All these aforementioned data are summarized in a .xlsx file which is read in the Matlab codes. Entries of elevation and horizontal distance within stations, as well as Manning's roughness coefficients within stations, are the data required to simulate the irregular cross-sectional shapes. Details of how to use the model and how to enter the input data can be found in the Supplemental Material. Moreover, all the code is also included in detail. Subsequently, we derive flow areas, wetted perimeters, hydraulic radius, section factor (ϕ), conveyance (k), and interpolate cross-section coordinates assuming linear relationships within known breakpoint data. A schematic of a typical river cross-section is presented in Fig. 6.1, where we detail the rapid increases in area and perimeter due to polygons formed for specific water surface depths.

6.2.2 Unique Elevation Values

To avoid points with the same elevation or with the same station, and to be able to treat all cross-sections as irregular cross-sections, we define a tiny number ($\sigma \approx 1 \times 10^{-4}$ m) and replace elevations and station values as follows:

$$z^i = z^i + \sigma,\ \forall\ z^{i-1} = z^i,\ i \in [1,\ 2, \ldots, n_s]^T \tag{6.1a}$$

$$x^i = x^i + \sigma,\ \forall\ x^{i-1} = x^i,\ i \in [1,\ 2, \ldots, n_s]^T \tag{6.1b}$$

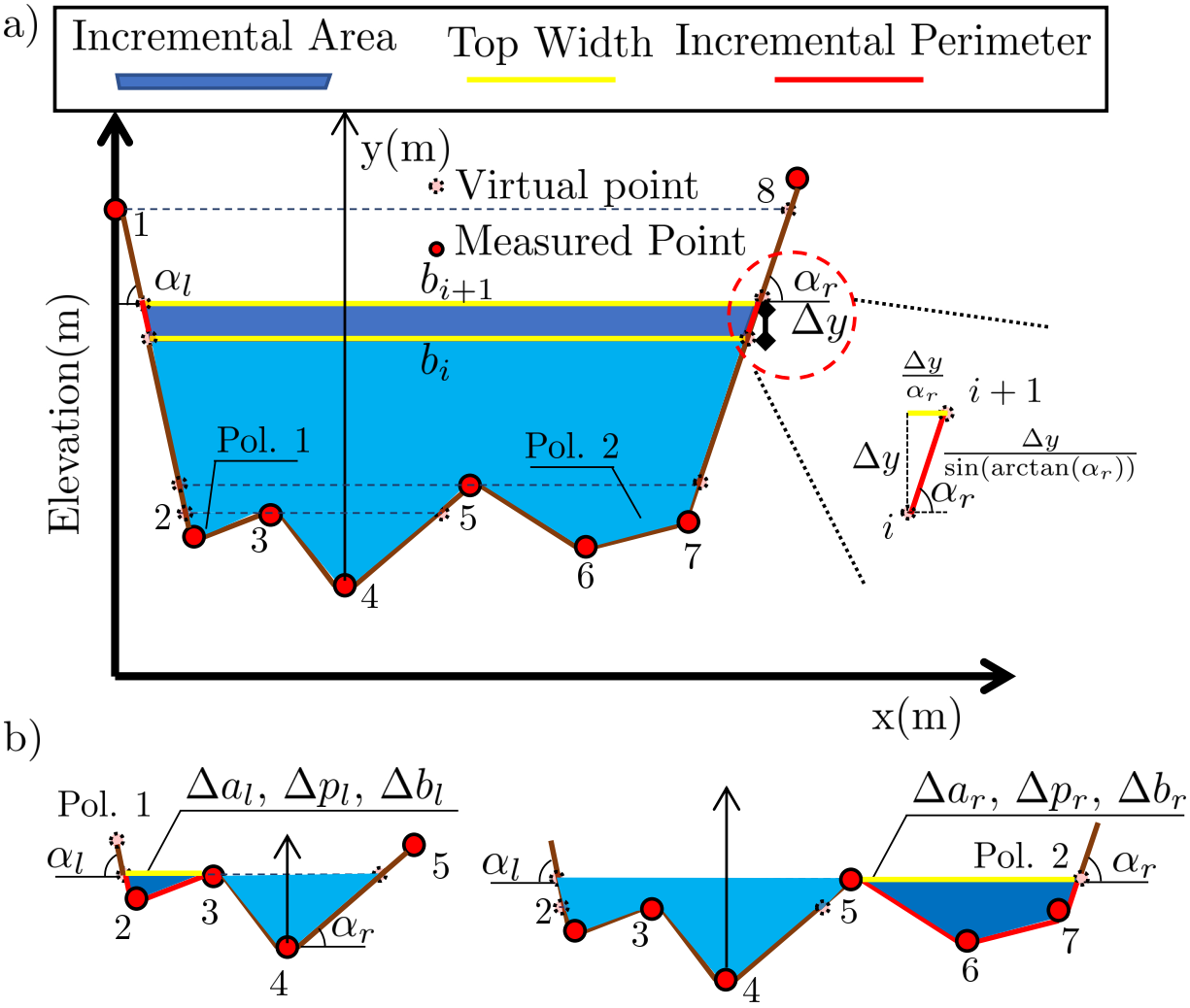

Figure 6.1. Example of cross-section schematics including areas with incremental polygons and areas with linear increasing of perimeter and area. Part a) is the cross-section and part b) represents the polygons within the cross-section. In the modeling rating curves of this paper, we assume that the water level rises inside the inbank and only flows to the overbanks after reaching its elevation. This is equivalent to the case of simulating cross-sections with levees in HEC-RAS (Brunner, 2016b).

where n_s is the number of stations measured.

This allows us to use trapezoid formulas for determining areas and perimeters (see Fig. 6.2), and to identify horizontal or vertical segments by calculating coordinate differences, such that segments with a particular depth and station difference smaller than a threshold would be considered horizontal and/or vertical segments. We detail these cases in more detail in this section in 6.2.8.1.

6.2.3 Hydraulic Radius

Once the area and perimeter are calculated for each segment, the hydraulic radius can be calculated as the ratio within the flow area and its correspondent perimeter (Sturm, 2021), such that:

$$r_h^i = \frac{a^i}{p^i}, \forall\, i = [1, 2, \ldots, n_v]^T \tag{6.2}$$

where n_v is the number of vertical steps, a^i is the flow area, p^i is the perimeter, and i is the i^{th} vertical segment taken from the invert.

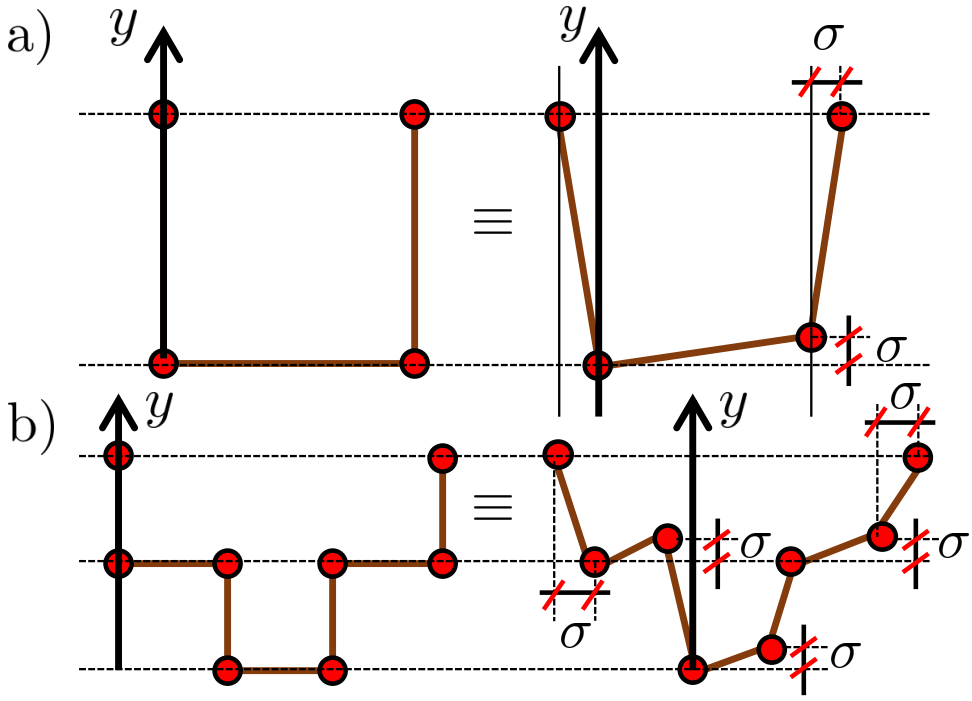

Figure 6.2. Cross-section equivalence within real-world cross-section and numerical cross-section, where parts a) and b) show equivalent cross-sections assuming a small noise σ altering x and y values and hence making them unique.

6.2.4 Section Factor

The section Factor ϕ is given by (Sturm, 2021):

$$\phi^i = a^i \left(r_h^i\right)^{2/3}, \forall\ i = [1, 2, \ldots, n_v]^T \tag{6.3}$$

The previous equation can also be equal to $Q/(\sqrt{s_0})$ for uniform flow, which indicates a biunivocal relationship of cross-section properties with normal flow if ϕ increases monotonically (Sturm, 2021).

6.2.5 Representative Manning's Coefficient for Single Channel Method

The values of $\boldsymbol{n}$ can change in terms of the surface roughness conditions, for example, in the overbanks, the presence of vegetation leads to a reduced flow velocity compared to that in the main channel (Fernandes, 2021a; Kidson et al., 2006). We assume herein that the representative Manning's coefficient for a cross-section in terms of water surface elevation depends on each value of n for each sub-segment if we are modeling using the single-section method. More specifically, we assume that n changes with a non-linear function of the perimeter (p) based on the hypothesis that the total cross-sectional mean velocity is equal to the subarea mean velocity (Einstein, 1934; Brunner, 2016b; Horton, 1933), such that:

$$\tilde{n}^i = \left[\frac{\sum_{j=1}^{i} (n_l^j)^{3/2} p_l^j + (n_r^j)^{3/2} p_r^j}{p^i}\right]^{2/3} \tag{6.4}$$

where n_l and n_r are the Manning's coefficients for left and right directions from the invert assuming piecewise continuous functions of the given $\boldsymbol{n}$ derived from surveyed data for each sub-segment. Similarly, p_l and p_r are the perimeters relative to the left and right slopes of the invert and p^i are the calculated total perimeter of a single section, further described in Eq. (6.10).

6.2.6 Conveyance Factor

The conveyance factor is derived with Manning's roughness coefficient and ϕ. The main hypothesis of Manning's equation is that average velocity is constant throughout the whole cross-section. This is approximately the case when we model the cross-section with a constant roughness coefficient with no discontinuities in hydraulic properties. However, two problems can occur. First, if ϕ is not a monotonic increasing function and if n increases, the velocity might decrease so that the flow in a further section would be smaller than that of a section with lower depth. This is the case for circular pipes (Sturm, 2021); however, this condition is rare in open irregular channels.

Generally, the function ϕ can have discontinuities and rapid changes when the flow reaches the overbank areas. In these cases, we can separate the channel and overbanks conveyances. The method used to calculate the conveyance varies with different types of software such as HEC-RAS (Brunner, 2016b) and MIKE-1D such that HEC-RAS separates the main channel and the overbanks. Here, we consider both methods: the Single Cross-section Method (SCM) and the Divided Cross-section Method (DCM) into conveyance calculations (Al-Khatib et al., 2012), such that:

$$k^i_{\text{SCM}} = \frac{1}{\tilde{n}^i}\phi^i, \forall\ i = [1, 2, \ldots, n_v]^T \tag{6.5a}$$

$$k^i_{\text{DCM}} = k^i_m + k^i_f \tag{6.5b}$$

where k_m and k_f are the main channel and the overbank conveyances.

6.2.7 Centroid Distance

Assuming a constant water density, the vertical centroid coordinate taken from the invert elevation can be derived using the first moment of area, as presented in Eq. (6.6). To solve the integral, we assume a moving trapezoid from i to $i-1$ given by:

$$\bar{y}(i) = \frac{1}{a^i}\int_0^{i\Delta y} a(y)\mathrm{d}y = \frac{\sum_{i=1}^{n_s}\left[(a^i - a^{i-1})(y^i + y^{i-1})\right]}{2a^i} \tag{6.6}$$

where Δy is the vertical discretization.

6.2.8 Algorithm 1 - Geometrical Procedure with a While Loops

6.2.8.1 Cross-section Lateral Angles

In this subsection, we show how to derive a generalized algorithm to estimate hydraulic properties in regular, composite, or irregular cross-sections. The differences between Algorithms 1 and 2 are: the first is based on plane geometry, whereas the second is based on the finite-element method.

The water surface elevation is assumed with no slope in the cross-section and the longitudinal slope is constant throughout the whole section. Therefore, we can use plane geometry to determine the areas and perimeters for a given water depth from the invert. For each depth y evaluated, we calculate the left and right tangents by defining vectors that represent the values of the breakpoints of the left (l) and right (r) of the invert. Let $\boldsymbol{x}_\text{l}$, $\boldsymbol{y}_\text{l}$, $\boldsymbol{x}_\text{r}$, and $\boldsymbol{y}_\text{r}$ be the coordinates left and right of invert. For a $y^i = i\Delta y$, we find the coordinates on the left and right larger (i^+) or smaller (i^-) than y^i, resulting in the following tangents:

$$\alpha^\text{i}_l = \left(\frac{y^{\text{i}^+}_r - y^{\text{i}^-}_r}{x^{\text{i}^+}_l - x^{\text{i}^-}_l}\right) \tag{6.7a}$$

$$\alpha_r^{\mathrm{i}} = \left(\frac{y_l^{\mathrm{i}^+} - y_l^{\mathrm{i}^-}}{x_r^{\mathrm{i}^+} - x_r^{\mathrm{i}^-}}\right) \tag{6.7b}$$

The previous formulae are only valid in inclined segments (i.e., lateral slopes are not 0 or $\pi/2$. Considering the coordinates of two consecutive breakpoints, 4 alternatives can occur. We classify them as (i) vertical segment, (ii) horizontal segment, (iii) vertical and horizontal segment, and (iv) regular segment. This classification is derived from the vertical and horizontal distances within consecutive breakpoints, such that if the differences are equal σ then a vertical and/or horizontal segment is identified. These cases are treated in the main code with a simple if − statements.

6.2.8.2 Top-width Geometry

Assuming a finite y discretization Δy, the increase of the top width (b) can be calculated with the angle defined in Eq. (6.7). However, in the cases where a drastic change in x occurs from i to $i+1$, we can calculate b^{i+1} as:

$$b^{\mathrm{i}+1} = b^{\mathrm{i}} + \Delta b_l^{\mathrm{i}+1} + \Delta b_r^{\mathrm{i}+1} + \Delta y\left(\frac{1}{\alpha_r{}^{\mathrm{i}}} + \frac{1}{\alpha_l^{\mathrm{i}}}\right) \tag{6.8}$$

where Δb_l and Δb_r are the additional values of b that must be added from the left and right directions of the invert y axis to consider horizontal changes in areas without slopes.

6.2.8.3 Flow Area Calculations

The basic idea for the area is to calculate trapezoid areas with bases b^{i+1} and b^i and depths Δy. However, similar to the increase in top width mentioned in Eq. (6.8), the area in section $i+1$ can also have a drastic increase. This is the case shown in Fig. 6.1 in the parts where the flow is retained within a surface. In these cases, the area calculation has to consider the polygon area formed by the surface generated from left and right overbanks, such that:

$$a^{\mathrm{i}+1} = \overbrace{(b^{\mathrm{i}+1} + b^{\mathrm{i}})\Delta y/2}^{a_t} + a^i + \Delta a_{\mathrm{l}}^{\mathrm{i}} + \Delta a_{\mathrm{r}}^{\mathrm{i}} \tag{6.9}$$

where Δa is the increase in area from discontinuities derived from the channel section from left and right directions calculated as a polygon area and a_t is the area of the incremental trapezoid from i to $i+1$.

6.2.8.4 Perimeter in terms of Water Surface Depth

The cross-section perimeter is a monotonic function in terms of $\boldsymbol{y}$. In parallel with calculations of a and b, the perimeter function might also have discontinuities. For example, these sharp changes in the perimeter can also be due to water reaching overbanks or increasing horizontal distances due to the deposition of sand in the main channels. The perimeter can be calculated in terms of lateral distances within the cross-sections, from incremental perimeters from overbanks, and the base at the invert. These distances can be calculated using the angles defined in Eq. (6.7). Therefore, we can write the perimeter functions as follows:

$$p^{i+1} = p^i + \Delta y\overbrace{\left(\frac{1}{\sin\left(\arctan\left(\alpha_l\right)\right)} + \frac{1}{\sin\left(\arctan\left(\alpha_r\right)\right)}\right)}^{f_\alpha} + \Delta p_{\mathrm{l}}^i + \Delta p_{\mathrm{r}}^i \tag{6.10}$$

As shown in the previous equation, the perimeter function could have issues for undefined values of α. To this end, we treat these cases with *if-statement* conditions in the algorithm identifying these points and assuming that $f_\alpha = 1$.

6.2.9 Single Channel Method (SCM)

In this method, there is no distinction between overbank and inbank flow conditions. An example of a cross-section where this hypothesis would be applicable is shown in Fig. 7.7 a), b) and c). The stage-roughness is determined in terms of the perimeter following Eq. (6.4). For inbank conditions, this method is identical to the Divided Channel Method described in the following section. The SCM method considers a stage-conveyance curve that ultimately converts depth into flows, such that:

$$Q^i = k^i \sqrt{s_0} \tag{6.11}$$

where Q is the normal flow rate and s_0 is the bottom slope, which is assumed as the friction slope for the normal flow estimates.

6.2.10 Divided Channel Method (DCM)

Herein, let $n_{fp} \in \mathbb{N}_{++} \in [0,\ 1,\ 2]^T$ be the number of floodplains in a cross-section as shown in Fig. 6.4. In this method, the cross-section is divided into main channel (m) and floodplains (f). The interface between the floodplains and the main channel introduces a new shear force that is considered by adding the wet perimeter in the main channel of a value equal to $n_{fp}(y - y_m)$. In the following subsection, we define the governing equations to determine the HP for the DCM.

6.2.10.1 Correcting Manning's Coefficient

A new system of equations is defined if we assume an additional shear stress acting in the interface between the main channel and the floodplains (see Fig. 6.4). Defining the break-point divider, we calculate the width of the main channel (b_m) by extending the line segment from the divider to the opposite overbank. Hence, the left and right sides of this line define the overbanks, while inside of this segment towards the invert is considered the main channel. In this paper, we consider that the wet perimeter of the main channel increases by h_f for each floodplain. Let n_m be the final representative Manning's coefficient for the main channel and n_f be the representative Manning's coefficient for the floodplains. If we assume different velocities on the floodplain and the main channel, we can estimate a new roughness coefficient $\bar{n}$ such that $k_{\text{SCM}} = k_{\text{f}} + k_{\text{m}}$ in Eq. (6.5b), resulting in Eq. (6.12f):

$$y_f = y - y_m \tag{6.12a}$$

$$a_f = a - (a_m + b_m y_f) \tag{6.12b}$$

$$p_f = p - p_m \tag{6.12c}$$

$$p_m^* = p_m + n_{fp} y_f \tag{6.12d}$$

$$a_m^* = a_m + b_m y_f \tag{6.12e}$$

$$\bar{n} = \frac{a(a/p)^{2/3}}{\left(\frac{1}{n_f} a_f (a_f/p_f)^{2/3} + \frac{1}{n_c} a_m^* (a_m^*/p_m^*)^{2/3}\right)} \tag{6.12f}$$

where b_m is the width of the main channel, the variables a and p are determined by Eqs. (6.9) and (6.10), and the superscript $*$ represents values corrected for by shear stress induced by the interface within the main channel and floodplains.

This new roughness coefficient accounts for vertical division within the main channel and overbank roughness by including the increase in wet perimeter in the main channel in terms of h_f, while allowing the use of the total stage-area and stage-perimeter algorithms derived in Sec. 6.2.8. Therefore, the normal flow can be calculated as follows:

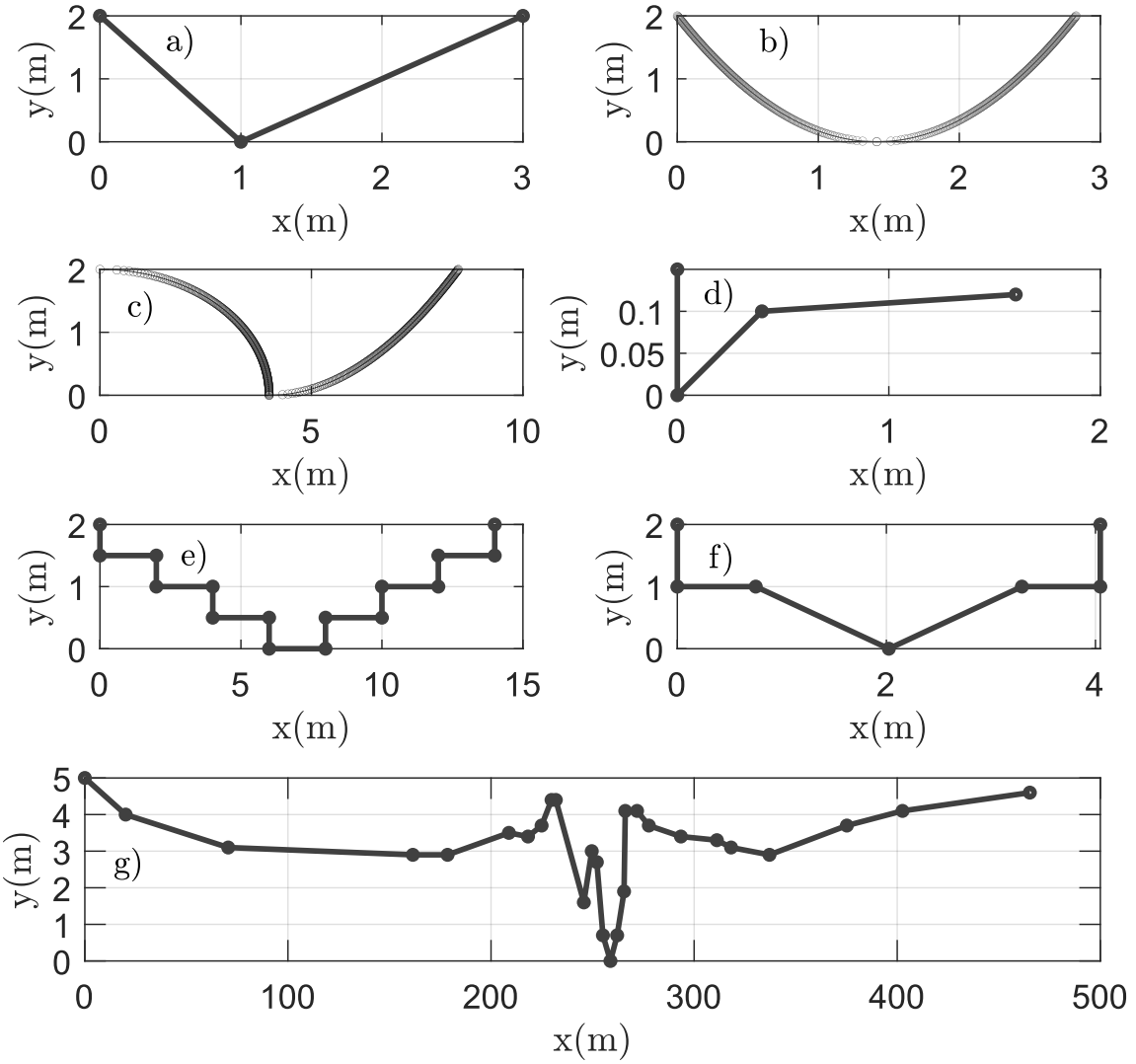

Figure 6.3. Cross-sections assessed in the numerical study cases. Parts a), b), c), d), e), and f) represent triangular, parabolic, semi-elliptical/semi-parabolic, road-gutter, composite v-notch and rectangular, trapezoidal gabion, and irregular cross-sections, respectively.

$$Q_{\mathrm{DCM}} = \bar{Q}_{\mathrm{SCM}} = \overbrace{\frac{1}{\bar{n}} a^* \left(\frac{a^{*\,2/3}}{p^*}\right)}^{\bar{k}_{\mathrm{SCM}}} \sqrt{s_0} \tag{6.13}$$

where $\bar{Q}_{\mathrm{SCM}}$ is the modified single-section method to account for overbanks and $\bar{k}_{\mathrm{SCM}}$ its respective conveyance.

6.2.10.2 Overbank Areas and Discontinuities

In this model, the elevation of the water surface is assumed to be continuous for the in-bank and overbanks. However, in case the algorithm identifies discontinuities in cross-section elevation (i.e., elevation data are not monotonically increasing and find left and/or right areas that are filled if water depth exceeds a threshold), the model can generate two sets of polygons to represent these cases. These polygons can increase areas and perimeters abruptly; which may increase or decrease flow rates depending on the increased values.

Let y_d be the depth taken from the invert elevation that starts to have overbank flows (see Fig. 6.1). If section i is such that $y_i = y_d$, the algorithm searches for left and right directions from the invert y-axis to find breakpoints with depths smaller than y_d. If depths are found, then a polygon can be defined and extra values of Δa, Δp, and Δb can be calculated from it. In Matlab, this problem can be solved using the functions polyshape and polyarea.

6.2.11 The 1D Shallow Water Equations

For the estimation of the 1D hydrodynamics, we focus on solving the complete one-dimensional Saint-Venant Equations (Gerbeau e Perthame, 2000). These equations are derived from the conservation of mass and momentum by applying Newtons second law in a finite fluid element. Let $\mathcal{D}$ be the set of computational nodes from 1 to N_x, for a node $i \in \mathcal{D}$, let $A(x,t)$ be the cross-section flow area at a given time t and space x and $v(x,t)$ be the depth-average flow velocity. All other states can be derived from these. Therefore, we can write the Saint Venant Equations as the following non-linear hyperbolic system of partial differential equations for a node i at coordinate x and in time as follows:

$$\frac{\partial \boldsymbol{q}(x,t)}{\partial x} + \frac{\partial \boldsymbol{f}(x,t)}{\partial t} = \boldsymbol{s}(x,t) \tag{6.14a}$$

$$\boldsymbol{q} = [A,\ Q]^T \tag{6.14b}$$

$$\boldsymbol{f} = [Q,\ (\beta |v| Av + gA\bar{y})]^T \tag{6.14c}$$

$$\boldsymbol{s} = [0,\ (gA(I_o - I_f))] \tag{6.14d}$$

$$I_f = \frac{n^2 Q|Q|}{R_h^{4/3} A^2} \tag{6.14e}$$

$$Q = |v| \text{signal}(v) A \tag{6.14f}$$

$$\beta = \left(1 + \frac{gn^2}{R_h^{1/3}\kappa^2}\right) \tag{6.14g}$$

where A is the cross-section area, v is the wave velocity, g is the gravity acceleration, $\bar{y}$ is the distance from the water surface to the centroid of the cross-section, I_o is the bottom slope and I_f is the friction slope, β is the Boussinesq coefficient for moment transfer corrections and κ is the von Kármáns coefficient (Yang et al., 2018) usually assumed as 0.41. Both A and v are the main states solved for the longitudinal distance x and time t, such that $A = A(x,t)$ and $v = v(x,t)$. In the following derivations of this paper, we neglect the x and t indexes for easier notation, as well as for other states dependent on A and v.

As shown in the previous sub-equations, functions describing the hydraulic radius and cross-section centroid distance from the water surface are required. Therefore, we first apply the hydraulic property estimation algorithm to determine these functions and solve the SVE by using the tabled results to find the required geometric functions.

To solve all nodes together, we collect the state vectors (e.g., $\boldsymbol{q}$, $\boldsymbol{s}$, and $\boldsymbol{f}$) for each internal node from $i = 2$ to $(N_x - 1)$, that is, from the second node to the second to last node, such that matrices $\boldsymbol{Q} = [\boldsymbol{q}_2, \boldsymbol{q}_3\ \ldots \boldsymbol{q}_{N_x-1}]^{\mathrm{T}}$, $\boldsymbol{F} = [\boldsymbol{f}_2, \boldsymbol{f}_3\ \ldots \boldsymbol{f}_{N_x-1}]^{\mathrm{T}}$, and $\boldsymbol{S} = [\boldsymbol{s}_2, \boldsymbol{s}_3\ \ldots \boldsymbol{s}_{N_x-1}]^{\mathrm{T}}$ can be derived. Therefore, we solve the vectorized set of hyperbolic partial differential equations for all nodes except the boundaries by numerically discretizing the problem using the Lax-Friedrichs method (Lax, 1954). This numerical scheme uses a forward discretization in time, centered discretization in space, and has first order accuracy in space in time (Kurganov, 2018). Expliciting Eq. (6.14a) for $\boldsymbol{Q}$, we can derive the following matrixwise expression such that:

$$\boldsymbol{Q}(t+\Delta t) = \frac{1}{2}\Big(\boldsymbol{Q}_b(t) + \boldsymbol{Q}_f(t)\Big) - \frac{\Delta t}{2\Delta x}\Big(\boldsymbol{F}_f(t) - \boldsymbol{F}_b(t)\Big) + \frac{1}{2}\Big(\boldsymbol{S}_b(t) + \boldsymbol{S}_f(t)\Big) \tag{6.15}$$

where subscripts b and f represent backward and forward states from each node i. Matrices

$$\boldsymbol{Q},\ \boldsymbol{Q}_b,\ \boldsymbol{Q}_f,\ \boldsymbol{F}_f,\ \boldsymbol{F}_b,\ \boldsymbol{S}_b,\ \boldsymbol{S}_f \in \mathbb{R}^{N_x-2}.$$

The boundary conditions are applied in matrices from backwards and forwards for $\boldsymbol{Q}$ and the source terms and flux terms for the boundary conditions are calculated using Eqs.(6.14c)-(6.14g). The connection between the SVE Model with the HP Estimator Model is presented in Fig. 6.5.

Algorithm 2: Geometrical Procedure with while loop

input: Breakpoint elevations ($\boldsymbol{e}$), sub-reach lengths $\boldsymbol{l}$, and sub-reach Manning's roughness coefficient ($\boldsymbol{n}$).
compute: $\boldsymbol{z} = \boldsymbol{f}_z(\boldsymbol{z}, \sigma)$ and $\boldsymbol{x} = \boldsymbol{f}_x(\boldsymbol{z}, \boldsymbol{x}, \sigma)$ from Eq. (6.1)
compute: $\boldsymbol{y} = \boldsymbol{z} - \min(\boldsymbol{z})$
find: Invert elevation index $\mathrm{p}_0 = \mathrm{find}(\boldsymbol{e} = \min(\boldsymbol{e}))$
sort y: Define two vectors $\boldsymbol{y}_l$ and $\boldsymbol{y}_r$ capturing left and right $\boldsymbol{y}$ values from p_0. Similarly, define the correspondent $\boldsymbol{x}_l$ and $\boldsymbol{x}_r$.
compute : Effective channel maximum depth ($y^{\max} = \min(\max(\boldsymbol{y}_l), \max(\boldsymbol{y}_r))$
compute : Intersection of $y^{\max}$ with either left or right directions and redefine $\boldsymbol{x}$ and $\boldsymbol{y}$.
Initialize : $s \leftarrow s+1$
while $s \neq b$ **do**
  if $s = 1$ **then**
    compute: α_l and α_r from Eq. (6.7), using invert coordinates
    compute: $y^s_{\max} = \min(y_l^{s^+}, y_r^{s^+})$
    compute: $n_p^s = y^s_{\max}/p$
    for $i = 1 : n_p^s$ **do**
      compute : Eqs. (6.8)-(6.10) and Eqs. (6.2)-(6.5)
    end for
  else
    compute: $y^s_{\max} = \min(y_l^{s^+}, y_r^{s^+})$
    compute: $n_p^s = y^s_{\max}/p$
    for $i = (n_p^{s-1}+1) : n_p^s$ **do**
      compute : Eqs. (6.8)-(6.10) and Eqs. (6.2)-(6.5)
    end for
  end if
  if $y^i = y^{\max}$ **then**
    $s = b$
  else
    $s = s+1$
  end if
end while

6.2.11.1 Adaptive Time-stepping

HydroHP - 1D model has an adaptive time-step scheme based on Courant Number (C) (Courant et al., 1928). Our model has to ensure $C \leq 1$ to guarantee convergence due to the explicit finite-difference scheme used to solve 1D SVE. Our 1D mesh is stationary and constant, therefore, the only manner to ensure computational stability is by changing the model time-step (Δt) accordingly, such that at the end of a computational time-step, we calculate the refreshed computational time-step as follows:

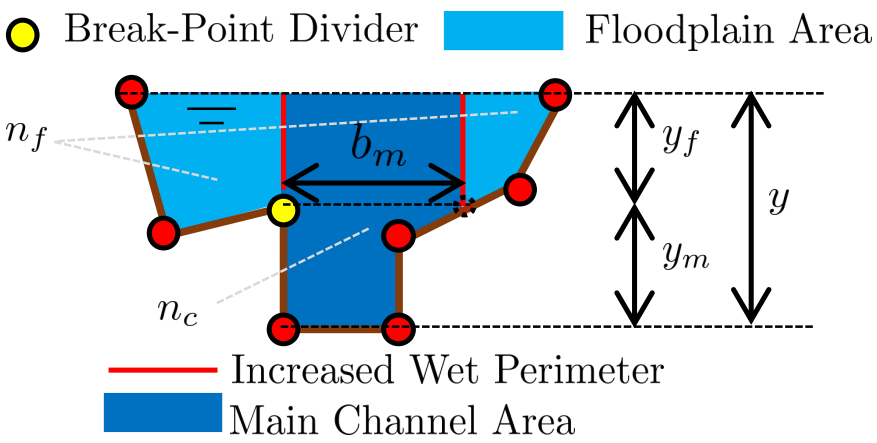

Figure 6.4. Incremental wet perimeter in the main channel due to shear stresses from the interface within floodplain and main channel, where b_m is the main channel width, y_f is the floodplain depth, y_m is the channel main depth, and y is the water flood depth.

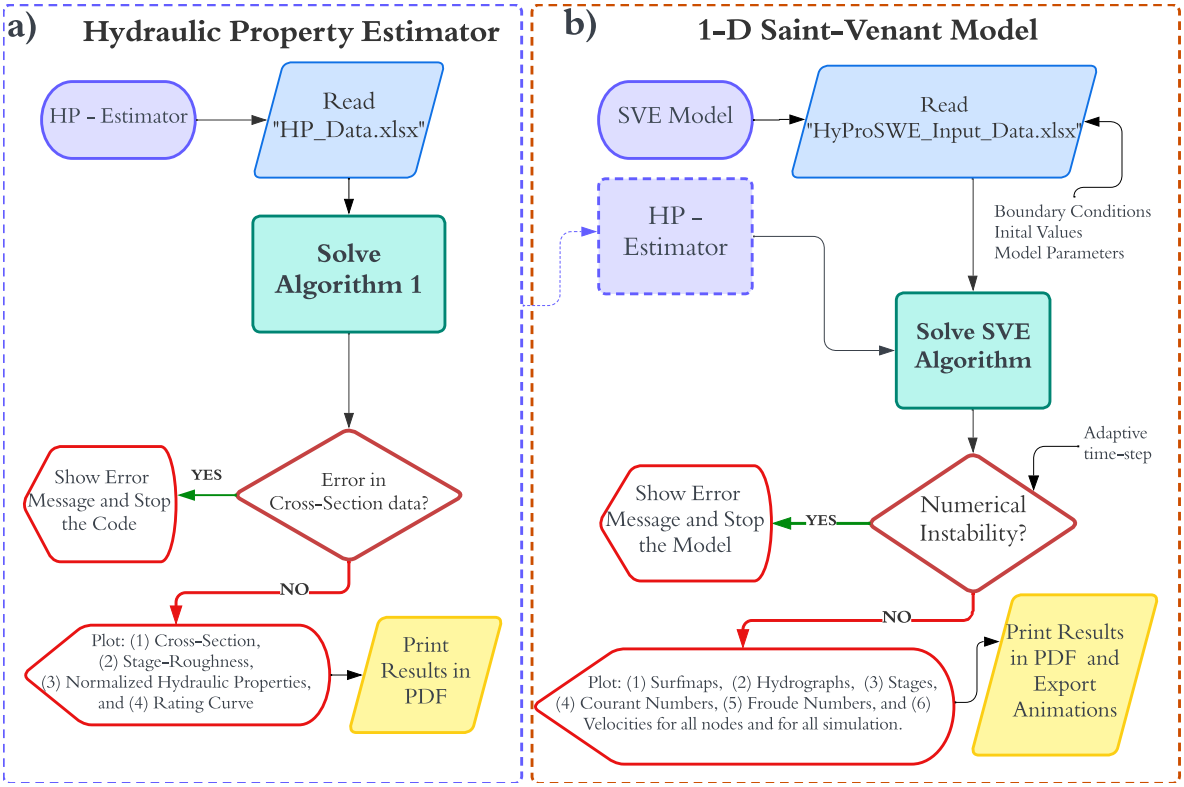

Figure 6.5. HP Model and SVE Model flowcharts. The HP - Estimator algorithm is a process for the SVE Model and is only used when modeling irregular cross-sections. Details of data entry are detailed and explained in the Supplemental Material, including the interfaces of data entry. Part a) represent the modeling steps for the HP algorithm and part b) shows it for the SVE model.

$$\Delta t(t) = \min_{\forall\, i \,\in\, \mathcal{D}} \left(\frac{C}{\left|u^i(t)\right| + \sqrt{g H_m^i(t)}} \right), \tag{6.16}$$

where C is the user-defined Courant number (e.g., typically assumed between 0.5 and 1 for 1D hydrodynamic modeling), $u(t) = Q(t)/A(t)$ is the flow velocity, $H_m(t) = A(t)/b_t(t)$ is a representative water depth for irregular channels, and $b_t(t)$ is the top width.

6.2.11.2 Boundary Conditions

In order to represent feasible hydraulic conditions in 1D channels, HydroHP - 1D has various options for combinations of boundary conditions. The current model version has 3 upstream boundary conditions and 2 downstream boundary conditions. The first node of the mesh can be subjected to a Nash inflow hydrograph (e.g., see Eq. (6.21)), tabular inflow hydrograph, and tabular stage-hydrograph. Tabular data is then interpolated to the model time-step via Piecewise Cubic Hermite Interpolating Polynomial method (Barker e McDougall, 2020). The downstream boundary conditions are twofold: normal slope boundary condition or stage-hydrograph boundary condition through the modeling of a wave function.

Since HydroHP - 1D uses the Lax-Friedrichs method that uses a central difference in space, the solution is only properly given in internal nodes. Therefore, numerical issues in the boundary may arise when poorly discretized meshes are used (Akan e Iyer, 2021). When either stage-hydrograph or inflow hydrograph boundary conditions are used in the borders of the domain, a zero-order extrapolation is used. More details of the treatment of the boundary conditions is explained in the supplemental material section.

6.3 Case studies

In this section, we show various model applications for different cross-sections. First, in Sec. 6.3.1, we apply the model in single sections for triangular, parabolic, and semi-elliptical/semi-parabolic cross-section. Moreover, the model is applied to estimate composite cross-sections in Sec. 6.3.2, followed by an example of an irregular cross-section with left and right overbanks in Sec. 6.3.3. The cross-section data are shown in Fig. 7.7. The assumed data for the sections can be found in the Supplemental Material. The variety of these sections was selected to represent the different common and complex shapes used in hydraulic design. In the particular case of irregular cross-section, this represents a real river section in the Little Washita River (Garbrecht, 1990).

6.3.1 Numerical Case Study 1 - Normal Flow in Complex Regular Cross-sections

In the first case study, we show three examples of determining stage-discharge relationships for well-known cross-sections. The tested cases are cross-sections of the following shapes: (a) triangular, (b) parabolic, (c) semi-elliptical/semi-parabolic. These sections can be represented by single closed-form equations for HP since the geometry functions are relatively easy to determine. For the particular case of (a), we can determine the cross-section with 3 coordinates. However, for cases (b) and (c), since geometry and slopes can change dramatically with x, we discretize the depth into 1 cm steps and determine x in terms of y with the governing equations of (b) and (c). Therefore, the number of coordinates entered to determine shapes (b) and (c) is primarily dependent on the maximum depth of the channel.

Section	$y^{\max}$ (m)	$p(y^{\max})$ (m)	$r_h(y^{\max})$ (m)	$\phi(y^{\max})$ ($m^{5/3}$)	$k(y^{\max})$ (m^3/s)	$k^{\max}_{\text{DCM}}(y^{\max})$ (m^3/s)	$k^{\max}_{\text{RAS}}(y^{\max})$ (m^3/s)	RE -	RE_{RAS} (m/s)	$v(y^{\max})$ (m^3/s)	$Q(y^{\max})$
T	2	5.06	0.59	2.11	105.58	105.58	105.60	0%	0	1.11	3.339
P	2	5.12	0.74	3.07	153.69	153.69	153.60	0%	0	1.29	4.860
EP	2	9.85	0.82	6.52	325.95	325.95	325.70	0%	0	1.38	10.307
Gu	0.12	1.73	0.04	0.00	0.16	0.22	0.20	-27%	1	-9.18	0.005
G	2	19.50	0.82	14.01	700.62	745.28	739.00	-6%	-1	1.39	22.156
VR	2	8.23	0.79	5.52	276.03	197.25	227.40	40%	15	1.35	8.729
I	4.6	525.38	2.05	626.00	31300.07	32293.42	31206.50	-3%	3	2.55	989.795

Table 6.1. Maximum values for different types of cross-sections, where RE is the relative error defined in Eq. (6.19). and RE_{RAS} is the relative error between SCM and HEC-RAS.

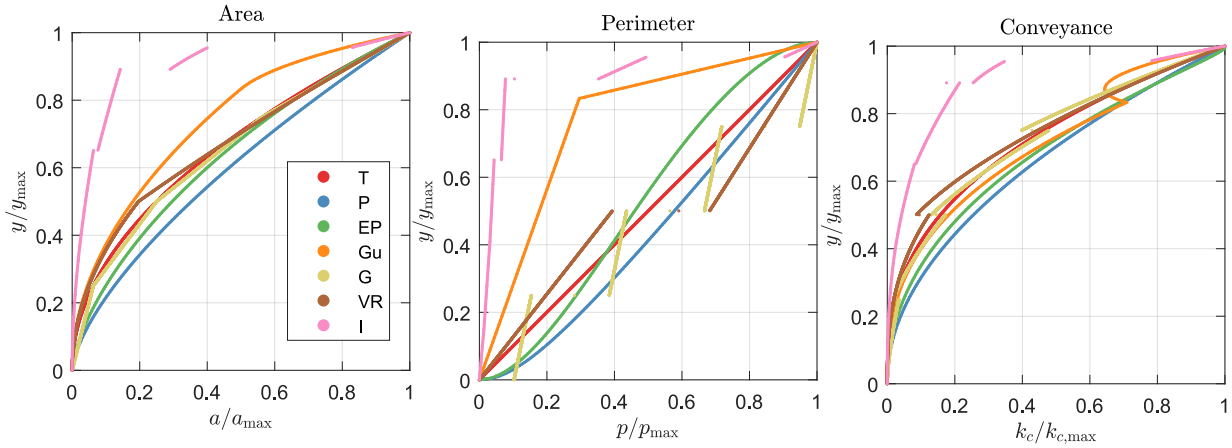

Figure 6.6. Normalized results of the perimeter, cross-section average velocity, and conveyance for the single-channel method. The captions T, P, EP, GU, G, VR, and I represent the triangular, parabolic, semi-elliptical/semi-parabolic, road-gutter, trapezoidal gabion, v-notch coupled with rectangular, and irregular cross-sections. Maximum values for each cross-section are shown in Table 6.1.

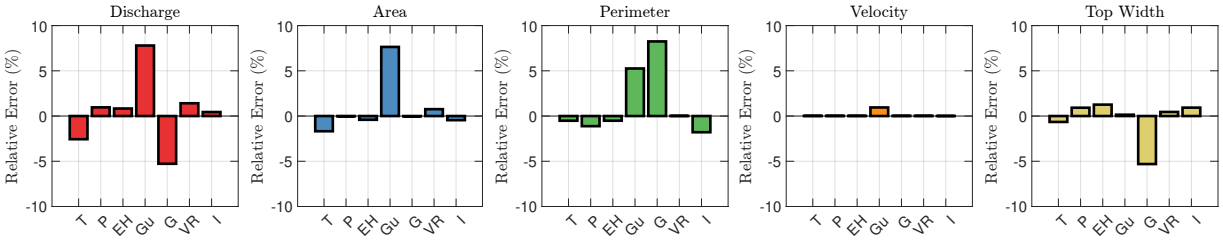

Figure 6.7. A relative error within modeled values at $y^{\max}$ compared to simulated values from NOAA normal depth solver (US Department of Commerce, 2016).

6.3.2 Numerical Case Study 2 - Normal Flow in Composite Regular Cross-Sections

Another common type of cross-section used in channels is the use of combinations of regular shapes. In this numerical case study, we estimate HP for the following cross-sections: (d) road-gutter, (e) composite triangular and rectangular, and (f) successive trapezoid gabion channel. We have chosen these sections to pinpoint common cross-sections used in hydraulic engineering design. As mentioned in 6.3.1, x is numerically discretized in terms of y for rapid changes in cross-section shapes. In these cases, all sections of this case study are only changed by changing slopes when a particular threshold depth occurs (d) and (f), or by increasing b^i (see Eq. (6.8)).

6.3.3 Numerical Case Study 3 - Irregular Cross-Sections with Overbanks

In this case study, we model a cross-section of the river presented in Garbrecht (1990). Two stage-roughness hypotheses were tested in this case study.

6.3.3.1 Single Manning Coefficient

Assuming a depth-invariant stage-roughness curve with a baseline roughness of $n_b = 0.02$ for all break-point segments, we model the stage-conveyance assuming certain eventually feasible values of roughness.

6.3.3.2 Depth Varying Coefficient

In this subsection, we test the role of uncertainty in the estimation of the roughness coefficient and its propagation in the conveyance. Three tests are performed as follows: scenario (i)

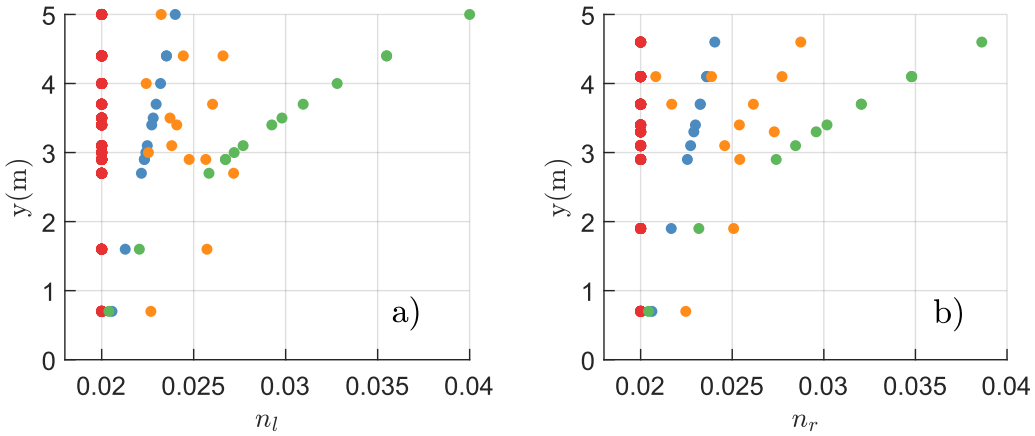

Figure 6.8. Manning's roughness coefficient for scenarios 1, 2, 3, and 4 defined in Eq. (6.17) and (6.18) for cross-section d) in Fig. 6.1, where red dots, blue dots, green dots, and orange dots represent scenarios 1, 2, 3, and 4, respectively. Parts a) and b) represent left and right points from invert.

assumes the baseline scenario shown in the previous section, scenario (ii) assumes a linear increasing stage-roughness relationship (Mustaffa et al., 2016), scenario (iii) considers a 2-order polynomial stage-roughness relationship, and scenario (iv) assesses a Monte-Carlo stage-roughness relationship with a known average variation (μ) and standard deviation (σ_n) varying from a base roughness coefficient from scenario (i). This scenario also accounts for cases where the roughness coefficient decreases with stage, as presented in Alves et al. (2020).

a) *Static Scenarios* The stage-roughness relationships for the static scenarios (i.e., only one depth series per scenario) are shown as follows:

$$n_1 = n_b \tag{6.17a}$$

$$n_2^d(y) = n_b + \alpha_d y \tag{6.17b}$$

$$n_3^d(y) = n_b + \alpha_d y^2 \tag{6.17c}$$

$$\tag{6.17d}$$

where d represents the left or right directions from the invert, and α are coefficients that describe the variation of the roughness.

b) *Monte Carlo Analysis*

The uncertainty in Manning's coefficient is evaluated assuming an average error ($\mu = 30\%$) and a standard deviation ($\sigma_n = 0.01$) based on (Kim et al., 2010). We perform 200 Monte-Carlo simulations to estimate the eventual variations of roughness in the channel. The signal $\pm$ in the following equation represents the cases where the roughness increases and decreases, on average.

$$n_4^d(y) = n_b\Big(1 \pm \mu\sqrt{(\sigma_n)} \sim \mathcal{N}(0,1)\Big) \tag{6.18}$$

Although only one series of n_4 is shown in Fig. 6.8, we estimate the flow discharge for 100 cases.

6.3.4 Numerical Case Study 4 - Divided Channel Method vs Single Channel

In this subsection, we define the analysis performed to compare the differences between SCM and DCM in modeling conveyances in regular, composite, and irregular cross-sections. We use the relative error index to calculate the percentage error between SCM and DCM as follows:

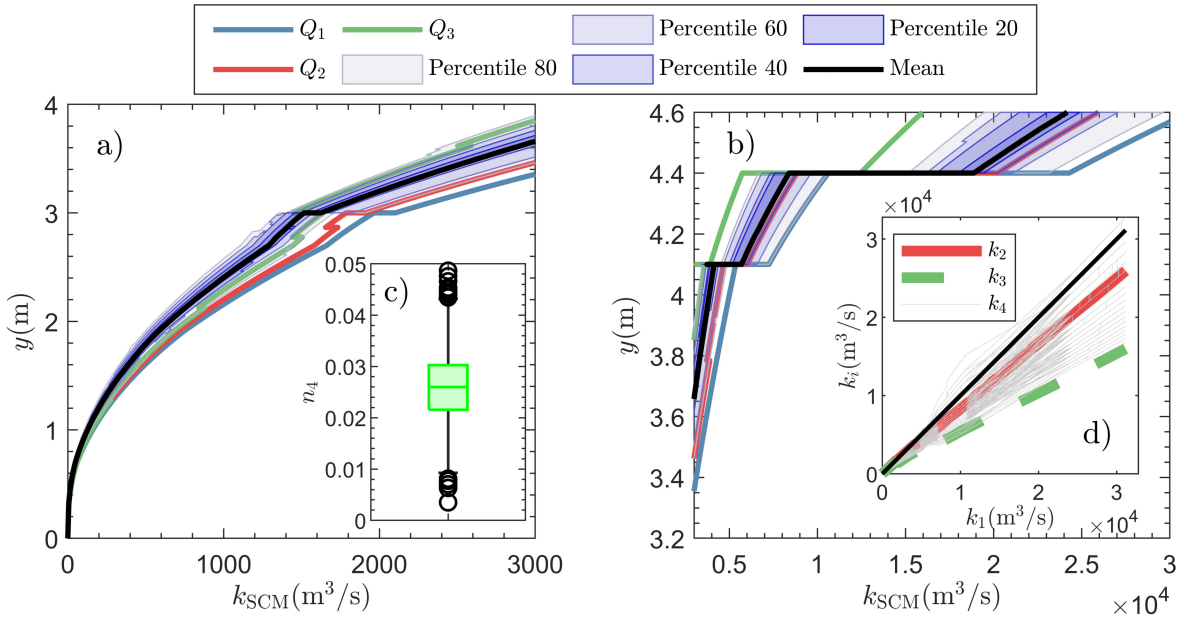

Figure 6.9. Uncertainty analysis in rating curves modeled with normal depths where a) is the stage-discharge curve for the main channel, b) for the interaction between overbanks and main channel, c) shows the variability of roughness coefficient for each inter-segment used in the Monte-Carlo analysis, and d) shows the relationship within each conveyance compared to scenario 1 where stage-roughness is constant.

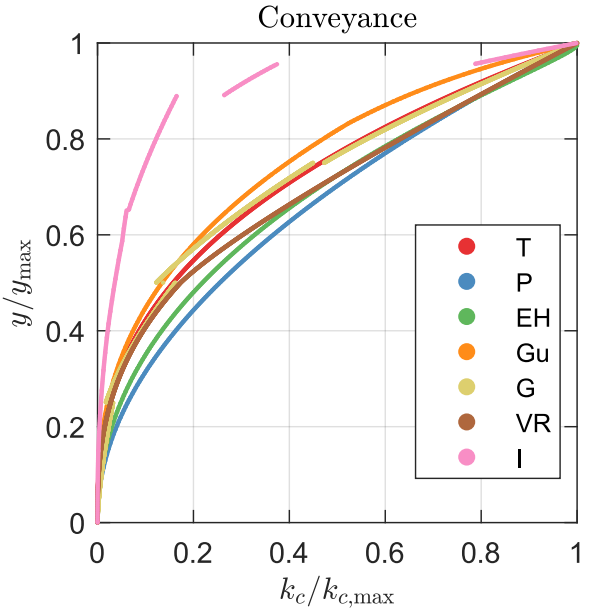

Figure 6.10. Results of conveyance for the DCM Method applied for cross-sections in Fig. 7.7 using Eq. (6.12f) for the representative Manning's coefficient

$$\mathrm{RE} = \frac{k_{\mathrm{SCM}} - k_{\mathrm{DCM}}}{k_{\mathrm{DCM}}} \times 100 \tag{6.19}$$

Similarly, we compute the relative error between SCM and HEC-RAS ($\mathrm{RE}_{\mathrm{RAS}}$) (Brunner, 2016b) analogy with Eq. (6.19).

6.3.5 Numerical Case-Study 5 - Modeling Unsteady-state Hydrodynamics and Rating Curves with a 1D SVE Model

6.3.5.1 Non-Breaking Wave Propagation Over a Horizontal Plane

This section compares solutions given by HydroHP - 1D, HEC-RAS 1D, and an analytical solution for a 1D wave propagating over a horizontal plane. The diffusive, convective, and inertial terms of SVE play important roles in this case and are tested. (Hunter et al., 2005) developed an analytical solution of SVE for this problem neglecting inertial and convective terms, such that the water depth in position x at time t can be written as:

$$h_x(t) = \left[\frac{7}{3}\left(C - n^2u^3(x-ut)\right)\right]^{7/3} \tag{6.20}$$

where u is the depth-averaged velocity in the x direction, C is a constant of integration solved by referring to the initial conditions of the problem (i.e. $h_0(t_0) = 0$), n is the stage-invariant roughness coefficient and t the elapsed time.

The parameters assumed are $u = 1$ m/s, $n = 0.03$ m.s$^{-1/3}$, and the channel width is assumed as 100 m. Results are compared within the developed model, HEC-RAS 1D Full Momentum Solver, and Analytical Solution given by Eq. (6.20).

6.3.5.2 Unsteady-State Inflow Hydrograph and Normal Flow at the Outlet

In this section, we compare the performance of HydroHP - 1D against HEC-RAS 1D model under different combinations of stage-hydrographs and inflow hydrographs. HEC-RAS is set to use the 1D Unsteady Finite Difference Numerical Solution with the Skyline/Gaussian solver (Brunner, 2016b), which uses an implicit numerical scheme and solves a series of non-linear system of equations, whereas HydroHP - 1D uses an explicit finite-difference method.

For this numerical testing, we adapt the problem 8.3 presented in Akan e Iyer (2021) to a different inflow hydrograph boundary condition with a relatively more complex cross-section. The problem consists in an unsteady-state simulation of an open channel with $n = 0.025$ m.s$^{-1/3}$, $s_0 = 0.00025$ m/m, with an inflow hydrograph boundary condition and a normal slope outlet boundary condition ($I_{f,N_x} = 0.00025$ m/m). The channel length is 1097.88 m and the elevation of the first node is 0.274 m. Simulation time is 360 min and detailed outputs are retrieved each 10 min. The differences from (Akan e Iyer, 2021) are the cross-section, number of nodes, and the tested and the inflow hydrograph. Herein, we apply HEC-RAS and HydroHP - 1D in the V-Notch (see Fig. 7.7) for an inflow hydrograph modeled with a Nash Function (i.e., Eq. (6.21)) with a peak flow of 2.5 m^3/s, time to peak of 3 hours, baseflow of 0.25 m^3/s and $\beta = 8.5$. Moreover, HEC-RAS 1D and HydroHP - 1D are discretized with 100 equally spaced cross-sections. HEC-RAS is set to solve the fully implicit scheme with a fixed time-step of 1 sec, while HydroHP - 1D adaptive time-step scheme (see Eq. (6.16)) is used with $\Delta t_{\min} = 0.5$ sec, $\Delta t_{\max} = 5$ sec, $C = 0.5$,

6.3.5.3 Irregular Cross-Section

In this case study, we simulate the diffusive and convective effects in flow propagation in an open channel with irregular geometry. The goal is to determine looped rating curves and to estimate another possible source of uncertainty in stage-discharge modeling (Holmes, 2016).

For this analysis, we consider a 1000 m channel, discretized into 50 sub-reaches with $20-$ m length each. The bottom slope was assumed as 2×10^{-4} to represent a feasible condition for rivers where convective and advective accelerations play important roles. We assumed a normal-depth outlet

boundary condition, meaning that the energy slope gradient at the outlet is the same as the bottom slope.

To simulate the effects of convective / advective acceleration and the diffusive/kinematic effects of the flood wave, looped stage-discharge curves are modeled using an inlet boundary condition modeled with a nash-function hydrograph (Akan e Iyer, 2021; Gomes Jr et al., 2023c), which is defined as:

$$q_{in}(t) = q_b + (q_p - q_b)\Big[\frac{t}{t_p}\exp\Big(1 - \frac{t}{t_p}\Big)\Big]^{\gamma} \tag{6.21}$$

where q_{in} is the inflow hydrograph, q_b is the baseflow, q_p is the peak flow, t_p is the peak time, and γ shapes the hydrograph.

The aforementioned parameters are typically derived from hydrology studies of the upstream watershed. Therefore, they represent the degree to which surface and sub-surface runoff are generated. In detail, q_p is closely related to the watershed area, shape, infiltration, and imperiousness rate. In addition, the factor γ, shapes the rate of q_{in}, defining the flow acceleration; therefore, it is closely related to the aforementioned parameters of q_p. However, the parameter q_b, is mostly related to groundwater properties and soil infiltration capacity.

As parameters for modeling, we assumed $q_b = 1$ m^3/s, $q_p = 75$ m^3/s, and $t_p = 2$ hr. These values typically represent inbank conditions for the assumed river slope for normal flow. The simulation time was assumed as $t_f = 6$ hrs and the computational time-step was set as $\Delta t = 5$ sec. In this study, we test the possible effects of different hydrographs on unstable rating curves by varying γ from 2 to 10, with steps of two units to represent the effects of eventual urbanization in the watershed.

6.3.5.4 V-Notch and Rectangular Weir

In this sub-section, we test the effect of varying roughness for inbank and overbank conditions into unsteady rating-curve modeling. Data assumed for this sub-section are the same as the previous subsection, except for q_p and q_b which were assumed as 2% of the values from the previous section. As mentioned, we model the channel with two roughness coefficients using the divided-channel method. The assumed roughness coefficients for inbank and overbanks were 0.020 and 0.035, respectively.

6.3.5.5 Upper Negro River Stage-Discharge Curves Compared to Observed Data

The algorithms developed in this paper are applied to a cross-section of the Upper Negro River, located in the state of Amazonas - Brazil (see Fig. 6.11). The Negro River is the seventh largest river in the world in terms of volume and is the largest affluent of the Amazon River, the largest in the world in terms of volume. Observed data of the Negro River were retrieved from the Agência Nacional de Águas (ANA) database (ANA, 2022) for the stream gauge code of 14330000. Post-processing in raw data from the ANA database was performed in HidroAPP, available at (https://www.labhidro.ufsc.br/hidroapp/) (Souza et al., 2021). The cross-sections tested in this section are shown in Fig. 6.12.

Only years with consistent data were used in this analysis. Water surface flow slopes at this station vary monthly, with the highest variations in September. Furthermore, the slopes vary throughout the river, so that the average slope value for the Upper Negro River can be assumed to be $s_0 = 8$ cm/km (Marinho, 2022). Moreover, Manning's roughness coefficient varies with the depth of the water surface (Alves et al., 2017); however, in this section, we fixed a single roughness and slope for the sake of simplicity and to test the model's ability to predict normal flows and their occurrence compared to the observed data. We assume $n = 0.042$, a value in accordance with previous estimates found in Alves et al. (2017). Cross-sectional data were only available for years up to 1993. As a result,

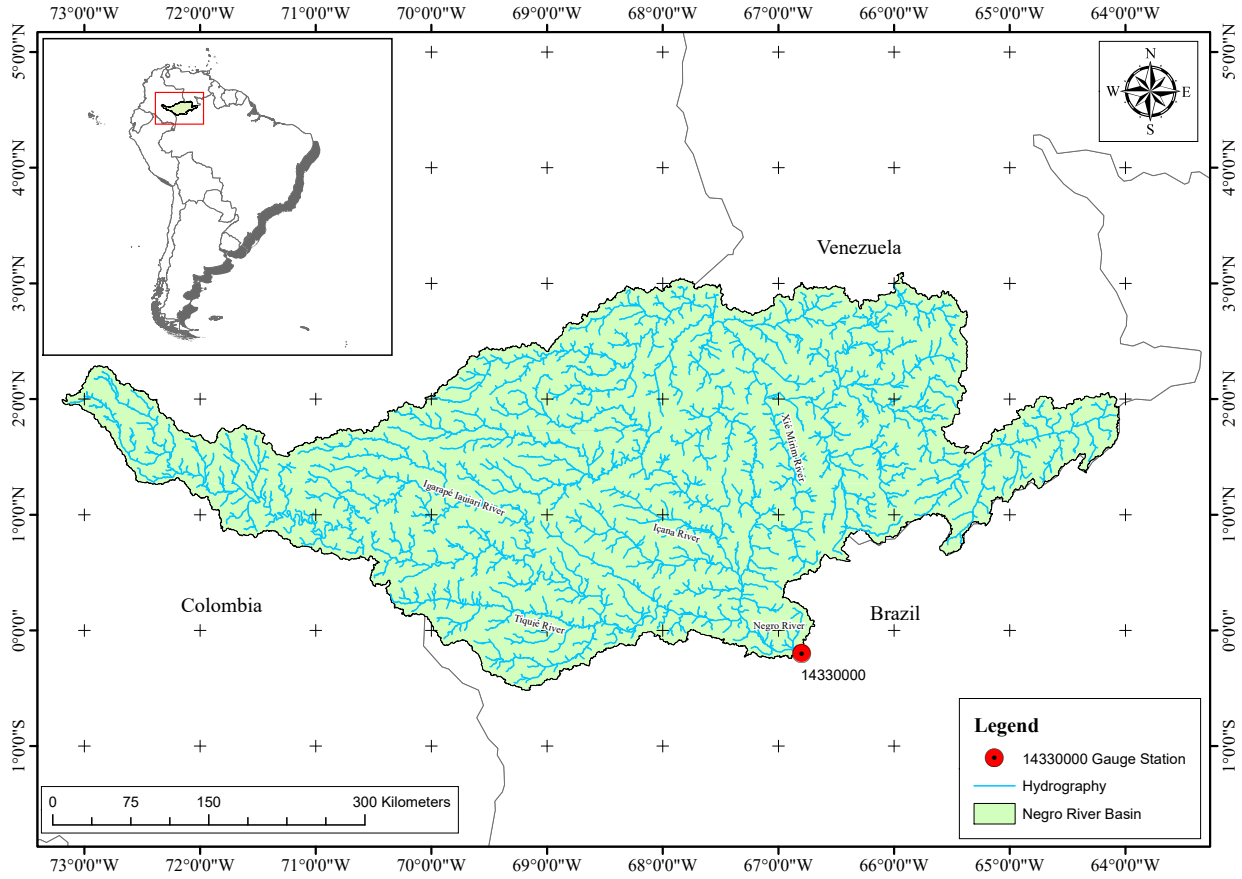

Figure 6.11. Upper Rio Negro River Basin with a drainage area of 200,204.6 km^2 , with an average yearly rainfall of 3,142 mm (Almagro et al., 2021).

the invert elevation of observed flow data from 1976 to 1999 was assumed to be the same as the last cross-section observation in 1993, (-6.97 m).

6.4 Results and Discussion

6.4.1 Numerical Case Study 1

6.4.1.1 Normal Flow in Complex Regular Cross-Sections

The results of the model application for triangular, parabolic, semi-elliptical/semi-parabolic cross-sections are presented in Fig. 6.6. The errors within the developed model and the NOAA normal depth solver are shown in Fig. 6.7. The HP values for $y^{\max}$ are shown in Table 6.1.

All relative errors of the developed model and the NOAA normal depth solver fault within a 10% difference, as presented in Fig. 6.7. For cross-sections T, P, and EP, errors were below 3% for discharge, area, perimeter, and top-width, and are almost negligible for velocity.

All HP curves are continuous and increase monotonically due to $\frac{\mathrm{d}y}{\mathrm{d}x}$ from the left or right directions. More specifically, although being relatively complex shapes (i.e., semi-elliptical/semi-parabolic) one could derive analytical expressions for perimeter, area, centroid, and others to solve SVE without requiring entering of HP values from tables. Examples of applications of SVE with complex but closed-form geometrical equations can be found in Simões et al. (2017).

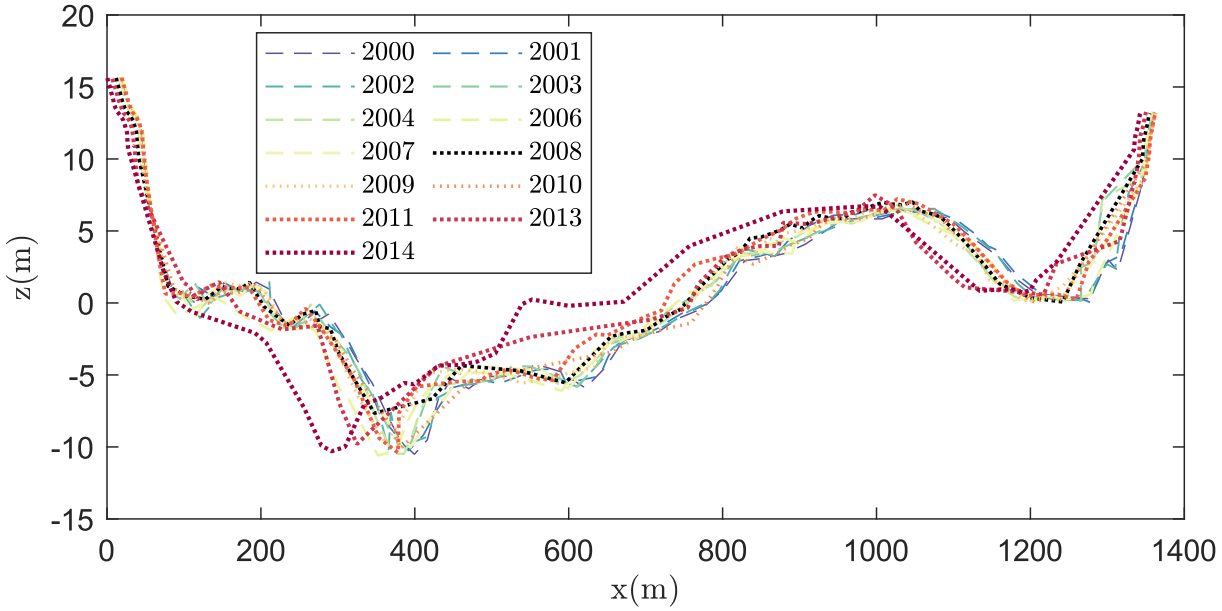

Figure 6.12. Cross-section data at stream gauge 14330000 in ANA's database (ANA, 2022), where validated years from 2000 to 2014 are plotted. Note that invert elevations change over cross-section different years.

6.4.2 Numerical Case Study 2

6.4.2.1 Normal Flow Modeling in Composite Cross-Sections

Cross-sections b), c) from Fig. 6.1 (i.e., P, EP) results are also presented in Fig. 6.6 and normal flow errors are shown in Fig. 6.7. The errors were approximately negligible compared to the NOAA solver and are mainly due to the introduction of noise (σ) into the x and y coordinates.

Although the stage-discharge relationship of sections P and EP was developed, a very fine numerical discretization in x and y was required for an accurate estimate of HP for these sections. We discretized y into 1 cm depth steps so that to define a 2-meter depth parabola and semi-ellipse/semi-parabola cross-sections we entered 400 coordinates in the model. In addition, in the model calculations, we assumed $\sigma = 1 \times 10^{-3}$ cm, which means 1,000 points each 1 cm. Ultimately, to properly capture the right HP in highly detailed cross-sections, one has to define proper numerical discretizations to avoid instabilities.

The greatest errors occurred for the Gabion (G) and Road Gutter (Gu) cross-sections. These errors occurred mainly due to the introduction of noise σ from Eq. (6.1) and due to the conceptualization of the SCM compared to the solution used in the NOAA solver (DCM).

6.4.3 Numerical Case Study 3

6.4.3.1 Normal Flow Modeling in Irregular Cross-Sections

We can see in Fig. 6.7 that the normal flow error was below 2%, even with different model conceptualizations from the NOAA solver and the model developed here. However, discontinuities occurred in geometrical functions such as area and perimeter, as shown in Fig. 6.6. These sharp changes occurred when the flow diverted from the main channel to overbanks. The conceptualization of the SCM model is a depth-based model assuming that the flow first propagates in the bank and after reaching the depth of the main channel y_{m} (see Fig. 6.10), the flow immediately diverts to the overbanks with the same elevation of the water surface elevation. In reality, more sophisticated software such as HEC-RAS, for example, can successfully model cross-section ineffective flow areas that could account

for effective oberbank flows (Brunner, 2016b).

6.4.3.2 Uncertainty in Steady Rating Curves for Inbank and Overbank Depths

The analytical determination of stage-conveyance figures for the irregular cross-section (g) in Fig. 7.7 is shown in Fig. 6.9. Two different behaviors were observed in the stage-conveyance modeling. First, for inbank conditions, flow is very similar to simpler cases of river rating curves as presented in Westerberg et al. (2011); Perumal et al. (2007). For the same design conveyance, water depths can have approximately 0.4 m difference for different scenarios of stage-roughness. As expected, the scenario with more hydraulic capacity was scenario (i), which assumed a single Manning's coefficient throughout the whole cross-section. On the contrary, scenario (iii) (i.e., stage variation of 2 orders in roughness) was the scenario with a lower hydraulic capacity (i.e., k). Part b) of Fig. 6.9 shows the stage-conveyance (i.e., $Q/\sqrt{s_0}$) after reaching y_{m} and the results show that 100% relative differences can occur when comparing different methods such as scenario (i) and scenario (iii), for the same depth. These results show the sensitivity of roughness coefficients in the modeling of rating curves and the importance of proper estimation of this parameter to accurately estimate flow discharges.

The Monte-Carlo analysis shows how various can be the conveyance and the at-station roughness coefficients, assuming typical uncertainty in roughness estimation with $\mu = 30\%$ and $\sigma_n = 0.01$, as presented in Part c) of Fig. 6.9. Part b) of Fig. 6.9 shows the plots of k for scenarios 2, 3, and 4 compared to k for scenario 1 (i.e., the baseline scenario). Generally, river cross-sections are assumed with constant roughness coefficients, and the results of this graph show that most of the time, comparisons within k_1 and k_i are below the 45° line, indicating that assuming a single roughness coefficient could be an overestimation of the hydraulic capacity of the cross-section up to 30% in inbank conditions and up to 100% in large overbank conditions. However, these results are obtained from a cross-section with overbanks of approximately 400 m and the main channel of nearly 10% of the overbanks.

6.4.4 Numerical Case Study 4

6.4.4.1 SCM x DCM Methods

The SCM and DCM differ specifically in two criteria: DCM herein considers an introduction of a shear stress acting at the interface between the overbanks and the main channel and considers an equivalent roughness that accounts for the divided conveyances. The SCM, however, considers a single section without the assumption of an increased perimeter in inbank-overbank interfaces. To this end, the differences in this method are most observed in cases where this new perimeter is comparable to the SCM perimeter increased by the overbank perimeter. This result can be observed in Table 6.1, where RE was only 3% for the irregular cross-section (i.e., $y_f = 0.4$ m, $b_m = 32.72$ m and $(p(y^{\max}) = 452.44$ m) but was 40% for the V-notch/Rectangular cross-section. The results of this section indicate that the SCM and DCM methods are more agreeable for sections with large overbanks widths and low overbank depths. Furthermore, they are the same for single sections, for complex sections, as shown in Table 6.1 for sections T, P and EP.

6.4.5 Numerical Case Study 5

6.4.5.1 Non-Breaking Wave - Comparing Analytical Solution with HydroHP - 1D and HEC-RAS

The modeling results are presented in Fig. 6.13 and shows the water surface elevation for different durations, varying from 12 min to 60 min. It is noted that neither HEC-RAS 1D model nor HydroHP - 1D model should match the analytical solution. The analytical solution is a simplification in 1D SWE to consider only diffusive effects. Therefore, in the interface between wet and dry sections,

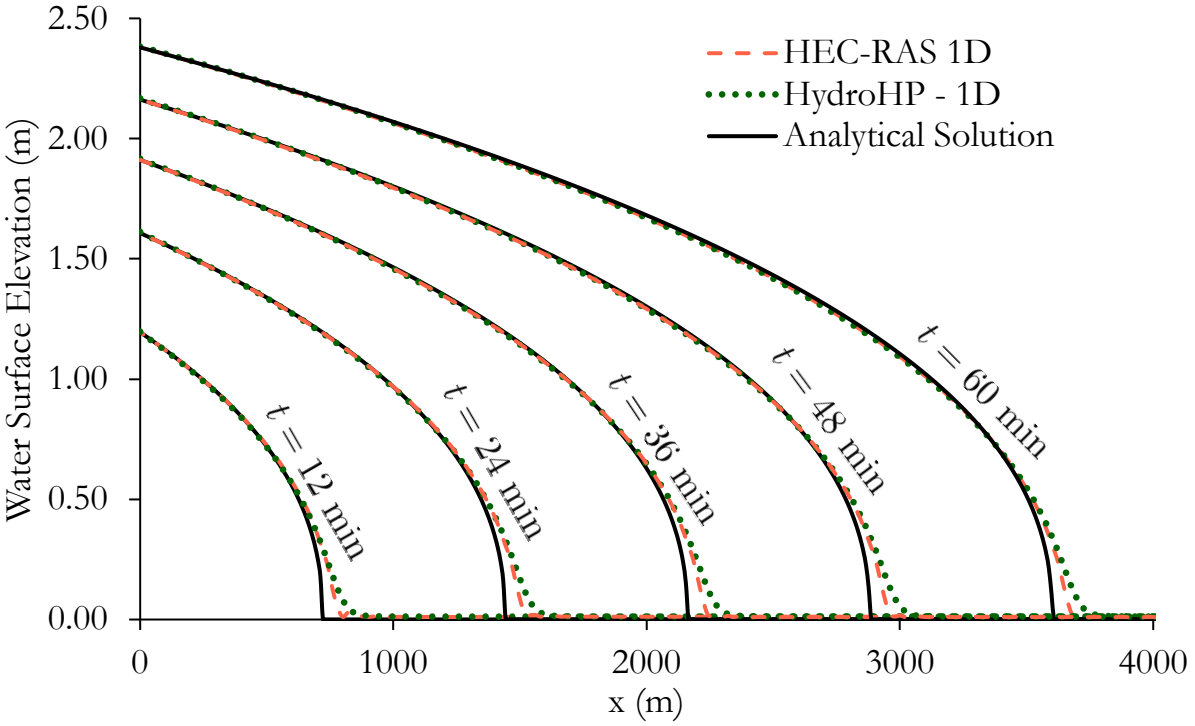

Figure 6.13. Dynamics of a Non-Breaking Wave simulated in HydroHP - 1D, HEC-RAS, compared with a diffusive-wave 1D analytical solution of the hydrodynamics under a flat surface modeled as a 100-m wide channel with no bottom slope. HEC-RAS and HydroHP - 1D models are built considering a stage-hydrograph boundary condition at the first cross-section of the domain following Eq. (6.20). All sections are modeled with stage-invariant roughness coefficient of 0.02 m.s$^{-1/3}$ and the wave has a 1 m/s celerity. . HEC-RAS model was built with cross-sections spanned 20 m, computational interval of 10 seconds, and the unsteady-state dynamics are solved via an implicit numerical scheme. HydroHP - 1D unsteady-state dynamics, however, are solved via explicit numerical scheme, requiring smaller time-steps and in this numerical case study is solved considering a 1 sec computational interval with cross-sections each 20 m.

HEC-RAS 1D and HydroHP - 1D should disagree with the analytical solution, especially because inertial effects become to play important roles in these cases. Similar results of the ones presented in Fig. 6.13 are shown in Bates et al. (2010); Hunter et al. (2005); Dottori e Todini (2011), indicating the inertial effects are responsible for changing the arrival time of the flood-wave in the dry frontier compared to a fully diffusive-like solution given by Eq. (6.20). HydroHP - 1D and HEC-RAS 1D model have slightly in the results of this problem due to differences related to mass conservation routines and numerical schemes used in both models.

6.4.5.2 Unsteady-State Inflow Hydrograph and Normal Flow at the Outlet

The results of the simulation of this numerical study are presented in Fig. 6.14. The HydroHP - 1D presented similar results with the HEC-RAS 1D implicit model, with Root Mean Square Errors (RMSE) of flows and discharges of 0.041 m^3/s and 0.053 m, respectively, as shown in Fig. 6.14a-b). Moreover, the coefficient of determination (r^2) for discharges and water surface elevations are 0.997 and 0.984. The largest differences between HEC-RAS 1D and HydroHP - 1D occurred in the inlet and in the falling limb of the hydrograph. Other studies indicate that the Lax-Friedrichs method can present numerical issues in the boundaries (Akan e Iyer, 2021; Kurganov, 2018) and this could be one of the reasons for this difference between the two models. Furthermore, since the discretization used for the solution of the partial differential equations is of first order accuracy, numerical diffusivity errors can propagate, even with the relatively fine mesh assumed (i.e., $\Delta x = 11.09$ m, $\Delta t_{\text{min}} = 0.5$ sec) (Kurganov, 2018). Although some differences are found between both models, the water surface elevation

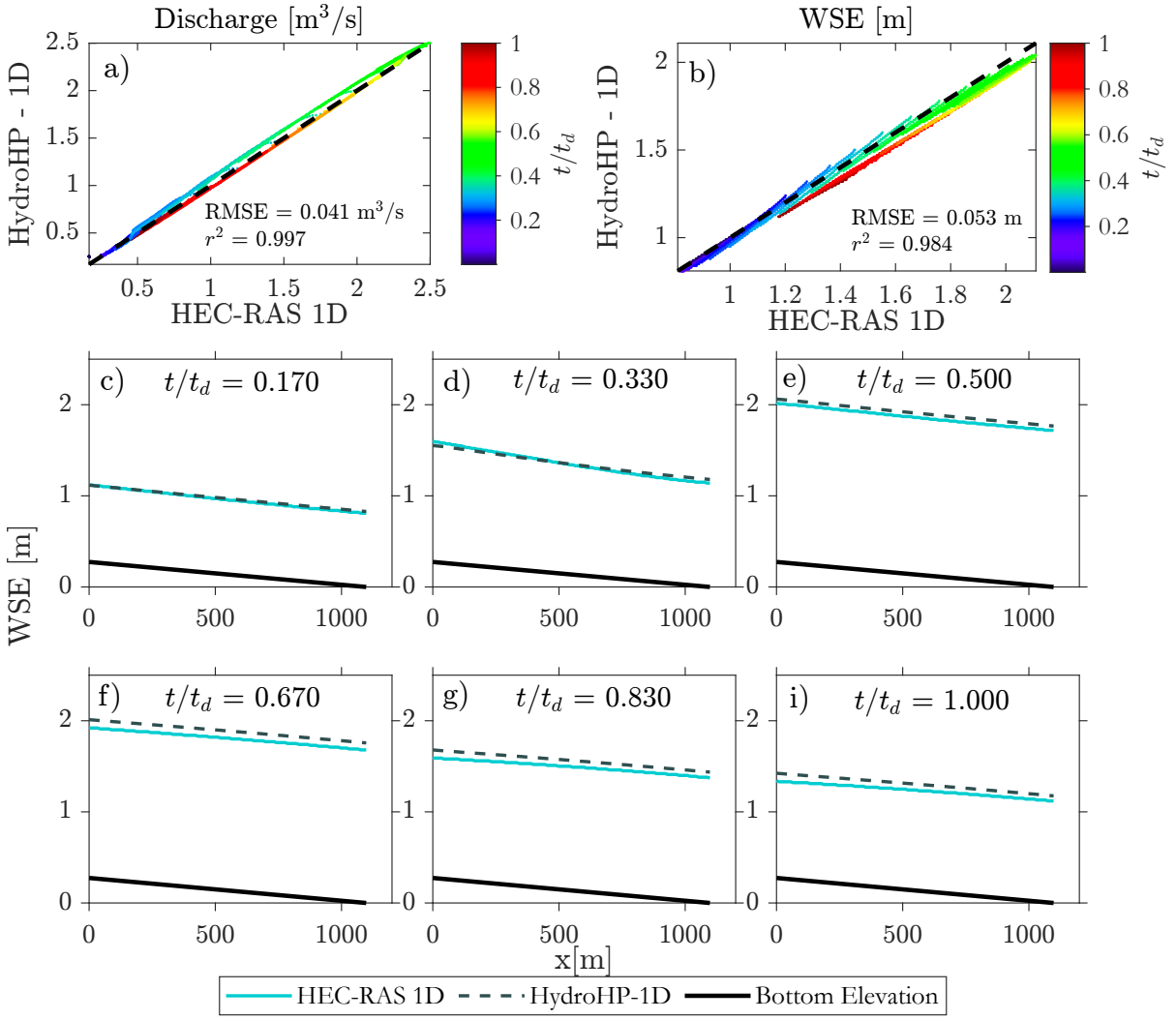

Figure 6.14. Modeling comparison within HEC-RAS 1D and HydroHP - 1D. Part a) shows the scatter plot of discharges for each section, for each time between both models, b) shows the same but for water surface elevation, plots c) to i) show water surface elevation profiles for 6 equally spaced intervals from $t = 0$ to $t = t_d$, where t_d is the simulation time of 360 minutes.

profiles shown in Fig. 6.14c-i) show the relatively small absolute differences between HEC-RAS 1D and HydroHP - 1D, indicating that the model can predict not only discharges but also water surface elevations.

6.4.5.3 Hysteresis Effect in Rating Curve Modeling

We compare results from steady and unsteady stage-discharge modeling for the irregular cross-section - the Little Washita River - in Fig. 7.7 g). The results indicate that the average errors within normal flows and flows modeled with a hydrodynamic model are up to 50% (e.g., see the stage at 2.5 m), as presented in Fig. 6.15. The results of this analysis are similar to the results shown in Muste e Lee (2013).

Differences in the rising limb of the hydrograph are relatively negligible for first inbank conditions (see part b at the stage of 3 meters, approximately); however, after reaching it, a sharp change in the flow discharge occurs due to the increased flow area from the second inbank region. The differences between the hydrodynamic cases of γ begin to increase after this stage, although they are getting closer to the normal flow towards the maximum stage. That indicates that local acceleration

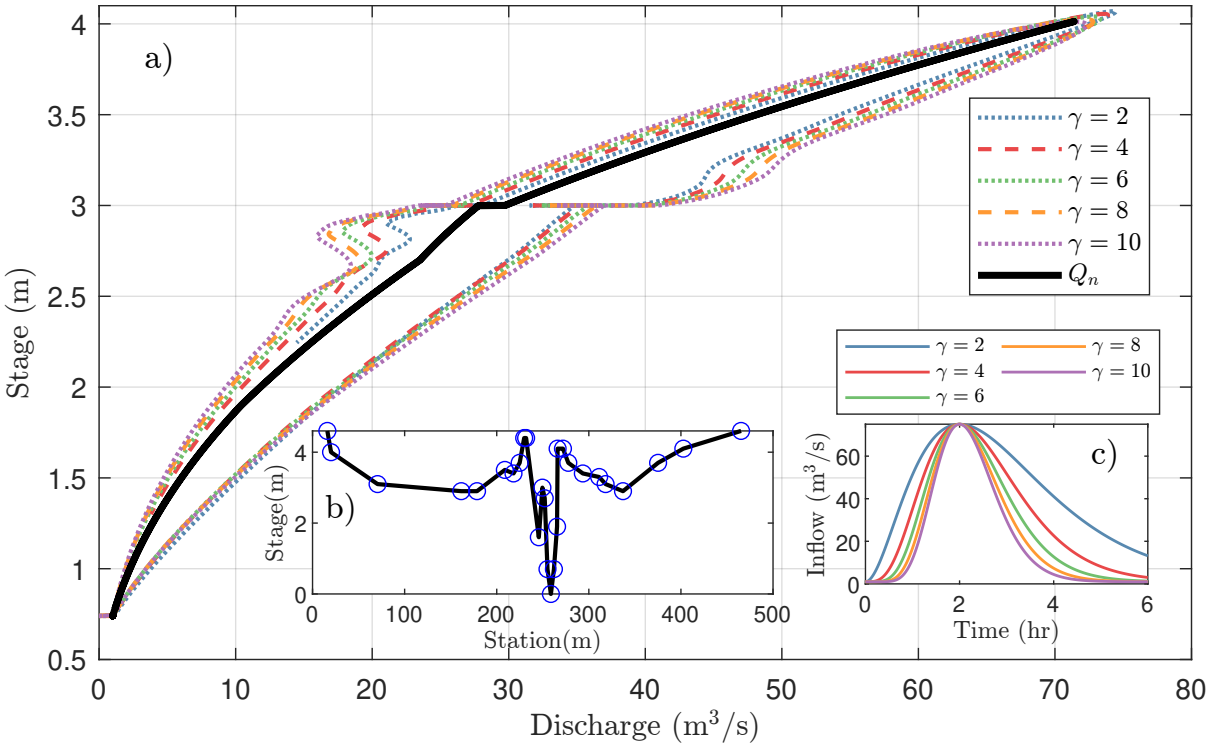

Figure 6.15. Inbank Unsteady Stage-Discharge compared with Steady Stage-Discharge for a composite irregular Cross-section with Manning's roughness coefficient of 0.020m.s$^{-1/3}$, where Q_n is the normal flow.

played a more important role at lower stages. The falling limb of the hydrograph shows a similar trend, with smaller flows for the highest γs. The results of this section can serve as a guide to model unsteady rating curves in the river and to assess the variation of complex rating curves variation for inbank conditions (Holmes, 2016).

The results of Fig. 6.16 show the results of the hydrodynamic simulation of the VR section of Fig. 7.7 with different roughness coefficients for inbank and overbank areas. As shown in this figure, the flow discharge can increase to 60% in the rising limb of the hydrograph, while it can decrease to 25% in the falling limb. This is particularly important when using v-notch weirs with a known material rugosity with walls and banks retrofitted with rougher materials such as rocks and local vegetation. Stage-discharge in weirs can carry large errors depending on the hydrograph properties of the inflow, as shown in Fig. 6.16. In addition, the role of changing the roughness of the overbanks is shown at the flow discharge rate of change after the stage of 1 m. Surprisingly, even when the roughness of the overbanks increases, the average roughness coefficient for the entire section using Eq. (6.12f) rapidly decreases after the stage of 1 m and starts to increase, reaching a value of 0.025 in the maximum stage. This reduction is due to the rapid increase in the perimeter, so that the average roughness coefficient would have to decrease to simulate the computation of the total conveyance as followed by Eq. (6.5b).

6.4.5.4 Normal Flow Rating Curve Modeling in Upper Negro River

Cross-section dynamic changes over time have not played the most important role in the modeling of the rating curve, except for 2008, as shown in Fig. 6.17. The invert elevation of the cross-section of this year is -7.66 m, whereas the invert elevations of the other years are -10.07 m $\pm$ 0.77 m, which explains the difference in y for the same flow discharge. However, we can visually infer from Fig. 6.12 that the cross-sections within years 2007 to 2009 have not dramatically changed, except for the invert. The difference in the invert elevation might be due to sediment deposition (de Almeida et al., 2016).

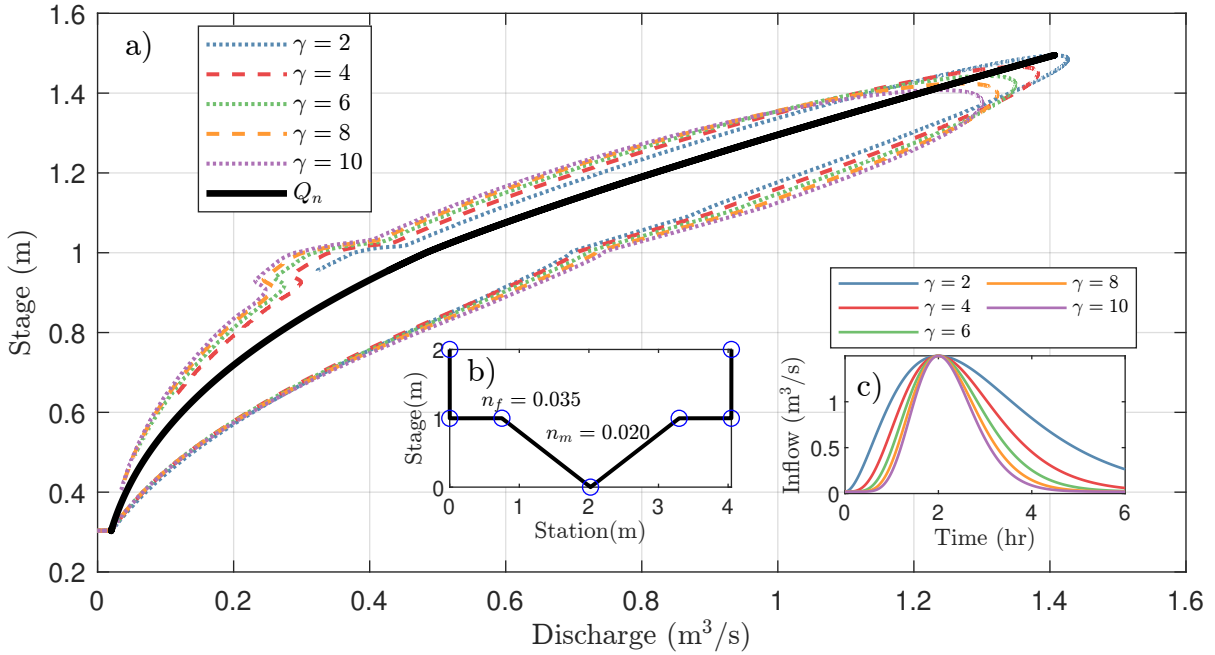

Figure 6.16. Unsteady Stage-Discharge compared with Steady Stage-Discharge for a composite V-Notch Rectangular Cross-section with inbank and overbank Manning's coefficients of 0.020 m.s$^{-1/3}$ and 0.035 m.s$^{-1/3}$, respectively, where Q_n is the normal flow.

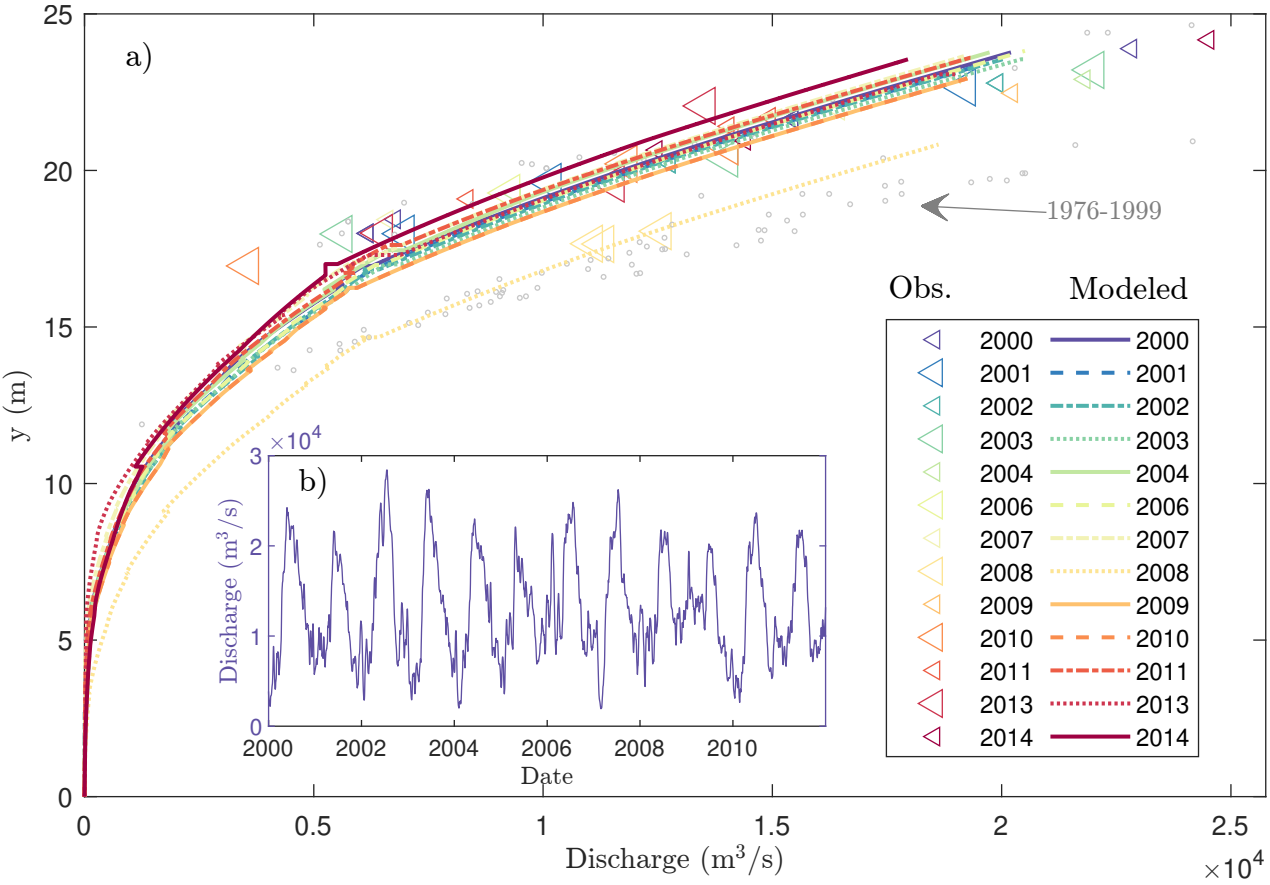

Figure 6.17. Stage-discharge curves for the Rio Negro, assuming normal flow with an 8 cm/km slope and a constant Manning's roughness coefficient of 0.042, where a) is the stage-discharge curves and b) the daily estimated hydrograph using ANA's rating curves. Surveyed stage elevations z(m) were converted to depths y(m) by subtracting the minimum values of z for each cross-section shown in Fig. 6.12

The daily hydrograph shown in Fig. 6.17b) shows average daily hydrographs. The values shown in this plot are calculated as follows: first, the average of two-stage measurements is calculated. Therefore, instantaneous peaks are generally smoothed. Following this, a fitted rating curve from ANA is used to convert stage to flow, resulting in this chart. The values of flow represent daily averages as mentioned above, whereas the plotted values of observations in Fig. 6.17a) are "instantaneous"observations. In other words, we can infer that observations are always upper-bounded by daily average maximum observations since maximum observations fall mostly below 2×10^4 m^3/s, while flow discharges have values above this threshold almost every year. It indicates that the measured data for flow discharges in this cross-section fail to capture the largest flows, which can impact statistically based rating curves derived from linear regression methods (Souza et al., 2021; Clarke et al., 2000).

The looped behavior found in the observed data from 1976-1999 could be from two main reasons: hysteresis effects, errors in the assumed invert-elevation dynamic change over the period due to deposition, erosion, and dunes formation, or due to changes in Manning's coefficient over time. Moreover, a systematic uncertainty is observed when comparing the model with observations. The model developed here assumes y_{max} as the maximum value within the left and right directions from the invert break-point. Therefore, the flow is not necessarily calculated for the maximum cross-section data z (see Fig. 6.12). However, observations of flows are found to be higher than these levels, as shown in Fig. 6.17. Values found at these stages are not modeled but can also be the result of hysteresis effects.

6.4.6 Strengths and Weaknesses of the Presented Model

The set of algorithms developed in this paper can be used to solve different types of hydraulic problems, varying from regular concrete channels, to complex shapes or irregular cross-sections with overbanks and depth-varying roughness. Some strengths and weaknesses of the model are presented as follows:

6.4.6.1 Strengths

- Flexibility to simulate all kinds of single cross-sections or composite sections with two overbanks.
- Simulate the role of stage-varying roughness
- Simulate the role of "at-station"roughness variation
- Assess the uncertainty in the estimation of rating curves by deploying Monte-Carlo analysis
- No need to define an iterative problem to solve Manning's equation, as required by other models (US Department of Commerce, 2016; Brunner, 2016b) either by performing polynomial approximations for cross-section segments or by defining linear interpolations.
- Relatively fast computations and the possibility of parallelization for normal flow estimations for large-scale cases.
- Simulate the hysteresis effect in unsteady rating-curve modeling

6.4.6.2 Weaknesses

- Time-invariant hydraulic parameters that could be conceptualized as time-varying parameters to consider riverine changes due to erosion and deposition. Moreover, this tool does not allow simulation of sediment-laden flows that can contribute to time-varying changes during flow propagation.
- The model did not explain cases with more than 2 overbanks (e.g., the case of the gabion channel is shown in Fig. 6.1 with results presented in Fig. 6.10 and Fig. 6.6).

- During the rising limb of the hydrograph in a cross-section with overbanks, flow is confined first to the inbank and later propagated to the overbanks after the level reaches the overbank level. However, this might not always be the case (e.g., HEC-RAS considers that flow can go for the overbanks even when the level has not reached the overbank level.

- The change in the cross-section by adding a noise σ can be important for channels with small dimensions (e.g., road gutter cross-section) due to being significant in the calculations of HP. Moreover, the proper definition of σ is required for simulating detailed cross-sections as the Parabolic and Semi-Elliptical/Semi-Parabolic cross-sections. Therefore, more points and more computational efforts are required to simulate these aforementioned sections with accurate results.

- The DCM method applied in this paper, although it solves the problem of non-monotonic conveyance curves by adding overbank and inbank conveyances due to the correction of $\bar{n}$ in Eq. (6.12e), still carries discontinuities when sharp areas and perimeters are added in inbank conditions.

- Overall, the modeling of the rating curve with fixed parameters for roughness and slope showed good results in the Upper Rio Negro. The model was able to predict flows within the cross-section range for most cases. Some outliers are found and could be explained by different friction slopes or roughness coefficients. However, defining the proper stage-roughness functions or the friction slopes is difficult and would require knowing a proper inflow hydrograph, which is typically unavailable for resolutions higher than 1 day in Brazil.

6.5 Conclusions and Future Work

The development of two algorithms for HP estimations in regular, composite, and irregular cross-sections capable of simulating stage-varying roughness and "at-station"varying roughness variation is performed. The results of model validation indicate predictions of normal flows within average relative errors of approximately 5% when compared to an established normal depth solver. Moreover, HydroHP - 1D results are consistent with HEC-RAS 1D model not only for a wave-propagation condition but also for unsteady-state simulation with inflow hydrograph at the inlet and normal slope at the outlet. From the results, we draw the following conclusions.

- The developed algorithms can represent normal flow conditions for complex cases and irregular cross-sections with the Single Method Channel and Divided Method Channel.

- The greater differences within SCM and DCM methods occurred for V-Notch Cross-sections and Road Gutter cross-sections. These are sections of relatively large overbanks compared to the cross-section height.

- Only a 3% difference between SCM and DCM occurred for the maximum water height in the irregular cross-section, indicating that flow discharges at the maximum stage for irregular channels with relatively large overbanks (i.e., $b_m/b_f \leq 0.1$, where b_f is the overbank width) assuming maximum levels, both methods are more comparable.

- Assuming feasible scenarios of stage-roughness in an irregular channel, inbank stage-discharge, for the same discharge, can have a stage variation of ($\sim$ 0.40 m). For overbank stage-discharge, however, this difference is typically smaller ($\sim$ 0.3 m). Additionally, for the same water depth, k can increase to 100%, indicating that the flow is highly influenced by the overbank areas and roughness.

- The unsteady rating curves modeled in this paper for an irregular cross-section indicated an increase of 50% and a decrease of 25% for the rising and falling limb of the hydrographs.

- Similar results were found for a composite V-Notch rectangular weir where errors between normal flow and unsteady flow would be up to 60% and 25% for the rising and falling limb of the hydrographs.
- Normal flow discharges in the Negro River assuming a constant Manning's roughness coefficient and bottom slope show good results without requiring calibrations or statistical analyses. The results show that, even with these assumptions, the developed model can accurately predict stage-discharge in real-world stream gauges.

Future application of the developed model will be in estimating rating curves for ungauged rivers in Brazil, where data in suitable resolution are sometimes available, but little information regarding flow discharges is displayed. Furthermore, we want to exploit the role of shear stress in more fundamental ways than by assuming a linear increase in the hydraulic perimeter on the main channel. Moreover, future versions will allow entering different cross-sections and interpolating them instead of simulating a single cross-section. In addition, sediment-laden flows and a movable overbed channel can be explored to explain dynamic changes on stage-discharge during monitored events in remote-sensed areas.

Acknowledgment

The authors appreciate the support from CAPES for funding this research. The authors also appreciate the effort made by Eng. Mateo Hernandez who gently helped with the HEC-RAS modeling.

Supplementary Material

Supplementary data related to this article can be found at

https://github.com/marcusnobrega-eng/HydroHP-1D.

Data Availability Statement

Algorithms and data used are available in an open repository at (Gomes Jr., M. N., 2022).

References

Abril, J. e Knight, D. (2004). Stage-discharge prediction for rivers in flood applying a depth-averaged model. *Journal of Hydraulic Research*, 42(6):616–629.

Akan, A. O. e Iyer, S. S. (2021). *Open channel hydraulics*. Butterworth-Heinemann.

Al-Khatib, I. A., Dweik, A. A., e Gogus, M. (2012). Evaluation of separate channel methods for discharge computation in asymmetric compound channels. *Flow Measurement and Instrumentation*, 24:19–25.

Almagro, A., Oliveira, P. T. S., Meira Neto, A. A., Roy, T., e Troch, P. (2021). Cabra: a novel large-sample dataset for brazilian catchments. *Hydrology and Earth System Sciences*, 25(6):3105–3135.

Alves, L. G. S., da Silva, D. D., Vauchel, P., Fraizy, P., e Filizola, N. P. (2020). Variable backwater and channel roughness: effects on solimões river discharge. *Comptes Rendus. Géoscience*, 352(3):185–198.

Alves, L. G. S., Silva, D., Filizola, N., e Pruski, F. (2017). Estimativa do coeficiente de manning para cálculo de vazão em regime sob efeito de remanso hidráulico na bacia amazônica. *XX Simpósio Brasileiro de Recursos Hídricos, 2017a. Florianópolis, Santa Catarina-Brasil*.

ANA (2022). Hidroweb. (http://www.snirh.gov.br/hidroweb/).

Barker, P. M. e McDougall, T. J. (2020). Two interpolation methods using multiply-rotated piecewise cubic hermite interpolating polynomials. *Journal of Atmospheric and Oceanic Technology*, 37(4):605–619.

Bates, P. D., Horritt, M. S., e Fewtrell, T. J. (2010). A simple inertial formulation of the shallow water equations for efficient two-dimensional flood inundation modelling. *Journal of hydrology*, 387(1-2):33–45.

Brunner, G. W. (2016b). Hec-ras river analysis system modeling user's manual us army corps of engineers hydrologic engineering center. *Information on http://www. hec. usace. army. mil*.

Chanson, H. (2004). *Hydraulics of open channel flow*. Elsevier.

Chen, W.-B., Liu, W.-C., e Wu, C.-Y. (2013). Coupling of a one-dimensional river routing model and a three-dimensional ocean model to predict overbank flows in a complex river–ocean system. *Applied Mathematical Modelling*, 37(9):6163–6176.

Chow, V. t. (2010b). *Applied hydrology*. Tata McGraw-Hill Education.

Clarke, R. T., Mendiondo, E., e Brusa, L. (2000). Uncertainties in mean discharges from two large south american rivers due to rating curve variability. *Hydrological Sciences Journal*, 45(2):221–236.

Courant, R., Friedrichs, K., e Lewy, H. (1928). Über die partiellen differenzengleichungen der mathematischen physik. *Mathematische annalen*, 100(1):32–74.

Cunge, J. (1980). Practical aspects of computational river hydraulics. *Pitman Publishing Ltd. London,(17 CUN), 1980, 420*.

de Almeida, R. P., Galeazzi, C. P., Freitas, B. T., Janikian, L., Ianniruberto, M., e Marconato, A. (2016). Large barchanoid dunes in the amazon river and the rock record: Implications for interpreting large river systems. *Earth and Planetary Science Letters*, 454:92–102.

Dingman, S. L. (2007). Analytical derivation of at-a-station hydraulic–geometry relations. *Journal of Hydrology*, 334(1-2):17–27.

Domeneghetti, A., Castellarin, A., e Brath, A. (2012). Assessing rating-curve uncertainty and its effects on hydraulic model calibration. *Hydrology and Earth System Sciences*, 16(4):1191–1202.

Dottori, F., Martina, M., e Todini, E. (2009). A dynamic rating curve approach to indirect discharge measurement. *Hydrology and Earth System Sciences*, 13(6):847–863.

Dottori, F. e Todini, E. (2011). Developments of a flood inundation model based on the cellular automata approach: testing different methods to improve model performance. *Physics and Chemistry of the Earth, Parts A/B/C*, 36(7-8):266–280.

Einstein, H. (1934). Der hydraulische oder profil-radius. *Schweizerische Bauzeitung*, 103(8):89–91.

Farina, G., Alvisi, S., Franchini, M., Corato, G., e Moramarco, T. (2015). Estimation of bathymetry (and discharge) in natural river cross-sections by using an entropy approach. *Journal of Hydrology*, 527:20–29.

Fernandes, J. N. (2021a). Apparent roughness coefficient in overbank flows. *Springer Science and Business Media LLC*, 3(7).

Fernandes, J. N. (2021b). Apparent roughness coefficient in overbank flows. *SN Applied Sciences*, 3(7):1–10.

Garbrecht, J. (1990). Analytical representation of cross-section hydraulic properties. *Journal of hydrology*, 119(1-4):43–56.

Gerbeau, J.-F. e Perthame, B. (2000). *Derivation of viscous Saint-Venant system for laminar shallow water; numerical validation*. PhD thesis, INRIA.

Ghanghas, A., Dey, S., e Merwade, V. (2022). Evaluating the reliability of synthetic rating curves for continental scale flood mapping. *Journal of Hydrology*, 606:127470.

Gleason, C. J. (2015). Hydraulic geometry of natural rivers: A review and future directions. *Progress in Physical Geography*, 39(3):337–360.

Gomes Jr, M. N., Rápalo, L. M., Oliveira, P. T., Giacomoni, M. H., do Lago, C. A., e Mendiondo, E. M. (2023c). Modeling unsteady and steady 1d hydrodynamics under different hydraulic conceptualizations: Model/software development and case studies. *Environmental Modelling & Software*, page 105733.

Gomes Jr., M. N. (2022). HP Estimator - Rating Curve - V5. https://github.com/marcusnobrega-eng/HyProSWE.

Holmes, R. (2016). River rating complexity. In *Proceedings of the International Conference on Fluvial Hydralics (River Flow 2016), St. Louis, USA*.

Horton, R. E. (1933). Separate roughness coefficients for channel bottom and sides. *Engineering News-Record*, 111(22):652–653.

HOSSEINI, S. M. (2004). Equations for discharge calculation in compound channels having homogeneous roughness. *IRANIAN JOURNAL OF SCIENCE AND TECHNOLOGY TRANSACTION B-ENGINEERING*.

Hrafnkelsson, B., Sigurdarson, H., Rögnvaldsson, S., Jansson, A. Ö., Vias, R. D., e Gardarsson, S. M. (2021). Generalization of the power-law rating curve using hydrodynamic theory and bayesian hierarchical modeling. *Environmetrics*.

Hua, W., Yang, K.-j., Cao, S.-y., e Liu, X.-n. (2007). Computation of momentum transfer coefficient and conveyance capacity in compound channels. *Journal of Hydrodynamics, Ser. B*, 19(2):225–229.

Hunter, N. M., Horritt, M. S., Bates, P. D., Wilson, M. D., e Werner, M. G. (2005). An adaptive time step solution for raster-based storage cell modelling of floodplain inundation. *Advances in water resources*, 28(9):975–991.

Khodashenas, S. R. e Paquier, A. (1999). A geometrical method for computing the distribution of boundary shear stress across irregular straight open channels. *Journal of Hydraulic Research*, 37(3):381–388.

Kidson, R., Richards, K., e Carling, P. (2006). Hydraulic model calibration for extreme floods in bedrock-confined channels: case study from northern thailand. *Hydrological Processes: An International Journal*, 20(2):329–344.

Kim, J.-S., Lee, C.-J., Kim, W., e Kim, Y.-J. (2010). Roughness coefficient and its uncertainty in gravel-bed river. *Water Science and Engineering*, 3(2):217–232.

Kuczera, G. (1996). Correlated rating curve error in flood frequency inference. *Water resources research*, 32(7):2119–2127.

Kurganov, A. (2018). Finite-volume schemes for shallow-water equations. *Acta numerica*, 27:289–351.

Lang, M., Pobanz, K., Renard, B., Renouf, E., e Sauquet, E. (2010). Extrapolation of rating curves by hydraulic modelling, with application to flood frequency analysis. *Hydrological Sciences Journal–Journal des Sciences Hydrologiques*, 55(6):883–898.

Lax, P. D. (1954). Weak solutions of nonlinear hyperbolic equations and their numerical computation. *Communications on pure and applied mathematics*, 7(1):159–193.

Manfreda, S. (2018). On the derivation of flow rating curves in data-scarce environments. *Journal of Hydrology*, 562:151–154.

Marinho, R. R. (2022). Perfil longitudinal do rio negro a partir da altimetria radar. In *Anais do Congresso de Iniciação Científica da UFAM*.

Moncoulon, D., Labat, D., Ardon, J., Leblois, E., Onfroy, T., Poulard, C., Aji, S., Rémy, A., e Quantin, A. (2014). Analysis of the french insurance market exposure to floods: a stochastic model combining river overflow and surface runoff. *Natural Hazards and Earth System Sciences*, 14(9):2469–2485.

Mustaffa, N., Ahmad, N., e Razi, M. (2016). Variations of roughness coefficients with flow depth of grassed swale. In *IOP Conference Series: Materials Science and Engineering*, volume 136, page 012082. IOP Publishing.

Muste, M., Kim, D., e Kim, K. (2022). A flood-crest forecast prototype for river floods using only in-stream measurements. *Communications Earth & Environment*, 3(1):1–10.

Muste, M. e Lee, K. (2013). Quantification of hysteretic behavior in streamflow rating curves. In *Proceeding of 2013 IAHR World Congress, Chengdu, China*.

Perret, E., Lang, M., e Le Coz, J. (2022). A framework for detecting stage-discharge hysteresis due to flow unsteadiness: Application to frances national hydrometry network. *Journal of Hydrology*, 608:127567.

Perumal, M., Moramarco, T., Sahoo, B., e Barbetta, S. (2007). A methodology for discharge estimation and rating curve development at ungauged river sites. *Water Resources Research*, 43(2).

Petersen-Øverleir, A. (2006). Modelling stagedischarge relationships affected by hysteresis using the jones formula and nonlinear regression. *Hydrological sciences journal*, 51(3):365–388.

Petikas, I., Keramaris, E., e Kanakoudis, V. (2020). Calculation of multiple critical depths in open channels using an adaptive cubic polynomials algorithm. *Water*, 12(3):799.

Roohi, M., Soleymani, K., Salimi, M., e Heidari, M. (2020). Numerical evaluation of the general flow hydraulics and estimation of the river plain by solving the saint–venant equation. *Modeling Earth Systems and Environment*, 6(2):645–658.

Rossman, L. A. et al. (2010). *Storm water management model user's manual, version 5.0*. National Risk Management Research Laboratory, Office of Research and Development, U.S. Environmental Protection Agency.

Sahu, M., Khatua, K., e Mahapatra, S. (2011). A neural network approach for prediction of discharge in straight compound open channel flow. *Flow Measurement and Instrumentation*, 22(5):438–446.

Simões, A. L. A., Schulz, H. E., e Porto, R. d. M. (2017). *Métodos computacionais em hidráulica*. EDUFBA.

Souza, K. I. S. d. et al. (2021). *Definição de áreas de preservação permanente com função de proteção aos recursos hídricos naturais*. PhD thesis, Universidade Federal de Santa Catarina.

Stephenson, D. e Kolovopoulos, P. (1990). Effects of momentum transfer in compound channels. *Journal of hydraulic engineering*, 116(12):1512–1522.

Strelkoff, T. (1970). Numerical solution of saint-venant equations. *Journal of the Hydraulics division*, 96(1):223–252.

Sturm, T. W. (2021). *Open channel hydraulics*. McGraw-Hill Education.

US Department of Commerce, N. (2016).

Vasconcelos, J. G., Wright, S. J., e Roe, P. L. (2006). Improved simulation of flow regime transition in sewers: Two-component pressure approach. *Journal of hydraulic engineering*, 132(6):553–562.

Westerberg, I., Guerrero, J.-L., Seibert, J., Beven, K., e Halldin, S. (2011). Stage-discharge uncertainty derived with a non-stationary rating curve in the choluteca river, honduras. *Hydrological Processes*, 25(4):603–613.

Wolfs, V. e Willems, P. (2014). Development of discharge-stage curves affected by hysteresis using time varying models, model trees and neural networks. *Environmental Modelling & Software*, 55:107–119.

Yang, F., Liang, D., e Xiao, Y. (2018). Influence of boussinesq coefficient on depth-averaged modelling of rapid flows. *Journal of Hydrology*, 559:909–919.

Zarmehi, F., Tavakoli, A., e Rahimpour, M. (2011). On numerical stabilization in the solution of saint-venant equations using the finite element method. *Computers & Mathematics with Applications*, 62(4):1957–1968.

Zheng, X., Tarboton, D. G., Maidment, D. R., Liu, Y. Y., e Passalacqua, P. (2018). River channel geometry and rating curve estimation using height above the nearest drainage. *JAWRA Journal of the American Water Resources Association*, 54(4):785–806.

7 INCREASING FLOOD AWARENESS THROUGH DAM-BREAK SERIOUS GAMES

A modified version was submitted as: Gomes Jr, M.N., Castro, M. A. R. A., da Silva, P. G. C., Giacomoni, M.H., Mendiondo E.M., 2023. Increasing Flood Awareness Through Dam-Breach Serious Games. *International Journal of Disaster Risk Reduction*.

Graphical Abstract

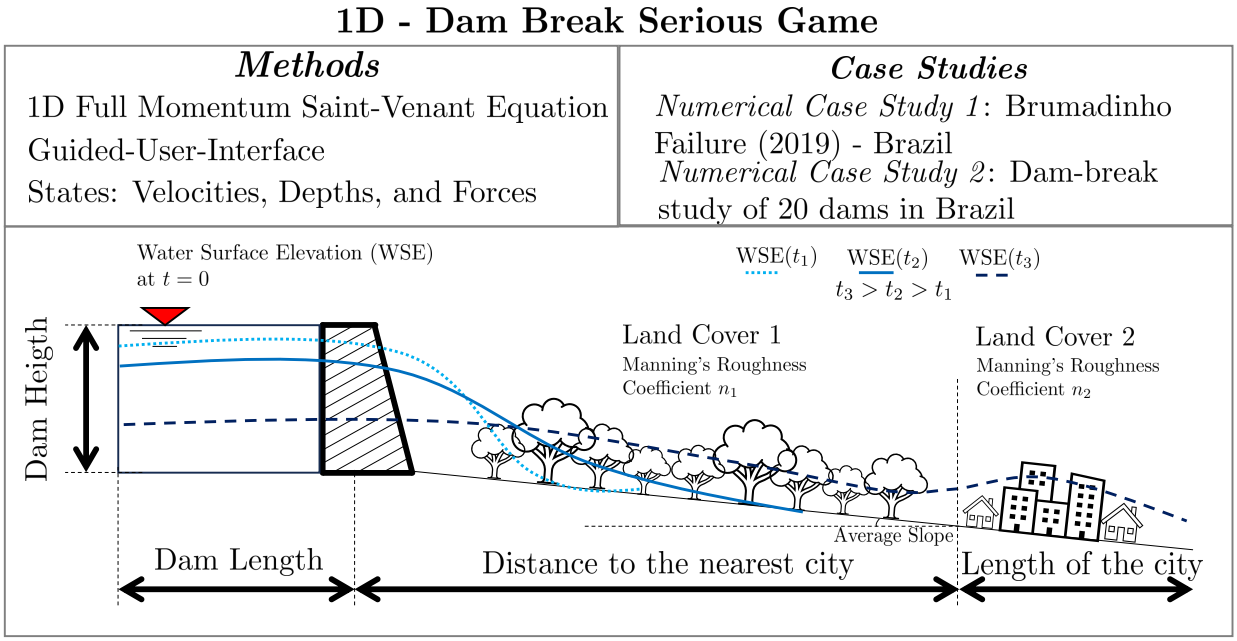

Highlights

- We develop a simplified model approach to assess the Dam Break problem.
- The model can be used for serious-gaming approaches.
- The model solves the 1D full momentum Saint-Venant equations assuming an inlet hydrograph boundary condition.
- Results of 21 dams in Brazil are presented and the potential dam-break hazards are discussed.

Abstract

Dams are one of the most important human-made structures ever conceptualized and allow the development of society by providing multiple uses, such as the development of hydroelectric plants and as a source of water supply. A dam break problem is a catastrophic event that evolves rapidly, causing uncontrollable large floods downstream. In this paper, we develop a simplified modeling approach to assess flood characteristics associated with dam-break problems. The method offers a useful tool to improve the perception of dam safety in terms of the hydrodynamic impacts associated with a dam break. We apply our framework to 20 dams in Brazil, in addition to the Brumadinho dam failure at Córrego do Feijão. This event occurred in Brazil in 2019 leading to almost 300 fatalities. The second case study demonstrates the use of the modelling framework developed in this paper through the simulation of 20 dams in Brazil. The modeling approach uses GIS databases, Google Earth, and

National Water Agency (ANA) databases and can be replicated whenever GIS information on dam characteristics, downstream channel, and downstream community is available. The results of this modeling approach indicate that several dams in the northeast of Brazil have relatively large flood hazards. A simplified dam-break hazard index was developed to establish a relative hazard impact that considers only deterministic factors such as the hydrodynamic force, velocity, and depth, as well as the arrival time of the maximum values of these states. These values are determined by a 1-D full momentum solver model (HydroHP-1D). *Keywords:* Flood Hazard, Serious Games, Risk Perception, Hydrodynamic Forces, Hydrodynamic Modeling

7.1 Introduction

Dams have contributed significantly to the development of civilization and are one of the most important human-made infrastructure. With a relatively high stored volume and relatively high depths, a dam break problem is a catastrophic event that evolves shortly and rapidly, causing uncontrollable large floods downstream. Despite the associated potential damages, dams are a versatile strategy used for multiple uses such as waste disposal, energy generation, and flood control (Aureli et al., 2021; Monte et al., 2017; Lauriano e Brasil, 2009).

Dam maintenance requires permanent monitoring throughout its lifespan to reduce the risk of failure. Dam safety can be defined in multiple ways, depending on the context of a country. The United States Federal Emergency Management Agency (FEMA) defines dam safety as the art and science of ensuring the integrity and viability of dams such that they do not present unacceptable risks to the public, property, and the environment, and the main steps to achieve proper dam safety are (a) adequate engineering design and construction, (b) regular surveillance (monitoring and inspections), (c) adequate operation and maintenance, and (d) plans to deal with emergencies (Burke et al., 2023).

The safety of these structures is an increasing concern in modern society, with a focus on the safety of dams and dikes (Toledo e Moran, 2022). Tailings dams, which are mining waste impounding structures, can pose higher failure rates and more safety concerns compared to conventional dams (Adamo et al., 2020a; Owen et al., 2020). Furthermore, embankment dams represent the most prevalent type of dam constructed on a global scale; however, their long-term stability poses a challenge due to a myriad of factors, including processes and human activities (Adamo et al., 2020b,a). Despite notable advances in dam construction practices, dam failures underscore persistent knowledge gaps within the realm of dam safety. The imperative for dam safety transcends the initial phases of design and construction, which requires ongoing vigilant monitoring throughout the entire dam lifecycle.

Assessing the potential impacts and damages caused by a failure depends on the accurate determination of the probabilities of dam failure (Psomiadis et al., 2021; Bilali et al., 2022). Even with the increased capacity to design and construct safer and more efficient dams in recent decades, more than 200 dams failed worldwide only in the 20th century (Luino et al., 2014).

Brazil had recently experienced two large dam failures. The Mariana dam failure (2015) and, more recently, Brumadinho dam failure (2019) caused almost 300 deaths combined. According to the National Dam Safety Information System (SNISB) of Brazil and with the 2010 Brazilian Institute of Geography and Statistics (IBGE) census, in Brazil, approximately 1 million people live up to 1 kilometer away from one of the 1,220 dams classified as high risk and high potential damage. According to an IBGE survey, 39 of these classified dams were designed for the storage of waste mines, which are considered highly unstable and responsible for the two aforementioned disasters that recently occurred in Brazil.

More countries are increasingly issuing dam safety legislation (Bradlow et al., 2002; Pisaniello et al., 2015), so that medium or large dam projects must incorporate studies to prepare and understand

impacts in downstream vulnerable communities to rapidly adapt and cope in an eventual dam-break case. These studies are generally called Emergency Action Plan (EAP) and aim at the planning of evacuation strategies for the riverine population living downstream of dams and also focus on the minimization of associated losses in the event of a dam failure. EAPs must contain the flood inundation and extent map, which is often derived from hydrodynamic models capable of estimating flood depths, velocities, and associated hydrodynamic forces (ANA, 2016). Herein, hydrodynamic forces are assumed to be the force derived from the static and dynamic pressure calculated with (7.1).

7.1.1 Literature Review

The cause associated with dam failure can be derived from an external force (e.g., earthquake) or internal erosion. Studies indicate that the appearance of this rupture may occur due to various causes such as infiltration, current overtopping due to insufficient spillway capacity, penetration, and even liquefaction due to earthquakes (Dincergok, 2007; Yi, 2011). Regardless of the reason, most failures are triggered by the formation of a breach. In other words, the rupture, responsible for the dam failure, can be understood as an opening formed in the body of the dam that causes the concentrated water behind the dam to flow downstream. Although the main types of failure have been identified as piping or overtopping, the actual mechanics of failure are not sufficiently understood for earth or concrete dams (Zhang et al., 2016). EAP studies typically assume different types of failure and estimate the associated downstream hydrograph in terms of the breach characteristics (Brunner, 2016b).

According to SNISB, Brazil classifies dam safety using two main indices: the associated potential damage (DPA) and the risk category (CRI). The first is calculated considering the damage that the dam can potentially cause to elements located downstream, through a mathematical expression that depends on the total volume of the reservoir, the number of human lives downstream, the existence of environmental preservation areas, and the existence of commercial facilities or economic activities. According to the DPA methodology, dams can be classified as high (DPA $\geq$ 16), medium (10 $<$ DPA $<$ 16) or low (DPA $\leq$ 10) damage. The second index (CRI) is calculated as the sum of a set of three subcategories: (I) technical characteristics (CT), (II) state of conservation (EC), and (III) security plan (PS). CRI classifies dams as high (CRI $\geq$ 62 or EC $\geq$ 8), medium (35 $<$ DPA $<$ 62) or low (CRI $\leq$ 35) risk. Using such a type of classification allows rapid identification of the potential risks of the dam, although they do not consider flood characteristics.

A study associated with dam failure requires knowledge of parameters such as the physical characteristics of the dam structure, the hydrograph of failure, and the time-varying evolution of the size of the breach. Currently, there are several methodologies in the literature to obtain the rupture gap and the peak flows that generate the rupture hydrograph (Hu et al., 2020). Disruption can occur gradually or instantaneously, depending on the cause of the failure and the type of dam.

In addition, the formation of the breach depends on the type of dam. For concrete dams, failure tends to be almost instantaneous and, in most cases, the total collapse of the dam is considered. In the case of earth structures, it may be appropriate to consider failure in a progressive manner, and, according to historical records, the final geometry of the breach has a trapezoidal shape (Mohr, 1998; Froehlich e Tufail, 2004).

Risk is a function of hazard (probability of a natural phenomenon) and vulnerability (harm potential) (Cardona et al., 2012). One way to assess the consequences of the risk of a dam is through a description of the severity of the impacts of its failure. Hazard can be defined as the possibility of the occurrence of physical events (natural or not) with effects on vulnerable and exposed elements. By vulnerability, we mean the propensity of exposed elements, their livelihoods, and assets to suffer adverse effects when affected by hazard events (Cardona et al., 2012; Youssef et al., 2021; Bathrellos et al.,

2017). The management of risk must be in terms of the hazard, and vulnerability. More practically, risk management is often expressed through the development and proper communication of a security plan to the vulnerable community, which, based on potential threats, suggests measures to be adopted (Balbi, 2008; Weichselgartner e Pigeon, 2015). However, the proper definition of these threats could not only be due to the presence of vulnerable people, but could also take into account the hydrodynamic effects of a dam-break such as the arrival time of the flood wave, the maximum depth, or the maximum velocity.

The level of detail and cost of Dam-Break studies are relatively high, and most dams have limited freely available information to build high-resolution hydrodynamic models that may be more appropriate to investigate the dam-break impacts. In this paper, we develop an alternative, simplified approach, fully based on freely worldwide available datasets, to assess flood characteristics associated with dam-break problems. As oppose to simplified diffusive methods (Paiva e Lima, 2024) that have limited performance against rapidly variable flows, we develop a full explicit solution of the SVE. To test the developed model, we apply our framework to 20 dams in Brazil and in the Brumadinho dam. This framework is adapted to be used as a serious game and can be used to increase awareness of floods induced by dam breaks (Bellotti et al., 2013a; Dandeneau e Baldwin, 2004; Cole et al., 2012).

Serious games are an elegant and visually effective form of discussing real-world problems. They are games that may or may not be digital, used for different purposes of mere entertainment (Gee, 2007; Greitzer et al., 2007). While it is desirable for these games to be engaging and enjoyable and capture users' attention, they are also designed for educational purposes. Thus, a serious game is designed both to be attractive and appealing to a broad target audience, similar to commercial games, and also to meet specific educational goals (Bellotti et al., 2013b; Susi et al., 2007). Therefore, the proposal of a serious game evaluating the impacts of a simulation of a dam break raises discussions regarding the perception and sensitivity of hazard from a simplified interface that makes it even more accessible to the public, but provides that feeling of reward for interaction and learning.

7.1.2 Fundamental Contributions and Objectives of the Paper

The fundamental contributions of this paper are:

- We developed a serious game with guided user interfaces (GUI) to solve the 1-D dam break problem.
- We allow two versions of the game: one with the GUI and another, more flexible, with the open source code and with input data derived from Excel spreadsheets.
- We solve the full momentum 1-D Saint-Venant Equations by simplifying the data entry to the minimum as possible; although still maintaining the physical meaning of the simulations for the GUI version. For the complete version, users can use several different types of cross-sections, including irregular cross-sections (Gomes Jr et al., 2023a).
- We create a framework that is in the state-of-the-art in the mathematical modeling of the hydrodynamics but can be adapted to require only simple input data that could be derived by students in a class of Hydraulics or Geographical Information Systems, for example. Therefore, the methods and results of this paper can be used in a serious gaming approach to increase the perception of flood impacts induced by dam-break events, as similarly presented in (Karpouza et al., 2023).

The objectives of this paper are twofold: (i) develop and validate a simple modeling framework for 1-D Dam Break problem that can be used for a serious-game approach to assess dam-break impacts, and (ii) assess the hydrodynamic impacts of 20 dams in Brazil according to the results obtained by the model.

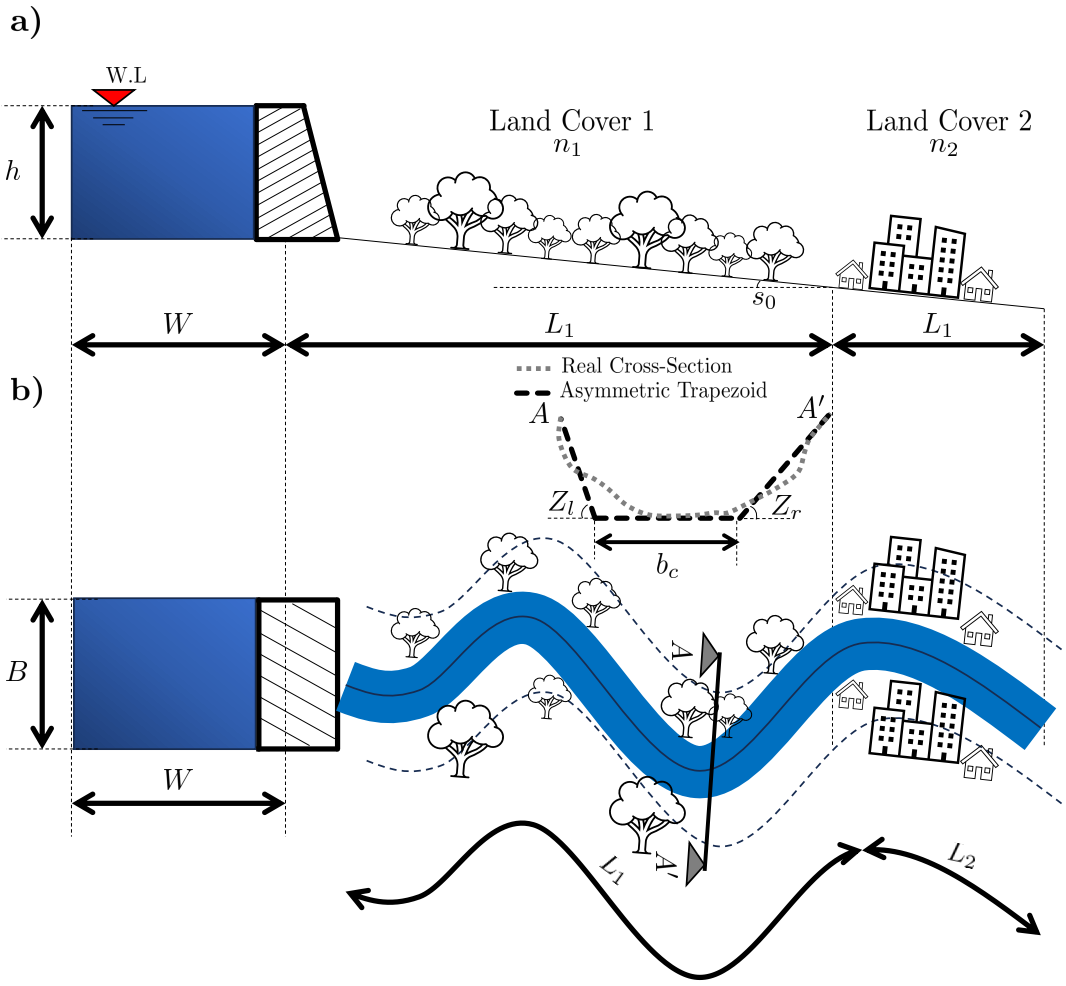

Figure 7.1. Input data schematics for the 1-D Dam Break Problem seem from a lateral view (a) and from a plan view (b). The dam dimensions are described by width B, length W, and height h. Three areas are defined from W, L_1, and L_2, that is, the reservoir, the floodplain, and the downstream vulnerable community. The downstream areas have an average slope s_0. In cases where one of these land uses does not exist, users can assume that the lengths are equal to zero. Dimensions are measured in the local axis of the downstream channel.

7.2 Materials and Methods

7.2.1 Problem Schematics

As opposed to the most accurate 1-D dam break problem that requires detailed cross-sections with relatively high resolution, we define a simplified hydrodynamic problem, but still physically based, that can have the least set of parameters to represent floodplain roughness, slope, and cross-sections. This problem is herein defined as the minimum viable problem as the one with the most simplifications possible, but capable of capturing most of the characteristics of the problem. To this end, we simplify the dam dimensions into a prism of width (B), length (W), and height (h), as shown in Fig. 7.1. The flood wave propagates as an asymmetric trapezoid channel of width b_c to downstream areas, following a bottom slope s_0. An inflow hydrograph upstream boundary condition is considered. The channel and floodplain downstream of the dam are divided into two different land uses with different Manning's roughness coefficients to represent the friction losses in these areas.

The determination of proper Manning's coefficients for downstream areas and urbanized areas can be aided by worldwide available information such as the dynamic world (Brown et al., 2022) that provides 10-m resolution classification of land use and land cover or by studies such as Papaioannou et al. (2022) that contain worldwide maps of Manning's roughness coefficients.

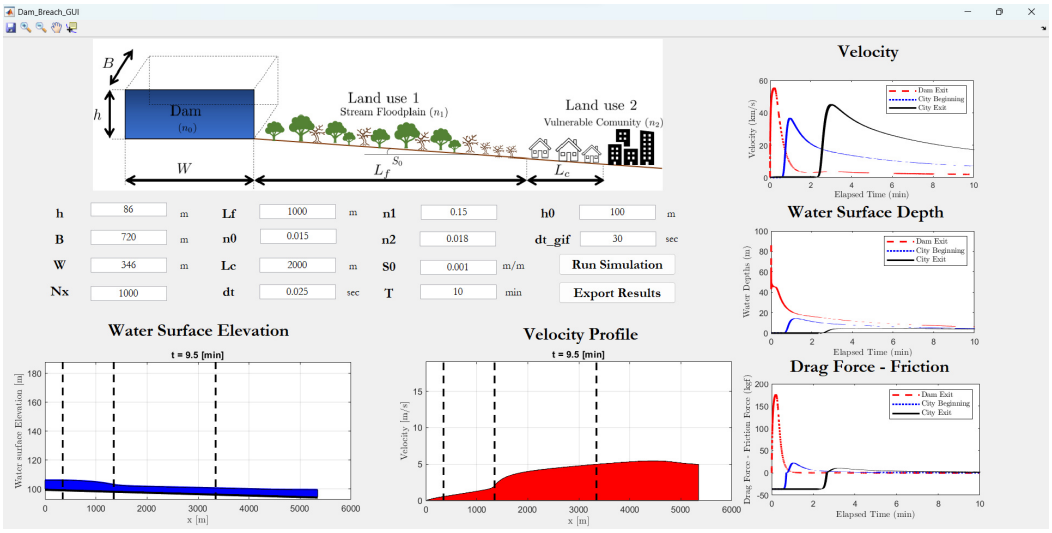

Figure 7.2. GUI of the Dam-Break model, where N_x is the number of nodes in the simulation, dt is the constant time-step, T is the end of the simulation, h_0 is the elevation of the first node, and dt_gif is the time-step used for generating the GIFs. The charts on the right contain plots of velocities, water surface depths, and net force (i.e., drag force from the hydrodynamics subtracted from the available static friction) for the exit of the dam (red), city beginning (blue) and city exit. The Neumann boundary condition of normal flow is set at the end of the domain defined by L_c, with the same energy slope as S_0. The black dashed lines in the bottom plots represent the dam exit, city beginning, and city end, respectively.

7.2.2 Guided-User-Interface Framework

The model is developed in Matlab and has an executable file that can be installed in the Matlab Apps section available in (Gomes Jr., M. N., 2023). An example of the GUI in the model is shown in Fig. 7.2. To run the serious game, users must have a Matlab 2021 version or higher and also must install the game on their Matlab. Another version of the model is available for those who are more familiar with Matlab coding, allowing more experienced users to change some parameters otherwise assumed for simplicity and parsimony. The model outputs are.mp4 videos, with a user-defined time resolution, of water surface elevation, flow velocity, and hydrodynamic force calculated from Eq. (7.1). In addition, colormaps of all states and of the Froude numbers are shown, allowing not only the spatial variation of the states but also their time variation. Finally, plots of these states with respect to time are done for 3 particular coordinates of the problem: the dam exit, the city beginning, and the end of the computational domain.

This GUI is designed for dam-break serious gaming; however, the underlying Matlab code contains a full-momentum hydraulic solver that can be used for wider applications since controlling upstream, downstream and internal boundary conditions is possible. Moreover, the hydraulic solver can also be associated with hydrological models to implement flow boundary conditions and represent other cases rather than only dam-break problems (see examples in (Gomes Jr et al., 2023a). To this end, using the code rather than the GUI is desirable for cases outside of dam-break analysis, since the GUI was designed for a relatively simple and fast estimation of flood impacts in a dam-break scenario.

7.2.3 1-D Dam Break Model

A fully description of the explicit 1D Saint-Venant equations (SVE) solved by the HydroHP-1D model is detailed in (Gomes Jr et al., 2023a) and explained in the Supplemental Materials. HydroHP-1D model is an explicit numerical model in the time domain that solves the SVE hyperbolic partial differential equations via the Lax-Friedrichs scheme (Lax, 1954) with user-defined Courant-Number values, herein this paper fixed as 0.5.. The performance of the model was compared to HEC-RAS

(Brunner, 2016b) and with analytical solutions. The full description of the model can be found in (Gomes Jr et al., 2023a). HydroHP-1D allows for the 1D simulation with varied cross-sections, such as: rectangular, assymetric trapezoids, hyperbolic sections, circular sections, and ultimately irregular cross-sections with overbanks. In addition, the model allows for the stage and space-varying assumption of Manning's roughness coefficient (Gomes Jr et al., 2023a).

The hydrodynamic forces associated with the flow can be calculated by determining the cross section depth-averaged flow velocity and pressure distribution for all computational nodes in space and time. The pressure is assumed to increase linearly with the water depth, such that for a given water depth h and depth-averaged velocity v, the integral of the pressure applied on a surface, that is, the total hydrodynamic force, can be written as:

$$\begin{aligned}\bar{F} &= \int_0^{\min(h,h_p)} P(h) A_p \mathrm{dh} \\ &= B_p\Big(\frac{\gamma h^2}{2} - \frac{\gamma[\max(h-h_p,0)]^2}{2}\Big) \\ &+ A_p \gamma \frac{v^2}{2g},\end{aligned} \tag{7.1}$$

where A_p is a person normal area to the flow direction, P is the normal pressure, $\bar{F}$ is the total hydrodynamic force, γ is the specific weight of the fluid, h is the water depth, h_p is the person height, v is the average velocity, and g is the gravity acceleration. Note that $A_p = B_p \times \max(h, h_p)$, where B_p is the average width of a person. For the sake of parsimony, we assume $h_p = 1.70$ m and $B_p = 0.35$ m.

The previous Eq. (7.1) considers the static and dynamic pressure of the flow dynamics and is valid for any case of h and models the integral of the water dynamic pressure bulb varying as a function of the water depth. The term $v^2/2g$ accounts for the hydrodynamic momentum of the water and is not neglected. The force $\bar{F}$ can be estimated for all computational nodes, including the one at the beginning of the city, which would represent the critical force to which a vulnerable person would be subjected. This result is tracked as a proxy of the drag hazard associated with the dam break.

7.2.3.1 Dam Break Hydrograph

The maximum discharge in a dam-break scenario can be calculated using a broad-crested weir equation such that:

$$Q_\mathrm{p} = \lambda B \sqrt{g} h^{3/2}, \tag{7.2}$$

where λ is a discharge coefficient that can be assumed as $8/27$ for rectangular weirs (Ritter, 1892).

During a dam break scenario, the time that Q_p is reached is considered instantaneous. This maximum flow is maintained for the peak time t_p, also called the initial stable stage duration, due to the reflection of the flood wave from the upstream wall. This duration depends on the finite length of the reservoir (W) and on the height of the reservoir (h), such that we can calculate t_p for a rectangular reservoir as follows:

$$t_p = \frac{15}{8}\frac{W}{\sqrt{gh}}. \tag{7.3}$$

The previous equation is derived by considering the reservoir as a storage node with a uniform water level for a given time and by assuming the reflected wave time to the upstream of the dam.

The reservoir storage (S) and stage (h_r) dynamic equations can be written in using a forward Euler explicit scheme as follows:

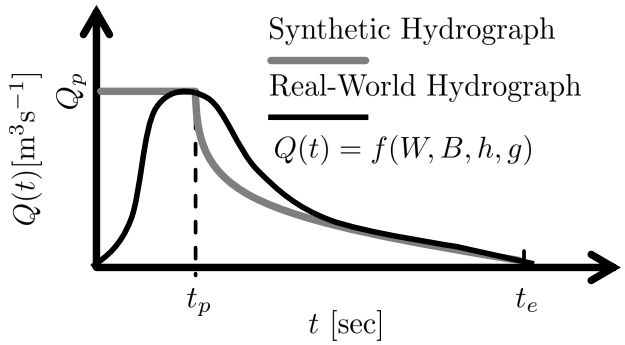

Figure 7.3. Simplified break hydrograph, where t_p is the peak time and t_e is the end of the hydrograph. Variables W, B, h, are further explained in Fig. 7.1, and g is the gravity acceleration. The black line represents the real-world dam-break hydrograph that contains time-varying information about the breach formation, as opposed to the synthetic hydrograph that assumes an instantaneous failure modeled with standard rectangular hydraulic cross-section equations.

$$S(t + \Delta t) = S(t) - \Delta t Q(t), \tag{7.4a}$$

$$h_r(t + \Delta t) = \frac{S(t + \Delta t)}{WB}, \tag{7.4b}$$

where h_r is the time-varying water depth in the reservoir.

After the period t_p, the remaining volume in the reservoir is

$$S(t_p) = BLh - Q_p t_p \tag{7.5}$$

and the depth is calculated by substituting Eq. (7.5) into (7.4b).

Therefore, the falling limb of the hydrograph is defined by a stage-discharge release equation using a broad-crested weir equation from Eq. (7.2) starting from the stage at t_p (i.e., $h(t_p)$). A schematic of the break hydrograph is shown in Fig. 7.3.

By tracking the reservoir water depth and using the weir equation, one can derive a flow hydrograph equation for the falling limb of the dam break as follows (Hu et al., 2020):

$$\begin{cases} Q(t) & = Q_\mathrm{p}, \;\; 0 \leq t < t_\mathrm{p} \\ Q(t) & = \left[\frac{-1/2h\left(t_p - t\right)\left(\lambda B \sqrt{g}\right)^{2/3}}{S(t_p)} + Q_p^{-1/3} \right]^{-3}, \;\; t_\mathrm{p} \leq t \leq t_\mathrm{e}. \end{cases} \tag{7.6}$$

7.2.4 Numerical Case Studies

To exemplify the use of the model, we developed a framework that was applied for students of Environmental Engineering and Civil Engineering at the University of Sao Paulo - Sao Carlos School of Engineering. Undergraduate students had to find dams in Brazil and gather all the required information shown in Fig. 7.1. The data were fully collected through GIS databases, Google Earth, and National Water Agency (ANA) databases. Subsequently, the teaching assistants of these classes filtered and validated the data collected by the graduate students, allowing the preparation of the input files to run the model.

7.2.5 Validation of the Numerical Approach - The Failure of Brumadinho Dam (2019)

The first case study presents detailed results of the Brumadinho dam failure, 2019. The Brumadinho Dam has approximately 12 milion $\mathrm{m^3}$ of storage, with a height of 80 m and width of 700 m and is parametrized following Figs. 7.1, resulting in $h = 80$ m, $B = 700$ m, $W = 214$ m. During

Figure 7.4. Dams simulated with HydroHP-1D from Numerical Case Study 2. The size of the point represents the relative volume of the dams. The inserted figure shows satellite imagery of dam 54 as an example.

the first 5 minutes after dam failure, more than 75% of the volume was released (Gibson et al., 2022). Here, we assume an inflow hydrograph as a boundary condition for the hydraulic model, such that the initial conditions of the model are a minimum discharge in all sections to avoid dry-wetting numerical issues. To guarantee a relatively more accurate representation of the terrain, we derive 16 cross-sections from the Shuttle Radar Topography Mission (SRTM) data from 2014, that is, before the dam failure. The detailed cross-sections for this simulation are available in the Supplemental Materials. We also linearly interpolate the cross-section values for each node of the domain to avoid abrupt changes in the cross-sections.

The digital elevation model of the area, the location of the dam, and of the cross-sections are shown in Fig. 7.6. To validate the proposed model, we compare the modeling results of HydroHP-1D with EMBREA-MUD (Petkovsek et al., 2021) results from (Lumbroso et al., 2021) obtained using a 5-m resolution digital elevation model (DEM). EMBREA-MUD simulates embankment dam breaches and models a water and tailings dynamics providing time series of the propagation. The points in the domain used for comparison are three, respectively named as C (Canteen), D (Railway bridge), and E (Paraopeba River) (Lumbroso et al., 2021). The 1D longitudinal lengths of these points taken from the dam are approximately 1.50, 3.70, and 9.44 km, respectively. A schematic figure of the lateral view of the dam is presented in the Supplemental Materials. The dam breach hydrograph is presented in Fig. 7.5. Note that this hydrograph is not derived from Eq. (7.6). The Brumadinho breach hydrograph was derived based on an expert panel report, which concluded that the dam failed progressively, in addition to high quality YouTube videos released of the dam failure (Lumbroso et al., 2021).

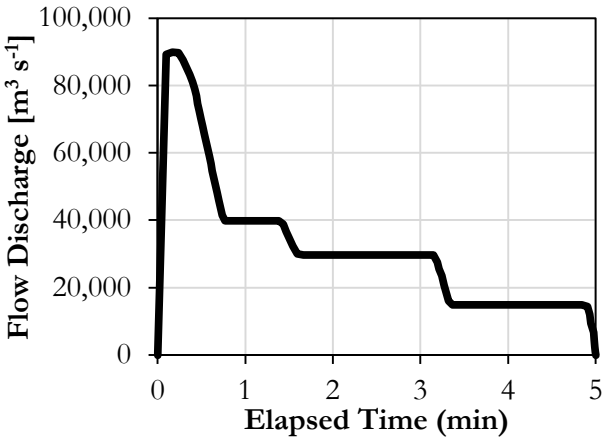

Figure 7.5. Dam failure hydrograph in Brumadinho Dam (2019), available at (Lumbroso et al., 2021). HydroHP model is subjected to this inflow hydrograph boundary condition.

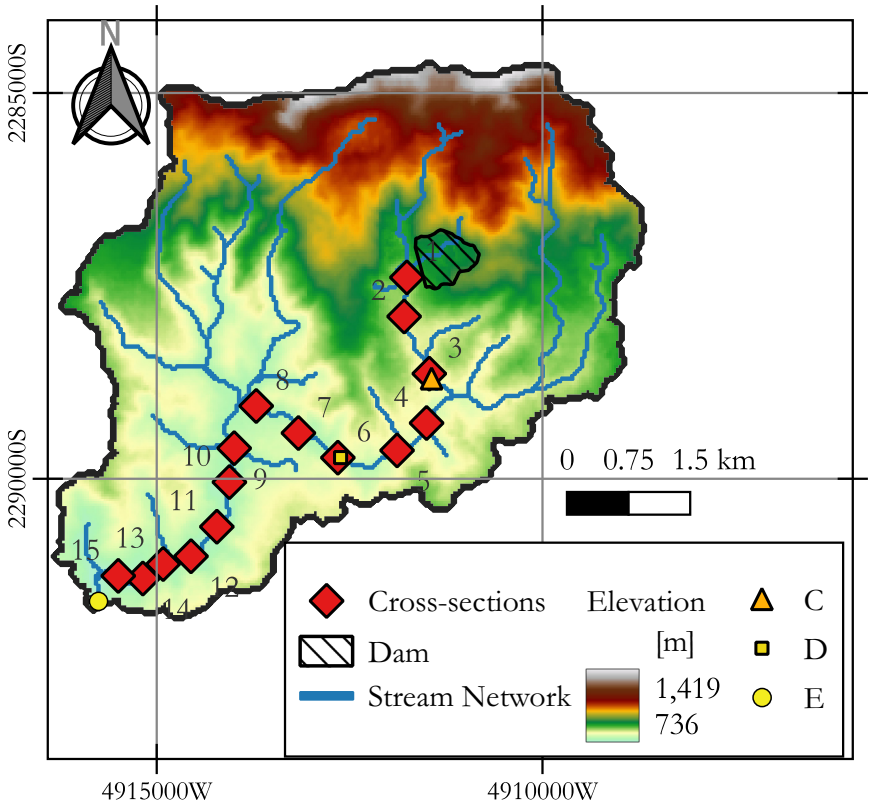

Figure 7.6. Córrego do Feijão Catchment. The cross-sections are arbitrarily defined downstream of the dam to present the open channel hydraulics. Projected coordinates in WGS 84 / Pseudo-Mercator.

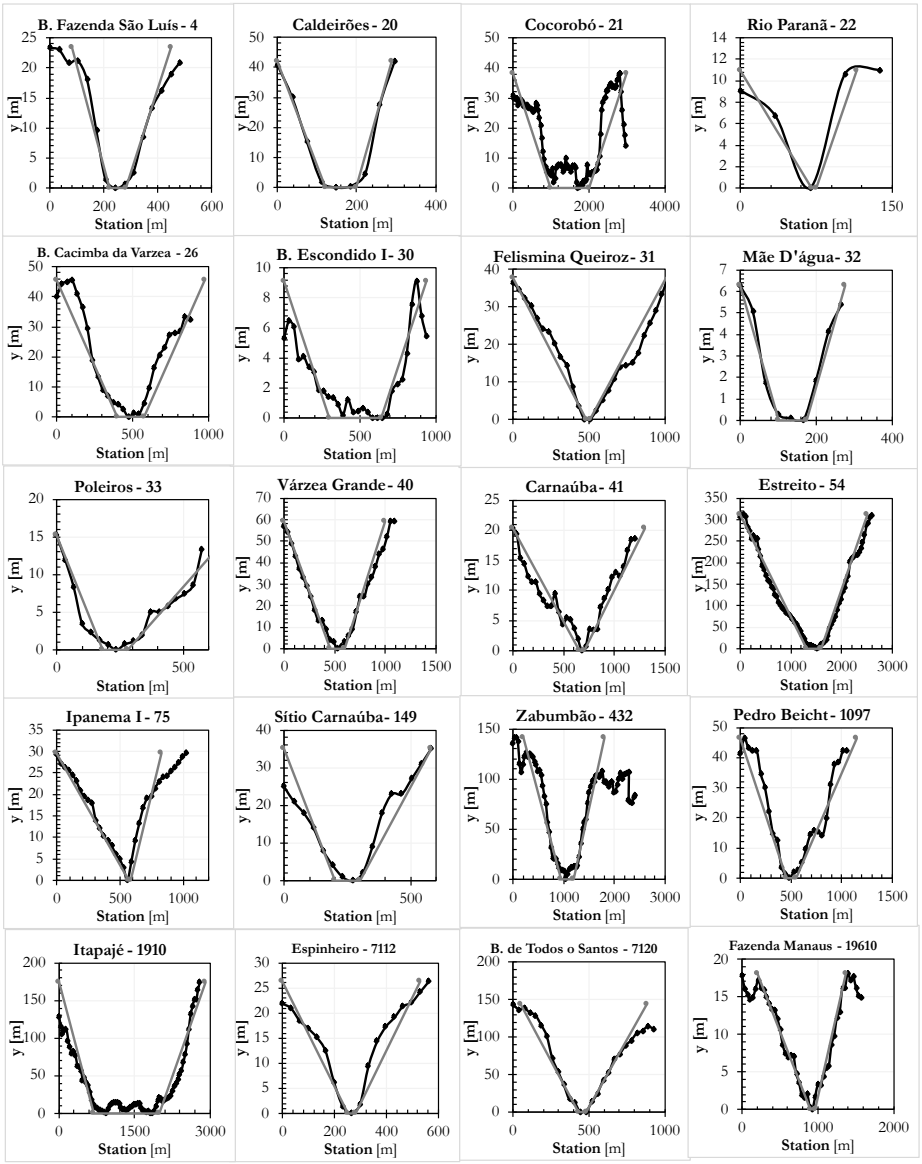

Figure 7.7. 1-D cross-sections derived from Copernicus DEM downloaded from OpenTopography and approximated by an asymmetric trapezoid defined by a width b_c, and cotangents of left and right angles. The title of each plot has the name of the dam and its ID, following the SNISB classification. Black lines are real cross-sections and gray lines are the approximated trapezoid cross-section.

7.2.6 Assessing the Potential Flood Hydrodynamic Impacts due to Dam-Break

We applied the simplified modeling approach presented in Fig. 7.2 for 20 dams shown in Fig. 7.4. The potential failure of these dams was estimated by simulating a breach-hydrograph following Eq. 7.6 in a constant, space-invariant, trapezoid simplification of the real-world cross-sections downstream of the dam, as shown in Fig. 7.7.

The slope was estimated by calculating the ratio between the elevation difference from the last and first node of the domain, divided by the distance of the center line of the floodplain between these points. This distance can be calculated by converting the stream network into vectors and later measuring the distance within the beginning and end of the study area using software such as QGIS. Most of the dams used in this case study are located in rural areas, with relatively little dense urbanized communities located downstream of these dams. This motivated the use of constant Manning's roughness coefficients for the floodplain and for the city, with values assumed as 0.035 $\mathrm{sm}^{-1/3}$ and 0.025 $\mathrm{sm}^{-1/3}$, respectively.

All simulations were carried out for 60-minutes of simulation time, with minimum time-steps of 0.001 seconds, maximum time-steps of 5 seconds and a maximum courant number of 0.5. We discretize the space into 1001 cross-sections such that 1000 discrete channel reaches are modeled. A normal slope boundary condition with the same slope of the downstream channel was assumed as the outlet boundary condition and an inflow hydrograph from Eq. 7.6 was assumed as an inlet boundary condition. Hydrodynamic forces were calculated by assuming a fluid density of 2.6 $\mathrm{tf/m^3}$, adapted from (Hu et al., 2017; Kossoff et al., 2014).

We perform an application of simple statistical description metrics to evaluate the representativeness of the selected dams. Metrics such as arithmetic average ($\bar{x}$), median ($\tilde{x}$), standard deviation (σ), and 10% and 90% exceedance percentiles, resulting in Tab. 7.3

7.2.7 Hydrodynamic Hazard (HH) Simplified Metric

To evaluate the overall impact of a dam failure, we consider five metrics as the governing factors related to the flood impact. We do not attempt to include socio-hydrological, demographic, or economic factors in this analysis; rather, we aim to assess only the factors associated with flood propagation. Therefore, we use the HH proposed in this paper as a metric only related to hydrodynamics of a dam break event. The metrics are: (1) inverse of the time to reach the maximum water depth $(1/t(h_{\max}))$, (2) maximum force at the entrance of the downstream community $(F_{\max})$, (3) inverse of the time to reach the downstream community $(1/t_f)$, (4) maximum velocity at the entrance of the community ($v_{\max}$), and (5) inverse of the time to reach the maximum velocity at the downstream of the community $(1/t(v_{\max}))$. We hypothesize that the maximization of each of these variables is somewhat related to a higher flood damage, such that one can write a simple flood-related hazard equation such that:

$$\bar{\eta^j} = \sum_{i=1}^{n_s} (\omega_i \eta_i^j), \tag{7.7}$$

where $0 \leq \bar{\eta} \leq 1$ represent an overall hazard metric that if maximized represent a relatively higher hazard, j is the index of the dam, and n_s is the number of metrics considered for the analysis.

For simplicity, we assume $\omega = 1$ for all metrics meaning all of them would have the relatively same importance for the overall HH metric. Although assumed with equal importance in this paper, the weights can vary to represent local preferences and significance in the analysis. In addition, the normalized metric η_i is calculated by the following:

$$\eta_i^j = \frac{x^* - x_{\min}}{x_{\max} - x_{\min}}, \tag{7.8}$$

where x^* represent a hydrodynamic state (e.g., maximum force at the community ($F_{\max}$)), $x_{\min}$ and $x_{\max}$ are the minimum and maximum values of state x for all simulated dams.

By normalizing the hydrodynamic states used in η, one can produce detailed information on the impacts of dam break analysis, resulting in an index for each dam-break case considered. The results of such methodology can be used to improve typical qualitative metrics (e.g., low, medium high risk, or potential damage) by giving an extra numeric layer that varies continuously from 0 to 1, where 1 represents the case with higher HH from the sample dams used in the analysis. We hypothesize that this metric can add valuable information for decision-makers and for the population that would be affected, in general, since it not only abstracts the complex hydrodynamic phenomena in a dam-break into a number but also presents the relativity HH among dams with different characteristics, as shown in Tab. 7.3.

ID	Dam name	Main Use	Material	Capacity [hm^3]	FU	City	Risk Category [CRI]	Potential Damage [DPA]	Latitude	Longitude
5	Fazenda São Pedro	Aquaculture	Earthen	0.72	MT	Porto Esperidião	Not applicable	Low	-16.27472	-59.17603
20	Caldeirões	Irrigation	Earthen	18.8	AL	Palmeira dos Índios	Medium	High	-9.31647	-36.64983
21	Cocorobó	Human supply	Earthen	245.4	BA	Canudos	High	High	-9.88225	-39.03900
22	Rio Paranã	Irrigation	Earthen	170.0	GO	São João D'Aliança	High	High	-14.69117	-47.27958
26	Cacimba da Várzea	Combating Droughts	Earthen	9.3	PB	Solânea	High	High	-6.69097	-35.78003
30	Escondido I	Human supply	Earthen	16.6	PB	Belém do Brejo do Cruz	Medium	High	-6.19358	-37.54228
31	Felismina Queiroz	Human supply	Earthen	2.1	PB	Pedra Lavrada	Medium	High	-6.85492	-36.40792
32	Mãe d'Água	Flow regulation	Concrete	640.0	PB	Coremas	Medium	High	-7.02428	-37.98547
33	Poleiros	Human supply	Earthen	7.9	PB	Barra de Santa Rosa	High	High	-6.73144	-36.08864
40	Várzea Grande	Human supply	Concrete	21.5	PB	Picuí	Medium	High	-6.42922	-36.35494
41	Carnaúba	Human supply	Concrete	25.7	RN	Caicó	Medium	High	-6.62878	-37.14739
54	Estreito	Human supply	Earthen	75.9	BA	Urandi	Medium	High	-14.82847	-42.80719
75	Ipanema I	Flow regulation	Earthen	1.1	PE	Águas Belas	Medium	High	-9.09075	-37.16031
149	Sítio Carnaúba	Human supply	Earthen	0.4	PE	Serrita	High	High	-7.81914	-39.27114
432	Zabumbão	Human supply	Earthen	60.9	BA	Paramirim	Medium	High	-13.43889	-42.21472
1097	Pedro Beicht	Human supply	Concrete	17.2	SP	Cotia	Medium	High	-23.71828	-46.96103
1910	Itapajé	Human supply	Earthen	4.9	CE	Granja	Low	High	-3.67207	-39.57486
7112	Espinheiro	Human supply	Earthen	0.3	BA	Presidente Jânio Quadros	High	High	-14.76394	-41.72417
7120	Todos os Santos	Human supply	Earthen	11.8	MG	Teófilo Otoni	Medium	High	-17.85888	-41.5721
19610	Fazenda Manaus	Irrigation	Masonry	0.3	BA	Itaju da Colônia	High	High	-15.15548	-39.76722

Table 7.1. Dam information collected from SNISB. The data from the downstream channel cross section is used to derive an approximate asymmetric trapezoid cross section, described by the width B_c, and the left and right angles θ_l and θ_r, as shown in Fig. 7.7.

ID	h [m]	B [m]	W [m]	L_1 [m]	L_2 [m]	n_1 [$sm^{-1/3}$]	n_2 [$sm^{-1/3}$]	b [m]	Z_l [m m^{-1}]	Z_r [m m^{-1}]	I_0 [m m^{-1}]
5	9.0	178.0	1492.8	8827.4	1743.8	0.035	0.025	100.0	15.1	13.9	0.18%
20	29.0	297.0	218.0	1000.0	4320.0	0.035	0.025	80.0	2.9	2.1	0.57%
21	33.5	1320.0	5549.0	72.0	257.0	0.035	0.025	1000.0	26.0	26.0	0.17%
22	33.0	1760.0	2926.0	6475.0	550.0	0.035	0.025	5.0	6.4	3.6	0.73%
26	22.3	311.0	1336.0	1000.0	500.0	0.035	0.025	180.0	8.8	8.8	0.16%
30	12.5	1200.0	1109.0	100.0	1470.0	0.035	0.025	340.0	33.7	33.7	0.10%
31	13.0	391.0	330.0	140.0	655.0	0.035	0.025	30.0	12.7	13.3	0.54%
32	35.0	175.0	7837.0	816.0	601.0	0.035	0.025	75.0	15.9	15.9	0.51%
33	25.0	430.0	2653.0	3055.0	3169.0	0.035	0.025	100.0	11.9	26.0	0.57%
40	25.0	544.0	2140.0	5145.2	1633.8	0.035	0.025	150.0	7.6	6.8	0.20%
41	19.0	550.0	3014.0	14600.0	366.0	0.035	0.025	50.0	31.8	30.1	0.22%
54	28.0	1091.0	2483.0	2165.0	1982.0	0.035	0.025	300.0	4.2	30.1	0.13%
75	16.4	724.0	218.0	132.0	404.0	0.035	0.025	10.0	19.1	8.5	1.83%
149	6.0	329.0	250.0	14500.0	1500.0	0.035	0.025	100.0	5.7	8.0	4.86%
432	65.0	365.0	2565.0	1171.0	4974.0	0.035	0.025	250.0	5.3	4.3	0.17%
1097	23.0	347.0	2151.0	3711.0	10590.0	0.035	0.025	100.0	9.7	13.0	0.28%
1910	17.9	436.0	2193.0	2170.0	685.0	0.035	0.025	1300.0	4.0	5.1	0.58%
7112	4.0	115.0	652.0	9010.0	1780.0	0.035	0.025	30.0	9.5	9.5	0.21%
7120	31.0	35.0	10808.0	4990.0	5710.0	0.035	0.025	50.0	2.7	2.8	0.50%
19610	7.0	156.0	276.0	3896.0	1317.0	0.035	0.025	70.0	38.2	22.0	0.24%

Table 7.2. Input data retrieved by the undergraduate students of Environmental Engineering and Civil Engineering of the University of Sao Paulo, Sao Carlos School of Engineering (2022). The nomenclature used in this table is following Figs. 7.1. ID is the SNISB Code of the dam

.

Metric	Capacity [hm^3]	h [m]	B [m]	W [m]	L1 [m]	L2 [m]	b [m]	ZL [m/m]	Zr [m/m]	I0 [m/m]
$\bar{x}$	66	23	538	2510	4149	2210	216	14	14	0.6%
$\tilde{x}$	14	23	391	2151	3055	1500	100	10	13	0.3%
σ	149	14	458	2719	4492	2530	336	11	10	1.1%
10% Perc.	0.3	6	119	221	103	370	12	3	3	0.1%
90% Perc.	238	35	1308	7608	13951	5636	934	34	30	1.7%

Table 7.3. Exploratory statistics of the input data used for the dam-break simulations, where 10% and 90% Perc. are the 10th and 90th non-exceedance percentiles.

.

7.3 Results and Discussion

7.3.1 Numerical Case Study 1

7.3.1.1 Spatio-temporal Dam-Break Analysis

A colormap with spatial-time mesh showing some of the states of HydroHP-1D (i.e., Froude Number, Water Depth, and Water Surface Elevation) for the Brumadinho Dam failure is presented in Fig. 7.8. As expected, this type of dam failure led to high froude numbers, especially in the interface between wet and dry areas, as shown in Fig. 7.8 a), indicating values larger than the unity for some areas and times. The manual calibration of Manning's roughness coefficient led to a relatively larger roughness increasing downstream of the dam in order to represent the proxy expected results shown in Tab. 7.4. As a result, deeper water persisted for longer times a few kilometers from the dam, as shown in Fig. 7.8b).

7.3.1.2 Model Validation

The lack of lateral flood propagation capability in 2D fashion of HydroHP-1D led to a faster floodplain propagation in HydroHP-1D model. The reasons for that are that in HydroHP-1D has (i) relatively smoother cross-section without overbanks by the approximation of a convex trapezoid section, and (ii) simple use of stage-invariant roughness coefficient. These simplifications, although

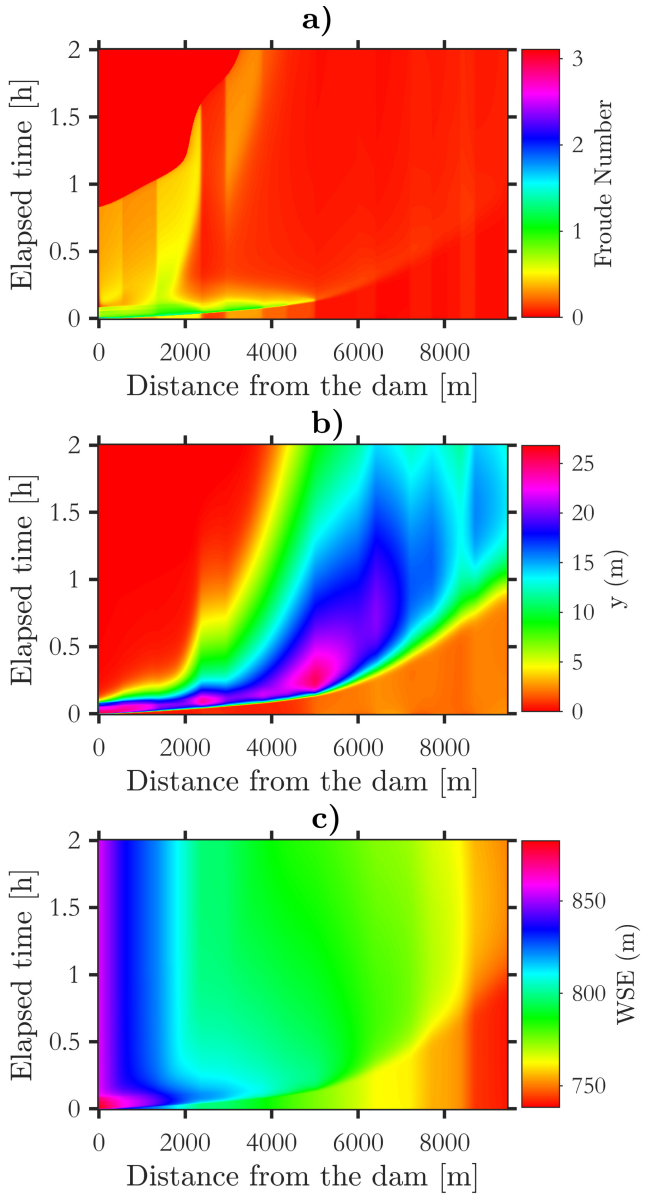

Figure 7.8. Spatio-temporal results of the 1D simulation of Brumadinho dam in Corrego do Feijao - Minas Gerais - Brazil. Part a)-c) shows spatio-temporal evolution the froude number, water depths, and water surface elevation, respectively.

not considered in the EMBREA-MUD model, were assumed in this analysis to understand the effects of such simplifications and to assess the potential implications of such a simplified scheme. However, even with these limitations, the HydroHP-1D with limited input data derived from 30-m resolution cross-sections from SRTM DEM still had sufficiently acceptable results, especially for points *C*, and *D*, as shown in Tab. 7.4. In addition, EMBREA-MUD model was applied with 5-m resolution DEM, not freely available.

The time series evolution of flow discharge, velocity, and water depth for the dam exit and for points *C*, *D*, and *E* from Tab. 7.4 are shown in Fig. 7.9. Part a) shows the breach hydrograph and the diffusive effects of the downstream propagation of the flodwave by the peak flow reduction from the Dam Exit to points *C*, *D*, and *E*. Point *C* experienced higher floodwave velocities than *D* due to the reduced roughness coefficient of its surrounding areas. The flood wave propagates slower at point *D* as shown in Fig. 7.9, in order to try to match the flood arrival time of 86.1 min.

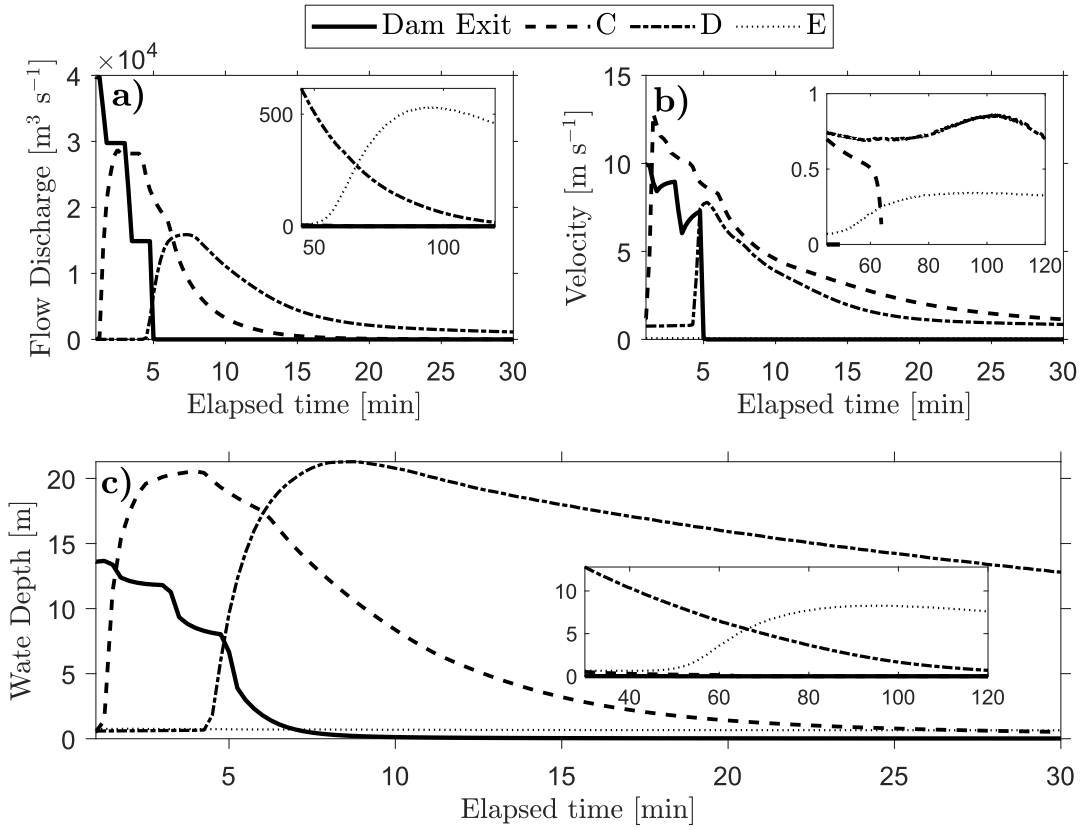

Figure 7.9. Plots of some states modeled in HydroHP-1D for the dam exit, the canteen (C), the bridge (D), and at river mouth at Paraopeba river in the end of the computational domain (E).

7.3.1.3 Maximum Water Surface Depth, Velocity, and Force for Brumadinho Dam Failure

The maximum results of water surface elevation, velocity, and hydrodynamic force are presented in Fig. 7.10. Results of this figure are the maximum values found during the simulation time. Veocities decrease rapidly as the flood propagates in the relatively rougher downstream channel. However, forces almost reach a plato around 40 tf due to the increasing roughness that increases flood depths but reduces the velocity, counter balancing the kinematic head with the pressure head of Eq. 7.1. As a reference, this force is equivalent to the weight of 8 average elephants acting as a horizontal force in a person.

7.3.1.4 Floodplain Extent

The evolution of the floodplain extent visualized from a plan view is shown in Fig. 7.11. The x-axis of this plot represents the center line of the downstream channel. As shown in this figure, this modeling approach allows not only to determine the flood wave arrival time but also the margin extent for each point. The plots each 0.1 min of all states are shown in the Supplemental Materials. The results presented in this section and in the Supplemental Materials illustrate how a simplified approach to serious games can be used to explain complex phenomena such as flood propagation in open channels In addition, results can be used to increase flood awareness by allowing users to have a sense of flood characteristics, such as arrival time, extent, and depth associated with a dam-break event.

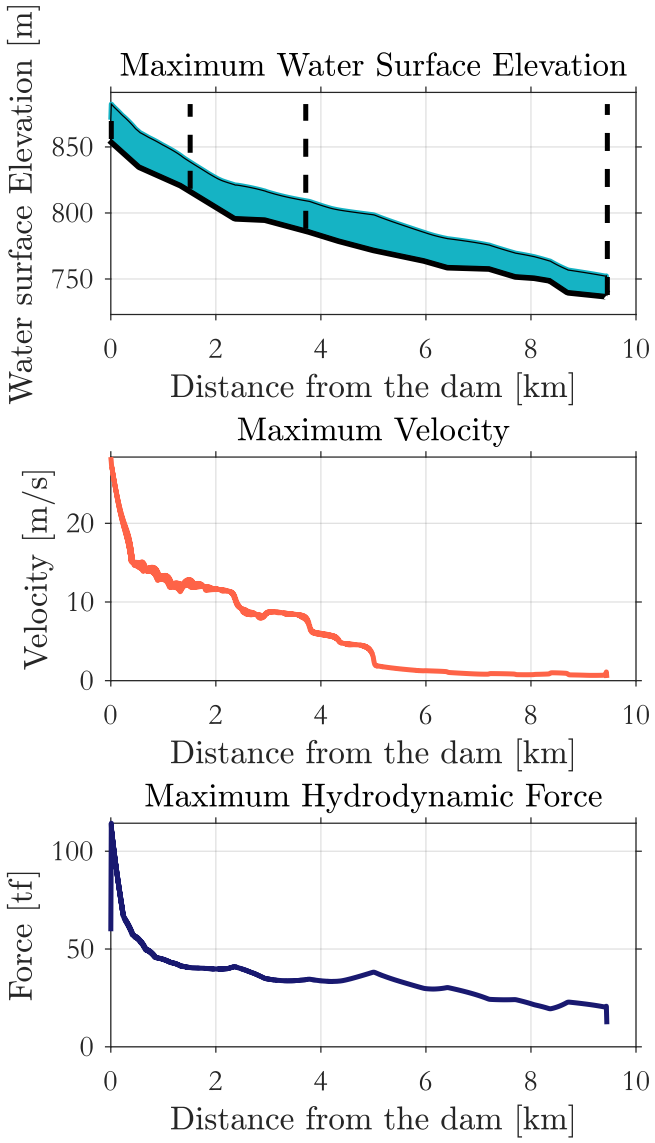

Figure 7.10. Maximum values of water surface elevation, velocity, and hydrodynamic force alongside the downstream of the Brumadinho dam. The black dashed lines in the first figure represent the distances of points C, D, and E from Tab. 7.4.

7.3.2 Numerical Case Study 2

7.3.2.1 Breach-Hydrographs of Several Dams Across Brazil

The breach-hydrographs for all dams simulated in Numerical Case Study 2 are presented in the Supplemental Materials. Discharges remain constant up to t_p, then are gradually reduced until the total release of the stored volume. The time to peak t_p depends on the dam length W; therefore, dams with higher width and smaller wave celerity (i.e., smaller water depth) typically have larger t_p, as shown in Eq. 7.3.

7.3.2.2 Detailed Results and Animations

Detailed results of all dams, containing videos of the spatial-temporal variation of the states (i.e., depths, velocities, and forces), are presented in the Supplemental Materials. In addition to videos, HydroHP-1D generates cross-section tables, similar to the HEC-RAS-1D model (Brunner, 2016b), al-

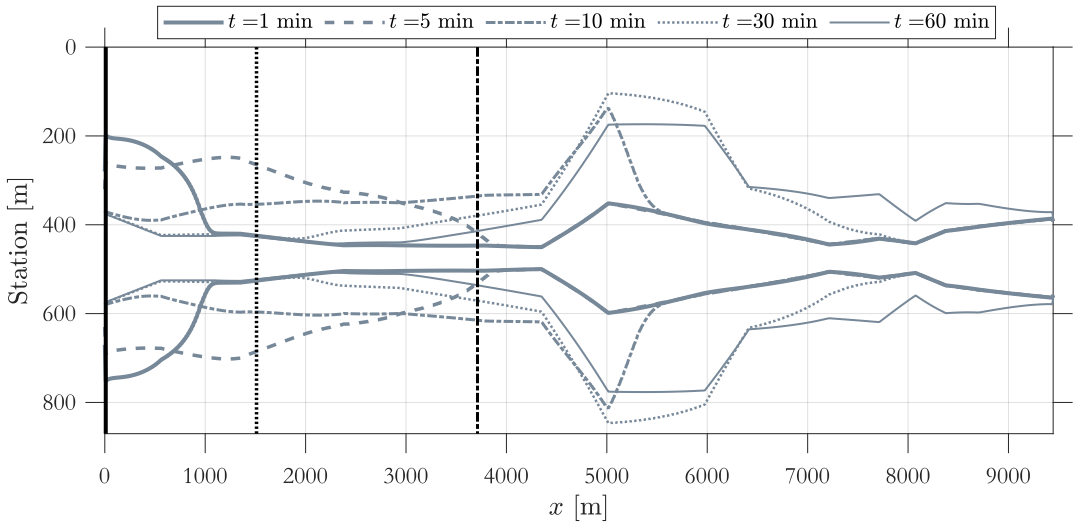

Figure 7.11. Temporal evolution of floodplain extent from a plan view in the downstream of the Brumadinho Dam. The black vertical line represents the dam exit, and the vertical dotted and dashed lines are the points C and D of Tab. 7.4.

lowing users to derive flow and stage hydrographs for each cross-section. It also generates a table with the summary results for the 1-D dam break case, containing the maximum values of each state, per each notable point (i.e., dam exit, internal nodes of interest up to 5 nodes).

7.3.2.3 Hydrodynamic Hazard (HH) Analysis

The plots of this metric applied to the dams assessed in this numerical case study are shown in Fig. 7.12. In this figure, we organize the dams into four groups of five dams. It is clearly noted a large discrepancy of dam 75 in comparison with the other dams. This particular dam had the largest velocity, force, and arrival times; however, this dam is not the one with the highest volume or dimensions of the dam, as shown in Tab. 7.1 and Tab. 7.2.

However, dam 75 had a very short (i.e., 132 m) distance from the dam to the city downstream and a relatively steep slope (i.e., 1.32%), favoring rapid flood propagation. Although dam 75 was critical, that is, the one with larger HH metrics for 4 of 5 selected hydrodynamic criteria, dam 22 had the critical water depth. Dam 22 was the largest in volume (i.e., 245.4 hm^3 as shown in Tab. 7.1). It was possibly not critical for the other criteria due to the relatively larger distance from the downstream community of nearly 6.5 km and the relatively mild slope of 0.18% as shown in Tab. 7.2. Although the slope might have contributed to the increase in flood depths, it contributes negatively to metrics related to the inverse of arrival times by the reduction in flow velocity.

The hydrodynamic hazard metric proposed in Eq. 7.7 requires the arrival times of the maximum values of each state, the arrival time of the floodwave, as well the values of maximum velocity, depth, and forces. In a simplified scenario, the metric proposed here could be visualized as the area of the radar plots presented in Fig. 7.12. The axes of Fig. 7.12 are assumed to be the states used to calculate the average HH, that is, a simple weighted average of each normalized state from the 20 dams. The results of the average HH are shown in Fig. 7.13. Part a) shows the spatial distribution of the dams with colors representing the average HH metric, and part b) shows a descending order of the dams in terms of the average HH hazard.

To compare the proposed HH metric with the CRI and DPA by SNISB classification, three classes were created for HH: $0 < \text{HH} \leq 30$ (low); $30 < \text{HH} \leq 60$ (medium); $60 < \text{HH} \leq 100$ (high). The dam Fazenda São Pedro (ID 5), for which CRI is not applied, was removed from the analysis.

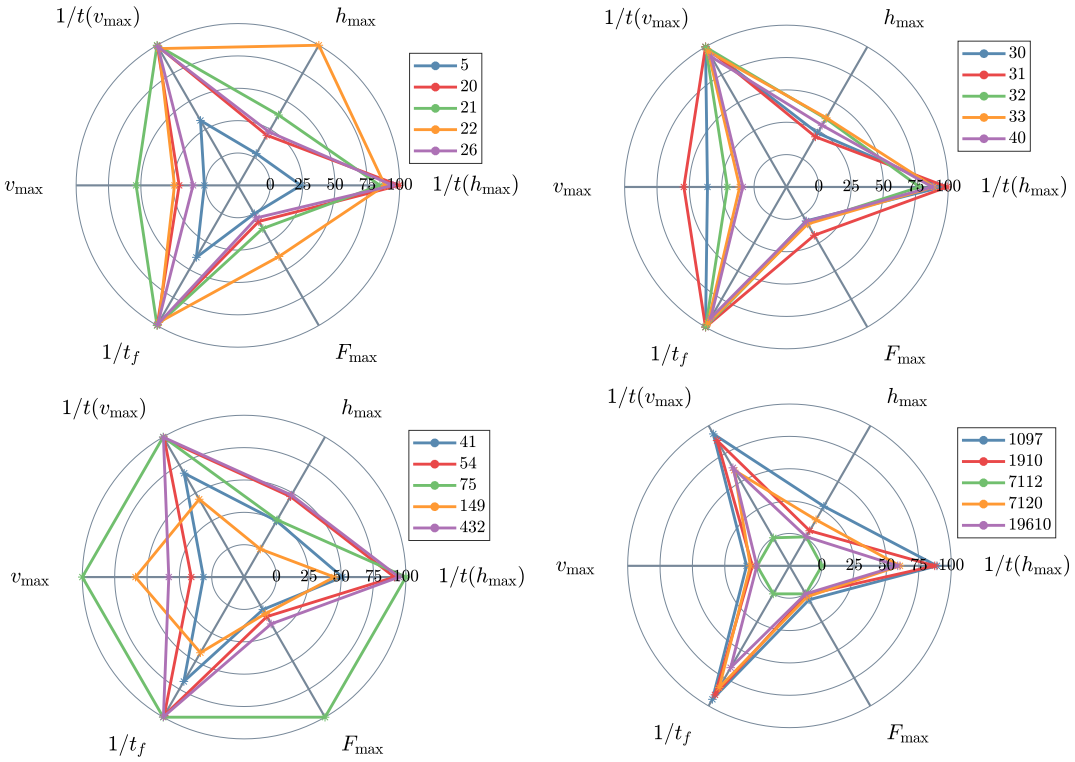

Figure 7.12. Normalized radar plot for states modeled at the entering the vulnerable community downstream of the dam. Variables are normalized by the maximum and minimum values obtained for all 20 dams tested such that a 0 value represent the minimum value and 100 a maximum value from the 20 dam samples. The arrival times are inverted such that higher values indicate shorter arrival times and, therefore, the overall hydrodynamic hazard is a function of the area of the radar plot.

Through that categorization, for CRI, it was perceived that 47% (for medium and high classes) of the dams presented the same category on both considered metrics. The CRI is related to the dam failure risk, whereas HH considers the dam damages and the 42% concordance is only a correlation. For the DPA, 32% of the dams agree in the definition of a high index. The DPA, however, is related to the potential damages associated with the dam failure and this result indicates that the metric might be different if hydrodyamic simulations are considered in the analysis. Although our classification of the chosen dams resulted in an HH qualitative metric with the distribution of the dams being 5% low, 63% medium and 32% high, these values only indicate the distribution of the sample used in the analysis, since they are normalized by the minimum and maximum values, as shown in Eq. (7.8).

The categorization of dam management by SNISB can be improved since DPA and CRI are only reported in qualitative indicators. By incorporating HH as a new numerical or qualitative criterion, even as a new indicator or by adding to the composition of DPA, we can provide more detailed information on the impact related to dam breaks. All DPA of the dams evaluated are considered high; however, our results indicate that the dam-break effects are higher in a few dams than in others due to the relatively short adaptation time, higher velocities, and hydrodynamic forces associated with the floodwave propagation in a dam-break scenario.

This simple metric can be used as a proxy representation of the hydrodynamic impact of the dam-break since it considers the arrival times of all states that are related to human instability, as well as the magnitudes of these states. By normalizing all values, one can derive a sense of the flood effect among them. It is important to note that this approach is fully deterministic and could be applied to all dams in Brazil that could be simplified following Fig. 7.1. However, this metric is only intended to be used to assess the hydrodynamic impacts that a dam can cause in the city or community closest to

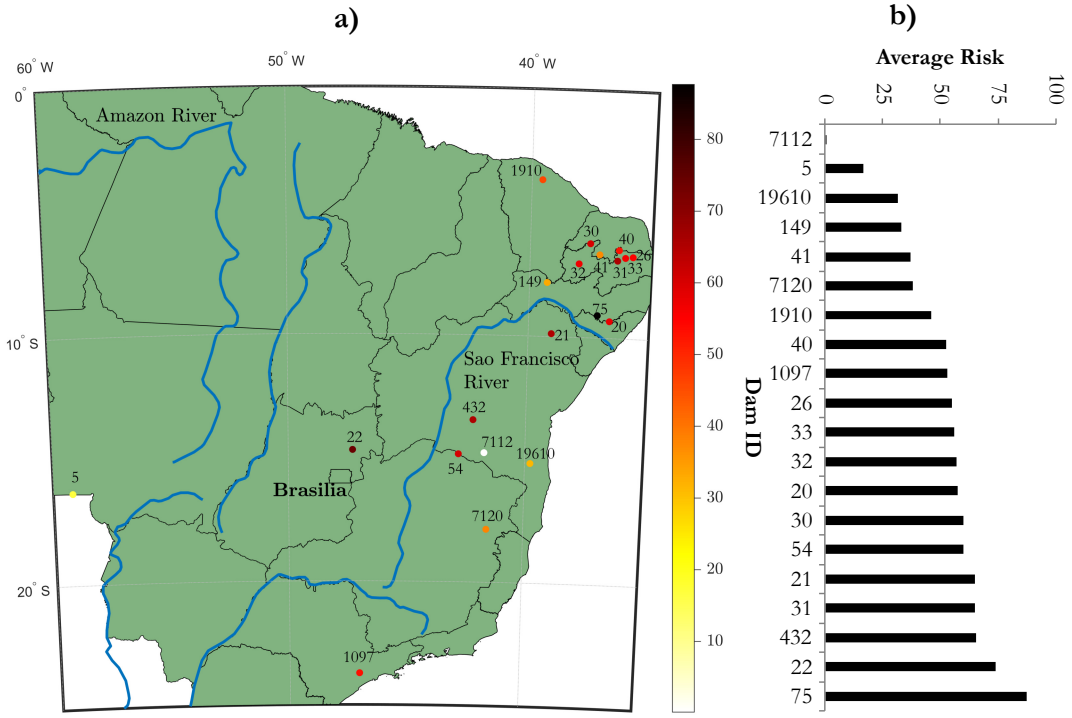

Figure 7.13. Relative Hydrodynamic Hazard Results. Part a) shows the geographical distribution of the simulated dams and the scatter colors represent the average HH. Part b) organizes the dams from the lowest to the highest relative average HH.

Point	L [km]	EMBREA-MUD		HydroHP-1D	
		Time [min]	h_{max} [m]	Time [min]	h_{max} [m]
C	1.5	1.5	18.7	1.3	20.6
D	3.7	9.2	16.2	4.5	21.3
E	9.4	86.1	11.6	50.3	8.3

Table 7.4. Modeled results from HydroHP-1D model in comparison with a EMBREA-MUD model (Lumbroso et al., 2021).

the dam.

In addition, the HH metric can be the score of a serious game approach that a user can play, such that it would indicate an overall effect of the flood impacts. To improve flood awareness, users can try to change the parameters of the game, such as the roughness coefficient by assuming a retrofit of a different land use or can try to increase the width of the downstream channel to accommodate the flood under in-bank conditions. These are only some of the examples that can be explored with such a serious gaming approach that can not only be used to derive a rapid HH assessment of a dam, but can also be used to explore and understand the effects associated with flood propagation.

7.4 Conclusions

A simplified approach was developed and applied to simulate the effects of the dam rupture in the Brumadinho dam failure (2019) and in other 20 dams located in Brazil. The modeling framework is adapted not only for a simple serious gaming approach requiring only geometrical and roughness coefficients but also can be used for more complex modeling cases such as by varying cross-sections with spatially varied roughness coefficient and slope.

The results of the validation case study of Brumadinho dam indicate that the HydroHP-1D model used in this paper can be used to simulate the flood dynamics even with simplied assumptions

such as trapezoid cross-sections without overbanks. However, the Manning's roughness coefficients had to be calibrated to represent the lack of overbank friction losses that are not considered in this case of simplification. Attention must be taken to avoid unrealistic values of n.

The results comparing the modeling performances of HydroHP-1D with EMBREA-MUD - a 2D mudflow model - show a good performance, especially for the areas near the dam that generally have less cumulative effects of overbank resistance. The results presented in this paper are obtained with freely available worldwide datasets and estimated with GIS tools and can serve as a preliminary estimate for dam-break analysis. Although this modeling framework can be used to understand and assess the impacts of dam-break scenarios, a 2D model is more appropriate, especially in cases of complex topography.

The results of the simulation of the other 20 dams in Brazil showed a scenario of dams with varied HH, with the majority of them, however, classified as with high HH. The distance from the dam to the nearest downstream comunity seems to be an important variable in the HH calculation. However, more factors have to be considered such as the cross-section characteristics, slope, and friction of the downstream channel. Ultimately, the combination of all morphometric characteristics of the downstream channel can be represented by the maximum hydrodynamic force associated with the streamflow at the entry of a downstream city. The force depends on the water depth, velicity (i.e., friction), cross-section, and is typically higher with the reduction of the flood arrival time. This metric seems to be a good indicator of the hydrodynamic impacts of dam-break and could have been considered with greater weight in the analysis, for example.

The framework presented in this paper is more applicable under some specific circumstances, such as: (i) the fluid incompressible and Newtonian, (ii) has a single density over the whole computational domain, (iii) and the flow is predominantly one-dimensional. These are fundamental limitations that certainly pose as a drawback in the numerical results, often requiring unfeasible assumptions such as adopting very high roughness coefficients to account for the lack of modeling capability. In addition to modeling limitations, the proper acquisition of model parameters can also be an issue for the wider application with the public.

For future studies, we recommend testing the modeling capability to increase flood hazard awareness by administering a pre- and post-survey to a selected group of individuals. In addition, future studies can develop a database of already parametrized dams to allow general users to only choose the dam and automatically assign the dam parameters, avoiding misleading and poor parameter estimations for the simulation. The game can be played, so players can evaluate their flood HH assessment by changes in the score due to the decisions of the users (i.e., changes in roughness, decreased slope, retrofit a different channel) after the first play (i.e., average simplified risk). The developed model code is fully open source and includes an executable file that can be downloaded and installed in Matlab, making it easy to apply this methodology in many locations around the world.

7.5 Data Availability Statement

Some or all data, models, or code generated or used during the study are available in a repository or online in accordance with funder data retention policies. All software, figures, and data can be freely downloaded in (Gomes Jr., M. N., 2022).

Acknowledgment

We greatly appreciate the support given by the undergraduate students of Environmental Engineering and Civil Engineering at the University of Sao Paulo - Sao Carlos School of Engineering,

who gently collected data for the simulations presented in this paper. The present study was supported by Conselho Nacional de Desenvolvimento Científico e Tecnológico (CNPq) and CAPES Ph.D Scholarship.

Supplemental Materials

Supplementary data related to this article can be found at https://github.com/marcusnobrega-eng/HydroHP.
Program size: Approximately 10 MB
Availability: Open source (github license)

References

Adamo, N., Al-Ansari, N., Sissakian, V. K., Laue, J., e Knutsson, S. (2020a). Dam safety : Monitoring of tailings dams and safety reviews.

Adamo, N., Al-Ansari, N., Sissakian, V. K., Laue, J., e Knutsson, S. (2020b). Dam safety : Use of instrumentation in dams.

ANA (2016). Guia de orientação e formulários para inspeções de segurança de barragem.

Aureli, F., Maranzoni, A., e Petaccia, G. (2021). Review of historical dam-break events and laboratory tests on real topography for the validation of numerical models. *Water*, 13(14):1968.

Balbi, D. A. F. (2008). Metodologias para a elaboração de planos de ações emergenciais para imundações induzidas por barragens: estudo de caso: Barragem de peti-mg.

Bathrellos, G. D., Skilodimou, H. D., Chousianitis, K., Youssef, A. M., e Pradhan, B. (2017). Suitability estimation for urban development using multi-hazard assessment map. *Science of the total environment*, 575:119–134.

Bellotti, F., Berta, R., De Gloria, A., D'ursi, A., e Fiore, V. (2013a). A serious game model for cultural heritage. *J. Comput. Cult. Herit.*, 5(4):1–27.

Bellotti, F., Kapralos, B., Lee, K., Moreno-Ger, P., e Berta, R. (2013b). Assessment in and of serious games: An overview. *Advances in human-computer interaction*, 2013:1–1.

Bilali, A. E., Taleb, I., Nafii, A., e Taleb, A. (2022). A practical probabilistic approach for simulating life loss in an urban area associated with a dam-break flood. *Int J Disast Risk Re*, 76:103011.

Bradlow, D. D., Palmieri, A., e Salman, S. M. (2002). *Regulatory frameworks for dam safety: A comparative study*. World Bank Publications.

Brown, C. F., Brumby, S. P., Guzder-Williams, B., Birch, T., Hyde, S. B., Mazzariello, J., Czerwinski, W., Pasquarella, V. J., Haertel, R., Ilyushchenko, S., et al. (2022). Dynamic world, near real-time global 10 m land use land cover mapping. *Scientific Data*, 9(1):251.

Brunner, G. W. (2016b). Hec-ras river analysis system modeling user's manual us army corps of engineers hydrologic engineering center. *Information on http://www. hec. usace. army. mil*.

Burke, E. R., Tront, J. M., Lyon, K. N., Rex, W., Castera Errea, M. I., Varughese, M. C., Newton, J. T., Becker, A. N., e Vale, A. L. (2023). What the future has in store: A new paradigm for water storage-overview for policy makers.

Cardona, O.-D., van Aalst, M. K., Birkmann, J., Fordham, M., McGregor, G., Perez, R., Pulwarty, R. S., Schipper, E. L. F., Sinh, B. T., Décamps, H., Keim, M., Davis, I., Ebi, K. L., Lavell, A., Mechler, R., Murray, V., Pelling, M., Pohl, J., Smith, A.-O., e Thomalla, F. (2012). Determinants of risk: Exposure and vulnerability. In Field, C. B., Barros, V., Stocker, T. F., e Dahe, Q., editors, *Managing the Risks of Extreme Events and Disasters to Advance Climate Change Adaptation*, pages 65–108. Cambridge University Press, Cambridge.

Cole, S. W., Yoo, D. J., e Knutson, B. (2012). Interactivity and reward-related neural activation during a serious videogame. *PLoS one*, 7(3):e33909.

Dandeneau, S. D. e Baldwin, M. W. (2004). The inhibition of socially rejecting information among people with high versus low self-esteem: The role of attentional bias and the effects of bias reduction training. *J Soc Clin Psychol*, 23(4):584–603.

Dincergok, T. (2007). The role of dam safety in dam-break induced flood management. In *Proceedings of International Congress on River Basin Management*, pages 682–697.

Froehlich, D. C. e Tufail, M. (2004). Evaluation and use of embankment dam breach parameters and their uncertainties. *Proceedings of the annual conference of the association of state dam safety officials*, 15.

Gee, J. (2007). What video games have to teach us about learning and literacy.(2a. edição).

Gibson, S., Moura, L. Z., Ackerman, C., Ortman, N., Amorim, R., Floyd, I., Eom, M., Creech, C., e Sánchez, A. (2022). Prototype scale evaluation of non-newtonian algorithms in hec-ras: Mud and debris flow case studies of santa barbara and brumadinho. *Geosciences*, 12(3):134.

Gomes Jr, M. N., Giacomoni, M. H., de Macedo, M. B., do Lago, C. A. F., Brasil, J. A. T., de Oliveira, T. R. P., e Mendiondo, E. M. (2023a). A modeling framework for bioretention analysis: Assessing the hydrologic performance under system uncertainty. *Journal of Hydrologic Engineering*, 28(9):04023025.

Gomes Jr., M. N. (2022). HP Estimator - Rating Curve - V5. https://github.com/marcusnobrega-eng/HyProSWE.

Gomes Jr., M. N. (2023). Dam Break Module. https://github.com/marcusnobrega-eng/Dam_Break_Module.

Greitzer, F. L., Kuchar, O. A., e Huston, K. (2007). Cognitive science implications for enhancing training effectiveness in a serious gaming context. *Journal on Educational Resources in Computing (JERIC)*, 7(3):2–es.

Hu, H., Zhang, J., Li, T., e Yang, J. (2020). A simplified mathematical model for the dam-breach hydrograph for three reservoir geometries following a sudden full dam break. *Nat Hazards*, 102:1515–1540.

Hu, L., Wu, H., Zhang, L., Zhang, P., e Wen, Q. (2017). Geotechnical properties of mine tailings. *J Mater Civil Eng*, 29(2):04016220.

Karpouza, M., Bathrellos, G. D., Kaviris, G., Antonarakou, A., e Skilodimou, H. D. (2023). How could students be safe during flood and tsunami events? *Int J Disast Risk Re*, 95:103830.

Kossoff, D., Dubbin, W., Alfredsson, M., Edwards, S., Macklin, M., e Hudson-Edwards, K. A. (2014). Mine tailings dams: Characteristics, failure, environmental impacts, and remediation. *Applied Geochemistry*, 51:229–245.

Lauriano, A. W. e Brasil, L. (2009). Estudo de ruptura da barragem de funil: comparação entre os modelos fldwav e hec-ras. *MsC Diss. Universidade Federal de Minas Gerais, Belo Horizonte-MG, Brasil*.

Lax, P. D. (1954). Weak solutions of nonlinear hyperbolic equations and their numerical computation. *Communications on pure and applied mathematics*, 7(1):159–193.

Luino, F., Tosatti, G., Bonaria, V., et al. (2014). Dam failures in the 20th century: nearly 1000 avoidable victims in italy alone. *Journal of Environmental Science and Engineering*, 3(1):19–31.

Lumbroso, D., Davison, M., Body, R., e Petkovšek, G. (2021). Modelling the brumadinho tailings dam failure, the subsequent loss of life and how it could have been reduced. *Nat Hazard Earth Sys*, 21(1):21–37.

Mohr, J. (1998). *Dam-break flood analysis: Review and recommendations*. International Commission on Large Dams.

Monte, B. E. O., Tschiedel, A. d. F., e Goldenfum, J. A. (2017). Índice de risco aplicado a potencial rompimento de barragem por simulações 1d e 2d. *Simpósio Brasileiro de Recursos Hídricos (22.: Florianópolis, 2017). Anais [recurso eletrônico].[Porto Alegre: ABRH, 2017]*.

Owen, J. R., Kemp, D., Lébre, É., Svobodova, K., e Murillo, G. P. (2020). Catastrophic tailings dam failures and disaster risk disclosure. *Int J Disast Risk Re*, 42:101361.

Paiva, R. C. e Lima, S. G. (2024). A simple model of flood peak attenuation. *Water Resources Research*, 60(2):e2023WR034692.

Papaioannou, G., Markogianni, V., Loukas, A., e Dimitriou, E. (2022). Remote sensing methodology for roughness estimation in ungauged streams for different hydraulic/hydrodynamic modeling approaches. *Water*, 14(7):1076.

Petkovsek, G., Hassan, M., Lumbroso, D., e Roca, M. (2021). A two-fluid simulation of tailings dam breaching. *Mine Water Environ*, 40:151–165.

Pisaniello, J. D., Dam, T. T., e Tingey-Holyoak, J. L. (2015). International small dam safety assurance policy benchmarks to avoid dam failure flood disasters in developing countries. *J Hydrol*, 531:1141–1153.

Psomiadis, E., Tomanis, L., Kavvadias, A., Soulis, K. X., Charizopoulos, N., e Michas, S. (2021). Potential dam breach analysis and flood wave risk assessment using hec-ras and remote sensing data: A multicriteria approach. *Water*, 13(3):364.

Ritter, A. (1892). Die fortpflanzung der wasserwellen. *Zeitschrift des Vereines Deutscher Ingenieure*, 36(33):947–954.

Susi, T., Johannesson, M., e Backlund, P. (2007). Serious games: An overview.

Toledo, M. . e Moran, R. (2022). Dam safety-overtopping and geostructural risks. *Water*, 14(18).

Weichselgartner, J. e Pigeon, P. (2015). The role of knowledge in disaster risk reduction. *Int J Disast Risk Sc*, 6:107–116.

Yi, X. (2011). A dam break analysis using hec-ras. *J. Water Res. Prot.*, 2011.

Youssef, A. M., Abu-Abdullah, M. M., AlFadail, E. A., Skilodimou, H. D., e Bathrellos, G. D. (2021). The devastating flood in the arid region a consequence of rainfall and dam failure: Case study, al-lith flood on 23th november 2018, kingdom of saudi arabia. *Z. Für Geomorphol*, 63:115–136.

Zhang, L., Peng, M., Chang, D., e Xu, Y. (2016). *Dam failure mechanisms and risk assessment*. John Wiley & Sons.

8 GENERAL CONCLUSIONS

In this Ph.D thesis, the development of new hydrodynamic and water quality models was carried out to comply with the proposed research objectives. Extensive testing of these models was evaluated using different numerical case studies, including analytical solutions of numerical problems and also real-world case studies. The models developed in this thesis can be used for a wide range of hydrology and environmental issues and can also be used for disaster education through the use of serious games.

More specifically, the research objective 1 allowed to investigate the potential effects of retrofitting stormwater reservoirs with valve control using a predictive strategy. The performance of peak flow reduction, attenuation, and flood mitigation in the downstream channel was substantially improved by using a model predictive control technique that optimizes valve operation by predicting inflows and reservoir behavior using rainfall forecasting. A full matrixwise mathematical description of the model was developed explaining the details behind the numerical details of simulating a watershed-reservoir-channel system via physically-based modeling equations.

Regarding research objective 2, the HydroPol2D model was developed and applied in a variety of different case studies to test its ability to accurately predict flood routing and pollutant transport and fate. HydroPol2D was evaluated against observations of flow discharges and pollutant concentrations. In addition, a global optimization algorithm was developed and tested to calibrate HydroPo2D in a real-world catchment - the Gregorio catchment in Sao Carlos Brazil. HydroPol2D was also used to estimate the risks of dragging forces and its sensitivity to different rainfall patterns in a case study in Bangalore - India. Overall, the model has potentially great flexibility and can be used to a variety of cases where overland flow governs; however, the model is not only limited to these cases. By having a component of simplified groundwater modeling, the model can be adapted to large scale, rain-on-the-grid, watershed modeling.

HydroPol2D lacks the full momentum terms of the shallow-water equations, and this is certainly a future implementation of the model. HydroHP-1D model (i.e., a 1D Saint-Venant model), however, has all terms required to simulate complex transient phenomena in open channels. Research objective 3 was attached by the development of this model and the whole mathematical description was detailed to adapt to different conceptualizations of friction. A later application of the model was to simulate dam breaks. With 21 dam-break simulations, including Brumadinho, the HydroHP-1D model showed accepted results and was used to develop a novel hydrodynamic-based risk formulation, indicating the relative impacts of flood-wave effects.

Regarding the RTC-Stormwater model, some future advances are warranted, such as allowing the model to have a larger flexibility in the cost-function. For example, users might want to mix water quantity and quality aspects by providing active control during flood events, while allowing for a longer detention time in the reservoirs during the recession periods. In addition, reservoirs can also have other sources of control, rather than only orifice valves, such as pumps or gates. Adapting the model to a plethora of different control actuators is also warranted.

Some advances are required in future directions for HydroPol2D. First, HydroPol2D can be easily adapted to accommodate full momentum effects by incorporating inertial terms into the governing equations. This would allow the HydroPol2D model to simulate 2D dam break problems more accurately, for example. The uncertainty associated with the simulation is also an area of investigation. Adapting HydroPol2D with filtering techniques, such as the use of Kalman Filters, would allow the model to self-correct its states based on field or remote sensing observations (e.g., soil moisture, flood depths, spatially distributed initial pollutant mass). In addition, adapting the model to serve as a digital twin is also a future direction. These features would advance the use of HydroPol2D towards

large-scale watersheds that can have more complexity in parameter estimation.

Finally, the HydroHP-1D model can also be advanced by including new modeling attributes. HydroHP-1D can be adapted to be used for real-time control by including channel gate operations in the Saint-Venant dynamics. In addition, this model can be adapted to serve as a tool for flood forecasting in rivers and urban channels. By coupling a catchment hydrological model to the HydroHP hydrodynamic model, users can rapidly create a simple tool to predict flood inundation in 1D channels.

Overall, the development of the models can be the basis for future applications in environmental issues modeling, and since all code is fully open source, it is encouraged to share and contribute to the implementation and enhancement of the tools. Therefore, the creation of a website with examples, descriptions, videos, and tutorials is in progress and will be available soon. The website will be released in my github account, available at: https://github.com/marcusnobrega-eng.

APPENDIXES

8.1 Appendix I - Supplementary Material of Chapter 2

The following table shows all variables used in the model. We categorize the variables into (i) system (i.e., coupled watershed, reservoir, and channel), (ii) watershed, (iii) reservoir, and (iv) channel. The following table has the variable description for each category with units in MLT units, where n is the number of states, q is the number of cells in the watershed, n_r is the number of reservoirs per watershed, n_c is the number of sub-reaches, and s is the number of systems composed of a watershed, n_r reservoirs per watershed, and a channel. Moreover, superscripts w, r, and c represent watersheds, reservoirs, and channels, respectively, whereas subscript i represents a specific sub-reach in the channel. The dimension N.A means not applicable.

8.2 Appendix II - Supplementary Material of Chapter 3

This supplemental material is organized as follows:

- Sec. 8.2.1: Performance Indicators.
- Sec. 8.2.2: HydroPol2D - Numerical Modeling Details.
  - Sec. 8.2.2.1: Matrixwise Stormwater Runoff Mass Balance Equation.
  - Sec. 8.2.2.2: Warm-up Process and Initial Values.
  - Sec. 8.2.2.3: Conversion Factor from SWMM Wash-Off model to HydroPol2D.
  - Sec. 8.2.2.4: Evapotranspiration Modeling.
  - Sec. 8.2.2.5: Soil Recovery and Groundwater Replenishing.
  - Sec. 8.2.2.6: Hydrograph Separation with Eckhart Filter.
  - Sec. 8.2.2.7: HydroPol2D Reservoir Modeling Routine.
- Sec. 8.2.3: Watershed Geometrical Indicators.
- Sec. 8.2.4: Water Quality Calibration Module.
- Sec. 8.2.5: HydroPol2D - Detailed Results of Water Quality Modeling - Event 4.
- Sec. 8.2.6: HydroPol2D - Input data structure.

Since we here present matrixwise expressions that increase modeling speed by avoiding elementwise calculations, let us define some numerical operations and definitions, as follows:

Supplemental Materials' Notation: Italicized, boldface upper and lower case characters represent matrices and column vectors: a is a scalar, $\boldsymbol{a}$ is a vector and $\boldsymbol{A}$ is a matrix. Matrix $\boldsymbol{I}_n$ denotes an identity square matrix of dimension n-by-n, whereas $\boldsymbol{O}_{m\times n}$ and $\boldsymbol{1}_{m\times n}$ denotes a zero and one matrix with size m-by-n, respectively. The notations $\mathbb{R}$ and $\mathbb{R}_{++}$ denote the set of real and positive real numbers. The notations $\mathbb{R}^n$ and $\mathbb{R}^{m\times n}$ denote a column vector with n elements and an m-by-n matrix in $\mathbb{R}$. The element-wise product or Hadamard product is defined as $\boldsymbol{x}\circ\boldsymbol{y} \coloneqq [x_1y_1, x_2y_2, \ldots, x_ny_n]^T$ multiplications. Similarly, the element-wise division or Hadamard is defined as $\boldsymbol{x}\oslash\boldsymbol{y} \coloneqq [\frac{x_1}{y_1}, \frac{x_2}{y_n}, \ldots, \frac{x_n}{y_n}]^T$. The element-wise p power of a matrix $\boldsymbol{A}$, $(\boldsymbol{A}^{\circ p})$, with $\boldsymbol{A}\in\mathbb{R}^{m\times n}$ and $p\in\mathbb{R}$ is given by $a_{i,j}^{p}$ for $i\in\mathbb{N}_{++}$, and $j\in\mathbb{N}_{++}$.

Table A.1. Variables used in the Hydrologic-Hydraulic Model

Category	Variable	Definition	Dimension	Unit
System	$\boldsymbol{E}$	Singular matrix for DAE dynamics	$\mathbb{R}^{n\times n}$	N.A
	$\boldsymbol{A}$	System matrix	$\mathbb{R}^{n\times n}$	N.A
	$\boldsymbol{B}$	Control matrix	$\mathbb{R}^{n\times n}$	N.A
	$\boldsymbol{\psi}$	Disturbance vector	$\mathbb{R}^{n\times n}$	N.A
	$\boldsymbol{C}$	Output matrix	$\mathbb{R}^{n\times n}$	L
	Δt	Time-step in time units	$\mathbb{R}$	T
Watershed	$\boldsymbol{h}^w_{ef}$	Water depth in watershed cells	$\mathbb{R}^q$	L
	$\boldsymbol{f}_d$	Cumulative infiltration depth	$\mathbb{R}^q$	L
	q^w_{out}	Watershed outflow	$\mathbb{R}$	L^3T^{-1}
	$\boldsymbol{c}$	Infiltration capacity	$\mathbb{R}^q$	LT^{-1}
	$\boldsymbol{k}_{sat}$	Saturated hydraulic conductivity	$\mathbb{R}^q$	LT^{-1}
	$\boldsymbol{\zeta}$	Suction head	$\mathbb{R}^q$	L
	$\boldsymbol{\theta}_s - \boldsymbol{\theta}_i$	Effective soil moisture	$\mathbb{R}^q$	N.A
	$\boldsymbol{q}_{in}$	Boundary inflows in watershed cells	$\mathbb{R}^q$	LT^{-1}
	$\boldsymbol{i}_p$	Rainfall intensity	$\mathbb{R}^q$	LT^{-1}
	$\boldsymbol{e}_{TR}$	Evapotranspiration	$\mathbb{R}^q$	LT^{-1}
	$\boldsymbol{f}$	Infiltration rate	$\mathbb{R}^q$	LT^{-1}
	$\boldsymbol{s}$	Surface runoff storage in each cell	$\mathbb{R}^q$	L^3
	ω^w	Cell area in watersheds	$\mathbb{R}$	L^2
	$\boldsymbol{q}_{out}$	Boundary outflows in watershed cells	$\mathbb{R}^q$	LT^{-1}
	Δx^w	Length of cells in watersheds	$\mathbb{R}$	L
	Δy^w	Width of cells in watersheds	$\mathbb{R}$	L
	$\boldsymbol{h}_0$	Initial abstraction	$\mathbb{R}^q$	L
	$\boldsymbol{s}_0$	Bottom slope in watersheds	$\mathbb{R}^q$	LL^{-1}
	$\boldsymbol{n}$	Manning's roughness coefficient in watersheds	$\mathbb{R}^q$	$TL^{-1/3}$
	$\boldsymbol{\lambda}$	Overland flow parameter for watershed cells	$\mathbb{R}^q$	$(LT^{-1})^{3/5}$
	$\boldsymbol{B}_d$	Direction matrix	$\mathbb{R}^{q\times q}$	N.A
	$\boldsymbol{\psi}^w$	Watershed disturbance vector	$\mathbb{R}^{2q+1}$	N.A
Reservoir	q_o	Orifice outflow	$\mathbb{R}$	L^3T^{-1}
	q_s	Spillway outflow	$\mathbb{R}$	L^3T^{-1}
	a_o	Orifice area	$\mathbb{R}$	L^2
	k_o	Orifice coefficient	$\mathbb{R}$	$L^{5/2}T^{-1}$
	$\hat{h}^r$	Effective orifice pressure	$\mathbb{R}$	L
	h_o	Orifice bottom depth	$\mathbb{R}$	L
	l_{ef}	Effective spillway length	$\mathbb{R}$	L
	p	Spillway elevation from reservoir bottom	$\mathbb{R}$	L
	k_s	Spillway coefficient	$\mathbb{R}$	$L^{3/2}T^{-1}$
	$c_{d,s}$	Spillway discharge coefficient	$\mathbb{R}$	N.A
	ω^r	Reservoir area	$\mathbb{R}$	L^2
	s^r	Reservoir storage	$\mathbb{R}$	L^3
	η	Reservoir porosity	$\mathbb{R}$	N.A
	$\boldsymbol{\varphi}^r_{out,s}$	Concatenated reservoir outflow	$\mathbb{R}^{n_r s}$	L^3T^{-1}
	$\boldsymbol{y}^r_s$	Concatenated reservoir water depths	$\mathbb{R}^{n_r s}$	L
	$\boldsymbol{\sigma}^r_s$	Concatenated reservoir control signals	$\mathbb{R}^{n_r s}$	N.A
	$\boldsymbol{q}^r_{out}$	Reservoir outflow	$\mathbb{R}^{n_r s}$	L^3T^{-1}
	$\boldsymbol{u}$	Control signal	$\mathbb{R}^{n_r}$	N.A
	$\boldsymbol{h}^r$	Water depth in reservoirs	$\mathbb{R}^{n_r}$	L
Channel	$\boldsymbol{q}^c_{out}$	Channel flow in all sub-reaches	$\mathbb{R}^{n_c}$	L^3T^{-1}
	a_i	Wetted area in channel in sub-reach i	$\mathbb{R}$	L^2
	$r_{h,i}$	Hydraulic radius in sub-reach i	$\mathbb{R}$	L
	n_i	Manning's roughness coefficient in sub-reach i	$\mathbb{R}$	$TL^{-1/3}$
	$\boldsymbol{a}^c$	Wetted area in all sub-reaches	$\mathbb{R}^{n_c}$	L^2
	$s_{f,i}$	Friction slope for sub-reach i	$\mathbb{R}$	LL^{-1}
	$\boldsymbol{h}^c$	Water depths in channel sub-reaches	$\mathbb{R}^{n_c}$	L
	Δx	Sub-reach width	$\mathbb{R}^{n_c}$	L
	Δy	Sub-reach length	$\mathbb{R}^{n_c}$	L
	$\boldsymbol{q}^c_{in}$	Inflow in sub-reaches	$\mathbb{R}^{n_c}$	$L^3.T^{-1}$
	$e_{l,i}$	Central elevation of sub-reach i	$\mathbb{R}$	L
	$\boldsymbol{A}_{slope}$	Boundary relationship between sub-reach cells	$\mathbb{R}^{n_c\times n_c}$	N.A
	$\boldsymbol{b}_{slope}$	Vector containing outlet boundary conditions	$\mathbb{R}^{n_c}$	N.A
	$\boldsymbol{B}^c_d$	Direction matrix for channel sub-reaches	$\mathbb{R}^{n_c\times n_c}$	N.A
	$\boldsymbol{w}$	Vector containing inlet and outlet boundary conditions	$\mathbb{R}^{n_c}$	N.A

8.2.1 Performance Indicators

Nash-Sutcliffe-Efficiency The Nash-Sutcliffe-Efficiency (NSE) metric is calculated in terms of the observed variable (e.g., generally flow discharge) and the modeled variable such that (Nash e Sutcliffe, 1970):

$$\text{NSE} = 1 - \frac{\sum_{i=1}^{n} \left(y_{\text{obs}}^{i} - y_{\text{m}}^{i}\right)^2}{\sum_{i=1}^{n} \left(y_{\text{obs}}^{i} - \overline{y_{\text{obs}}^{i}}\right)^2} \tag{8.1}$$

where y_{obs} is the observed or the assumed true variable, whereas y_{m} is the variable. The indexes herein expressed as i and n represent the time in which the observations were made and the number of observations, respectively. NSE ranges from $-\infty$ to 1 (inclusive), with negative values indicating that the observed mean has smaller squared error than the modeled results. Ideally, a NSE = 1 indicates a perfect match between modeled and observed values.

Coefficient of Determination The coefficient of determination determines the correlation between the observations. It ranges from 0 to 1, with 1 corresponding to a perfect correlation between modeled and observed data, and can be calculated as:

$$r^2 = \left(\frac{\sum_{i=1}^{n} \left(y_{\text{m}}^{i} - \overline{y_{\text{m}}^{i}}\right)\left(y_{\text{obs}}^{i} - \overline{y_{\text{obs}}^{i}}\right)}{\sqrt{\sum_{i=1}^{n} \left(y_{\text{m}}^{i} - \overline{y_{\text{m}}^{i}}\right)^2 \sum_{i=1}^{i} \left(y_{\text{obs}}^{i} - \overline{y_{\text{obs}}}\right)^2}} \right)^2 \tag{8.2}$$

Root-Mean-Square-Error The Root-Mean-Square-Error (RMSE) index measures the average difference between predicted and observed variables and can be calculated as follows (Fisher et al., 1920):

$$\text{RMSE} = \sqrt{\frac{\sum_{i=1}^{n} \left(y_{m}^{i} - y_{\text{obs}}^{i}\right)^2}{n}} \tag{8.3}$$

PBIAS The Percent bias (PBIAS) measures the average tendency of the modeled values to be larger or smaller than observations. PBIAS ranges from $-\infty$ to $+\infty$. Ideally, PBIAS should be zero, with positive values indicating overestimation bias, whereas negative values indicates model underestimation bias. PBIAS can be calculated as (Neyman e Pearson, 1936):

$$\text{PBIAS} \ = \frac{\sum_{i=1}^{n} \left(y_{\text{obs}}^{i} - y_{\text{m}}^{i}\right)}{\sum_{i=1}^{n} y_{\text{obs}}^{i}} \tag{8.4}$$

8.2.2 HydroPol2D - Numerical Modeling Extra Details

HydroPol2D is a numerical hydrodynamic and pollutant transport and fate model. A pseudo-code of the model is presented in Algorithm 3.

8.2.2.1 Matrixwise Stormwater Runoff Mass Balance Equation

The mass balance equation can be written as follows:

$$\frac{\mathrm{d}\boldsymbol{H}(t)}{\mathrm{d}t} = \boldsymbol{B}_i \circ \boldsymbol{I}(t) + \frac{1}{A}\boldsymbol{B}_Q \circ \boldsymbol{Q}(t) - \boldsymbol{F}(\boldsymbol{H}(t), \boldsymbol{F}_d(t)) - \boldsymbol{E}_{TR}(t) + \sum_{i=1}^{m} \left(\overbrace{\boldsymbol{B}_d(\boldsymbol{H}(t))\boldsymbol{Q}_{out}(\boldsymbol{H}(t))}^{\boldsymbol{Q}_{in}(\boldsymbol{H}(t))} - \boldsymbol{Q}_{out}(\boldsymbol{H}(t)) \right) \tag{8.5}$$

where $\boldsymbol{B}_i$ and $\boldsymbol{B}_Q \in \mathbb{R}^{n \times p}$ are boolean time invariant matrices representing cells that receive rainfall and inflow, respectively, $\boldsymbol{B}_d(\boldsymbol{H}(t)) \in \mathbb{R}^{n \times p}$ is the flow distribution time-variant matrix function derived

from the celullar automata rules, $\boldsymbol{H}(t) \in \mathbb{R}^{n \times p}$ is the water surface depths, $\boldsymbol{I}(t) \in \mathbb{R}^{n \times p}$ is the rainfall intensity, $\boldsymbol{F}(\boldsymbol{H}(t), \boldsymbol{F}(t)) \in \mathbb{R}^{n \times p}$ is the infiltration rate, $\boldsymbol{F}_d \in \mathbb{R}^{n \times p}$ is the accumulated infiltration depth, $\boldsymbol{E}_{TR}(t) \in \mathbb{R}^{n \times p}$ is the evapotranspiration rate, $\boldsymbol{Q}_{in}(t)$ and $\boldsymbol{Q}_{out}(t) \in \mathbb{R}^{n \times p}$ are inflows and outflows from each cell, assuming a Von-Neumann squared grid, m is the the number of neighbor cells from a given cell, n and p represents the number of cells in Cartesian coordinates in the domain and t is a time index.

Expanding Eq. (8.5) by a 1st order Taylor's approximation, we can derive an explicit numerical solution for the water surface due to overland flow problem neglecting high order, such that:

$$\boldsymbol{H}(t+\Delta t) = \overbrace{\boldsymbol{H}(t) + \Delta t \left(\boldsymbol{B}_i \boldsymbol{I}(t) + \frac{1}{A} \boldsymbol{B}_Q \boldsymbol{Q}(t) - \boldsymbol{F}(\boldsymbol{H}(t), \boldsymbol{F}_d(t), \boldsymbol{E}_{TR}) - \boldsymbol{E}_{TR}(t) \right)}^{\boldsymbol{H}_{ef}(t)} + \Delta t \sum_{i=1}^{m} \left(\boldsymbol{Q}_{in}^{i}(\boldsymbol{H}(t)) - \boldsymbol{Q}_{out}^{i}(\boldsymbol{H}(t)) \right) \tag{8.6}$$

where $\boldsymbol{H}_{ef}(t) \in \mathbb{R}^{n \times p}$ is the effective depth for overland flow routing. To solve Eq. (8.6), we develop a weighted cellular automata approach using Manning's equation to estimate matrix $\boldsymbol{Q}_{out}$, and using topological relationships between cells, we derive $\boldsymbol{Q}_{in}(t)$ in terms of $\boldsymbol{Q}_{out}(t)$ by calculating $\boldsymbol{B}_d(\boldsymbol{H}(t))$. Details of how to solve the WCA2D model can be found in Ghimire et al. (2013) and (Guidolin et al., 2016) and are described later in Algorithm 4.

8.2.2.2 Warm-Up Process and Initial Values for Modeling

Before starting the hydrodynamic simulations, a warm-up process was simulated to represent the initial conditions of water depths in the TPS and the initial mass of pollutants in the catchment. Initial tests indicated that simulating an event with a hydrograph in the channel inlet provides better warm-up depths in the channel than a rainfall simulation on the grid (i.e., water accumulates only in the channel). Thus, a constant hydrograph with a flow of 0.3 $m^3s^{-1}$for 24 hours was simulated at the beginning of the open stream (coordinates 202762.24; 7563794.99 UTM 23S). This initial flow can represent an eventual base flow and clandestine sewage releases that are often released into the creek. The same inflow is also considered in rain-on-the-grid events. The downstream boundary condition of the domain was assumed to be the critical flow condition, and the outlet pixels were considered the two lowest elevation pixels on the domain boundary. The outlet represents a 25-m wide area with 2 pixels.

A different warm-up process was used to represent the initial conditions of the pollutant mass of the cells. Typically, build-up models assume that the accumulation of pollutants in the catchment is uniform for each type of land use (Rossman e Huber, 2016). Therefore, in a scenario in which the entire catchment had been washed previously (e.g., a relatively large storm), for an accumulated mass equivalent to an ADD, permeable and impermeable areas would deterministically have the same accumulated mass of pollutants in each cell. A previous simulation was performed with ADD = 10 days and rainfall of RP = 1/12 years to determine more realistic conditions for the accumulation of pollutants, which is equal to the rainfall event with a probability exceedance relative to the period of 1 month, assuming a duration of 60 min. The hypothesis is that this event theoretically represents an initial condition of the catchment not fully washed, where a pattern of accumulation is established on the streets, buildings, and channels.

8.2.2.3 Conversion Factor from SWMM to HydroPol2D

Converting wash-off parameters from concentrated modeling to distributed modeling requires a conversion factor f_c that can be estimated as:

Table A.2. Variable definitions, dimensions, and units, where n and p define the domain, and m represent the number of boundary cells per cell.

Class	Symbol	Description	Dimension	Units
Input Matrices and Data	$\boldsymbol{I}(t)$	Rainfall intensity	$\mathbb{R}^{n\times p}$	LT^{-1}
	$\boldsymbol{E}_{TR}(t)$	Evapotranspiration rate	$\mathbb{R}^{n\times p}$	LT^{-1}
	$\boldsymbol{Q}(t)$	Inflow hydrograph	$\mathbb{R}^{n\times p}$	L^3T^{-1}
	ω	Cell area	$\mathbb{R}$	L^2
	$\mathbb{C}$	Set of cells	N.A	N.A
	$\mathbb{O}$	Set of outlet cells	N.A	N.A
	$\mathbb{B}$	Set of domain borders	N.A	N.A
	Δx	Average cell width	$\mathbb{R}$	L
	Δt	Model time-step	$\mathbb{R}$	T
	α_1	Time-step coefficient for water quantity	$\mathbb{R}$	T
	α_2	Time-step coefficient for water quality	$\mathbb{R}$	T
	σ	Slope tolerance	$\mathbb{R}$	LL^{-1}
Infiltration model	$\boldsymbol{F}(t)$	Infiltration rate	$\mathbb{R}^{n\times p}$	LT^{-1}
	$\boldsymbol{F}_d(t)$	Infiltrated depth	$\mathbb{R}^{n\times p}$	L
Flood routing model	$\boldsymbol{H}(t)$	Water surface depth	a	L
	$\boldsymbol{B}_i$	Rainfall incidence matrix	$\mathbb{R}^{n\times p}$	N.A
	$\boldsymbol{B}_q$	Inflow hydrograph incidence matrix	$\mathbb{R}^{n\times p}$	N.A
	$\boldsymbol{B}_d(H(t))$	Flow distribution matrix	$\mathbb{R}^{n\times p}$	N.A
	$\boldsymbol{Q}_{in}(t)$	Inflows in each cell	$\mathbb{R}^{n\times p}$	L^3T^{-1}
	$\boldsymbol{Q}_{out}(t)$	Outflows in each cell	$\mathbb{R}^{n\times p}$	L^3T^{-1}
	$\boldsymbol{H}_{ef}(t)$	Effective depth for overland flow	$\mathbb{R}^{n\times p}$	L
Cellular Automata	**WSE**	Water surface elevation	$\mathbb{R}^{n\times p}$	L
	s_0^b	Outlet slope boundary condition	$\mathbb{R}$	L.L-1
	g	Gravity acceleration	$\mathbb{R}$	L^3T^{-2}
	$\boldsymbol{N}$	Manning's roughness coefficient	$\mathbb{R}^{n\times p}$	$TL^{-1/3}$
	Δh_{min}	Minimum assumed water level difference	$\mathbb{R}$	L
	$\Delta \boldsymbol{V}$	Available free volume within boundary cells	$\mathbb{R}^{n\times p\times(m+1)}$	L^3
	$\Delta \boldsymbol{H}_{ef}$	Available water depth within boundary cells	$\mathbb{R}^{n\times p\times(m+1)}$	L
	$\Delta \boldsymbol{V}_{min}$	Minimum intercell volume transfer	$\mathbb{R}^{n\times p}$	L^3
	$\Delta \boldsymbol{V}_{max}$	Maximum intercell volume transfer	$\mathbb{R}^{n\times p}$	L^3
	$\boldsymbol{\Omega}$	Weights for each direction	$\mathbb{R}^{n\times p\times m}$	N.A
	$\boldsymbol{V}_m$	Maximum outflow velocity per each cell	$\mathbb{R}^{n\times p}$	LT^{-1}
	$\boldsymbol{I}_{tot}^*$	Total intercell volume	$\mathbb{R}^{n\times p}$	L^3
	$\boldsymbol{V}_{min}$	Minimum intercell transferable volume	$\mathbb{R}^{n\times p}$	L^3
Build-up and wash-off	$\boldsymbol{\Phi}$	Wash-off rate	$\mathbb{R}^{n\times p}$	MT^{-1}
	$\boldsymbol{C}_1$	Build-up coefficient	$\mathbb{R}^{n\times p}$	ML^{-2}
	$\boldsymbol{C}_2$	Build-up exponent	$\mathbb{R}^{n\times p}$	T^{-1}
	$\boldsymbol{C}_3$	Wash-off coefficient	$\mathbb{R}^{n\times p}$	$(LT^{-1})^{C_4}T^{-1}$
	$\boldsymbol{C}_4$	Wash-off exponent	$\mathbb{R}^{n\times p}$	N.A
	$\boldsymbol{B}_{out}^i$	Mass of pollutant washed for direction i	$\mathbb{R}^{n\times p}$	M
	$\boldsymbol{W}_{out}^{tot}$	Sum of washed pollutant for all directions	$\mathbb{R}^{n\times p}$	M
	$\boldsymbol{B}$	Available mass of pollutant in each cell	$\mathbb{R}^{n\times p}$	M
	$\boldsymbol{C}(t)$	Instantaneous pollutant concentration	$\mathbb{R}^{n\times p}$	$ML^{-3'}$

Algorithm 3: Main Algorithm, where $\gamma, \tau, \theta,$ and β are time vectors and F_d is the accumulated infiltration depth. The details of all input data are described in Table S1 in the supplemental material section.

input: Input maps and parameters from .TIFF and .xlsx files (i.e., Digital Elevation Model, Land Use and Land Cover Map) time, minimum and maximum time-step, stability method, outlet boundary cells, cells receiving rainfall, cells receiving inflow hydrograph, recording times for maps and for hydrographs, outlet boundary condition type, outlet boundary condition slope, flag to correct water balance, flag to simulate water quality, antecedent dry days, flag do correct time-step
set: Hydrologic, Hydrodynamic, and Water Quality distributed parameters according to input maps
while $t <$ *Routing Time* **do**
    compute: Infiltration Capacity through Green-Ampt Model
    compute: Inflow Rate from rainfall, inflow hydrograph and neighbor cells outflow
    compute: Infiltration Rate = min(Infiltration Capacity, Inflow Rate)
    compute: Cellular Automata Weighted System from Algorithm 4 and find $Q_{out}, H_{ef}, I^*_{tot}$
    compute: Build-up and Wash-off problem and determine spatial washed mass of pollutant and concentration
    if $t \in \gamma$ **then**
        Check stability criteria and refresh time-step
    end if
    compute: Disaggregation of inflow and rainfall to the time-step used
    if $t \in \tau$ **then**
        Resize all state matrices to the new coordinate system
    end if
    compute: 2-D discretized solution of the mass balance of stormwater runoff and pollutant mass
    compute: Water Balance Error
    if *Water Balance Error* $>$ *Tolerance* **then**
        Redistribute water balance error in the inflow cells
    end if
    if $t \in \theta$ **then**
        Save maps of water surface depths and pollutant concentration
    end if
    if $t \in \beta$ **then**
        Save hydrographs and pollutugraphs at the outlet
    end if
end while
output: Export Hydrographs, Pollutographs, .TIFF maps, and GIFs of water surface elevations and pollutant distributions over time

Algorithm 4: Cellular automata pseudocode

input: Cell elevations, initial surface water depths, $\boldsymbol{N}$, $\boldsymbol{H}_0$, Δt, Δx, s_0^b, c, Velocity to the steepest direction $\boldsymbol{V}_m$, Intercell Volume $\boldsymbol{I}_{tot}$ previous outflow volumes, Minimum water depth Δh_{min} Set of cells $\mathbb{C}$, Outlet cells $\mathcal{O}$, Domain borders $\mathbb{B}$
for *i = 1 to m* **do**
  compute: $\Delta \boldsymbol{H}_{ef,i} = \mathbf{WSE} - \mathbf{WSE}_i$, $\Delta \boldsymbol{H}_{ef} \in \mathbb{R}^{n \times p \times (m+1)}$, $\mathbf{WSE} \in \mathbb{R}^{n \times p}$
end for
if *Outlet Type = 1* **then**
  compute: $\Delta \boldsymbol{H}_{ef,m+1} = s_0^b \Delta x \; \forall \; \mathbb{C} \in \mathbb{O}$
else
  compute: $\Delta \boldsymbol{H}_{ef,m+1} = \boldsymbol{H}_{ef}^{\circ -1/6} g^{0.5} \circ \boldsymbol{N} \; \forall \; \mathbb{C} \in \mathbb{O}$
end if
$\boldsymbol{H}_{ef,m+1} \leftarrow 0 \; \forall \; \mathbb{C} \in \mathbb{B}$
$\boldsymbol{\Delta H}_{ef} \leftarrow 0 \; \forall \; \Delta \boldsymbol{H}_{ef} \leq \Delta h_{min}$
compute: $\Delta \boldsymbol{V} = A \Delta \boldsymbol{H}_{ef}$, $\Delta \boldsymbol{V} \in \mathbb{R}^{n \times p \times (m+1)}$
$\Delta \boldsymbol{V} \leftarrow c, \; \forall \; \Delta \boldsymbol{V} = 0$
compute: $\Delta \boldsymbol{V}_{max} = \max(\Delta \boldsymbol{V})$, $\Delta \boldsymbol{V}_{max} \in \mathbb{R}^{n \times p}$
compute: $\Delta \boldsymbol{H}_{ef,max} = \max(\Delta \boldsymbol{H}_{ef})$, $\Delta \boldsymbol{H}_{ef,max} \in \mathbb{R}^{n \times p}$
compute: $\Delta \boldsymbol{V}_{min} = \min(\Delta \boldsymbol{V})$, $\Delta \boldsymbol{V}_{min} \in \mathbb{R}^{n \times p}$
compute: $\boldsymbol{\Omega} = (\Delta \boldsymbol{V}_{tot} + \Delta \boldsymbol{V}_{min}) \oslash \Delta \boldsymbol{V}$, $\boldsymbol{\Omega} \in \mathbb{R}^{n \times p \times (m+1)}$
compute: $\boldsymbol{\Omega}_{max} = \max(\boldsymbol{\Omega})$, $\boldsymbol{\Omega}_{max} \in \mathbb{R}^{n \times p}$
compute:
$\boldsymbol{V}_m = \min\left(\sqrt{g} \boldsymbol{H}_{ef}^{\circ 0.5}, \boldsymbol{N} \oslash \max(\boldsymbol{H}_{ef} - \boldsymbol{H}_0)^{\circ 2/3} \circ (\boldsymbol{H}_{ef,max}(1/\Delta x))^{\circ 0.5}\right)$, $\boldsymbol{V}_m \in \mathbb{R}^{n \times p}$
compute: $\boldsymbol{I}_{tot}^* = \min(\omega \boldsymbol{H}_{ef}, (\Delta x / \Delta t) \boldsymbol{V}_m \circ \boldsymbol{H}_{ef}, \boldsymbol{I}_{tot}^p + \Delta \boldsymbol{V}_{min})$, $\boldsymbol{I}_{tot}^* \in \mathbb{R}^{n \times p}$
compute: $\boldsymbol{I}_{tot}^* \leftarrow \text{sum}_3(\boldsymbol{\Omega} \circ \boldsymbol{I}_{tot}^*)$
compute: $\boldsymbol{Q}_{out} = 1/(\Delta t A) \boldsymbol{I}_{tot}^*$, $\boldsymbol{Q}_{out} \in \mathbb{R}^{n \times p \times m}$
compute: $\boldsymbol{H}_{ef} \leftarrow \boldsymbol{H}_{ef} - (1/\omega) \boldsymbol{I}_{tot}^*$
output: $\boldsymbol{Q}_{out}$, , $\boldsymbol{H}_{ef}$, $\boldsymbol{I}_{tot}^*$

$$f_c = \left(\frac{3600 \times 1000}{\Delta x^2} \right)^{C_3^*} \tag{8.7}$$

where Δx is the pixel size (m) and f_c converts C_3^*, the wash-off coefficient for concentrated modeling, to C_3, the wash-off coefficient for distributed modeling.

The application of the aforementioned equation for different pixel resolutions and C3 and C4 values are shown in the following figure:

8.2.2.4 Evapotranspiration Modeling

Although not often considered in rapid and intense flood modeling, evapotranspiration (ET) is important in continuous simulation models. ET is the process of evaporation in the soil-plant system transferring water to the atmosphere (Sentelhas et al., 2010). Several models are available to estimate the reference evapotranspiration (E_{to}) flux in monthly (Thornthwaite, 1948), daily (Hargreaves e Samani, 1985), or even sub-daily scale (Allen et al., 1989). The input data required to simulate it varies, and the proper selection of the model should be done according to data availability at the catchment. In this paper, we use the Penman-Monteith model, which requires spatialized data of wind speed at 2m from surface, relative humidity, temperature, and radiation. However, the latter can be indirectly estimated using the method presented as follows. Let (i, j) collect the central coordinates of a specific cell. The rate of evapotranspiration can be estimated as:

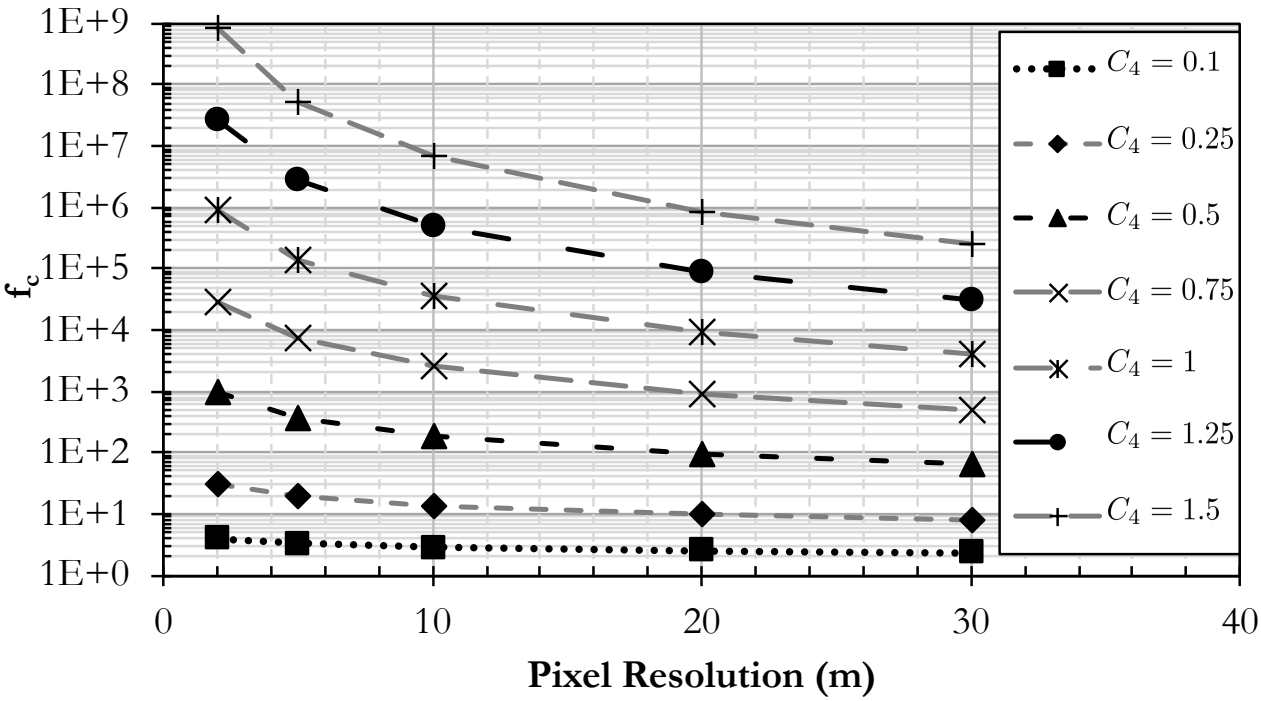

Figure A.1. Conversion factor from SWMM to HydroPol2D wash-off parameters.

$$e_{to}^{i,j} = \frac{0.408 \times \Delta^{i,j}(r_n^{i,j} - g^{i,j}) + \gamma^{i,j} \times \frac{900}{t^{i,j}+273} \times u_2^{i,j} \times (e_s^{i,j} - e_a^{i,j})}{\Delta^{i,j} + \gamma^{i,j} \times (1 + 0.34 \times u_2^{i,j})} \tag{8.8}$$

where $\Delta^{i,j}$ = slope vapor pressure curve (kPa°C^{-1}), $r_n^{i,j}$ = net radiation at the crop surface (MJm^{-2}day^{-1}), $g^{i,j}$ = soil heat flux density (MJm^{-2}day^{-1}), $\gamma^{i,j}$ = psychrometric constant constant (kPa°C^{-1}), $t^{i,j}$ = mean daily air temperature at 2 m height in (°C), $u_2^{i,j}$ = wind speed at 2 m height (ms^{-1}), $e_s^{i,j}$ = saturation vapor pressure (kPa) and $e_a^{i,j}$ = actual vapor pressure (kPa).

This model is programmed to be implemented with all the inputs required in Penman Monteith ($\Delta^{i,j}$, $r_n^{i,j}$, $g^{i,j}$, $fl^{i,j}$, $u_2^{i,j}$, $e_s^{i,j}$, $e_a^{i,j}$ and $t^{i,j}$), but due to the lack of sub-day data in several regions, we applied methods to simplify the database and reduce the number of input data. To this end, parameters such as $fl^{i,j}$, $r_n^{i,j}$, $e_s^{i,j}$ and $e_a^{i,j}$ can be estimated with the input of spatially referenced areas, altitudes, temperatures for each watershed cell and, considering, some coefficients according to the location and the day of the year (Allen et al., 1998; Conceição, 2006). The $fl^{i,j}$ variable can be quantified by establishing a relationship with atmospheric pressure (8.9), which will only require the altitude data extracted from the digital elevation model ($z^{i,j}$) (8.10).

$$\gamma^{i,j} = 0.665 \times 10^{-3} \times p_{atm}^{i,j} \tag{8.9}$$

$$p_{atm}^{i,j} = 101.3 \times \left(\frac{293 - 0.0065 \times z^{i,j}}{293}\right)^{5.26} \tag{8.10}$$

where $p_{atm}^{i,j}$ = atmospheric pressure (kPa) and $z^{i,j}$ = altitude (meters).

The simplifications made for $e_s^{i,j}$ (kPa) (8.11), $e_a^{i,j}$ (kPa) (8.12), $\Delta^{i,j}$ (kPa°C^{-1}) (8.13), and $r_n^{i,j}$ (MJm^{-2}day^{-1}) (8.14) are presented below. The only input required for them is $g^{i,j}$ (MJm^{-2}day^{-1}), day of the year (d) (1 to 366 $\in \mathbb{N}_{++}$), latitude ($Œ^{i,j}$) (rad) and maximum ($t_{max}^{i,j}$) (°C), minimum ($t_{min}^{i,j}$) (°C) and average temperatures ($t^{i,j}$) (°C).

$$e_s^{i,j} = 0.6108 \times \exp\left[\frac{17.27 \times t^{i,j}}{t^{i,j} + 237.3}\right] \tag{8.11}$$

$$e_a^{i,j} = 0.61 \times \left(\frac{17.27 \times t_{min}^{i,j}}{t_{\text{min}}^{i,j} + 237.3}\right) \tag{8.12}$$

$$\Delta^{i,j} = \frac{4098 \times \left[0.6108 \times \exp\left(\frac{17.2 \times t^{i,j}}{t^{i,j}+237.3}\right)\right]^2}{t^{i,j} + 237.3} \tag{8.13}$$

$$r_n^{i,j} = r_{ns}^{i,j} - r_{nl}^{i,j} \tag{8.14}$$

where $\text{r}_{\text{ns}}^{\text{i,j}}$ = short-wave radiation ($\text{MJm}^{-2}\text{day}^{-1}$), expressed in following equation (8.15) and $\text{r}_{\text{nl}}^{\text{i,j}}$ = long-wave radiation ($\text{MJm}^{-2}\text{day}^{-1}$), later detailed in (8.21).

$$r_{ns}^{i,j} = (1 - \alpha) \times r_s^{i,j} \tag{8.15}$$

where $\text{r}_{\text{s}}^{\text{i,j}}$ = incident solar radiation ($\text{MJm}^{-2}\text{day}^{-1}$) (8.16) and ff = 0.23, albedo coefficient for the culture referee (grass). Note that α can change according to the land cover in the watershed. Therefore, r_s can be calculated as:

$$r_s^{i,j} = k_{rs} \times r_a^{i,j} \times \sqrt{(t_{max}^{i,j} - t_{min}^{i,j})} \tag{8.16}$$

where $\text{r}_{\text{a}}^{\text{i,j}}$ = solar radiation at the top of the atmosphere ($\text{MJm}^{-2}\text{day}^{-1}$) (8.17) and k_{rs} = coefficient of 0.16 for continental areas and 0.19 to coastal areas. The solar radiation, however, is a periodic function of ϕ and is related to the relative distance between the sun and the surface, such that:

$$r_a^{i,j} = \frac{118.08}{\pi} \times d_r^{i,j} \times \left[w_s^{i,j} \times \sin(\phi^{i,j}) \times \sin(\delta^{i,j}) + \cos(\phi^{i,j}) \times \cos(\delta^{i,j}) \times \sin(w_s^{i,j})\right] \tag{8.17}$$

where $\text{d}_{\text{r}}^{\text{i,j}}$ = inverse relative distance between Earth and Sun (rad) (8.18), $\text{w}_{\text{s}}^{\text{i,j}}$ = sunrise angle (rad) (8.19) and $\text{ffi}^{\text{i,j}}$ = solar declination (rad) (8.20). We can estimate d_r as a periodic function of d, such that:

$$d_r^{i,j} = 1 + 0.33 \times \cos\left(\frac{2 \times \pi}{365} \times \text{d}\right) \tag{8.18}$$

Moreover, w_s from (8.17) is a function of the latitude and δ, such that:

$$w_s^{i,j} = \frac{\pi}{2} - \text{arctg} \times \left[\frac{-\tan(\phi^{i,j}) \times \tan(\delta^{i,j})}{(1 - [\tan(\phi^{i,j})]^2 \times [\tan(\delta^{i,j})]^2)^{0.5}}\right] \tag{8.19}$$

if $(1 - [\tan(\text{Œ}^{\text{i,j}})]^2 \times [\tan(\text{ffi}^{\text{i,j}})]^2) \leq 0$, we use $1\text{e} - 5$. Variable δ can be estimated as:

$$\delta^{i,j} = 0.409 \times \sin\left(\frac{2}{\pi} \times \text{d} - 1.39\right) \tag{8.20}$$

$$r_{nl}^{i,j} = \sigma \times \left[\frac{(t_{max}^{i,j} + 273.16)^4 + (t_{min}^{i,j} + 273.16)^4}{2}\right] \times (0.34 - 0.14 \times \sqrt{(e_a^{i,j})}) \times \left(1.35 \times \frac{r_s^{i,j}}{r_{so}^{i,j}} - 0.35\right) \tag{8.21}$$

where $\text{œ} = 4.903 \times 10^{-9}$ ($\text{MJm}^{-2}\text{day}^{-1}$) and $\text{r}_{\text{so}}^{\text{i,j}}$ = incident solar radiation without clouds ($\text{MJm}^{-2}\text{day}^{-1}$), resulting in:

$$r_{so}^{i,j} = (0.75 + 2 \times 10^{-5} \times \text{z}^{\text{i,j}}) \times r_a^{i,j} \tag{8.22}$$

More background and rationale of these methods can be found in Conceição (2006).

8.2.2.5 Soil Recover and Groundwater Replenishing

Three hydrological processes are assumed to occur in the soil media. The evapotranspiration and sub-surface drainage reduce the water content in the media, whereas infiltration from the upper zone increases it. We focus here on the methods to estimate sub-surface exfiltration rate (f_g), which depends on the replenishing rate k_r and on the uppermost layer depth l_u, written as (Rossman, 2010):

$$k_r = \frac{\sqrt{k_{sat}/25.4}}{75} \tag{8.23}$$

$$t_r = \frac{4.5}{\sqrt{k_{sat}/25.4}} \tag{8.24}$$

$$l_u = 4\sqrt{k_{sat}/25.4} \tag{8.25}$$

where k_r = replenishing rate (1/h), t_r = recovery time (h), and l_u = uppermost layer depth (m).

From previous equations, we can infer that the sub-surface exfiltration rate is given by:

$$f_g = (\theta_{sat} - \theta_i) k_r l_u 1000 \tag{8.26}$$

where f_g = sub-surface exfiltration rate (mm/h), θ_{sat} = saturated soil content (−), and θ_i = initial soil content (−). Therefore, f_g is a constant sub-surface exfiltration rate applied in the water balance equation.

8.2.2.6 Hydrograph Separation with Eckhart Filter

The Eckhart digital filter allows separation of surface runoff from the baseflow using observed streamflow data and can be used in HydroPol2D to estimate groundwater fluxes. Therefore, observed streamflow data is required. Usually, this data is derived from fitted rain curves using daily stage observations that ultimately convert the stage into discharges (Gomes Jr et al., 2023a). By considering a filter that separates runoff (i.e., rapid response) from the baseflow (i.e., slow reservoir), one can estimate the proportion of observed hydrograph that corresponds to each flow clasification. Therefore, it is possible to obtain daily flow and baseflow hydrographs. The total observed stream flow is composed by the runoff and baseflow, given by Eq. (8.27a). The baseflow-index, which is the long-term ratio between the baseflow and the total volume, depends on the aquifer porosity properties and can be estimated by a regression made for several brazilian watersheds as a function of the 90th and 50th percentile discharges (Collischonn e Fan, 2013) as shown in Eq. (8.27b). During periods of hydrograph recession, the decay in the hydrograph is assumed by the releasing of the aquifer water from the groundwater linear reservoir. The aquifer decay coefficient k can be calculated by defining two points on the recession curve and solving Eq. (8.27c). The solution of the digital filter using the signal processing theory require another paramter a, that is given by Eq. (8.27d) and the baseflow for a time t can be estimated in Eq. 8.27e.

$$Q_{\text{obs}}(t) = Q_{\text{r}}(t) + b(t) \tag{8.27a}$$

$$\text{BFI}_{\text{max}} = 0.8344\frac{Q_{90}}{Q_{50}} + 0.2146 \tag{8.27b}$$

$$k = \frac{-\Delta t^d}{\ln\left(\frac{Q_{\text{obs}}(t+\Delta t^d)}{Q_{\text{obs}}(t)}\right)} \tag{8.27c}$$

$$a = e^{\frac{-\Delta t^b}{k}} \tag{8.27d}$$

$$b(t) = \frac{(1 - \mathrm{BFI_{max}})\, ab(t - \Delta t^b) + (1 - a)\mathrm{BFI_{max}} Q_{\mathrm{obs}}(t)}{1 - a\mathrm{BFI_{max}}} \tag{8.27e}$$

where $b(t)$ is the baseflow, Δt^b is the baseflow time-step, Δt^d is a time-step where two points of the recession curve are obtained, Q_{r} is the runoff discharge, Δt^d is a drought time-step, Q_{obs} is the total observed streamflow, $\mathrm{BFI_{max}}$ is the baseflow index, k is the aquifer decay constant, Q_{90} is the 90th percentile of exceedance of stream flow, and Q_{50} is the streamflow of the 50th percentile.

We perform hydrograph separation for all stream gauges and calculate the specific average daily baseflow and average lateral ground flux as follows:

$$\bar{q_A}^i = \frac{1}{A^i n \Delta t^b} \sum_{j=1}^{n} b_j \tag{8.28a}$$

$$\bar{q_L}^i = \frac{1}{L^i n \Delta t^b} \sum_{j=1}^{n} b_j \tag{8.28b}$$

where q_A is the specific baseflow per unit of superficial drainage area, q_L is the specific baseflow per unit of stream, n is the number of time-steps, L is the streamflow length, A is the upstream drainage area, n is the number of observations, and i is the location of the stream gauge.

In this paper, to allow for a simple conceptualization of groundwater flux, we average all lateral stream fluxes such that the dependency of sub-catchments is disregarded by an assumption of a single average lateral groundflux, such that:

$$\bar{q}_L = \frac{1}{n_g} \sum_{i=1}^{n_g} \bar{q}_L^i \tag{8.29}$$

where $\bar{q}_L$ is the average lateral groundflux calculated from all observed streamgauges in the watershed, and n_g is the number of streamgauges.

HydroPol2D is a sub-hourly rainfall-runoff model that is typically solved with relatively smaller time-steps. To this end, the baseflow hydrograph can be incorporated into the mass balance by a lateral flux that enters the streamlines, such that a lateral groundwater flux $\bar{q}_l$ calculated from Eq. (8.29) changes the mass balance equation such that (Gomes et al., 2023):

$$\frac{\partial d^{i,j}(t)}{\partial t} = \Big[\sum_{\mathcal{N}^{i,j}} I^{i,j}(t) - \sum_{\mathcal{N}^{i,j}} O^{i,j}(t) + i^{i,j}(t) - f^{i,j}\Big(d^{i,j}(t), F_d^{i,j}(t)\Big) - e_{\mathrm{T}}^{i,j}(t) - \bar{q}_L \Delta x \Big] \tag{8.30}$$

where $d^{i,j}(t)$ is the water surface depth (m), $I^{i,j}(t)$ is the inflow rate ($\mathrm{LT^{-1}}$), $O^{i,j}(t)$ is the outflow rate ($\mathrm{LT^{-1}}$), $i^{i,j}(t)$ is the rainfall intensity ($\mathrm{LT^{-1}}$), $f^{i,j}(t)$ is the infiltration rate ($\mathrm{LT^{-1}}$), $F_d(t)$ is the infiltrated depth of water into the soil (L), and $e_T^{i,j}(t)$ is the evapotranspiration rate ($\mathrm{LT^{-1}}$).

The previous equation is solved using a forward Euler discretization and gives states from $t + \Delta t$ in terms of inputs and states from t.

8.2.2.7 HydroPol2D Reservoir Modeling Routine

To simulate reservoir control in a 2D fashion, we imply a boundary condition at the reservoir dam, such that flow is limited to the available volume of water in the upstream cell and the spillway capacity. Let (i_g, j_g) be the gate location coordinates in the domain. The spillway capacity can be modeled through a Francis-type spillway equation such that:

$$Q^{i_g j_g}(t) = \max\Big(C d^{i_g, j_g} L_{ef}^{i_g, j_g} (z^u + d^u(t) - p^{i_g, j_g})^{3/2}, \frac{\Delta x^2 d^u(t)}{\Delta t} \Big), \ \forall \text{ gates} \tag{8.31}$$

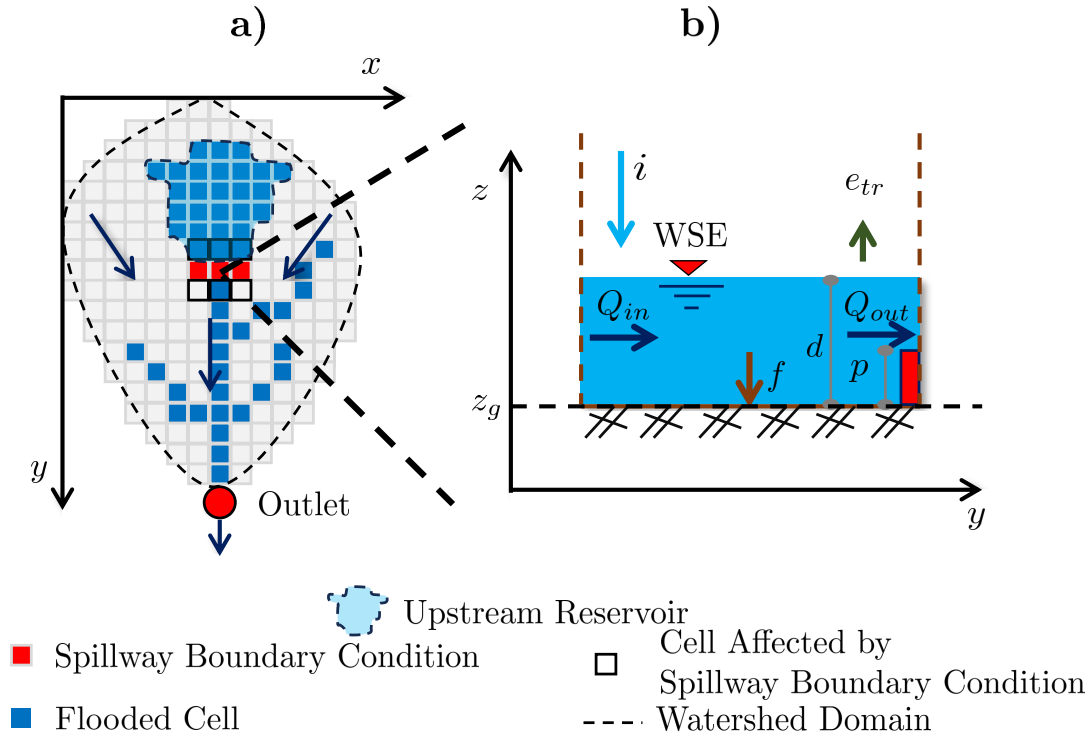

Figure A.2. Effect of a reservoir in a 2D meshgrid of HydroPol2D. Part a) shows the flooded cells, the cells with spillway boundary conditions, and the cells affected to this boundary conditions. Part b) shows how the flow is confined in the upstream reservoir. Hydrological variables i = rainfall intensity, f = infiltration rate, d = water surface depth, WSE = water surface elevation, Q_{in} = inflow discharge are used to estimate the spillway boundary condition expressed by Q_{out}.

where $(z^u + d^u)$ is the water surface elevation of the upstream cell connected to the gate cell, C_d is the spillway discharge coefficient, L_{ef} is the effective spillway length, p is the spillway elevation, Δx is the cell length, and Δt is the computational time-step.

The gate is then categorized by the effective length of the spillway, its discharge coefficient, its height, and the downstream cell ($i = 1, 2, \ldots m$, such that 1 = rightwards, 2 = leftwards, 3 = upwards, 4 = downwards for a Von-Neuman grid. Knowing the downstream cell of a gate allows us to define the upstream cell, which is assumed to be the diametral opposite cell to the downstream one.

Although the boundary condition described is designed for reservoir gates, it can represent channels and other hydraulic structures that follow a power relationship with the water depth.

8.2.2.8 Interpolation of Rainfall ETP and Climatological Forcing

HydroPol2D allows interpolating spatially distributed input data using the Inverse-Distance-Weightning method (Bartier e Keller, 1996), which is calculated as follows. Given a n_s number of stations with recorded values, we store the station values for a given time t in $\boldsymbol{z}_s(t) = [z_s^1(t),\, z_s^2(t), \ldots z_s^{n_s}(t)]^T$. The stations are located at known projected coordinates x and y described by vectors $\boldsymbol{x}_s$ and $\boldsymbol{y}_s$, respectively. We apply the IDW method (Bartier e Keller, 1996) by calculating the p-norm (i.e., projected distance for a euclidean norm) between each point of the meshgrid and the stations.

$$\hat{z}(\mathbf{x_s}, \mathbf{y_s}) = \frac{\sum_i^{n_c} w_i z_s^i}{\sum_i^n w_i},\; w_i = ||(\mathbf{x_s}, \mathbf{y_s}) - (\mathbf{x_i}, \mathbf{y_i})||_2^{-\beta} \tag{8.32}$$

where n_c is the number of cells in the catchment, β is the weighting factor and is typically asssumed equals 2 to represent the Euclidean distance.

8.2.3 Watershed Geometrical Indicators

8.2.3.1 Compactness Coefficient

The compactness coefficient relates the perimeter of the catchment and a perimeter of a circle with the same area such that:

$$k_c = \frac{0,28P}{\sqrt{A}} \tag{8.33}$$

where P is the perimeter of the catchment and A is its area.

8.2.3.2 Form Factor

It is the relationship between the average width of the catchment (W) and the length of the catchment axis (L) (from the mouth to the farthest point in the area). The average width of the basin is typically determined by geoprocessing software. However, in the developed model, this width is estimated as follows:

$$\bar{L} = \sqrt{W^2 + H^2} \tag{8.34}$$

where W and H are the largest $x - x$ length, and $y - y$ length in the 2-D spatial domain, respectively.

Therefore, the factor form is given by:

$$K_f = \frac{A}{\bar{L}} \tag{8.35}$$

8.2.3.3 Circularity Index

The circularity index is the ratio between the catchment area and the correspondent perimeter of a circle with the same perimeter such that:

$$IC = 12,57\frac{A}{P^2} \tag{8.36}$$

8.2.4 Water Quality Calibration Module

The decision variables for the optimization problem are the wash-off coefficients C_3 and C_4 and the problem is solved with the genetic algorithm for a 40 generation and population size of 100. The build-up coefficients C_1 and C_2 were not used in the calibration since the initial mass of salt is known. Let x be the decision vector collecting the optimized water quality parameters, such that $x = [C_3^{\text{opt}}, C_4^{\text{opt}}]^T$. Let $\boldsymbol{x}_l$ collect the lower boundary conditions of C_3 and C_4, such that $\boldsymbol{x}_l = [C_3^l, C_4^l]^T$. Similarly, let $\boldsymbol{x}_m$ collect upper bounds of the water quality parameters, such that $\boldsymbol{x}_m = [C_3^m, C_4^m]^T$. We want to formulate a calibration optimization problem such that the root mean square error (RMSE) between the observed solute concentration and modeled solute concentration is minimized. Therefore, we can write the objective function as follows:

$$\text{OF} = \text{RMSE} = \sqrt{\frac{\sum_{i=1}^{n} \left(C_{mod}^i - C_{obs}^i\right)^2}{n}} \tag{8.37}$$

where C_{mod} and C_{obs} are the modeled and observed solute concentrations and n is the number of concentration observations.

The inputs for the optimization problem are:

- Hyetograph

- Watershed Parameters
- Observed Pollutograph (i.e., pollutant concentration)

The algorithm developed can also work with equality and inequality constraints. These are defined by matrices $\boldsymbol{A}_{\text{eq}}$, $\boldsymbol{B}_{\text{eq}}$, and $\boldsymbol{A}$, $\boldsymbol{B}$. Therefore, we can formally describe the optimization problem as follows:

$$\min_{C_3, C_4} \text{Eq. (8.37)}$$

$$\begin{aligned} \text{s.t. } & \text{HydroPol2D Dynamics} \\ & \boldsymbol{A}_{\text{eq}}\boldsymbol{x} = \boldsymbol{B}_{\text{eq}} \\ & \boldsymbol{A}\boldsymbol{x} \leq \boldsymbol{B} \\ & \boldsymbol{x}_l \leq \boldsymbol{x} \leq \boldsymbol{x}_m \end{aligned} \tag{8.38}$$

In Matlab, several solvers can be used to solve the previous equation (e.g., global search, pattern search. In this paper, we used the genetic algorithm solver. Since the problem is non-linear and non-convex, we aimed to provide relatively enough numbers of population and generation in the simulation to try catching global solutions. We assumed a 100-population and 40-generations in the modeling for both calibration, that is, for events with 0.5° and 2° slopes.

The optimized results for events with 0.5° are shown in Fig. A.3. The resulting water quality parameters from the optimization simulation are $C_3^{\text{opt}} = 9036.83813876743$ and $C_4^{\text{opt}} = 0.243545935909623$.

8.2.5 Detailed Results of Water Quality Modeling - Event 4

In the HydroPol2D model, users can access detailed reports, summary figures, and GIF files with spatial states shown in time. In this section, we show the HydroPol2D automatic results generated from the post-processing codes. The following graphs show (i) hydrographs and Rainfall, (ii) Concentrations and loads, (iii) Discharges and Concentrations, (iv) rating curve, (v) M(V) Curve, (vi) EMC variation with time. In addition to graphs, as mentioned above, all data are also saved and exported in .csv files. Finally, GIFs and .tifs from spatial data are generated and shown automatically on the screen.

8.2.6 HydroPol2D - Input data structure

For the HydroPol2D input data structure, we use .xlsx sheets to facilitate the procedure of feeding the model with input data. In Fig. A.10 is shown a general view of the general input data structure. Here, we briefly explain each input data section:

1. Running Control:this section defines the time-steps for each sub-component of the model. In addition, it defines the running control, that is, the beginning and end of the simulation. This section also includes the parameters of the CFL stability criteria.
2. General Flags: This section defines the model options allowed in HydroPol2D. Each value equal to 1 indicates that a condition is implied in the model (e.g., $flag\_rainfall = 1$ means that rainfall is being model, whereas $flag\_rainfall = 0$ indicates that no infiltration is modeled). The user defines the modeling conditions, e.g., rainfall (lumped or distributed), model hydrodynamic structure (kinematic or diffusive), consideration of ETP calculation, among others.

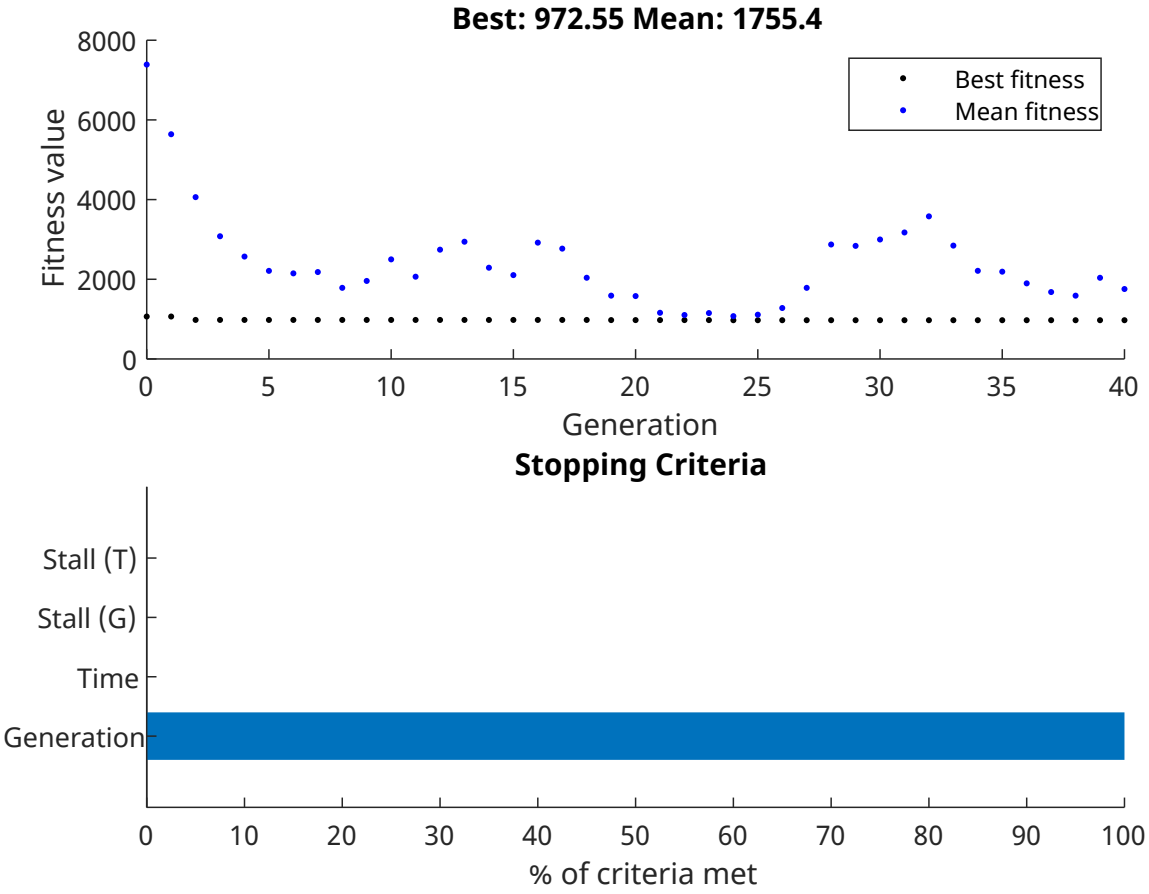

Figure A.3. Optimization Summary for Events with 0.5° slope. Results obtained using the genetic Algorithm to minimize the RMSE (mg/L) between the modeling and the observed solute concentrations.

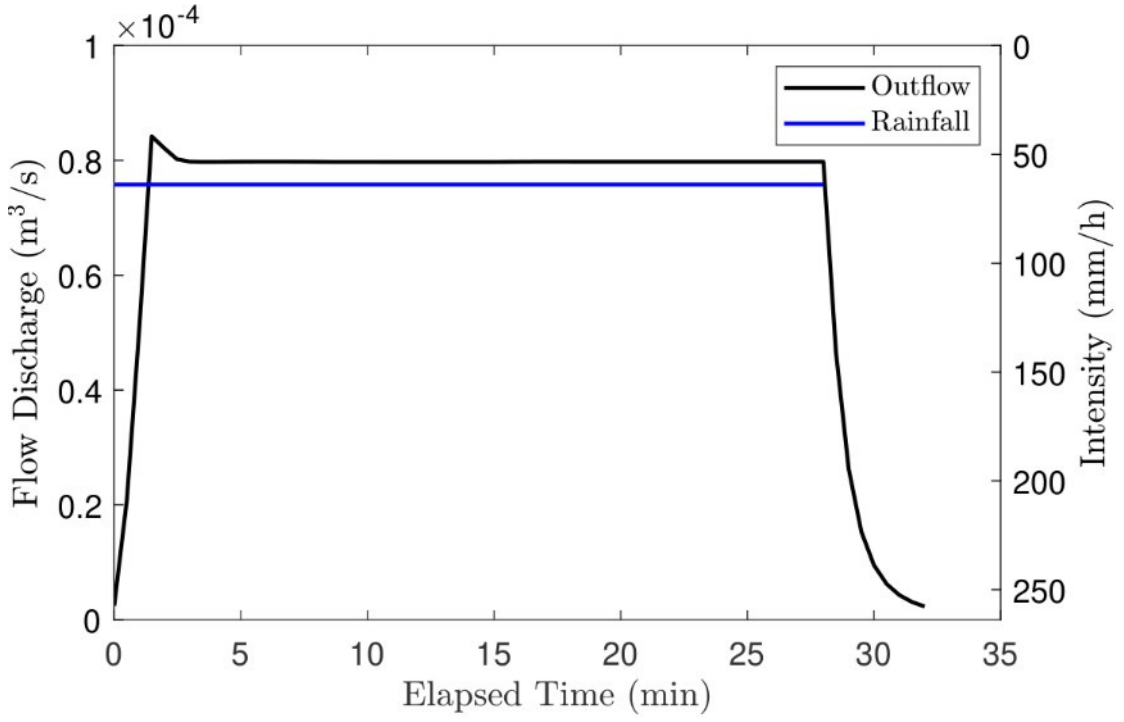

Figure A.4. Outlet hydrograph and Rainfall Intensity.

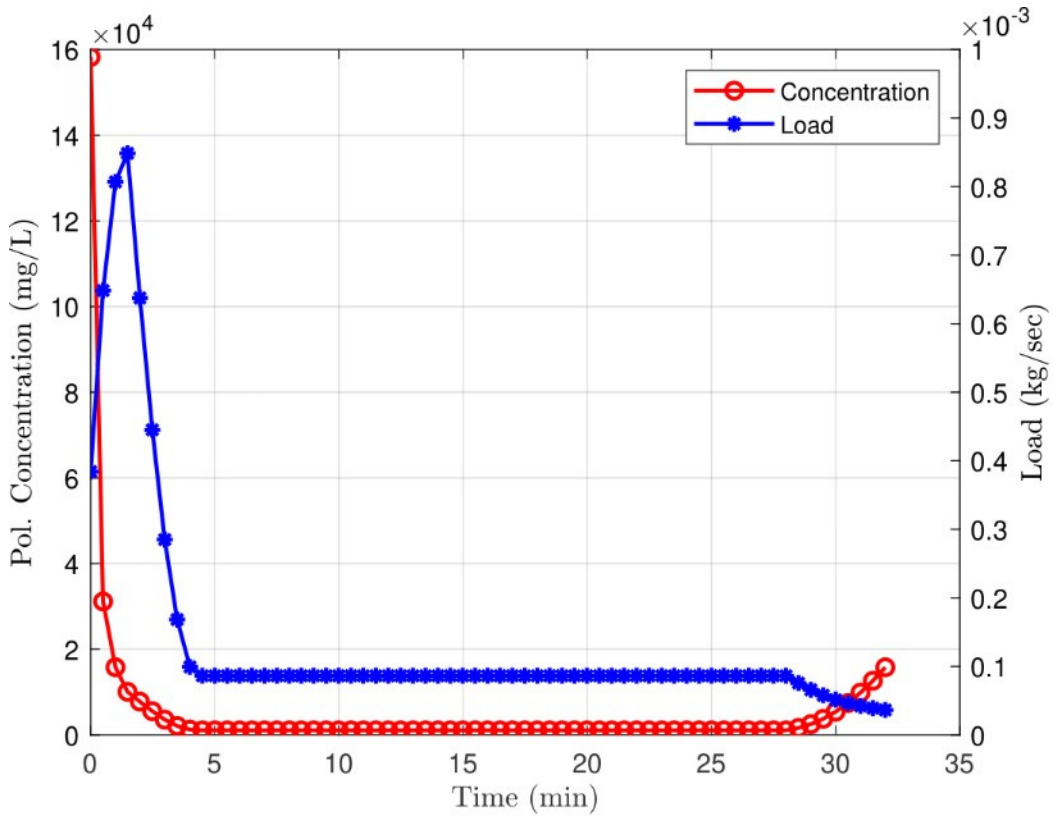

Figure A.5. Pollutograph and Load of diluted salt.

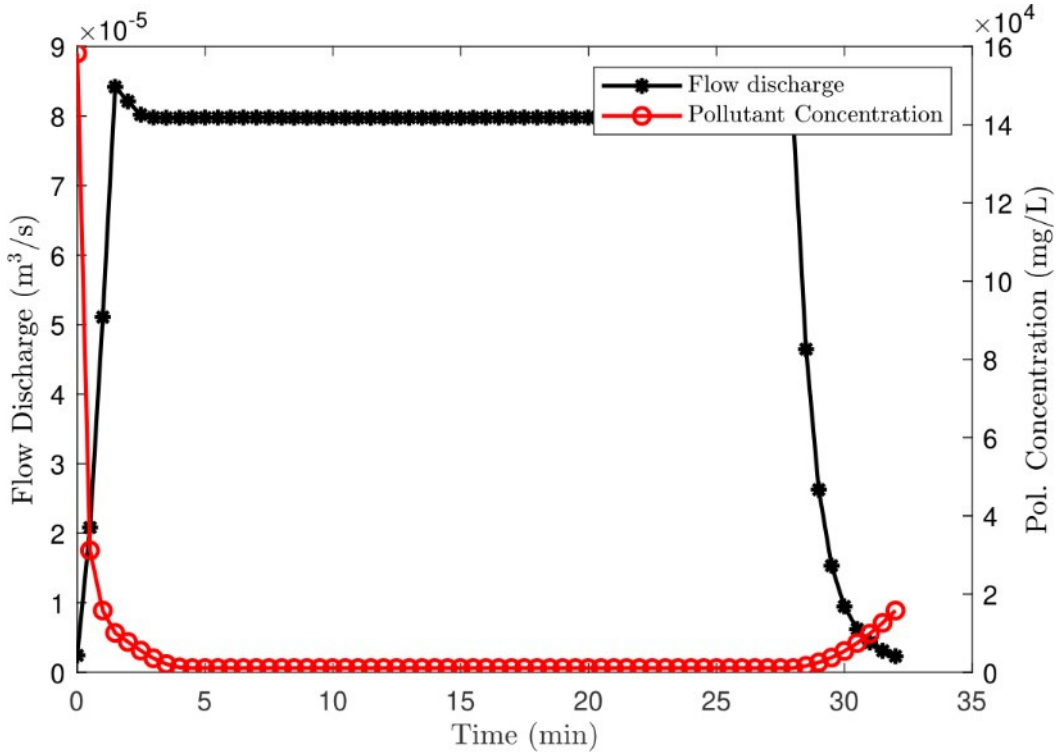

Figure A.6. Hysteresis effect where the peak of the concentration occurs before the flow discharge peak.

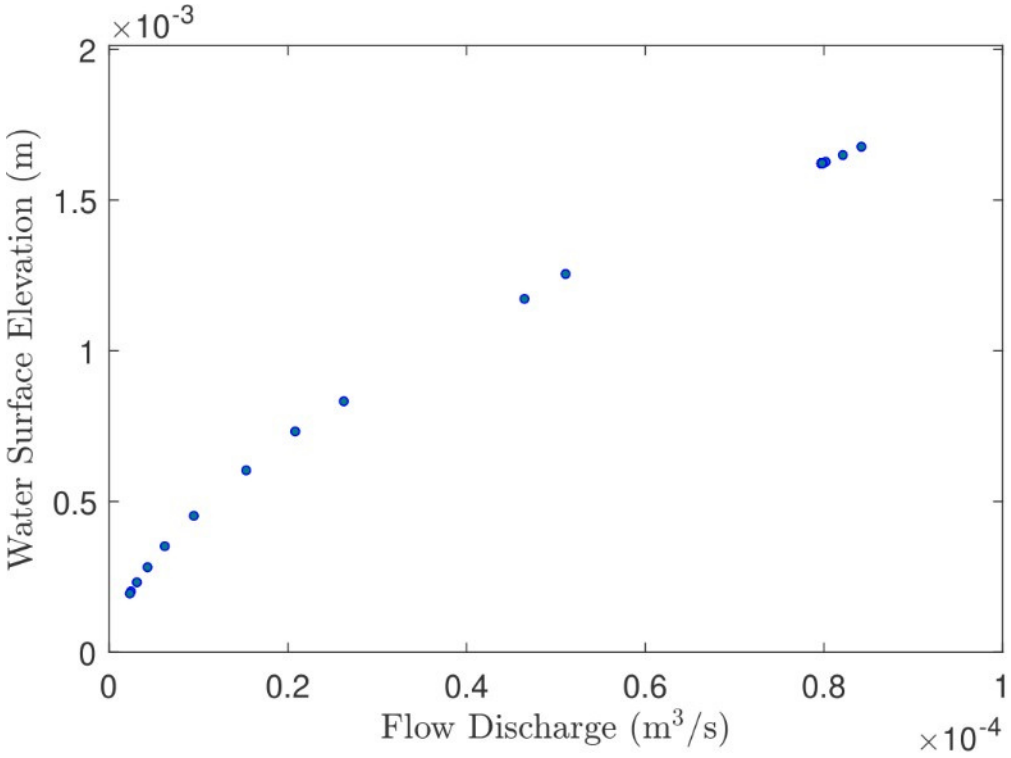

Figure A.7. Rating Curve at the outlet where the flow discharge is known for each stage.

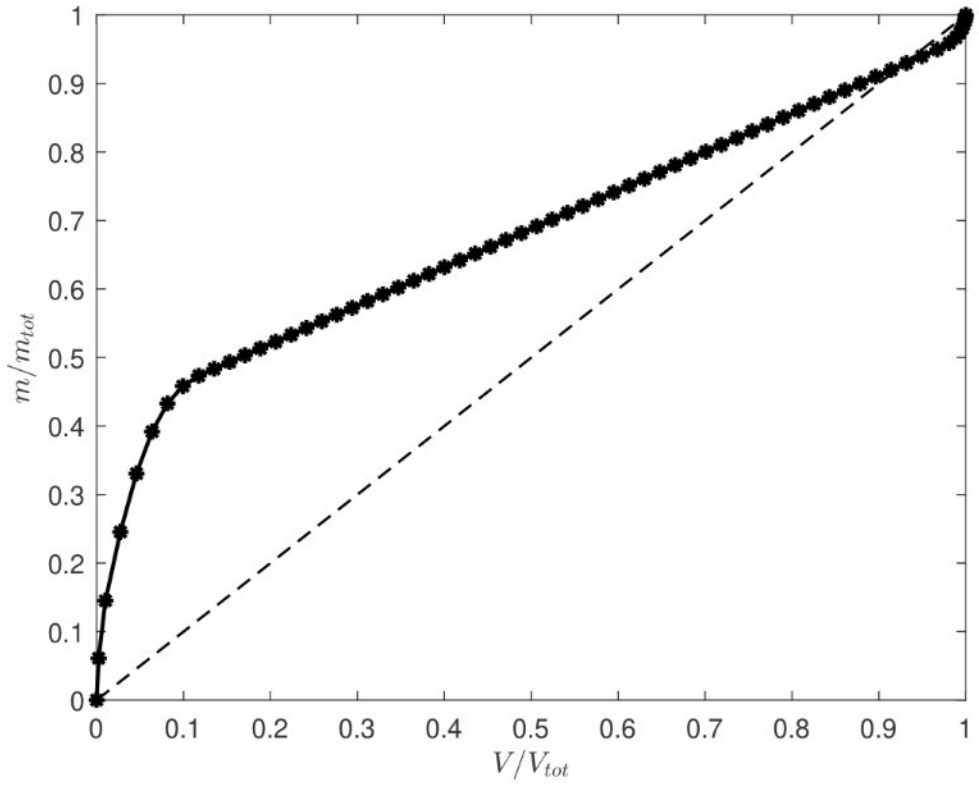

Figure A.8. M(V) Curve relating normalized runoff volume and normalized pollutant mass.

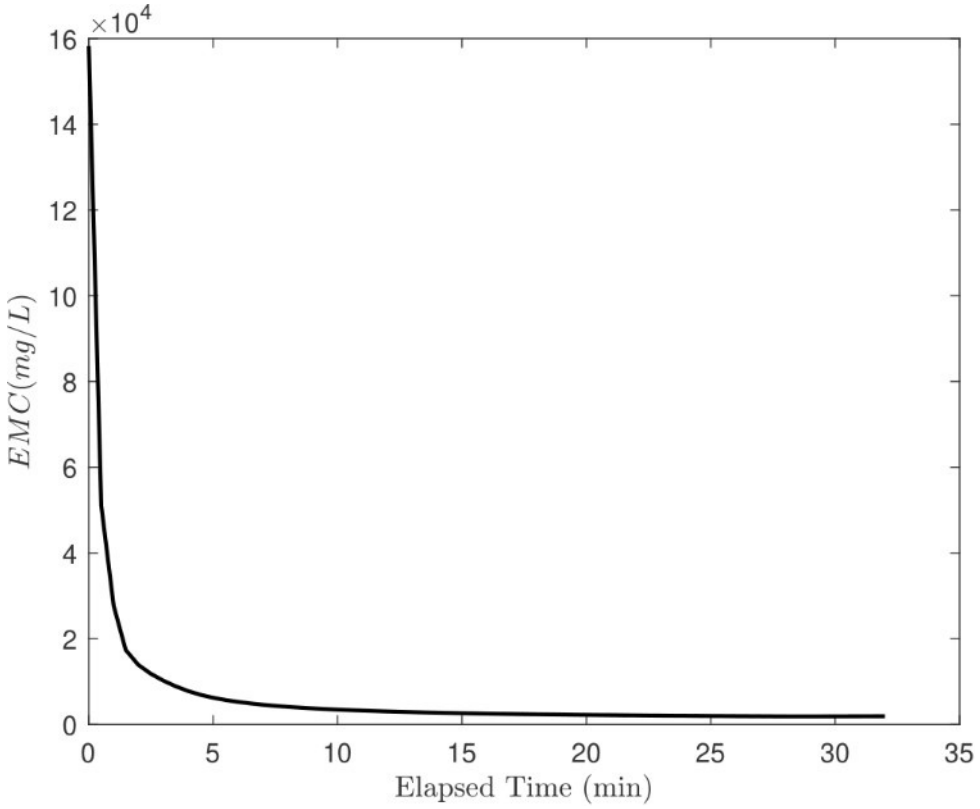

Figure A.9. EMC Curve relating the EMC variation with time.

3. Matricial Variables: This is used if and only if an inflow hydrograph is used and allows the model to use a different one to avoid calculations in large matrices. Therefore, the model changes the size of the matrices according to the wet cells that were derived from the inflow hydrograph propagation.

4. Watershed Inputs and Cuts: Definition of outlet conditions. The outlet type defines which outlet boundary condition is used, that is, normal or critical flow. Also, if the user wants to define more outlets than those already defined by finding the cells with the smallest elevation, she can define it by choosing the n_outlets_data. This variable adds more outlets close to those already defined by the topology.

5. Maps and Plots Control: In this section, we define the time at which the spatial and source variables are recorded. Users must be aware of memory and processing capabilities of their machines such that the recording of the spatial variables is sufficiently accurate but yet suitable for their computer memory. It also defines the threshold to map the variables.

6. CA Parameters: Definition of some thresholds for cellular automata.

7. Abstractions: coordinates definition to establish an initial area of interest to improve modeling performance (applicable for warm-up procedure and CPU execution). The model allows the user to delineate a region of interest, defined by a squared region, using the local x and y coordinates (units or pixels) taken from the center of the left upper corner

8. Water Quality Inputs: here are defined the water quality model parameters.

9. DEM Smoothing, Imposemin, Resample, Bathymetry: Optional procedures to treat the used digital elevation model.

10. Directories: Here are defined the directories for the DEM, land use and land cover, soil type, warm-up depths (if apply), among others. Please note that Matlab must have access to these folders.

11. Human Instability: Here are the set variables to calculate human stability against drag forces.

12. Observation Points: In this section are defined the coordinates for all the relevant point within the study area to analyze the modeling results and derive hydrographs, stages, and other charts related to the coordinates.

13. Synthetic Design Storms: The user can define synthetic storms with different return periods, durations, and time intervals. Two options are allowed: Alternated Blocks and Huff rainfall distributions. However, in both cases users need to have a Sherman-type IDF curve.

14. Satellite Or Radar Rainfall: The HydroPol2D is capable to read rainfall data in .TIFF format, .bin binary data from compressed data, e.g., satellite data, or HDF5 data from radar.

In Fig. A.11 is shown the HydroPol2D input structure related to rainfall (distributed or lumped) and evapotranspiration processes. For spatial rainfall data, it is necessary to inform the index code, the coordinates of the gauges, and their respective rainfall intensity records. The time is discretized with constant time-steps. Please, note that the coordinates must be in a projected coordinate system and must be the same reference from the DEM, LULC, and Soil maps. However, for lumped rainfall data, it is only necessary to inform the rainfall intensity records. Similarly, from the distributed rainfall case, for the ETP data, coordinates and gauge code stations are required, and the record data are such as: maximum, median and minimum air temperature, air speed above two meters from the surface (U_2), relative air humidity (UR), and solar radiation (G).

In Fig. A.12 is shown the structure for inflow data, soil type and land use and land cover. For the inflow data, it is necessary to specify the hydrograph and coordinates from where the stream flow is entered as a boundary condition. Related to soil type, name of the soil, relative index, and hydraulic properties such as saturated conductivity (k_{sat}), suction head (ψ), initial water content (I_0), and water deficit (θ_{sat} - θ_i). In relation to land use and land cover, it is necessary to specify the name and index for each class. Please, note that the indexes used in these folders must match with information stored in the input rasters .tif used when reading the general data. Furthermore, parameters for the hydraulic and water quality behavior are necessary, such as: manning roughness coefficient (n), initial abstraction (h_0), initial water depth condition (d_0), pollutant build-up and wash-off coefficients (C_1, C_2, C_3, C_4).

8.3 Appendix III - Supplementary Material of Chapter 4

This supplemental material is organized as follows:

- Sec. 8.3.1: Fitness Functions.
  - Sec. 8.3.1.1: NSE
  - Sec. 8.3.1.2: Coefficient of Determination
  - Sec. 8.3.1.3: Root-Mean-Squared-Error
  - Sec. 8.3.1.4: Peak Flow Bias
  - Sec. 8.3.1.4: Relative Volume Error
- Sec. 8.3.2: Input Data
- Sec. 8.3.3: Parallel Plotting

Figure A.10. HydroPol2D - General data input data structure. Sections 1, 2, 3, 4, 5, 6, 10, 12 are always required to be entered while the remainder sections are optional and might be only act.

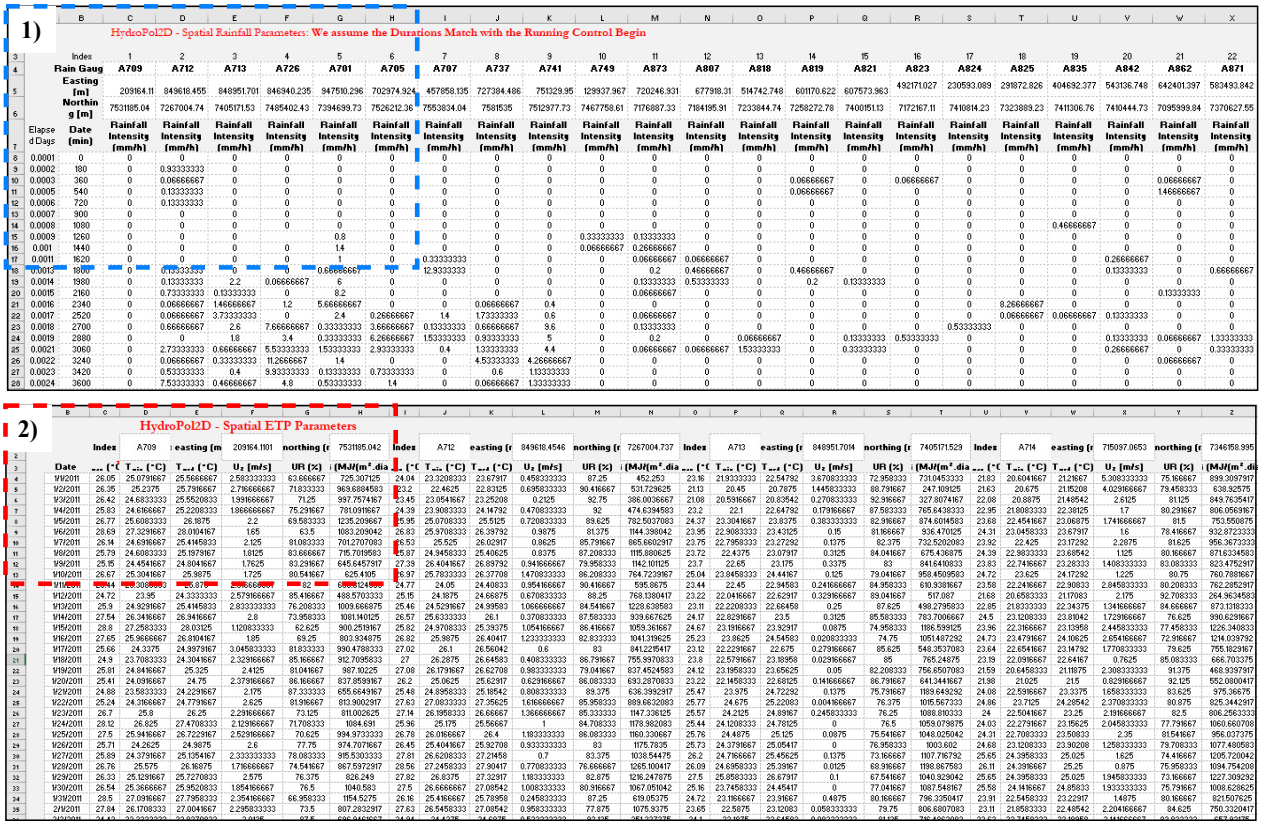

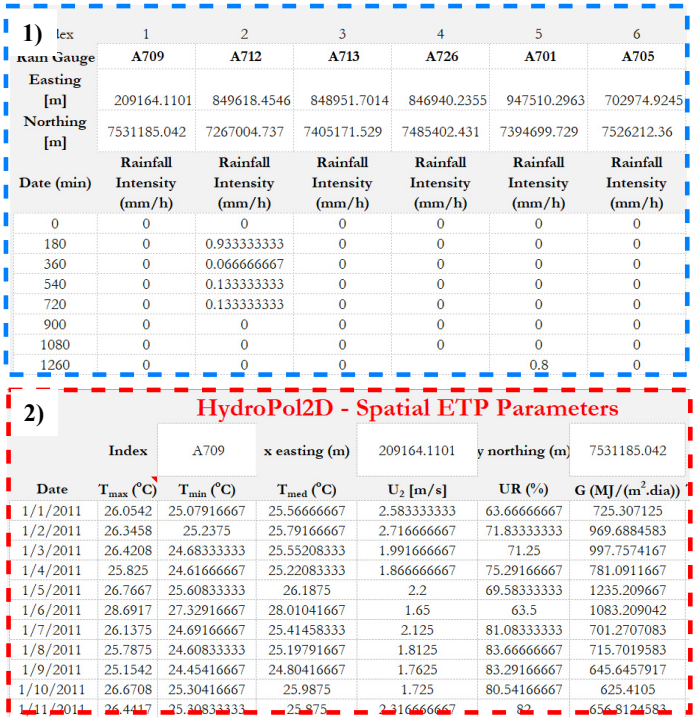

Figure A.11. HydroPol2D - ETP and rainfall input data structure.

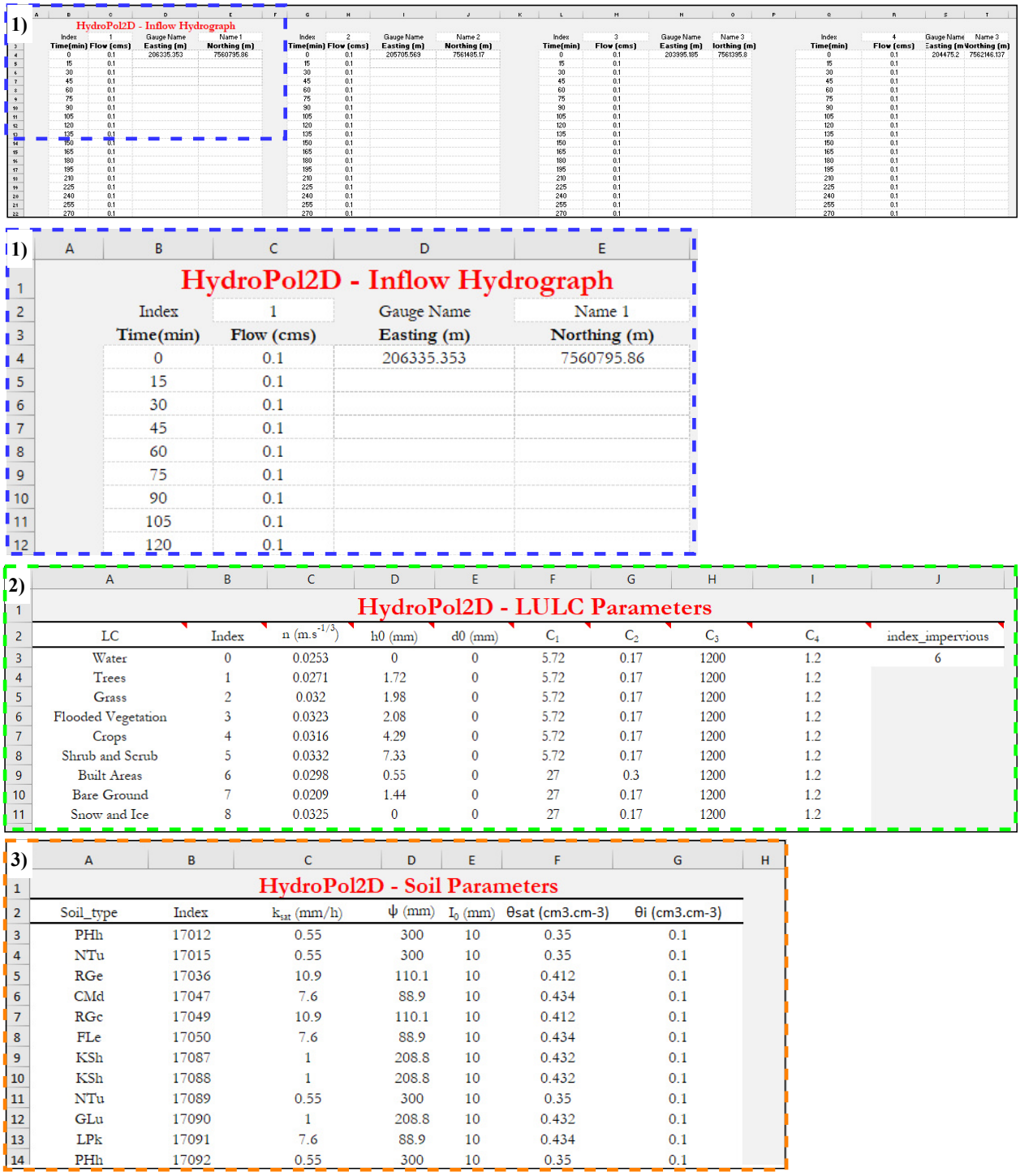

1)

HydroPol2D - Inflow Hydrograph

Index	1	Gauge Name	Name 1
Time(min)	Flow (cms)	Easting (m)	Northing (m)
0	0.1	206335.353	7560795.86
15	0.1		
30	0.1		
45	0.1		
60	0.1		
75	0.1		
90	0.1		
105	0.1		
120	0.1		

2)

HydroPol2D - LULC Parameters

LC	Index	n ($m.s^{-1/3}$)	h0 (mm)	d0 (mm)	C_1	C_2	C_3	C_4	index_impervious
Water	0	0.0253	0	0	5.72	0.17	1200	1.2	6
Trees	1	0.0271	1.72	0	5.72	0.17	1200	1.2	
Grass	2	0.032	1.98	0	5.72	0.17	1200	1.2	
Flooded Vegetation	3	0.0323	2.08	0	5.72	0.17	1200	1.2	
Crops	4	0.0316	4.29	0	5.72	0.17	1200	1.2	
Shrub and Scrub	5	0.0332	7.33	0	5.72	0.17	1200	1.2	
Built Areas	6	0.0298	0.55	0	27	0.3	1200	1.2	
Bare Ground	7	0.0209	1.44	0	27	0.17	1200	1.2	
Snow and Ice	8	0.0325	0	0	27	0.17	1200	1.2	

3)

HydroPol2D - Soil Parameters

Soil_type	Index	k_{sat} (mm/h)	ψ (mm)	I_0 (mm)	θsat (cm3.cm-3)	θi (cm3.cm-3)
PHh	17012	0.55	300	10	0.35	0.1
NTu	17015	0.55	300	10	0.35	0.1
RGe	17036	10.9	110.1	10	0.412	0.1
CMd	17047	7.6	88.9	10	0.434	0.1
RGc	17049	10.9	110.1	10	0.412	0.1
FLe	17050	7.6	88.9	10	0.434	0.1
KSh	17087	1	208.8	10	0.432	0.1
KSh	17088	1	208.8	10	0.432	0.1
NTu	17089	0.55	300	10	0.35	0.1
GLu	17090	1	208.8	10	0.432	0.1
LPk	17091	7.6	88.9	10	0.434	0.1
PHh	17092	0.55	300	10	0.35	0.1

Figure A.12. HydroPol2D - Inflow, Land use and Land cover, and soil type input data structure.

- Sec. 8.3.4: Numerical Case Study 4 - Equifinality
  - Sec. 8.3.4.1: Parameter Ranges
  - Sec. 8.3.4.2: Hydrographs and Hyetographs
  - Sec. 8.3.4.3: Results of the 10.8 mmh^{-1} Rainfall
  - Sec. 8.3.4.4: Results of the 21.6 mmh^{-1} Rainfall
  - Sec. 8.3.4.5: Results of the 32.4 mmh^{-1} Rainfall
  - Sec. 8.3.4.6: Near-Optimal Parameters for 1 Event
- Sec. 8.3.5: DEM Treatment Tools
  - Sec. 8.3.5.1: Gaussian Filter
  - Sec. 8.3.5.2: Flow-Accumulation-Based Filter
  - Sec. 8.3.5.3: Constrained Regularized Smoothing of the Channel Length Profile
- Sec. 8.3.6: Antecedent Moisture Condition (AMC)

8.3.1 Fitness Functions

8.3.1.1 Nash-Sutcliffe-Efficiency

The Nash-Sutcliffe-Efficiency (NSE) metric is calculated in terms of the observed variable (e.g., generally flow discharge) and the modeled variable such that (Nash e Sutcliffe, 1970):

$$\text{NSE} = 1 - \frac{\sum_{i=1}^{n_{\text{obs}}} \left(y_{\text{obs}}^i - y_{\text{m}}^i\right)^2}{\sum_{i=1}^{n_{\text{obs}}} \left(y_{\text{obs}} - \overline{y_{\text{obs}}^i}\right)^2} \tag{8.39}$$

where y_{obs} is the observed or the assumed true variable, whereas y_{m} is the variable. The indexes herein expressed as i and n_{obs} represent the time in which the observations were made and the number of observations, respectively. NSE ranges from $-\infty$ to 1 (inclusive), with negative values indicating that the observed mean has smaller squared error than the modeled results. Ideally, a NSE = 1 indicates a perfect match between modeled and observed values.

8.3.1.2 Coefficient of Determination

The coefficient of determination determines the correlation between the observations. It ranges from 0 to 1, with 1 corresponding to a perfect correlation between the modeled and observed data, and can be calculated as:

$$r^2 = \left(\frac{\sum_{i=1}^{n_{\text{obs}}} \left(y_{\text{m}} - \overline{y_{\text{m}}^i}\right) \left(y_{\text{obs}}^i - \overline{y_{\text{obs}}^i}\right)}{\sqrt{\sum_{i=1}^{n_{\text{obs}}} \left(y_{\text{m}} - \overline{y_{\text{m}}^i}\right)^2 \sum_{i=1}^{i} \left(y_{\text{obs}}^i - \overline{y_{\text{obs}}}\right)^2}} \right)^2 \tag{8.40}$$

8.3.1.3 Root-Mean-Square-Error

The Root-Mean-Square-Error (RMSE) index measures the average difference between the predicted and observed variables and can be calculated as follows (Fisher et al., 1920):

$$\text{RMSE} = \sqrt{\frac{\sum_{i=1}^{n_{\text{obs}}} \left(y_m^i - y_{\text{obs}}^i\right)^2}{n}} \tag{8.41}$$

a)

LULC-Based Paramters

Class	Type	Hydrodynamic Modeling				Water Quality Modeling							
		n_{min} ($sm^{-1/3}$)	n_{max} ($sm^{-1/3}$)	$h_{0,min}$ (mm)	$h_{0,max}$ (mm)	$C_{1,min}$ (kg/ha)	$C_{1,max}$ (kg/ha)	$C_{2,min}$ (1/day)	$C_{2,max}$ (1/day)	$C_{3,min}$ (mm/h)^{C4}/h	$C_{3,max}$ (mm/h)^{C4}/h	$C_{4,min}$ (-)	$C_{4,max}$ (-)
1	Water	0.025	0.04	0	0								
2	Trees	0.025	0.04	0	10								
3	Grass	0.02	0.035	0	5								
4	Flooded Vegation	0.025	0.04	0	10								
5	Crops	0.02	0.035	0	10								
6	Scrub/Schrub	0.03	0.04	0	10								
7	Built Areas	0.015	0.03	0	2								
8	Bare Ground	0.02	0.03	0	2								
9	Snow/Ice	0.0325	0.0325	0	0								

Water Quality Parameters - Not Used in Numerical Case Study 3

b)

Class	Type	$k_{sat,min}$ (mm/hr)	$k_{sat,max}$ (mm/hr)	$\Delta\theta_{min}$ (-)	$\Delta\theta_{max}$ (-)	ψ_{min} (mm)	ψ_{max} (mm)
1	SOIL - 1	0	10	0.25	0.5	0	110
2	SOIL - 2	0	10	0.25	0.5	0	110

c)

Event		Gauge 1		Gauge 2	
Event	1	x(m)	202710.043	x(m)	
ADD	10	y(m)	7561755.866	y(m)	
Time (min)	Rainfall Intensity (mm/h)	Flow Discharge (m^3/s)	Pollutant Concentration (mg/L)	Flow Discharge (m^3/s)	Pollutant Concentration (mg/L)
0	30	0.05			
5	94.8	0.24			
10	97.2	3.06			
15	70.8	10.05			
20	39.6	39.39			
25	43.2	56.90			
30	54	53.88			

d)

Event	Initial Water Surface Depth (m)	Initial Soil Moisture (mm)	Number of Gauges	flag_calibrate_wq	Number of Events
1	D:\Google_drive\Datos maquetilladeo\JDCAWQ_Model\Estudio_Completo \Version_10\Gaugeo_Catchment_Calibration\Water_Depths.tif	D:\Google_drive\Datos maquetilladeo\JDCAWQ_Model\Estudio_Completo \Version_10\Gaugeo_Catchment_Calibration\Initial_Moisture\Events1_1.tif	1	0	1

Figure A.13. Automatic calibration input data used in Numerical Case Study 3. Part a) shows the LULC-Based parameters for each LULC classification. Part b) shows the SOIL-Based parameters for each soil type whereas part c) shows the label of the events simulated, observed rainfall, discharge, pollutant concentration, and x and y coordinates of each observed gauge. Part d) shows the file directories of the initial maps of water surface depths, initial soil moisture, as well as defines the number of gauges for each event, number of events, and checks if water quality is used or not in the optimization.

8.3.1.4 Peak-Flow Bias

The peak flow bias is defined as the relative error between the modeled peak flow and the observed peak flow, and can be written as:

$$\eta_q = \frac{\left|\max_{\forall\ i}\left(y^i_{\mathrm{m}}\right) - \max_{\forall\ i}\left(y^i_{\mathrm{obs}}\right)\right|}{\max_{\forall\ i}\left(y^i_{\mathrm{obs}}\right)},\ \text{for i } = 1 \text{ to } n_{\mathrm{obs}} \tag{8.42}$$

Ř This metric measures the percentual bias between the surface runoff volume error and the total observed runoff error, given by:

$$\eta_v = \frac{\sum_{i=1}^{T}\left(V_m - V_{obs}\right)}{\sum_{i=1}^{T} V_{obs}} \tag{8.43}$$

8.3.2 Input Data

The input data used for the calibration algorithm is shown in Fig. A.13.

8.3.3 Parallel Plotting

The parallel graph showing the evolution of the parameters in terms of the generation number is shown in Fig. A.14, for the LULC parameters, and Fig. A.15, for the Soil parameters. In addition, the box-plot variation of the parameters for the last generation is shown in Fig. A.16.

8.3.4 Numerical Case Study 4 - Equifinality

The wide parameter ranges used to mimic no prior knowledge of the system are presented in Tab. A.3.

8.3.4.1 Parameter Ranges

The wide parameter ranges used to mimic no prior knowledge of the system are presented in Tab. A.3.

8.3.4.2 Hydrographs and Hyetographs

The hyetographs and hydrographs for the simulated events are presented in Fig. A.18.

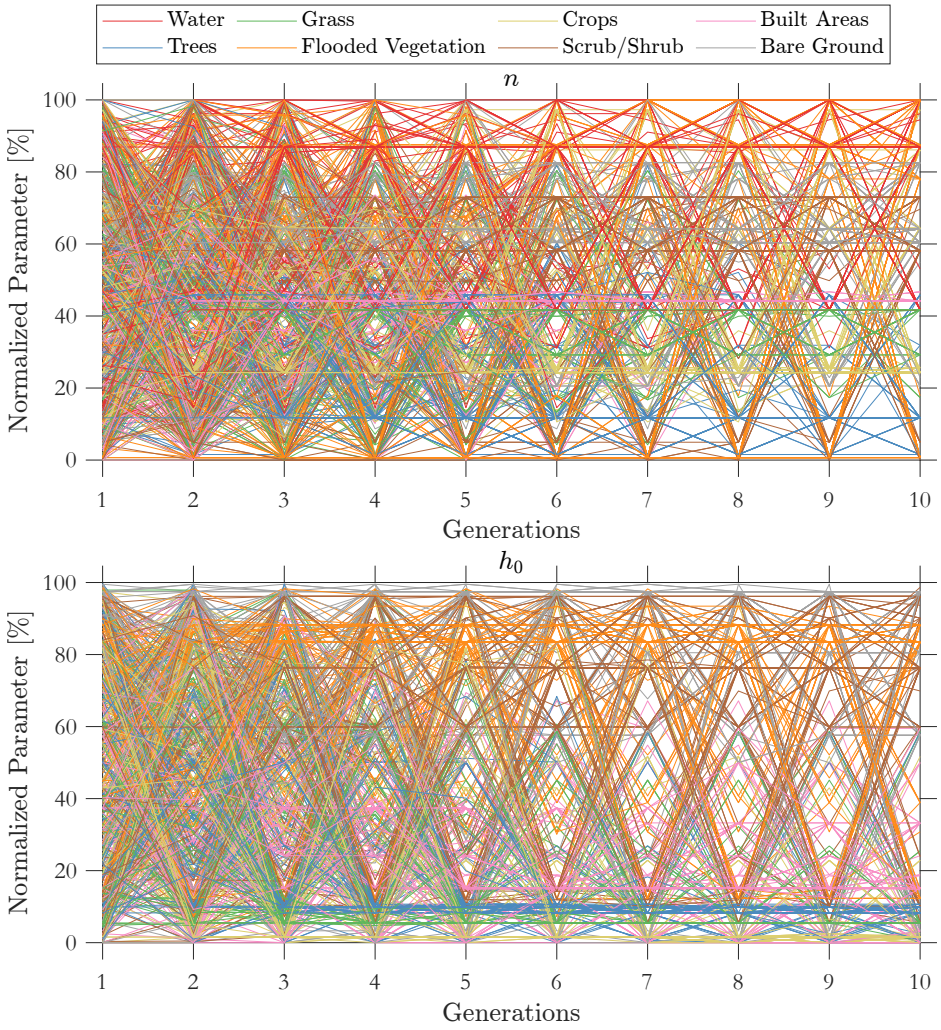

Figure A.14. Parallel Plotting of each LULC-Based parameter for Numerical Case Study 3, where parameter are normalized by the upper and lower bounds.

Classification	n_{min}	n_{max}	$h_{0,min}$	$h_{0,max}$x	$k_{sat,min}$	$k_{sat,max}$	$\Delta\theta_{min}$	$\Delta\theta_{max}$	ψ_{min}	ψ_{max}
	$[sm^{-1/3}]$	$[sm^{-1/3}]$	[mm]	[mm]	$[mmh^{-1}]$	$[mmh^{-1}]$	[–]	[–]	[mm]	[mm]
Left Hillslope	0.01	0.1	0	10	0	25	0.0001	0.8	0	200
Channel	0.15	0.15	0	0	0	0	0.0001	0.0001	0	0
Right Hillslope	0.01	0.1	0	10	0	25	0.0001	0.8	0	200

Table A.3. Parameter Ranges of Numerical Case Study 4 for the case with no prior knowledge (i.e., wide parameter range) of the system.

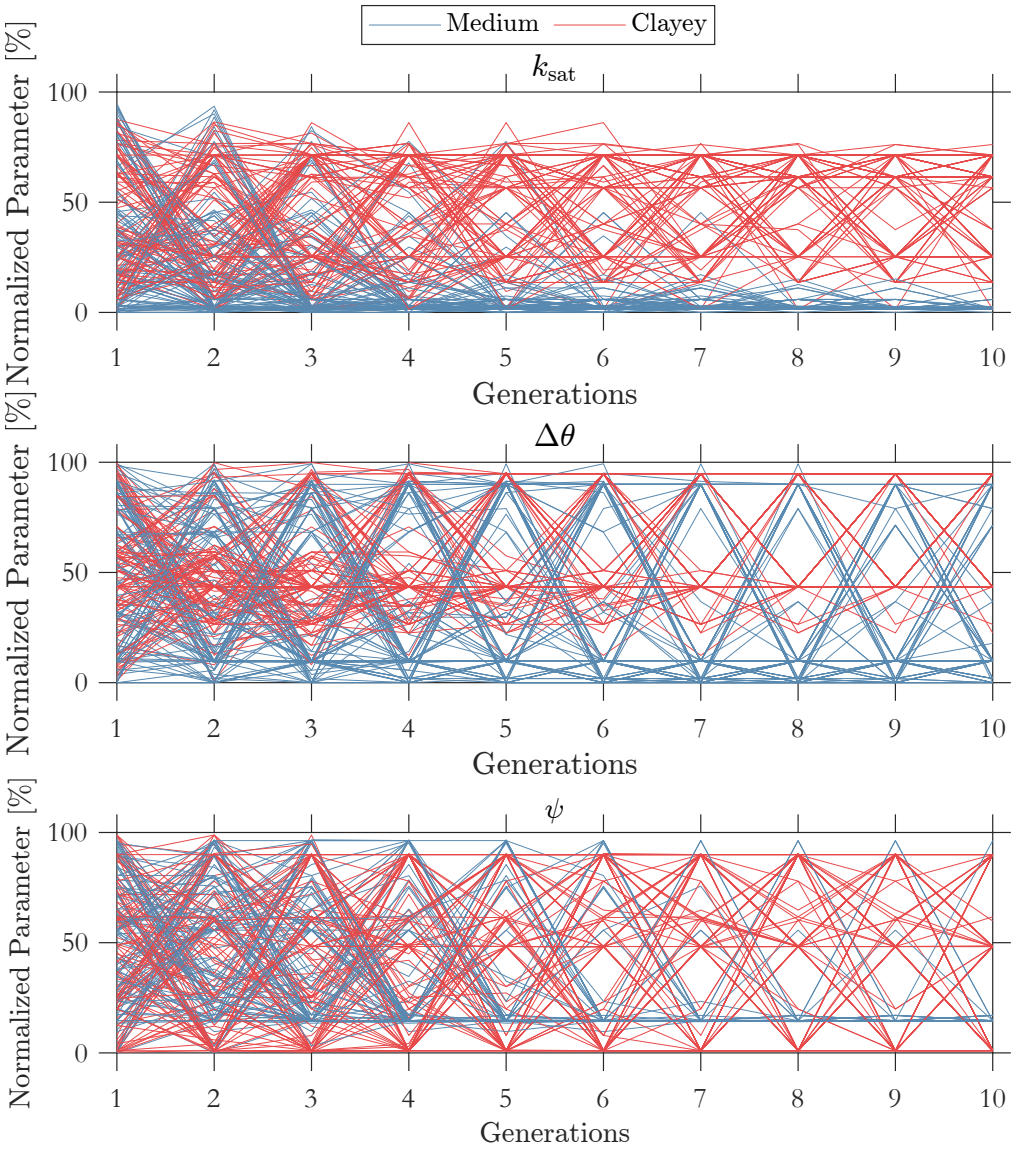

Figure A.15. Parallel Plotting of each SOIL-Based parameter for Numerical Case Study 3, where parameter are normalized by the upper and lower bounds.

8.3.4.3 Results of the 10.8 mm/h Rainfall

The results of the 10.8 mm/h Rainfall are presented in Fig. A.19. The stage-hydrograph of this event is shown in Fig. A.20.

8.3.4.4 Results of the 21.6 mm/h Rainfall

The results of the 21.6 mm/h Rainfall are presented in Fig. A.21. The stage-hydrograph of this event is shown in Fig. A.22.

8.3.4.5 Results of the 32.4 mm/h Rainfall

The results of the 21.6 mm/h Rainfall are presented in Fig. A.23. The stage-hydrograph of this event is shown in Fig. A.24.

8.3.4.6 Near-Optimal Parameters for 1 Event

The near-optimal parameters relative error chart for Event 1, only, is shown in Fig. A.25.

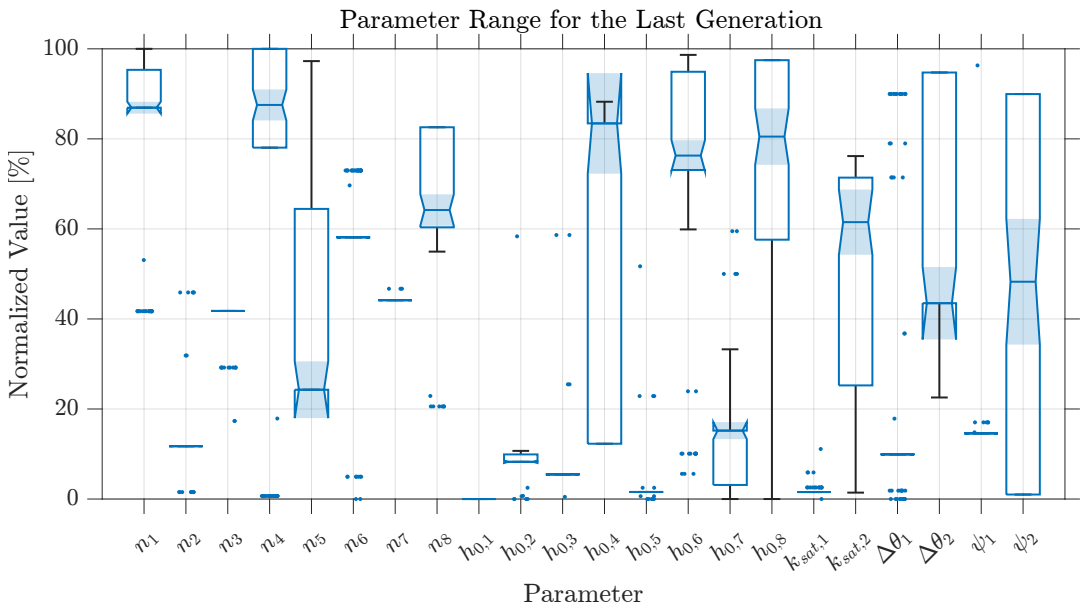

Figure A.16. Box-plot of the parameters at the last generation of the optimization algorithm for the optimization problem of Numerical Case Study 3.

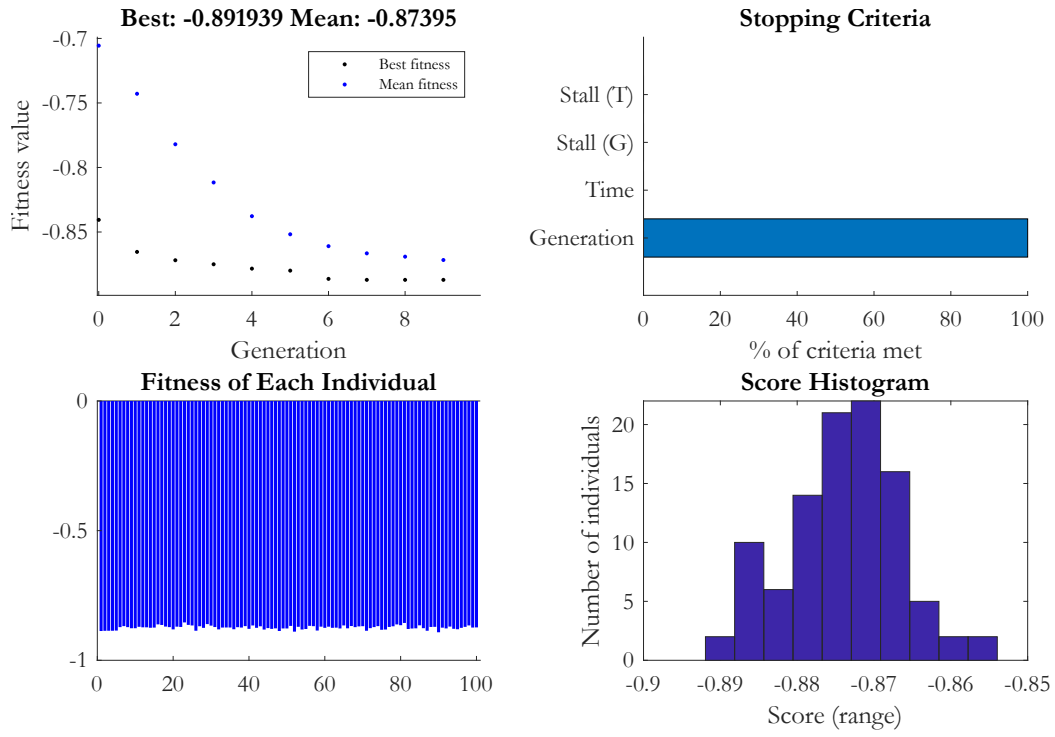

Figure A.17. GA Results for the calibration of the Numerical Case Study 3.

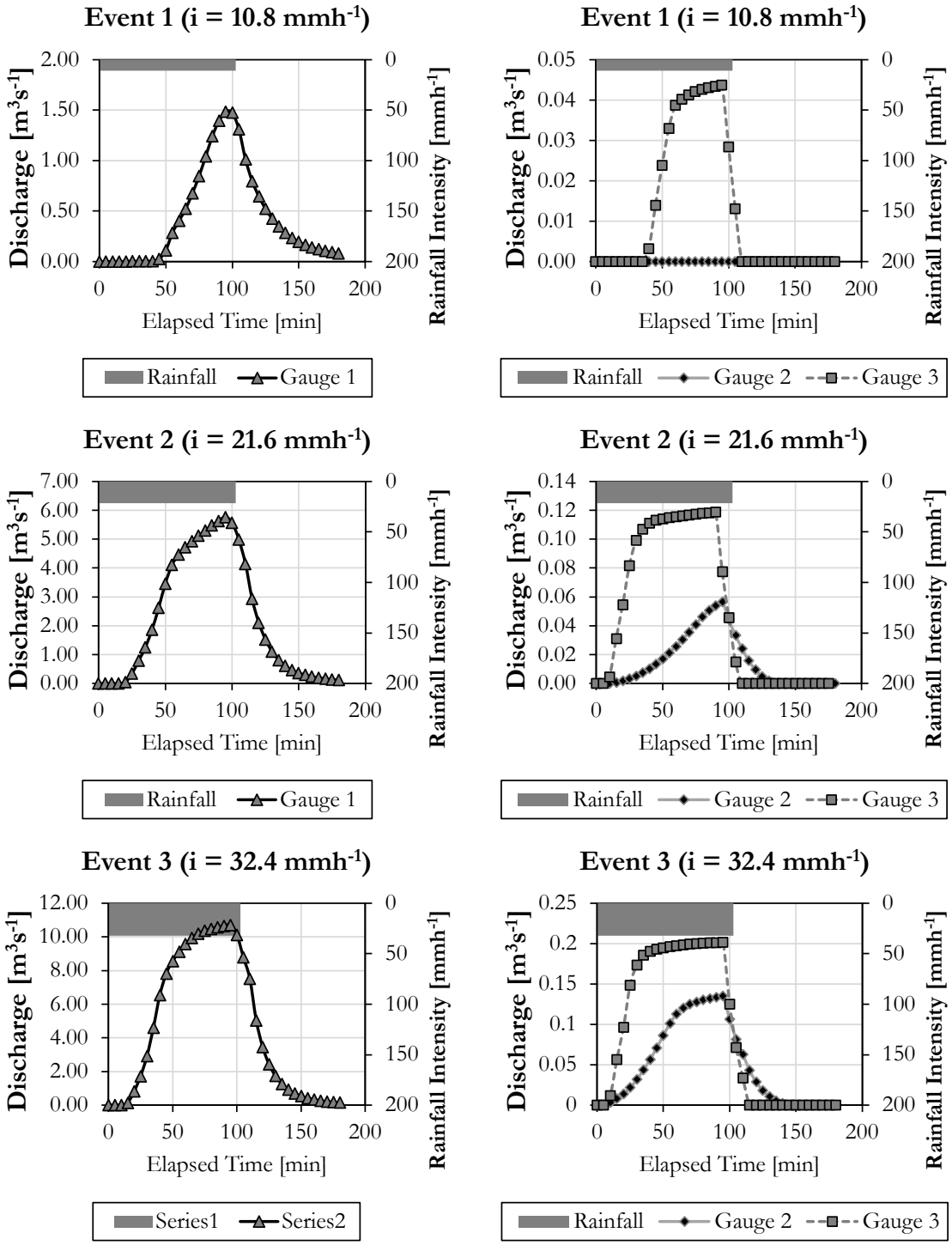

Figure A.18. Hyetographs and hydrographs for all events and gauges used for calibration used in Numerical Case Study 4.

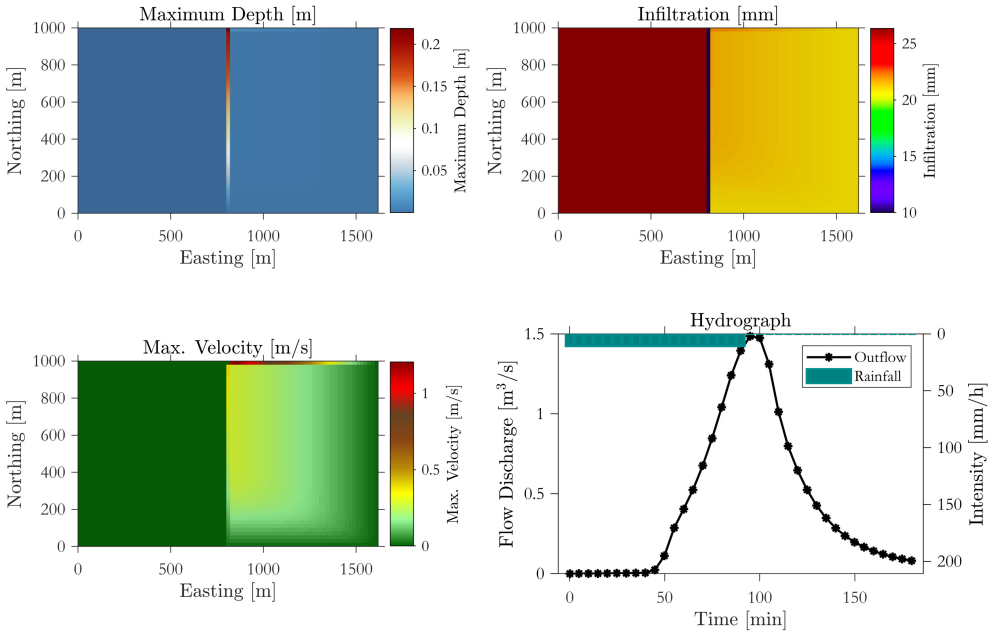

Figure A.19. Summary results of the simulation of Numerical Case Study 4 with rainfall of 10.8 mmh^{-1}.

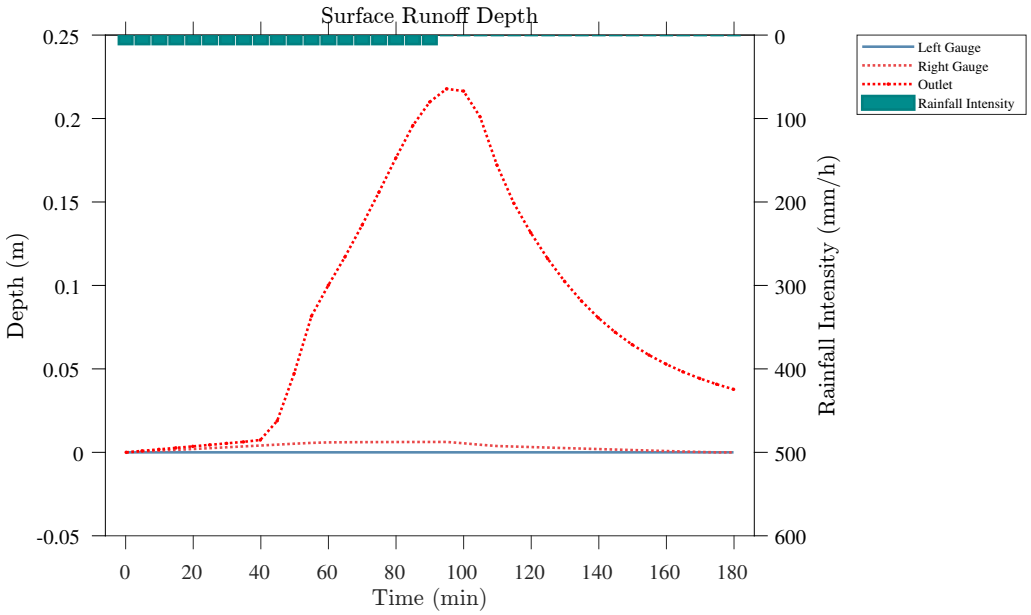

Figure A.20. Stage Hydrograph for the outlet and observed gauges for the event of 10.8 mmh^{-1}.

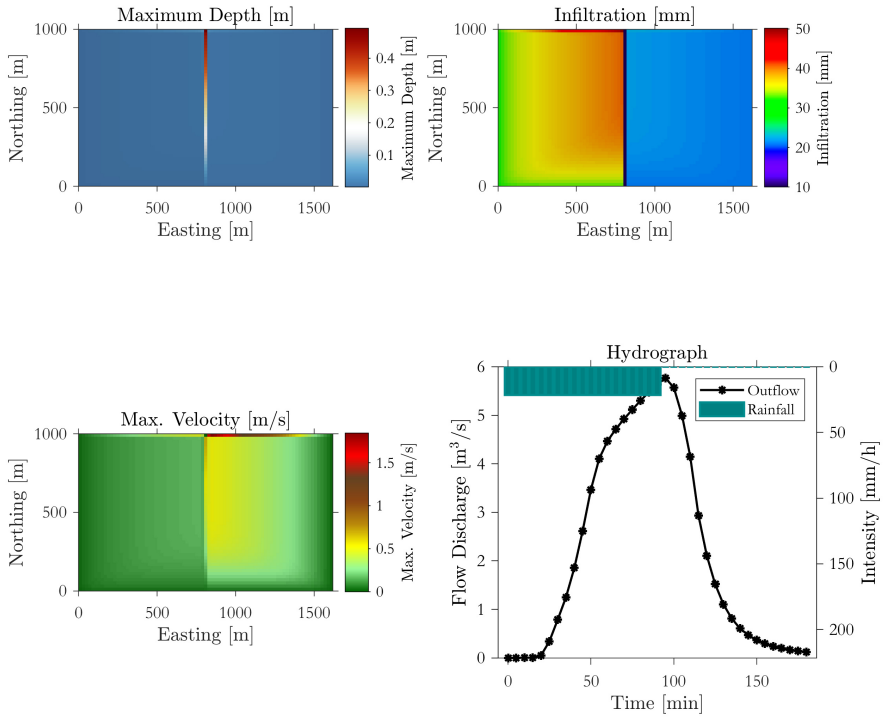

Figure A.21. Summary results of the simulation of Numerical Case Study 4 with rainfall of 21.6 mmh^{-1}.

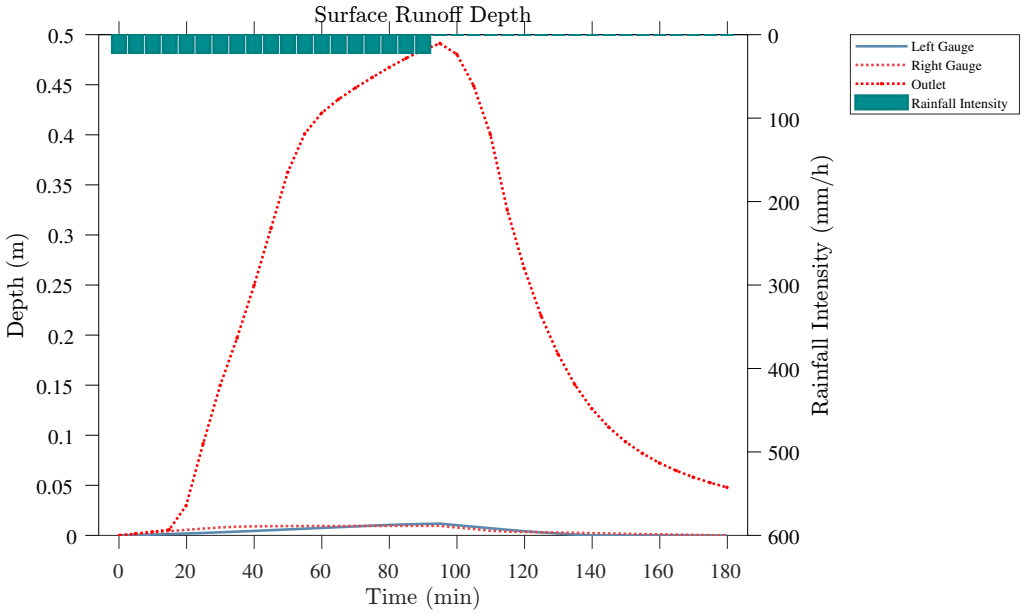

Figure A.22. Stage Hydrograph for the outlet and observed gauges for the event of 21.6 mmh^{-1}.

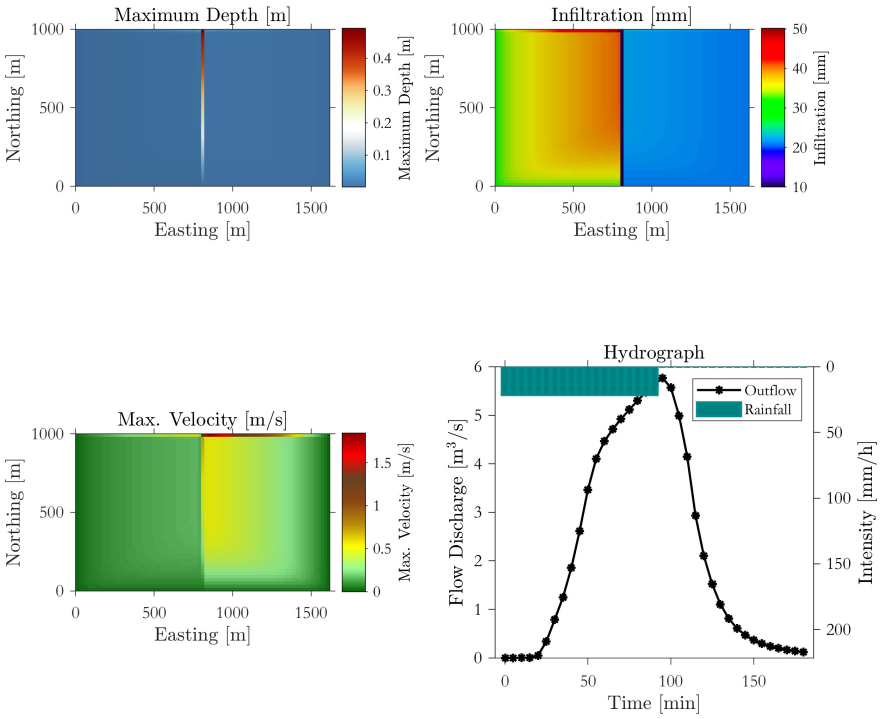

Figure A.23. Summary results of the simulation of Numerical Case Study 4 with rainfall of 32.4 mmh^{-1}.

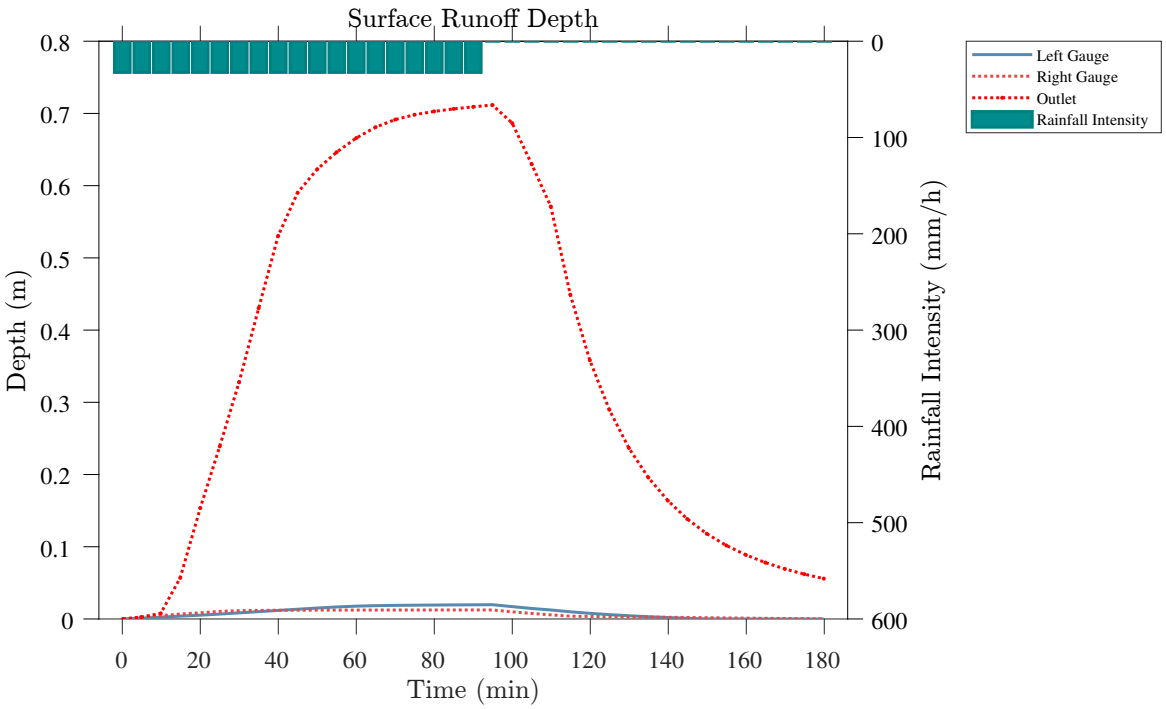

Figure A.24. Stage Hydrograph for the outlet and observed gauges for the event of 32.4 mmh^{-1}.

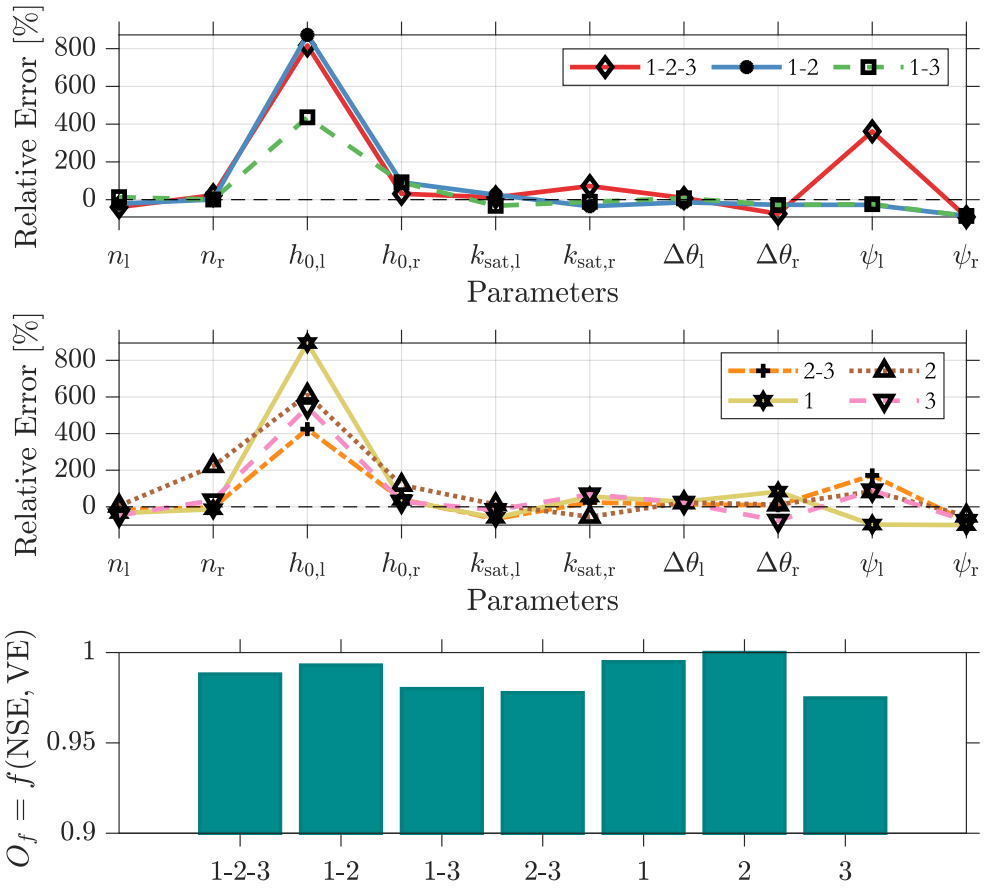

Figure A.25. Near-optimal parameters relative error for the calibration using only Event 1. The black dashed line represents the expected optimal parameters.

8.3.5 DEM Treatment Tools

8.3.5.1 Gaussian Filter

A Gaussian filter calculates the weighted average of all pixels in a 3-x-3-pixel frame and assigns the value to the center pixel in the frame.

$$g(x,y) = \frac{1}{2\pi\sigma^2} e^{-(x^2+y^2)/(2\sigma^2)} \tag{8.44}$$

where x is the distance from the origin in the horizontal axis, y is the distance from the origin in the vertical axis, and σ is the standard deviation of the Gaussian distribution.

8.3.5.2 Flow Accumulation-Based Filter

Let $\boldsymbol{F_a}$ be the flow accumulation matrix that indicates the number of pixels that drain to a particular cell (i,j) in the domain. Let $\boldsymbol{R}$ be a mask matrix defining the pixels that are considered as streams, that is, pixels that have a flow accumulation larger than a pre-defined threshold τ. As shown in De Paiva et al. (2013), the width of the river $\boldsymbol{B}$ and height $\boldsymbol{H}$ can be written as:

$$\boldsymbol{B} = \alpha_1 \boldsymbol{F_a}^{\circ\alpha_2} \boldsymbol{R} \tag{8.45}$$

$$\boldsymbol{H} = \beta_1 \boldsymbol{F_a}^{\circ\beta_2} \tag{8.46}$$

Soil state	AMC	5-day antecedent rainfall in mm	
		Dormant period	Growth period
Dry	I	12.7	35.56
Under average moisture conditions	II	12.7 - 27.94	35.56 - 53.34
Saturated moist	III	27.94	53.34

Table A.4. Antecedent Moisture Condition (AMC) index classification for each 5-day cumulative rainfall class.

where parameters α_1, α_2, β_1, and β_2 are derived from fitting regression models in cross-section data.

Therefore, the estimated cross-section area under normal flow conditions is:

$$\boldsymbol{A} = \boldsymbol{B} \circ \boldsymbol{H} \tag{8.47}$$

If we impose that this area needs to be connected to only one pixel, we can calculate the DEM depth reduction (H_r) as follows:

$$\boldsymbol{H_r} = \frac{1}{\Delta x}\boldsymbol{A} \tag{8.48}$$

where Δx is the pixel resolution in meters.

Finally, a raster operation is performed in the $\boldsymbol{DEM}$, such that:

$$\mathbf{DEM} = \mathbf{DEM} - \boldsymbol{H_r} \tag{8.49}$$

8.3.5.3 Constrained Regularized Smoothing of the Channel Length Profile

A detailed definition of the algorithm is presented in Schwanghart e Scherler (2017). For smoothing the streams, we assume $K = 10$ and $\sigma = 0.2$. The parameter K dictates the degree of smoothing.

8.3.6 Antecedent Moisture Condition (AMC)

In order to calculate the soil moisture condition prior to the calibration event, the water balance was performed based on the Antecedent Moisture Condition (AMC) methodology. It uses the 5-day Antecedent Precipitation Index (API) (Kohler et al., 1951) to classify the soil condition. Several authors have employed the API for the calculation of an initial soil moisture condition (Durbude et al., 2011; McCuen, 1998; Suresh Babu e Mishra, 2012), defines the status of the soil state as dry, under average moisture conditions, and saturated moist in relation to the dormant and vegetation growth periods. The ranges of these states are presented in Tab. A.4.

The water balance considers that the total precipitation (P) is equal to the effective precipitation (P_e) plus the infiltrated precipitation (P_o), the latter would be the moisture stored in the soil or soil moisture prior to the calibration event. For the calculation of P_e the SCS-CS methodology was used where:

$$P_e = \frac{(P - I_a)^2}{(P - I_a) + S} \tag{8.50}$$

$$I_a = 0.2S \tag{8.51}$$

$$S = \frac{25400}{\mathrm{CN}} \tag{8.52}$$

Class	LULC/Soil	AMC II				AMC I			
		A	B	C	D	A	B	C	D
0	Water	100	100	100	100	100	100	100	100
1	Trees	25	55	70	77	11	35	51	60
2	Grass	68	79	86	89	49	63	72	77
3	Flooded Vegetation	100	100	100	100	100	100	100	100
4	Crops	72	81	88	91	54	65	75	80
5	Scrub/Schrub	39	61	74	80	21	41	56	64
6	Built Areas	89	92	94	95	77	81	84	86
7	Bare Soil	72	82	87	89	54	67	74	77

Table A.5. CN values for each LULC in the two AMC conditions.

where CN is the curve number. The CN values were modified considering an initial dry soil condition (Condition I). Table XX shows the CN of the LULC for the 9 classes and their modification for Condition I according to soil type.

For the conversion of the soil type, the sandy texture was considered that corresponds to soil type A, the medium texture corresponds to the average of the values of soils B and C and the clayey or very clayey texture to the values of soil D.

For event used for calibration, it was observed a total precipitation of 163.9 mm antecedent rainfall in the last 5 days.

8.4 Appendix IV - Supplementary Material of Chapter 5

8.4.1 Intensity-Duration-Frequency Curve

The IDF was derived from 30 years of daily rainfall obtained by the Intensity-Duration-Frequency curve using data gathered from the India Meteorological Department(IMD) and Karnataka State Natural Disaster Monitoring Centre (KSNDMC). The resulting IDF curve is as follows:

$$r = \frac{447.01\mathrm{RP}^{0.19}}{(0.03 + t_r)^{0.67}}, \tag{8.53}$$

where r is the rainfall intensity (mm/h), RP is the return period (years), and t_r is the rainfall duration (min).

This IDF was derived by disaggregating daily rainfall into sub-daily rainfall. To this end, we use the following relationship (Palaka et al., 2016)

$$P_{t_r} = P_{24}\left(\frac{t_r}{24}\right)^{1/3}, \tag{8.54}$$

where P is the rainfall volume (mm), and P_{24} is the rainfall depth of 24 hours duration.

We use the Gumbel distribution to fit the intensity-duration-frequency curve presented in Eq. (8.53). The plot of the IDF is shown in Fig. A.26.

Once with the IDF developed, the HydroPol2D model can also create synthetic distribution hyetographs of Huff and Alternating Blocks Method (ABM).

8.4.2 Model Setup

The HydroPol2D model was set to a maximum time-step of 0.0001 sec, with a maximum Courant-Friedrics-Lewy (CFL) of 0.4, such that numerical time-steps are adjusted each 30 seconds to

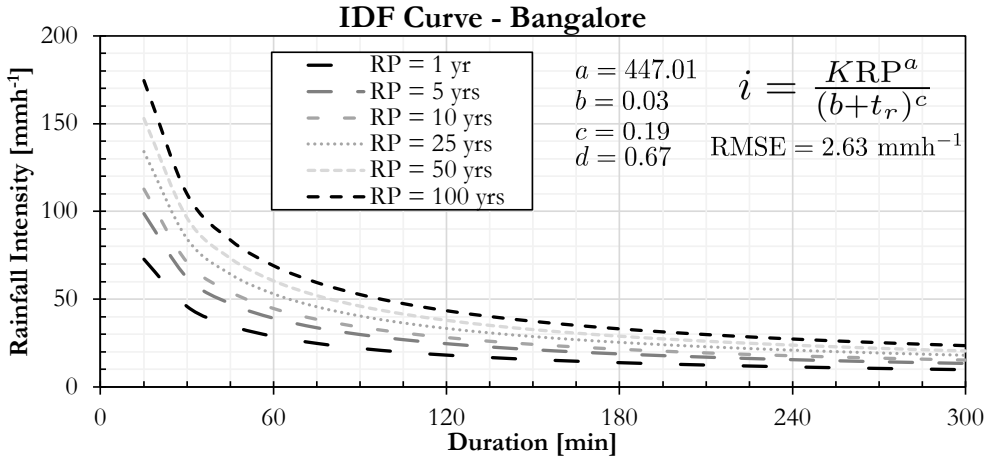

Figure A.26. Fitted IDF curve for Bangalore with 15-min intervals.

match this CFL number. Mapping results are retrieved each 30 min and maps of maximum depths, velocities, and infiltration are calculated each model time-step.

8.4.3 Model Validation

The lack of observed streamflow makes proper calibration of the model unfeasible. However, we performed a validation of the model by simulating a critical event recorded on October 31, 2012. Cyclone Nilam, a formidable meteorological event that occurred in the Bay of Bengal from October 28th to November 1st, 2012, etched its name as one of the most lethal storms in recent history. With economic losses amounting to an estimated 56 million USD (2012), the cyclone's impact resonated profoundly across the southern coastal plains of India, inflicting substantial damage to both human lives and infrastructure. Even Bangalore City, located inland, experienced consequential effects, manifested through a drop in temperatures and a deluge of precipitation. The aftermath, characterized by uprooted trees and inundated roads, particularly in regions like Koramangala recording daily rainfall figures ranging from 25mm to 110mm according to media reports and meteorological satellite rainfall data obtained from the Persiann, engendered traffic congestion and urban disarray, accentuating the cyclone's cascading repercussions well beyond its epicenter.(Timesofindia, 2012).

To simulate spatially-varied rainfall, we used the Persian satellite rainfall dataset coupled in a File Transfer Protocol (FTP) in Matlab, gathering hourly rainfall data at 5 km spatial resolution (Hsu et al., 1997).

8.4.4 Modeling the Cyclone Nilam

The daily rainfall volume is shown in Fig. A.27. The rainfall volume is distributed more towards the southwest with values of approximately 108 mm. Most of the storm, however, is temporally distributed between 15h (i.e., 3 pm) to 18h (i.e., 6 pm) of this day, with cumulative values of 72 mm in 3 hours, as shown in Fig. A.28. The summary of the results of this cyclone is presented in Fig. A.29, where the maximum flood depths (a), maximum velocity (b), cumulative infiltration (c), and outlet hydrograph (d). Maximum depths are expected to be on the order of 5 m near the downstream reservoirs, whereas velocities can be up to 15 m/s in these areas of large flow accumulation. This availability of water allows for a larger infiltration of up to 400 mm in some areas where the stream line passes.

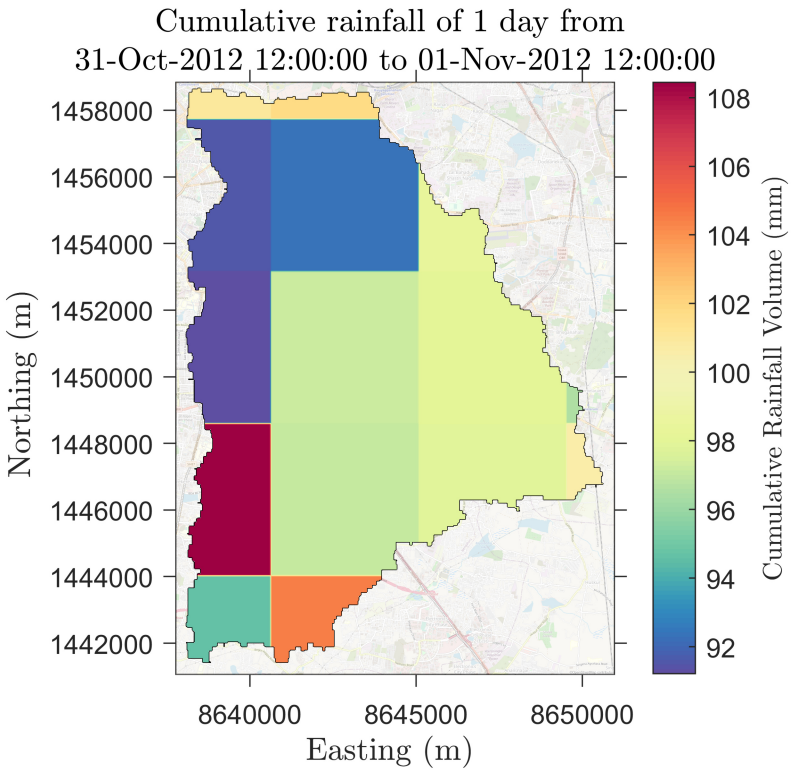

Figure A.27. Accumulated rainfall volume during the cyclone. Rainfall is recorded in 0.04° resolution and is clipped using the watershed boundaries. The nearest method is used for downscalling the rainfall into the HydroPol2D spatial resolution.

Rainfall Distribution	Rainfall Duration				
	2h	6h	12h	24h	48h
ABM	3.12	5.59	5.94	6.10	6.06
Huff	3.36	4.01	3.39	2.47	1.57
Observed	3.69	4.87	6.17	3.89	1.47

Table A.6. Area of flood risk instability in km^2 for different rainfall durations and distributions for a 100-yr storm event.

In order to quantify the specific contributions of each subcatchment derived from the virtual gauges upstream areas, we calculate the ratio between the flow discharge and drainage area. Gauge 9 has the larger specific contribution of 12 $m^3s^{-1}km^{-2}$, followed by gauge 10, as shown in Fig. A.30. The delay in hydrograph effect of reservoirs is clearly seen by visualizing the peak flow delay in the normalized outlet hydrograph. Given that the rainfall is time-spatially varied, the standard deviation of the rainfall intensities in the catchment, however, is relatively low, as presented in the error bars of Fig. A.30. The rainfall pixels are approximately 5 km long, with 25 km^2 catchment areas, resulting in fewer than 12 complete rainfall pixels.

8.5 Appendix V - Supplementary Material of Chapter 6

This supplemental material presents the following:

- HydroHP - 1D Input Data in Sec. 8.5.1
- Data Derived from ANA in Sec. 8.5.3
- Mathematical Treatment at Domain Boundaries in Sec. 8.5.4

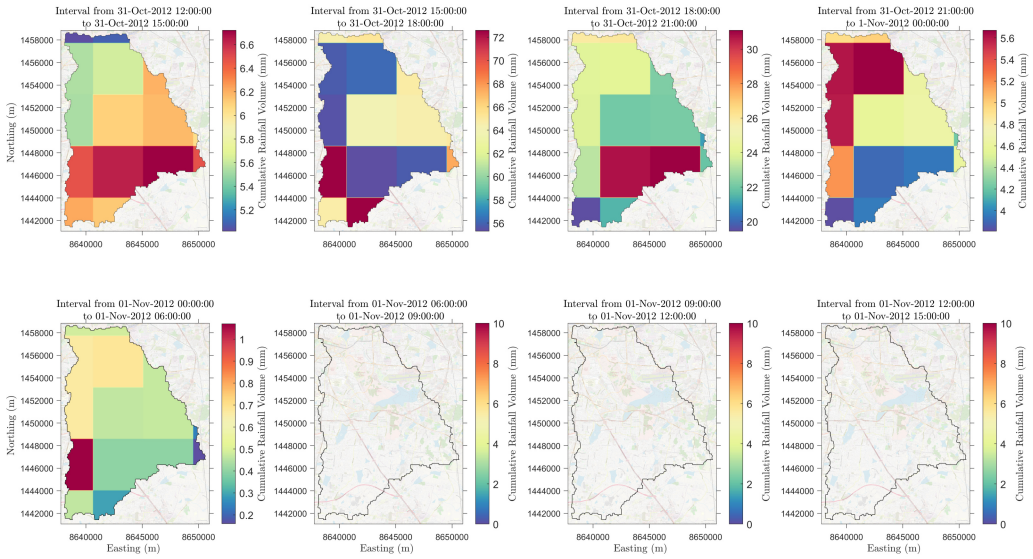

Figure A.28. Rainfall temporal distribution in 3-hour intervals. The rainfall maps derived from Persian are in a 5 km resolution with 1 hour time steps and are aggregated each 3 hour for this illustration.

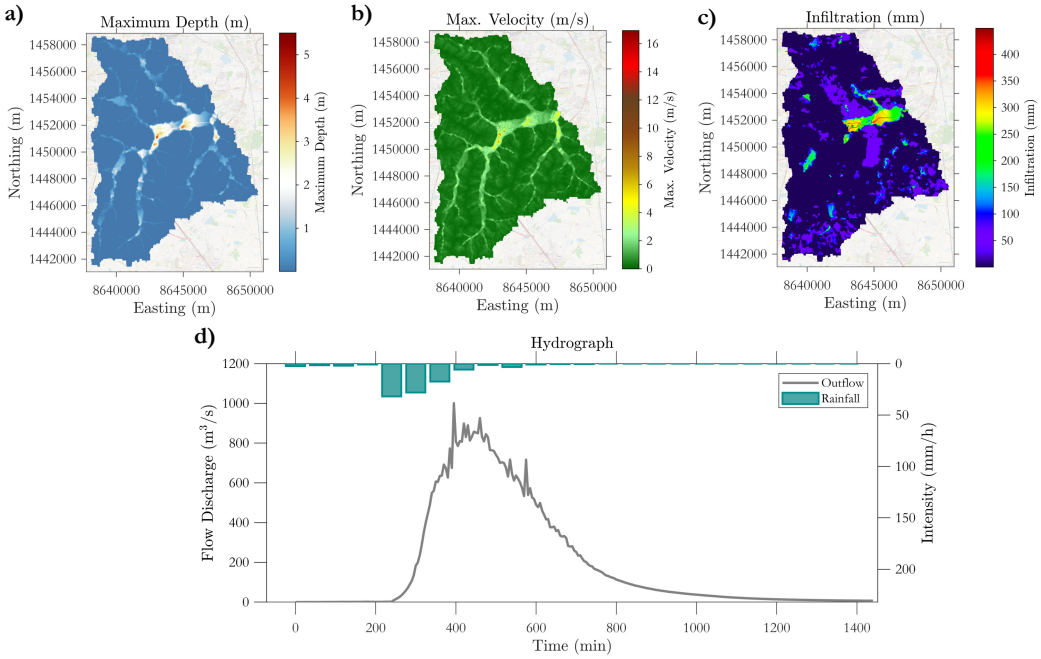

Figure A.29. Event summary results modeled with HydroPol2D. Part a) shows the maximum water surface depths, b) shows the maximum instantaneous velocity, c) the total infiltrated depth, and part d) shows the outlet hydrograph and average areal hyetograph in the catchment.

Rainfall Distribution	Rainfall Duration				
	2h	6h	12h	24h	48h
ABM	9.43	11.65	11.94	12.06	12.04
Huff	8.71	8.30	6.83	5.35	4.03
Observed	10.17	11.01	11.70	8.43	4.03

Table A.7. Flood areas with depths larger than 0.5 m in km^2 for different rainfall durations and distributions for a 100-yr storm event.

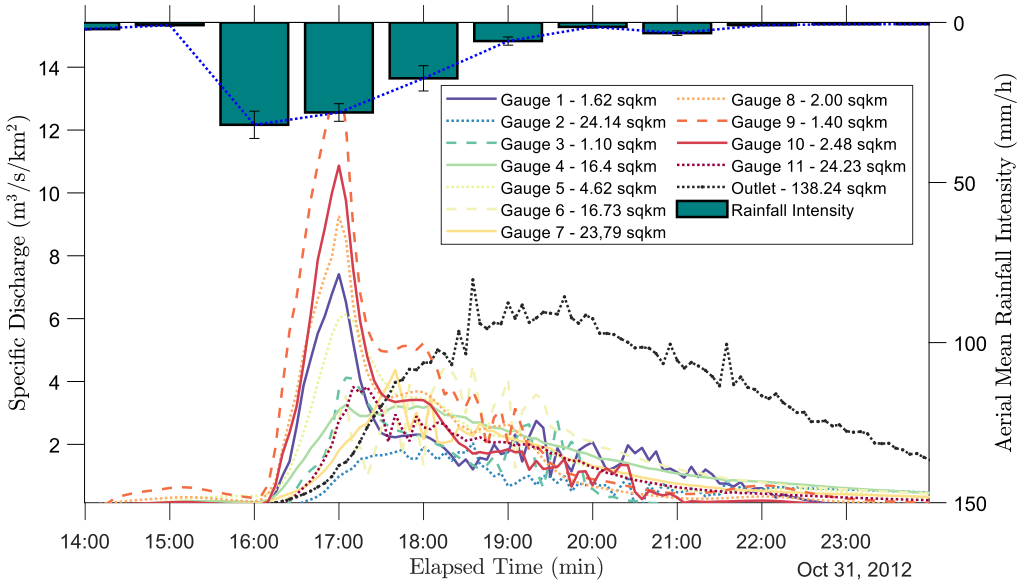

Figure A.30. Specific discharges for each virtual gauge presented in the study area map.

Rainfall Distribution	Rainfall Duration				
	2h	6h	12h	24h	48h
ABM	0.57	1.38	1.72	1.79	1.81
Huff	0.41	0.69	0.44	0.14	0.04
Observed	0.66	0.96	1.93	0.64	0.04

Table A.8. Flood areas with velocities larger than 3 ms^{-1} in km^2 for different rainfall durations and distributions for a 100-yr storm event.

Rainfall Distribution	Rainfall Duration				
	2h	6h	12h	24h	48h
ABM	0.02	4.83	9.07	27.52	27.52
Huff	0.20	5.26	9.78	27.52	27.52
Observed	0.00	4.61	6.32	23.22	27.52

Table A.9. Areas with infiltration larger than 100 mm in km^2 for different rainfall durations and distributions for a 100-yr storm event.

- Appendix 2 - Algorithm 2 for HP Estimation on Python language in Sec. 8.5.5
- Matlab codes of:
  - (i) HP Estimator Sec. 8.5.6.1
  - (ii) Read Input Data for SVE Model Sec. 8.5.6.2
  - (iii) SVE Model in Sec. 8.5.6.3
  - (iv) post-processing in Sec. 8.5.6.4
  - (v) Cross-Section, Top Width, and Water Surface Elevation Profiles in Sec. 8.5.6.5
  - (vi) Top Width, and Water Surface Elevation Profiles in regular sections in Sec. 8.5.6.6
  - (vii) Detailed output algorithm in Sec. 8.5.6.7

8.5.1 HydroHP - 1D Input Data

In order to improve the HydroHP - 1D use, the model is aided with Excel sheets with an interface to enter input data such as boundary conditions, and cross-sections data. All input data entered in Excel has comments to assist users. Excel version 2013 or higher is required.

8.5.2 General Data

In this sub-topic, we enter the basic geometrical data of the channel such as the length, the number of nodes, and the elevation of the first node. Fig. A.31 shows an example.

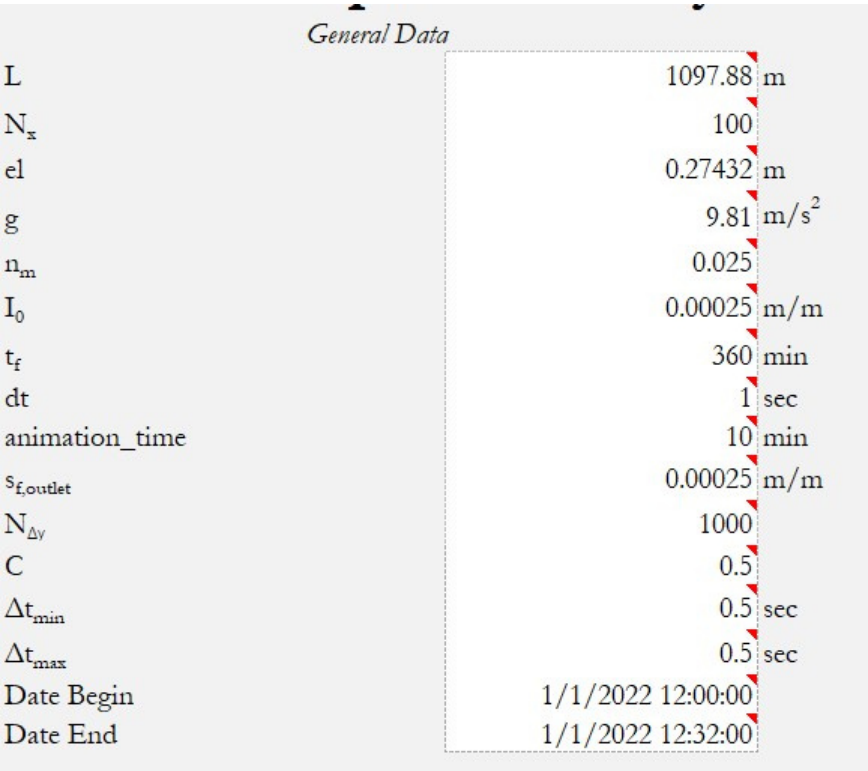

General Data		
L	1097.88	m
N_x	100	
el	0.27432	m
g	9.81	m/s^2
n_m	0.025	
I_0	0.00025	m/m
t_f	360	min
dt	1	sec
animation_time	10	min
$s_{f,outlet}$	0.00025	m/m
$N_{\Delta y}$	1000	
C	0.5	
Δt_{min}	0.5	sec
Δt_{max}	0.5	sec
Date Begin	1/1/2022 12:00:00	
Date End	1/1/2022 12:32:00	

Figure A.31. Example of general data for the model set up. The parameters presented here control the spatial domain, some of the outlet boundary conditions, adaptive time-step scheme, and output recording time.

- L is the channel lengths (m).
- N_x is the number of sections that the channel lengths will be divided into.
- e_l is the elevation of the first reach of the channel.
- g is the gravity acceleration magnitude (9.81 m/s^2).
- n_m is the manning roughness coefficient for cases with a constant roughness coefficient.
- I_0 is the bottom slope along the channel lengths (this not includes the outlet).
- t_f is the simulation period of time (min).
- Δt is the time-step if a constant time-step is used.
- animation_time is the interval of time considered for the results post-processing.
- $s_{f,outlet}$ is the outlet slope if normal condition are established (see sec. 8.5.2.1).

- $N_{\Delta v}$ is the number of discretization for the cross-section depths. C is the desired Courant number in order to ensure numerical stability.
- $\Delta t_{\min}$ is the minimum time-step.
- and $\Delta t_{\max}$ is the maximum time-step for the adaptive scheme employed in this paper.
- Date Begin is the date that starts the simulation. It is only activated if flag_elapsed_time is 1.
- Date End is the date that the simulation ends. It is only activated if flag_elapsed_time is 1.

8.5.2.1 Boundary conditions

The boundary conditions and other modeling conditions are activated by flags. A flag equal to 1 represents that a condition is imposed in the model. Fig. A.32a) shows the flags that are required and Fig. A.32b) summarize the HydroHP - 1D set up, where a) represent the general data, b) shows the model boundary conditions and simulating cases according to the flags entered, c) controls the Nash hydrograph, d) controls the tidal outlet boundary condition, e) enters the trapezoid cross-section data, f) controls either the circular or parabolic cross-section data, g) enters the tabular inflow hydrograph, h) inputs the stage hydrograph data, and i) controls the varying slope or elevation data.

8.5.2.2 Hydrograph Conditions

The flag_hydrograph indicates the hydrograph shape, if it is defined by the user as showed in Fig. A.32g), otherwise, it is assumed to employ a hydrograph with Nash shape (flag_nash==1). For the latter, Fig. A.32c) shows the parameters for this condition. T_p indicates when the peak time of the hydrograph (h). Q_b is the base flow along the hydrograph (m^3/s). Beta is a the shape factor of the Nash hydrograph. Q_p is the magnitude of the peak flow (m^3/s).

8.5.2.3 Outlet Conditions

Regarding the flag_outlet, this indicates if normal conditions are assumed for the flow, otherwise, a wave function is employed (flag_outlet = 0) which is defined by the user, as shown in Fig. A.32h). Herein, in Fig. A.32d) are shown the wave properties: $h_{0,wave}$ is the mean wave depth (m); $H_{0,wave}$ is the wave amplitude (m); L_{wave} is the wave length (m); T_{wave} is the wave period (hr); x_{wave} is the relative position from the reference (m). It is worth mentioning that if normal conditions are assumed, the flag_friction should be equals to 1.

8.5.2.4 Channel Conditions

If the conditions will not be considered as constant along the channel, the flag_slope and flag_elevation (equal to 1) allow us to specify the slope and elevation for each node within the channel, as shown in Fig. A.32i).

8.5.2.5 Cross-section Conditions

The HydroHP - 1D includes four types of cross-section along the channel: Trapezoidal (1); Circular (2); Parabolic (3); Irregular (4). Once the kind of cross-section is defined in flag_section, it is necessary to set the parameters for the desired section as shown in Fig. A.32e) and Fig. A.32f). b is the bottom channel width (m). z_1 and z_2 are the left and right slopes (m/m), respectively. D is the channel diameter (m) and a is the parabola coefficient (1/m).

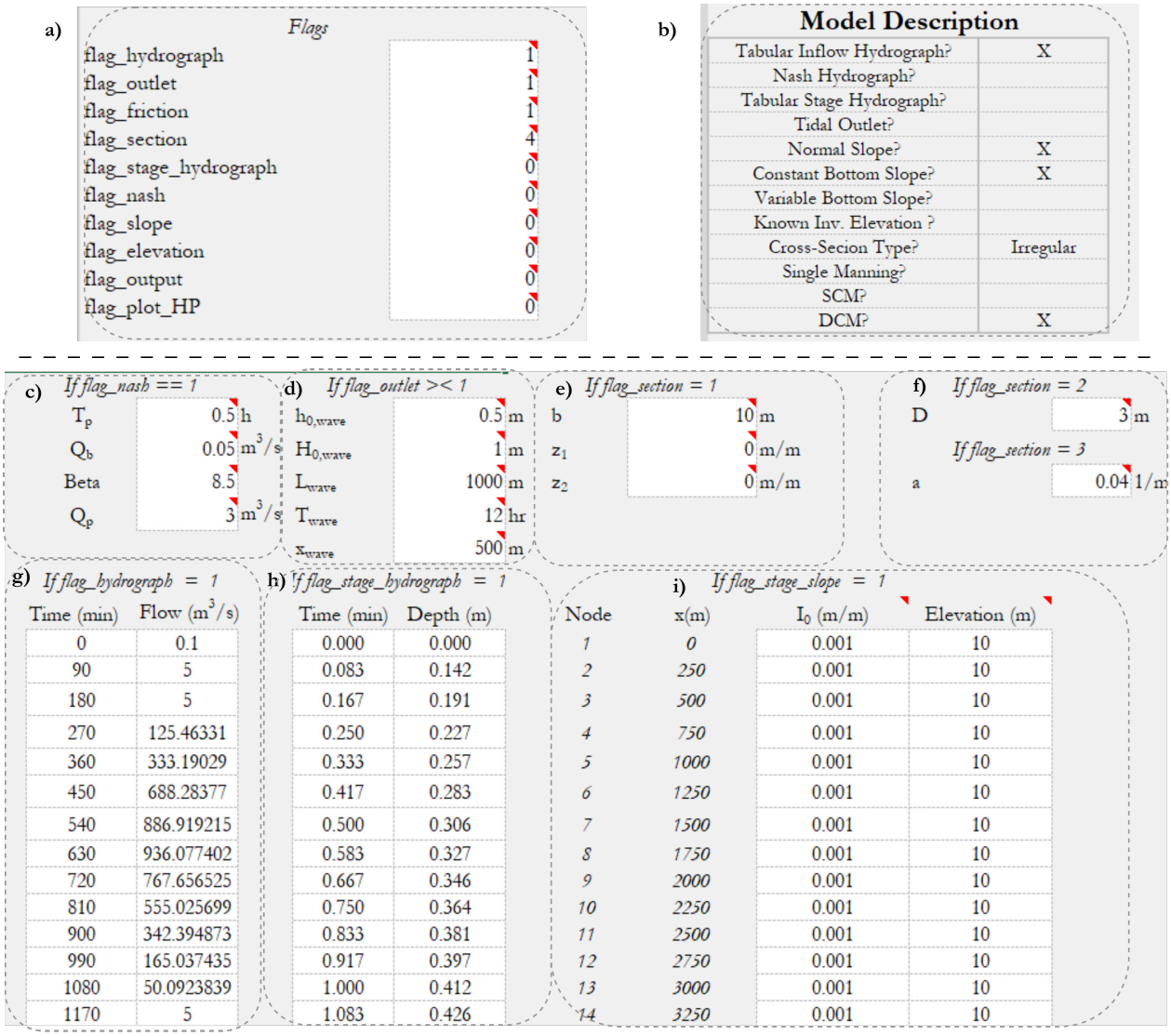

Figure A.32. Boundary conditions for the HydroHP - 1D model.

For the irregular cross-section case, as shown in Fig. A.33, it is necessary to indicate the kind of model (flag_method) to calculate the hydraulic properties of the section: 1 indicates that the single cross-section method (SCM) will employed considering only the depth-varying manning coefficient modeled via Einstein's equation and entered in the table; and 2 indicates that the discrete cross-section method (DCM) will be used and considers the difference between the in-bank and the over-banks roughness. n_m is the in-bank roughness coefficient and n_f is the over-bank roughness coefficient.

```
%% Algorithm - Section Coordinates
% Developer: Marcus Nobrega
% Date 5/16/2022
% Goal - Determine cross-section coordinates for different types of
% cross-sections
%%%%%%%%%%%%%% All Rights Reserved - contact: marcusnobrega.engcivil@
    gmail.com

clear all
% Single Sections
```

Readme			Section Discretization				
flag_length	0		Station (m)	Elevation (m)	Lengths (m)	n(i,i+1)	break_point divider
flag_method	2		0	195.05		0.035	
S_0	0.0001	m/m	5.0002	194.81		0.035	
n_m	0.035		10.0004	194.57		0.035	
n_f	0.035		15.0007	194.32		0.035	
			20.0014	194.05		0.035	
			25.0018	193.23		0.035	
			30.0028	192.38		0.035	
			35.003	191.55		0.035	
			40.0036	190.73		0.035	
			45.0041	190.41		0.035	
			50.0044	190.1		0.035	

Figure A.33. Irregular cross-section input data.

```
n_test = 0.02; % Roughness assumed
%% Triangular Section
hmax = 2; % maximum depth in m
b1 = 1; % left length in m
b2 = 2; % right length in m
x_1 = 0; % inicial x_coordinate for first value
y_1 = hmax; % inicial y_coordinate for first value
x = [x_1 (x_1 + b1) (x_1 + b1 + b2)]';
y = [y_1 (y_1 - hmax) (y_1)]';
x_triangular = x;
y_triangular = y;
n_channel_triangular = repmat(n_test,length(x_triangular)-1,1);
%% Parabolic Section
a = 1; % 1/m such that y = a*x^2 or x = sqrt(y/a)
hmax = 2; % maximum depth in m
step = 0.01; % height step in m
n_steps = floor(hmax/step);
y = linspace(0,hmax,n_steps);
x_right = sqrt(y/a);
x_left = flip(-x_right,2);
y_left = flip(y,2);
x = [x_left x_right]';
y = [y_left y]';
x_parabolic = x;
xmin = min(x_parabolic);
x_parabolic = x_parabolic + abs(xmin);
y_parabolic = y;
n_channel_parabolic = repmat(n_test,length(x_parabolic)-1,1);
%% Semi-Hyperbolic and Semi-Parabolic
% Hyperbole Equation -> y^2/a^2 - x^2/b^2 = 1
% a = 0.1;
% b = 0.01;
% xc = 0;
% yc = 0;
```

```
% hmax = 1; % maximum depth in m
% step = 0.01; % height step in m
% n_steps = floor(hmax/step);
% y = linspace(0,hmax,n_steps);
% x_left = xc + sqrt(a^2*(-1 + (y - yc).^2/(b^2)));
% x_left = flip(-x_left,2);
% % Parabolic Equation
% a = 0.01; % 1/m such that y = a*x^2 or x = sqrt(y/a)
% x_right = sqrt(y/a);
% % Final
% x = [x_left x_right]';
% y = [flip(y,2) y]';
% Composite Sections
%% Semi-Elliptical and Semi-Parabolic
% Ellipse Equation -> (x-xc)^2/a^2 + (y-yc)^2/b^2 = 1\
hmax = 2; % maximum depth in m
a = 2*hmax;
b = hmax;
xc = -a;
yc = 0;
step = 0.01; % height step in m
n_steps = floor(hmax/step);
y = linspace(0,hmax,n_steps);
x_left = xc + sqrt(a^2*(1 - (y - yc).^2/(b^2)));
x_left = flip(x_left,2);
% Parabolic Equation
a = 0.1; % 1/m such that y = a*x^2 or x = sqrt(y/a)
x_right = sqrt(y/a);
% Final
x = [x_left x_right]';
y = [flip(y,2) y]';
x_semi = x;
xmin = min(x_semi);
x_semi = x_semi + abs(xmin);
y_semi = y;
n_channel_semi = repmat(n_test,length(x_semi)-1,1);
%%%%%%%%%%%%%%%% Composite Sections%%%%%%%%%%%%%%%%
%% Road Gutter Cross-Section
hmax = 2; % maximum depth in m
b_1 = 0; % gutter width in m, typycally 0 if vertical
b_2 = 0.4; % gutter width in m
b_3 = 1.2; % wetted road width in (m)
h_1 = 0.15; % curb height (m)
h_2 = 0.10; % gutter height (m)
h_3 = 0.12; % water depth (m) <= h_1
x_1 = 0; % inicial x_coordinate for first value
y_1 = max([h_1 h_2 h_3]); % inicial y_coordinate for first value
```

```
x = [x_1 (x_1 + b_1) (x_1 + b_1 + b_2) (x_1 + b_1 + b_2 + b_3)]';
y = [y_1 (y_1 - h_1) (y_1 - h_1 + h_2) (y_1 - h_1 +  h_3)]';
x_gutter = x;
xmin = min(x_gutter);
x_gutter = x_gutter + abs(xmin);
y_gutter = y;
n_channel_road = repmat(n_test,length(x_gutter)-1,1);
%% Sucessive Trapezoid Gabion Channel
b0 = 0; % width within vertical points (m)
b = 2; % width of horizontal gabion (m)
h = 0.5; % height of the gabion (m)
n_vertical = 4; % number of vertical gabions
x_1 = 0; % inicial x_coordinate for first value
y_1 = h*n_vertical; % inicial y_coordinate for first value
x = 0;
y = 0;
for i = 1:(n_vertical*2)
    if i == 1
        x(i,1) = x_1;
        y(i,1) = y_1;
    else
        if mod(i,2) == 1 % Odd number
            x(i,1) = x(i-1,1) + b;
            y(i,1) = y(i-1,1);
        else
            x(i,1) = x(i-1,1) + b0;
            y(i,1) = y(i-1,1) - h;
        end
    end
end
x_left = x;
y_left = y;
x_right = 0; y_right = 0;
for i = 1:(n_vertical*2)
    if i == 1
        x_right(i,1) = x_left(end,1) + b;
        y_right(i,1) = y_left(end,1);
    else
        if mod(i,2) == 1 % Odd number
            x_right(i,1) = x_right(i-1,1) + b;
            y_right(i,1) = y_right(i-1,1);
        else
            x_right(i,1) = x_right(i-1,1) + b0;
            y_right(i,1) = y_right(i-1,1) + h;
        end
    end
end
```

```
x = [x_left;x_right]';
y = [y_left;y_right]';
x_gabion = x;
xmin = min(x_gabion);
x_gabion = x_gabion + abs(xmin);
y_gabion = y;
n_channel_triangular = repmat(n_test,length(x_gabion)-1,1);
%% Composite V-Notch and Francis Weir
b_rec = 0.75; % width of rectangular weir besides the v-notch (m)
hrec = 1; % rectangular height
h_vnot = 1; % v-notch height
alfa = pi/4; % 45 degree
x_1 = 0;
y_1 = hrec + h_vnot;
x = [x_1 (x_1) (x_1 + b_rec) (x_1 + b_rec + h_vnot/tan(atan(alfa))) (x_1
    + b_rec + 2*h_vnot/tan(atan(alfa))) (x_1 + b_rec + 2*h_vnot/tan(atan
   (alfa)) + b_rec) (x_1 + 2*h_vnot/tan(atan(alfa)) + 2*b_rec)]';
y = [y_1 (y_1 - hrec) (y_1 - hrec) (y_1 - hrec - h_vnot) (y_1 - hrec) (
   y_1 - hrec) (y_1)]';
x_vnot = x;
y_vnot = y;
n_channel_trapezoid = repmat(n_test,length(x_vnot)-1,1);
%% Irregular Channel
y_irr = [343.6  342.6   341.7   341.5   341.5   342.1   342     342.3
   343     343     340.2   341.6   341.3   339.3   338.6   339.3   340.5
      342.7   342.7   342.3   342     341.9   341.7   341.5   342.3
   342.7   343.2]';
l_irr = [20.1   50.5    90.9    17.1    30.2    9.4     6.7     4.9
   2.1     13.8    3.9     2.5     3       3.7     3.3     3.4     0.6
        5.8     5.8     15.8    17.7    7       18.9    38.1    27.4
   62.7]';
x_irr(i,1) = 0;
for i = 1:length(l_irr)
    x_irr(i+1,1) = x_irr(i,1) + l_irr(i,1);
end
n_channel_triangular = repmat(n_test,length(x_irr)-1,1);
% x_final = [x_triangular x_parabolic x_semi x_gutter x_gabion x_vnot
   x_irr]';
% y_final = [y_triangular y_parabolic y_semi y_gutter y_gabion y_vnot
   x_irr]';
%% Plot Cross-Sections
subplot(4,2,1)
line_w = 2;
c = [64 64 64]/255;
font = 12;
set(gcf,'units','inches','position',[4,4,6.5,4])
set(gca,'FontSize',font)
```

```
plot(x_triangular,y_triangular,'LineWidth',line_w,'color',c)
xlabel('x(m)','Interpreter','latex','FontSize',font)
ylabel('y(m)','Interpreter','latex','FontSize',font)
grid on
set(gca,'FontSize',font)
subplot(4,2,2)
plot(x_parabolic,y_parabolic,'LineWidth',line_w,'color',c)
xlabel('x(m)','Interpreter','latex','FontSize',font)
ylabel('y(m)','Interpreter','latex','FontSize',font)
grid on
set(gca,'FontSize',font)
subplot(4,2,3)
plot(x_semi,y_semi,'LineWidth',line_w,'color',c)
xlabel('x(m)','Interpreter','latex','FontSize',font)
ylabel('y(m)','Interpreter','latex','FontSize',font)
grid on
set(gca,'FontSize',font)
subplot(4,2,4)
plot(x_gutter,y_gutter,'LineWidth',line_w,'color',c)
xlabel('x(m)','Interpreter','latex','FontSize',font)
ylabel('y(m)','Interpreter','latex','FontSize',font)
grid on
set(gca,'FontSize',font)
subplot(4,2,5)
plot(x_gabion,y_gabion,'LineWidth',line_w,'color',c)
xlabel('x(m)','Interpreter','latex','FontSize',font)
ylabel('y(m)','Interpreter','latex','FontSize',font)
grid on
set(gca,'FontSize',font)
subplot(4,2,6)
plot(x_vnot,y_vnot,'LineWidth',line_w,'color',c)
xlabel('x(m)','Interpreter','latex','FontSize',font)
ylabel('y(m)','Interpreter','latex','FontSize',font)
grid on
set(gca,'FontSize',font)
% Irr
subplot(4,2,[7:8])
y_irr = y_irr - min(y_irr);
plot(x_irr,y_irr,'LineWidth',line_w,'color',c)
xlabel('x(m)','Interpreter','latex','FontSize',font)
ylabel('y(m)','Interpreter','latex','FontSize',font)
grid on
set(gca,'FontSize',font)
exportgraphics(gcf,'Cross_Sections.pdf','ContentType','vector')
```

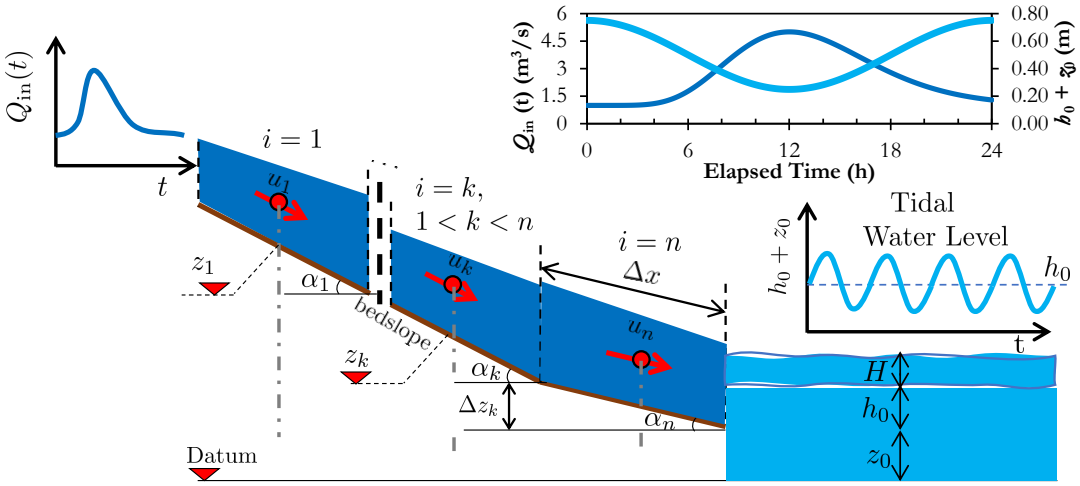

Figure A.34. Example of problem schematics that HydroHP - 1D can solve. The model allow simulating inflow hydrographs, stage hydrographs, normal slope, rating curves and other types of boundary conditions

8.5.3 Data derived from ANA

Data can be obtained from hydroweb website, available at (https://www.snirh.gov.br/hidroweb/). The data format is given in .csv and requires a treatment to convert it into cross-sections, flows, and stages. The data treatment is performed in (https://www.labhidro.ufsc.br/hidroapp/), using the research conducted in Souza et al. (2021).

8.5.4 Mathematical Treatment at Domain Boundaries

The Lax-Friedrichs method uses a central difference in space, which requires known state values on the neighborhoods. Therefore, in the borders of domain (i.e., $i = 1$ or $i = N_x$), one has to assume some sort of extrapolation. Herein, we use a zero-order extrapolation that varies according to the chosen boundary condition simulated.

8.5.4.1 Inflow Hydrograph Boundary Condition

For an inflow hydrograph boundary condition, we can write:

$$Q_1(t + \Delta t) - Q_h(t + \Delta t) = 0 \tag{8.55a}$$

$$A_1(t + \Delta t) - A_2(t) = 0 \tag{8.55b}$$

where Q_h is the known inflow hydrograph.

We can see from the previous equation that if a very long time-step is used, problems might arise, making the boundary sharped or curved by the zero-order extrapolation. Moreover, since $A_1(\Delta t)$ can be estimated, all other hydraulic properties can be derived from the table containing the hydraulic properties.

8.5.4.2 Stage-Hydrograph Boundary Condition

When the depths are known over time in the inlet of the channel, we can write:

$$h_1(t + \Delta t) - h_s(t + \Delta t) = 0 \tag{8.56a}$$

$$Q_1(t + \Delta t) = Q_2(t) \tag{8.56b}$$

With known values of $h_1(t+\Delta t)$, we seek values of every other state, such as $A_1(t+\Delta t)$, in the hydraulic properties table.

8.5.4.3 Stage-Hydrograph with Inflow Hydrograph Boundary Condition

When both information is known, we can write:

$$h_1(t+\Delta t) - h_s(t+\Delta t) = 0 \tag{8.57a}$$
$$Q_1(t+\Delta t) - Q_h(t+\Delta t) = 0 \tag{8.57b}$$

8.5.4.4 Known Friction Slope at Outlet

In this case, the outlet friction slope is a constant value given by:

$$I_{f,N_x}(t+\Delta t) - s_{out} = 0 \tag{8.58a}$$
$$A_{N_x}(t+\Delta t) - A_{N_x-1}(t) = 0 \tag{8.58b}$$

where s_{out} is given.

8.5.4.5 Tidal Outlet Boundary Condition

For tidal water level, we use a wave equation boundary condition such as:

$$h_{N_x}(t+\Delta t) = h_0 + \frac{H}{2}\cos\left(k_w x_w - \sigma t\right) \tag{8.59a}$$
$$I_{f,N_x}(t+\Delta t) = \frac{(z_{N_x-1} + h_{N_x-1}(t)) - (z_{N_x} + h_{N_x}(t))}{\Delta x} \tag{8.59b}$$
$$u_{N_x}(t+\Delta t) = \frac{1}{n_{Nx}} R_{h,N_x}(t)^{2/3}\sqrt{I_{f,N_x}} \tag{8.59c}$$
$$Q_{N_x}(t+\Delta t) = A_{N_x}(t)u_{N_x}(t) \tag{8.59d}$$

where h_{N_x} is the water depth at node n, x_w is the relative position of the wave from a given reference, L_w is the wave length, $k_w = 2\pi/L_w$ is the wave number, T_w is the wave period, and σ is the wave angular frequency such that $\sigma = 2\pi/T_w$.

8.5.5 Algorithm 2: Finite Element discretization procedure with Nested For Loops

To assess depth-varying HP for the second algorithm, the finite element method (FEM) was used as a basis to discretize the hole cross section area into n regular elements, this results in a 2-D mesh of squares (a matrix), where the number of elements in the mesh are established by a resolution r as commonly done in many engineering applications (Sabat e Kundu, 2020). The grid size is determined by the r which splits vertical and horizontal distances between coordinates; for example, a r equal to 0.1m will divide into 10 elements a horizontal distance of 1 meter between two coordinates, and similarly for a vertical distance.

The algorithm begins by finding the lowest bottom elevation of the riverbed ly, then, two vectors are defined ($\boldsymbol{seg_x}$ and $\boldsymbol{seg_y}$) with consecutive pairs or coordinates for both axis, this aims to determine the flow area between the water depth j and the boundaries of the riverbed (see Fig. A.35). The main loop is used to represent the water depth increasing, then, inside of this, three individual loops are used to 1) define the riverbed boundaries; 2) calculate the flow area, and 3) calculate the wet perimeter. The left HP are determined in terms of the aforementioned variables. Considering

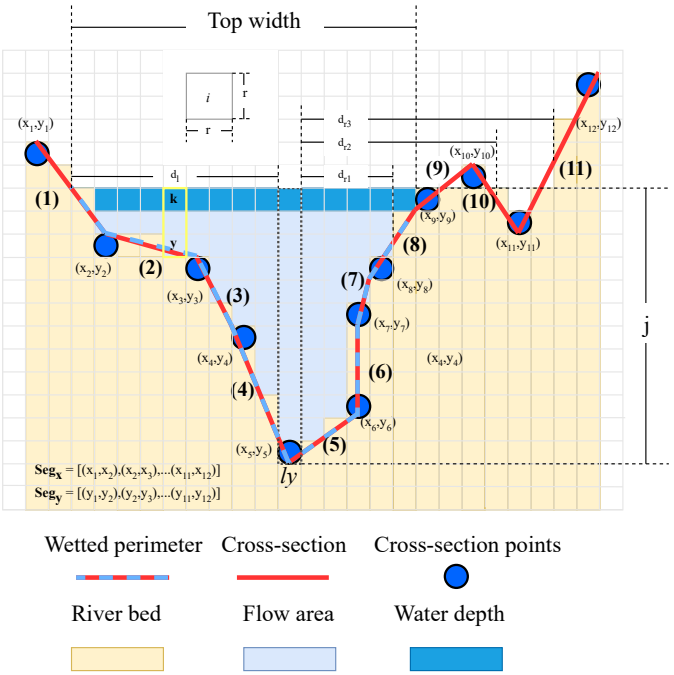

Figure A.35. Example of cross-section discretization with finite element and riverbed boundaries identification according to a water depth j.

that the water depth is monotonically increasing from ly for every pixel in the mesh on the vertical axis, boundaries from the riverbed topography are identified for every j iteration, hence defining new boundaries to be reached before the water can overflow to the next height of the cross-section for each side. To this end, first, in the vector $\boldsymbol{seg_y}$ is identified between of which pair of coordinates or segments j belongs to. It is worth mentioning that through this method many segments could be considered, as shown in Fig. A.35 where j intersect segments 1, 8, 10, and 11, to solve this, the pairs of horizontal coordinates from those segments in $\boldsymbol{seg_x}$ are filtered by considering the closer distance of the average of those pair of coordinates related to the station of ly for left and right sides, for instance, on the right side the distance d_{r1} is lower than d_{r2} and d_{r3}, for the left side there is only a segment to be considered.

8.5.5.1 Flow area and centroid

To calculate any HP is necessary to define which elements in the mesh belong to the flow area, for this, and considering the previous method to find boundaries in the riverbed, the value of 1 is assigned to elements in the flow area, otherwise, 0 is assigned to the left elements in the matrix. To this end, it was defined the function f_1, which returns the riverbed elevation for a specific station k within the cross-section, in this case, for every column in the matrix. According to Eq. (8.60) as shown in Fig. A.35, this result comes for 24 hours was simulated at the beginning o from a linear interpolation between the two coordinates of the segment 2. It is worth mentioning that there is also a second function f_2 (Eq. (8.61)) with similar logic of f_1 with the difference that f_2 returns the value of the k station in a segment according to an elevation y of the riverbed. Once every element in the matrix has a value, calculate the area as just the sum of all elements within the matrix.

$$f_1(i) = y_{i+1} - \left(\frac{y_i - y_{i+1}}{x_i - x_{i+1}}\right)(x_i - k) \tag{8.60}$$

$$f_2 = x_{i+1} - \left(\frac{y_{i+1} - y}{y_i - y_{i+1}}\right)(x_{i+1} - x_i) \tag{8.61}$$

where: y is the riverbed elevation; y_i and y_{i+1} are the two riverbed elevations in the segment in analysis; x_i and x_{i+1} are the two riverbed horizontal coordinates of the segment in analysis, and k is the horizontal coordinate of the station.

On the other hand, the vertical centroid for every column is calculated through the sum of all the values on the column and divided by two, plus the riverbed elevation obtained with the f_1 shown in Eq. (8.60).

8.5.5.2 Wetted Perimeter

This procedure is divided into two steps: first, with the f_3 (Eq. (8.62)) are calculated and accumulated the hypotenuses for all segments within the flow area (2, 3, 4, 5, 6, and 7), excluding those which are intersected by the j water depth (1 and 8). Second, for the hypotenuses' calculation of the first and last segments, is necessary to determine the intersection points on them due to the water depth j using (Eq. (8.60)) and (Eq. (8.61)), thus, knowing the coordinates, the distances are calculated using (Eq. (8.62)).

$$f_3(i) = \sqrt{(y_i - y_{i+1})^2 + (x_i - x_{i+1})^2} \tag{8.62}$$

where y_i, y_{i+1}, x_i and x_{i+1} represent the segment's coordinates.

8.5.5.3 Main Python Code

```
# %%% Cross Section Hydraulic Properties Estimator %%% #
# Developer: Luis Castillo and Marcus Nobrega
# Date 5/20/2022
# Goal: Determine hydraulic properties for regular or irregular cross-section

import numpy as np
import pandas as pd
import math
import matplotlib.pyplot as plt
from matplotlib import pyplot
from numpy import exp

noise = 0.01
res = 10  # To be defined by the user, this resolution means the quantity of elements between point, i.e., between
        # two coordinates (1 and 2) on the vertical axis, and for a res = 10, 10 elements will be discretized between
        # 1 and 2 coordinates. the bigger the quantity of elements, the better representation, however, it takes more
        # time of processing.
man = 0.012  # To be defined by the user, Manning roughness coefficient
s = 0.00398  # To be defined by the user, slope of the cross-section

file = open("D:/Google_drive/Meu Drive/Papers/Paper - Nota_tecnica/j1.csv")
```

```
coors = pd.read_csv(file, delimiter=';', header=None).values
plt.plot(coors[:, 0], coors[:, 1])

Ymax, Ymin, Xmax, Xmin = max(coors[:, 1]), min(coors[:, 1]), max(coors
    [:, 0]), min(coors[:,0 ])   # Maximum and minimum values of the list
    of coordinates
for m in range(len(coors)):
    if coors[m][1] <= Ymin:  # Looking for the middle part of the cross-
        section
        middle = coors[m][0]
# --- Preallocate HP --- #
area, top, = np.zeros((int(Ymax*res - Ymin*res), 1)), np.zeros((int(Ymax
    *res - Ymin*res), 1))
perimeter_2, y = np.zeros((int(Ymax*res - Ymin*res), 1)), np.zeros((int(
    Ymax*res - Ymin*res), 1))
RH, centroid = np.zeros((int(Ymax*res - Ymin*res), 1)), np.zeros((int(
    Ymax*res - Ymin*res), 1))
con, phi = np.zeros((int(Ymax*res - Ymin*res), 1)), np.zeros((int(Ymax*
    res - Ymin*res), 1))
Q, center = np.zeros((int(Ymax*res - Ymin*res), 1)), np.zeros((int(Ymax*
    res - Ymin*res), 1))
seg_x, seg_y = np.zeros((len(coors[:, 0]) - 1, 2)), np.zeros((len(coors
    [:, 0]) - 1, 2))

for i in range(len(coors) - 1):
    seg_x[i, 0], seg_x[i, 1] = coors[i, 0], coors[i+1, 0]
    seg_y[i, 0], seg_y[i, 1] = coors[i, 1], coors[i+1, 1]


def per(i):
    return math.sqrt(pow(seg_y[i, 0]- seg_y[i, 1], 2) + pow(seg_x[i, 0]-
        seg_x[i, 1], 2))


def image_x(i, j):  # Function that according to the horizontal position
    of K, returns the vertical image of the segment
    if seg_y[i, 0] == seg_y[i, 1]:  # if there is a vertical wall
        return (seg_x[i, 0]) - (((seg_y[i, 0] - j)*(seg_x[i, 0]-seg_x[i,
            1])) / ((seg_y[i, 0]-seg_y[i, 0]*noise) - (seg_y[i, 1]+seg_y
            [i, 1]*noise)))
    return (seg_x[i, 0]) - (((seg_y[i, 0] - j)*(seg_x[i, 0]-seg_x[i, 1])
        ) / (seg_y[i, 0] - seg_y[i, 1]))


def image_y(i, j):  # Function that according to the horizontal position
    of K, returns the vertical image of the segment
    if seg_x[i, 0] == seg_x[i, 1]:  # if there is a horizontal wall
```

```
54          return (seg_y[i, 0]) - ((seg_y[i, 0] - seg_y[i, 1])/((seg_x[i,
                0]-seg_x[i, 0]*noise)-(seg_x[i, 1]+seg_x[i, 1]*noise)))*(
                seg_x[i, 0] - j)
55      return (seg_y[i, 0]) - ((seg_y[i, 0] - seg_y[i, 1])/(seg_x[i, 0]-
            seg_x[i, 1]))*(seg_x[i, 0] - j)
56
57
58  mg = np.zeros((int(round((Ymax-Ymin)*res)), int(round((Xmax-Xmin)*res)))
        , dtype=int)  # Main Grid
59
60  for j in range(int(round(Ymin*res))+1, int(round(Ymax*res))):  # Looping
        thought the vertical axis
61      seg_{x2}, seg_{y2} = np.zeros((len(seg_y), 1)), np.zeros((len(seg_y)
            , 1))
62      for i in range(len(seg_y)):  # finding the upper boundary of the
            water deep
63          if (seg_y[i, 0] >= j/res > seg_y[i, 1]) or (seg_y[i, 0] <= j/res
                <= seg_y[i, 1]):
64              seg_y_2[i, 0] = i
65              seg_{x2}[i, 0] = (seg_x[i, 0]+seg_x[i, 1])/2 - middle
66      left_wall = np.where(seg_{x2} < 0, seg_{x2}, -np.inf).argmax()  #
            Finding the walls that contains the current
67      right_wall = np.where(seg_{x2} > 0, seg_{x2}, np.inf).argmin()   #
            water level
68
69      if left_wall == right_wall:  # this condition is meet when water
            level is higher the profile
70          break
71
72      for i in np.arange(round(image_x(left_wall, j/res)*res) - Xmin*res,
            # Looping thought the horizontal axis
73                         round(image_x(right_wall, j/res)*res) - Xmin*res)
                               :   # Modifying the main grid
74          for k in range(len(seg_x)):
75              if (seg_x[k, 0] <= (i / res + Xmin) < seg_x[k, 1]):  #
                    Looking for what segment "i" belongs to.
76                  break
77          mg[round(Ymax*res-j): int(round(Ymax*res)) - int(round(image_y(k
                , (i/res + Xmin))*res)), int(i)] = 1
78          center[int(j - Ymin*res), 0] = ((np.count_nonzero(mg[:, int(i)]
                == 1)/2)/res + (image_y(k, (i/res)))) * (np.count_nonzero(mg
                [:, int(i)] == 1)/pow(res, 2))
79
80      perimeter = []
81      for i in range(left_wall,
82                     right_wall):  # all segments between the walls but
                           not including they selfs
```

```
83          perimeter.append(per(i))
84      perimeter.append(math.sqrt(pow(j/res - seg_y[left_wall, 1], 2) +
85                                 pow(image_x(left_wall, j/res) - seg_x[
                                       left_wall, 1],
86                                     2)))  # perimeter for the left
                                           boundary
87      perimeter.append(math.sqrt(pow(j/res - seg_y[right_wall, 0], 2) +
88                                 pow(image_x(right_wall, j/res) - seg_x[
                                       right_wall, 0],
89                                     2)))  # perimeter for the right
                                           boundary
90
91      area[int(j - Ymin*res), 0] = np.sum(mg) / pow(res, 2)
92      y[int(j - Ymin*res), 0] = j / res - Ymin
93      perimeter_2[int(j - Ymin*res), 0] = np.sum(perimeter)
94      RH[int(j - Ymin*res), 0] = (np.sum(mg) / pow(res, 2))/np.sum(
            perimeter)
95      top[int(j - Ymin*res), 0] = image_x(right_wall, j/res)-image_x(
            left_wall, j/res)
96      centroid[int(j - Ymin*res), 0] = np.sum(center)/(np.sum(mg))
97      con[int(j - Ymin*res), 0] = (1/man)*(np.sum(mg) / pow(res, 2))*pow((
            np.sum(mg) / pow(res,2))/(np.sum(perimeter)), 2/3)
98      phi[int(j - Ymin*res), 0] = (np.sum(mg) / pow(res, 2))*pow((np.sum(
            mg) / pow(res,2))/(np.sum(perimeter)), 2/3)
99      Q[int(j - Ymin*res), 0] = (1/man)*(np.sum(mg) / pow(res, 2))*pow((np
            .sum(mg) / pow(res,2))/(np.sum(perimeter)), 2/3)*pow(s, 1/2)
100
101 # --- Filling with Nan all extra elements in the arrays --- #
102 area[int(j - Ymin*res): , 0], y[int(j - Ymin*res): , 0], perimeter_2[int
        (j - Ymin*res): , 0] = math.nan, math.nan, math.nan
103 RH[int(j - Ymin*res): , 0], top[int(j - Ymin*res): , 0], centroid[int(j
        - Ymin*res): , 0] = math.nan, math.nan, math.nan
104 con[int(j - Ymin*res): , 0], phi[int(j - Ymin*res): , 0], Q[int(j - Ymin
        *res): , 0] = math.nan, math.nan, math.nan
105 plt.imshow(mg)
106
107 # ---  Plotting the HP curves --- #
108 fig, (ax1, ax2, ax3, ax4, ax5, ax6, ax7, ax8) = plt.subplots(1, 8)
109 fig.suptitle('2b')
110 ax1.plot(area, y)
111 ax1.set_xlabel('Area $(m^2)$')
112 ax1.set_ylabel('water depth $(m)$')
113 ax2.plot(perimeter_2, y)
114 ax2.set_xlabel('Perimeter $(m)$')
115 ax3.plot(top,y)
116 ax3.set_xlabel('Top lenght $(m)$')
117 ax4.plot(RH, y)
```

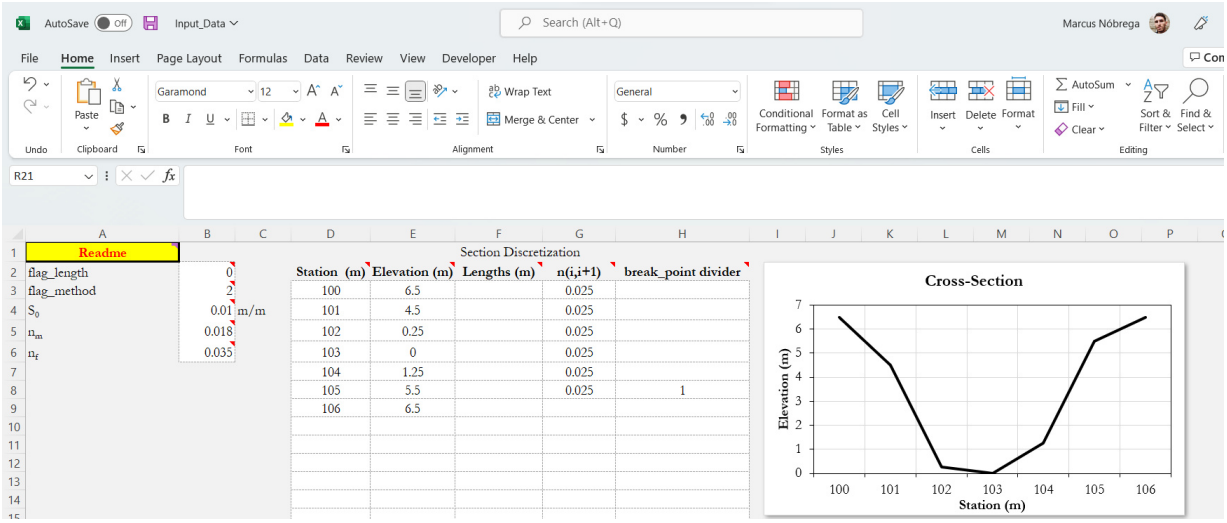

Figure A.36. Excel Spreadsheet input data file. Column B allows selecting the data entry method and the hydraulic assumption of the DCM or SCM model. Moreover, it allows entering the roughness coefficient for inbank and overbank areas. Columns D to H are relative to the cross-section. An automatic plot of the cross-section is displayed in the right of the data entry.

```
ax4.set_xlabel('Hydraulic radius $(m)$')
ax5.plot(centroid,y)
ax5.set_xlabel('Centroid $(m)$')
ax6.plot(con, y)
ax6.set_xlabel('Conveyance $(m^3/s)$')
ax7.plot(phi, y)
ax7.set_xlabel('Phi $(m^3/s)$')
ax8.plot(Q, y)
ax8.set_xlabel('Flow $(m^3/s)$')
```

8.5.6 Matlab Codes

8.5.6.1 HP Estimator

A read-me file gives all details of how to fill the data in the spreadsheet. In summary, the user can select the method used to enter the coordinates (e.g., flag length) and the method used to calculate flows. Moreover, the user can enter the bottom slope and roughness coefficients of the inbank and outbank areas if the DCM is used.

A table with cells painted white allows the entry of x and y coordinates, as well as roughness coefficients, lengths, and the breakpoint dividers of the channel.

Overall, this function reads the input data and return plots of

- Cross-section geometry and stage-roughness plot
- Normalized Hydraulic Properties such as: a)

```
%%% Determining Irregular Cross-section Functions %%%
% Developer: Marcus Nobrega Gomes Junior
% Date: 2022/05/03
% Goal - Calculate Hydraulic Properties of Irregular and Regular
    Sections
```

```
5  % for a given cross-sections and Manning's roughness coefficients
6
7  function [y_table, A, P, Rh, y_bar, n_med, Beta, v, B, Q, x_absolute, y,
       s0] = HP_estimator(flag_plot_HP,dh)
8  input_table = xlsread('HyProSWE_Input_Data.xlsx','
       Irregular_Cross_Section');
9  input_data = input_table(1:5,1);
10 input_data_coordinates = input_table(2:end,3:end);
11 flag_length = input_data(1,1); % If == 1, use lengths as main input data
       , otherwise use absolute values of x (m)
12 flag_method = input_data(2,1); % If == 1, SCM, else DCM
13 s0 = input_data(3,1); % Slope in m/m
14 nm = input_data(4,1); % Main channel roughness
15 nf = input_data(5,1); % Overbanks channel roughness
16
17 if flag_method == 1
18     n_channel = input_data_coordinates(1:(end-1),4);
19 end
20
21 % Retrieving Data
22 x_absolute = input_data_coordinates(:,1);
23 elevations = input_data_coordinates(:,2);
24 lengths = input_data_coordinates(1:(end-1),3);
25 break_point_divider = input_data_coordinates(1:(end),5);
26
27 delta = zeros(length(elevations),1);
28 for i = 1:(length(elevations)-1)
29     delta(i) = abs(elevations(i+1,1) - elevations(i,1));
30 end
31 delta_h = min(delta(delta > 0));
32 tic
33
34 % Checking input data consistency
35 if length(elevations) <= 3
36     error('Please, enter at least 4 points for elevation and 3 points
           for manning and lengths. If you have a triangular shape, please
           enter the invert elevation twice and add a 0 length and 0 manning
           , such that you have 4 points for elevation and 3 points for
           manning and lengths')
37 end
38
39 points = (1:1:length(elevations))'; % stations from 1 to n
40
41 % Let's assume a maximum 1 cm difference in the depths
42 % Noise
43 noise_max = 0.01; % m
44 % Let's also assume a minimum 0.1 cm difference in the depths, that is,
```

```
    the
% noise
noise_min = 0.001; % m
noise = delta_h/dh; % Noise in m from user input data
if noise > noise_max
    noise = noise_max; % m
elseif noise < noise_min
    noise = noise_min; % m
end

factor = 1; %precision = 1/factor * noise

[au,ia] = unique(elevations,'stable');
Same = ones(size(elevations));
Same(ia) = 0; % repetitive values
noise_i = rand(1,1)*noise;
small_number = noise/100;
% New Elevation and X_values
ii = 0;
for i = 1:(length(elevations) - 1)
    el1 = elevations(i); el2 = elevations(i+1);
    x1 = x_absolute(i); x2 = x_absolute(i+1);
    if el1 == el2 || abs(el1 - el2) == noise
        elevations(i+1) = elevations(i+1) + noise;
        if elevations(i+1) == elevations(i)
            elevations(i+1) = elevations(i+1) + noise;
        end
    end
    if x1 == x2 || abs(x2 - x1) == noise
        x_absolute(i+1) = x_absolute(i+1) + noise;
        if x_absolute(i+1) == x_absolute(i)
            x_absolute(i+1) = x_absolute(i+1) + noise;
        end
    end
end

% if max(isnan(n_channel)) > 0
%     error('Please, enter (n-1) data for Manning coefficient, where n
    is the number of break-points')
% end

% Roughness Boundary Condition
if flag_method == 1
    n_channel(end+1,1) = 0; % adding last boundary condition
end

% Minimum elevation
```

```
min_el = min(elevations); % m
% y (bottom to up)
y = elevations - min_el;
pos_inv = find(y == 0); % position of invert elevation
% If we have more than 1 invert
pos_inv = pos_inv(1);

% x (left to right)
if flag_length == 1
    for i = 1:length(y) % coordinates of each measured point
        if i == 1
            x_absolute(i,1) = 0 + noise;
        else
            x_absolute(i,1) = x_absolute(i-1) + lengths(i-1) + noise;
        end
    end
else % Lengths are already assumed from the input data table
    for i = 1:length(y)
        if i ~= length(y)
            lengths(i) = x_absolute(i+1) - x_absolute(i);
        end
    end
end

%  Alfa min
alfa_min_bound = noise/max(lengths(lengths>1e-8));
big_n = 100000*atan(asin(1)); % big number making sure it is a multiple
    of 1 rad, so that sin(atan(big_n)) = 1
min_length = min(lengths(lengths>0));

% Invert coordinates
x_invert = x_absolute(pos_inv,1);
y_invert = 0;

% Slopes (taking from x (left-right) y (down-up)
% For point 1 and for the last point
alfa_l = (y(1,1) - y(2,1))/lengths(1,1);

% Unsorted Values
x_left_unsorted = x_absolute(1:(pos_inv-1),1);
y_left_unsorted = y(1:(pos_inv-1),1);
x_right_unsorted = x_absolute(pos_inv + 1:end,1);
y_right_unsorted = y(pos_inv + 1:end,1);
if flag_method == 1
    n_left_unsorted = n_channel(1:(pos_inv-1),1);
    n_right_unsorted = n_channel(pos_inv:(end-1),1);
end
```

```
136
137 % Maximum depth (left and right)
138 max_left = max(y_left_unsorted); max_right = max(y_right_unsorted);
139 max_y = min(max_left, max_right);
140
141 % Refreshing values of ymax
142 pos_r = length(y_right_unsorted);
143 if max_left ~= max_right
144     if max_left > max_y % the maximum is located at left
145         z = sort(y_left_unsorted,1,'descend');
146         if length(z) == 1 % Case where we have a vertical wall
147             z(2,1) = y_invert;
148         end
149         x_left_first = round(x_absolute(2) - (max_y - z(2))/alfa_l,2);
150         % New values of x and y
151         x_absolute(1) = x_left_first;
152         y(1) = max_y;
153         pos_r = length(y_right_unsorted);
154     else
155         pos_r = find(y_right_unsorted > max_y ,1,'first');
156         alfa_r = (y_right_unsorted(pos_r) - y_right_unsorted(pos_r - 1))
               /lengths(length(y_left_unsorted) + 1 + pos_r-1);
157         z = sort(y_right_unsorted,1,'descend');
158         x_rigth_last = round(x_absolute(end-1) + (max_y - z(2))/alfa_r
               ,2);
159         % New values of x and y
160         x_absolute(end) = x_rigth_last;
161         y(length(y_left_unsorted) + 1 + pos_r) = max_y;
162     end
163 end
164 dim = 1:(length(y_left_unsorted) + 1 + pos_r);
165 y = y(dim,1);
166 x_absolute = x_absolute(dim,1);
167 % n_channel = n_channel(dim,1);
168 points = points(dim);
169
170 % New Unsorted Values with New max
171 x_left_unsorted = x_absolute(1:(pos_inv-1),1);
172 y_left_unsorted = y(1:(pos_inv-1),1);
173 x_right_unsorted = x_absolute(pos_inv + 1:end,1);
174 y_right_unsorted = y(pos_inv + 1:end,1);
175 if flag_method == 1
176     n_left_unsorted = n_channel(1:(pos_inv-1),1);
177     n_right_unsorted = n_channel(pos_inv:(end-1),1);
178 end
179
180 % Main Matrix
```

```
% table = [points,x_absolute,y,n_channel];

% % Vlookup Function
% Vlookup_eq = @(data,col1,val1,col2) data((find(data(:,col1)==val1,1)),
    col2); %Vlookup function as Excel
% Vlookup_leq = @(data,col1,val1,col2) data((find(data(:,col1)<=val1,1))
    ,col2); %Vlookup function as Excel

% Sections left
numb_left = length(find(y_left_unsorted >= y_left_unsorted(end)));
% Sections right
numb_right = length(find(y_right_unsorted >= y_right_unsorted(1)));
% Tot sections
tot_sections = numb_left + numb_right - 1; % take one out because both
    sides are equal

y_l_prev = y_left_unsorted(2:length(y_left_unsorted));
y_l_next = y_left_unsorted(1:(length(y_left_unsorted)-1));

%%%% Precision
precision = 1/factor*noise; % m

%%%% small number >= 1 < 1e-8 + 1
sm = (1e-8 + 1);

%%%% Total_Noise
tot_noise = noise*sum(Same);
% Main loop
i = 0; int_n_p = 0; % integral of n*perimeter

%% Define Main Channel and Overbanks
pos_break = find(break_point_divider == 1); % Position where the divider
    occurs
% Main Channel Height
ym = y(pos_break); % Main channel height (m)
if pos_break > pos_inv % Left intersection
    % Left intersection
    posm_left = find(y_left_unsorted >= ym,1,'last');
    ym_left_up = y_left_unsorted(posm_left);
    xm_left_up = x_left_unsorted(posm_left);
    ym_left_down = y_left_unsorted(min(posm_left+1,length(
        y_left_unsorted)));
    xm_left_down = x_left_unsorted(min(posm_left+1,length(
        y_left_unsorted)));
    % Angles
    if (ym_left_up - ym_left_down <= length(y_left_unsorted)*noise)
        alfa_m_l = big_n;
```

```
222     else
223         alfa_m_l = (ym_left_up - ym_left_down )/(xm_left_down -
                xm_left_up); % Slope
224     end
225     xm_left = xm_left_down - (ym - ym_left_down )/alfa_m_l;
226     ym_left = ym;
227     % Polygons (left - inv - right)
228     x_pol = [xm_left; x_left_unsorted((posm_left + 1:end),1); x_invert;
            x_right_unsorted(1:(pos_break-pos_inv),1)];
229     y_pol = [ym_left; y_left_unsorted((posm_left + 1:end),1); y_invert;
            y_right_unsorted(1:(pos_break-pos_inv),1)];
230     % Top-Width
231     bm = abs(x_pol(1) - x_pol(end));
232     % Area
233     am = polyarea(x_pol,y_pol);
234     % Perimeter
235     polyin = polyshape(x_pol,y_pol);
236     pm = perimeter(polyin) - bm; % Taking away the top width
237 else
238     % Right Intersection
239     posm_right = find(y_right_unsorted >= ym,1,'first');
240     ym_right_up = y_right_unsorted(posm_right);
241     xm_right_up = x_right_unsorted(posm_right);
242     ym_right_down = y_right_unsorted(max(posm_right-1,1));
243     xm_right_down = x_right_unsorted(max(posm_right-1,1));
244     % Angles
245     if (ym_right_up - ym_right_down < noise*length(y_right_unsorted)) %
            No depth
246         alfa_m_r = big_n;
247     else
248         alfa_m_r = (ym_right_up - ym_right_down )/(xm_right_up -
                xm_right_down); % Slope
249     end
250     xm_right = xm_right_down + (ym - ym_right_down )/alfa_m_r;
251     ym_right = ym;
252     % Polygons (left - inv - right)
253     x_pol = [x_left_unsorted(pos_break:end,1); x_invert;
            x_right_unsorted(1:(posm_right - 1),1); xm_right];
254     y_pol = [y_left_unsorted(pos_break:end,1); y_invert;
            y_right_unsorted(1:(posm_right - 1),1); ym_right];
255     % Top-Width
256     bm = abs(x_pol(1) - x_pol(end));
257     % Area
258     am = polyarea(x_pol,y_pol);
259     % Perimeter
260     polyin = polyshape(x_pol,y_pol);
261     pm = perimeter(polyin) - bm; % Taking away the top width
```

```
end
if flag_method ~= 1
    % Number of floodplains
    if pos_break == 1 || pos_break == length(y)
        n_fp = 1;
    else
        n_fp = 2;
    end
end
while i < big_n
    %% Case where i == 1
    i = i + 1;
    n_P_left = 0;
    n_P_right = 0;
    n_P_left_extra = 0;
    n_P_right_extra = 0;
    B_extra = 0;
    P_extra = 0;
    P_extra_left = 0;
    P_extra_right = 0;
    if i == 1 % We are talking about the first point

        %%% Initializing variables
        y_table = 0; h = 0; B = 0; A = 0; Rh = 0; P = 0; Phi = 0; K_c =
            0;
        % Look to both sides from pos_inv (invert point)

        % Left Direction
        pos_left = find(y_left_unsorted>sm*y_invert,1,'last');
        y_left_point = y_left_unsorted(pos_left,1);
        x_left_point = x_left_unsorted(pos_left,1);
        if flag_method == 1
            n_left_segment = n_left_unsorted(pos_left,1);
        else
            n_left_segment = nm; % Main channel
        end

        % Right Direction
        pos_right = find(y_right_unsorted>sm*y_invert,1,'first');
        y_right_point = y_right_unsorted(pos_right,1);
        x_right_point = x_right_unsorted(pos_right,1);
        if flag_method == 1
            n_right_segment = n_right_unsorted(pos_right,1);
        else
            n_right_segment = nm; % Main channel
        end

```

```
308         %%%%%%%%%%% Angles Calculations %%%%%%%%%%%
309         %%%% Alfa Left %%%%
310         % Case 01 - Vertical Point
311         if (x_invert - x_left_point <= tot_noise) && (y_left_point -
                y_invert > tot_noise)
312             alfa_l = big_n;
313             alfa_l_tang = big_n;
314         end
315         % Case 02 - Horizontal Point
316         if (x_invert - x_left_point > tot_noise) && (y_left_point -
                y_invert <= tot_noise)
317             alfa_l = big_n;
318             alfa_l_tang = big_n;
319         end
320         % Case 03 - Horizontal and Vertical Point
321         if (x_invert - x_left_point <= tot_noise) && (y_left_point -
                y_invert <= tot_noise)
322             alfa_l = big_n;
323             alfa_l_tang = big_n;
324         end
325         % Case 04 - Poit with normal slopes
326         if (x_invert - x_left_point > tot_noise) && (y_left_point -
                y_invert > tot_noise)
327             alfa_l = (y_left_point - y_invert)/(x_invert - x_left_point)
                    ;
328             alfa_l_tang = alfa_l;
329         end
330
331         %%%% Alfa Right %%%%
332         % Case 01 - Vertical Point
333         if (x_right_point - x_invert <= tot_noise) && (y_right_point-
                y_invert > tot_noise)
334             alfa_r = big_n;
335             alfa_r_tang = big_n;
336         end
337         % Case 02 - Horizontal Point
338         if (x_right_point - x_invert > tot_noise) && (y_right_point -
                y_invert <= tot_noise)
339             alfa_r = big_n;
340             alfa_r_tang = big_n;
341         end
342         % Case 03 - Horizontal and Vertical Point
343         if (x_right_point - x_invert <= tot_noise) && (y_right_point -
                y_invert <= tot_noise)
344             alfa_r = big_n;
345             alfa_r_tang = big_n;
346         end
```

```
347         % Case 04 - Poit with normal slopes
348         if (x_right_point - x_invert > tot_noise) && (y_right_point -
                y_invert > tot_noise)
349             alfa_r = (y_right_point - y_invert)/(x_right_point -
                    x_invert);
350             alfa_r_tang = alfa_r;
351         end
352
353         % Min Angle
354         if alfa_l <= alfa_min_bound
355             alfa_l_tang = big_n;
356         end
357         if alfa_r <= alfa_min_bound
358             alfa_r_tang = big_n;
359         end
360
361         if y_left_point <= y_right_point
362             y_moving = y_left_point;
363             xleft_point = x_absolute(pos_inv - 1,1);
364             precision_section = min(y_left_point - y_invert,precision);
365             n_points = floor((y_left_point - y_invert)/(
                    precision_section)); % number of interpolated points
366             if n_points == 1 % only one point means no slope
367                 if x_invert - x_left_point >= sm*noise && alfa_l ==
                        big_n
368                     P_extra_left = sqrt((x_invert - x_left_point)^2 + (
                            y_invert - y_left_point)^2);
369                     n_P_left_extra = P_extra_left*n_left_segment^(3/2);
370                     B_extra = (x_invert - x_left_point);
371                 else
372                     B_extra = 0;
373                     n_P_left_extra = 0;
374                     P_extra_left;
375                 end
376             end
377             if n_points == 1 % only one point means no slope
378                 if x_right_point - x_invert > 1.0001*noise && alfa_r ==
                        big_n
379                     P_extra_right = sqrt((x_invert - x_right_point)^2 +
                            (y_invert - y_right_point)^2) + B_extra;
380                     B_extra = B_extra + (x_right_point - x_invert);
381                     n_P_right_extra = (P_extra_right)*n_right_segment
                            ^(3/2);
382                 else
383                     n_P_left_extra = 0;
384                     P_extra_right = 0;
385                 end
```

```
386             end
387             P_extra = P_extra_right + P_extra_left;
388
389             %%%%%%%%%%% Main loop for i == 1 %%%%%%%%%%%
390             for j = 1:(n_points)
391                 h = precision_section;
392                 y_table(j+1,1) = y_table(j,1) + h;
393                 B(j+1,1) = h/alfa_l_tang + h/alfa_r_tang + B(j,1);
394                 A(j+1,1) = (B(j+1,1) + B(j,1))*h/2 + A(j,1); % Trapezoid
395                 P(j+1,1) = h/sin(atan(alfa_l_tang)) + h/sin(atan(
                        alfa_r_tang)) + P(j,1);
396                 Rh(j+1,1) = A(j+1,1)/P(j+1,1);
397                 Phi(j+1,1) = A(j+1,1)*Rh(j+1,1)^(2/3);
398                 int_n_p = n_P_left_extra + n_P_right_extra +
                        n_left_segment^(3/2)*h/sin(atan(alfa_l_tang)) +
                        n_right_segment^(3/2)*h/sin(atan(alfa_r_tang)) +
                        int_n_p;
399                 % Representative Roughness Coefficient
400                 if flag_method == 1
401                     n_med(j+1,1) = (int_n_p/P(j+1,1))^(2/3);
402                 else
403                     if y_table(j+1,1) > ym
404                         yf = max(y_table(j+1,1) - ym,0); % Overbank
                                depth
405                         af = max(A(j+1,1) - (am + bm*yf),0); % Overbank
                                flow area
406                         pf = max(P(j+1,1) - pm,0); % Floodplain
                                perimeter (m)
407                         pm_star = max(pm + n_fp*yf,0);
408                         am_star = max(am + bm*yf,0);
409                         n_med(j+1,1) = (Phi(j+1,1))/(1/nf*af*(af/pf)
                                ^(2/3) + 1/nm*am_star*(am_star/pm_star)^(2/3)
                                );
410                     else
411                         yf = 0; % Overbank depth
412                         af = 0; % Overbank flow area
413                         pf = 0; % Floodplain perimeter (m)
414                         pm_star = 0;
415                         am_star = 0;
416                         n_med(j+1,1) = nm;
417                     end
418                 end
419                 K_c(j+1,1) = 1/n_med(j+1,1)*Phi(j+1,1);
420
421                 if j == (n_points) % final point
422                     % Final point - make sure you have the exact
                            surveyed point at the end
```

```
423                     h_ = y_right_point - y_table(j,1);
424                     y_table(j+1,1) = y_table(j,1) + h_;
425                     B(j+1,1) = h_/alfa_l_tang + h_/alfa_r_tang + B(j,1)
                            + B_extra;
426                     A(j+1,1) = (B(j+1,1) + B(j,1))*h/2 + A(j,1); %
                            Trapezoid
427                     P(j+1,1) = h_/sin(atan(alfa_l_tang)) + h_/sin(atan(
                            alfa_r_tang)) + P(j,1) + P_extra;
428                     Rh(j+1,1) = A(j+1,1)/P(j+1,1);
429                     Phi(j+1,1) = A(j+1,1)*Rh(j+1,1)^(2/3);
430                     if n_points == 1
431                         int_n_p =  n_left_segment^(3/2)*h/sin(atan(
                                alfa_l_tang)) + n_right_segment^(3/2)*h/sin(
                                atan(alfa_r_tang)) + n_P_right_extra +
                                n_P_left_extra;
432                     else
433                         int_n_p =  n_left_segment^(3/2)*h/sin(atan(
                                alfa_l_tang)) + n_right_segment^(3/2)*h/sin(
                                atan(alfa_r_tang)) + int_n_p;
434                     end
435                     % Representative Roughness Coefficient
436                     if flag_method == 1
437                         n_med(j+1,1) = round((int_n_p/P(j+1,1))^(2/3),3)
                                ;
438                     else
439                         if y_table(j+1,1) > ym
440                             yf = max(y_table(j+1,1) - ym,0); % Overbank
                                    depth
441                             af = max(A(j+1,1) - (am + bm*yf),0); %
                                    Overbank flow area
442                             pf = max(P(j+1,1) - pm,0); % Floodplain
                                    perimeter (m)
443                             pm_star = max(pm + n_fp*yf,0);
444                             am_star = max(am + bm*yf,0);
445                             n_med(j+1,1) = round((Phi(j+1,1))/(1/nf*af*(
                                    af/pf)^(2/3) + 1/nm*am_star*(am_star/
                                    pm_star)^(2/3)),3);
446                         else
447                             yf = 0; % Overbank depth
448                             af = 0; % Overbank flow area
449                             pf = 0; % Floodplain perimeter (m)
450                             pm_star = 0;
451                             am_star = 0;
452                             n_med(j+1,1) = nm;
453                         end
454                     end
455                     K_c(j+1,1) = 1/n_med(j+1,1)*Phi(j+1,1);
```

```
456                 end
457             end
458         else
459             x_right_point = x_absolute(pos_inv + 1,1);
460             precision_section = min(y_right_point - y_invert,precision);
461             n_points = floor((y_right_point - y_invert)/(
                    precision_section)); % number of interpolated points
462             if n_points == 1 % only one point means no slope
463                 if x_right_point - x_invert >= sm*noise && alfa_r ==
                        big_n % Additional B_extra
464                     P_extra = sqrt((x_right_point - x_invert)^2 + (
                            y_right_point - y_invert)^2);
465                     B_extra = x_right_point - x_invert;
466                     n_P_right_extra = P_extra*n_right_segment^(3/2);
467                 else
468                     B_extra = 0;
469                     n_P_right_extra = 0;
470                     P_extra = 0;
471                 end
472             end
473             y_moving = y_right_point;
474             % For loop to calculate functions
475             for j = 1:(n_points)
476                 h = precision_section;
477                 B(j+1,1) = h/alfa_l_tang + h/alfa_r_tang + B(j,1);
478                 y_table(j+1,1) = y_table(j,1) + h;
479                 A(j+1,1) = (B(j+1,1) + B(j,1))*h/2 + A(j,1); % Trapezoid
480                 P(j+1,1) = h/sin(atan(alfa_l_tang)) + h/sin(atan(
                        alfa_r_tang)) + P(j,1);
481                 Rh(j+1,1) = A(j+1,1)/P(j+1,1);
482                 Phi(j+1,1) = A(j+1,1)*Rh(j+1,1)^(2/3);
483                 int_n_p = n_P_left_extra + n_P_right_extra +
                        n_left_segment^(3/2)*h/sin(atan(alfa_l_tang)) +
                        n_right_segment^(3/2)*h/sin(atan(alfa_r_tang)) +
                        int_n_p;
484                 % Representative Roughness Coefficient
485                 if flag_method == 1
486                     n_med(j+1,1) = round((int_n_p/P(j+1,1))^(2/3),3);
487                 else
488                     if y_table(j+1,1) > ym
489                         yf = max(y_table(j+1,1) - ym,0); % Overbank
                                depth
490                         af = max(A(j+1,1) - (am + bm*yf),0); % Overbank
                                flow area
491                         pf = max(P(j+1,1) - pm,0); % Floodplain
                                perimeter (m)
492                         pm_star = max(pm + n_fp*yf,0);
```

```
493                     am_star = max(am + bm*yf,0);
494                     n_med(j+1,1) = (Phi(j+1,1))/(1/nf*af*(af/pf)
                            ^(2/3) + 1/nm*am_star*(am_star/pm_star)^(2/3)
                            );
495                 else
496                     yf = 0; % Overbank depth
497                     af = 0; % Overbank flow area
498                     pf = 0; % Floodplain perimeter (m)
499                     pm_star = 0;
500                     am_star = 0;
501                     n_med(j+1,1) = nm;
502                 end
503             end
504             K_c(j+1,1) = 1/n_med(j+1,1)*Phi(j+1,1);
505             if j == (n_points) % final point
506                 % Final point - make sure you have the exact
                        surveyed point at the end
507                 h_ = y_right_point - y_table(j,1);
508                 y_table(j+1,1) = y_table(j,1) + h_;
509                 B(j+1,1) = h_/alfa_l_tang + h_/alfa_r_tang + B(j,1)
                        + B_extra;
510                 A(j+1,1) = (B(j+1,1) + B(j,1))*h/2 + A(j,1); %
                        Trapezoid
511                 P(j+1,1) = h_/sin(atan(alfa_l_tang)) + h_/sin(atan(
                        alfa_r_tang)) + P(j,1) + P_extra;
512                 Rh(j+1,1) = A(j+1,1)/P(j+1,1);
513                 Phi(j+1,1) = A(j+1,1)*Rh(j+1,1)^(2/3);
514                 if n_points == 1
515                     int_n_p =  n_left_segment^(3/2)*h/sin(atan(
                            alfa_l_tang)) + n_right_segment^(3/2)*h/sin(
                            atan(alfa_r_tang)) + n_P_right_extra +
                            n_P_left_extra;
516                 else
517                     int_n_p =  n_left_segment^(3/2)*h/sin(atan(
                            alfa_l_tang)) + n_right_segment^(3/2)*h/sin(
                            atan(alfa_r_tang)) + int_n_p;
518                 end
519                 % Representative Roughness Coefficient
520                 if flag_method == 1
521                     n_med(j+1,1) = (int_n_p/P(j+1,1))^(2/3);
522                 else
523                     if y_table(j+1,1) > ym
524                         yf = max(y_table(j+1,1) - ym,0); % Overbank
                                depth
525                         af = max(A(j+1,1) - (am + bm*yf),0); %
                                Overbank flow area
526                         pf = max(P(j+1,1) - pm,0); % Floodplain
```

```
                                perimeter (m)
527                         pm_star = max(pm + n_fp*yf,0);
528                         am_star = max(am + bm*yf,0);
529                         n_med(j+1,1) = (Phi(j+1,1))/(1/nf*af*(af/pf)
                                ^(2/3) + 1/nm*am_star*(am_star/pm_star)
                                ^(2/3));
530                     else
531                         yf = 0; % Overbank depth
532                         af = 0; % Overbank flow area
533                         pf = 0; % Floodplain perimeter (m)
534                         pm_star = 0;
535                         am_star = 0;
536                         n_med(j+1,1) = nm;
537                     end
538                 end
539                 K_c(j+1,1) = 1/n_med(j+1,1)*Phi(j+1,1);
540             end
541         end
542     end
543     % Previous Positions
544     pos_left_previous = pos_left;
545     pos_right_previous = pos_right;
546 else
547     %% Case where i ~= 1
548
549     % Look to left sides from x_point_left and from right side of
550     % x_point_right
551     y_moving = y_table(end,1); % actual water depth
552
553     % Left Direction
554     pos_left = find(y_left_unsorted>sm*y_moving,1,'last');
555     y_left_point = y_left_unsorted(pos_left,1);
556     x_left_point = x_left_unsorted(pos_left,1);
557
558     % Right Direction
559     pos_right = find(y_right_unsorted>sm*y_moving,1,'first');
560     y_right_point = y_right_unsorted(pos_right,1);
561     x_right_point = x_right_unsorted(pos_right,1);
562
563     % Roughness
564     if y_moving <= ym % Inside of the channel
565         if flag_method == 1
566             n_left_segment = n_left_unsorted(pos_left,1);
567             n_right_segment = n_right_unsorted(pos_right,1);
568         else
569             if (abs(y_left_unsorted(pos_left) - ym) <= noise*length(
                    y_left_unsorted))
```

```
570                 n_left_segment = nf; % Attention here
571             else
572                 n_left_segment = nm; % Attention here
573             end
574             if (abs(y_right_unsorted(pos_right) - ym) <= noise*
                    length(y_right_unsorted))
575                 n_right_segment = nf;  % Attention here
576             else
577                 n_right_segment = nm;  % Attention here
578             end
579         end
580     else % Overbanks
581         if flag_method == 1
582             n_left_segment = n_left_unsorted(pos_left,1);
583             n_right_segment = n_right_unsorted(pos_right,1);
584         elseif y_left_unsorted(pos_left) - ym < noise*length(
                y_left_unsorted)% Check Noises
585             n_left_segment = nm; % Attention here
586             n_right_segment = nm;  % Attention here
587         else
588             n_left_segment = nf; % Attention here
589             n_right_segment = nf;  % Attention here
590         end
591     end
592
593
594     % Checking Discontinuities
595     %%% Initializing Varaibles
596     Delta_Area_left = 0; Delta_Area_right = 0;
597     Delta_B_left = 0; Delta_B_right = 0;
598     Delta_P_left = 0; Delta_P_right = 0;
599
600     %%%%%%%%%%% Angles Calculation %%%%%%%%%%%
601     if pos_left + 1 > length(y_left_unsorted)
602         x_prev_left = x_invert;
603         y_prev_left = y_invert;
604     else
605         x_prev_left = (x_left_unsorted(pos_left + 1,1));
606         y_prev_left = (y_left_unsorted(pos_left + 1,1));
607     end
608
609     %%%% Alfa Left %%%%
610     % Case 01 - Vertical Point
611     if (x_prev_left - x_left_point <= tot_noise) && (y_left_point -
            y_prev_left > tot_noise)
612         alfa_l = big_n;
613         alfa_l_tang = big_n;
```

```
614         end
615         % Case 02 - Horizontal Point
616         if (x_prev_left - x_left_point > tot_noise) && (y_left_point -
               y_prev_left <= tot_noise)
617             alfa_l = big_n;
618             alfa_l_tang = big_n;
619         end
620         % Case 03 - Horizontal and Vertical Point
621         if (x_prev_left - x_left_point <= tot_noise) && (y_left_point -
               y_prev_left <= tot_noise)
622             alfa_l = big_n;
623             alfa_l_tang = big_n;
624         end
625         % Case 04 - Poit with normal slopes
626         if (x_prev_left - x_left_point > tot_noise) && (y_left_point -
               y_prev_left > tot_noise)
627             alfa_l = (y_left_point - y_prev_left)/(x_prev_left -
                   x_left_point);
628             alfa_l_tang = alfa_l;
629         end
630         if pos_right == 1
631             x_prev_right = x_invert;
632             y_prev_right = y_invert;
633         else
634             x_prev_right = x_right_unsorted(pos_right - 1,1);
635             y_prev_right = y_right_unsorted(pos_right - 1,1);
636         end
637         %%%% Alfa Right %%%%
638         % Case 01 - Vertical Point
639         if (x_right_point - x_prev_right <= tot_noise) && (y_right_point
               - y_prev_right > tot_noise)
640             alfa_r = big_n;
641             alfa_r_tang = big_n;
642         end
643         % Case 02 - Horizontal Point
644         if (x_right_point - x_prev_right > tot_noise) && (y_right_point
               - y_prev_right <= tot_noise)
645             alfa_r = big_n;
646             alfa_r_tang = big_n;
647         end
648         % Case 03 - Horizontal and Vertical Point
649         if (x_right_point - x_prev_right <= tot_noise) && (y_right_point
                - y_prev_right <= tot_noise)
650             alfa_r = big_n;
651             alfa_r_tang = big_n;
652         end
653         % Case 04 - Poit with normal slopes
```

```
654         if (x_right_point - x_prev_right > tot_noise) && (y_right_point
               - y_prev_right > tot_noise)
655             alfa_r = (y_right_point - y_prev_right)/(x_right_point -
                   x_prev_right);
656             alfa_r_tang = alfa_r;
657         end
658
659         % Min Angle
660         if alfa_l <= alfa_min_bound
661             alfa_l_tang = big_n;
662         end
663         if alfa_r <= alfa_min_bound
664             alfa_r_tang = big_n;
665         end
666
667
668         if (pos_left_previous - pos_left) > 1 % More than one movement
669
670             % intersect
671             if alfa_l_tang == 0
672                 x_intersect = x_left_unsorted(pos_left + 1,1);
673             else
674                 x_intersect = x_left_unsorted(pos_left + 1,1) - (
                       y_moving - y_left_unsorted(pos_left + 1,1))/alfa_l;
675             end
676             x_pol = []; y_pol = [];
677             for nn = 1:(pos_left_previous - pos_left)
678                 x_pol = [x_pol; x_left_unsorted(pos_left_previous - nn +
                        1)];
679                 y_pol = [y_pol; y_left_unsorted(pos_left_previous - nn +
                        1)];
680             end
681             % Adding intersection
682             x_pol = [x_pol;x_intersect];
683             y_pol = [y_pol;y_moving];
684             % Delta B
685             Delta_B_left = abs(x_pol(1) - x_pol(end));
686             % Delta A
687             Delta_Area_left = polyarea(x_pol,y_pol);
688             % Delta P
689             polyin = polyshape(x_pol,y_pol);
690             Delta_P_left = perimeter(polyin) - Delta_B_left; % Taking
                    away top width
691             n_P_left = Delta_P_left*n_left_segment^(3/2);
692             % Delta Rh left
693             % Phi left
694             % Conductance Left
```

```
695         end
696
697
698         % Checking Discontinuities
699         if (pos_right - pos_right_previous) > 1 % More than one movement
700             % intersect
701             if alfa_r_tang == 0
702                 x_intersect = x_right_unsorted(pos_right - 1,1);
703             else
704                 x_intersect = x_right_unsorted(pos_right - 1,1) + (
                        y_moving - y_right_unsorted(pos_right - 1,1))/alfa_r;
705             end
706             x_pol = []; y_pol = [];
707             for nn = 1:(pos_right - pos_right_previous)
708                 x_pol = [x_pol; x_right_unsorted(pos_right_previous + nn
                        - 1)];
709                 y_pol = [y_pol; y_right_unsorted(pos_right_previous + nn
                        - 1)];
710             end
711             % Adding intersection
712             x_pol = [x_pol;x_intersect];
713             y_pol = [y_pol;y_moving];
714             % Delta B
715             Delta_B_right = abs(x_pol(1) - x_pol(end));
716             % Delta A
717             Delta_Area_right = polyarea(x_pol,y_pol);
718             % Delta P
719             polyin = polyshape(x_pol,y_pol);
720             Delta_P_right = perimeter(polyin) - Delta_B_right; % Taking
                    away top width
721             % Manning * Perimeter
722             n_P_right = Delta_P_right*n_right_segment^(3/2);
723         end
724         y_moving_end = min(y_right_point,y_left_point);
725         %         if (y_moving_end - y_moving)/(precision/100) < 1
726         %             error('Please, increase precision. Instability!')
727         %         end
728         precision_section = min(y_moving_end - y_moving,precision); %
                meters
729         if y_moving_end - y_moving < precision
730             ttt = 1;
731         end
732         n_points = floor((y_moving_end - y_moving)/(precision_section));
                % number of interpolated points
733         % For loop to calculate functions
734         if n_points == 1 % only one point means no slope
735             if y_moving_end == y_right_point && y_moving_end ==
```

```
            y_left_point && alfa_l == big_n && alfa_r == big_n
736             B_extra = x_right_point - x_prev_right + x_prev_left -
                    x_left_point;
737             P_extra_left = sqrt((x_prev_left - x_left_point)^2 + (
                    y_prev_left - y_left_point)^2);
738             P_extra_right = sqrt((x_right_point - x_prev_right)^2 +
                    (y_right_point - y_prev_right)^2);
739         elseif y_moving_end == y_right_point && alfa_r == big_n
740             if pos_right == 1
741                 P_extra_right = sqrt((x_right_point - x_invert)^2 +
                        (y_right_point - y_invert)^2);
742                 B_extra = x_right_point - x_invert;
743             else
744                 P_extra_right = sqrt((x_right_point - x_prev_right)
                        ^2 + (y_right_point -  y_prev_right)^2);
745                 B_extra = x_right_point - x_prev_right;
746             end
747         else % y_moving == y_left
748             if pos_left + 1 > length(x_left_unsorted) && alfa_l ==
                    big_n
749                 P_extra_left = sqrt((x_invert - x_left_point)^2 + (
                        y_invert - y_left_point)^2);
750                 B_extra = x_invert - x_left_point;
751             elseif alfa_l == big_n
752                 P_extra_left = sqrt((x_prev_left - x_left_point)^2 +
                         (y_prev_left - y_left_point)^2);
753                 B_extra = x_prev_left - x_left_point;
754             end
755             % Right
756             if pos_right == 1 && alfa_r == big_n
757                 P_extra_right = sqrt((x_invert - x_right_point)^2 +
                        (y_invert - y_right_point)^2);
758                 B_extra = x_right_point - x_invert + B_extra;
759             elseif alfa_r == big_n
760                 P_extra_left = sqrt((x_prev_right - x_right_point)^2
                         + (y_right_point -  y_prev_right^2));
761                 B_extra = x_right_point - x_prev_right + B_extra;
762             end
763
764         end
765         P_extra = P_extra_left + P_extra_right;
766         n_P_right_extra = P_extra_right*n_right_segment^(3/2);
767         n_P_left_extra = P_extra_left*n_left_segment^(3/2);
768     else
769         B_extra = 0;
770         n_P_right_extra = 0;
771         n_P_left_extra = 0;
```

```
772             P_extra = 0;
773             P_extra_left = 0;
774             P_extra_right = 0;
775         end
776
777         dim_table = length(y_table);
778         %%%%%%%%%%% Main loop for i ~= 1 %%%%%%%%%%%
779
780         for j = 1:(n_points)
781             k = dim_table + j;
782             if  j == 1 % We have to add values from discontinuity (
                    Deltas)
783                 h = precision_section; % meters
784                 y_table(k,1) = y_table(k-1,1) + h;
785                 % Roughness
786                 if y_table(k,1) <= ym % Inside of the channel
787                     if flag_method == 1
788                         n_left_segment = n_left_unsorted(pos_left,1);
789                         n_right_segment = n_right_unsorted(pos_right,1);
790                     else
791                         if (abs(y_left_unsorted(pos_left) - ym) <= noise
                                *length(y_left_unsorted))
792                             n_left_segment = nf; % Attention here
793                         else
794                             n_left_segment = nm; % Attention here
795                         end
796                         if (abs(y_right_unsorted(pos_right) - ym) <=
                                noise*length(y_right_unsorted))
797                             n_right_segment = nf;  % Attention here
798                         else
799                             n_right_segment = nm;  % Attention here
800                         end
801                     end
802                 else % Overbanks
803                     if flag_method == 1
804                         n_left_segment = n_left_unsorted(pos_left,1);
805                         n_right_segment = n_right_unsorted(pos_right,1);
806                     elseif y_left_unsorted(pos_left) - ym < noise*length
                            (y_left_unsorted)% Check Noises
807                         n_left_segment = nm; % Attention here
808                         n_right_segment = nm;  % Attention here
809                     else
810                         n_left_segment = nf; % Attention here
811                         n_right_segment = nf;  % Attention here
812                     end
813                 end
814                 B(k,1) = B(k-1,1) + Delta_B_left + Delta_B_right +  h/
```

```
                alfa_l_tang + h/alfa_r_tang;
815             A(k,1) = A(k-1,1) + (B(k,1) + B(k-1,1))*h/2 +
                    Delta_Area_left + Delta_Area_right;
816             P(k,1) = h/sin(atan(alfa_l_tang)) + h/sin(atan(
                    alfa_r_tang)) + P(k-1,1) + Delta_P_left +
                    Delta_P_right;
817             Rh(k,1) = A(k,1)/P(k,1);
818             Phi(k,1) = A(k,1)*Rh(k,1)^(2/3);
819             int_n_p =  n_P_left + n_P_right + n_P_right_extra +
                    n_P_left_extra + n_left_segment^(3/2)*h/sin(atan(
                    alfa_l_tang)) + n_right_segment^(3/2)*h/sin(atan(
                    alfa_r_tang)) + int_n_p;
820             % Representative Roughness Coefficient
821             if flag_method == 1
822                 n_med(k,1) = (int_n_p/P(k,1))^(2/3);
823             else
824                 if y_table(k,1) > ym
825                     yf = max(y_table(k,1) - ym,0); % Overbank depth
826                     af = max(A(k,1) - (am + bm*yf),0); % Overbank
                            flow area
827                     pf = max(P(k,1) - pm,0); % Floodplain perimeter
                            (m)
828                     pm_star = max(pm + n_fp*yf,0);
829                     am_star = max(am + bm*yf,0);
830                     n_med(k,1) = (Phi(k,1))/(1/nf*af*(af/pf)^(2/3) +
                             1/nm*am_star*(am_star/pm_star)^(2/3));
831                 else
832                     yf = 0; % Overbank depth
833                     af = 0; % Overbank flow area
834                     pf = 0; % Floodplain perimeter (m)
835                     pm_star = 0;
836                     am_star = 0;
837                     n_med(k,1) = nm;
838                 end
839             end
840             K_c(k,1) = 1/n_med(k,1)*Phi(k,1);
841         else
842             % Functions in terms of depth
843             h = precision_section;
844             y_table(k,1) = h + y_table(k-1,1);
845             % Roughness
846             if y_table(k,1) <= ym % Inside of the channel
847                 if flag_method == 1
848                     n_left_segment = n_left_unsorted(pos_left,1);
849                     n_right_segment = n_right_unsorted(pos_right,1);
850                 else
851                     if (abs(y_left_unsorted(pos_left) - ym) <= noise
```

```
                    *length(y_left_unsorted))
852                  n_left_segment = nf; % Attention here
853              else
854                  n_left_segment = nm; % Attention here
855              end
856              if (abs(y_right_unsorted(pos_right) - ym) <=
                    noise*length(y_right_unsorted))
857                  n_right_segment = nf;  % Attention here
858              else
859                  n_right_segment = nm;  % Attention here
860              end
861          end
862      else % Overbanks
863          if flag_method == 1
864              n_left_segment = n_left_unsorted(pos_left,1);
865              n_right_segment = n_right_unsorted(pos_right,1);
866          elseif y_left_unsorted(pos_left) - ym < noise*length
                (y_left_unsorted)% Check Noises
867              n_left_segment = nm; % Attention here
868              n_right_segment = nm;  % Attention here
869          else
870              n_left_segment = nf; % Attention here
871              n_right_segment = nf;  % Attention here
872          end
873      end
874      B(k,1) = h/alfa_l_tang + h/alfa_r_tang + B(k-1,1);
875      A(k,1) = (B(k,1) + B(k-1,1))*h/2 + A(k-1,1); % Trapezoid
876      P(k,1) = h/sin(atan(alfa_l_tang)) + h/sin(atan(
             alfa_r_tang)) + P(k-1,1);
877      Rh(k,1) = A(k,1)/P(k,1);
878      Phi(k,1) = A(k,1)*Rh(k,1)^(2/3);
879      int_n_p = n_left_segment^(3/2)*h/sin(atan(alfa_l_tang))
             + n_right_segment^(3/2)*h/sin(atan(alfa_r_tang)) +
             int_n_p;
880      % Representative Roughness Coefficient
881      if flag_method == 1
882          n_med(k,1) = (int_n_p/P(k,1))^(2/3);
883      else
884          if y_table(k,1) > ym
885              yf = max(y_table(k,1) - ym,0); % Overbank depth
886              af = max(A(k,1) - (am + bm*yf),0); % Overbank
                    flow area
887              pf = max(P(k,1) - pm,0); % Floodplain perimeter
                    (m)
888              pm_star = max(pm + n_fp*yf,0);
889              am_star = max(am + bm*yf,0);
890              n_med(k,1) = (Phi(k,1))/(1/nf*af*(af/pf)^(2/3) +
```

```
                        1/nm*am_star*(am_star/pm_star)^(2/3));
891                 else
892                     yf = 0; % Overbank depth
893                     af = 0; % Overbank flow area
894                     pf = 0; % Floodplain perimeter (m)
895                     pm_star = 0;
896                     am_star = 0;
897                     n_med(k,1) = nm;
898                 end
899             end
900             K_c(k,1) = 1/n_med(k,1)*Phi(k,1);
901         end
902
903         if j == (n_points) % final point
904             % Final point - make sure you have the exact surveyed
                    point at the end
905             h_ = y_moving_end - y_table(k-1,1);
906             y_table(k,1) = y_table(k-1,1) + h_;
907             % Roughness
908             if y_table(k,1) <= ym % Inside of the channel
909                 if flag_method == 1
910                     n_left_segment = n_left_unsorted(pos_left,1);
911                     n_right_segment = n_right_unsorted(pos_right,1);
912                 else
913                     if (abs(y_left_unsorted(pos_left) - ym) <= noise
                            *length(y_left_unsorted))
914                         n_left_segment = nf; % Attention here
915                     else
916                         n_left_segment = nm; % Attention here
917                     end
918                     if (abs(y_right_unsorted(pos_right) - ym) <=
                            noise*length(y_right_unsorted))
919                         n_right_segment = nf;  % Attention here
920                     else
921                         n_right_segment = nm;  % Attention here
922                     end
923                 end
924             else % Overbanks
925                 if flag_method == 1
926                     n_left_segment = n_left_unsorted(pos_left,1);
927                     n_right_segment = n_right_unsorted(pos_right,1);
928                 elseif y_left_unsorted(pos_left) - ym < noise*length
                        (y_left_unsorted)% Check Noises
929                     n_left_segment = nm; % Attention here
930                     n_right_segment = nm;  % Attention here
931                 else
932                     n_left_segment = nf; % Attention here
```

```
933                         n_right_segment = nf;  % Attention here
934                     end
935                 end
936                 B(k,1) = h_/alfa_l_tang + h_/alfa_r_tang + B(k-1,1) +
                        B_extra;
937                 A(k,1) = (B(k,1) + B(k-1,1))*h_/2 + A(k-1,1); %
                        Trapezoid
938                 P(k,1) = h_/sin(atan(alfa_l_tang)) + h_/sin(atan(
                        alfa_r_tang)) + P(k-1,1) + P_extra;
939                 Rh(k,1) = A(k,1)/P(k,1);
940                 Phi(k,1) = A(k,1)*Rh(k,1)^(2/3);
941                 int_n_p = n_left_segment^(3/2)*h/sin(atan(alfa_l_tang))
                        + n_right_segment^(3/2)*h/sin(atan(alfa_r_tang)) +
                        int_n_p;
942                 % Representative Roughness Coefficient
943                 if flag_method == 1
944                     n_med(k,1) = (int_n_p/P(k,1))^(2/3);
945                 else
946                     if y_table(k,1) >= ym
947                         yf = max(y_table(k,1) - ym,0); % Overbank depth
948                         af = max(A(k,1) - (am + bm*yf),0); % Overbank
                                flow area
949                         pf = max(P(k,1) - pm,0); % Floodplain perimeter
                                (m)
950                         pm_star = max(pm + n_fp*yf,0);
951                         am_star = max(am + bm*yf,0);
952                         n_med(k,1) = (Phi(k,1))/(1/nf*af*(af/pf)^(2/3) +
                                1/nm*am_star*(am_star/pm_star)^(2/3));
953                     else
954                         yf = 0; % Overbank depth
955                         af = 0; % Overbank flow area
956                         pf = 0; % Floodplain perimeter (m)
957                         pm_star = 0;
958                         am_star = 0;
959                         n_med(k,1) = nm;
960                     end
961                 end
962                 K_c(k,1) = 1/n_med(k,1)*Phi(k,1);
963             end
964         end
965         % Previous Positions
966         pos_left_previous = pos_left;
967         pos_right_previous = pos_right;
968     end
969     % Checking i
970     if round(y_table(end),3) == round(max_y,3) % Stop de algorithm
971         i = big_n;
```

```
    end
end

% Centroid Coordinates
int_a_y = 0; % Integral of A(y)dy
for i = 1:(length(A))
    if i == 1
        y_bar(i,1) = 0;
        int_a_y(i,1) = 0;
    else
        int_a_y(i,1) = (A(i) - A(i-1))*(y_table(i) + y_table(i-1))/2 +
           int_a_y(i-1);
        y_bar(i,1) = int_a_y(i,1)/A(i,1);
    end
end

% Flow Discharge Calculations
Q = K_c*sqrt(s0);

% Velocity
v = Q./A; % m/s

% Beta - Boussinesq factor
kappa = 0.41;
g = 9.81; % m/s2
Beta = (1 + (g*n_med.^2)./(Rh.^(1/3)*kappa^2));

%% Plotting Results
% Plotting Channel
if flag_plot_HP == 1
close all
subplot(1,2,1)
set(gcf,'units','inches','position',[4,4,6.5,4])
mark_size = 5;
plot(x_absolute,y,'linewidth',2,'color','black')
xlabel('x ($m$)','Interpreter','latex');
ylabel('y ($m$)','Interpreter','latex');
xlim([min(x_absolute) max(x_absolute)])
grid on
hold on
scatter(x_absolute,y,'black')
subplot(1,2,2)
n_med(1,1) = inf;
plot(n_med(2:end,1),y_table(2:end,1),'linewidth',2,'color','black')
xlabel('Manning`s coefficient (SI)','Interpreter','latex');
ylabel('y ($m$)','Interpreter','latex');
xlim([0.9*min(n_med) 1.1*max(n_med(~isinf(n_med)))])
```

```
grid on
exportgraphics(gcf,'Cross_Section.pdf','ContentType','vector')


subplot(2,4,1)
set(gcf,'units','inches','position',[4,2,7.5,5])
sz = 5;
c = linspace(1,sz,length(y_table));
scatter(A,y_table,sz,c,'filled')
grid on
grid on
xlabel('Area ($m^2$)','Interpreter','latex');
ylabel('y ($m$)','Interpreter','latex');
% xlim([0 4])
subplot(2,4,2)
grid on
scatter(P,y_table,sz,c,'filled')
grid on
xlabel('Perimeter ($m$)','Interpreter','latex');
ylabel('y ($m$)','Interpreter','latex');
% xlim([0 4])
subplot(2,4,3)
grid on
scatter(Rh,y_table,sz,c,'filled')
grid on
xlabel('Hydraulic Radius ($m$)','Interpreter','latex');
ylabel('y ($m$)','Interpreter','latex');
% xlim([0 4])
subplot(2,4,4)
grid on
scatter(B,y_table,sz,c,'filled')
grid on
xlabel('Top width ($m$)','Interpreter','latex');
ylabel('y ($m$)','Interpreter','latex');
subplot(2,4,5)
grid on
scatter(K_c,y_table,sz,c,'filled')
grid on
xlabel('Conveyance ($m^3/s$)','Interpreter','latex');
ylabel('y ($m$)','Interpreter','latex');
subplot(2,4,6)
sz = 5;
c = linspace(1,sz,length(y_table));
scatter(Phi,y_table,sz,c,'filled')
grid on
xlabel('$\Phi$ ($m^{5/3}$)','Interpreter','latex');
ylabel('y ($m$)','Interpreter','latex');
```

```
subplot(2,4,7)
scatter(y_bar,y_table,sz,c,'filled')
grid on
xlabel('$\bar{y}$ (m)','Interpreter','latex');
ylabel('y ($m$)','Interpreter','latex');
subplot(2,4,8)
scatter(Q,y_table,sz,c,'filled')
grid on
xlabel('Flow discharge ($m^3/s$)','Interpreter','latex');
ylabel('y ($m$)','Interpreter','latex');
exportgraphics(gcf,'Hydraulic_Properties.pdf','ContentType','vector')
toc

% Rating Curve
close all
subplot(3,1,1)
set(gcf,'units','inches','position',[4,4,6.5,4])
mark_size = 5;
plot(x_absolute,y,'linewidth',2,'color','black')
xlabel('x ($m$)','Interpreter','latex');
ylabel('y ($m$)','Interpreter','latex');
xlim([min(x_absolute) max(x_absolute)])
grid on
subplot(3,1,2)
scatter(Q,y_table,sz,c,'filled')
xlabel('Flow discharge ($m^3/s$)','Interpreter','latex');
ylabel('y ($m$)','Interpreter','latex');
grid on
box on
% Velocity
subplot(3,1,3)
scatter(Q./A,y_table,sz,c,'filled')
xlabel('Velocity ($m/s$)','Interpreter','latex');
ylabel('y ($m$)','Interpreter','latex');
grid on
box on
exportgraphics(gcf,'Rating Curve.pdf','ContentType','vector')

% Plotting Normalized Values
set(gcf,'units','inches','position',[4,2,8,4])
subplot(1,5,1)
scatter(Q/max(Q),y_table/max(y_table),sz,c,'filled')
xlabel('$Q/Q_p$','Interpreter','latex');
ylabel('$y/y_{max} $','Interpreter','latex');
title(['$Q_p (m^3/s) = $ ',num2str(round(max(Q),2))],'interpreter','
    latex')
axis equal
```

```
grid on
xlim([0 1]); ylim([0 1]);
subplot(1,5,2)
scatter(A/max(A),y_table/max(y_table),sz,c,'filled')
xlabel('$A/A_{max}$','Interpreter','latex');
ylabel('$y/y_{max}$','Interpreter','latex');
title(['$A_{max} (m^2) = $ ',num2str(round(max(A),2))],'interpreter','
    latex')
axis equal
grid on
xlim([0 1]); ylim([0 1]);
subplot(1,5,3)
scatter(Phi/max(Phi),y_table/max(y_table),sz,c,'filled')
xlabel('$\Phi/\Phi_{max}$','Interpreter','latex');
ylabel('$y/y_{max} $','Interpreter','latex');
title(['$\Phi_{max} (m^2) = $ ',num2str(round(max(Phi),2))],'interpreter
    ','latex')
axis equal
grid on
xlim([0 1]); ylim([0 1]);
subplot(1,5,4)
scatter(K_c/max(K_c),y_table/max(y_table),sz,c,'filled')
xlabel('$K_c/K_{c,max}$','Interpreter','latex');
ylabel('$y/y_{max} $','Interpreter','latex');
title(['$K_{c,max} (m^3/s) = $ ',num2str(round(max(K_c),2))],'
    interpreter','latex')
axis equal
grid on
xlim([0 1]); ylim([0 1]);
subplot(1,5,5)
scatter((Q./A)/(max(Q./A)),y_table/max(y_table),sz,c,'filled')
xlabel('$v/v_{c,max}$','Interpreter','latex');
ylabel('$y/y_{max} $','Interpreter','latex');
title(['$v_{max} (m/s) = $ ',num2str(round(max(Q./A),2))],'interpreter',
    'latex')
axis equal
grid on
xlim([0 1]); ylim([0 1]);
exportgraphics(gcf,'Normalized_Values.pdf','ContentType','vector')
close all

end
end
```

8.5.6.2 Read Input Data - SVE

This script reads the excel input data and converts them into Matlab arrays.

```
%%% --------- HyProSWE Model ----------- %%%
% Script to read input data
% Developer: Marcus Nobrega Gomes Junior
% 5/1/2023
% Goal: Solution of 1-D SVE for given cross-section functions of Area,
   Perimeter, and
% top Width
% If you have any issues, please contact me at
% marcusnobrega.engcivil@gmail.com

% ---------- Please, don't change anything below ------------ %

%% Read Input Data %%
data = readtable('HyProSWE_Input_Data.xlsx','Sheet','Input_Data');
b = 0; Z1 = 0; Z2 = 0; a = 0; D = 0;


% General Data
general_data = table2array(data(1:16,2));
L = general_data(1,1);
Nx = general_data(2,1);
el = general_data(3,1);
g = general_data(4,1);
nm = general_data(5,1);
I0 = general_data(6,1);
tf = general_data(7,1);
dt = general_data(8,1);
animation_time = general_data(9,1);
s_outlet = general_data(10,1);
dh = general_data(11,1);
alpha = general_data(12,1);
dtmin = general_data(13,1);
dtmax = general_data(14,1);


% Flags
flags = table2array(data(19:29,2));
flag_hydrograph = flags(1,1);
flag_outlet = flags(2,1);
flag_friction = flags(3,1);
flag_section = flags(4,1);
flag_stage_hydrograph = flags(5,1);
flag_nash = flags(6,1);
flag_slope = flags(7,1);
flag_elevation = flags(8,1);
flag_output = flags(9,1);
```

```
flag_plot_HP = flags(10,1);
flag_elapsed_time = flags(11,1);
if flag_elapsed_time ~= 1
    Date_Begin = general_data(15,1);
    Date_Begin = datetime(datestr(Date_Begin+datenum('30-Dec-1899')));
    Date_End = general_data(16,1);
    Date_End = datetime(datestr(Date_End+datenum('30-Dec-1899')));
end

if flag_nash == 1
    nash_data = table2array(data(1:4,5));
    % Hydrograph
    Tp = nash_data(1,1);
    Qb = nash_data(2,1);
    Beta = nash_data(3,1);
    Qp = nash_data(4,1);
else
    % Input Hydrograph
    input_hydrograph_data = table2array(data(8:end,4:5));
    time_ = input_hydrograph_data(1:end,1);
    Qe1_ = input_hydrograph_data(1:end,2);
    Qe1 = zeros(size(Qe1_,1) - sum(isnan(Qe1_)),1);
    time = zeros(size(time_,1) - sum(isnan(time_)),1);
    % Taking away nans
    for i = 1:length(Qe1)
        if isnan(Qe1_(i)) || isnan(time_(i))
            break
        else
            Qe1(i,1) = Qe1_(i,1);
            time(i,1) = time_(i,1);
        end
    end
    clear Qe1_ time_
end

if flag_stage_hydrograph ~= 0
    % Stage Hydrograph
    input_stage_data = table2array(data(8:end,7:8));
    time_stage_ = input_stage_data(1:end,1);
    he1_ = data(1:end,2);
    he1 = zeros(size(he1_,1) - sum(isnan(he1_)),1);
    time_stage = zeros(size(time_stage_,1) - sum(isnan(time_stage_)),1);
    % Taking away nans
    for i = 1:length(he1)
        if isnan(he1_(i)) || isnan(time_stage_(i))
            break
        else
```

```
93              he1(i,1) = he1_(i,1);
94              time_stage(i,1) = time_stage_(i,1);
95          end
96      end
97      clear Qe1_ time_stage_
98  end
99
100 if flag_slope ~= 0
101     % Slope
102     input_slope_data = table2array(data(8:end,7:8));
103     station = input_slope_data(1:end,1);
104     bottom_slope = input_slope_data(2:end,2);
105     slopes_not_nan = zeros(size(bottom_slope,1) - sum(isnan(bottom_slope
            )),1);
106     station_index = zeros(size(station,1) - sum(isnan(station)),1);
107     % Taking away nans
108     for i = 1:length(station_index)
109         if isnan(bottom_slope(i)) || isnan(station(i))
110             break
111         else
112             slopes_not_nan(i,1) = bottom_slope(i,1);
113             station_index(i,1) = station(i,1);
114         end
115     end
116     clear station_index station bottom_slope
117     bottom_slope = slopes_not_nan;
118 end
119
120 if flag_elevation ~= 0
121     % Slope
122     input_slope_data = table2array(data(8:end,7:8));
123     station = input_slope_data(1:end,1);
124     elevation_cell = table2array(data(8:end,7:8));
125     inv_el_ = zeros(size(elevation_cell,1) - sum(isnan(elevation_cell))
            ,1);
126     station_index = zeros(size(station,1) - sum(isnan(station)),1);
127     % Taking away nans
128     for i = 1:length(station_index)
129         if isnan(elevation_cell(i)) || isnan(station(i))
130             break
131         else
132             inv_el_(i,1) = elevation_cell(i,1);
133             station_index(i,1) = station(i,1);
134         end
135     end
136     inv_el = inv_el_; % Invert Elevation
137     clear station_index station elevation_cell inv_el_
```

```
138 end
139
140 % Outlet
141 if flag_outlet ~=1
142     input_slope_wave = table2array(data(8:5,8));
143     h_0_wave = input_slope_wave(1,1);
144     H_0_wave = input_slope_wave(2,1);
145     L_wave = input_slope_wave(3,1);
146     T_wave = input_slope_wave(4,1);
147     x_wave = input_slope_wave(5,1);
148 end
149
150 % Section
151 if flag_section == 1
152     input_slope_trapezoid = table2array(data(1:3,11));
153     b = input_slope_trapezoid(1,1);
154     Z1 = input_slope_trapezoid(2,2);
155     Z2 = input_slope_trapezoid(3,3);
156 elseif flag_section == 2
157     input_slope_circular = table2array(data(1,14));
158     D = input_slope_circular(1,1);
159 elseif flag_section == 3
160     input_slope_parabolic = table2array(data(3,14));
161     a = data(1,1);
162 else
163     % Read HP estimator data
164     [y_irr, A_irr, P_irr, Rh_irr, y_bar_irr, n_med_irr, Beta_irr, u_irr,
            B_irr, Q_irr, x_cross, y_cross,s0] = HP_estimator(flag_plot_HP,
        dh);
165     irr_table = [y_irr, A_irr, P_irr, Rh_irr, y_bar_irr, n_med_irr,
        Beta_irr, u_irr, B_irr, Q_irr];
166
167     % Some Boundary Conditions
168     % [y_irr, A_irr, P_irr, Rh_irr, y_bar_irr, n_med_irr, Beta_irr,
        u_irr, B_irr, Q_irr];
169     % [   1,    2,     3,      4,    5,            6,          7,  8,
            9,  10]
170     irr_table(1,6) = irr_table(2,6); irr_table(1,7) = 0; irr_table(1,8)
        = 0;
171     % Second Line
172     irr_table(2,2) = 0; irr_table(2,3) = 0; irr_table(2,4) = 0;
        irr_table(2,5) = 0; irr_table(2,7) = 0; irr_table(2,8) = 0;
        irr_table(2,9) = 0;
173 %     z = irr_table;
174 %     second = 0*z(2,:);
175 %     second(1,1) = 0.5*10^-3; second(1,6) = z(1,6); second(1,10) = z
    (1,10)/2;
```

```
%      z = [z(1,:) ; second; z(2:end,:)];
%      irr_table = z;
end


% Contraint at observed flow
if flag_hydrograph == 1
    if max(time) ~= tf
        z = round(tf - max(time),0);
        for i = 1:z
            Qe1(end + 1,1) = 0;
            time(end+1,1) = time(end,1) + 1;
        end
    end
end


% Contraint at stage hydrograph
if flag_stage_hydrograph == 1
    if max(time_stage) ~= tf
        z = round(tf - max(time_stage),0);
        for i = 1:z
            he1(end + 1,1) = 0;
            time_stage(end+1,1) = time_stage(end,1) + 1;
        end
    end
end
```

8.5.6.3 SVE Model

The following algorithm solves the 1-D SVE using the Lax-Friedrichs method. To run the SVE Model, 3 functions are required: The SVE Model V1, the Read Input Data, and the HP Estimator, explained in the previous section.

```
%%% --------- HyProSWE Model ----------- %%%
% Developer: Marcus Nobrega Gomes Junior
% 5/1/2023
% Goal: Solution of 1-D SVE for given cross-section functions of Area,
    Perimeter, and
% top Width
% If you have any issues, please contact me at
% marcusnobrega.engcivil@gmail.com


% -------------------- All Rights Reserved ---------------------- %

%% 1.0 -  Pre-Processing

```

```
clear all
clc
warning('off') % Deactivate Warnings

% Reading the Input Data
Read_Input_Data % Here we read the .xlsx input data file. Please don't
    change the name of this file.

% Checking if at least one boundary condition is considered
if flag_hydrograph ~= 1 && flag_nash ~= 1 && flag_stage_hydrograph ~= 1
   && flag_outlet ~= 0
    error('Please enter at least 1 internal boundary condition.')
end

% Checking if there is conflicting boundary conditions
if flag_hydrograph == 1 && flag_nash == 1
    error('Please choose either an observed inflow hydrograph entered in
        a tabular format or a nash-type hydrograph.')
end

% Checking if there is conflicting cross section
if flag_section > 4
    error('Please, enter a the index indicating which type of cross-
       section is being simulated. Read the instruction in the .xlsx
       file')
end

% Checking if there is conflicting cross section
if flag_stage_hydrograph == 1 && flag_hydrograph == 1
    error('Please, the inlet can only have either a stage hydrograph or
       a flow hydrograph')
end
%% 2.0 - Initial Boundary Conditions
% ------------- Inflow Hydrograph ------------- %
if flag_hydrograph == 1
    % We already read the hydrograph in Read_Input_Data file
elseif flag_nash == 1
    % 2nd option - Model the hydrograph using a nash function
    %%% Q(t) = Qb(t) + (Qp(t) - Qb(t))*(t/TP*EXP(1 - t/TP))^Beta
    Inflow_Hydrograph_fun = @(t)(Qb + (Qp - Qb).*(t/(Tp*3600).*exp(1 - (
       t)/(Tp*3600))).^Beta);
    time = [0 tf]'; % begin and end in min
else
    time = [0 tf]'; % begin and end in min
end

if flag_stage_hydrograph == 1
```

```
54      Stage_Hydrograph = he1;
55  end
56
57  % -------------  Outlet Boundary Condition ------------- %
58  % flag_outlet = 1; % 1 = normal depth, flag_outlet >< 1, stage
        hydrograph
59  % at the outlet following a wave function
60
61  if flag_outlet ~= 1
62      %%% Wave Properties for Outlet Stage Hydrograph
63      %     x_wave = L_wave/1; % point position in wave x direction;
64      k_wave = 2*pi/L_wave;
65      sigma_wave = 2*pi./(T_wave*3600);
66      h_wave_function = @(t)(h_0_wave + H_0_wave/2.*cos(k_wave.*x_wave -
            sigma_wave*t));
67  end
68
69  % Time Calculations
70  time = time*60; % time in seconds
71  [a1,~] = size(time); % Length of time
72  tt_h = time(a1,1); % End of hydrograph in seconds
73  tt = min(tf*60,tt_h); % End of simulation in seconds
74  Nt = tt/dt; % Number of time-steps in the simulations
75
76  % Recording Times
77  time_records_min = animation_time; % Minutes
78  time_store = [0:time_records_min*60:tt]; % number of steps necessary to
        reach the recording vector
79  Nat = time_records_min*60/dt; % Number of time-steps within an animation
        time
80  tint = linspace(0,tt,Nt); % Generate Nt points within 0 and tt(sec)
81
82  time_save = zeros(length(time_store),1); % Time
83  Flow_Area = zeros(length(time_store),Nx); % Flow area
84  Discharge = zeros(length(time_store),Nx); % Flow discharge
85  Depth = zeros(length(time_store),Nx); % Depth
86  Velocity = zeros(length(time_store),Nx); % Velocity
87  Froude = zeros(length(time_store),Nx); % Froude
88  Courant = zeros(length(time_store),Nx); % Courant number
89
90  if flag_hydrograph == 1
91      Qe1int = max(interp1(time,Qe1(:,1),tint,'pchip'),0); % Interpolated
            flow
92      % Assuming no negative flows
93      Qe1int = Qe1int';
94  elseif flag_nash == 1
95      Qe1int = Inflow_Hydrograph_fun(tint)';
```

```
else
    tiny_flow = 1e-8;
    Qe1int = tiny_flow*ones(1,length(tint)); % No inflow hydrograph
end

if flag_stage_hydrograph == 1
    he1int = max(interp1(time_stage*60,he1(:,1),tint,'pchip'),0); %
        Interpolated depth
    he1int = he1int';
end

%% 3.0 - Pre-Allocation of Arrays

% Channel Discretization
dx = L/(Nx-1); % Channel discretization length in meters

% Friction Data
flag_friction = 1; % If 1, Manning, otherwise DW

% Manning
nm = repmat(nm,Nx,1); % Bottom slope in m/m for all reaches

% Pre-allocating arrays
% Matrices
x = (0:dx:L)'; % x discretization in meters
y = zeros(Nx,2);
q1 = zeros(Nx,2);
q2 = zeros(Nx,2);
f1 = zeros(Nx,2);
f2 = zeros(Nx,2);
J2 = zeros(Nx,2);
q1_back = q1(1:(Nx-2),2);
q1_forward = zeros(Nx-2,2);
q2_back = zeros(Nx-2,2);
q2_forward = zeros(Nx-2,2);
f1_back = zeros(Nx-2,2);
f1_forward = zeros(Nx-2,2);
f2_back = zeros(Nx-2,2);
f2_forward = zeros(Nx-2,2);
J2_back = zeros(Nx-2,2);
J2_forward = zeros(Nx-2,2);
ybar = zeros(Nx,2);
Fr = zeros(Nx,2);
Cn = zeros(Nx,2);

%% 4.0 Channel Data (Cross Section)
% Slope
```

```
142 if flag_slope ~= 1 && flag_elevation ~= 1
143     I0 = repmat(I0,(Nx-1),1); % Bottom slope in m/m for all reaches.
        This is only valid for closed-form sections
144 elseif flag_slope == 1
145     I0 = bottom_slope; % From read input data script
146 end
147
148 if flag_elevation == 1 % We are entering the elevations of each node
149     for i = 1:(Nx-1)
150         if i+1 > length(inv_el)
151             error('Please make sure to add enough invert elevation data.
                ')
152         end
153         I0(i,1) = (inv_el(i+1) - inv_el(i))/dx;
154     end
155 end
156
157 % Outlet Slope
158 if flag_outlet == 1
159     I0(end+1) = s_outlet;
160 else
161     I0(end+1) = s_outlet; % Let's assume a boundary condition
162 end
163
164 % Intializing channel data
165 sm = 1e-12; % Small number
166 b = sm + b; Z1 = sm + Z1; Z2 = sm + Z2; D = sm + D; a = sm + a;
167 % flag_section - If 1, trapezoid, if 2, circular, if 3, paraboloid, if 4
      - Irregular
168
169 % Invert Elevations
170 if flag_elevation ~=1
171     inv_el = zeros(Nx,1);
172     for i = 1:Nx
173         if i == 1
174             inv_el(i) = el;
175         else
176             inv_el(i) = inv_el(i-1) - (I0(i-1)*dx);
177         end
178     end
179 end
180
181 % -------------  Geometrical Functions for all Cros-Sections
    ------------ %
182 syms b_ y_ Z1_ Z2_ Q_ I0_ D_ a_
183 dim_all = 1e-6*(y_ + Z1_ + Z2_ + a_ + D_ + b_);
184 if flag_section == 1
```

```
185     B = b_ + y_*(Z1_ + Z2_) + + dim_all; % user defined function (top
            width)
186     B_function = matlabFunction(B);
187     P = b_ + y_*(sqrt(1 + Z1_^2) + sqrt(1 + Z2_^2)) + dim_all; %
            Perimeter Function % user defined function
188     P_function = matlabFunction(P);
189     A = (2*b_ + y_*(Z1_ + Z2_))*y_/2 + dim_all; % Area function % user
            defined function
190     A_function = matlabFunction(A); % Function describing the area in
            terms of y
191     centroid = y_ - int(A,y_)./A + dim_all; % 1st order momentum
192     ybar_function = matlabFunction(centroid); % Function describing ybar
             in terms of y
193 end
194 if flag_section == 2
195     % Circular Section
196     theta = 2*acos(1 - 2.*y_./D_) + dim_all;
197     B = D_.*sin(theta/2) ; % top width
198     B_function = matlabFunction(B);
199     P = theta.*D_/2 ; % perimeter
200     P_function = matlabFunction(P);
201     A = D_.^2/8.*(theta - sin(theta)) ; % area
202     A_function = matlabFunction(A); % Function describing the area in
            terms of y
203     Ybar = y_ - (D_.*(- cos(theta/2)/2 + 2.*sin(theta/2).^3./(3*(theta -
             sin(theta))))); % Very much attention here
204     ybar_function = matlabFunction(Ybar);
205 end
206
207 if flag_section == 3
208     % Parabolic Section
209     % Area Function
210     A = 4.*(y_.^3/2)./(3*sqrt(a_)) + dim_all; % m2
211     A_function = matlabFunction(A); % Function describing the area in
            terms of y
212     % Top Width
213     B = 3/2.*A./y_ + dim_all; % m
214     B_function = matlabFunction(B);
215     % Hydraulic Perimeter
216     P = dim_all + sqrt(y_)./sqrt(a_).*(sqrt(1 + 4*a_.*y_) + 1./(2*a_).*(
            log(2*sqrt(a_).*sqrt(y_) + sqrt(1 + 4*a_.*y_))));
217     P_function = matlabFunction(P);
218     Y_bar = y_ - 2/5*y_ + dim_all;
219     ybar_function = matlabFunction(Y_bar);
220 end
221
222 if flag_section ~= 4
```

```
223     %%%%%% Hydraulic Radius %%%%%%
224     Rh = A/P; % Hydraulic Radius Function
225     Rh_function = matlabFunction(Rh); % Function describing the
            hydraulic radius in terms of y
226 end
227
228 % Vlookup Function
229 Vlookup_eq = @(data,col1,val1,col2) data((find(data(:,col1)==val1,1,'
        first')),col2); %Vlookup function as Excel
230 Vlookup_l = @(data,col1,val1,col2) data((find(data(:,col1)<val1,1,'last'
        )),col2); %Vlookup function as Excel]
231 Vlookup_g = @(data,col1,val1,col2) data((find(data(:,col1)>val1,1,'first
        ')),col2); %Vlookup function as Excel
232 fv = 1 + 1e-4; % Factor to avoid fails in vlookup function
233
234 % Minimum Value
235 min_depth = 0.02; % m
236 min_area = Vlookup_l(irr_table,1,min_depth*fv,2);
237
238 % Initial Guess
239 if flag_section == 1
240     y0_guess = 1;
241 elseif flag_section == 2
242     y0_guess = D/2;
243 elseif flag_section == 3
244     y0_guess = 1;
245 end
246
247 %% 5.0- Initial Values for Simulation
248 Q0 = Qe1int(1,1); % Flow at inlet section at time 0
249 if flag_stage_hydrograph == 1
250     h0 = he1int(1,1); % Water depth at x = 0 at time = 0
251 end
252 if flag_friction == 1
253     if flag_section ~= 4
254         if Q0 == 0
255             Q0 = sm; % Numerical Constraint
256         end
257         y0 = uniformeM(nm,Q0,b,Z1,Z2,a,D,I0,P,A,y0_guess)    ; % normal
                depth using manning equation
258         % Stage_Hydrograph Boundary Condition
259         if flag_stage_hydrograph == 1
260             y0(1,1) = h0;
261         end
262         % More Initial Boundary Conditions for Area, Velocity, Perimeter
                and Rh
263         A0 = A_function(D,Z1,Z2,a,b,y0); % Cross section area in m2
```

```
264         u0 = (Q0./A0)'; % Initial velocity in m/s
265         P0 = P_function(D,Z1,Z2,a,b,y0); % Hydraulic perimeter in m
266         Rh0 = A0./P0; % Hydraulic radius at time 0
267         % Boundary Conditions
268         y(:,1) = y0; % all sub-reaches with y0 at the beginning
269         q1(:,1) = A0; % all sub-reaches with same area A0 at the
                beginning
270         q2(:,1) = Q0; % Assuming permanent conditions at the beginning
271         f1(:,1) = q2(:,1);
272         % f2 depends on ybar
273     else % Irregular Cross-Section
274         % [y_irr, A_irr, P_irr, Rh_irr, y_bar_irr, n_med_irr, Beta_irr,
                u_irr, B_irr, Q_irr];
275         % [   1,     2,      3,       4,     5,             6,           7,
                8,       9,     10]
276
277         if max(irr_table(:,10)) == 0 % No outflow and S = 0
278             % Here we are modeling a channel with no slope
279             % We search Everything Using the Depth instead of the Flow
280             col1 = 1; % Searching with the Col of Y
281             % Stage_Hydrograph Boundary Condition
282             if flag_stage_hydrograph == 1
283                 y0(1,1) = max(h0,irr_table(2,1));
284                 s_v = y0; % Searching Variable
285             else
286                 error('Please, add a minimum slope value or enter a
                        stage-hydrograph boundary condition.')
287             end
288             y0 = Vlookup_g(irr_table,col1,s_v*fv,1);
289             A0 = Vlookup_g(irr_table,col1,s_v*fv,2);
290             P0 = Vlookup_g(irr_table,col1,s_v*fv,3);
291             Rh0 = Vlookup_g(irr_table,col1,s_v*fv,4);
292
293         else % Now we are modeling a channel with slope
294             if (flag_hydrograph == 1 || flag_nash == 1) &&
                    flag_stage_hydrograph ~= 1
295                 col1 = 10; % Col with Q
296                 Q_min_table = irr_table(3,10); % ATTENTION HERE
297                 s_v = max(Q0,Q_min_table); % Searching Variable
298             elseif flag_stage_hydrograph == 1
299                 col1 = 1; % Col with y or h
300                 h_min_table = irr_table(3,1);
301                 s_v = max(h_min_table,h0); % Searching Variable
302             elseif flag_outlet == 0
303                 col1 = 1; % Col with y or h
304                 h_min_table = irr_table(3,1);
305                 s_v = max(h_min_table,0); % Searching Variable
```

```
306                 Q_min_table = irr_table(3,10);
307                 Q0 = Q_min_table;
308             end
309             Q0 = max(irr_table(2,end),Q0); % Allowing minimum value of
                    Q0 larger than 0
310             y0 = Vlookup_l(irr_table,col1,s_v*fv,1);
311             A0 = Vlookup_l(irr_table,col1,s_v*fv,2);
312             P0 = Vlookup_l(irr_table,col1,s_v*fv,3);
313             Rh0 = Vlookup_l(irr_table,col1,s_v*fv,4);
314         end
315         % Boundary Conditions
316         y(:,1) = y0; % all sub-reaches with y0 at the beginning
317         q1(:,1) = A0; % all sub-reaches with same area A0 at the
                beginning
318         q2(:,1) = Q0; % Assuming permanent conditions at the beginning
319         f1(:,1) = q2(:,1);
320     end
321     if flag_outlet ~=1 % Bay or Ocean Boundary Condition
322         % Stage Hydrograph Boundary Condition
323         time_wave = 0; % time in seconds
324         y(Nx,1) = h_wave_function(time_wave);
325         if flag_section ~= 4
326             q1(Nx,1) = A_function(D,Z1,Z2,a,b,y(Nx,2));
327         else
328             % We search Everything Using the Depth instead of the Flow
329             col1 = 1; % Searching with the Col of Flow
330             q1(Nx,1) = Vlookup_g(irr_table,col1,y(Nx,2)*fv,2);
331         end
332     end
333
334     % Hydraulic Radius
335     if flag_section ~= 4
336         Rh_outlet = Rh_function(D,Z1,Z2,a,b,y(Nx,2));
337     else
338         for mm = 1:(length(irr_table(1,:))-1)
339             interp_base = q1(Nx,1); % Value that will be used for
                    interpolation (area)
340             area_smaller = Vlookup_l(irr_table,2,interp_base,2); %
                    Smaller values
341             if isempty(area_smaller)
342                 area_smaller = 0;
343             end
344             area_larger = Vlookup_g(irr_table,2,interp_base,2); % Larger
                     values
345             col1 = 2; % Interpolating from area values
346             if interp_base <= min_area
347                 var_outlet(mm,1,1) = irr_table(2,mm); % Smaller values
```

```
348             else
349                 var_outlet(mm,1,1) = Vlookup_l(irr_table,col1,
                        interp_base,mm); % Smaller values
350             end
351             var_outlet(mm,1,2) = Vlookup_g(irr_table,col1,interp_base,mm
                    ); % Larger values
352             alfa_var_outlet(mm,1) = sqrt((interp_base - area_smaller)/(
                    area_larger - area_smaller));
353         end
354
355
356         % [y_table, A, P, Rh, y_bar, n_med, Beta, v, B, Q]
357         % [   1,    2, 3, 4,    5,    6,      7,  8,  9, 10]
358         col_var = 4; % Calculating Hydraulic Radius
359         % Var* = Var(-) + alfa*(Var(+) - Var(-))
360         Rh_outlet = var_outlet(col_var,1,1) + alfa_var_outlet(col_var,1)
                *(var_outlet(col_var,1,2) - var_outlet(col_var,1,1)); %
                Interpolated Hydraulic Radius
361         % Var* = Var(-) + alfa*(Var(+) - Var(-))
362         col_var = 6;
363         nm(end,1) = var_outlet(col_var,1,1) + alfa_var_outlet(col_var,1)
                *(var_outlet(col_var,1,2) - var_outlet(col_var,1,1));
364     end
365
366         if flag_outlet == 1
367             u = (1./nm(Nx)).*Rh_outlet^(2/3)*I0(Nx)^0.5; % Normal depth
                    at the outlet
368             flow_dir = 1;
369         else
370             wse_dif = y(Nx-1,2-1) + inv_el(Nx-1) - y(Nx,2) - inv_el(Nx);
                     % Difference in wse
371             out_slope = abs(wse_dif)/dx; % Friction slope at the outlet
                    as a diffusive model
372             if wse_dif < 0
373                 ttt = 1;
374             end
375
376             if flag_stage_hydrograph ~= 1 && flag_nash ~= 1 &&
                    flag_hydrograph ~= 1
377                 % Only Outlet Tidal B.C.
378                 if wse_dif > 0 && y(Nx-1,2-1) <= fv*1e-3
379                     out_slope = 0;
380                 end
381             end
382             u = (1./nm(Nx)).*Rh_outlet^(2/3)*out_slope^0.5; % Normal
                    velocity at the outlet
383             if wse_dif > 0
```

```
                flow_dir = 1; % Flowing towards the outlet
            else
                flow_dir = -1; % Flowing to inside of the channel
            end
        end
else
    error('HyProSWE not coded for Darcy-Weisbach. Wait for the new
        version or change the method for Manning.')
end
q2(Nx,1) = q1(Nx,1)*u*flow_dir; % Area x Velocity

%%% State Space Format %%%
% dq/dt + dF/dx = S, we solve for A(x,t) and Q(x,t)
% q = [A Q]' = [q1 q2]'
% F [Q (Qv + gAybar]' = [q2 (q2^2)/q1 + g.q1.ybar]' = [f1 f2]'
% where ybar is the centroid depth from the top
% S = [0 gA(I0 - If)]'

% ybar = y - int(A(y)) / A(y) from y = 0 to y = y0
if flag_section ~= 4
    ybar = ybar_function(D,Z1,Z2,a,b,y0);
else
    % [y_irr, A_irr, P_irr, Rh_irr, y_bar_irr, n_med_irr, Beta_irr,
        u_irr, B_irr, Q_irr];
    % [   1,    2,     3,      4,    5,            6,          7,     8,
            9,
    % ybar = y - ybar*
    %     ybar(:,1) =  Vlookup_leq(irr_table,col1,Q0*fv,1) - Vlookup_leq
        (irr_table,col1,Q0*fv,5);
    ybar(:,1) = Vlookup_g(irr_table,col1,s_v*fv,5);
end
f2(:,1) = q2(:,1).*abs(q2(:,1))./q1(:,1) + g*q1(:,1).*ybar(:,1);
f2(isnan(f2)) = 0; % Attention Here

% Friction S = [J1 J2]' with J1 = 0 and J2 calculated as follows:
if flag_friction == 1
    J2(:,1) = g*q1(:,1).*(I0(:) - q2(:,1).*abs(q2(:,1)).*nm(:)./(q1(:,1)
        .^2.*Rh0.^(4/3))); % Manning
else
    J2(:,1) = g*q1(:,1).*(I0(:) - f*q2(:,1).*abs(q2(:,1))./((q1(:,1).^2)
        .*8*g.*Rh0));
end

J2(isnan(J2)) = 0; % Attention Here

% Froude Number
if flag_section ~= 4
```

```
425     Fr(:,1)=abs(q2(:,1)./q1(:,1))./((g*A_function(D,Z1,Z2,a,b,y0)./
            B_function(D,Z1,Z2,a,b,y0)).^0.5);% Froude Number
426 else
427     % [y_irr, A_irr, P_irr, Rh_irr, y_bar_irr, n_med_irr, Beta_irr,
            u_irr, B_irr, Q_irr];
428     % [   1,     2,     3,      4,     5,             6,          7,     8,
                9,
429     A_f_irr = Vlookup_g(irr_table,col1,s_v*fv,2)*ones(length(q1(:,1)),1)
            ;
430     B_f_irr = Vlookup_g(irr_table,col1,s_v*fv,9)*ones(length(q1(:,1)),1)
            ;
431     Fr(:,1)=abs(q2(:,1)./q1(:,1))./((g*A_f_irr./B_f_irr).^0.5);% Froude
            Number
432 end
433 % Courant Number
434 % Cn = c / (dx / dt), where c = v + sqrt(g.Hm), where Hm = A / B
435 if flag_section ~= 4
436     Hm = A_function(D,Z1,Z2,a,b,y0)./B_function(D,Z1,Z2,a,b,y0);
437     Cn(:,1)=(abs(q2(:,1)./q1(:,1))+(g*Hm).^0.5)/(dx/dt);% Courant Number
438 else
439     Hm = A_f_irr./B_f_irr;
440     Cn(:,1) = (abs(q2(:,1)./q1(:,1))+(g*Hm).^0.5)/(dx/dt);
441 end
442
443 % Depth in terms of Area function
444 % let c be the area in terms of Z1,Z2,b, and y, such that A(y) = c
445 % we want to solve y for A(y) = c
446
447 syms c_
448 if flag_section ~= 4
449     fun_solve = (A - c_); % with c = area, we solve for y.
450     options = optimoptions ('fsolve', 'Display', 'none','
            FunctionTolerance',1e-2,'MaxFunctionEvaluations',Nx*10);
451 end
452 if flag_section == 1
453     % We have an analytical solution for this case
454     z = solve(fun_solve,y_); % solving for y_ = y and c = A(y)
455     h_function = matlabFunction(z); % h(A) = z;
456 else
457     % Non-linear set of equations for circular pipe, we need to use
            fsolve
458 end
459 if flag_section ~= 4
460     fun_solve = matlabFunction(fun_solve); % Transforming into an
            equation
461 end
462 %% 6.0 -  Main Loop %%
```

```
463 n = 1; % initializing counter
464 x_i = 2:(Nx-1); % vector for interior sections varying from 2 to (Nx -
        1)
465 tic % starts measuring time
466 % Interpolation Variables
467 if flag_section == 4
468     var_inlet = zeros((length(irr_table(1,:))-1),1,2); var_outlet =
            var_inlet;
469     alfa_var_inlet = zeros((length(irr_table(1,:))-1),1,1);
            alfa_var_outlet = alfa_var_inlet;
470     var_middle = zeros((length(irr_table(1,:))-1),length(x_i),2);
471     alfa_var_middle = zeros((length(irr_table(1,:))-1),length(x_i),1);
472 end
473
474 % Initialization of some variables
475 time_end_min = (Nt)*dt;
476 time = 0;
477 time_previous = 0;
478 time_step = dt; % sec
479 t_store_prev = 0;
480
481 while time <= (time_end_min) % Main loop
482     try
483     n = n + 1; % Time-step index
484     time = time + time_step; % Seconds
485     time_save_model(n) = time; % Seconds
486
487     % Model Status
488     percentage_timestepsec_maxCourant_maxh = [time/(tt)*100, time_step,
            max(max(Cn)), max(max(y))]
489
490     % Agregating Inflows to the New Time-step
491     if flag_hydrograph == 1 || flag_nash == 1
492         z1 = find(tint > time_previous,1,'first'); % begin of the time-
                step
493         z2 = find(tint <= time,1,'last'); % end of the time-step
494         if isempty(z1)
495             z1 = 1;
496         end
497         if isempty(z2) || z2 < z1
498             z2 = z1;
499         end
500         if time_step >= dt
501             Q0 = mean(Qe1int(z1:z2));
502         else
503             Q0 = Qe1int(z1);
504         end
```

```
505     end
506     if time > 4.08*10^3
507         ttt = 1;
508     end
509     % Agregating Stages to the New Time-step
510     if flag_stage_hydrograph == 1
511         z1 = find(tint > time_previous,1,'first'); % begin of the time-
                step
512         z2 = find(tint <= time,1,'last'); % end of the time-step
513         if isempty(z1)
514             z1 = 1;
515         end
516         if isempty(z2) || z2 < z1
517             z2 = z1;
518         end
519         if time_step >= dt
520             h0 = mean(he1int(z1:z2));
521         else
522             h0 = he1int(z1);
523         end
524     end
525
526     % Stop Program if Complex Number Occurs
527     if imag(max(Cn(:,2-1))) > 0 || imag(max(q2(:,2-1)))
528         error('Complex number possibly due to changing the regime from
                free flow to pressurized flow.')
529     end
530     %%%%% -  Boundary Conditions -  %%%%%
531     %% Channel's begin (INLET)
532     if flag_stage_hydrograph == 1
533         %         h0 = he1int(n,1); % Water depth at x = 0 at time =
                time
534         if flag_section == 4
535             if h0 > max(irr_table(:,1))
536                 error('The maximum water depth is larger than the
                        channel height.')
537             end
538             q1(1,2) = Vlookup_g(irr_table,1,h0,2); % Smaller values
539         else
540             q1(1,2) = A_function(D,Z1,Z2,a,b,h0);
541         end
542     else
543         q1(1,2) = q1(2,1); % Area at section 1 is equals area of section
                2 from previous time-step
544     end
545     if flag_hydrograph == 1 || flag_nash == 1
546         %         q2(1,2) = Qe1int(n,1); % Flow at section 1 is the
```

```
            inflow hydrograph
547         q2(1,2) = Q0; % Flow at section 1 is the inflow hydrograph
548     else
549         q2(1,2) = q2(2,1); % Flow at section 1 equals flow at section 2
                from previous time-step
550     end
551
552     if flag_hydrograph == 0 && flag_nash == 0 && flag_stage_hydrograph
            == 0 && flag_outlet == 0
553         q2(1,2) = q2(2,1); % Flow at section 1 equals flow at section 2
                from previous time-step
554 %         q2(1,1) = q2(2,1);
555     end
556
557     % Interpolating All Values from I_rr_table using q1 as basis
558     % Explanation: area is given in m2. P, Rh, and other variables are
559     % in m. So we have a quadratically similar triangle relationship
560     if flag_section == 4
561         for mm = 1:(length(irr_table(1,:))-1)
562             interp_base = q1(1,2); % Value that will be used for
                    interpolation (area)
563             if interp_base <= min_area % Col with area = 0
564                 area_smaller = 0; % Smaller values
565             else
566                 area_smaller = Vlookup_l(irr_table,2,interp_base,2); %
                        Smaller values
567             end
568             area_larger = Vlookup_g(irr_table,2,interp_base,2); % Larger
                    values
569             col1 = 2; % Interpolating from area values
570             if interp_base <= min_area % Col with area = 0
571                 var_inlet(mm,1,1) = irr_table(2,mm); % Smaller values
572             else
573                 var_inlet(mm,1,1) = Vlookup_l(irr_table,col1,interp_base
                        ,mm); % Smaller values
574             end
575             var_inlet(mm,1,2) = Vlookup_g(irr_table,col1,interp_base,mm)
                    ; % Larger values
576             alfa_var_inlet(mm,1) = sqrt((interp_base - area_smaller)/(
                    area_larger - area_smaller));
577         end
578     end
579
580     if flag_section == 1 % Trapezoid or Rectangular
581         if Z1 > 0 || Z2 > 0 % Trapezoidal channel
582             y(1,2) = max(h_function(D,Z1,Z2,a,b,q1(1,2)')); % water
                    depth in terms of area q1
```

```
583             % In this previous function, we solve h = y in terms of A =
                    q1 = c
584         else
585             y(1,2) = q1(1,2)/b; % water depth in terms of area q1 for
                    rectangular channels
586         end
587     elseif flag_section > 1 % circular or paraboloid or irregular
588         y0_guess = y(1,2-1);
589         c = q1(1,2)*fv;  % WEIRDO. I HAVE TO CHECK IT OUT ... ISNT IT
                (2-1)?
590         if flag_section ~= 4
591             fun = @(y_)fun_solve(D,Z1,Z2,a,b,c,y_);
592             y(1,2) = fsolve(fun,y0_guess,options); % non-linear solver
593         else % Irregular section
594             % [y_irr, A_irr, P_irr, Rh_irr, y_bar_irr, n_med_irr,
                    Beta_irr, u_irr, B_irr, Q_irr];
595             % [   1,    2,     3,      4,    5,            6,
                    7,     8,      9,
596             col1 = 2; % Col with A
597             col_var = 1;
598             % Var* = Var(-) + alfa*(Var(+) - Var(-))
599             y(1,2) = var_inlet(col_var,1,1) + alfa_var_inlet(col_var,1)
                    *(var_inlet(col_var,1,2) - var_inlet(col_var,1,1));
600             %             y(1,2) = Vlookup_leq(irr_table,col1,c,1);
601         end
602     end
603     % ybar
604     if flag_section ~= 4
605         ybar(1,2) = ybar_function(D,Z1,Z2,a,b,y(1,2));
606         % f1 and f2
607         f1(1,2) = q2(1,2);
608         f2(1,2) = q2(1,2).*abs(q2(1,2))./q1(1,2) + g*q1(1,2).*ybar(1,2);
609         % Hydraulic Radius
610         Rh_inlet = Rh_function(D,Z1,Z2,a,b,y(1,2));
611         % Friction
612         if flag_friction == 1
613             J2(1,2) = g*q1(1,2).*(I0(1) - q2(1,2).*abs(q2(1,2)).*nm(1)
                    .^2./(q1(1,2).^2*Rh_inlet.^(4/3))); % Manning
614         else
615             J2(1,2) = (I0(1) - f*q2(1,2).*abs(q2(1,2))./((q1(1,2).^2)*8*
                    g.*Rh_inlet));
616         end
617         % Froude
618         Fr(1,2)=abs(q2(1,2)./q1(1,2))./((g*A_function(D,Z1,Z2,a,b,y(1,2)
                ))./B_function(D,Z1,Z2,a,b,y(1,2)))^0.5);% Froude Number
619         % Courant
620         Hm = A_function(D,Z1,Z2,a,b,y(1,2))./B_function(D,Z1,Z2,a,b,y
```

```
            (1,2));
621         Cn(1,2)=(abs(q2(1,2)./q1(1,2))+(g*Hm).^0.5)/(dx/time_step);%
                Courant Number
622         if isinf(Cn(1,2)) || isinan(Cn(1,2))
623             Cn(1,2) = 0;
624         end
625     else
626         % [y_irr, A_irr, P_irr, Rh_irr, y_bar_irr, n_med_irr, Beta_irr,
                u_irr, B_irr, Q_irr];
627         % [   1,    2,     3,      4,    5,            6,          7,
                8,       9,   10]
628         col1 = 2; % Col with A
629         col_var = 5;
630         % Var* = Var(-) + alfa*(Var(+) - Var(-))
631         ybar(1,2) = var_inlet(col_var,1,1) + alfa_var_inlet(col_var,1)*(
                var_inlet(col_var,1,2) - var_inlet(col_var,1,1));
632         % f1 and f2
633         f1(1,2) = q2(1,2);
634         f2(1,2) = q2(1,2).*abs(q2(1,2))./q1(1,2) + g*q1(1,2).*ybar(1,2);
635         % Hydraulic Radius
636         col_var = 4;
637         % Var* = Var(-) + alfa*(Var(+) - Var(-))
638         Rh_inlet = var_inlet(col_var,1,1) + alfa_var_inlet(col_var,1)*(
                var_inlet(col_var,1,2) - var_inlet(col_var,1,1));
639         % Friction
640         if flag_friction == 1
641             col_var = 6;
642             % Var* = Var(-) + alfa*(Var(+) - Var(-))
643             nm(1) = var_inlet(col_var,1,1) + alfa_var_inlet(col_var,1)*(
                    var_inlet(col_var,1,2) - var_inlet(col_var,1,1));
644             if isnan(nm(1,1))
645                 nm = irr_table(2,6)*ones(length(q1(:,1)),1);
646             end
647             J2(1,2) = g*c.*(I0(1) - q2(1,2).*abs(q2(1,2)).*nm(1).^2./(c
                    .^2*Rh_inlet.^(4/3))); % Manning
648         else
649             J2(1,2) = (I0(1) - f*q2(1,2).*abs(q2(1,2))./((q1(1,2).^2)*8*
                    g.*Rh_inlet));
650         end
651         % Froude
652         % Var* = Var(-) + alfa*(Var(+) - Var(-))
653         A_f_irr = q1(1,2);
654         col_var = 9;
655         B_f_irr = var_inlet(col_var,1,1) + alfa_var_inlet(col_var,1)*(
                var_inlet(col_var,1,2) - var_inlet(col_var,1,1));
656         %         B_f_irr = Vlookup_leq(irr_table,col1,c,9);
657         Fr(1,2) = abs(q2(1,2)./q1(1,2))./((g*A_f_irr./B_f_irr)^0.5);%
```

```
            Froude Number
658         % Courant
659         Hm = A_f_irr./B_f_irr;
660         Cn(1,2) = (abs(q2(1,2)./q1(1,2))+(g*Hm).^0.5)/(dx/time_step);%
                Courant Number
661     end
662
663     %% Right side of the channel (outlet)
664     if flag_outlet == 1 % Normal Depth
665         q1(Nx,2) = q1(Nx-1,2-1); % Boundary Condition (same area)
666         % Interpolating All Values from I_rr_table using q1 as basis
667         % Explanation: area is given in m2. P, Rh, and other variables
                are
668         % in m. So we have a quadratically similar triangle relationship
669         if flag_section == 4
670             for mm = 1:(length(irr_table(1,:))-1)
671                 interp_base = q1(Nx,2); % Value that will be used for
                        interpolation (area)
672                 if interp_base <= min_area % Area
673                     area_smaller = 0;
674                 else
675                     area_smaller = Vlookup_l(irr_table,2,interp_base,2);
                            % Smaller values
676                 end
677                 area_larger = Vlookup_g(irr_table,2,interp_base,2); %
                        Larger values
678                 col1 = 2; % Interpolating from area values
679                 if interp_base <= min_area % Area
680                     var_outlet(mm,1,1) = irr_table(2,mm); % Smaller
                            values
681                 else
682                     var_outlet(mm,1,1) = Vlookup_l(irr_table,col1,
                            interp_base,mm); % Smaller values
683                 end
684                 var_outlet(mm,1,2) = Vlookup_g(irr_table,col1,
                        interp_base,mm); % Larger values
685                 alfa_var_outlet(mm,1) = sqrt((interp_base - area_smaller
                        )/(area_larger - area_smaller));
686             end
687         end
688         if flag_section == 1
689             if Z1 > 0 || Z2 > 0
690                 y(Nx,2) = max(h_function(D,Z1,Z2,a,b,q1(Nx,2)')); %
                        water depth in terms of area q1
691             else
692                 y(Nx,2) = q1(Nx,2)/b; % water depth in terms of area q1
                        for rectangular channels
```

```
693             end
694         elseif flag_section >= 2 % circular or paraboloid or irregular
695             % If we do not have a stage-hydrograph boundary condition
696             y0_guess = y(Nx,2-1);
697             if flag_section ~= 4
698                 fun = @(y_)fun_solve(D,Z1,Z2,a,b,c,y_);
699                 y(Nx,2) = fsolve(fun,y0_guess,options); % non-linear
                        solver
700             else
701                 % [y_table, A, P, Rh, y_bar, n_med, Beta, v, B, Q]
702                 % [   1,    2, 3, 4,    5,    6,      7,  8,  9, 10]
703                 col_var = 1;
704                 % Var* = Var(-) + alfa*(Var(+) - Var(-))
705                 y(Nx,2) = var_outlet(col_var,1,1) + alfa_var_outlet(
                        col_var,1)*(var_outlet(col_var,1,2) - var_outlet(
                        col_var,1,1));
706             end
707         end
708     else
709         % Stage Hydrograph Boundary Condition. We are modeling a tidal
710         % outlet condition
711         time_wave = time; % time in seconds
712         y(Nx,2) = h_wave_function(time_wave);
713         if flag_section ~= 4
714             q1(Nx,2) = A_function(D,Z1,Z2,a,b,y(Nx,2));
715         else
716             % We search Everything Using the Depth instead of the Flow
717             col1 = 1; % Searching with the Col of Flow
718
719
720             area_smaller = Vlookup_l(irr_table,col1,y(Nx,2)*fv,2);
721             area_greater = Vlookup_g(irr_table,col1,y(Nx,2)*fv,2);
722             y_smaller = Vlookup_l(irr_table,col1,y(Nx,2)*fv,1);
723             y_greater = Vlookup_g(irr_table,col1,y(Nx,2)*fv,1);
724
725             delta_y = y(Nx,2) - Vlookup_l(irr_table,col1,y(Nx,2)*fv,1);
726             q1(Nx,2) = area_smaller + (area_greater - area_smaller)*(
                    delta_y/(y_greater - y_smaller))^2;
727         end
728         %          q1(Nx,2) = q1(Nx-1,2-1)
729     end
730     % Hydraulic Radius
731     if flag_section ~= 4
732         Rh_outlet = Rh_function(D,Z1,Z2,a,b,y(Nx,2));
733     else
734         for mm = 1:(length(irr_table(1,:))-1)
735             interp_base = q1(Nx,2); % Value that will be used for
```

```
                interpolation (area)
736             if interp_base <= min_area
737                 area_smaller = 0; % Smaller values
738             else
739                 area_smaller = Vlookup_l(irr_table,2,interp_base,2); %
                        Smaller values
740             end
741             area_larger = Vlookup_g(irr_table,2,interp_base,2); % Larger
                    values
742             col1 = 2; % Interpolating from area values
743             if interp_base <= min_area
744                 var_outlet(mm,1,1) = irr_table(2,mm);
745             else
746                 var_outlet(mm,1,1) = Vlookup_l(irr_table,col1,
                        interp_base,mm); % Smaller values
747             end
748             var_outlet(mm,1,2) = Vlookup_g(irr_table,col1,interp_base,mm
                    ); % Larger values
749             alfa_var_outlet(mm,1) = sqrt((interp_base - area_smaller)/(
                    area_larger - area_smaller));
750         end
751         % [y_table, A, P, Rh, y_bar, n_med, Beta, v, B, Q]
752         % [   1,    2, 3, 4,    5,    6,      7,  8,  9, 10]
753         col_var = 4; % Calculating Hydraulic Radius
754         % Var* = Var(-) + alfa*(Var(+) - Var(-))
755         Rh_outlet = var_outlet(col_var,1,1) + alfa_var_outlet(col_var,1)
                *(var_outlet(col_var,1,2) - var_outlet(col_var,1,1)); %
                Interpolated Hydraulic Radius
756         % Var* = Var(-) + alfa*(Var(+) - Var(-))
757         col_var = 6;
758         nm(end,1) = var_outlet(col_var,1,1) + alfa_var_outlet(col_var,1)
                *(var_outlet(col_var,1,2) - var_outlet(col_var,1,1));
759     end
760     if flag_friction == 1
761         if flag_outlet == 1
762             u = (1./nm(Nx)).*Rh_outlet^(2/3)*I0(Nx)^0.5; % Normal depth
                    at the outlet
763             flow_dir = 1;
764         else
765             wse_dif = y(Nx-1,2-1) + inv_el(Nx-1) - y(Nx,2) - inv_el(Nx);
                    % Difference in wse
766             out_slope = abs(wse_dif)/dx; % Friction slope at the outlet
                    as a diffusive model
767             if wse_dif < 0
768                 ttt = 1;
769             end
770
```

```
771             u = (1./nm(Nx)).*Rh_outlet^(2/3)*out_slope^0.5; % Normal
                    velocity at the outlet
772             if wse_dif > 0
773                 flow_dir = 1; % Flowing towards the outlet
774             else
775                 flow_dir = -1; % Flowing to inside of the channel
776             end
777         end
778     else
779         u = sqrt(8*g*Rh_outlet*I0(Nx)/f); % outlet velocity
780     end
781     % Outlet Flow
782     q2(Nx,2) = q1(Nx,2)*u*flow_dir; % Area x Velocity
783     if isnan(q2(Nx,2))
784         ttt = 1;
785     end
786     % Outlet Flow Under No Inflow Hydrograph & Not Enough WSE_dif
787     if flag_stage_hydrograph ~= 1 && flag_nash ~= 1 && flag_hydrograph
            ~= 1
788         % Only Outlet Tidal B.C.
789         if wse_dif > 0 && y(Nx-1,2-1) <= fv*1e-3
790             q2(Nx,2) = q1(Nx,2)*dx/(time_step); % Making sure all
                    available depth becomes outflow in the outlet
791         end
792     end
793
794     % ybar
795     if flag_section ~= 4
796         ybar(Nx,2) = ybar_function(D,Z1,Z2,a,b,y(Nx,2));
797     else
798         % [y_irr, A_irr, P_irr, Rh_irr, y_bar_irr, n_med_irr, Beta_irr,
                u_irr, B_irr, Q_irr];
799         % [   1,     2,     3,      4,     5,            6,          7,
                8,       9,   10]
800         % ybar = y - ybar*
801         col1 = 2; % A
802         %         ybar(Nx,2) =  Vlookup_leq(irr_table,col1,c,1) -
                Vlookup_leq(irr_table,col1,c,5);
803 %         if q1(Nx,2) == 0
804 %             ybar(Nx,2) = 0;
805 %         else
806 %             ybar(Nx,2) = Vlookup_l(irr_table,col1,q1(Nx,2),5);
807 %         end
808         col_var = 5;
809         % Var* = Var(-) + alfa*(Var(+) - Var(-))
810         ybar(Nx,2) = var_outlet(col_var,1,1) + alfa_var_outlet(col_var
                ,1)*(var_outlet(col_var,1,2) - var_outlet(col_var,1,1));
```

```
811     end
812     % f1 and f2
813     f1(Nx,2) = q2(Nx,2); % f1 - Flow
814     zzz = q2(Nx,2).*abs(q2(Nx,2))./q1(Nx,2) + g*q1(Nx,2).*ybar(Nx,2); %
            f2 = (Qv + gAy_bar)
815     zzz(isnan(zzz)) = 0;
816     f2(Nx,2) = zzz; % f2 = (Qv + gAy_bar)
817
818     % J2
819     % Friction
820     if flag_friction == 1
821         J2(Nx,2) = g*q1(Nx,2).*(I0(Nx) - q2(Nx,2).*abs(q2(Nx,2)).*nm(Nx)
                .^2./(q1(Nx,2).^2*Rh_outlet.^(4/3))); % Manning --> gA*(I0 -
                If), If = n^2*Q*abs*Q)/(Rh^(4/3)*A^2)
822     else
823         J2(Nx,2) = g*q1(Nx,2).*(I0(Nx) - f*q2(:,2).*abs(q2(Nx,2))./((q1(
                Nx,2).^2)*8*g*Rh_outlet));
824     end
825     J2(isnan(J2)) = 0; % Attention Here
826     % Froude
827     if flag_section ~= 4
828         Fr(Nx,2)=abs(q2(Nx,2)./q1(Nx,2))./((g*A_function(D,Z1,Z2,a,b,y(
                Nx,2))./B_function(D,Z1,Z2,a,b,y(Nx,2)))^0.5);% Froude Number
829         % Courant
830         Hm = A_function(D,Z1,Z2,a,b,y(Nx,2))./B_function(D,Z1,Z2,a,b,y(
                Nx,2));
831         Cn(Nx,2)=(abs(q2(Nx,2)./q1(Nx,2))+(g*Hm).^0.5)/(dx/time_step);%
                Courant Number
832         if isnan(Cn(Nx,2)) || isinf(Cn(Nx,2))
833             Cn(Nx,2) = 0;
834         end
835     else
836         % Froude
837         % [y_irr, A_irr, P_irr, Rh_irr, y_bar_irr, n_med_irr, Beta_irr,
                u_irr, B_irr, Q_irr];
838         % [   1,    2,     3,      4,    5,            6,           7,
                8,       9,   10]
839         col1 = 2; % Col with A
840         A_f_irr = c;
841         col_var = 9;
842         % Var* = Var(-) + alfa*(Var(+) - Var(-))
843         B_f_irr = var_outlet(col_var,1,1) + alfa_var_outlet(col_var,1)*(
                var_outlet(col_var,1,2) - var_outlet(col_var,1,1));
844         %          B_f_irr = Vlookup_l(irr_table,col1,c,9);
845         Fr(Nx,2) = abs(q2(Nx,2)./q1(Nx,2))./((g*A_f_irr./B_f_irr)^0.5);%
                Froude Number
846         % Courant
```

```
847         Hm = A_f_irr./B_f_irr;
848         if y(Nx,2) <= min_depth
849             Cn(Nx,2) = 0;
850         else
851             Cn(Nx,2)=(abs(q2(Nx,2)./q1(Nx,2))+(g*Hm).^0.5)/(dx/time_step
                );% Courant Number
852             if isnan(Cn(Nx,2)) || isinf(Cn(Nx,2))
853                 Cn(Nx,2) = 0;
854             end
855         end
856     end
857
858     %% Main Loop for Non-Boundary Cells from 2 to (Nx - 1)
859     % vectorized calculations
860     q1_back = q1(1:(Nx-2),(2-1));
861     q1_forward = q1(3:(Nx),(2-1));
862     q2_back = q2(1:(Nx-2),(2-1));
863     q2_forward = q2(3:(Nx),(2-1));
864     f1_back = f1(1:(Nx-2),(2-1));
865     f1_forward = f1(3:(Nx),(2-1));
866     f2_back = f2(1:(Nx-2),(2-1));
867     f2_forward = f2(3:(Nx),(2-1));
868     J2_back = J2(1:(Nx-2),(2-1));
869     J2_forward = J2(3:(Nx),(2-1));
870
871     % Lax-Friedrichs Method
872     % Given a hyperbolic partial derivative system of equations
            described
873     % by:
874     % pq/pt + pF/px - S = 0, where p is the partial derivative, one can
875     % solve this equation by performing a forward discretization for q
            and a
876     % central discretization for F. Moreover, S = (Sback + Sforward)/2
877     % Expliciting the system of equations for q, it follows that:
878
879     q1(x_i,2) = 0.5.*(q1_forward + q1_back) - 0.5*time_step/dx*(
            f1_forward - f1_back); %% attention here in f1forward
880     q2(x_i,2) = 0.5*(q2_forward + q2_back) - 0.5*time_step/dx*(
            f2_forward - f2_back) + 0.5*time_step*(J2_back + J2_forward);
881
882     if q1(Nx-1,2) > 0.0
883         ttt = 1;
884     end
885     % There is no such thing as a negative water depth, so we apply a
886     % constraint
887 %     if min(q1(x_i,2)) < 0
888 %         zzz = q1(x_i,2); zzz(zzz<0) = 0; q1(x_i,2) = zzz;
```

```
%          ttt = 1;
%      end
    % Interpolating All Values from I_rr_table using q1 as basis
    if flag_section == 4
        for mm = 1:(length(irr_table(1,:))-1)
            for hh = 1:length(x_i)
                interp_base = q1(hh+1,2); % Value that will be used for
                    interpolation (area)
                if interp_base <= min_area
                    area_smaller = 0;
                else
                    area_smaller = Vlookup_l(irr_table,2,interp_base,2);
                        % Smaller values
                end
                area_larger = Vlookup_g(irr_table,2,interp_base,2); %
                    Larger values
                col1 = 2; % Interpolating from area values
                if interp_base <= min_area
                    var_middle(mm,hh,1) = irr_table(2,mm); % Smaller
                        values
                else
                    var_middle(mm,hh,1) = Vlookup_l(irr_table,col1,
                        interp_base,mm); % Smaller values
                end
                var_middle(mm,hh,2) = Vlookup_g(irr_table,col1,
                    interp_base,mm); % Larger values
                alfa_var_middle(mm,hh,1) = sqrt((interp_base -
                    area_smaller)/(area_larger - area_smaller));
            end
        end
    end

    if flag_section == 1
        if Z1>0 || Z2>0
            y(x_i,2) = max(h_function(D,Z1,Z2,a,b,q1(x_i,2)')); % water
                depth in terms of area q1
        else
            y(x_i,2)=q1(x_i,2)/b;
        end
    elseif flag_section > 1
        y0_guess = y(x_i,2-1);
        c = q1(x_i,2)*fv; % It has to be a line vector (area)
        if flag_section ~= 4
            fun = @(y_)fun_solve(D,Z1,Z2,a,b,c,y_);
            y(x_i,2) = fsolve(fun,y0_guess,options); % non-linear solver
        else
            % [y_irr, A_irr, P_irr, Rh_irr, y_bar_irr, n_med_irr,
```

```
                Beta_irr, u_irr, B_irr, Q_irr];
928             % [   1,    2,     3,      4,    5,            6,
                    7,  8,      9,  10]
929             col1 = 2; % Col with A
930             for i = 1:length(x_i)
931                 cc = c(i); % be careful here
932                 col_var = 1;
933                 % Var* = Var(-) + alfa*(Var(+) - Var(-))
934                 y(i+1,2) = var_middle(col_var,i,1) + alfa_var_middle(
                        col_var,i)*(var_middle(col_var,i,2) - var_middle(
                        col_var,i,1));
935             end
936         end
937     end
938     % Hydraulic Radius
939     if flag_section ~= 4
940         Rh_middle = Rh_function(D,Z1,Z2,a,b,y(x_i,2));
941         % ybar
942         ybar(x_i,2) = ybar_function(D,Z1,Z2,a,b,y(x_i,2));
943         % f1 and f2
944         f1(x_i,2) = q2(x_i,2);
945         f2(x_i,2) = q2(x_i,2).*abs(q2(x_i,2))./q1(x_i,2) + g*q1(x_i,2).*
                ybar(x_i,2);
946         % Froude
947         Hm = A_function(D,Z1,Z2,a,b,y(x_i,2))./B_function(D,Z1,Z2,a,b,y(
                x_i,2));
948         Fr(x_i,2)=abs(q2(x_i,2)./q1(x_i,2))./((g*Hm).^0.5);% Froude
                Number
949         % Courant
950         Cn(x_i,2)=(abs(q2(x_i,2)./q1(x_i,2))+(g*Hm).^0.5)/(dx/time_step)
                ;% Courant Number
951         % Friction
952         if flag_friction == 1
953             J2(x_i,2) = g*q1(x_i,2).*(I0(x_i) - q2(x_i,2).*abs(q2(x_i,2)
                    .*nm(x_i).^2./(q1(x_i,2).^2.*Rh_middle.^(4/3))));
954         else
955             J2(x_i,2) = g*q1(x_i,2).*(I0(x_i) - f*q2(x_i,2).*abs(q2(x_i
                    ,2))./((q1(x_i,2).^2)*8*g*Rh_midle));
956         end
957         % Stability Check
958         if max(Cn(:,2)) > 1
959             error('Please, decrease the time-step')
960         end
961     else
962         for jj = 1:length(x_i)
963             cc = c(jj); % Area
964             % [y_irr, A_irr, P_irr, Rh_irr, y_bar_irr, n_med_irr,
```

```
    Beta_irr, u_irr, B_irr, Q_irr];
% [   1,    2,     3,      4,    5,            6,
    7,  8,      9,  10]
col_var = 4;
% Var* = Var(-) + alfa*(Var(+) - Var(-))
Rh_middle(jj,1) = var_middle(col_var,jj,1) + alfa_var_middle
    (col_var,jj)*(var_middle(col_var,jj,2) - var_middle(
    col_var,jj,1));
col_var = 5;
ybar(jj+1,2) = var_middle(col_var,jj,1) + alfa_var_middle(
    col_var,jj)*(var_middle(col_var,jj,2) - var_middle(
    col_var,jj,1));
col_var = 6;
nm(jj+1,1) = var_middle(col_var,jj,1) + alfa_var_middle(
    col_var,jj)*(var_middle(col_var,jj,2) - var_middle(
    col_var,jj,1));
% f1 and f2
f1(jj+1,2) = q2(jj+1,2);
f2(jj+1,2) = q2(jj+1,2).*abs(q2(jj+1,2))./q1(jj+1,2) + g*q1(
    jj+1,2).*ybar(jj+1,2);
% Froude
A_f_irr = q1(jj+1,2);
col_var = 9;
B_f_irr = var_middle(col_var,jj,1) + alfa_var_middle(col_var
    ,jj)*(var_middle(col_var,jj,2) - var_middle(col_var,jj,1)
    );
Hm = A_f_irr./B_f_irr;
Fr(jj+1,2) = abs(q2(jj+1,2)./q1(jj+1,2))./((g*Hm).^0.5);%
    Froude Number
% Courant
if y(jj+1,2) > 0.005 % 0.5 cm
    Cn(jj+1,2) = (abs(q2(jj+1,2)./q1(jj+1,2))+(g*Hm).^0.5)/(
        dx/time_step);% Courant Number
else
    Cn(jj+1,2) = 0;
end
if isinf(Cn(jj+1,2))
    Cn(jj+1,2) = 0;
end
% Friction
if flag_friction == 1
    J2(jj+1,2) = g*A_f_irr.*(I0(jj+1,1) - q2(jj+1,2).*abs(q2
        (jj+1,2).*nm(jj+1,1).^2./(A_f_irr.^2.*Rh_middle(jj,1)
        ^(4/3))));
else
    J2(jj+1,2) = g*q1(jj+1,2).*(I0(jj+1,2) - f*q2(jj+1,2).*
        abs(q2(jj+1,2))./((q1(jj+1,2).^2)*8*g*Rh_midle(jj,1))
```

```
                    );
996             end
997             % Stability Check
998             if Cn(jj+1,2) > 1 && y(jj+1,2) >= min_depth && q1(jj+1,2) >=
                    min_area
999                 error('Please, decrease the time-step')
1000            end
1001        end
1002    end
1003
1004
1005    % Constraint at dry areas
1006    % -- the idea is that dry cells have no hydraulic properties
1007    if min(q1(:,2)) <=  min_area || min(y(:,2)) <=  min_depth
1008        idx1 = q1(:,2) <= min_area; idx2 = y(:,2) <= min_area; idx =
               idx1 + idx2; % Both
1009        idx = logical([zeros(size(idx,1),1), idx]);
1010        q1(idx) = 0; q2(idx) = 0; f1(idx) = 0; f2(idx) = 0; J2(idx) = 0;
                y(idx) = 0;
1011        Fr(idx) = 0; Cn(idx) = 0;
1012    end
1013        % Adaptive Time-Step - Outlet not considered
1014        idx_courant = Cn(1:end-1,2) <= 0;
1015        zzz = Cn(1:end-1,2); zzz(idx_courant) = nan;
1016        dt_courant_1 = zzz/time_step; % Cn/time_step = dx/ (v + sqrt(Hm*
               g)), this the the time-step for Courant = 1
1017        time_step = min(alpha./dt_courant_1); % Calculated
1018        time_step = min(time_step,dtmax);
1019        time_step = max(time_step,dtmin);
1020        time_previous = time;
1021
1022        if time_step < 1
1023            ttt = 1;
1024        end
1025
1026    % Saving hydrographs and depths with user defined recording time-
           step
1027    if n == 1
1028        % Do nothing, it is already solved, we just have to save the
               data
1029        % for the next time-step
1030        t_store = 1;
1031        time_save(1,1) = time;
1032    else
1033        t_store = find(time_store <= time,1,'last'); % Time that is
               being recorded in min
1034        if t_store > t_store_prev
```

```
            time_save(t_store,1) = time;
            Flow_Area(t_store,:) = q1(:,2); % m2
            Discharge(t_store,:) = q2(:,2); % m3/s
            Depth(t_store,:) = y(:,2); % m
            Velocity(t_store,:) = q2(:,2)./q1(:,1); % m/s
            Froude(t_store,:) = Fr(:,2);
            Courant(t_store,:) = Cn(:,2);
            t_store_prev = t_store;
        end
    end
    % Refreshing States
%       idx = y < 1e-3; q1(idx) = 0; q2(idx)

    q1(:,1) = q1(:,2);
    q2(:,1) = q2(:,2);
    f1(:,1) = f1(:,2);
    f2(:,1) = f2(:,2);
    J2(:,1) = J2(:,2);
    y(:,1) = y(:,2);
    Cn(:,1) = Cn(:,2);
    Fr(:,1) = Fr(:,2);

    if time > 2*1000
        ttt = 1;
    end

    catch ME
        % If this condition is reached, we are reducing the time-step to
        % 50% and doing the calculations again
        idx = q1(:,2) <= min_area;
        vel = abs(q2(:,2)./q1(:,2)) + sqrt(g*y(:,2)); vel(idx) = 0;
        dtnew = min(alpha*dx./(vel));
        time = time - time_step; % Seconds
        time_step = dtnew; % Halving the time-step
        n = n - 1;
    end
end
%% 7.0 - Post-Processing
water_depths = Depth;
%%% Post Processing Figures %%%
% Call function
warning('on');
post_processing
close all
toc
disp(['Thank you for using HyProSWE. If you have any questions, please
   contact me at marcusnobrega.engcivil@gmail.com).'])
```

```
disp(['Also, please check your current matlab folder. The outputs are
    there.'])
```

8.5.6.4 SVE Post Processing

```
%%% --------- HyProSWE Model ----------- %%%
% Post-Processing Routine
% Developer: Marcus Nobrega Gomes Junior
% 5/1/2023
% Goal: Solution of 1-D SVE for given cross-section functions of Area,
    Perimeter, and
% top Width
% If you have any issues, please contact me at
% marcusnobrega.engcivil@gmail.com

%% Creating Modeling Results Folder
% Create the folder name
folderName = 'Modeling_Results';

% Check if the folder already exists
if ~exist(folderName, 'dir')
    % If it doesn't exist, create the folder
    mkdir(folderName);
    disp('Folder "Modeling_Results" created successfully!');
else
    disp('Data sucessfully exported in Modeling_Results Folder');
end

%% Post Processing Graphs
clf
close all


color_plot = [21, 179, 196]/255; % You can change it if you want

% Surfplot
t_save = [0:Nat:tt/dt];
t_save(1,1) = 1;
set(gcf,'units','inches','position',[2,0,8,10])
subplot(3,1,1)
surf(x,tint(t_save)/3600,Froude);
view(0,90);
kk = colorbar ; colormap('jet')
shading interp
xlabel('x (m)','Interpreter','latex')
ylabel('t (h)','Interpreter','latex')
ylabel(kk,'Froude Number','Interpreter','latex')
```

```
zlabel ('Froude Number','Interpreter','Latex');
xlim([0 L]);
ylim([0 tt/60/60]);
set(gca,'FontName','Garamond','FontSize',12,'FontWeight','Bold','
    LineWidth', 1.5);
set(gca,'TickLength',[0.02 0.01])
set(gca,'TickDir','out')

subplot(3,1,2)
surf(x,tint(t_save)/60/60,Depth);
view(0,90);
kk = colorbar ; colormap('jet')
shading interp
xlabel('x (m)','Interpreter','latex')
ylabel('t (h)','Interpreter','latex')
ylabel(kk,'y (m)','Interpreter','latex')
zlabel ('y (m)','Interpreter','Latex');
xlim([0 L]);
ylim([0 tt/60/60]);
set(gca,'FontName','Garamond','FontSize',12,'FontWeight','Bold','
    LineWidth', 1.5);
set(gca,'TickLength',[0.02 0.01])
set(gca,'TickDir','out')

subplot(3,1,3)
wse = Depth + repmat(inv_el',[size(Depth,1),1]);
surf(x,tint(t_save)/60/60,wse);
view(0,90);
kk = colorbar ; colormap('jet')
shading interp
xlabel('x (m)','Interpreter','latex')
ylabel('t (h)','Interpreter','latex')
ylabel(kk,'WSE (m)','Interpreter','latex')
zlabel ('WSE (m)','Interpreter','Latex');
xlim([0 L]);
ylim([0 tt/60/60]);
set(gca,'FontName','Garamond','FontSize',12,'FontWeight','Bold','
    LineWidth', 1.5);
set(gca,'TickLength',[0.02 0.01])
set(gca,'TickDir','out')
exportgraphics(gcf,fullfile(folderName,'Surf_Plots.pdf'),'ContentType','
    image','Colorspace','rgb','Resolution',600)
clf
close all

if flag_section == 2 % circular
% Video
```

```
obj = VideoWriter('Circular_Depth.avi','Motion JPEG AVI');
obj.Quality = 100;
obj.FrameRate = 20;
open(obj)
set(gcf,'units','inches','position',[2,2,10,3])
    for n=1:1:(Nt/Nat)
        if n == 1
            t = 1;
            pos = 1;
        else
            t=time_save(n);
            pos = n;
        end
        % Circle Function
        xcir = linspace(0,2*pi,100); % 100 points within 0 and 360 deg
        cir = @(r,ctr) [r*cos(xcir)+ctr(1); r*sin(xcir)+ctr(2)];
        c1 = cir(D/2, [D/2; D/2]);

        % Boundary Circle
        % (x - xc)^2 + (y - yc)^2 = D^2/4
        % where xc = D/2 and yc = D/2
        xc = D/2; yc = D/2;
        y01 = Depth(pos,1);
        y02 = Depth(pos,ceil(ceil(Nx/2)));
        y03 = Depth(pos,Nx);
        y0_c = [y01; y02; y03];
        % For a given known y, we have to find two xs, such that
        % x^2 + (-2xc)x + ( (y0 - yc)^2 - xc^2 - D^2/4 )
        % or ax^2 + bx + c, with
        % a = 1; b = -2xc; c = (y0 - yc)^2 - xc^2 - D^2/4
        % x = (- b +- sqrt(b^2 - 4ac)) / (2a)
        a = 1;
        b = -2*xc;
        c = xc^2 + (y0_c - yc).^2 - D^2/4;
        Delta = b^2 - 4*a.*c;
        x1 = (-b + sqrt(Delta))/(2*a);
        x2 = (-b - sqrt(Delta))/(2*a);
        % Now we found the intersection of the circle and a line with
            know
        % depth
        subplot(1,3,1)
        title(['t = ',num2str(round(round(t,2),0)),' [sec]'])
        ylim([0 D]);
        xlim([0 D]);
        viscircles([D/2 D/2],D/2,'Color','black');
%         plot(c1(1,:),c1(2,:),'Color','black');
        hold on
```

```
131         x_water = linspace(x2(1),x1(1),100);
132         y_water = repmat(y01,1,100);
133         plot(x_water,y_water,'Color',color_plot,'linewidth',2);
134 %           fill([c1(1,:) fliplr(c1(1,:))], [y_water fliplr(c2(1,:))],
        color_plot)
135         ylabel('y(m)','Interpreter','latex')
136         xlabel('B(m)','Interpreter','latex')
137         legend('Entrance','interpreter','latex')
138         hold off
139         grid on
140         set(gca,'FontName','Garamond','FontSize',12);
141         set(gca,'TickLength',[0.02 0.01])
142         set(gca,'TickDir','out');
143         box on
144         % second section
145         subplot(1,3,2)
146         title(['t = ',num2str(round(round(t,2),0)),' [sec]'])
147         ylim([0 D]);
148         xlim([0 D]);
149         viscircles([D/2 D/2],D/2,'Color','black');
150         hold on
151         x_water = linspace(x2(2),x1(2),100);
152         y_water = repmat(y02,1,100);
153         plot(x_water,y_water,'Color',color_plot,'linewidth',2);
154         ylabel('y(m)','Interpreter','latex')
155         xlabel('B(m)','Interpreter','latex')
156         legend('x = L/2','interpreter','latex')
157         hold off
158         legend('L/2','interpreter','latex')
159         % third section
160         grid on
161         set(gca,'FontName','Garamond','FontSize',12);
162         set(gca,'TickLength',[0.02 0.01])
163         set(gca,'TickDir','out');
164         box on
165         subplot(1,3,3)
166         title(['t = ',num2str(round(round(t/60),0)),' [sec]'])
167         ylim([0 D]);
168         xlim([0 D]);
169         viscircles([D/2 D/2],D/2,'Color','black');
170         hold on
171         x_water = linspace(x2(3),x1(3),100);
172         y_water = repmat(y03,1,100);
173         plot(x_water,y_water,'color',color_plot,'linewidth',2);
174         hold off
175         ylabel('y(m)','Interpreter','latex')
176         xlabel('B(m)','Interpreter','latex')
```

```
177         legend('Exit','interpreter','latex')
178         grid on
179         set(gca,'FontName','Garamond','FontSize',12);
180         set(gca,'TickLength',[0.02 0.01])
181         set(gca,'TickDir','out');
182         box on
183         % Save frame
184         title(['t = ',num2str(round(round(t,2),0)),' [sec]'])
185         f = getframe(gcf);
186         writeVideo(obj,f);
187         hold off
188         clf
189     end
190 obj.close();
191 end
192 
193 if flag_section == 3 % paraboloid
194 % Video
195 obj = VideoWriter('Parabolic_Depth.avi','Motion JPEG AVI');
196 obj.Quality = 100;
197 obj.FrameRate = 20;
198 open(obj)
199 set(gcf,'units','inches','position',[2,2,10,3])
200     for n=1:1:(Nt/Nat)
201         if n == 1
202             t = 1;
203             pos = 1;
204         else
205             t=time_save(n);
206             pos = n;
207         end
208         % Save frame
209         Plot_Title = 'Time = %d (sec)';
210         sgtitle(sprintf(Plot_Title, time_store(n)),'fontsize',18,'
              interpreter','latex')
211         % Parabolic Function
212         % y = a*x^2 => xmax = sqrt((ymax/a))
213         ymax = max(max(Depth));
214         xmax = sqrt(ymax/a); % x to left and right directions
215         xpar = linspace(-xmax,xmax,100); % 100 points within -xmax and
              xmax deg
216         ypar = a.*xpar.^2;
217         % Now we found bottom of the channel
218         % We still need to find xleft and xright for a given y
219         y01 = Depth(pos,1);
220         y02 = Depth(pos,ceil(Nx/2));
221         y03 = Depth(pos,Nx);
```

```
y0_c = [y01; y02; y03];
xright = sqrt(y0_c/a);
xleft = - xright;
subplot(1,3,1)
title(['t = ',num2str(round(round(t/60,2),0)),' [min]'])
ylim([0 ymax]);
xlim([0 ymax]);
plot(xpar,ypar,'Color','black','LineWidth',2);
hold on
x_water = linspace(xleft(1),xright(1),100);
y_water = linspace(y01,y01,100);
plot(x_water,y_water,'color',color_plot,'linewidth',2);
ylabel('y(m)','Interpreter','latex')
xlabel('B(m)','Interpreter','latex')
legend('Entrance','interpreter','latex')
grid on
set(gca,'FontName','Garamond','FontSize',12);
set(gca,'TickLength',[0.02 0.01])
set(gca,'TickDir','out');
hold off
% second section
subplot(1,3,2)
title(['t = ',num2str(round(round(t/60,2),0)),' [min]'])
ylim([0 ymax]);
xlim([0 ymax]);
plot(xpar,ypar,'Color','black','LineWidth',2);
hold on
x_water = linspace(xleft(2),xright(2),100);
y_water = linspace(y02,y02,100);
plot(x_water,y_water,'color',color_plot,'linewidth',2);
ylabel('y(m)','Interpreter','latex')
xlabel('B(m)','Interpreter','latex')
legend('x = L/2','interpreter','latex')
grid on
set(gca,'FontName','Garamond','FontSize',12);
set(gca,'TickLength',[0.02 0.01])
set(gca,'TickDir','out');
hold off
% third section
subplot(1,3,3)
title(['t = ',num2str(round(round(t/60,2),0)),' [min]'])
ylim([0 ymax]);
xlim([0 ymax]);
plot(xpar,ypar,'Color','black','LineWidth',2);
hold on
x_water = linspace(xleft(3),xright(3),100);
y_water = linspace(y03,y03,100);
```

```
269         plot(x_water,y_water,'Color',color_plot,'linewidth',2);
270         ylabel('y(m)','Interpreter','latex')
271         xlabel('B(m)','Interpreter','latex')
272         legend('Outlet','interpreter','latex')
273         grid on
274         set(gca,'FontName','Garamond','FontSize',12);
275         set(gca,'TickLength',[0.02 0.01])
276         set(gca,'TickDir','out');
277         f = getframe(gcf);
278         writeVideo(obj,f);
279         hold off
280         clf
281     end
282 obj.close();
283 end
284
285
286 %% Plots
287 % Time Scale
288 if flag_elapsed_time == 1
289     close all
290     flag_date = 3; % 1 min, 2 hour, 3 day, 4 month
291     date_string = {'Elased time (min)','Elapsed time (h)','Elapsed time
            (days)','Elapsed time (months)'};
292     if flag_date == 1
293         time_scale = 1;
294     elseif flag_date == 2
295         time_scale = 1/60;
296     elseif flag_date == 3
297         time_scale = 1/60/24;
298     else
299         time_scale = 1/60/24/30;
300     end
301     set(gcf,'units','inches','position',[2,0,8,10])
302     subplot(3,2,1)
303     % Flows
304     plot(time_save/60,Discharge(:,1),'LineStyle','--','LineWidth',2,'
            Color','k')
305     hold on
306     plot(time_save/60,Discharge(:,ceil(Nx/2)),'LineStyle',':','LineWidth
            ',2,'Color','k')
307     hold on
308     plot(time_save/60,Discharge(:,Nx),'LineStyle','-','LineWidth',2,'
            Color','k')
309     hold on
310     xlabel(date_string(flag_date),'interpreter','latex');
```

```
311     ylabel('Flow Discharge (m\textsuperscript{3}/s)','Interpreter','
            latex');
312     legend('Entrance','L/2','Outlet','Interpreter','Latex','location','
            best')
313     % Velocity
314     subplot(3,2,2)
315     plot(time_save/60,Velocity(:,1),'LineStyle','--','LineWidth',2,'
            Color','k')
316     hold on
317     plot(time_save/60,Velocity(:,ceil(Nx/2)),'LineStyle',':','LineWidth'
            ,2,'Color','k')
318     hold on
319     plot(time_save/60,Velocity(:,Nx),'LineStyle','-','LineWidth',2,'
            Color','k')
320     %%% Normal Depth Velocity %%%
321     xlabel(date_string(flag_date),'interpreter','latex');
322     ylabel('Velocity (m/s)','Interpreter','latex');
323     legend('Entrance','L/2','Outlet','Interpreter','Latex','Location','
            best')
324     % Water Depth
325     subplot(3,2,3)
326     plot(time_save/60,Depth(:,1),'LineStyle','--','LineWidth',2,'Color',
            'k')
327     hold on
328     plot(time_save/60,Depth(:,ceil(Nx/2)),'LineStyle',':','LineWidth',2,
            'Color','k')
329     hold on
330     plot(time_save/60,Depth(:,Nx),'LineStyle','-','LineWidth',2,'Color',
            'k')
331     xlabel(date_string(flag_date),'interpreter','latex');
332     ylabel('Water Depths (m)','Interpreter','latex');
333     legend('Entrance','L/2','Outlet','Interpreter','Latex','Location','
            best')
334     % Froude Number
335     subplot(3,2,4)
336     plot(time_save/60,Froude(:,1),'LineStyle','--','LineWidth',2,'Color'
            ,'k')
337     hold on
338     plot(time_save/60,Froude(:,ceil(Nx/2)),'LineStyle',':','LineWidth'
            ,2,'Color','k')
339     hold on
340     plot(time_save/60,Froude(:,Nx),'LineStyle','-','LineWidth',2,'Color'
            ,'k')
341     xlabel(date_string(flag_date),'interpreter','latex');
342     ylabel('Froude Number','Interpreter','latex');
343     legend('Entrance','L/2','Outlet','Interpreter','Latex','Location','
            best')
```

```
344
345     % Courant Number
346     subplot(3,2,5)
347     plot(time_save/60,Courant(:,1),'LineStyle','--','LineWidth',2,'Color
            ','k')
348     hold on
349     plot(time_save/60,Courant(:,ceil(Nx/2)),'LineStyle',':','LineWidth'
            ,2,'Color','k')
350     hold on
351     plot(time_save/60,Courant(:,Nx),'LineStyle','-','LineWidth',2,'Color
            ','k')
352     xlabel(date_string(flag_date),'interpreter','latex');
353     ylabel('Courant Number','Interpreter','latex');
354     legend('Entrance','L/2','Outlet','Interpreter','Latex','Location','
            best')
355
356     % Rating Curve
357     % Solving for normal Depth
358     ymin = min(min(Depth));
359     ymax = max(max(Depth));
360     hs = 1; % 1 node
361     % hs = ceil(1);
362     if flag_section ~= 4
363             y_m = [ymin:0.01:ymax]'; % meters
364             Qn = 1/nm(hs).*A_function(D,Z1,Z2,a,b,y_m).*Rh_function(D,Z1
                    ,Z2,a,b,y_m).^(2/3).*I0(hs)^0.5;
365     else
366         % [y_table, A, P, Rh, y_bar, n_med, Beta, v, B, Q]
367         % [   1,    2, 3, 4,    5,    6,      7,  8,  9, 10]
368         col1 = 2; % Col with A
369         for jj = 1:length(Flow_Area(:,1))
370             Qn(jj,1) = Vlookup_g(irr_table,col1,Flow_Area(jj,hs),10); %
                    Attention here
371             y_m(jj,1) = Vlookup_g(irr_table,col1,Flow_Area(jj,hs),1);
372             rh_i = Vlookup_g(irr_table,col1,Flow_Area(jj,hs),4);
373         end
374     end
375     subplot(3,2,6)
376     tbegin = 30; % (steps), considering initial stabilization of the
            domain
377     plot(Discharge(2:end,hs),Depth(2:end,hs),'LineStyle','--','LineWidth
            ',2,'Color','k')
378     hold on
379     plot(Discharge(2:end,ceil(Nx/2)),Depth(2:end,ceil(Nx/2)),'LineStyle'
            ,':','LineWidth',2,'Color','k')
380     hold on
381     plot(Qn,y_m,'LineStyle','-','LineWidth',2,'Color','k')
```

```
382     xlabel('Flow Discharge (m\textsuperscript{3}/s)','Interpreter','
            latex');
383     ylabel('Water Depth (m)','Interpreter','latex');
384     ylim([ymin 1.1*max([max(y_m),max(y(ceil(Nx)))])]);
385     legend('Q(Inlet)','Q(Nx/2)','$Q_{n}$ (L)','Interpreter','Latex','
            Location','best')
386     hold off
387     exportgraphics(gcf,fullfile(folderName,'Summary_Charts.pdf'),'
            ContentType','vector')
388     clf
389     close all
390 else
391     close all
392     % Time Calculation
393     time_duration = time_save/3600/24 + Date_Begin;
394     set(gcf,'units','inches','position',[2,0,8,10])
395     date_string = {''};
396     flag_date = 1;
397     subplot(3,2,1)
398     % Flows
399     plot(time_duration,Discharge(:,1),'LineStyle','--','LineWidth',2,'
            Color','k')
400     hold on
401     plot(time_duration,Discharge(:,ceil(Nx/2)),'LineStyle',':','
            LineWidth',2,'Color','k')
402     hold on
403     plot(time_duration,Discharge(:,Nx),'LineStyle','-','LineWidth',2,'
            Color','k')
404     hold on
405     xlabel(date_string(flag_date),'interpreter','latex');
406     ylabel('Flow Discharge (m\textsuperscript{3}/s)','Interpreter','
            latex');
407     legend('Entrance','L/2','Outlet','Interpreter','Latex','location','
            best')
408     % Velocity
409     subplot(3,2,2)
410     plot(time_duration,Velocity(:,1),'LineStyle','--','LineWidth',2,'
            Color','k')
411     hold on
412     plot(time_duration,Velocity(:,ceil(Nx/2)),'LineStyle',':','LineWidth
            ',2,'Color','k')
413     hold on
414     plot(time_duration,Velocity(:,Nx),'LineStyle','-','LineWidth',2,'
            Color','k')
415     %%% Normal Depth Velocity %%%
416     xlabel(date_string(flag_date),'interpreter','latex');
417     ylabel('Velocity (m/s)','Interpreter','latex');
```

```
418     legend('Entrance','L/2','Outlet','Interpreter','Latex','Location','
            best')
419     % Water Depth
420     subplot(3,2,3)
421     plot(time_duration,Depth(:,1),'LineStyle','--','LineWidth',2,'Color'
            ,'k')
422     hold on
423     plot(time_duration,Depth(:,ceil(Nx/2)),'LineStyle',':','LineWidth'
            ,2,'Color','k')
424     hold on
425     plot(time_duration,Depth(:,Nx),'LineStyle','-','LineWidth',2,'Color'
            ,'k')
426     xlabel(date_string(flag_date),'interpreter','latex');
427     ylabel('Water Depths (m)','Interpreter','latex');
428     legend('Entrance','L/2','Outlet','Interpreter','Latex','Location','
            best')
429     % Froude Number
430     subplot(3,2,4)
431     plot(time_duration,Froude(:,1),'LineStyle','--','LineWidth',2,'Color
            ','k')
432     hold on
433     plot(time_duration,Froude(:,ceil(Nx/2)),'LineStyle',':','LineWidth'
            ,2,'Color','k')
434     hold on
435     plot(time_duration,Froude(:,Nx),'LineStyle','-','LineWidth',2,'Color
            ','k')
436     xlabel(date_string(flag_date),'interpreter','latex');
437     ylabel('Froude Number','Interpreter','latex');
438     legend('Entrance','L/2','Outlet','Interpreter','Latex','Location','
            best')
439
440     % Courant Number
441     subplot(3,2,5)
442     plot(time_duration,Courant(:,1),'LineStyle','--','LineWidth',2,'
            Color','k')
443     hold on
444     plot(time_duration,Courant(:,ceil(Nx/2)),'LineStyle',':','LineWidth'
            ,2,'Color','k')
445     hold on
446     plot(time_duration,Courant(:,Nx),'LineStyle','-','LineWidth',2,'
            Color','k')
447     xlabel(date_string(flag_date),'interpreter','latex');
448     ylabel('Courant Number','Interpreter','latex');
449     legend('Entrance','L/2','Outlet','Interpreter','Latex','Location','
            best')
450
451     % Rating Curve
```

```
452     % Solving for normal Depth
453     ymin = min(min(Depth));
454     ymax = max(max(Depth));
455     hs = 1; % 1 node
456     % hs = ceil(1);
457     if flag_section ~= 4
458             y_m = [ymin:0.01:ymax]'; % meters
459             Qn = 1/nm(hs).*A_function(D,Z1,Z2,a,b,y_m).*Rh_function(D,Z1
                    ,Z2,a,b,y_m).^(2/3).*I0(hs)^0.5;
460     else
461         % [y_table, A, P, Rh, y_bar, n_med, Beta, v, B, Q]
462         % [   1,    2, 3, 4,    5,    6,      7,  8,  9, 10]
463         col1 = 2; % Col with A
464         for jj = 1:length(Flow_Area(:,1))
465             Qn(jj,1) = Vlookup_g(irr_table,col1,Flow_Area(jj,hs),10); %
                    Attention here
466             y_m(jj,1) = Vlookup_g(irr_table,col1,Flow_Area(jj,hs),1);
467             rh_i = Vlookup_g(irr_table,col1,Flow_Area(jj,hs),4);
468         end
469     end
470     subplot(3,2,6)
471     tbegin = 30; % (steps), considering initial stabilization of the
            domain
472     plot(Discharge(2:end,hs),Depth(2:end,hs),'LineStyle','--','LineWidth
            ',2,'Color','k')
473     hold on
474     plot(Discharge(2:end,ceil(Nx/2)),Depth(2:end,ceil(Nx/2)),'LineStyle'
            ,':','LineWidth',2,'Color','k')
475     hold on
476     plot(Qn,y_m,'LineStyle','-','LineWidth',2,'Color','k')
477     xlabel('Flow Discharge (m\textsuperscript{3}/s)','Interpreter','
            latex');
478     ylabel('Water Depth (m)','Interpreter','latex');
479     ylim([ymin 1.1*max([max(y_m),max(y(ceil(Nx)))])]);
480     legend('Q(Inlet)','Q(Nx/2)','$Q_{n}$ (L)','Interpreter','Latex','
            Location','best')
481     hold off
482     exportgraphics(gcf,fullfile(folderName,'Summary_Charts.pdf'),'
            ContentType','vector')
483     clf
484     close all
485 end
486
487 %% States Post-Processing
488 states_post_processing
489 %% Cross-Section Post-Processing
490 if flag_section == 4
```

```
    cross_section_post_processing
end

%% Lateral Profiles
if flag_section ~= 4
    wse_top_width_regular
end
%% Detailed Output
Detailed_Output_Script
```

8.5.6.5 Cross-Section Post Processing

The following matlab script shows the post processing of cross-section data.

```
    % Post-Processing Routine
% Model: HyPro-SWE
% Developer: Marcus Nobrega
% Last Update: 4/29/2023
% Goal: Create animations of water depth, top width, and water surface
% elevation

close all
close(video);

Video_Name = 'Depth_WSE_Top_Width.mp4';

% Set up video
video = VideoWriter(Video_Name,'MPEG-4');
open(video);

% Define water depths for each time
depths = Depth(:,1)';

% Preallocate Top Width
B2 = zeros(size(Flow_Area));

% Time
t = time_save; % Sec

% Define tick size
ticksize = [0.015 0.01];

% Define Tick Position
tickposition = 'in';


% Define polygon for the cross-section
polygon = polyshape(x_cross,y_cross);
```

```
35
36 % Water Surface Elevation
37 wse = Depth + repmat(inv_el',[size(Depth,1),1]);
38
39 % Color
40 color_plot = [21, 179, 196]/255;
41 set(gcf,'units','inches','position',[2,0,8,10])
42
43 if flag_elapsed_time ~= 1
44     % Time Calculation
45     time_duration = time_save/3600/24 + Date_Begin;
46 end
47
48 % Iterate through all time steps
49 set(gca,'FontSize',14,'FontName','Garamond')
50 for i=1:(length(t))
51
52     if flag_elapsed_time == 1
53         Plot_Title = 'Time = %d (sec)';
54         sgtitle(sprintf(Plot_Title, time_store(i)),'fontsize',18,'
              interpreter','latex')
55     else
56         sgtitle(string(time_duration(i)),'fontsize',18,'interpreter','
              latex');
57     end
58     for j = 1:3 % 3 Cross-sections
59         if j == 1
60             sec = 1;
61         elseif j == 2
62             sec = ceil(Nx/2);
63         else
64             sec = Nx;
65         end
66         depths = Depth(i,sec)';
67         hold on
68         subplot(3,3,(j))
69         % Set title with time and water depth
70         % Define the water depth for this time step
71         depth_line = depths*ones(1,length(x_cross));
72         plot(x_cross, y_cross, '-k', 'LineWidth', 2,Marker='*'); hold on
73         % Find where depth line intersects cross-section polygon
74         [x_intersect, y_intersect] = polyxpoly(x_cross,y_cross,x_cross,
              depth_line);
75         if length(x_intersect)  > 1
76             % Finding Inside Values
77             idx1 = x_cross >= x_intersect(1);
78             idx2 = x_cross <= x_intersect(end);
```

```
            idx = logical(idx1.*idx2); % Both cases
            x_pol = [x_intersect(1), x_cross(idx)', x_intersect(end)];
            y_pol = [y_intersect(1), y_cross(idx)', y_intersect(2)];
            hold on
            % If the depth line intersects the polygon, plot it
            if ~isempty(x_intersect) && ~isempty(y_intersect)
                depth_plot = depth_line(1)*ones(size(x_pol));
                fill([x_pol fliplr(x_pol)], [y_pol fliplr(depth_plot)],
                    color_plot)
            else
                error('Call developer')
            end
        end
        box on
        if j == 1
            ylabel('Depth [m]','Interpreter','latex')
        end
        xlabel('Station [m]','Interpreter','latex')
        title(sprintf('x = %0.2f m, h = %0.2f m', round((sec-1)*dx,2),
            depths),'fontsize',16,'interpreter','latex');
        set(gca,'FontSize',12,'FontName','Garamond')
        % Set Tick Postion and Tick Size
        set(gca,'TickLength',ticksize)
        set(gca,'TickDir',tickposition)
    end

    % --------------- Plotting Channel Width ----------------- %
    subplot(3,3,[4 5 6]);
    if flag_section ~= 4
        B2 = B_function(D,Z1,Z2,a,b,y);
    else
        for pos_b = 1:length(Flow_Area(1,:))
            % [y_table, A, P, Rh, y_bar, n_med, Beta, v, B, Q]
            % [   1,    2, 3, 4,    5,    6,      7,  8,  9, 10]
            B2(i,pos_b) = Vlookup_g(irr_table,col1,Flow_Area(i,pos_b),9)
                ;
        end
    end
    offset = max(x_cross)/2; % From station data
    right_margin = B2(i,:)/2 + offset; left_margin = -B2(i,:)/2 + offset
        ;
    plot(x,right_margin,'k','LineWidth',2); set(gca,'YDir','reverse');
    hold on
    plot(x,left_margin,'k','LineWidth',2); set(gca,'YDir','reverse');
    hold on
    fill([x' fliplr(x')], [left_margin fliplr(right_margin)],color_plot)
    xlabel('$x$ [m]','Interpreter','latex');
```

```
    ylabel('Station [m]','Interpreter','latex');
    ylim([0, max(x_cross)]);
    grid on
    title(sprintf('$B_{{max}}(t)$ = %0.2f m', max(right_margin -
        left_margin)),'fontsize',16,'interpreter','latex');
    set(gca,'FontSize',12,'FontName','Garamond')
    % Set Tick Postion and Tick Size
    set(gca,'TickLength',ticksize)
    set(gca,'TickDir',tickposition)

    % ---------------------  Ploting Water Surface Elevation ------- %
    subplot(3,3,[7 8 9])
    plot(x,inv_el,'LineWidth',4,'LineStyle','-','Color','k');
    hold on
    plot(x,wse(i,:),'k','LineWidth',2,'LineStyle','-','Color',color_plot
        );
    fill([x' fliplr(x')], [inv_el' fliplr(wse(i,:))],color_plot)
    xlabel('$x$ [m]','Interpreter','latex');
    ylabel('Water Surface Elevation [m]','Interpreter','latex');
    ylim([0.98*min(min(wse - Depth)) max(max(1.01*wse))])
    grid on
    title(sprintf('$WSE_{{max}}(t)$ = %0.2f m', max(wse(i,:))),'fontsize
        ',16,'interpreter','latex');
    set(gca,'FontSize',12,'FontName','Garamond')
    % Set Tick Postion and Tick Size
    set(gca,'TickLength',ticksize)
    set(gca,'TickDir',tickposition)

    % Save the frame for the video
    % Set background color and write to video
    frame = getframe(gcf);
    writeVideo(video,frame);
    hold off
    clf
end
% Close video writer
close(video);
close all
```

8.5.6.6 Water Surface Elevation Profiles

The following matlab script shows the code to generate water surface elevation profiles in regular sections.

```
    % Post-Processing Routine
% Model: HyPro-SWE
% Developer: Marcus Nobrega
% Last Update: 4/29/2023
```

```
% Goal: Create animations of WSE and Top Width for regular sections

close all

Video_Name = 'WSE_Top_Width.avi';

% Set up video
video = VideoWriter(Video_Name,'MPEG-4');
open(video);

% Define water depths for each time
depths = Depth(:,1)';

% Preallocate Top Width
B2 = zeros(size(Flow_Area));

% Time
t = time_save; % Sec

% Define tick size
ticksize = [0.02 0.01];



% Water Surface Elevation
wse = Depth + repmat(inv_el',[size(Depth,1),1]);

% Color
color_plot = [21, 179, 196]/255;
set(gcf,'units','inches','position',[2,0,8,10])

% Iterate through all time steps
set(gca,'FontSize',14,'FontName','Garamond')
for i=1:length(t)
    Plot_Title = 'Time = %d (sec)';
    sgtitle(sprintf(Plot_Title, time_store(i)),'fontsize',18,'
       interpreter','latex')
        % --------------- Plotting Channel Width ----------------- %
    subplot(2,3,[1 2 3]);
    if flag_section ~= 4
        B2 = B_function(D,Z1,Z2,a,b,Depth);
    else
        for pos_b = 1:length(Flow_Area(1,:))
            % [y_table, A, P, Rh, y_bar, n_med, Beta, v, B, Q]
            % [   1,    2, 3, 4,    5,    6,      7,  8,  9, 10]
            B2(i,pos_b) = Vlookup_g(irr_table,col1,Flow_Area(i,pos_b),9)
               ;
```

```
        end
    end
    if flag_section == 1
         offset = b/2 + (Z1 + Z2)/2*max(max(depths));
         xmax_plot = (Z1 + Z2)*max(max(depths)) + b;
    elseif flag_section == 2
        offset = D/2;
        xmax_plot = D;
    elseif flag_section == 3
        offset = xmax/2;
        xmax_plot = xmax;
    else
        offset = max(x_cross)/2; % From station data
        xmax_plot = max(x_cross);
    end
    right_margin = B2(i,:)/2 + offset; left_margin = -B2(i,:)/2 + offset
       ;
    plot(x,right_margin,'k','LineWidth',2); set(gca,'YDir','reverse');
    hold on
    plot(x,left_margin,'k','LineWidth',2); set(gca,'YDir','reverse');
    hold on
    fill([x' fliplr(x')], [left_margin fliplr(right_margin)],color_plot)
    xlabel('$x$ [m]','Interpreter','latex');
    ylabel('Station [m]','Interpreter','latex');
    ylim([0, xmax_plot]);
    xlim([0, max(x)]);
    grid on
    title(sprintf('$B_{{max}}(t)$ = %.2f m', max(right_margin -
       left_margin)),'fontsize',16,'interpreter','latex');
    set(gca,'FontSize',12,'FontName','Garamond')

    % ---------------------  Ploting Water Surface Elevation ------- %
    subplot(2,3,[4 5 6])
    plot(x,inv_el,'LineWidth',4,'LineStyle','-','Color','k');
    hold on
    plot(x,wse(i,:),'k','LineWidth',2,'LineStyle','-','Color',color_plot
       );
    fill([x' fliplr(x')], [inv_el' fliplr(wse(i,:))],color_plot)
    xlabel('$x$ [m]','Interpreter','latex');
    ylabel('Water Surface Elevation [m]','Interpreter','latex');
    ylim([0.98*min(min(wse - Depth)) max(max(1.01*wse))])
    grid on
    title(sprintf('$WSE_{{max}}(t)$ = %.2f m', max(wse(i,:))),'fontsize'
       ,16,'interpreter','latex');

    % Save the frame for the video
    set(gca,'FontSize',12,'FontName','Garamond')
```

```
    % Set background color and write to video
    frame = getframe(gcf);
    writeVideo(video,frame);
    hold off
end
% Close video writer
close(video);
close all
```

8.5.6.7 Detailed Output

The following script generates .csv outputs summarizing the collected data from the simulation.

```
    % HyProSWE Model
% Output .csv script
% Developer: Marcus Nobrega
% Goal: Create a detailed output from modeling results
% Last updated: 4/30/2023


%%% ----------------------- All rights reserved --------------------- %%

% Number of states
ns = 6;
% 0 - time, 1 - flow, 2 - depth, 3 - velocity, 4 - Courant, 5 - Froude,
    6,
% 7 WSE

% Concatenate data
t = time_store; % time vector
h = Depth; % water level matrix
q = Discharge; % flow rate matrix
v = Velocity; % velocity matrix
f = Froude; % Froude number matrix
c = Courant; % Courant number matrix
z = x; % distance matrix

% Round Data
decimal_places = 3;

data = zeros(size(Depth,1),size(Depth,2),ns);

data(:,:,1) = Depth;
data(:,:,2) = Discharge;
data(:,:,3) = Velocity;
data(:,:,4) = Froude;
data(:,:,5) = Courant;
```

```
data(:,:,6) = wse;


if flag_output == 1
    for i = 1:(Nx*ns)
        j = floor((i-1)/ns);
        x_cell = j*dx;
        if mod(i-1,ns) == 0 || (i-1)/ns == 1
            states_title(1,i) = cellstr(sprintf('Depth (m), x(m) = %0.2f
                ',x_cell));
        elseif mod(i-1,ns) == 1 || (i-1)/ns == 2
            states_title(1,i) = cellstr(sprintf('Discharge (m^3/s), x(m)
                 = %0.2f',x_cell));
        elseif mod(i-1,ns) == 2 || (i-1)/ns == 3
            states_title(1,i) = cellstr(sprintf('Velocity (m/s), x(m) =
                %0.2f',x_cell));
        elseif mod(i-1,ns) == 3 || (i-1)/ns == 4
            states_title(1,i) = cellstr(sprintf('Froude (-), x(m) = %0.2
                f',x_cell));
        elseif mod(i-1,ns) == 4 || (i-1)/ns == 5
            states_title(1,i) = cellstr(sprintf('Courant Number (-), x(m
                ) = %0.2f',x_cell));
        elseif mod(i-1,ns) == 5 || (i-1)/ns == 6
            states_title(1,i) = cellstr(sprintf('Water Surface Elevation
                 (m), x(m) = %0.2f',x_cell));
        end
    end
else
    for i = 1:(Nx*ns)
        if mod(i,Nx) ~= 0
            j = mod(i,Nx);
            x_cell = (j-1)*dx; % m
        else
            j = Nx;
            x_cell = (j-1)*dx; % m
        end
        if floor(i/Nx) == 0 || i/Nx == 1
            states_title(1,i) = cellstr(sprintf('Depth (m), x(m) = %0.2f
                ',x_cell));
        elseif floor(i/Nx) == 1 || i/Nx == 2
            states_title(1,i) = cellstr(sprintf('Discharge (m^3/s), x(m)
                 = %0.2f',x_cell));
        elseif floor(i/Nx) == 2 || i/Nx == 3
            states_title(1,i) = cellstr(sprintf('Velocity (m/s), x(m) =
                %0.2f',x_cell));
        elseif floor(i/Nx) == 3 || i/Nx == 4
            states_title(1,i) = cellstr(sprintf('Froude (-), x(m) = %0.2
```

```
                f',x_cell));
        elseif floor(i/Nx) == 4 || i/Nx == 5
            states_title(1,i) = cellstr(sprintf('Courant Number (-), x(m
                ) = %0.2f',x_cell));
        elseif floor(i/Nx) == 5 || i/Nx == 6
            states_title(1,i) = cellstr(sprintf('Water Surface Elevation
                 (m), x(m) = %0.2f',x_cell));
        end
    end
end
% states_title(1,end+1) = cellstr(sprintf('Water Surface Elevation (m),
    x(m) = %0.2f',dx*(Nx-1)));
time_string = {'Time (sec)'};
% Table Headers
table_headers = [time_string, states_title];
data_save = zeros(length(time_store),ns*Nx);


if flag_output == 1
    % Detailed Output for each section with all states together
    for i = 1:length(time_store)
        % For all time
        for j = 1:ns
            if j == 2
                ttt = 1;
            end
            % For all states
            for k = 1:Nx
                % For all nodes
                %                 data_table = round(data(i,k,j),
                    decimal_places);
                %                 data_save(i,ns*(k-1) +  j) =
                    data_table;
                data_table = round(data(i,k,j),decimal_places);
                data_save(i,ns*(k-1) +  j) = data_table;
            end
        end
    end
else
    % Detailed Output for each state for each section
    for i = 1:length(time_store)
        % For all time
        for j = 1:ns
            % For all states
            for k = 1:Nx
                % For all nodes
                data_table = round(data(i,k,j),decimal_places);
```

```
                data_save(i,k + (j-1)*Nx) = data_table;
            end
        end
    end
end



data_save = [time_save, data_save]; % Concatenating dataset to the time
T = array2table(data_save,'VariableNames',table_headers);
writetable(T,'Detailed_Output.csv','Delimiter',',');
disp('Attention: Data exported in .CSV');


%% Detailed Output per Cross-Section (Similarly as HEC-RAS)
i_prev = 1;
if flag_elapsed_time == 1
    time_str = 'Elapsed Time (sec)';
else
    time_str = 'Time';
end
Titles_Section = {'x(m)',time_str,' Depth (m)','Discharge (m3/s)','
   Velocity (m/s)','Froude (-)','Courant Number (-)','WSE (m)'};
for i = 1:Nx
    % Through each section
    for j = 1:length(time_store)
        % Through each time
        for k = 1:ns
            row = length(time_store)*(i-1) + j;
            data_save_XS(row,k) = data(j,i,k);
        end
    end
end

zzz = data_save_XS;
clear data_table data_save_XS
for i = 1:Nx
    x_cell = (i-1)*dx;
    if i == 1
        section(1,1) = x_cell;
    end
    row = length(time_store)*(i-1) + 1;
    row_i = length(time_store)*(i);
    data_save_XS((row + i-1):(row_i + i-1),:) = zzz(row:row_i,:);
    data_save_XS(row_i+1 + i - 1,:) = nan;

    section((row + i-1):(row_i + i-1),:) = x_cell;
```

```
159     section(row_i+1 + i - 1,:) = NaN;
160 end
161 section(size(data_save_XS,1),1) = x_cell;
162 % section(end:size(data_save_XS,1)) = [];
163 % section(section == 0) = NaN;
164 if flag_elapsed_time == 1
165     time_vector = time_save;
166 else
167     time_vector = time_begin + time_save/86400; % Days minutes and
        seconds
168 end
169
170 delta = 0;
171 for i = 1:Nx
172     row = length(time_store)*(i-1) + 1;
173     row_i = length(time_store)*(i);
174     time_vector_total((row + i-1):(row_i + i-1),1) = time_vector;
175     time_vector_total(row_i+1 + i - 1,:) = nan;
176 end
177
178 data_save = [section, time_vector_total, data_save_XS]; % Concatenating
    dataset to the time
179 T = array2table(data_save,'VariableNames',Titles_Section);
180
181 T.Properties.VariableNames(1:size(data_save,2)) = Titles_Section;
182 writetable(T,'Detailed_Output_XS.csv','Delimiter',',');
183 disp('Attention: XS Data exported in .CSV');
```

8.6 Appendix VI - Supplementary Material of Chapter 7

This supplemental material is organized as follows:

- Sec. 8.6.1: 1-D Dam Break Hydrodynamic Model.
- Sec. 8.6.2: Brumadinho Cross-Section Data.
- Sec. 8.6.3: Brumadinho Lateral View.
- Sec. 8.6.4: Breach Hydrographs.

8.6.1 1-D Dam Break Hydrodynamic Model

Derived from the Navier-Stokes equation for cases where (2-D) spatial dimension scale is orders of magnitude larger than the vertical scale, the full-momemtum Saint-Venant Equations (SVE) are the combination of conservation of mass and momentum. These two equations can be written in a vector state-space representation given by:

$$\frac{\partial \mathbf{q}(x,t)}{\partial x} + \frac{\partial \mathbf{f}(x,t)}{\partial t} = \mathbf{s}(x,t) \tag{8.63}$$

where x is the space, t is the time, and vectors $\boldsymbol{q}(x,t)$, $\boldsymbol{f}(x,t)$ and $\boldsymbol{s}(x,t)$ are described as follows, neglecting indexes x and t.

To solve Eq. (8.63), we define:

$$\boldsymbol{q} = [A,\ Q]^T \tag{8.64a}$$
$$\boldsymbol{f} = [Q,\ (\beta|v|Av + gA\bar{y})]^T \tag{8.64b}$$
$$\boldsymbol{s} = [0,\ (gA(I_o - I_f))] \tag{8.64c}$$
$$I_f = \frac{n^2 Q|Q|}{R_h^{4/3} A^2} \tag{8.64d}$$
$$Q = |v|\text{signal}(v)A \tag{8.64e}$$
$$\beta = \left(1 + \frac{gn^2}{R_h^{1/3}\kappa^2}\right) \tag{8.64f}$$

where A is the cross-section area, v is the wave velocity, g is the gravity acceleration, $\bar{y}$ is the distance from the water surface to the centroid of the cross-section, I_o is the bottom slope and I_f is the friction slope, β is the Boussinesq coefficient for moment transfer corrections and κ is the von Kármáns coefficient (Yang et al., 2018) usually assumed as 0.41. Both A and v are the main states solved for the longitudinal distance x and time t, such that $A = A(x,t)$ and $v = v(x,t)$. In the following derivations of this paper, we neglect the x and t indexes for easier notation, as well as for other states dependent on A and v.

Vector $\boldsymbol{q}$ from Eq. (8.64a) collects the main state variables, whereas $\boldsymbol{f}$ from Eq. (8.64b) has the terms of mass balance and momentum conservation in their terms, respectively. The source terms are given by $\boldsymbol{s}$ in Eq. (8.64c), where the sink/source of fluid can be added by changing the zero value in the first term of $\boldsymbol{s}$. The second term of $\boldsymbol{s}$ refers to the gravity and friction forces represented by the bottom slope (I_o) and the friction slope (I_f). The friction slope is calculated using Manning's equation given in Eq. (8.64d). Flow can change direction and is modeled considering the signal of the velocity by Eq. (8.64e). Finally, the change in floodplain momentum transfer is expressed by β.

The 1-D dam breach model is a set of hyperbolic partial differential equations (HPDE) presented in Eq. 8.63 only have analytical solutions for simplified cases and are usually numerically solver either by implicit (Akan e Iyer, 2021) or by explicit (Gomes Jr et al., 2023a) schemes. Using the latter with a Lax-Friedrichs (Lax, 1954) discretization of the HPDE presented in Eq. 8.63, we can write:

$$\begin{aligned}\mathbf{q}_i(t+\Delta t) = &\frac{1}{2}\Big(\mathbf{q}_{i-1}(t) + \mathbf{q}_{i+1}(t)\Big) \\ &- \frac{\Delta t}{2\Delta x}\Big(\mathbf{f}_{i+1} - \mathbf{f}_{i-1}(t)\Big) \\ &+ \frac{1}{2}\Big(\mathbf{s}_{i-1}(t) + \mathbf{s}_{i+1}(t)\Big)\end{aligned}$$

where Δt is the model time-step and Δx is the space discretization

The numerical solution of Eq. (8.65) requires depth-varying functions of flow area, hydraulic radius, wet perimeter, and the calculation of the centroid of the cross-section. These functions are typically not available for complex real-world cross sections (Gomes Jr et al., 2023a). However, approximate solutions, such as fitting an asymmetric trapezoid, can be an efficient mathematical solution (Ferreira et al., 2017). The distance from the surface to the centroid, the wetted area, the wetted perimeter, the maximum width, and the hydraulic radius are given by Eq. 8.65. An schematic of the trapezoid section is shown in Fig. A.37.

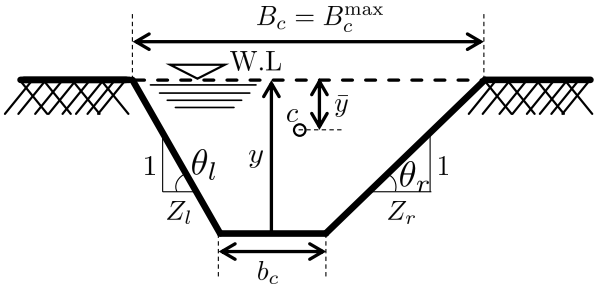

Figure A.37. Asymmetric trapezoid schematics, where b_c is the bottom width, B_c is the top width, θ_l is the left angle, Z_l is the cotangent of this angle, θ_r is the angle of the right margin, Z_r is the cotangent of this angle, c is the centroid coordinate of the cross-section, and y is the water depth taken from the invert elevation.

XS	Elevation [m]	b [m]	Z_l [m/m]	Z_r [m/m]	Segment	Δx [m]	L [m]	s_0 [m/m]	Node
1	856	200	6.25	7.50	1-2	560	560	3.57%	59
2	836	100	6.04	9.43	2-3	790	1350	1.77%	143
3	822	100	7.58	10.61	3-4	1030	2380	2.43%	252
4	797	50	4.78	5.65	4-5	560	2940	0.18%	312
5	796	50	6.90	4.14	5-6	840	3780	1.07%	401
6	787	50	3.13	7.81	6-7	570	4350	1.23%	461
7	780	40	4.38	7.19	7-8	665	5015	1.05%	531
8	773	200	5.56	19.44	8-9	960	5975	0.83%	633
9	765	100	14.67	13.33	9-10	440	6415	0.80%	680
10	761.5	100	6.58	4.74	10-11	800	7215	0.50%	765
11	757.5	30	7.33	7.33	11-12	500	7715	0.90%	818
12	753	60	5.91	8.18	12-13	360	8075	0.42%	856
13	751.5	50	2.40	6.00	13-14	300	8375	0.50%	888
14	750	100	7.24	5.17	14-15	340	8715	2.65%	924
15	741	120	5.68	4.73	15-16	730	9445	0.41%	1001
16	738	120	5.68	4.73					

Table A.10. Cross-section data of Brumadinho downstream area.

$$\bar{y} = y - \frac{y^2}{6A}\left[y\left(Z_l + Z_r\right) + 3b_c\right] \tag{8.65a}$$

$$A = \left[2b_c + y\left(Z_l + Z_r\right)\right]\frac{y}{2} \tag{8.65b}$$

$$P = b + y\left(\sqrt{1 + Z_l^2} + \sqrt{1 + Z_r^2}\right) \tag{8.65c}$$

$$B_c = b_c + y\left(Z_l + Z_r\right) \tag{8.65d}$$

$$R_h = \frac{A}{P} \tag{8.65e}$$

8.6.2 Brumadinho Cross-Section Data

The Brumadinho cross-sections used to simulate the dam-break is presented in Fig. A.38. The data derived from these cross-sections are summarized in Tab. A.10 and shown in Figs. A.38 to A.42.

8.6.3 Brumadinho Lateral View

The lateral view of the dam and the simplification used in the model are shown in Fig. A.43.

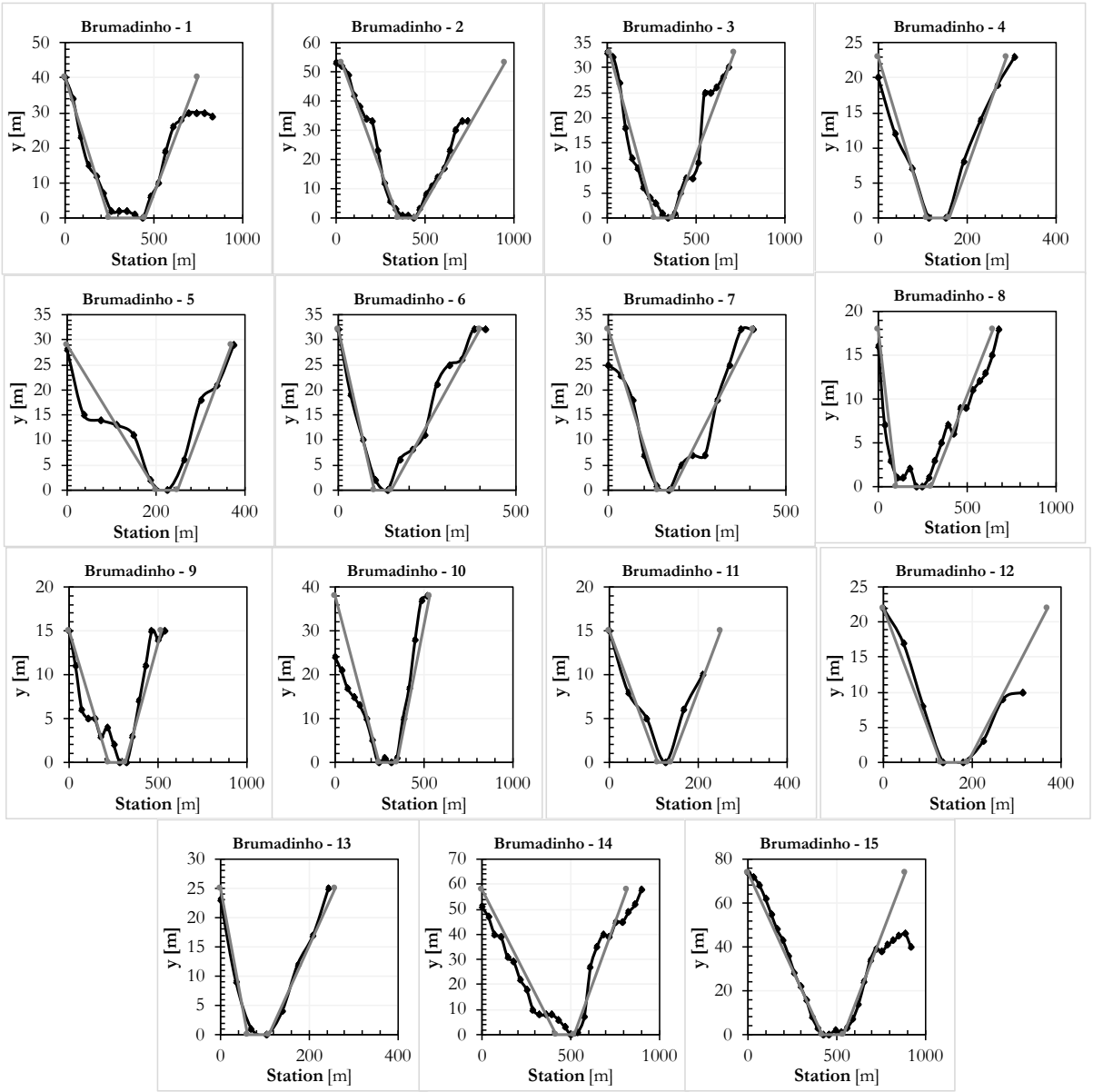

Figure A.38. Asymmetric trapezoid approximation on Brumadinho's downstream cross-sections.

8.6.4 Breach Hydrographs

The breach hydrograph as well as the temporal evolution of water depth for all 20 dams simulated are presented in Fig. A.44

References

Akan, A. O. e Iyer, S. S. (2021). *Open channel hydraulics*. Butterworth-Heinemann.

Allen, R. G., Jensen, M. E., Wright, J. L., e Burman, R. D. (1989). Operational estimates of reference evapotranspiration. *Agronomy journal*, 81(4):650–662.

Allen, R. G., Pereira, L. S., Raes, D., Smith, M., et al. (1998). Crop evapotranspiration-guidelines for computing crop water requirements-fao irrigation and drainage paper 56. *Fao, Rome*, 300(9):D05109.

Bartier, P. M. e Keller, C. P. (1996). Multivariate interpolation to incorporate thematic surface data using inverse distance weighting (idw). *Computers & Geosciences*, 22(7):795–799.

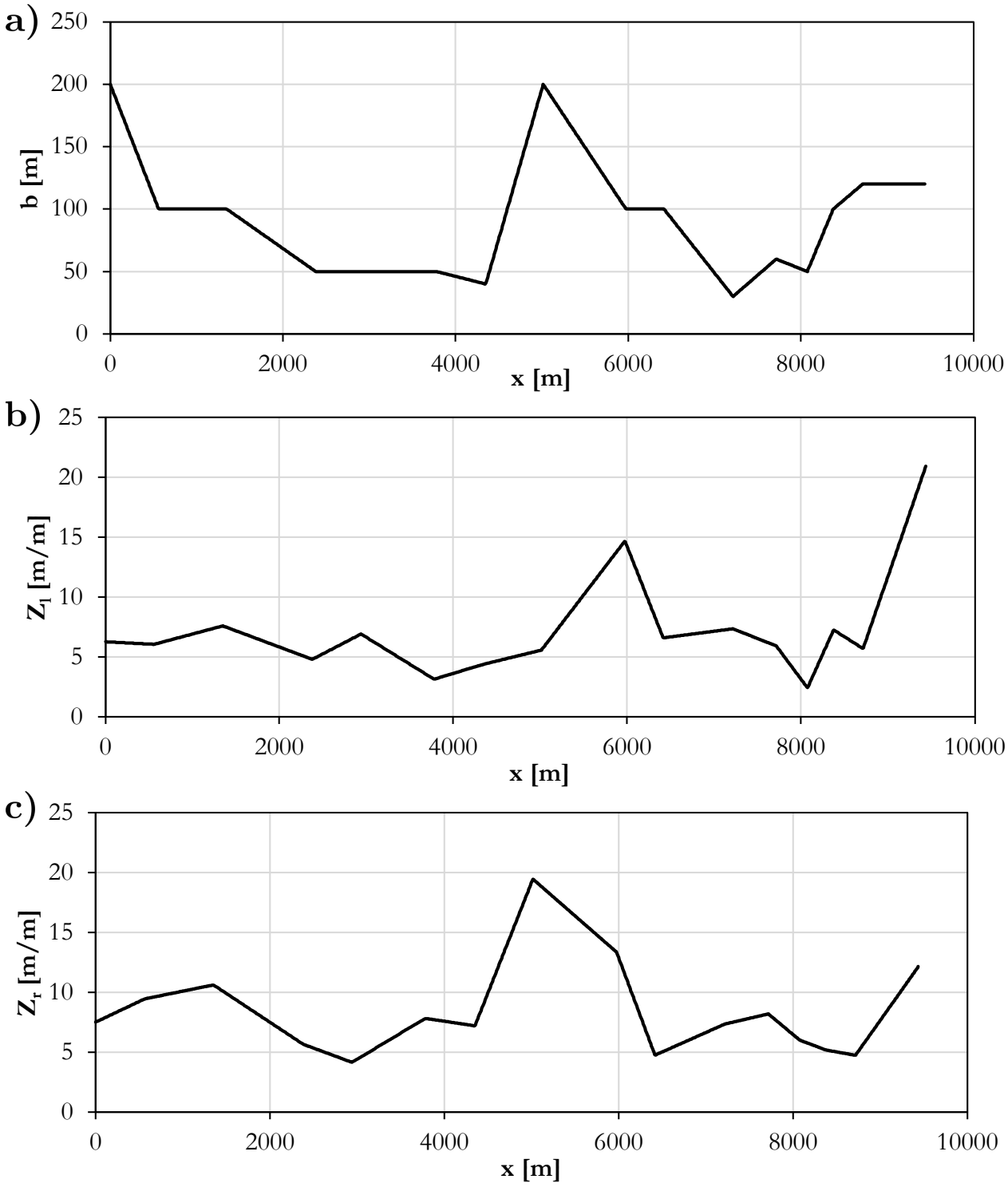

Figure A.39. Cross-section characteristics over the downstream channel.

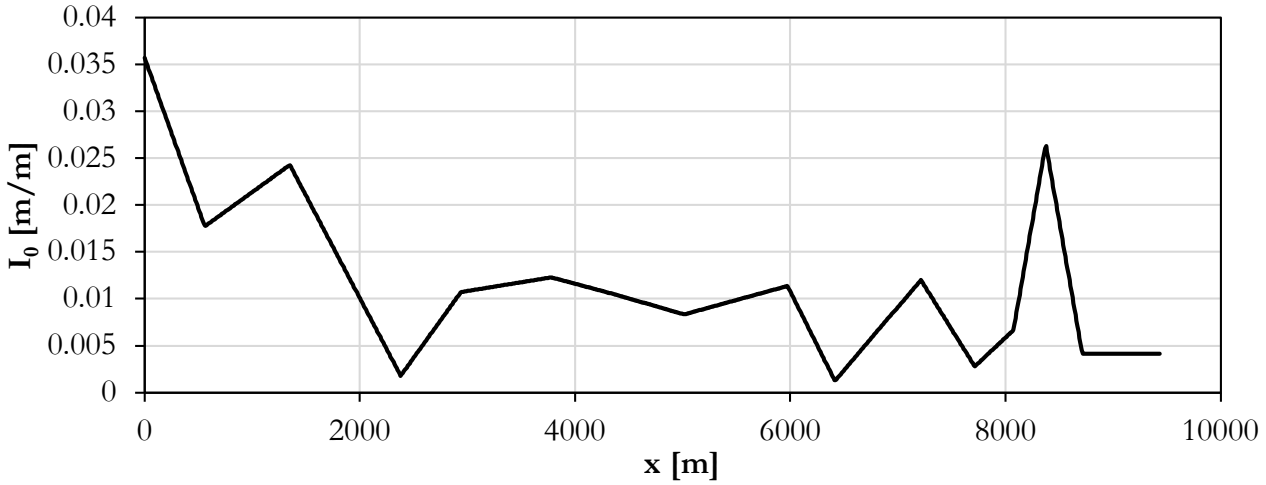

Figure A.40. Slope profile of the Brumadinho's dam downstream channel.

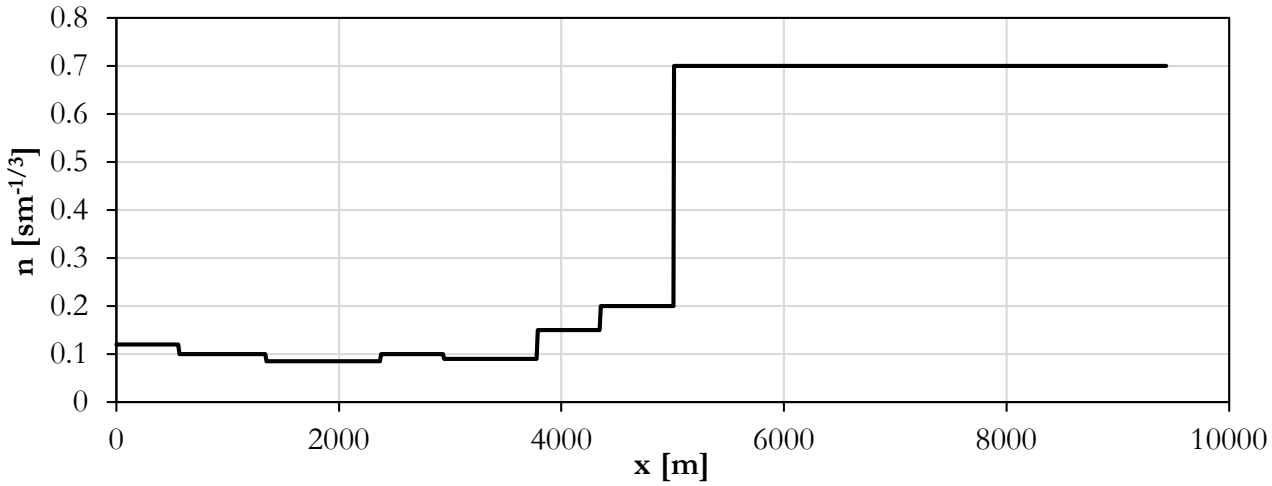

Figure A.41. Calibrated Manning's roughness coefficient.

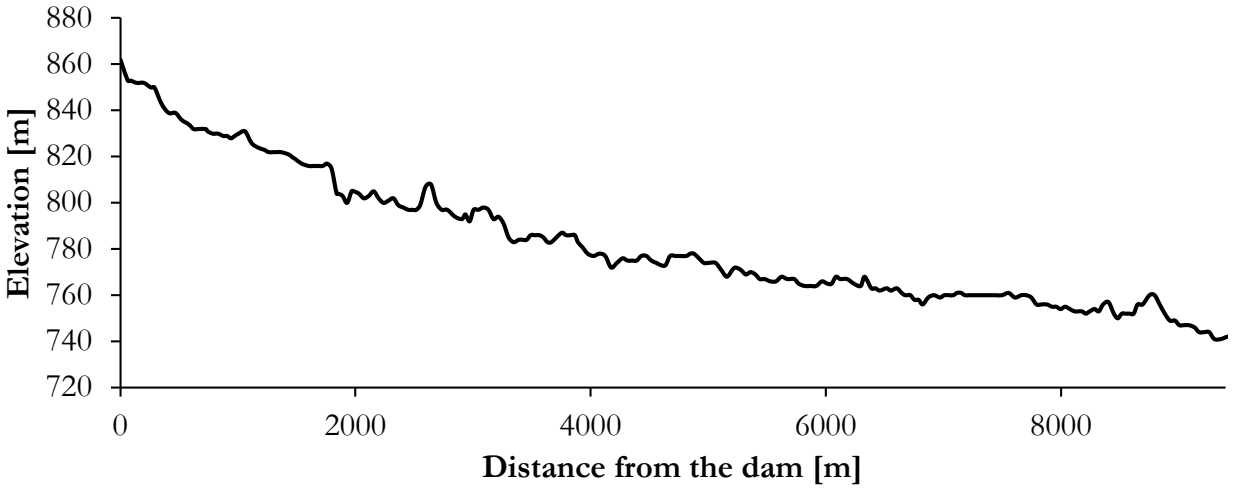

Figure A.42. Channel profile of the Brumadinho downstream channel.

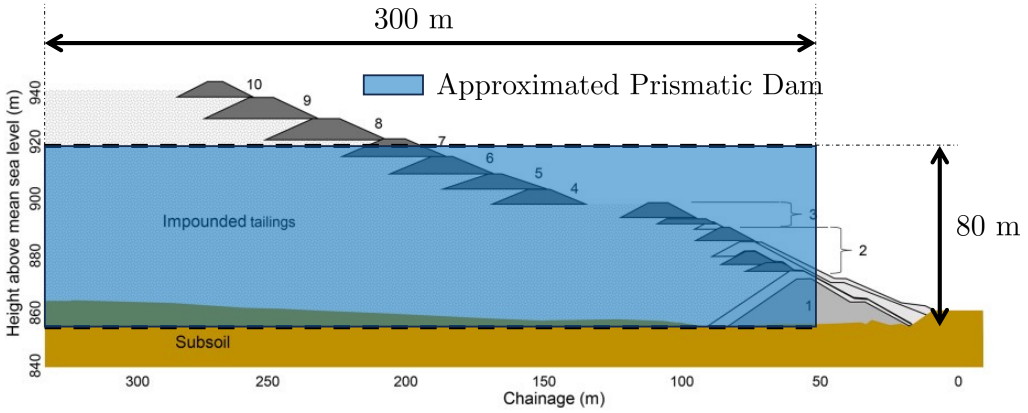

Figure A.43. Brumadinho Dam approximate dimensions. Figure adapted from (Lumbroso et al., 2021).

Collischonn, W. e Fan, F. M. (2013). Defining parameters for eckhardt's digital baseflow filter. *Hydrological Processes*, 27(18):2614–2622.

Conceição, M. A. (2006). Roteiro de cálculo da evapotranspiração de referência pelo método de penman-monteith-fao. *Embrapa Uva e Vinho. Circular Técnica*.

De Paiva, R. C. D., Buarque, D. C., Collischonn, W., Bonnet, M.-P., Frappart, F., Calmant, S., e Bulhões Mendes, C. A. (2013). Large-scale hydrologic and hydrodynamic modeling of the amazon river basin. *Water Resources Research*, 49(3):1226–1243.

Durbude, D., Jain, M., e Mishra, S. (2011). Longterm hydrologic simulation using scscnbased improved soil moisture accounting procedure. *Hydrological Processes*, 25:561–579.

Ferreira, D. M., Fernandes, C. V. S., e Gomes, J. (2017). Verification of saint-venant equations solution based on the lax diffusive method for flow routing in natural channels. *RBRH*, 22.

Fisher, R. A. et al. (1920). 012: A mathematical examination of the methods of determining the accuracy of an observation by the mean error, and by the mean square error. *Monthly Notices of the Royal Astronomical Society*.

Ghimire, B., Chen, A. S., Guidolin, M., Keedwell, E. C., Djordjević, S., e Savić, D. A. (2013). Formulation of a fast 2d urban pluvial flood model using a cellular automata approach. *Journal of Hydroinformatics*, 15(3):676–686.

Gomes, M. N., do Lago, C. A. F., Rápalo, L. M. C., Oliveira, P. T. S., Giacomoni, M. H., e Mendiondo, E. M. (2023). Hydropol2d distributed hydrodynamic and water quality model: Challenges and opportunities in poorly-gauged catchments. *Journal of Hydrology*, 625:129982.

Gomes Jr, M. N., Giacomoni, M. H., de Macedo, M. B., do Lago, C. A. F., Brasil, J. A. T., de Oliveira, T. R. P., e Mendiondo, E. M. (2023a). A modeling framework for bioretention analysis: Assessing the hydrologic performance under system uncertainty. *Journal of Hydrologic Engineering*, 28(9):04023025.

Guidolin, M., Chen, A. S., Ghimire, B., Keedwell, E. C., Djordjević, S., e Savić, D. A. (2016). A weighted cellular automata 2d inundation model for rapid flood analysis. *Environmental Modelling & Software*, 84:378–394.

Hargreaves, G. H. e Samani, Z. A. (1985). Reference crop evapotranspiration from temperature. *Applied engineering in agriculture*, 1(2):96–99.

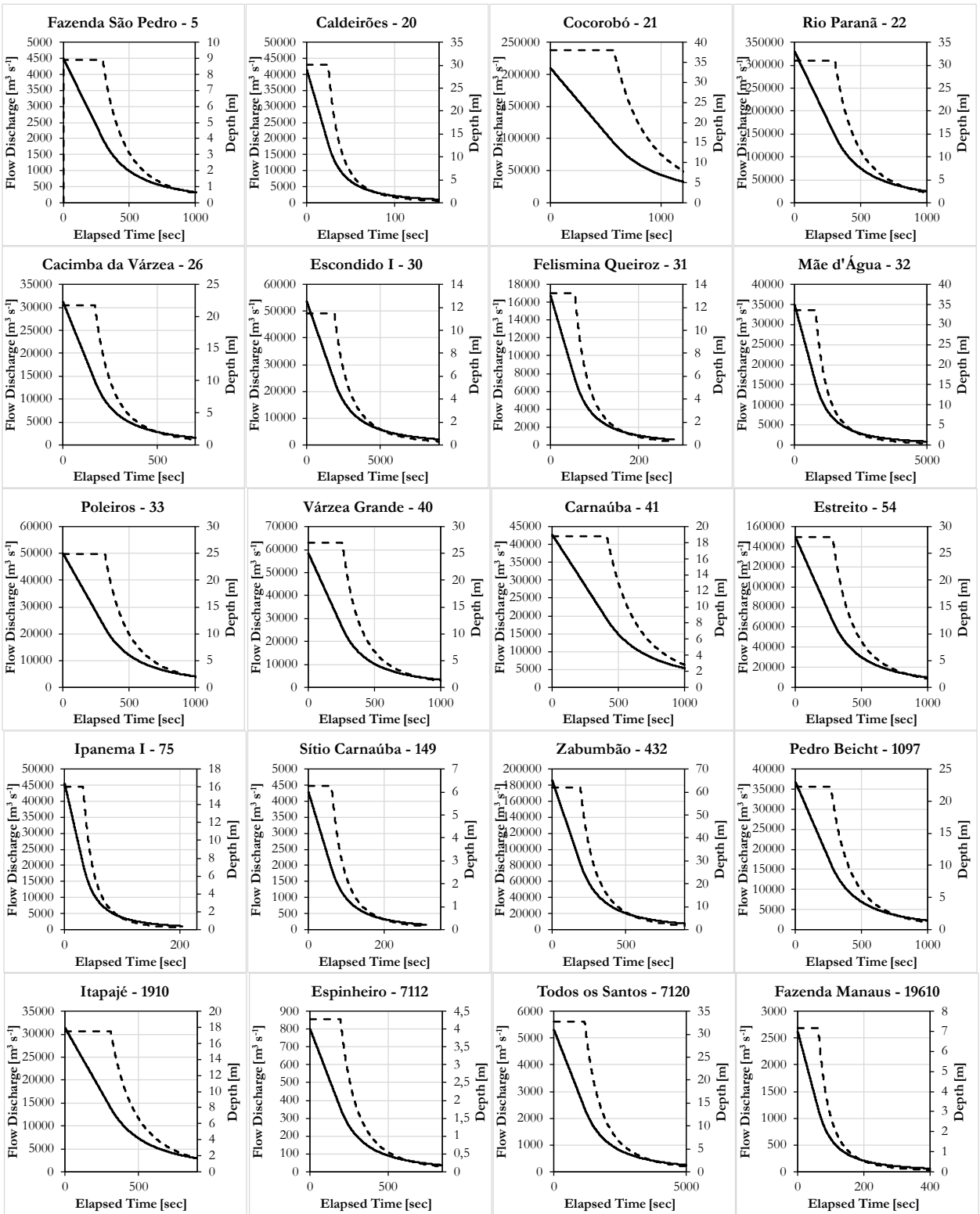

Figure A.44. Breach hydrographs. The black dashed lines are hydrographs and the solid lines are the reservoir water depth.

Hsu, K.-l., Gao, X., Sorooshian, S., e Gupta, H. V. (1997). Precipitation estimation from remotely sensed information using artificial neural networks. *Journal of Applied Meteorology and Climatology*, 36(9):1176–1190.

Kohler, M., Linsley, R., e Bureau, U. S. W. (1951). *Predicting the Runoff from Storm Rainfall*. Number v. 30 in Predicting the Runoff from Storm Rainfall. U.S. Department of Commerce, Weather Bureau.

Lax, P. D. (1954). Weak solutions of nonlinear hyperbolic equations and their numerical computation. *Communications on pure and applied mathematics*, 7(1):159–193.

Lumbroso, D., Davison, M., Body, R., e Petkovšek, G. (2021). Modelling the brumadinho tailings dam failure, the subsequent loss of life and how it could have been reduced. *Nat Hazard Earth Sys*, 21(1):21–37.

McCuen, R. (1998). *Hydrologic Analysis and Design*. Hewlett Packard Professional Books. Prentice Hall.

Nash, J. E. e Sutcliffe, J. V. (1970). River flow forecasting through conceptual models part ia discussion of principles. *Journal of hydrology*, 10(3):282–290.

Neyman, J. e Pearson, E. S. (1936). Contributions to the theory of testing statistical hypotheses. *Statistical research memoirs*.

Palaka, R., Prajwala, G., Navyasri, K., e Anish, I. S. (2016). Development of intensity duration frequency curves for narsapur mandal, telangana state, india. *International Journal of Research in Engineering and Technology*, 5(6):109–113.

Rossman, L. e Huber, W. (2016). Storm water management model reference manual. *Volume II–Hydraulics, Tech. Rep. EPA/600/R-17/111, US EPA Office of Research and Development, Water Systems Division, avaialable at: https://nepis. epa. gov/Exe/ZyPDF. cgi*.

Rossman, L. A. (2010). *Storm water management model user's manual, version 5.0*. National Risk Management Research Laboratory, Office of Research andă. . . .

Sabat, L. e Kundu, C. K. (2020). History of finite element method: A review.

Schwanghart, W. e Scherler, D. (2017). Bumps in river profiles: uncertainty assessment and smoothing using quantile regression techniques. *Earth Surface Dynamics*, 5(4):821–839.

Sentelhas, P. C., Gillespie, T. J., e Santos, E. A. (2010). Evaluation of fao penman–monteith and alternative methods for estimating reference evapotranspiration with missing data in southern ontario, canada. *Agricultural water management*, 97(5):635–644.

Souza, K. I. S. d. et al. (2021). *Definição de áreas de preservação permanente com função de proteção aos recursos hídricos naturais*. PhD thesis, Universidade Federal de Santa Catarina.

Suresh Babu, P. e Mishra, S. (2012). Improved scs-cn–inspired model. *Journal of Hydrologic Engineering*, 17(11):1164–1172.

Thornthwaite, C. W. (1948). An approach toward a rational classification of climate. *Geographical review*, 38(1):55–94.

Timesofindia (2012). Cyclone nilam leaves bangalore chilled to the bone. *The Times of India*.

Yang, F., Liang, D., e Xiao, Y. (2018). Influence of boussinesq coefficient on depth-averaged modelling of rapid flows. *Journal of Hydrology*, 559:909–919.


EESC • USP